DOT/FAA/AR-xx/xx

Federal Aviation Administration
William J. Hughes Technical Center
Aviation Research Division
Atlantic City International Airport
New Jersey 08405

Annex B
NIAR Final Report
Task A14: UAS Ground Collision Severity Evaluation 2017-2018

Date: 24 March 2019

Final Report

U.S. Department of Transportation
Federal Aviation Administration

NOTICE

TABLE OF CONTENTS

LIST OF FIGURES

LIST OF TABLES

EXECUTIVE SUMMARY

This research effort aimed to characterize the injury severity of sUAS impacts with the non-participating public through testing and numerical simulation. Tests were conducted utilizing the FAA Hybrid-III 50th percentile anthropomorphic test device (ATD), to quantify the head kinematics and neck loads associated with sUAS impacts. Eleven sUAS articles were tested, quadcopter and fixed-wing configurations, with masses ranging from 0.73 lbm to 9.82 lbm. These articles represented a range of construction materials from composite and metal to plastic and foam. Impact velocities covered a spectrum from 10 fps to 71 fps; energy levels of 2.4 ft-lbf to 209 ft-lbf. This energy range encompasses parachute velocities for heavier sUAS as well as the general flight performance of middle and lower weight sUAS. Injury severity was quantified in terms of standard aerospace and automotive criteria: HIC, head peak acceleration, and Nij. In support of the testing effort, NIAR developed and validated three sUAS FE models for use in impact simulations. The sUAS articles represent the DJI Phantom3 quadcopter (2.67 lbm), the SenseFly eBeePlus pusher prop (2.4 lbm), and the Lancaster PrecisionHawk MKIII fixed-wing puller UAS (4.4 lbm). In addition to the numerical sUAS and ATD simulations, NIAR utilized the A11 test data to develop and calibrate the THUMS numerical instrumentation methodology. With these calibrated models, ATD and THUMS simulations were used to determine the critical sUAS orientation and impact conditions for the PMHS test matrix, reducing the cost and effort associated with physical testing. THUMS simulations predicted the most injurious sUAS impact test from the PMHS test matrix as the DJI Phantom3 angled frontal condition, impacting front first, at 71 ft/s. The A14 studies provided data from four perspectives: ATD testing, ATD simulation, HBM simulation, and PMHS testing. ATD testing provided head and neck injury metrics as well as high speed video of the impact kinematics. ATD simulations provided head and neck injury metrics, detailed model kinematics, and the potential to quantify energy transfers. HBM simulations provided head and neck injury metrics, detailed model kinematics, potential to quantify energy transfers, and also material stress and strain results related to skull fracture and brain injury potentials. PMHS testing provided head injury metrics, high speed video kinematics, VICON marker tracking, and physical injury observations. Through the research, it was found that one of the main variables related to injury potential is the amount of energy transferred from the sUAS to the impact target. As such, the parameters that govern this energy transfer are the initial impact energy of the sUAS due to its mass and velocity, the energy absorbing characteristics of the materials in combination with the sUAS architecture (fixed-wing pusher / puller, multirotor, or other configurations), and the impact orientation of the sUAS at the time of contact. It was also found that the impact location and direction with respect to the THUMS or ATD head form could cause a 30% difference in HIC and peak acceleration, and a 20% difference in neck compression loading. The testing and numerical analyses data strongly support that the preliminary injury thresholds for sUAS head impacts developed in earlier work are overly conservative. Until additional work is conducted to develop specific injury criteria for the sUAS impact scenarios, it seems appropriate to use the injury criteria described in this report to assess when additional operational risk mitigations are required to reduce the probability of serious injury due to a sUAS ground collision. Finally, this test and simulation comparison effort demonstrates that verified and validated models can predict real-world physics, and that simulations can leverage computing power to investigate a broader range of conditions than are typically available in a test program.

1. INTRODUCTION

Unmanned Aircraft Systems (UASs) continue to be one of the fastest growing sectors of the aviation industry. The Association for Unmanned Vehicles International (AUVSI), the largest trade group concerning UASs, estimates that by 2025 more than 100,000 jobs will be created, corresponding to an economic impact of $82 billion [1]. In support of this growth the FAA began awarding waivers for small UAS (sUAS) operations over populated or semi-populated areas via Title 14 of the Code of Federal Regulations (CFR), Part 107. As of this writing, a small number of documented ground collisions have occurred, resulting in minor injuries to persons involved. This demonstrates the potential danger sUAS pose to the non-participating public at-large, and signals the need to perform investigations into the damage causing characteristics associated with these vehicles and their flight patterns.

Findings from this research can be used to help define ground collision hazard severity thresholds for impacts between sUAS and persons on the ground. The results presented in this report will focus on small UAS configurations impacting 50th percentile male representatives such as ATDs and PMHS.

1.1 BACKGROUND

1.1.1 sUAS Usage Over Populated Areas

As the UAS industry expands to meet ever growing needs and to provide innovative new services, the potential for unintended collisions between UASs and the non-participating public increases. Existing applications for sUAS over populated areas include uses such as infrastructure inspection, land / real estate surveying, and media coverage of sporting and entertainment events, to name just a few examples.

1.1.2 Ground Collision Conditions

sUAS operations and flight patterns occurring near or over populated areas have the potential that unforeseen system failures can result in ground collisions with the non-participating public. The most common flight failure modes are discussed in Annex A, UAH flight failure test report [2]. These failure modes indicate that vertical and downward angled impacts are most common. Additional impact orientations were studied for the purpose of determining general worst-case conditions. The impact velocities used in testing and simulation represent a range of performance characteristics from the respective sUAS articles, as well as from impact mitigation parachutes.

1.1.3 sUAS Configuration Architectures

The most common sUAS architectures are identified as the following types.

- **Quadcopter**: UAS design having 4 rotors allowing VTOL flight patterns and typically carrying a camera payload.
- **Multi-rotor:** UAS design having 4 or more rotors allowing VTOL flight patterns and typically carrying a camera payload.
- **Fixed-wing Puller:** traditional aircraft configuration with a wing and front mounted motor which pulls the vehicle forward.
- **Fixed-wing Pusher:** traditional aircraft configuration with a wing and rear mounted motor which pushes the vehicle forward.

1.1.4 Proposed Injury Mechanisms

Injury potential has the following proposed mechanisms in terms of the features of a sUAS. The most readily identifiable parameter is the impact energy carried by the sUAS as a product of its mass and flight velocity (KE), and/or vertical altitude (PE). Following the impact energy, the construction stiffness of the sUAS plays a crucial role in the transfer of energy during a collision. The construction stiffness is a term to describe the combined effect of the construction materials and the structural layout of the sUAS. This combined stiffness allows the design and the material to be evaluated together in full-scale impact tests. Additionally, the impact orientation of the sUAS at the start of the ground collision effects the amount of energy transferred.

1.1.5 Injury Metrics

These proposed injury mechanisms were evaluated throughout the course of the research in terms of the commonly accepted injury metrics used by the automotive and aerospace industries. Some examples include: HIC, the peak head acceleration, neck compression, neck shear, and Nij. Additional criteria, which are not current standards, were used to give a better view of the potential, such as the BrIC, CP, and modified Nij.

1.2 PROJECT SCOPE

The research was conducted over an 18-month period that included peer reviews of the research plan at the beginning of the research task, and a peer review of the final reports occurring at the end of the program. The research is broken down into six fundamental tasks, intended to answer the following research questions, and any related questions that may be developed through the research process. NIAR's major responsibilities were within Task A and B. Details regarding these two sections are provided in the following sections.

1.2.1 Task A: Simple and Repeatable Test Method Development

The intention of this simplified test was to define the basic testing methodology and data outputs that are necessary to characterize the injury severity of sUAS impacts.

NIAR assisted in the development of a clear and easily repeatable test method to determine the injury potential to a person impacted by a UAS under various conditions and scenarios. The test method relies on the usage of a full-scale ATD. The data post-processing methods address the acceptable levels of safety for the non-participating public, including neck injury, skull fracture, and concussion based on existing aerospace and automotive criteria thresholds, as well as for a proposed set of criteria limits representing a 30% chance of incurring an AIS3+ type of injury, as proposed by ARC [4].

1.2.2 Task B: Human Body Modeling

The THUMS human body model (HBM) was used in combination with calibrated sUAS models to determine the injury potential of various impact conditions over a spectrum of kinetic energy from 2.4 ft-lbf to 209 ft-lbf. The energy range under consideration includes quadcopter and fixed-wing configurations, with masses ranging from 0.73 lbm to 9.82 lbm at impact velocities from 10 fps to 71 fps. This methodology functions equally well for all of the sUAS configurations studied for flight speeds ranging from terminal falling velocity to parachute descent rates, without a measurable loss of fidelity.

Data collected from these sUAS impact studies include head and neck injury metrics, detailed sUAS and HBM kinematics, impact energy quantities, and also material stress and strain results related to skull fracture and brain injury potentials. Based on this data and the supporting test efforts [2, 3], NIAR provides recommendations regarding the injury severity of the various test conditions.

1.3 TECHNICAL APPROACH

1.3.1 Testing of Impact Conditions

Testing was performed with FAA Hybrid III 50th percentile male representative ATDs instrumented with a 6aw internal sensor array and neck load cells. Impact tests are conducted with a selection of sUAS articles representing many of the common configurations available today.

1.3.2 Simulated Impact Tests

NIAR utilized numerical simulations to develop the spectrum of test conditions, to predict the worst case sUAS orientations and impact conditions, and finally to represent the ATD and PMHS tests performed on the Phantom3, eBeePlus, and PrecisionHawk MKII. Simulation results are post-processed to provide insights regarding injury producing mechanisms pertaining to sUAS architectures, materials, and impact conditions.

1.4 REPORT ORGANIZATION

This report provides details regarding the activities performed by NIAR in the following sections.

Chapter 2 provides details regarding ATD physical testing. Discussion includes topics concerning test equipment, test procedure, test matrix, and the ATD data outputs compared against injury criteria.

Chapter 3 gives information covering the sUAS models' definitions. Information regarding the materials, structural layout, and performance are provided along with reverse engineering processes, model creation details, and the validation testing results.

Chapter 4 documents the full-scale sUAS model verification tests. The A11 test data is presented with comparisons to simulated tests using the sUAS model and the numerical ATD. Parametric studies are documented as a means of characterizing the worst-case orientation of the DJI Phantom3. A14 test results are given with comparisons to simulations of the same test conditions.

Chapter 5 provides documentation of the HBM development and verification work. Numerical instrumentation definitions are discussed along with demonstrations of model outputs compared to test data. An evaluation of the A11 test conditions, as applied to the THUMS model, is given as verification of the digital instrumentation methodologies. Critical orientations of the Phantom3 sUAS are investigated in terms of standard injury metrics and skull effective plastic strains. Lastly, a set of preparatory impact simulations are evaluated to determine the most injurious impact conditions for the PMHS test campaign.

Chapter 6 covers the A14 PMHS test matrix simulations for impacts with the Phantom3 and the eBeePlus against the THUMS model. Vertical, side, and angled frontal impact conditions are discussed with example simulations for each direction. The most injurious PMHS test is reviewed in detail, with observations drawn from supplementary modeling studies. ATD test replications of the most injurious PMHS test are presented with injury results. Injury threshold recommendations are discussed in terms of a 30% probability of producing an AIS3+ injury. Subsequently, conclusions are drawn from the data provided by testing and simulations.

Chapter 7 gives a summary of the activities performed under this research task, conclusions derived from the effort as a whole, and finally, recommendations for future work with rationale and commentary.

2. ATD PHYSICAL TESTING

The ATD testing was completed with a FAA Hybrid III 50th Percentile. This ATD represents the size of an average male. The ATD was instrumented with accelerometers, angular rate sensors, and load cells. In all tests, the ATD was in a seated position in a rigid seat.

2.1 TEST SETUP

2.1.1 Test Equipment

2.1.1.1 sUAS Impact System

The sUAS Impact System is composed of a pneumatically actuated cylinder, sUAS mounting cart and rail system, shown in Figure 1. The entire assembly is mounted to a 6" wide C-channel beam, allowing the system to be rotated to various angles. The cylinder contains a piston and rod connected to the sUAS mounting platform. The steel cylinder is approximately 6 ft long with 5.5 ft of total travel (4.5 ft of pressurized travel and 1 ft of venting and air cushion). The sUAS mounting platform has two linear roller bearing carriages that are attached two a single 6 ft rail.

Figure 1. sUAS Impact System, Horizontal Configuration

The propulsion system is composed of a nitrogen tank, an accumulator, a burst disc value, and a control system. The control system allows for automatic operation of system pressurization, test operations, and gas release. A solenoid value is used to control the supply of nitrogen gas. Next, an electronic pressure regulator controls the pressure of the accumulator. Once the accumulator reaches the desired pressure, the supply valve is closed and the operator is instructed to fire the test or abort the test. When firing the test, a 10 second count occurs, and then the burst disc valve is opened, releasing the nitrogen in the pressurized accumulator to pass through a large hose to actuate the cylinder.

The sUAS mounting platform was designed to accommodate a large assortment of models with various weights, from 0.5 lb to 12 lb, and associated geometries. The platform contains multiple hole patterns to attach an inertia based release mechanism. The release mechanism allows for different clamping forces to hold the sUAS models in various orientations with multiple impact angles. While the mechanism is sufficient to hold the sUAS test article while idle, the geometry also provides more clamping force while accelerating, and rotates to release the test article at the end of the rail. Two energy absorbers were also placed at the end of the rail to support the deceleration of the cart and actuation of the release mechanism; see Figure 2. At higher velocities, aluminum honeycomb panels were used along with the energy absorbers.

Figure 2. sUAS Mounting System and Energy Absorbers

2.1.1.2 ATD and Instrumentation

The FAA Hybrid III 50th percentile ATD used in this test program was fitted with a specialized skull with the ability to mount various accelerometer array packages, part number 78051-61X-1846-DN; Figure 3. This testing utilized the 6aω system, combining six linear accelerometers and three angular rate sensors. Upper neck and lower neck load cells were also installed in the ATD. Test instrumentation is documented in Table 1.

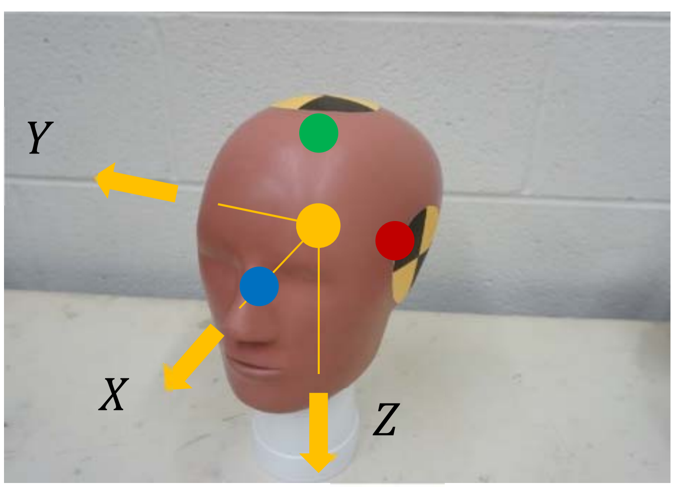

Figure 3. FAA Hybrid III 50th Head Instrumentation Locations

Table 1. FAA Hybrid II 50th Instrumentation

FAA Hybrid III 50th	Instrumentation	Location	Direction	Manufacturer	Model
Head	Acceleration	Head CG	Ax	Endevco	7264C-2k
		Head CG	Ay	Endevco	7264C-2k
		Head CG	Az	Endevco	7264C-2k
		Head Lat	Ax	Endevco	7264C-2k
		Head Sup	Ay	Endevco	7264C-2k
		Head Ant	Az	Endevco	7264C-2k
	Angular Velocity	Head CG	Rx	DTS	PRO-8k
		Head CG	Ry	DTS	PRO-8k
		Head CG	Rz	DTS	PRO-8k
Neck	Force	Upper Neck	Fx	Humanetics	IF-205
		Upper Neck	Fy	Humanetics	IF-205
		Upper Neck	Fz	Humanetics	IF-205
	Moment	Upper Neck	Mx	Humanetics	IF-205
		Upper Neck	My	Humanetics	IF-205
		Upper Neck	Mz	Humanetics	IF-205
	Force	Lower Neck	Fx	Humanetics	1794AJLN2
		Lower Neck	Fy	Humanetics	1794AJLN2
		Lower Neck	Fz	Humanetics	1794AJLN2
	Moment	Lower Neck	Mx	Humanetics	1794AJLN2
		Lower Neck	My	Humanetics	1794AJLN2
		Lower Neck	Mz	Humanetics	1794AJLN2

Two Smarteye EZ-Pro optical sensors were installed on the sUAS impact system mounting rail. One sensor was used as the T0 trigger for the data acquisition and high-speed cameras and the other sensor was used in conjunction with a fin structure to determine velocity. Velocity was calculated from the known dimension of each fin and the time required for each fin to pass the sensor.

2.1.1.3 Data Acquisition

The data acquisition system was used to record the instrumentation results during the impact event. Two DTS SlicePro Sensor Input Modules were used to record all data channels at 20,000 samples per second.

2.1.1.4 High-Speed Video and Photographs

Two high-speed cameras were used to record each test impact event. The cameras were positioned perpendicular to the sUAS and ATD impact when applicable. In most cases, this was horizontal from the side of the impact and vertical from the top of the impact. In a few test orientations, the top camera was positioned in front of the ATD parallel to the sUAS impact. The two high speed cameras were PCO dimax.CS4 and were recorded with a resolution of 1920 x 1080 pixels at 2,000 frames per second.

2.1.2 Test Procedure

The sUAS ATD test procedure was controlled through a dedicated checklist developed for this program. The checklist also allowed data, such as sUAS model, serial number, weight, etc., to be imported into the test report. The sUAS test article was prepared, weighed, and photographed for documentation prior to mounting in the test apparatus. The sUAS impact system was adjusted to account for appropriate mounting configuration and energy absorber setting depending on velocity. The ATD was set in the rigid seat in the correct test orientation and then adjusted using a CMM to ensure the sUAS CG would impact in alignment with the ATD head CG. The impact alignment tolerance for the ATD head CG was +/- 0.05 inches from the sUAS CG; shown in Figure 4.

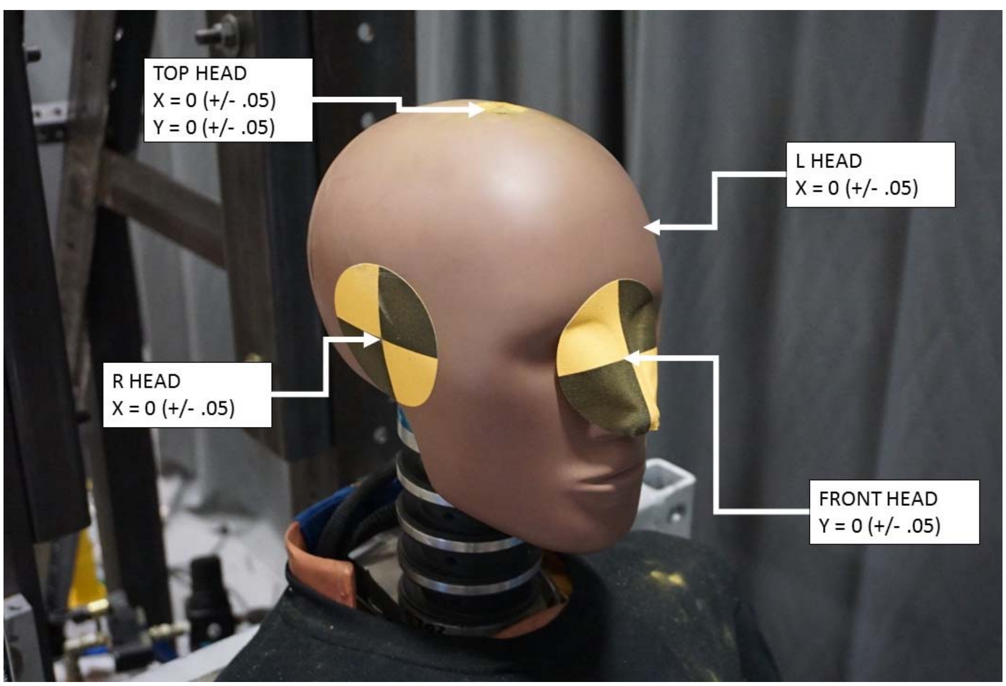

Figure 4. CMM ATD Point Locations and Tolerances, Vertical Test

Next, chalk was applied to the test article at the projected location of the area of impact. Small, one-inch quadrature adhesive targets were placed on the test article in multiple locations for better visualization of the sUAS impact angle, and for aid in determining if any rotation occurred upon release. The sUAS test article was then securely mounted to the impact system cart. Final photographs were taken of the test article, ATD, and overall test setup. The sUAS impact system cart and test article were moved into the firing position, and final setups were taken to charge the pneumatic accumulator. Once fired, data and high-speed videos were downloaded and saved, and photographs were taken to document the impact location and test article condition, shown in Figure 5.

Figure 5. Frames for photos (left) and directions for photos (right)

2.2 TEST MATRIX

Table 2. sUAS ATD Testing Matrix

UAH Test #	NIAR ID Number	Impact Trajectory Relative to Head	Model	Impact Speed (fps)	Impact Speed (kts)	Head Impact Location	Vehicle Orientation wrt Head	Impact KE (ft-lbs)
1	UA19A-23	Vertical Impact	DJI Phantom 3	25	15	Top	Top Into Head	26.7
2	UA19A-25	Vertical Impact	DJI Phantom 3	25	15	Top	Side Into Head	26.7
3	UA19A-27	Vertical Impact	DJI Phantom 3	25	15	Top	Arm Into Head	26.7
4	UA19A-24	Vertical Impact	DJI Phantom 3	36	21	Top	Top Into Head	53.4
5	UA19A-26	Vertical Impact	DJI Phantom 3	36	21	Top	Side Into Head	53.4
6	UA19A-28	Vertical Impact	DJI Phantom 3	36	21	Top	Arm Into Head	53.4
7	UA19A-21	Vertical Impact	DJI Phantom 3	25	15	Top	Bottom Into Head	26.7
8	UA19A-22	Vertical Impact	DJI Phantom 3	36	21	Top	Bottom Into Head	53.4
9	UA19A-83	Horizontal Impact	DJI Phantom 3	36	21	Sideward	Between Arms Forward	53.8
10	UA19A-84	Horizontal Impact	DJI Phantom 3	56	33	Sideward	Between Arms Forward	130.1
11	UA19A-85	Horizontal Impact	DJI Phantom 3	61	36	Sideward	Between Arms Forward	154.4

12	UA19A-86	Horizontal Impact	DJI Phantom 3	65	39	Sideward	Between Arms Forward	175.3
13	UA19A-29	Vertical Impact	DJI Phantom 3	55	33	Top	Between Arms Forward	125.5
14	UA19A-30	Vertical Impact	DJI Phantom 3	65	38	Top	Between Arms Forward	175.3
15	UA19A-43	Angled Impact	DJI Phantom 3	56	33	58 deg forward	Between Arms Forward	130.1
16	UA19A-44	Angled Impact	DJI Phantom 3	61	36	58 deg forward	Between Arms Forward	154.4
17	UA19A-45	Angled Impact	DJI Phantom 3	65	38	58 deg forward	Between Arms Forward	175.3
18	UA19A-46	Angled Impact	DJI Phantom 3	56	33	58 deg rearward	Between Arms Forward	130.1
19	UA19A-47	Angled Impact	DJI Phantom 3	61	36	58 deg rearward	Between Arms Forward	154.4
20	UA19A-48	Angled Impact	DJI Phantom 3	65	38	58 deg rearward	Between Arms Forward	175.3
21	UA19A-39	Angled Impact	DJI Phantom 3	36	21	58 deg - Sideward	Between Arms Forward	53.8
22	UA19A-40	Angled Impact	DJI Phantom 3	56	33	58 deg - Sideward	Between Arms Forward	130.1
23	UA19A-41	Angled Impact	DJI Phantom 3	61	36	58 deg - Sideward	Between Arms Forward	154.4
24	UA19A-42	Angled Impact	DJI Phantom 3	65	38	58 deg - Sideward	Between Arms Forward	175.3
25	UA19A-31	Vertical Impact	eBee +	50	30	Top	Nose Into Head	93.2
26	UA19A-32	Vertical Impact	eBee +	60	36	Top	Nose Into Head	134.2
27	UA19A-87	Horizontal Impact	eBee +	25	15	Sideward	Nose Into Head	23.3
28	UA19A-88	Horizontal Impact	eBee +	36	21	Sideward	Nose Into Head	48.3
29	UA19A-89	Horizontal Impact	eBee +	59	35	Sideward	Nose Into Head	129.7
30	UA19A-90	Horizontal Impact	eBee +	64	38	Sideward	Nose Into Head	152.6
31	UA19A-49	Angled Impact	eBee +	25	15	58 deg - Sideward*	Nose Into Head	23.3
32	UA19A-50	Angled Impact	eBee +	36	21	58 deg - Sideward*	Nose Into Head	48.3
33	UA19A-51	Angled Impact	eBee +	59	35	58 deg - Sideward*	Nose Into Head	129.7
34	UA19A-52	Angled Impact	eBee +	64	38	58 deg - Sideward*	Nose Into Head	152.6
35	UA19A-01	Vertical Impact	Vendor 1	25	15	Top	Bottom Into Head	7.3
36	UA19A-03	Vertical Impact	Vendor 1	25	15	Top	Top Into Head	7.3
37	UA19A-05	Vertical Impact	Vendor 1	25	15	Top	Side Into Head	7.3
38	UA19A-02	Vertical Impact	Vendor 1	36	21	Top	Bottom Into Head	14.6
39	UA19A-04	Vertical Impact	Vendor 1	36	21	Top	Top Into Head	14.6
40	UA19A-06	Vertical Impact	Vendor 1	36	21	Top	Side Into Head	14.6
41	UA19A-07	Vertical Impact	Vendor 1	25	15	Top	Arm Into Head	7.3
42	UA19A-08	Vertical Impact	Vendor 1	36	21	Top	Arm Into Head	14.6
43	UA19A-15	Vertical Impact	Vendor 1	25	15	Top	Top Into Head	7.3
44	UA19A-16	Vertical Impact	Vendor 1	36	21	Top	Top Into Head	14.6
45	UA19A-17	Vertical Impact	Vendor 1	25	15	Top	Top Into Head	7.3
46	UA19A-18	Vertical Impact	Vendor 1	36	21	Top	Top Into Head	14.6
47	UA19A-19	Vertical Impact	Vendor 1	45	27	Top	Top Into Head	23.0
48	UA19A-20	Vertical Impact	Vendor 1	55	33	Top	Top Into Head	34.3

49	UA19A-35	Angled Impact	Vendor 1	45	27	80 deg forward	Top Into Head	23.0
50	UA19A-36	Angled Impact	Vendor 1	55	33	80 deg forward	Top Into Head	34.3
51	UA19A-37	Angled Impact	Vendor 1	45	27	80 deg - Sideward	Top Into Head	23.0
52	UA19A-38	Angled Impact	Vendor 1	55	33	80 deg - Sideward	Top Into Head	34.3
53	UA19A-09	Vertical Impact	Block, Wood	10	6	Top	Flat Surface Forward	4.2
54	UA19A-10	Vertical Impact	Block, Wood	20	12	Top	Flat Surface Forward	16.8
55	UA19A-11	Vertical Impact	Block, Wood	30	18	Top	Flat Surface Forward	37.8
56	UA19A-103	Horizontal Impact	Block, Wood	20	12	Forward	Flat Surface Forward	16.8
57	UA19A-101	Horizontal Impact	Block, Wood	30	18	Forward	Flat Surface Forward	37.8
58	UA19A-102	Horizontal Impact	Block, Wood	40	24	Forward	Flat Surface Forward	67.1
59	UA19A-91	Horizontal Impact	Block, Wood	20	12	Sideward	Flat Surface Forward	16.8
60	UA19A-92	Horizontal Impact	Block, Wood	30	18	Sideward	Flat Surface Forward	37.8
61	UA19A-93	Horizontal Impact	Block, Wood	40	24	Sideward	Flat Surface Forward	67.1
62	UA19A-62	Angled Impact	Block, Wood	20	12	58 deg - Forward	Flat Surface Forward	16.8
63	UA19A-63	Angled Impact	Block, Wood	30	18	58 deg - Forward	Flat Surface Forward	37.8
64	UA19A-64	Angled Impact	Block, Wood	40	24	58 deg - Forward	Flat Surface Forward	67.1
65	UA19A-56	Angled Impact	Block, Wood	20	12	58 deg - Sideward	Flat Surface Forward	16.8
66	UA19A-57	Angled Impact	Block, Wood	30	18	58 deg - Sideward	Flat Surface Forward	37.8
67	UA19A-58	Angled Impact	Block, Wood	40	24	58 deg - Sideward	Flat Surface Forward	67.1
68	UA19A-12	Vertical Impact	Block, Foam	10	6	Top	Flat Surface Forward	4.2
69	UA19A-13	Vertical Impact	Block, Foam	20	12	Top	Flat Surface Forward	16.8
70	UA19A-14	Vertical Impact	Block, Foam	30	18	Top	Flat Surface Forward	37.8
71	UA19A-97	Horizontal Impact	Block, Foam	20	12	Forward	Flat Surface Forward	16.8
72	UA19A-98	Horizontal Impact	Block, Foam	40	24	Forward	Flat Surface Forward	67.1
73	UA19A-99	Horizontal Impact	Block, Foam	60	36	Forward	Flat Surface Forward	151.1
74	UA19A-96	Horizontal Impact	Block, Foam	20	12	Sideward	Flat Surface Forward	16.8
75	UA19A-94	Horizontal Impact	Block, Foam	40	24	Sideward	Flat Surface Forward	67.1
76	UA19A-95	Horizontal Impact	Block, Foam	60	36	Sideward	Flat Surface Forward	151.1
77	UA19A-59	Angled Impact	Block, Foam	20	12	58 deg - Forward	Flat Surface Forward	16.8
78	UA19A-60	Angled Impact	Block, Foam	40	24	58 deg - Forward	Flat Surface Forward	67.1
79	UA19A-61	Angled Impact	Block, Foam	60	36	58 deg - Forward	Flat Surface Forward	151.1
80	UA19A-53	Angled Impact	Block, Foam	20	12	58 deg - Sideward	Flat Surface Forward	16.8
81	UA19A-54	Angled Impact	Block, Foam	40	24	58 deg - Sideward	Flat Surface Forward	67.1
82	UA19A-55	Angled Impact	Block, Foam	60	36	58 deg - Sideward	Flat Surface Forward	151.1

93	UA19A-75	Vertical Impact	DJI Mavic Pro	50	30	Top	Top Into Head	63.7
94	UA19A-76	Vertical Impact	DJI Mavic Pro	61	36	Top	Top Into Head	94.8
95	UA19A-72	Angled Impact	DJI Mavic Pro	40	24	58 deg forward	Top Into Head	40.8
96	UA19A-73	Angled Impact	DJI Mavic Pro	50	30	58 deg forward	Top Into Head	63.7
97	UA19A-74	Angled Impact	DJI Mavic Pro	61	36	58 deg forward	Top Into Head	94.8
98	UA19A-69	Angled Impact	DJI Mavic Pro	40	24	58 deg - Sideward	Top Into Head	40.8
99	UA19A-70	Angled Impact	DJI Mavic Pro	50	30	58 deg - Sideward	Top Into Head	63.7
100	UA19A-71	Angled Impact	DJI Mavic Pro	61	36	58 deg - Sideward	Top Into Head	94.8
109	UA19A-77	Vertical Impact	Karma	40	24	Top	Side Into Head	101.2
110	UA19A-78	Vertical Impact	Karma	50	30	Top	Side Into Head	158.1
111	UA19A-65	Angled Impact	Karma	40	24	58 deg forward	Side Into Head	101.2
112	UA19A-66	Angled Impact	Karma	50	30	58 deg forward	Side Into Head	158.1
113	UA19A-67	Angled Impact	Karma	40	24	58 deg - Sideward	Side Into Head	101.2
114	UA19A-68	Angled Impact	Karma	50	30	58 deg - Sideward	Side Into Head	158.1
115	UA19A-81	Vertical Impact	Vendor 3	40	24	Top	Between Arms Forward	109.4
116	UA19A-82	Vertical Impact	Vendor 3	50	30	Top	Between Arms Forward	170.9
117	UA19A-106	Angled Impact	Vendor 3	40	24	58 deg - Angled	Between Arms Forward	109.4
118	UA19A-107	Angled Impact	Vendor 3	50	30	58 deg - Angled	Between Arms Forward	170.9
119	UA19A-79	Vertical Impact	DJI Phantom 3 battery	40	24	Top	Impact with smallest surface	20.0
120	UA19A-80	Vertical Impact	DJI Phantom 3 battery	60	36	Top	Impact with smallest surface	45.0
121	UA19A-104	Horizontal Impact	DJI Phantom 3 battery	40	24	Forward	Impact with smallest surface	20.0
122	UA19A-105	Horizontal Impact	DJI Phantom 3 battery	60	36	Sideward	Impact with smallest surface	45.0
129	UA19A-33	Vertical Impact	DJI Inspire 2	9	5	Vertical to Top of Head	Nose into top of head	12.4
130	UA19A-34	Vertical Impact	DJI Inspire 2	15	9	Vertical to Top of Head	Nose into top of head	34.3
131	UA19A-100	Angled Impact	DJI Inspire 2	30	18	20 deg to Right Side of Skull	Nose into top of head	137.3
132	UA19A-108	Angled Impact	DJI Phantom 3	71	42	58 deg forward	Between Arms Forward	209.2
133	UA19A-109	Angled Impact	DJI Phantom 3	71	42	58 deg forward	Between Arms Forward	209.2
112B	UA19A-66B	Angled Impact	Karma	50	30	58 deg forward	Side Into Head	158.1
23B	UA19A-41B	Angled Impact	DJI Phantom 3	61	36	58 deg - Sideward	Between Arms Forward	154.4
98B	UA19A-69B	Angled Impact	DJI Mavic Pro	40	24	58 deg - Sideward	Top Into Head	40.8

2.3 ATD TEST RESULTS

2.3.1 Injury Criteria Limits

NIAR was tasked to evaluate the level of injury potential the various sUAS had for impacts with the human body. Since the specific test conditions are an emerging field of study, existing injury metrics were used to guide injury assessments. The majority of these criteria came from existing automotive and FAA standards. Table 3 presents the wide range of criteria that were evaluated. It was desired to cast a wide net of measured injury values, so as to best guide where and how injuries would occur. Section 2.4 discusses the injury criteria that became most relevant for overall A14 conclusions in more detail.

The criteria were documented with their own limit or threshold at which injury was predicted. However, the level and probability of injury associated with each criterion differed for any given test. In an effort to have common injury metrics to compare with and draw conclusions from, the equivalent threshold value for 30% probability of an AIS3+ injury was found when applicable, as per ARC recommendations [2]. The conclusions in Section 7. also discuss this topic and rationale in more detail. Note that the ATD simulations in this report use only the automotive and FAA standards, but that the THUMS model uses the proposed threshold values for 30% probability of an AIS3+ injury.

Table 3. Injury criteria for assessment of various sUAS accompanied by their thresholds, applicable 30% AIS3 equivalent thresholds, and relevant regulatory sources.

Injury Criteria	Limit	Limit Source	Injury Risk Limit for 30% AIS 3	Injury Risk Source	Units
HIC	700	FMVSS 208	1170	NCAP	N/A
N_{ij}	1	FMVSS 208	1.21	NCAP	N/A
Fzc Compression	-1384.82 (-6160)	FMVSS 208	None Found	-	lbf , (N)
Fzc Tension	1530.05 (6806)	FMVSS 208	None Found	-	lbf , (N)
Myc Flexion	228.64 (310)	FMVSS 208	None Found	-	ft-lbf , (N*m)
Myc Extension	-99.57 (-135)	FMVSS 208	None Found	-	ft-lbf , (N*m)
Mod N_{ij}	1	Duma	None Found	-	N/A
Tension	937 (4170)	FMVSS 208	966 (4297)	NCAP	lbf , (N)
Compression	899 (4000)	FMVSS 208	966 (4297)	NCAP	lbf , (N)
Flexion	140 (190)	IARV	None Found	-	ft-lbf , (N*m)
Extension	42 (57)	UN R94	None Found	-	ft-lbf , (N*m)
Shear	696 (3100)	UN R94	None Found	-	lbf , (N)
*Mod Shear – Side Cond.	244 (1093)	NIAR	**244 (1093)	FAA/AR-09/41	lbf , (N)
Head 3ms	80	UN R94 / FAA ANM-03-115-31	None Found / WSTC	-	g
Peak Head Acceleration	200	FAA ANM-03-115-31	237***	Hertz (2016) Stapp	g
Peak Lateral Moment (M_x)	106 (144)	IARV (Lund)	None Found	-	ft-lbf , (N*m)
Peak Twisting Moment (M_z)	72 (97)	IARV (Lund)	None Found	-	ft-lbf , (N*m)
****BrIC	0.69	Takhounts	0.69	Takhounts (2013) Stapp	N/A
****VT CP	0.95	Duma	.95*****	Duma	N/A

*Task A14 obtained by direct comparison and scaling of ES-2 shear value when using a FAA HIII ATD: 186 lbf for AIS 3 injury
** This represents 25% probability of an AIS 3 injury - Based on Note 1
*** This represents 30% probability of an AIS 2 injury
**** Not currently used as limits by any regulatory agency
*****This represents 95% probability of an AIS 1 concussion

HIC: This criterion relates the scaled area under a head C.G. acceleration curve, for a specified time window, to probability of skull fracture. It is one of the oldest and most developed of the referenced criteria. It is currently in use by both the automotive industry and FAA for evaluating head injury.

N_{ij}: This criterion evaluates a combination of upper-neck Z-force and Y-moment, both individually divided by respective compression or tension and flexion or extension limits. The Y-moment is corrected for moments to be resolved about the occipital condyle. The resulting maximum combination of measured values are used by the automotive industry to evaluate neck injury and how it is occurring.

Mod N_{ij}: Based on a work by Duma [5], this is simply a modification of the typical N_{ij} equation, which seeks to better account for neck injury from side loading conditions. In this application, it takes the Y-moment input from the typical N_{ij} equation and replaces it with the square root of the sum of the squared values for upper neck Y-moment and X-moment combined. Both are corrected to have moments about the occipital condyle. These modified moments are compared against the same limits as the standard Nij for the 50th percentile male.

Tension: This criterion is simply a measure of the positive (tensile) Z-force on the upper-neck. It is most commonly used in the automotive industry as a part of neck injury evaluation.

Compression: This criterion is simply a measure of the negative (compressive) Z-force on the upper-neck. It is most commonly used in the automotive industry as a part of neck injury evaluation.

Flexion: This criterion is simply a measure of the positive (bending forward) Y-moment on the upper-neck. It is corrected for the moment to be about the occipital condyle, and is most commonly used in automotive industry as a part of neck injury evaluation.

Extension: This criterion is simply a measure of the negative (bending backward) Y-moment on the upper-neck. It is corrected for the moment to be about the occipital condyle, and is most commonly used in automotive industry as a part of neck injury evaluation.

Shear: This criterion is the evaluated as the square root of the squares for upper-neck X-force and Y-force combined. It is most commonly used in the automotive industry as a part of neck injury evaluation.

Mod Shear for Side Impact: This modification on shear is calculated the same way as regular shear, but has a different limit to better account for lateral impact scenarios. APPENDIX B— discusses the rationale and methodology in detail.

Head 3ms: This criterion relates head C.G. acceleration values to skull fracture. This is measured by finding a single or multiple summed rectangular pulse(s) within the acceleration curve that exist for a total of 3 ms. The maximum acceleration pulse value is then compared to the limit.

Peak Head Acceleration: This criterion relates the peak head C.G. acceleration value to skull fracture. It is currently in use by both NHTSA and FAA for evaluating head injury.

Peak Lateral Moment: This injury evaluation is simply a measure of the X-moment on the upper-neck. It is a developing criterion for neck injury based on work from Lund [6].

Peak Twisting Moment: This injury evaluation is simply a measure of the Z-moment on the upper-neck. It is a developing criterion for neck injury based on work from Lund [6].

BrIC: This injury evaluation relates head C.G. rotational velocities to concussion. It is found by measuring the square root of the squares for X, Y, and Z peak rotational velocities, each divided by a respective critical value first. The peak rotational velocity value used is also irrespective of time, for all three. It is a developing criterion for concussion evaluation from Takhounts [7].

VT CP: This injury evaluation relates head C.G. linear acceleration and rotational acceleration to probably of an AIS1 concussion. It is found by measuring the peak linear acceleration and rotational acceleration, which are then used in a probability relation. The peak values are also irrespective of time for both accelerations. It is a developing criterion for AIS1 concussion evaluation from Duma [8] and is primarily used in contact sports scenarios.

2.3.2 Rotational Velocity and Acceleration Data

The rotational velocities and accelerations are important components of the BrIC and VT CP injury evaluations. Typically, these angular values would be obtained from the sensor package at the CG of the ATD's head, as with linear acceleration values. However, it was discovered that the physical rotational sensors at the head CG had sensitivity issues in some of the impact conditions this project tested. The option of head CG sensors would not be available for PMHS testing either, due to the mechanical sensors requiring a firm and dense mounting location. In an effort to align testing methodologies with the PMHS tests conducted by OSU and to eliminate potential sources of error, rotational values were determined via the peripheral accelerometers. This methodology is described in the documentation by Kang et al. [9]. Rotational accelerations are calculated directly using the peripheral accelerometer outputs. Rotational velocities are determined by integrating these calculated angular accelerations.

An exception to the above methodology is required for tests #59, #60, and #61. In those cases, the rotational velocities were determined using an ARS due to a damaged peripheral accelerometer giving eratic output. This exception is applied to the selected cases so that BrIC values can be determined for the wood block in the sideward impact condition; see APPENDIX A— and APPENDIX C—. Since these cases used the ARS instead of the typical instrumentation set, the values are only considered to be an indication of the injury potential for those test conditions.

2.3.3 ATD Test Output - Injury Metrics vs Impact Kinetic Energy

The various injury metrics were plotted with respect to the kinetic energy of each impact condition in order to demonstrate trends regarding the injury-causing potential of each sUAS configuration and test condition. A selection of the full data set is provided in this section; the remaining figures can be found in APPENDIX C—. The test results were tabulated according to their respective injury criteria and the number of exceedances were quantified in Table 4. This table includes results for the wood and foam block too. Table 5 shows the tabulated test results for just sUAS articles.

Figure 6 presents the vertical impact test results for the peak head acceleration criteria. Note that there are wood block, foam block, and additional sUAS results that will not have a simulation comparison.

Table 4. Tabulated injury criteria exceedances for all A14 ATD tests

Criteria	Threshold	# Tests This Criteria is Used	# Tests Exceeding Threshold	Precentage of Exceedances
Head Resultant(g)	237	109	35	32.11%
HIC15	1170	109	16	14.68%
Head > 80g (g)	80	109	2	1.83%
Tension(lbf)	937	109	0	0.00%
Compression(lbf)	899	109	26	23.85%
Flexion(lbf-ft)	140	109	0	0.00%
Extension(lbf-ft)	42	109	0	0.00%
Shear(lbf)	696	70	2	2.86%
Nij	1	70	7	10.00%
NCE	1	70	2	2.86%
NCF	1	70	8	11.43%
NTE	1	70	0	0.00%
NTF	1	70	0	0.00%
ModifiedNij	1	39	2	5.13%
mNCE	1	39	2	5.13%
mNCF	1	39	1	2.56%
mNTE	1	39	0	0.00%
mNTF	1	39	0	0.00%
Modified Shear (lbf)	244	39	11	28.21%
Lateral Moment (lbf-ft)	71.5	109	0	0.00%
Twisting Moment (lbf-ft)	106.2	109	0	0.00%
BrIC	0.687	109	8	7.34%
CP	0.95	109	47	43.12%

Table 5. Tabulated injury criteria exceedances for sUAS A14 ATD tests

Criteria	Threshold	# Tests This Criteria is Used	# Tests Exceeding Threshold	Precentage of Exceedances
Head Resultant(g)	200	75	16	21.33%
HIC15	700	75	4	5.33%
Head > 80g (g)	80	75	1	1.33%
Tension(lbf)	937	75	0	0.00%
Compression(lbf)	899	75	16	21.33%
Flexion(lbf-ft)	140	75	0	0.00%
Extension(lbf-ft)	42	75	0	0.00%
Shear(lbf)	696	49	0	0.00%
Nij	1	49	3	6.12%
NCE	1	49	1	2.04%
NCF	1	49	3	6.12%
NTE	1	49	0	0.00%
NTF	1	49	0	0.00%
ModifiedNij	1	26	0	0.00%
mNCE	1	26	0	0.00%
mNCF	1	26	0	0.00%
mNTE	1	26	0	0.00%
mNTF	1	26	0	0.00%
Modified Shear (lbf)	244	26	1	3.85%
Lateral Moment (lbf-ft)	71.5	75	0	0.00%
Twisting Moment (lbf-ft)	106.2	75	0	0.00%
BrIC	0.687	75	8	10.67%
CP	0.95	75	26	34.67%

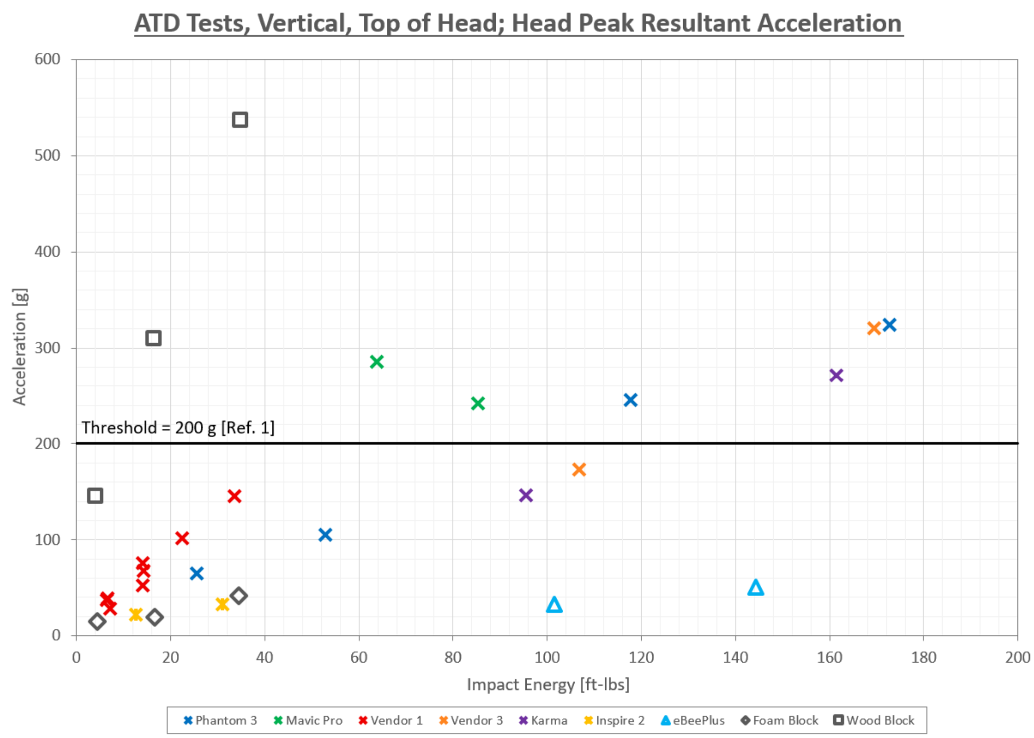

Figure 6. A14 ATD test results; vertical impacts; peak head resultant acceleration

Figure 7 shows a specific trend in the injury pattern obtained from the foam block as compared to the eBeePlus. The angled sideward test conditions produced impacts with the side of the ATD's head. Note that the foam block has a mass that is equivalent to the eBeePlus, but appears to induce more significant head accelerations for a given energy level. This is attributed to the structural layout of the eBeePlus allowing for bending and buckling deformations along the loading axis in addition to the energy absorbing capability of the EPP foam. The foam block, on the other hand, is a cubic shape and can only absorb energy through material compression.

Furthermore, it can be demonstrated that the injury potential of a given projectile is different for each injury criterion. In most cases the wood block is the most injurious projectile, but in terms of the upper neck Nij, the foam block showed more severe results in the sideward test condition; Figure 8.

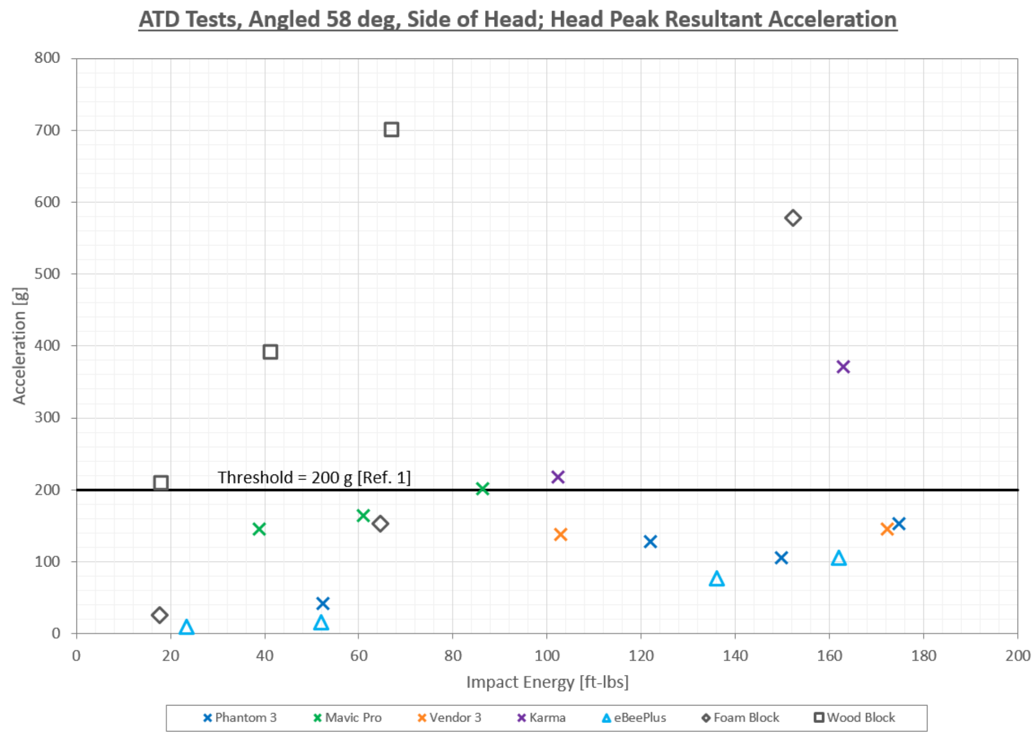

Figure 7. A14 ATD test results; 58 degree angled sideward impacts; HIC15

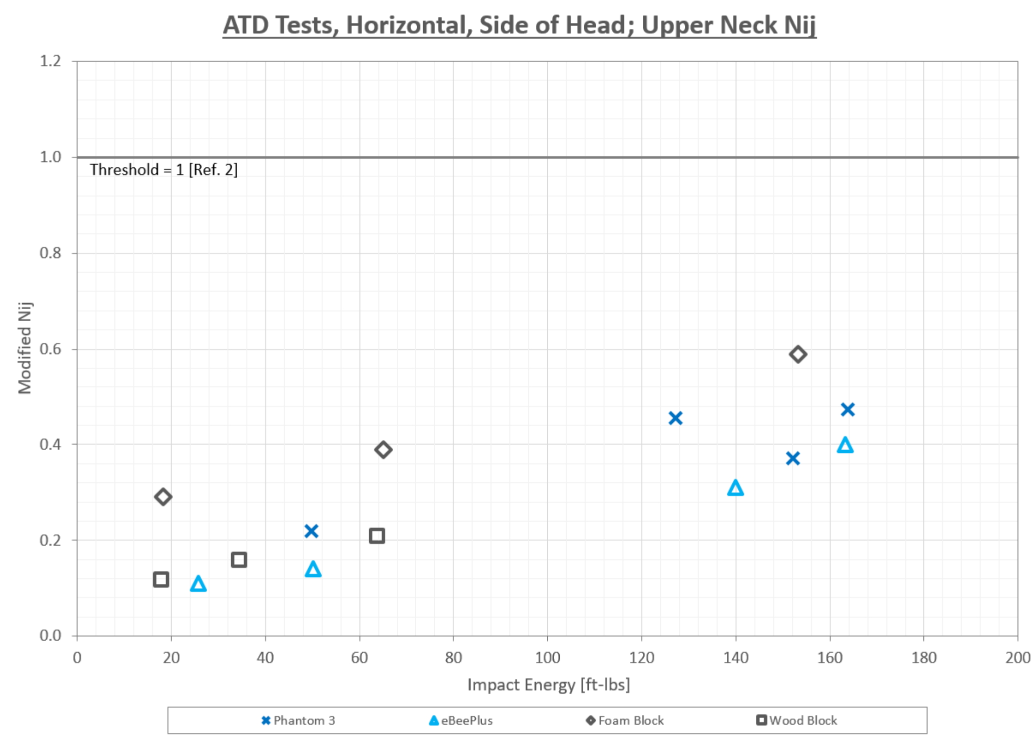

Figure 8. A14 ATD test results; horizontal sideward impacts; Nij injury criterion

2.4 CONCLUSIONS AND RECOMMENDATIONS

Test equipment:

Overall, the performance of the sUAS impact system was as good as expected. The propulsion system was very efficient and extremely repeatable. Achieved velocities during the impacts were typically +/- 0.5 ft/s of the desired test velocity. The release mechanism also worked well; it was able to hold all of the sUAS models with minimal change. The release mechanism also allowed for accurate sUAS impact locations on the ATD head. In the few cases where specific tests were repeated, the impact location was also quite repeatable. Generally, the impact location was within +/-0.25 inches of the desired location, through the CG of the head.

Test results:

The first significant parameter to be identified as a predictor of injury potential was the sUAS impact energy; increasing kinetic energy was shown to increase potential for injury. This trend can be seen from the plots in Figure 6 showing the NIAR ATD test results as a function impact energy.

Additionally, injury potential has been shown to be a function of the construction stiffness of a given sUAS. The construction stiffness is a product of both the materials and the structural layout of the sUAS. This trend is observed by comparing the test results for the eBeePlus and the foam block. The materials of both articles are energy absorbing foams which generally allow impact energy to be absorbed through material compliance, but the eBeePlus can also bend and buckle along its longitudinal axis, while the foam block can only compress axially without any significant bending. So, for a similar mass between the two articles, the foam block has a greater potential to cause injury due to its cubic shape, while the eBeePlus tends to absorb more energy through axial buckling; Figure 7.

Tabulated Injury Criteria Exceedances

The greatest number of current automotive and aerospace injury criteria exceedances based on ATD testing correspond to the head peak acceleration, HIC, neck compression, the modified shear criterion, and combined probability of concussion (CP) as shown in Section [2.3.3].

Acceleration Based Criteria Thresholds

The HIC metric shows a conservative threshold when applied to ATD tests with sUAS impacts. The low incidence of skull fracture injury seen from PMHS testing is not accurately represented by the probabilities predicted by ATD tests, when compared against the current injury threshold level. <u>We therefore recommend to use a threshold value of 1170 for HIC15, corresponding to 30% of AIS3+, to better represent the PMHS observed injuries.</u>

The existing peak acceleration criteria seems to provide a conservative threshold. Since the PMHS test results showed fewer occurences of skull fracture injuries, the threshold of 200 g appears to be conservative. It is recommended to expand the basis of these conclusions with further ATD testing and numerical analysis in order to verify the applicability of the Injury Assessment Reference Values (IARV's) correlating ATD outputs to known head accelerations that resulted in skull fractures. As the injury levels predicted by the H3 ATD were not consistent with the PMHS tests, this underlines the necessity to do matched pair testing to determine the appropriate acceptance values.

Neck Loading Criteria

Compression and modified shear criteria have conservative thresholds when applied to ATD test output. This determination is based on the observation that the existing criteria thresholds over-predict compression and shear type injuries for the tested conditions. No neck injuries were attributed to the PMHS impact cases tested by OSU [3].

3. UAS MODELS DEFINITION

NIAR performed reverse engineering activities, FE modeling, and testing to define three numerical sUAS FE models representing quadcopter and fixed-wing sUAS architectures.

In order to build the UAS and target FE models, researchers followed a physics based modeling approach. This methodology developed by the NIAR takes advantage of advances in computational power, the latest computational tools, years of research in understanding the fundamental physics of the crashworthiness event, generated test-to-test variability data, and verification & validation modeling methods. The method follows the building block approach, illustrated in Figure 9.

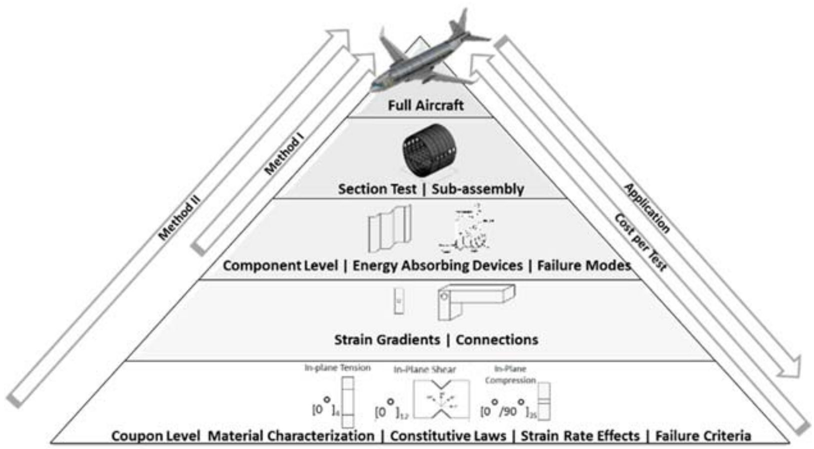

Figure 9. Building block approach for NIAR's FE modeling methodology

The building block approach is the incremental development of analysis and supporting tests where typically there is an increase in size and complexity of the test article and a decrease in number of supporting tests. In order to develop this method, it is necessary to have a good understanding of the physics and testing variability from the coupon to the system level. Full-scale level test results do not drive the definition of the numerical model; it is driven by a predefined, verification and validation building block modeling methodology.

Using this approach, simulations should be able to predict the system level test results within the scatter of the physical system test results. Objective verification criteria were used to evaluate the numerical models, where the correlation level between simulation and testing was defined by an understanding of the test-to-test variability of the physical system under evaluation.

3.1 FINITE ELEMENT MODELING PROCESS

This section describes the process followed to produce the FE model of every UAS, starting from the geometry model (CAD) and ending with the final mass check. The following procedure was carried out to create the UAS FE models. For more details on specifics of the process, refer to the airborne collision report [10].

- Obtain CAD data (STEP format) for each part of the model.
- Clean up geometry and prepare for meshing (i.e. split surfaces where symmetric, de-feature small elements, etc.).

- Select element type (e.g. shell, solid, etc.) for each of the different parts depending on geometry and element size constraints.
- Discretize the geometry (i.e. meshing).
- Check quality criteria with NIAR standards.
- Assign section properties: shell thicknesses and beam cross section.
- Assemble meshed parts to create complete FE model.
- Check model for non-desired entities (free-nodes, free-edges, mesh overlap, duplicated elements, non-aligned element normals, etc.).
- Assign corresponding material properties.
- Add non-structural mass to nodes wherever a part is not being modeled.
- Perform mass check, comparing individual components to its physical counterpart.
- Renumber model components, assigning a reserved range to avoid clashes.

The methods for defining internal contacts, connections, and adhesives follow a similar methodology as in the airborne collision project [10]. Nevertheless, the material definitions used to model various compositions in the UAS models are described in this section.

3.1.1 Material Definitions

The process of obtaining material properties, the sources of the information, and the final material identification are discussed in this section. The material description is presented in different subsections based on the type of material. Notice that not all of the materials are present in every UAS FE model.

3.1.1.1 Structural Plastic

Small UAS typically contain abundant plastic components. Most of these components are secondary and support structure, to attach components to the main frame. This is the case of the eBeePlus and the Precision Hawk Lancaster 4, where plastic is used for brackets, attachment points for carbon rods and motor mounts, while the main structural components are made of EPP foam and glass fiber laminate, respectively. These plastic polymers were identified from the bill of materials provided by the UAS manufacturer, and their properties were obtained to recreate the corresponding bilinear plasticity material model (MAT_024).

Contrary to the eBeePlus and Precision Hawk, most of the DJI Phantom 3 parts, including the main structure, are made of polycarbonate plastic. Consequently, a more advanced material model was selected for the polycarbonate definition, because of its importance for the energy absorption capabilities at impact. The material properties were obtained from an Army Research Lab publication [12]. The constitutive properties follow the Johnson-Cook material model (**MAT_JOHNSON-COOK*), and ultimate strain was fine-tuned during the Airborne Collision project [10]. This advanced material model is capable of capturing not only elastic and plastic deformation but also strain-rate and temperature effects. Table 6 summarizes the parameter selected.

Table 6. Material properties and Johnson-Cook parameters of polycarbonate polymer

Density *(kg/m³)*	Modulus of Elasticity *(GPa)*	Shear Modulus *(GPa)*	A *(MPa)*	B *(MPa)*	C	m	n	C_v *(KJ/kgK)*	Tmelt *(K)*
1197.8	2.59	0.93	80	75	0.052	0.548	2	1.3	562

3.1.1.2 Metallic Alloys

The most common metallic components in sUAS are the motor(s) and the camera payload. Typically, brushless motors for sUAS applications are constructed with an aluminum or steel alloy rotor and a laminated steel core with copper wire winding. Because the FE models were simplified to an aluminum or steel rotor and the steel core stator, only those two material models were needed.

The aluminum body of the motor and camera for this type of applications is often made of casting alloy A520.0-F, according to a market research performed for this project. Mechanical properties for this alloy were obtained from ASM handbook [13] and added in to a **MAT_PIECEWISE_LINEAR_PLASTICITY* LS-DYNA material card [14]. In addition, the steel stator was assumed to be of the alloy AISI 4030. Properties were obtained from MMPDS [15].

3.1.1.3 Electronic Printed Circuit Board

The electronic boards of consumer UAS typically consist of a printed circuit board (PCB) to which other electronic components (e.g. capacitors, IC chips, etc.) are connected. In the FE models, the PCB was modeled as only a shell composite. Some of the larger electronic components (e.g. chips) were modeled as a rigid cube to represent its volume. It was assumed that the rest of the elements would add little stiffness, and only the mass of the components was considered, by being applied as non-structural masses.

It is common that PCBs manufactured for the consumer industry are made of glass melamine fiber-epoxy composite laminate, embedded with and/or covered with a layer(s) of copper. A typical composite laminate for this application is G-10. Ravi-Chandar and Satapathy [16] investigated the mechanical properties of G-10, which were determined from compression and tension quasi-static tests. Table 7 summarizes these properties.

**MAT_ENHANCED_COMPOSITE_DAMAGE* was used from the LS-DYNA material model library [14] to model the G-10 composite. The properties given in Table 7 were added directly in to the material card and applied to the PCB components of the FE model.

Table 7. Material properties of G-10 glass-epoxy composite for PCB components

Density *(kg/m³)*	Young's Modulus *(GPa)*		Compressive Strength *(MPa)*		Tensile Strength *(MPa)*		Shear Modulus *(MPa)*	Shear Strength *(MPa)*	Poisson's Ratio	
	X	Y	X	Y	X	Y			XY	XZ/YZ
1850	18.83	19.26	365	300	233	310	8,275	152	0.136	0.118

3.1.1.4 Battery Cells

The UAS battery cells are constructed using lithium-ion polymer (LiPo) technology. Based on the information published by Sahraei, Meier and Wierzbicki [17], a **MAT_CRUSHABLE_FOAM* [14] material card was created to represent the bulk behavior of the battery cells. Table 8 shows the parameters specified in literature and used for the battery cells of the UAS in this research project.

Table 8. Battery cells properties

Young's Modulus *(MPa)*	Poisson's Ratio	Density *(kg/m³)*
500	0.01	1755

LS-OPT, an optimization software developed by LSTC [18], was used to fit some parameters in the material card to obtain greater correlation between the test and simulation. More details about this study can be found in the Airborne Collision report [10].

Additionally, the aluminum pouch covering each of the battery cells was modeled with the alloy 1145-O, typical for aluminum foil applications. The mechanical properties of this alloy were obtained from ASM handbook [13] and input to a **MAT_PIECEWISE_LINEAR_PLASTICITY* material card of LS-DYNA [14].

3.1.1.5 Low-density Foam

The eBeePlus and PrecisionHawk Lancaster 3 have extensive low-density foam in their components. For instance, concerning the eBeePlus, the load path of a frontal impact event mainly involves foam components of the body. For the most part, both body and wings are made of expanded polypropylene foam (EPP).

The constitutive material properties, for the eBeePlus body and wing foams and for the PrecisionHawk wing, were extracted from compression coupon testing performed in NIAR facilities. The results were processed and compiled in a **MAT_LOW_DENSITY_FOAM* LS-DYNA material card [14].

Apart from the loading curve for the foam, the material card allows inputting recovery parameters for the unloading. The values from hysteric unloading (HU) and SHAPE factors, that allow a close fitting with the experimental data, were selected through an iterative process. The HU and SHAPE factors are numerical parameters that govern the loading and unloading behavior of the material model.

3.2 DJI PHANTOM III MODEL DETAILS

3.2.1 Model Preparation for Ground Collision

The existing model of the DJI Phantom 3 was calibrated for high-speed impacts, using experimental data from ballistic tests. The maximum impact speeds in this project are of less than

20% of those used for calibration in the A3 project. Consequently, existing impact tests of the DJI Phantom 3 on an FAA Hybrid III 50th male ATD, executed during A11 project [REF] were used to fine-tune the FE model for ground collision type of impacts.

In the airborne collision studies, the gimbal structure and camera were less significant contributors to the impact dynamics. However, for ground collision studies, especially for UAS impacts with the bottom first, gimbal and camera are directly involved in the impact load path and the load transfer mechanism. During task A3 [10], the camera was developed in detail, and calibrated through ballistic testing, but the gimbal was simplified (discussed below). Preliminary simulations with the A11 ATD test conditions identified this gimbal assembly as having too rigid of a response, so the modeling of the assembly was enhanced to improve the accuracy of the simulation predictions.

The gimbal of a DJI Phantom 3 Standard was disassembled, and reverse engineered into a CAD model, and subsequently into a detailed FE model, following the process listed in Section 3.1. The mechanism of the three servos was captured with revolute joints. Stop angles that coincide with the actual allowed actuation on the Phantom 3 gimbal and rotational friction were defined. Figure 10 shows the evolution of the gimbal FE model from airborne to ground collision projects. The FE model validation studies performed with the A11 ATD test conditions showed a high level of correlation, as will be shown in Chapter 4. Therefore, the gimbal FE model shown below was judged appropriate.

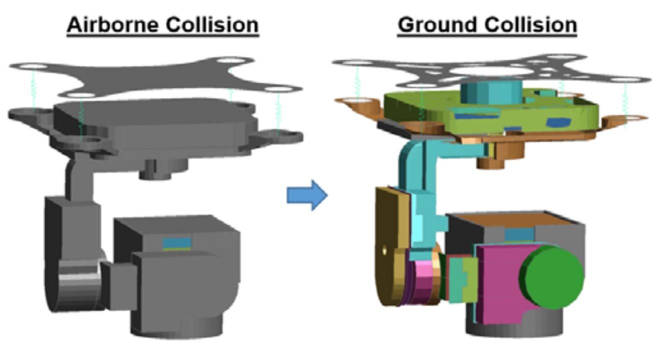

Figure 10. Comparison of the airborne and ground collision versions of the gimbal FE model

The DJI Phantom 3 body is constructed with mainly two shells that attach with plastic clips. The FE model from the airborne collision project, represented those clips with ideal spot-weld connections, with no failure defined. However, it was identified that during ground collision testing from the A11 project, the two shells separated during frontal impact (horizontal case). Therefore, it was necessary to add failure to the spot-weld connections to allow a more realistic separation.

3.2.2 Model Details

Table 9 shows the most relevant specifications and dimensions of the DJI Phantom 3. More details can be found in the airborne collision project technical report [10].

Table 9. Relevant specifications of the DJI Phantom 3

Selected UAS	DJI Phantom 3
Image	
Mass	1,216 g (2.68 lbm)
Dimensions	290x289x186 mm (11.4”x11.4”x7.3”)
Max. Horizontal Speed	16.0 m/s (52.5 ft/s)
Max. Service Ceiling	6,000 m (19685 ft)
Battery - LiPo	364 g (4 cell) (0.8 lbm)
Motor(s) – Brushless DC	56 g (0.12 lbm) x 4
Max. Motor Speed	1,240 rad/s
Camera	52 g (0.11 lbm)

Figure 11 presents the level of detail achieved with the quadcopter FE model, in which features as small as 0.8 mm (0.031 in) have been captured by the mesh. Summarizing, the complete FE UAS model is comprised of 137,325 elements and 191,455 nodes. Figure 12 shows the breakdown of the UAS per type of material. More details can be found in the Airborne Collision project report [10].

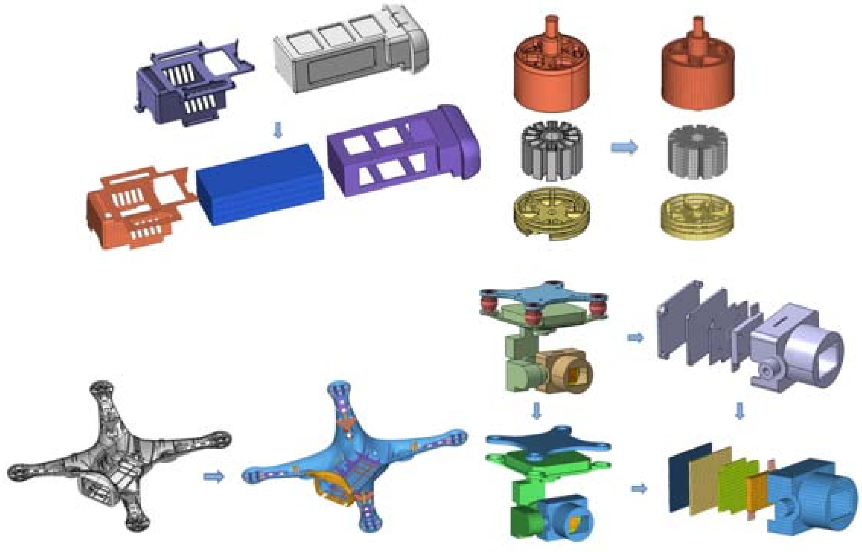

Figure 11. Quadcopter UAS FE model overview

Code	Material
	Polycarbonate
	Nylon
	Cast Aluminum 520-F
	Steel 4030
	G-10 Fiberglass (PCB)
	Li-Po Battery Cell
	Aluminum Film 1145-O

Figure 12. DJI Phantom 3 materials

3.3 SENSEFLY EBEE PLUS MODEL DETAILS

This chapter presents the work performed to validate the eBeePlus FEM created for ground collision events. NIAR carried out coupon level, component, and full assembly tests to validate the virtual model, in accordance with the building block approach. Because of the majority of external foam surfaces in this UAS, most of the tests emphasized the study of the foam behavior at impact.

3.3.1 Model Details

The eBeePlus is a fixed-wing UAS with a particular foam construction that protects the internal stiffer components, such as battery and camera. This material choice is justified by the low density of foam and the energy absorption requirements of this UAS while landing. The eBeePlus model lands by reducing its speed and dragging its body on the ground. Table 10 summarizes the most relevant specification of the eBeePlus model.

Table 10. eBeePlus specifications

MTOW	2.4 lb
Wingspan	3 ft 7.3 in
Length	1 ft 7 in
Cruise Speed	36-98 ft/s

SenseFly [20] provided NIAR with a detailed geometry CAD model of the eBeePlus. This geometry was meshed with a minimum element size that captured the majority of the geometry details while avoiding excessively penalizing the timestep of the FEM solver. Table 11 compiles the element quality criteria followed to mesh the eBeePlus geometry.

Table 11. eBeePlus element quality criteria

	2D elements	3D elements
Warpage	15°	15°
Minimum element size	1 mm	1mm
Maximum element size	5 mm	5 mm
Jacobian	0.7	0.5
Minimum Tria angle	30°	-
Maximum Tria angle	120°	-
Minimum Quad angle	45°	-
Maximum Quad angle	140°	-

Some areas of the eBeePlus, such as the winglets, were simplified with a coarser mesh because they are not a likely area of impact on a ground collision event for this specific UAS, and would not present as high a risk of injury, as the central body does. Figure 13 shows the mesh details of the FEM by comparing geometry and mesh per sub-assembly.

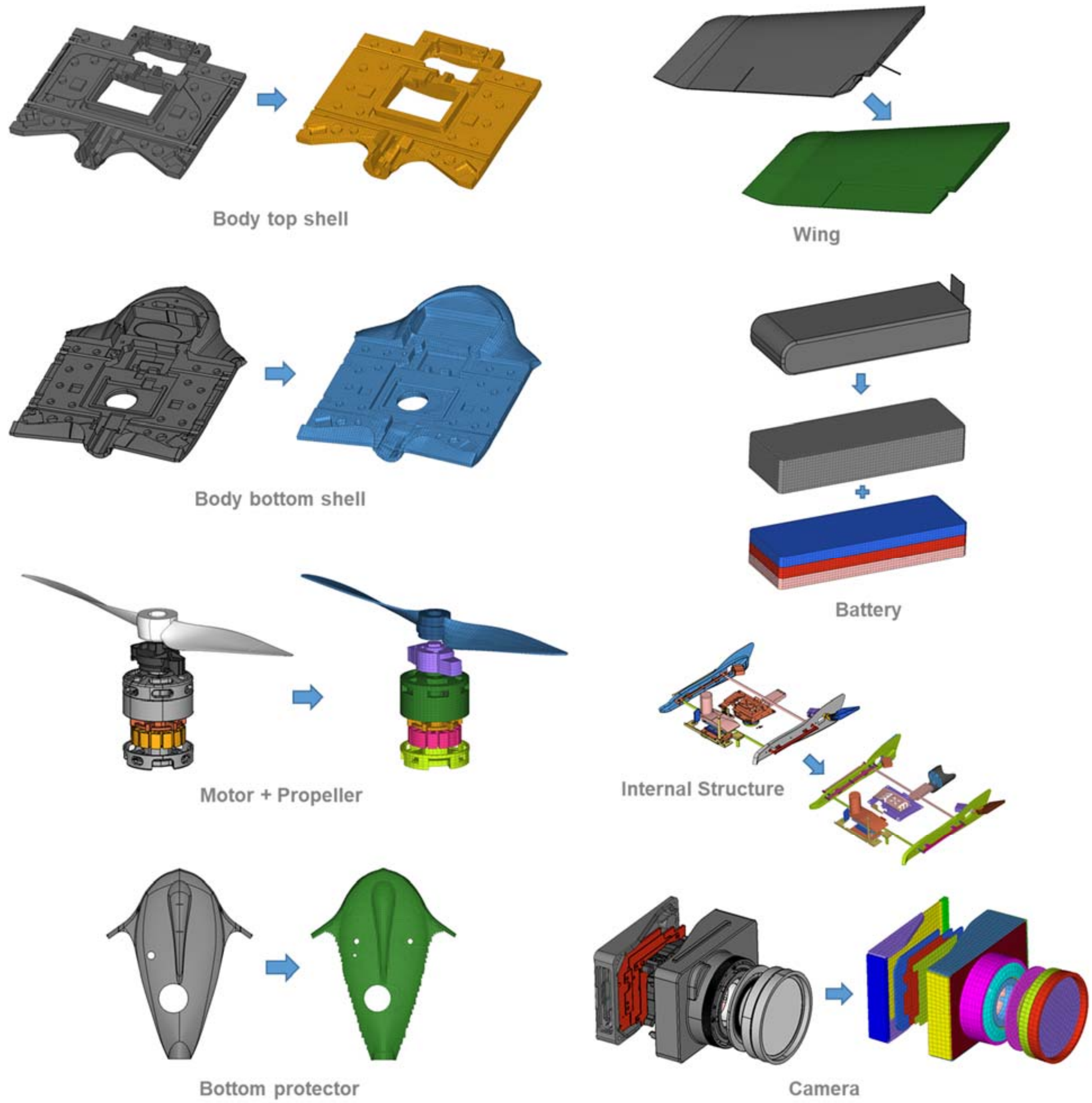

Figure 13. eBeePlus mesh details

The individual sub-assemblies were merged, resulting in approximately 200k elements throughout the model. Beam elements (one-dimensional elements) were selected to represent the carbon fiber wing spar rods, as the wing struts that connect the wings to the main body. Table 12 presents the element quantity summary of the eBeePlus FEM. Figure 14 shows a collection of views of the assembled FEM.

Table 12. eBeePlus FEM elements summary

	1D elements	2D elements	3D elements
Body top shell	-	-	20,775
Body bottom shell	-	-	27,163
Wing (each)	14	665	41,244
Battery	-	15,386	16,896
Motor + Propeller	-	428	6,077
Internal structure	56	21,626	630
Camera	-	5,100	-
Bottom protector	-	3,628	-
TOTAL	**84**	**47,498**	**154,029**

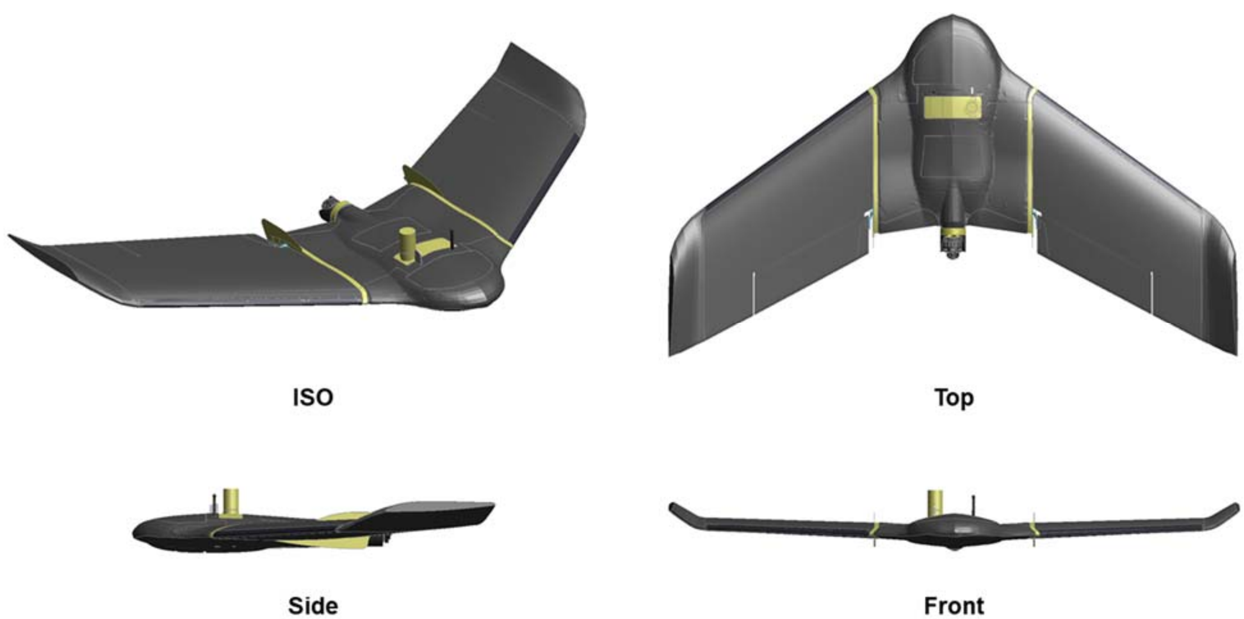

Figure 14. eBeePlus Finite Element Model

Table 13 summarizes the different type of connection techniques and contact definitions applied to the eBeePlus FEM. Some connections were simplified for the sake of avoiding intersections within the model. For instance, the wing struts were attached to the wing foam by means of nodal rigid bodies (NRB's), avoiding the intersection that a contact definition would cause between the strut 1D elements and the foam 3D elements.

Table 13. eBeePlus connection and contact definition summary

	Type	Components	Quantity
Connections	NRB	Wing struts to foam, plastic embedded into foam parts...	96
	Spotwelds	Screws	11
Automatic Contact	Single Surface	Foam to foam	2
	Surface to Surface	Plastic parts to foam	4
Tied Contact	Nodes to Surface	Motor controller to foam	1
	Surface to Surface	Plastic parts glued to foam	4
Tiebreak Contact	Nodes only	Battery and camera foam lids magnets	9

3.3.2 Material Level Tests & Validation

In order to characterize the foam material of the eBeePlus, NIAR extracted four foam specimens from an available eBeePlus article to carry out testing at the coupon level. Two coupons were obtained from the UAS body and two others from the wing. The type of test selected to validate this foam material was a quasi-static test under compressive loading conditions.

The stress-strain results were used to characterize a LS-DYNA material card specified for low-density foams. The unloading section of the curve was captured by means of the HU and SHAPE parameters, which are specified within the LS-DYNA **MAT_LOW_DENSITY_FOAM* material card [14]. These parameters were adjusted through an iterative process described in the validation sub-chapter.

3.3.2.1 Test Setup

Four foam coupons were extracted from an eBeePlus article reserved for FE modeling validation purposes. The location selected for the coupon extraction were:

- Top half center body, where the nominal foam density is of 30 g/l as specified by the manufacturer (see Figure 15). This gave two prismatic coupons.
- Right wing, as close as possible to the root, where the nominal foam density is 26 g/l (see Figure 15). This gave two prismatic coupons.

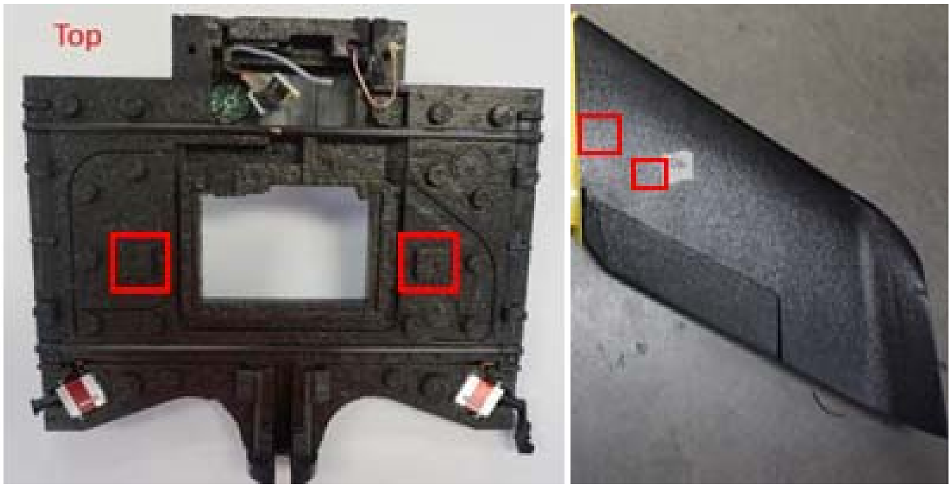

Figure 15. eBeePlus foam coupon extraction location from body (left) and wing (right)

A servo hydraulic MTS testing machine was used for the quasi-static coupon tests. This testing machine is equipped with a hydraulic actuator which has a 15-inch maximum stroke and a load capacity of 110 kip. Figure 16 illustrates the setup selected for the four specimens tested.

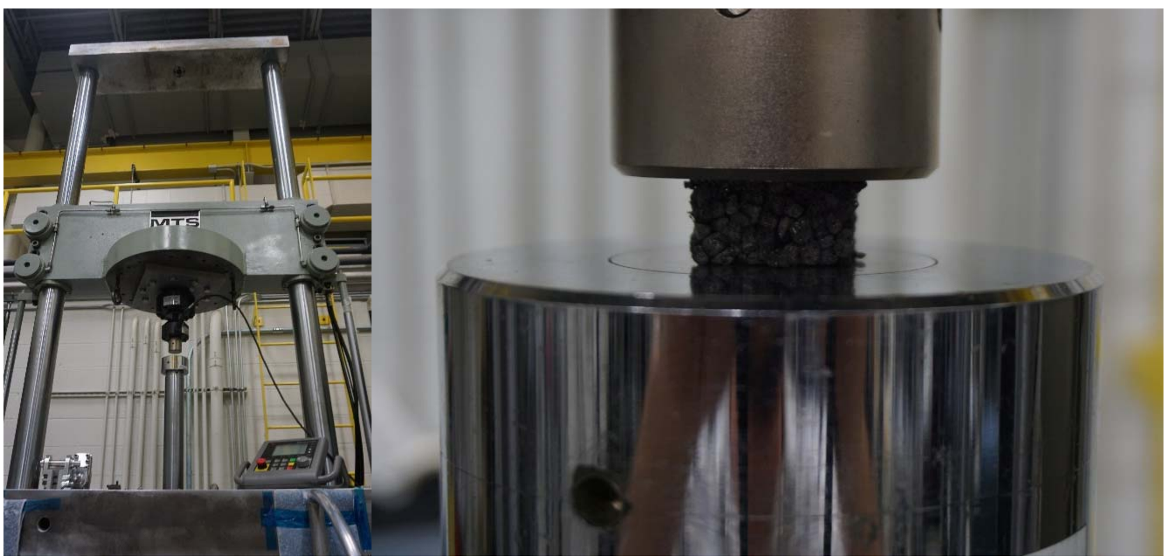

Figure 16. Foam coupon quasi-static compression test setup

3.3.2.2 eBee Plus Wing Foam: Test Results, FE Model Fitting and Validation

The experimental data was processed, and a stress-strain curve was obtained for each of the test repetitions. Figure 17 compares experimental data for both test repetitions against the simulation results. Concerning the experimental data, it is observed that both specimens produced good repeatability. The data overlaps each other at the loading phase, and closely matches in the unloading portion of the curve.

The stress-strain curve, along with other parameters measured in the test (*e.g.* density), were directly entered into the LS-DYNA material card. A virtual model was created following the test coupon dimensions, with mesh specifications similar to the element size of the equivalent full-assembly FEM regions from where the coupons were extracted. The virtual coupon was confined between two virtual rigid walls. Similar to the test conditions, the top rigid wall was constrained through a single point constraint (SPC), while a prescribed motion was applied to the bottom rigid wall. Simulation force-displacement outputs were converted into stress-strain format for comparison against the experimental data.

An iteration exercise was conducted to investigate the influence of the parameters HU and SHAPE, which control the unloading phase (see LS-DYNA manual [21] for more details on these parameters). Figure 17 presents the stress-strain curve for the optimum values of these two parameters. The simulation shows high accuracy in its prediction of the loading phase, and an acceptable performance in the subsequent unloading phase. Therefore, the material model validation for the 30 g/l EPP foam is completed.

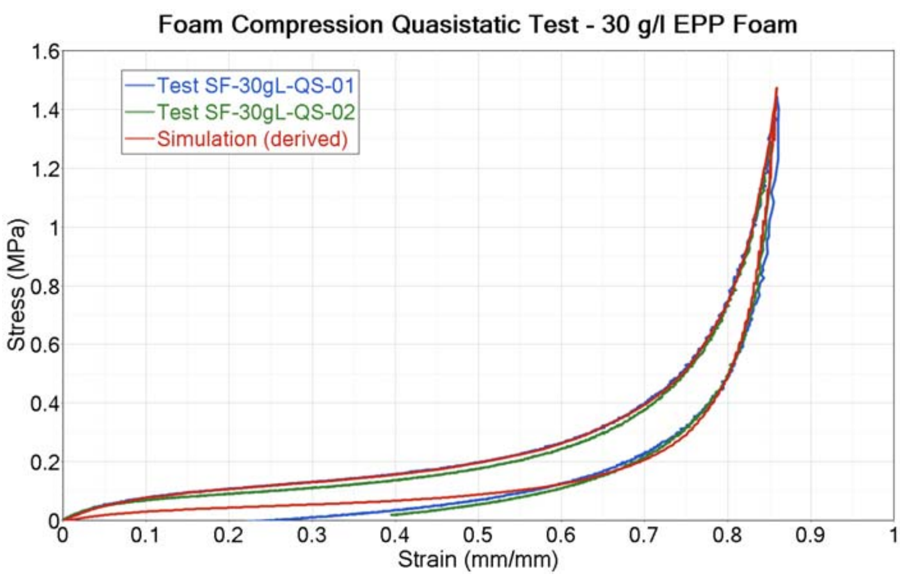

Figure 17. 30 g/l EPP foam material model validation

3.3.2.3 eBee Plus Body Foam: Test Results, FE Model Fitting and Validation

Two quasi-static compression coupon tests were conducted for the 26 g/l wing foam. The experimental data in Figure 18 presents a high level of repeatability. The unloading parameters were fixed to the same values as the body foam. The final material card was simulated applying the test boundary conditions. The simulation results indicate a good correlation with the experimental data, as shown in Figure 18.

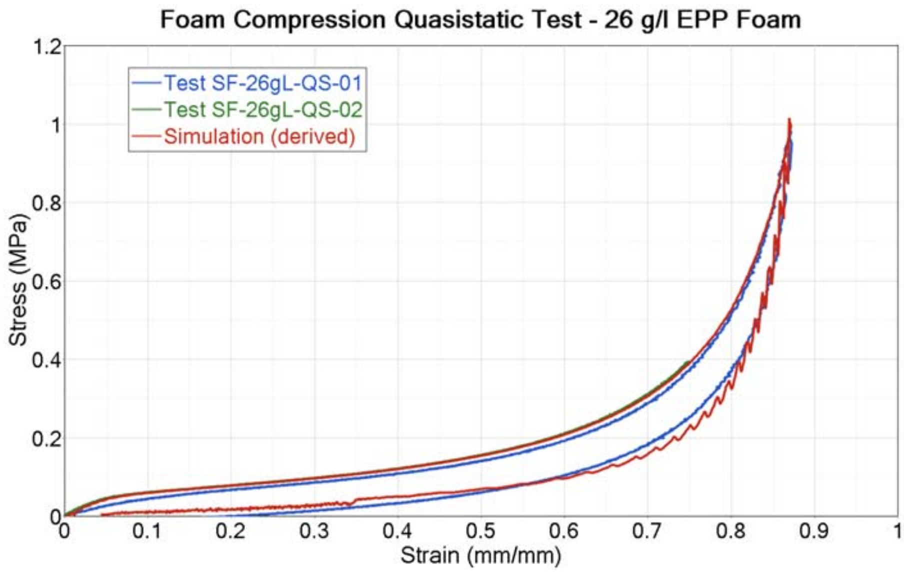

Figure 18. 26 g/l EPP foam material model validation

3.3.3 Component Level Tests and Validation

This section provides a brief review of the vertical drop tower test performed on the UAS foam of the body, followed by the validation of the UAS material model. The objective of this test was to validate the FE modeling of the EPP foam under dynamic loading. To achieve this, the test was set up so it would drop an impactor on the different sections of the UAS body. The test results obtained were used to replicate the test by simulation, and helped validating the FE model of the foam by correlating the simulation to the test.

3.3.3.1 Test Setup

Three foam specimens were extracted from different regions of the eBeePlus main body, accounting for specimens' thickness variability, with the aim of extending the validation of the material card verified at the coupon level test.

Figure 19 defines the three specimen regions and shows the actual specimens extracted for testing purposes.

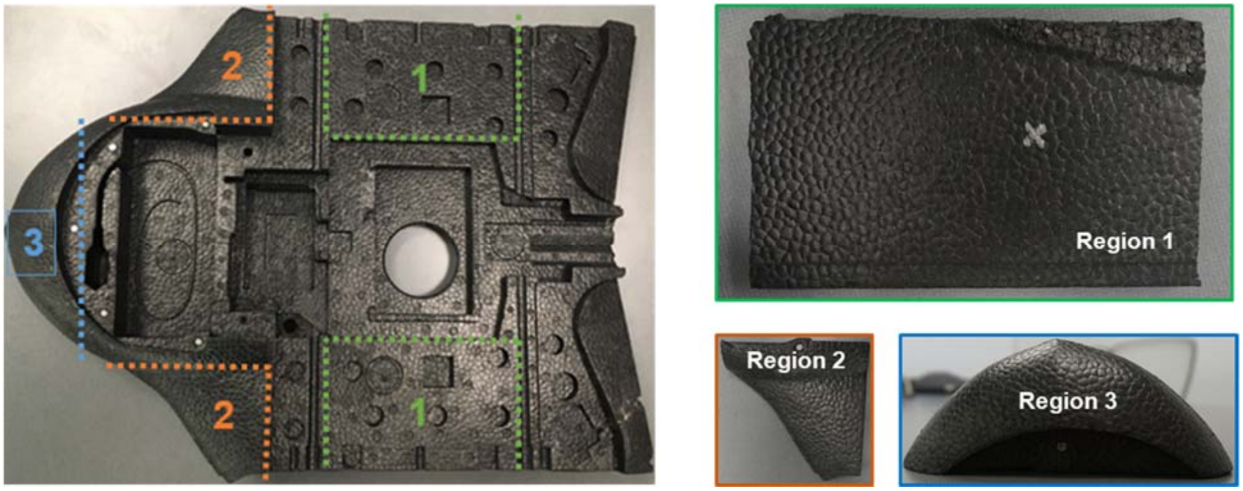

Figure 19. Specimen extraction regions and eBeePlus foam specimens

The specimens were placed on top of the drop tower aluminum base, and aligned for the center of the impactor head in order to hit the specimen in the selected impact regions. The specimens were constrained with tape to prevent them from sliding sideward during the impact.

Figure 20 illustrates the test setup of the three specimens individually.

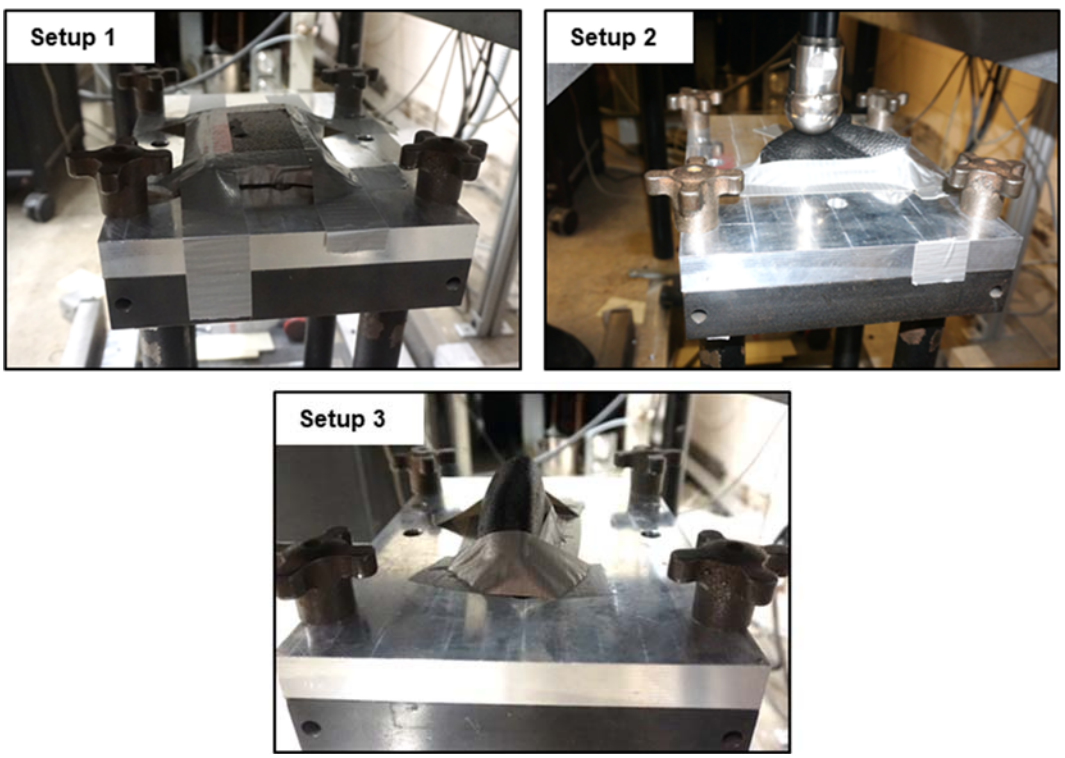

Figure 20. Component level test setup for each foam specimen

3.3.3.2 Test Equipment

The following equipment was necessary to conduct the test and record the data.

I. Drop tower:
The drop tower is composed of a steel spherical impactor attached to a mass. The drop height, along with the preselected mass, define the impact energy of the test. The largest impactor diameter available was selected to avoid failure of the foam. The equipment contains instrumentation to measure the time history of load reactions and displacements of the impactor. Figure 21 shows the drop tower and the spherical impactor which was chosen for the tests.
Table 14 presents the configuration selected for the component level test conducted.

Table 14. Drop tower impactor characteristics

Diameter [in]	Mass [lb]
2	9.46

II. High speed video cameras:
Two high-speed cameras were placed on the side and bottom of the impact location to record the event at 1000 frames per second. Figure 21 presents the camera type used for this series of tests.

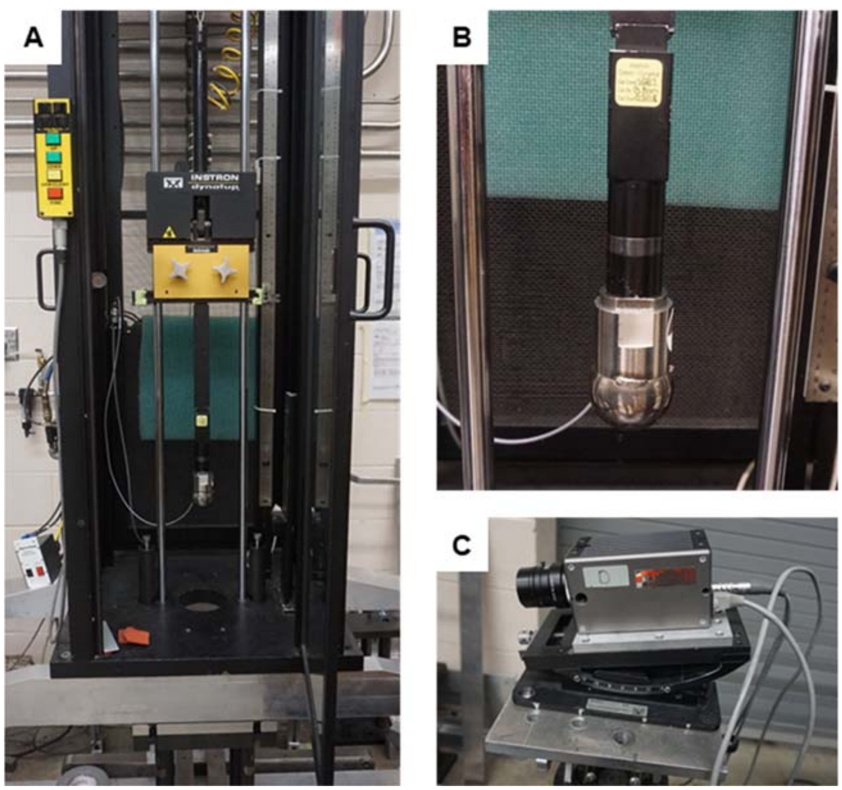

Figure 21. A: drop tower; B: 2 in. diameter spherical impactor; C: high-speed camera

3.3.3.3 Body Foam Dynamic Test: Results and Validation

Table 15 summarizes some of the most notable data values recorded for each foam component test.

Table 15. Summary of the drop tower test data for each EPP specimen

Test Reference	Impact Velocity [*ft/s*]	Drop Mass [*lb*]	Impact Energy [*in-lbf*]
Specimen 1	5.26	9.45	49.70
Specimen 2	6.69	9.45	79.03
Specimen 3	8.45	9.45	125.98

Figure 22 through Figure 24 present the kinematics comparison between test and simulation results.

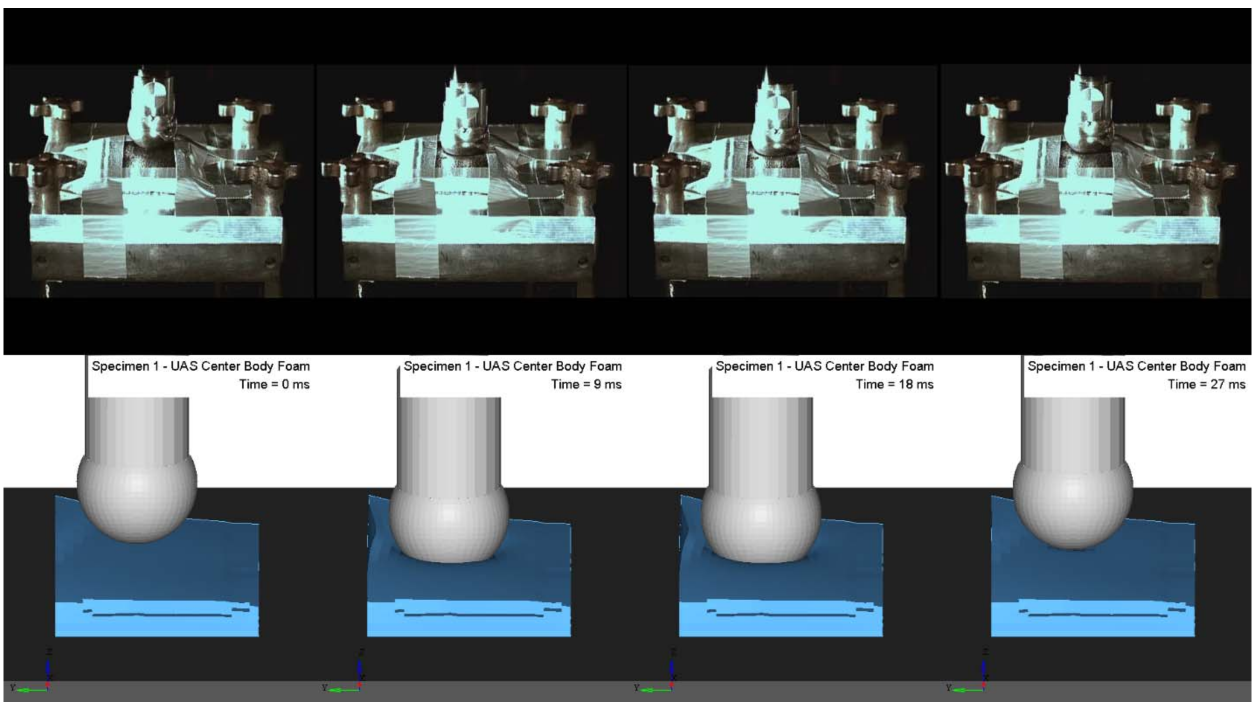

Figure 22. Test vs simulation comparison; EPP specimen-1, 5.26 ft/s; kinematics

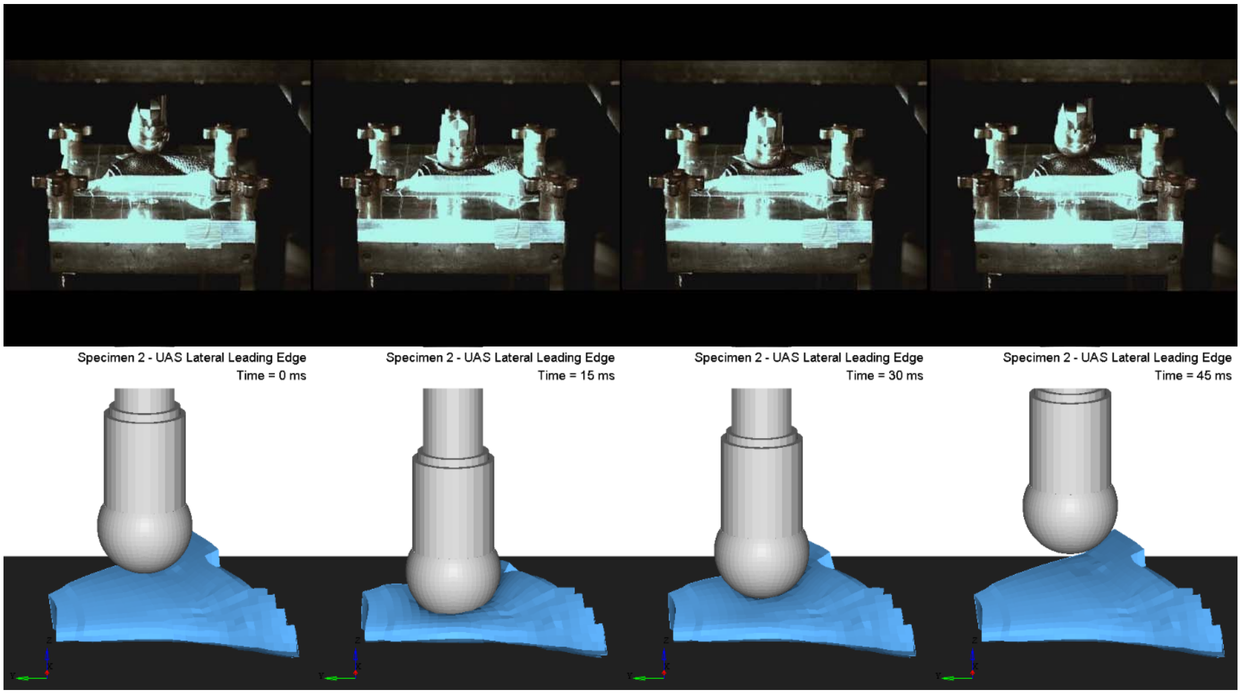

Figure 23. Test vs simulation comparison; EPP specimen-2, 6.69 ft/s; kinematics

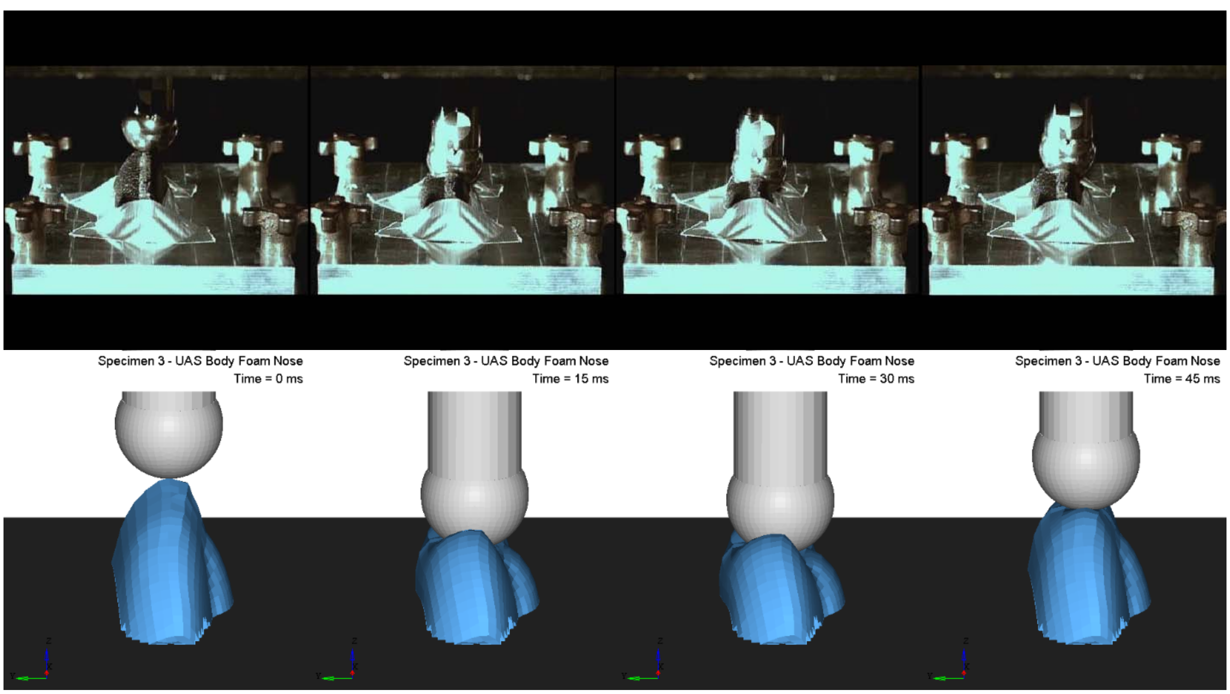

Figure 24. Test vs simulation comparison; EPP specimen-3, 8.45 ft/s; kinematics

Figure 25 shows the verification between experimental and simulation data for each of the drop tower tests. Results indicate good correlation for the three different foam specimens obtained from independent UAS locations, which increases the confidence on the material card performance for the eBeePlus EPP and validates the material card.

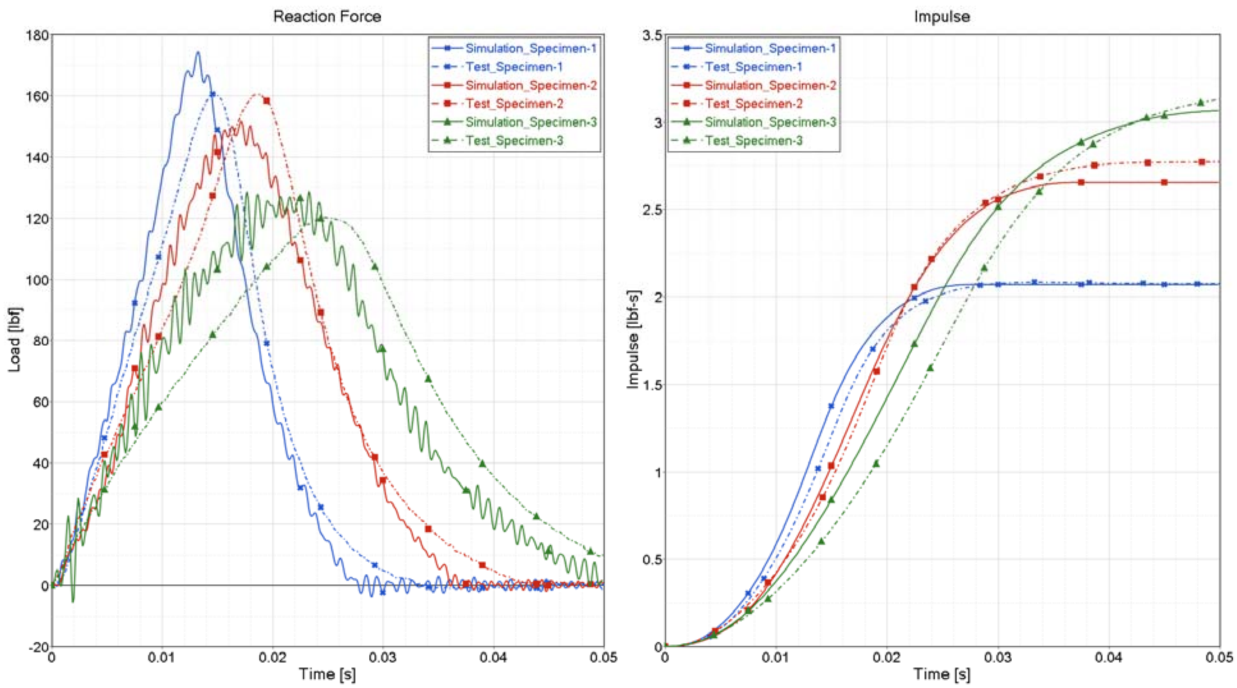

Figure 25. Comparison of the reaction force and impulse of the eBeePlus EPP foam specimens

3.3.4 Full Assembly Impact Tests and Validation

This section provides a description of the impact test performed on the eBeePlus followed by the validation of the UAS model. The objective of this test was to assess the behavior of the full UAS assembly FE model (with and without wings) under similar impact velocities that exist in the ATD tests. This was achieved by accelerating the entire UAS assembly into a rigid plate.

3.3.4.1 Test Setup

The setup selected for this test consisted of a flat aluminum plate attached to a load cell, which recorded the load profile of the impact event. To accelerate the UAS to the desired impact velocity, the UAS was launched with the equipment described in Section 2.1.1 against a 1.0 inch thick flat aluminum plate.

High-speed cameras were placed around the set to strategically capture the most details during the crash event. Figure 26 illustrates the test setup used for the full-assembly eBeePlus impact test.

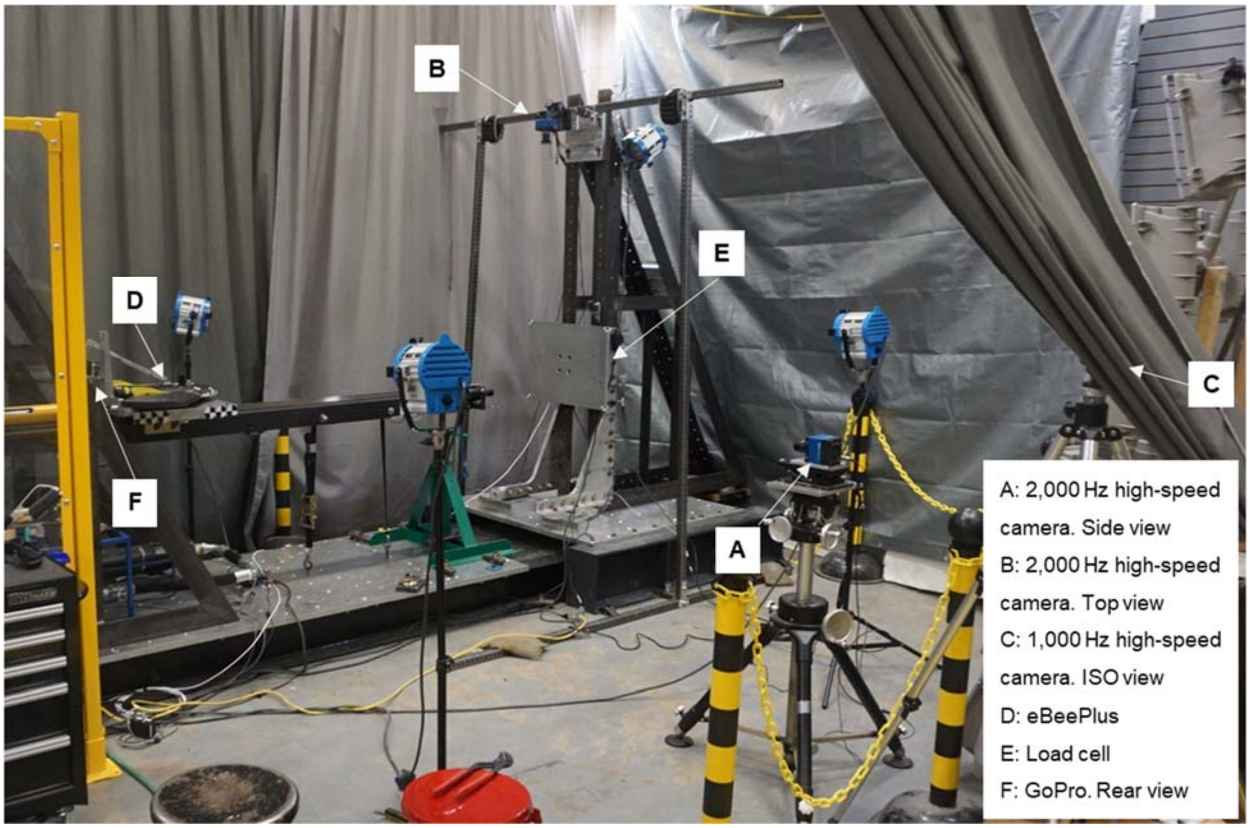

Figure 26. eBeePlus full-assembly test setup

3.3.4.2 Test Equipment

The following equipment was necessary to conduct the test and record the data.

I. Load cell force gage of a range of 10,000 lbf and sampling rate of 20 kHz.
II. Two high-speed video cameras placed around the setup to record the event at 2000 frames per second. Figure 26 shows the positioning of the two cameras.
III. One high-speed camera with recording specifications of 1000 frames per second and a GoPro camera.

3.3.4.3 Test Results and Validation

A finite element discretization of the test fixture was developed by capturing the plate, beams and main attachments. The model aimed to capture the transfer load path within the structure for an adequate correlation with the experimental results. Load cell recordings in the FEM were obtained by means of an LS-DYNA cross-section definition. Interactions between components were specified through LS-DYNA contact cards [21]. *AUTOMATIC_SURFACE_TO_SURFACE* and *AUTOMATIC_NODES_TO_SURFACE* were applied to surfaces attached through fasteners, while *TIED_NODES_TO_SURFACE* was applied to welded surfaces. Figure 27 shows the FEM assembly created to represent the flat panel set up. Table 16 summarizes the material definition chosen for the FEM creation of the test fixture.

Figure 27. Flat plate test fixture for full-assembly impacts

Table 16. Material bill summary of the flat plate test fixture

Parts	Material	LS-DYNA card
Plates and floor structure	Aluminum	*MAT_PIECEWISE_LINEAR_PLASTICITY*
Beams and frames	Steel	*MAT_PIECEWISE_LINEAR_PLASTICITY*
Load cell	Aluminum	*MAT_ELASTIC*

Figure 28 and Figure 29 presents the side and top kinematics of the eBeePlus full-assembly impact respectively. Simulation results capture the front foam components buckling, as well as the wing detachment at impact.

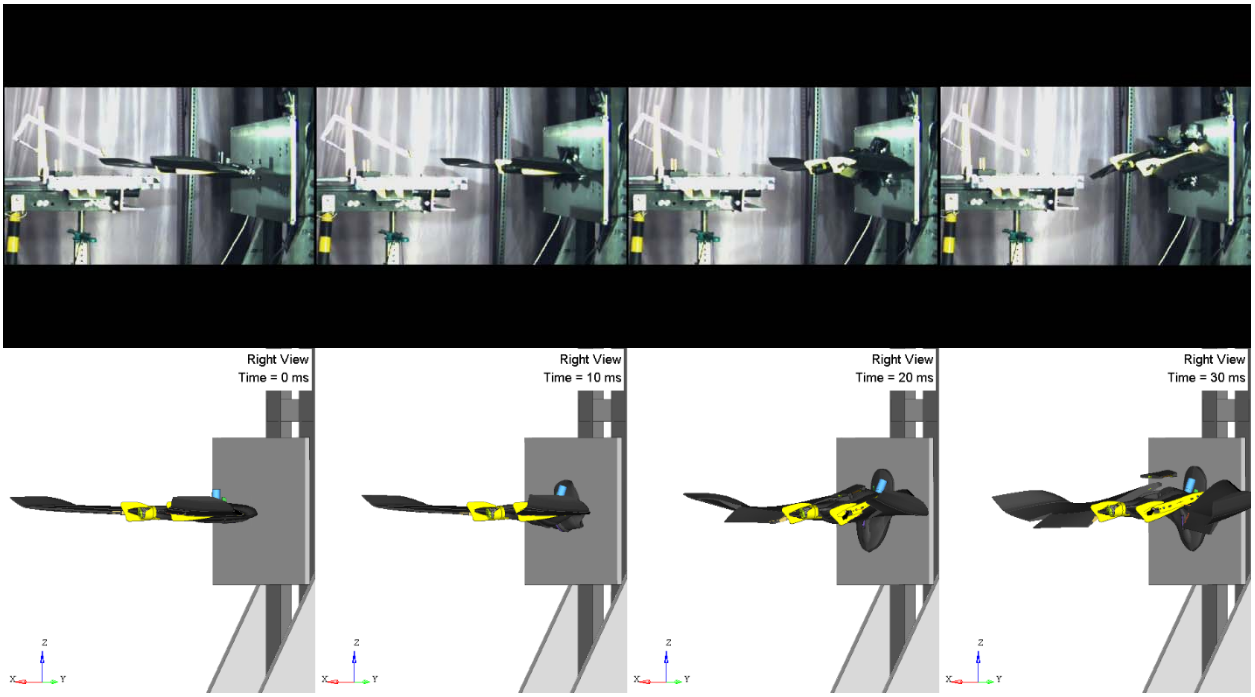

Figure 28. eBeePlus full-assembly impact kinematics; side view

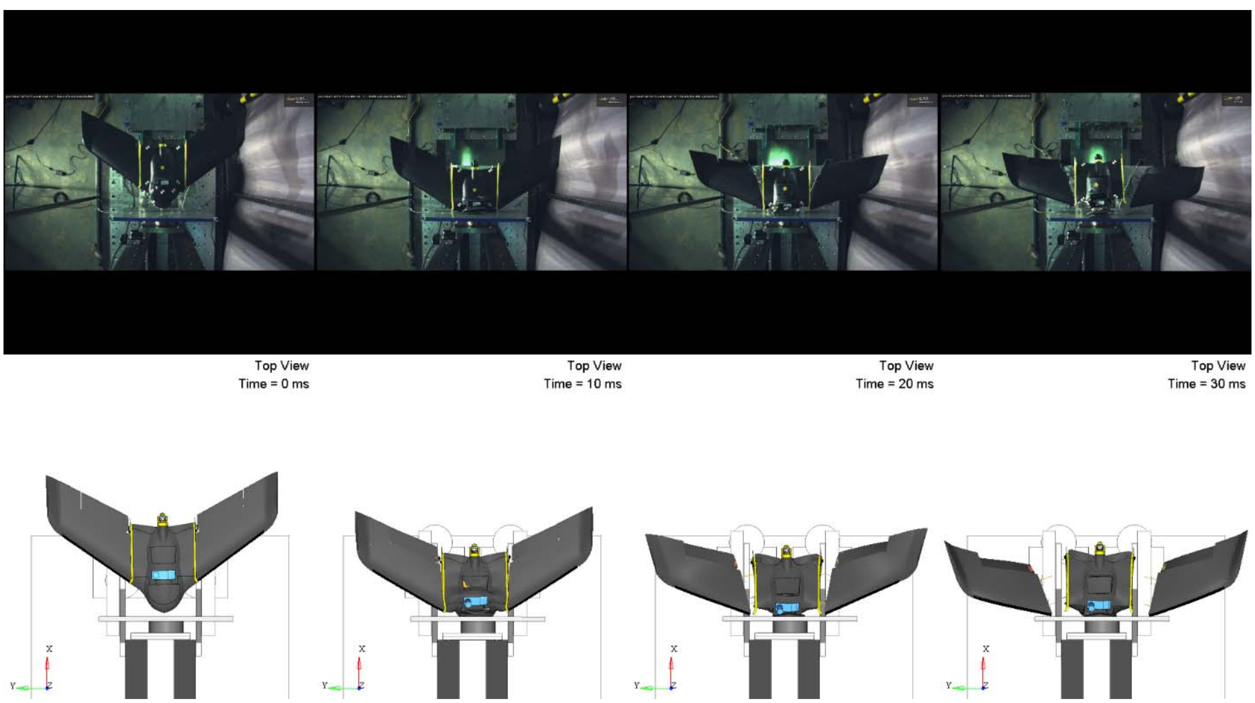

Figure 29. eBeePlus full-assembly impact kinematics; top view

Figure 30 compares the plate reaction force along the impact direction, as well as the impulse between test and simulation. Both plots indicate a good level of correlation. The small discrepancies in the load profile could be caused by the lack of failure parameters in the foam material card, which could have introduced a different vibration mode within the FEM test fixture. Nevertheless, the close match of the impulse time-history indicates that the impact load transfer was effectively the same for the test and the simulation. This implies that the virtual model is capable of producing similar damage on the target structure as the actual test article.

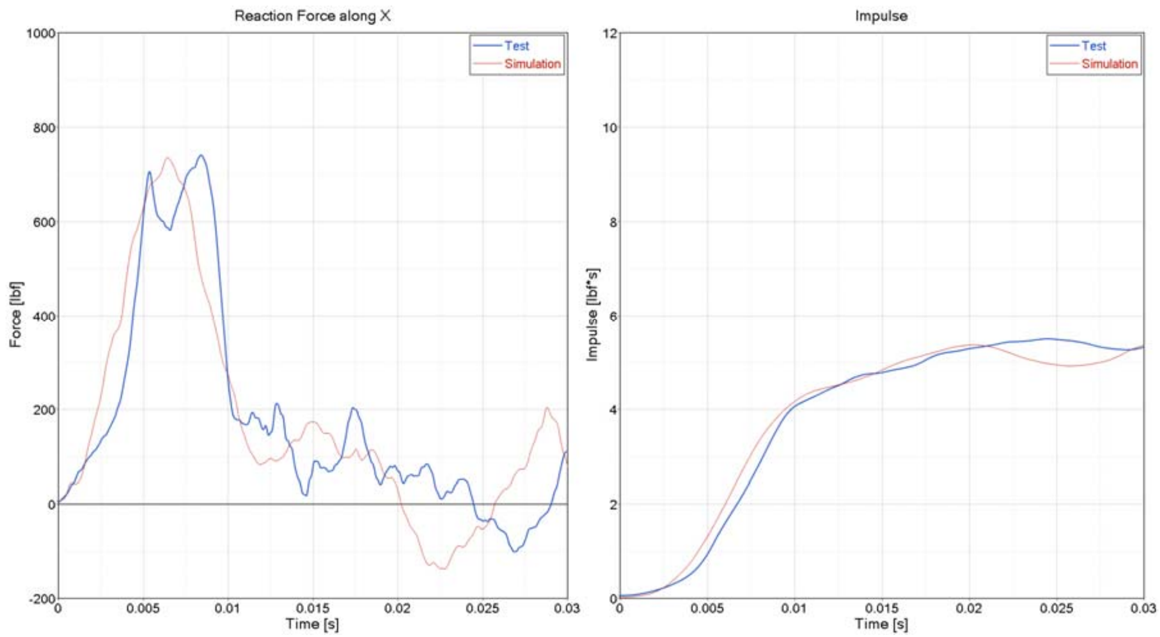

Figure 30. eBeePlus full-assembly impact test; plate reaction force and impulse

The building block approach validation process, followed from the coupon until the full-assembly level, is a good foundation to confirm the validation of the eBeePlus full-assembly FEM created for ground collision impacts.

3.4 PRECISION HAWK LANCASTER III REV 3 MODEL DETAILS

Previous work carried out by the ASSURE team for airborne collision scenarios led to the development of a fixed-wing UAS FEM. Airborne collision task [11] required the creation of a representative Precision Hawk Lancaster Hawkeye Mark III FEM for high-speed impact conditions at 250 knot (422 ft/s). Component level tests were performed for the battery and the camera of this UAS model. These test results helped to validate their destruction behavior for high-speed impact events. Material properties were applied based on available data in literature.

The present ground collision studies take into consideration the probability of a fixed-wing UAS colliding against a pedestrian. As a continuation of previous efforts carried out by the ASSURE-UAS alliance in [11], the present work required the update of the Precision Hawk model created in the previous airborne collision task [11] to develop a representative FEM for low velocity impacts, which are related to ground collision events. Some of the modifications affecting the previous model are the characterization of material properties for low speed impacts, such as foam and PCB.

3.4.1 Model Preparation for Ground Collisions

Two scaled models of the standard Precision Hawk Lancaster Hawkeye Mark III were created for previous ASSURE efforts [11], with the aim of evaluating airborne collision damage of representative 4.0 lb and 8.0 lb fixed-wing UASs against a commercial aviation.

A scaling exercise was performed to return the airborne collision Precision Hawk model to its original mass of 4.4 lb. Table 17 presents the mass distribution of the Precision Hawk Lancaster Mark III per sub-assembly system as described in [11]. Previous researchers determined masses by weighing the different sub-assemblies from the physical model available in [11].

Table 17. Precision Hawk physical model mass distribution [11]

Sub-assembly	Mass [lb]
Frame	1.07
Wing	0.91
Aft Fuselage	0.55
Propulsion system	0.29
Battery	0.74
Camera	0.87
TOTAL	4.43

While developing the FEM and adjusting sub-assembly masses, non-structural parts such as wires and printed lines on PCB surfaces and motor stator cabling were simplified by means of attached mass elements.

3.4.2 Model Details

Table 18 gathers the most relevant specifications of the Precision Hawk Lancaster Hawkeye Mark III. Figure 31 shows several views of the ground collision updated fixed-wing model, which complies with the mass and dimensions specified in Table 18.

Table 18. Precision Hawk Lancaster Hawkeye Mark III specifications

MTOW	5.5 lb
Model TOW	4.4 lb
Wingspan	4 ft 11 in
Length	2 ft 7.5 in
Max. Horizontal Speed	64 ft/s
Max. Service Ceiling	13,120 ft

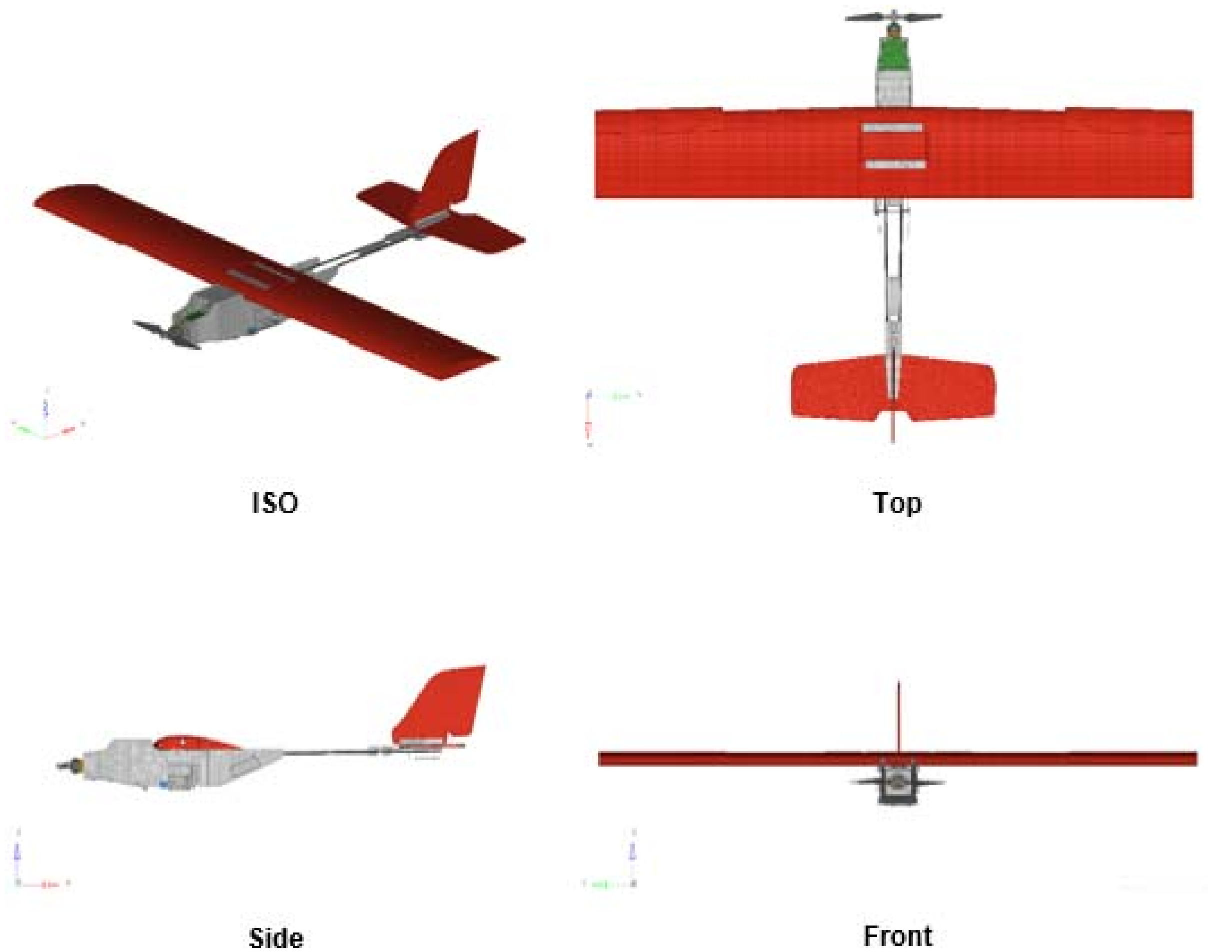

Figure 31. Precision Hawk Lancaster Hawkeye Mark III ground collision FEM

Table 19 summarizes the different type of elements, which forms the ground collision FEM of the Precision Hawk Lancaster Hawkeye Mark III.

Table 19. Mesh elements summary

	1D elements	2D elements	3D elements
Frame	14	6,655	540
Wing	8	2,742	43,556
Aft Fuselage	12	3,930	9,070
Propulsion system	20	720	3,623
Battery	-	14,141	10,524
Camera	6	1,853	2,252
TOTAL	**60**	**30,041**	**69,565**

3.4.3 Material Level Tests & Validation

In order to update the FEM foam material properties, two coupons were tested at quasi-static stroke rate under compressive loading conditions.

Stress-strain results were used to build the updated EPS material card in LS-DYNA. The unloading section of the curve was captured with two parameters (HU and SHAPE) from the **MAT_LOW_DENSITY_FOAM* material card [14]. Parameter values were obtained by means of an iterative process, as discussed in Chapter 3.3.2.2 .

3.4.3.1 Lancaster Wing Foam

Two coupons were extracted from an available Precision Hawk Lancaster Revision 4 wing, whose polystyrene composition was determined to be similar to its previous Lancaster version. Figure 32 shows the specimen extraction region selected to obtain the quasi-static test coupons.

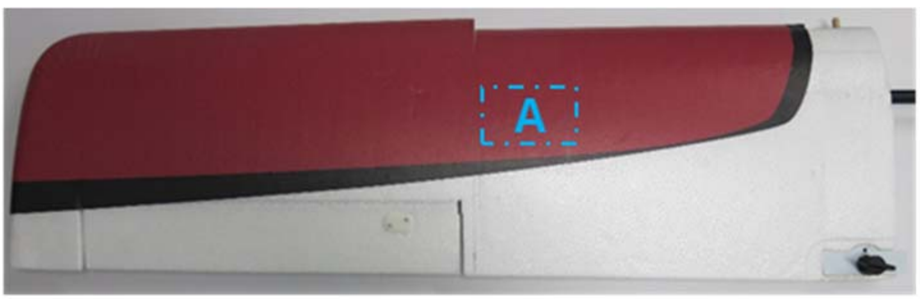

Figure 32. Specimen extraction region from the Precision Hawk Lancaster Revision 4 foam wing

Figure 33 presents the two foam coupons extracted to be tested under quasi-static compressive loading. Both specimens had similar dimensions to account for repeatability.

Figure 33. Polystyrene foam specimens for quasi-static compression test

NIAR used MTS equipment available at its facilities to conduct the two coupon level tests. Figure 34 illustrates the test setup for the quasi-static tests under compressive loading conditions.

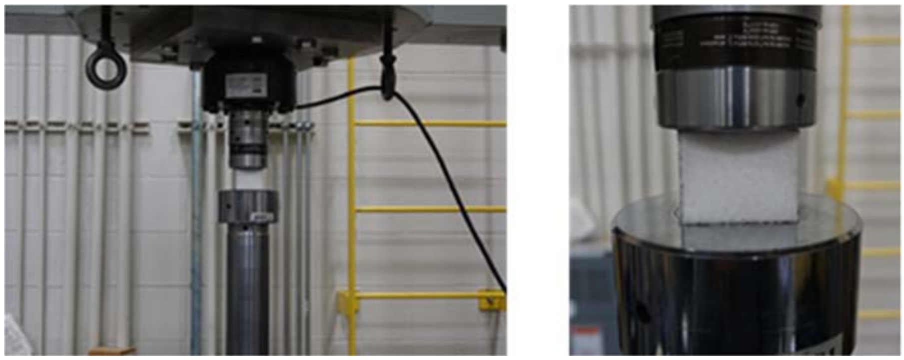

Figure 34. Polystyrene foam coupon quasi-static compression test setup

The quasi-static compression test consisted of a constant loading speed of 0.5 in/min compressing the foam coupon until it reaches 10% of its original thickness. There was then a subsequent unloading motion at the same stroke rate as the loading process. Figure 35 shows the comparison between experimental and simulation kinematics.

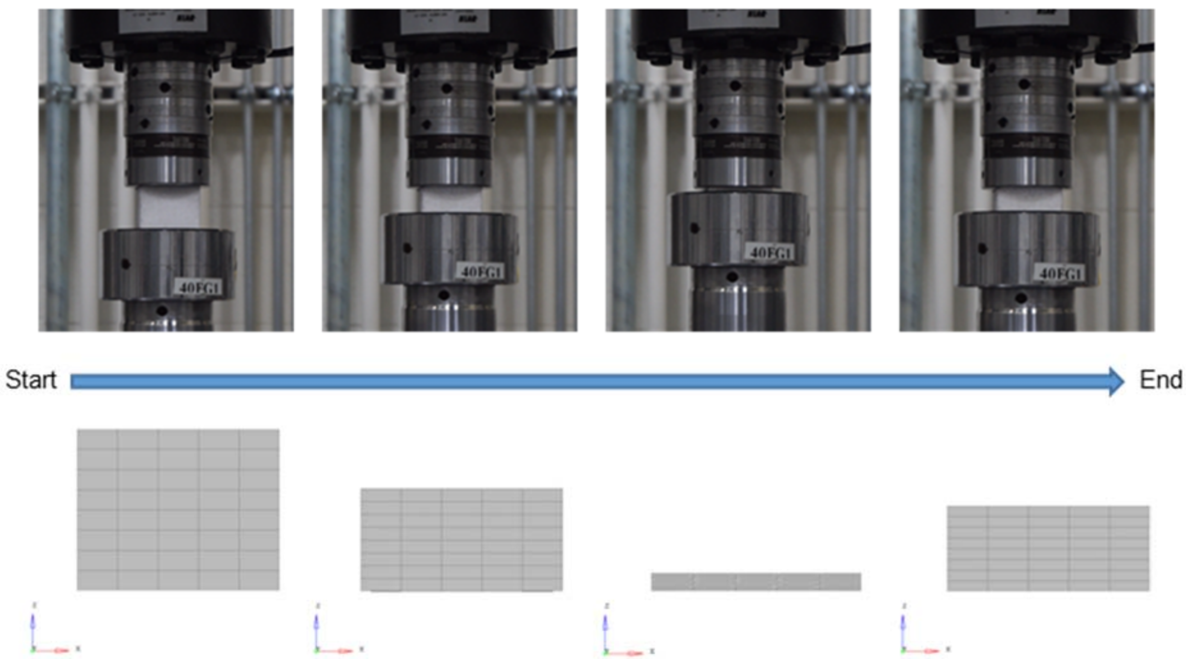

Figure 35. Polystyrene quasi-static compression test vs simulation kinematics

For the creation of the coupon FEM, the element size was determined in accordance to the foam component's element size on the existing Precision Hawk FEM. This practice reduces any major mesh dependence in the material card performance due to mesh size.

Figure 36 compares the experimental loading curves to the simulation curve, which was adjusted through the **MAT_LOW_DENSITY_FOAM* material card parameters HU and SHAPE for better results correlation [14].

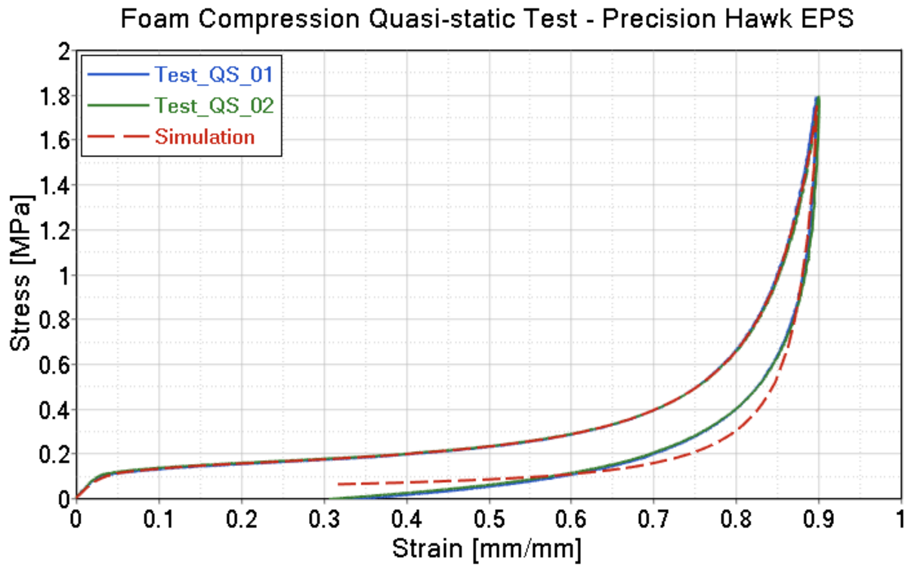

Figure 36. Foam compression quasi-static test of Precision Hawk polystyrene

3.4.4 Full Assembly Impact Tests and Validation

With the aim of correlating the crash behavior of the Precision Hawk FEM for low velocity impacts, NIAR carried out an impact test of the Precision Hawk main frame against an aluminum flat plate.

3.4.4.1 Test Setup

The full UAS FEM was simplified to match the composition of the test article. Figure 37 compares the physical test article to the equivalent FEM. Similar to the full FEM model, non-structural masses such as printed lines and wires were kept by adding element masses to achieve a representative mass distribution along the assembly.

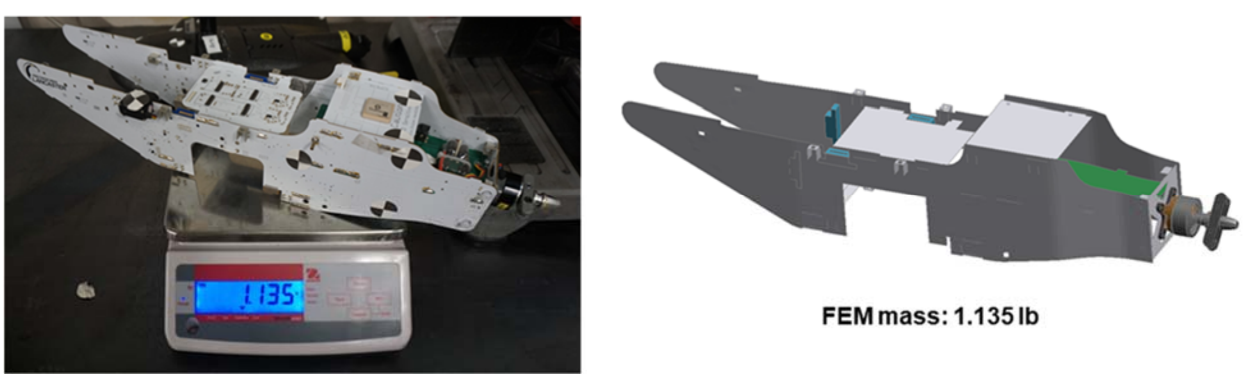

Figure 37. Test article vs frame FEM.

This experiment used the test structure and instrumentation previously built at NIAR facilities for the eBeePlus validation efforts. Figure 38 illustrates the test setup used for this experiment.

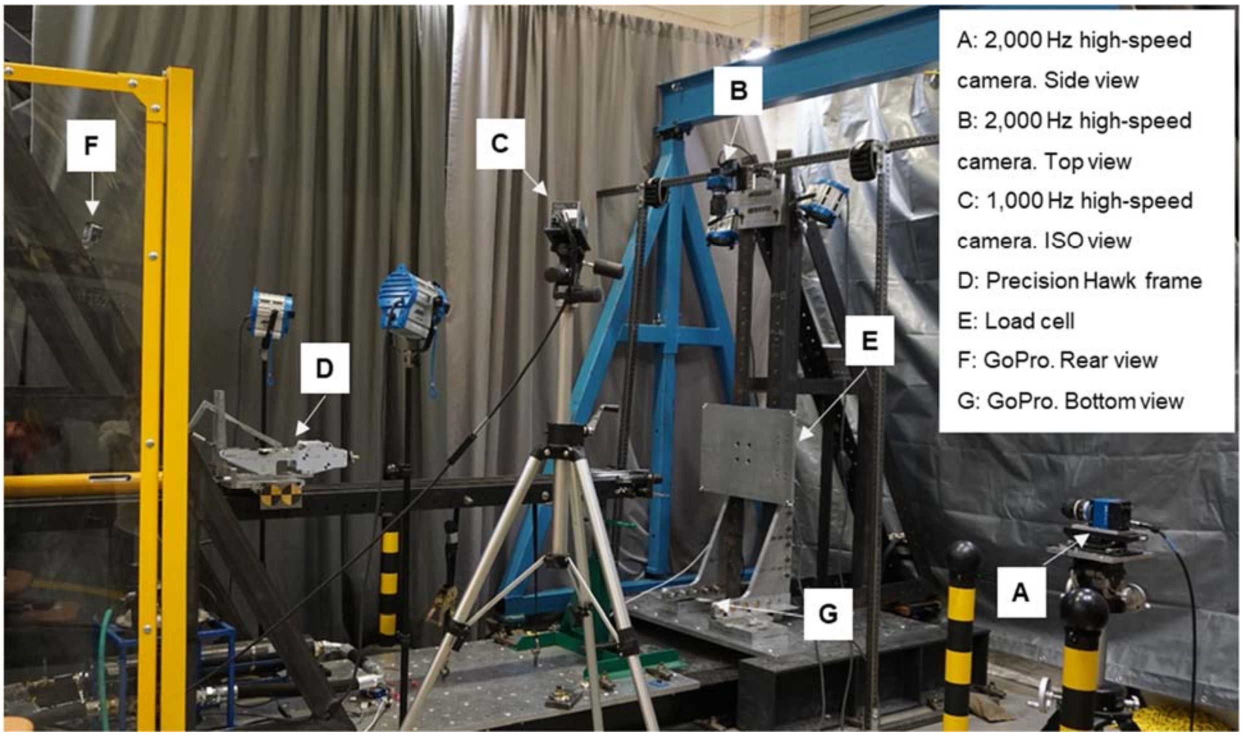

Figure 38. Precision Hawk Lancaster Hawkeye Mark III frame test setup

The UAS was accelerated along the rail and released by means of a mechanical fixture before colliding against the aluminum plate. The desirable release velocity was determined at 36 ft/s based on the Lancaster *return to home* speed, which was measured through flight-testing.

3.4.4.2 Test Equipment

Refer to Chapter 3.3.4.2 .

3.4.4.3 Test Results and Validation

The desirable low impact velocity for the Lancaster model was determined to be 36 ft/s, however, due to the adjustments applied to the eBeePlus full-assembly launching system for the present test configuration and the difference in mass between eBeePlus and Precision Hawk, a higher velocity than planned was recorded at impact. Such velocity deviation remains within the ground collision flight speed range, and extends the validity of the model for a higher velocity range. Figure 39 compares experimental and simulation kinematics of the Lancaster frame impact.

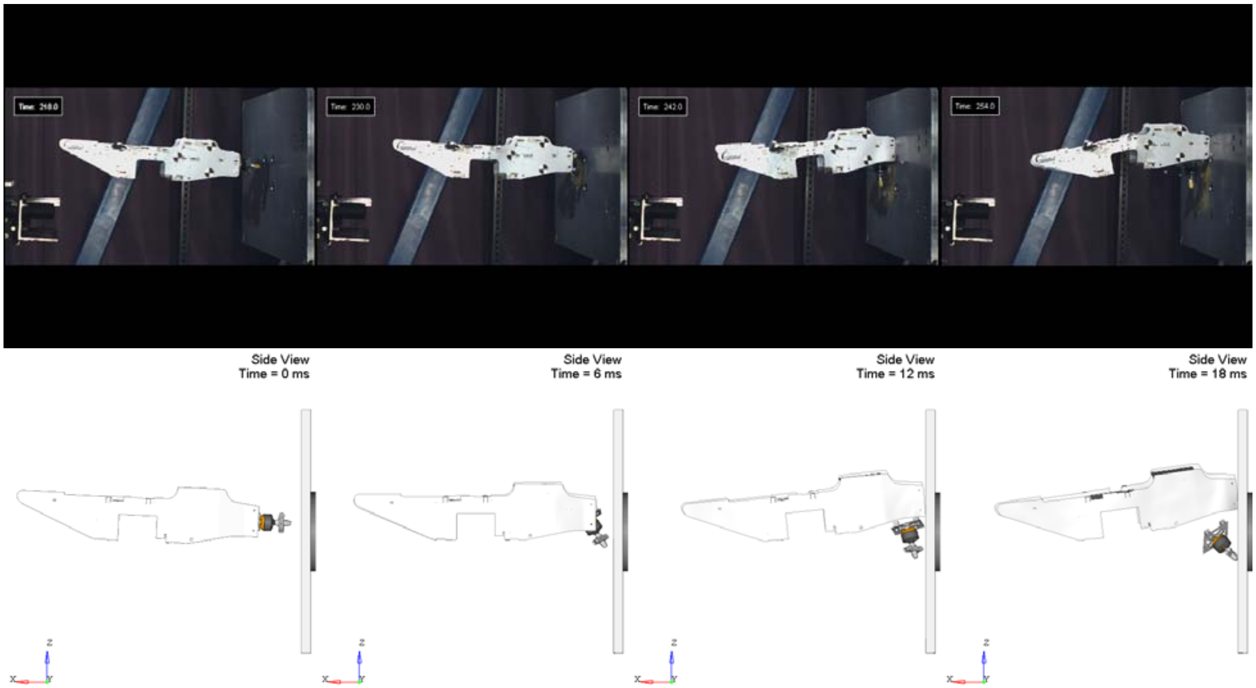

Figure 39. Test vs simulation comparison; Precision Hawk Lancaster Hawkeye Mark III frame, 1.135 lb, 42.5 fps, horizontal; kinematics.

Figure 40 compares load cell readings between test and simulation along the impact direction, and it includes impulse calculations for both events. Both plots highlight three instants of interest in terms of contact: *End Nozzle contact*, which indicates the time at which the propeller nose ends contacting the aluminum plate due to the rebound motion; *Start Frame contact*, which defines the moment at which the PCB frame contacts the aluminum plate; and *End contact*, which determines the last instant of contact between the Precision Hawk frame and the aluminum plate.

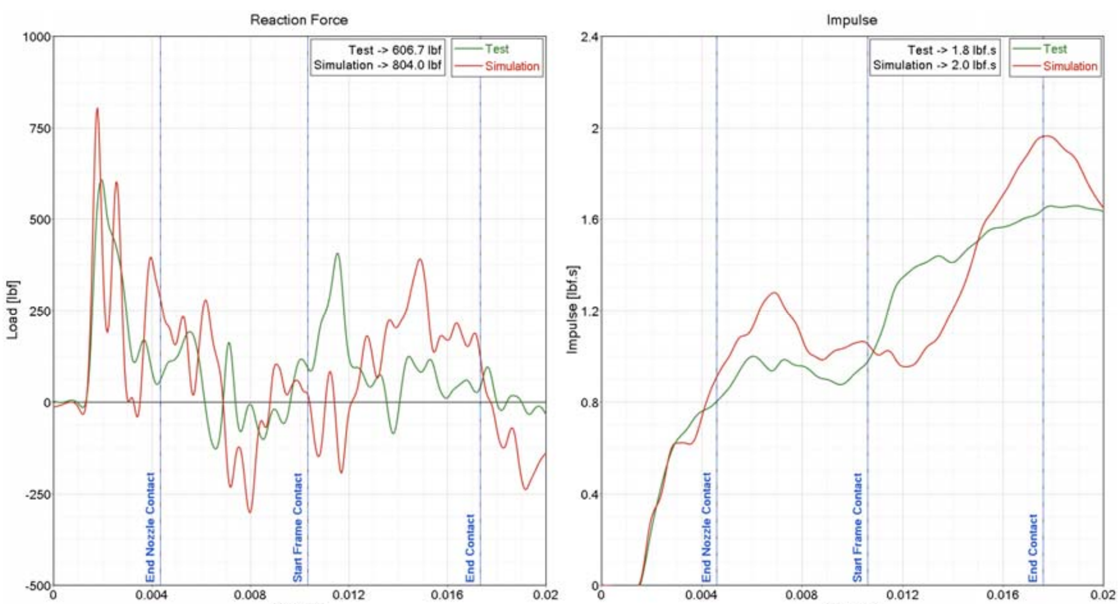

Figure 40. Load and Impulse.

3.5 sUAS FINITE ELEMENT MODEL RECOMMENDATION

Chapter 3 has presented the LS-DYNA finite element models of a DJI Phantom III, an eBeePlus and a Precision Hawk MKII. All these numerical models have been developed for ground collision impact simulations. They were verified and validated with coupon, component level, and full-scale tests to ensure good correlation with physics within the envelope of conditions tested.

These numerical models are intended to be used for assessing impact dynamics with human body or ATD models during ground collisions. It is recommended to limit the applications to impact velocities of 75 ft/s or less, for which tests validated the behavior of the sUASs discussed here.

4. UAS PROJECTILES MODEL VERIFICATION FOR GROUND COLLISION

The calibrated version of the Quadcopter FEM, which was developed under Task A3 for Airborne Collision [10], was evaluated against existing physical tests. Prior to the present project, NIAR conducted the referenced physical tests with the Hybrid III 50th percentile male ATD, as part of Task A11 [19].

The simulations analyzed the six different impact orientations specified for Task A11 [19]:

- Vertical maximum velocity
- Vertical minimum velocity
- Horizontal
- Combined impact 65 deg. angle
- Combined impact 58 deg. angle minimum velocity
- Combined impact 58 deg. angle maximum velocity

Figure 41 illustrates the six configurations analyzed to calibrate the Quadcopter FEM for ground collision events.

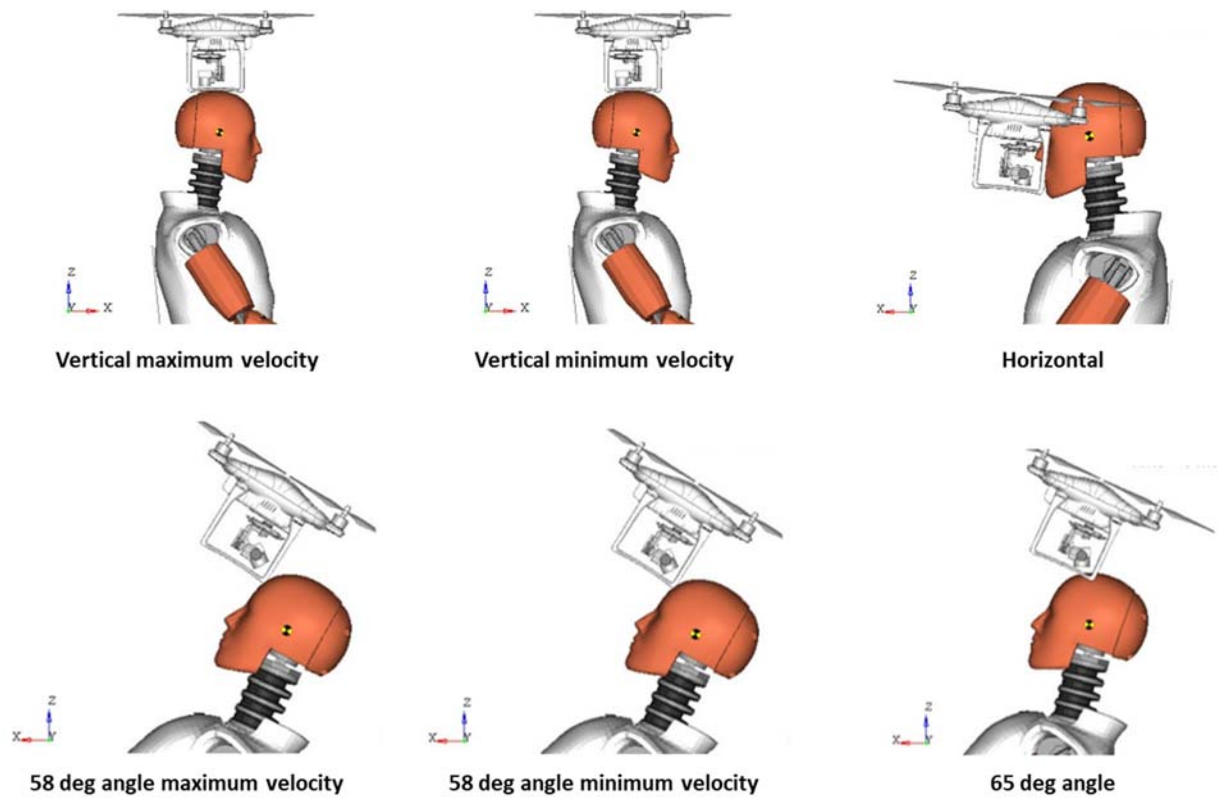

Figure 41. Task A11 test impact configurations analyzed

The modifications presented in Chapter 3, which were applied to the Quadcopter UAS model from the airborne collision project, were accepted based on the preliminary results from these impact scenarios. The gimbal and camera area were modeled in detail to achieve a better level of correlation with the experimental tests. Furthermore, a breakaway connection was defined for the two main plastic body shells to separate in a similar way as the tests.

In order to increase the level of confidence in the DJI Phantom III and eBeePlus FEM, additional simulations were performed and compared to the physical tests conducted for this project, which were previously introduced in Chapter 2.

The following sections present the details on the ATD virtual model used for the correlation simulations, as well as the results for the different test scenarios.

4.1 HUMANETICS VIRTUAL FAA HYBRID III 50TH ATD FE MODEL

For the simulations involving the ATD, it was decided to use Humanetics FAA Hybrid III 50th Percentile Male Dummy FE model, version 1.2.2 for LS-DYNA. Humanetics User's Manual [24] provides extensive information on the FE model, recommendations regarding injury criteria extraction, and instructions on dummy positioning. Several case studies report the level of accuracy achieved with the ATD virtual model [24] [26]. This section will present some of the most relevant information to this project.

Table 20 summarizes the number of parts, elements, and nodes in the ATD FE model. Figure 42 illustrates the physical and the virtual ATD.

Table 20. Humanetics FAA H3-50 finite element model summary

Entity	Count
Parts	409
Nodes	132,227
1D elements	9,070
2D elements	76,874
3D elements	131,820
Accelerometer elements	12

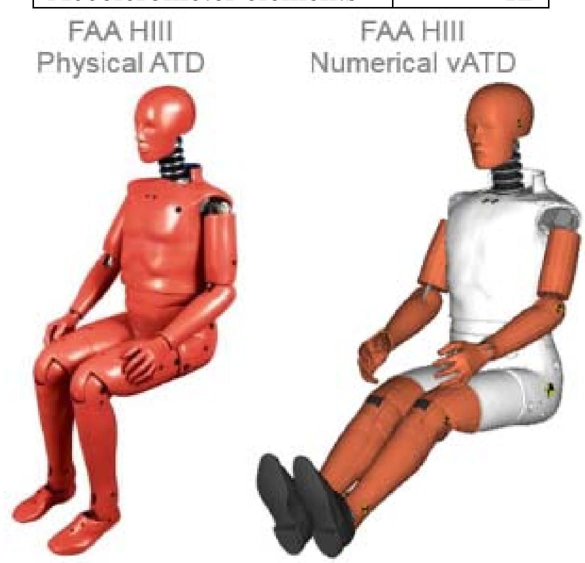

Figure 42. Comparison of physical and numerical versions of the FAA Hybrid-III 50th ATDs

The virtual model contains several sensors that coincide with accelerometer and load cell locations on the physical model. All sensors were defined with the same sign convention and local coordinate systems as the physical dummy. The output of the sensors can be directly exported from the simulation results. The following list enumerates the virtual sensors that apply to the channels used in the experimental tests.

- Tri-axial accelerometer mounted at the head CG.
    - This sensor can also be used to output the rotational velocities at the CG. However, the location of the sensor does not coincide with the angular rate sensor of the dummy.
- Six-axis upper neck load cell, located at the physical load cell's neutral axis.
- Six-axis lower neck load cell.

The neck lower cell bracket of the physical ATD was adjusted so as to orient the neck angle with respect to the thorax. The virtual neck bracket was adjusted to match the experimental setup of the neck assembly angle.

Additionally, three tri-axial accelerometers were virtually modeled in order to account for the peripheral accelerometers of the physical dummy. These accelerometers were positioned based on measurements taken on the physical dummy. The sensor elements were rigidly connected to the skull in the FE model.

4.2 DJI PHANTOM III

This section presents the verification outcomes for the DJI Phantom 3 FE model against the experimental results derived from the test campaigns performed under task A11 and this present effort. The summary of all injury criteria results for both experimental test and simulation are tabulated and compared in this section. In addition, this section discusses a sample case for tests and simulation, comparing kinematics, the time history of the accelerometer, and the time history of the upper load cell sensor. This exercise will demonstrate the level of accuracy achieved by the simulation predictions. The remaining data comparisons can be found in APPENDIX D—.

In order to provide a brief label that accurately describes each combination of impact orientation, angle, and velocity, the following convention was created to name each impact case presented in this project:

Every impact condition will be coded using following characters X(YYZ)-VV

- X – UAS approach global direction
    - Angled trajectory
    - Horizontal flight
    - Vertical drop
- YY – Impact angle respect to the horizon
- Z – Impact direction relative to target's head orientation
    - Frontal impact
    - Rear impact
    - Sideward impact
- VV – Impact velocity in ft/s

Example A(55S)-65

- Angled
- 55 degree
- Sideward
- 65 ft/s

4.2.1 A11 Conditions

During A11 project [22], the DJI Phantom 3 was impacted against an FAA Hybrid III 50th ATD for eight different test configurations, with varying impact angles and speed. Three repetitions were executed for each impact configuration. Six of the eight conditions tested were simulated with the respective FE models. For A11, only UAS bottom orientations - first impact were investigated for vertical and angled impacts. These tests were used to calibrate the UAS model, which was originally created for airborne collision events. The calibration process aimed to enhance the predictions of the FE model for ground collision scenarios. The changes made in the UAS model, which were presented in Chapter 3, were implemented based on the feedback obtained by comparing all six tests against their corresponding simulation. The results of the most up-to-date UAS version are collected in this chapter. Table 21 presents the test matrix of the A11 test campaign for the DJI Phantom 3.

Table 21. Test matrix for A11 cases used for DJI Phantom 3 finite element model validation

Test No.	Impact Trajectory	Nominal Mass (lb)	Nominal Impact Speed (ft/s)	Achieved Impact Speed (ft/s)	Nominal Impact KE (ft-lb)	Achieved Impact KE (ft-lb)
V(90)-20-1	Vertical	2.67	36.0	32.5	53.8	43.8
V(90)-20-2	Vertical	2.67	36.0	32.3	53.8	43.3
V(90)-20-3	Vertical	2.67	36.0	32.5	53.8	43.8
V(90)-50-1	Vertical	2.67	57.0	49.6	134.8	102.1
V(90)-50-2	Vertical	2.67	57.0	49.2	134.8	100.4
V(90)-50-3	Vertical	2.67	57.0	49.1	134.8	100.0
H(0)-4.5-1	Horizontal	2.67	17.0	17.3	12.0	12.4
H(0)-4.5-2	Horizontal	2.67	17.0	17.3	12.0	12.4
H(0)-4.5-3	Horizontal	2.67	17.0	17.2	12.0	12.3
A(65)-36.5-1	65 deg angle	2.67	36.5	37.0	55.3	56.8
A(65)-36.5-2	65 deg angle	2.67	36.5	36.8	55.3	56.2
A(65)-36.5-4	65 deg angle	2.67	36.5	36.6	55.3	55.6
A(58)-46.1-1	58 deg angle	2.67	46.1	46.0	88.2	87.8
A(58)-46.1-2	58 deg angle	2.67	46.1	46.1	88.2	88.2
A(58)-46.1-3	58 deg angle	2.67	46.1	46.1	88.2	88.2
A(58)-51.7-1	58 deg angle	2.67	51.7	50.4	110.9	105.4
A(58)-51.7-2	58 deg angle	2.67	51.7	50.5	110.9	105.8
A(58)-51.7-3	58 deg angle	2.67	51.7	50.5	110.9	105.8

As mentioned previously, six different test configuration were used for correlation purposes with the UAS FE model. Table 22 presents a summary of the results for the injury criteria, both experimental and simulated.

Table 22. A11 Test and simulation result comparison

Injury Criteria	V(90)-20				V(90)-50			
	Test 1	Test 2	Test 3	Sim	Test 1	Test 2	Test 3	Sim
Head Acceleration (g)	54.3	56.7	49.2	44.7	82.4	71.5	119.1	88.2
HIC15	12.0	15.0	15.6	23.0	59.5	48.0	42.2	91.4
Upper Neck Tension (lbf)	75.9	76.8	74.8	39.0	43.9	42.2	25.8	18.9
Upper Neck Compression (lbf)	536.2	574.4	564.9	553.9	826.2	776.8	753.5	793.5
Upper Neck Flexion (lbf-ft)	7.16	6.95	6.45	1.44	6.99	7.68	7.60	2.21
Upper Neck Extension (lbf-ft)	11.40	10.87	14.24	8.24	15.76	15.45	16.71	10.46
Upper Neck Shear (lbf)	35.9	31.9	34.8	37.2	48.2	46.8	62.7	63.0
Upper Neck Nij	0.42	0.45	0.47	0.42	0.65	0.62	0.63	0.59

Injury Criteria	H(0)-4.5				A(65)-36.5			
	Test 1	Test 2	Test 3	Sim	Test 1	Test 2	Test 3	Sim
Head Acceleration (g)	25.1	60.7	43.2	52.4	60.1	60.9	55.6	59.0
HIC15	7.8	29.2	19.9	29.4	39.6	30.3	26.3	39.4
Upper Neck Tension (lbf)	12.4	27.3	20.6	45.8	68.1	54.6	49.2	43.8
Upper Neck Compression (lbf)	65.2	118.2	93.5	91.3	626.5	596.3	579.9	550.0
Upper Neck Flexion (lbf-ft)	4.02	4.00	4.14	1.38	23.50	29.17	28.65	28.45
Upper Neck Extension (lbf-ft)	5.45	6.12	6.22	4.77	5.96	6.14	5.22	0.46
Upper Neck Shear (lbf)	32.0	71.5	50.7	62.3	133.6	139.5	135.5	87.9
Upper Neck Nij	0.08	0.10	0.09	0.07	0.53	0.52	0.51	0.43

Injury Criteria	A(58)-46.1				A(58)-51.7			
	Test 1	Test 2	Test 3	Sim	Test 1	Test 2	Test 3	Sim
Head Acceleration (g)	112.7	120.5	130.5	131.2	119.8	139.2	126.6	151.1
HIC15	107.9	119.1	147.8	143.5	137.2	165.1	123.6	181.0
Upper Neck Tension (lbf)	49.7	62.9	65.1	97.6	57.6	92.0	82.9	91.6
Upper Neck Compression (lbf)	619.6	593.6	612.1	603.7	581.4	602.6	601.7	634.3
Upper Neck Flexion (lbf-ft)	34.05	28.74	33.22	14.06	22.54	27.96	25.57	13.68
Upper Neck Extension (lbf-ft)	7.92	8.63	9.93	1.37	9.63	10.07	9.80	3.43
Upper Neck Shear (lbf)	171.2	174.8	196.5	144.3	192.9	208.2	183.0	153.4
Upper Neck Nij	0.53	0.50	0.52	0.46	0.48	0.50	0.50	0.48

Figure 43 summarizes the injury values for all test repetitions and simulations in bar chart format. Table 22 values have been normalized with the injury limits introduced in Chapter 2. For all six test configurations, simulation injury values are within the test scatter for most criteria, and within 10% of the test mean value for all the criteria.

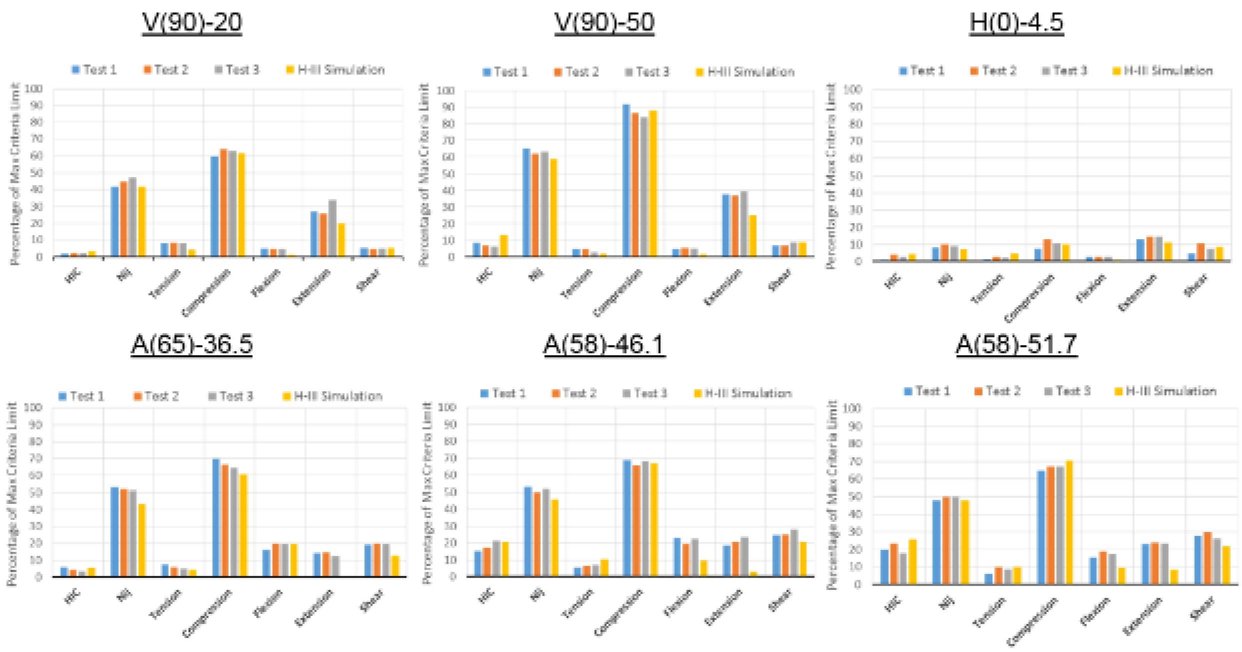

Figure 43. Bar chart with summary of injury criteria for A11 test vs simulation comparison.

The following set of images compares the kinematics between test case V(90)-50 and its corresponding simulation. This case produced the highest level of injury values, and was selected to present the level of accuracy achieved by the model. The remaining five cases are attached in APPENDIX D—. These results show that, not only are the peak load values matching the experimental data, but also the whole time history of the event presents a similar profile. The kinematics show a good correlation in the deformations and rigid body motion of the UAS during and after impact. Moreover, the time history of the head translational acceleration, angular rate, upper neck forces, and upper neck moments lie within the test plot scatter. To summarize, the simulation demonstrates the capability to predict the physics of the impact event accurately.

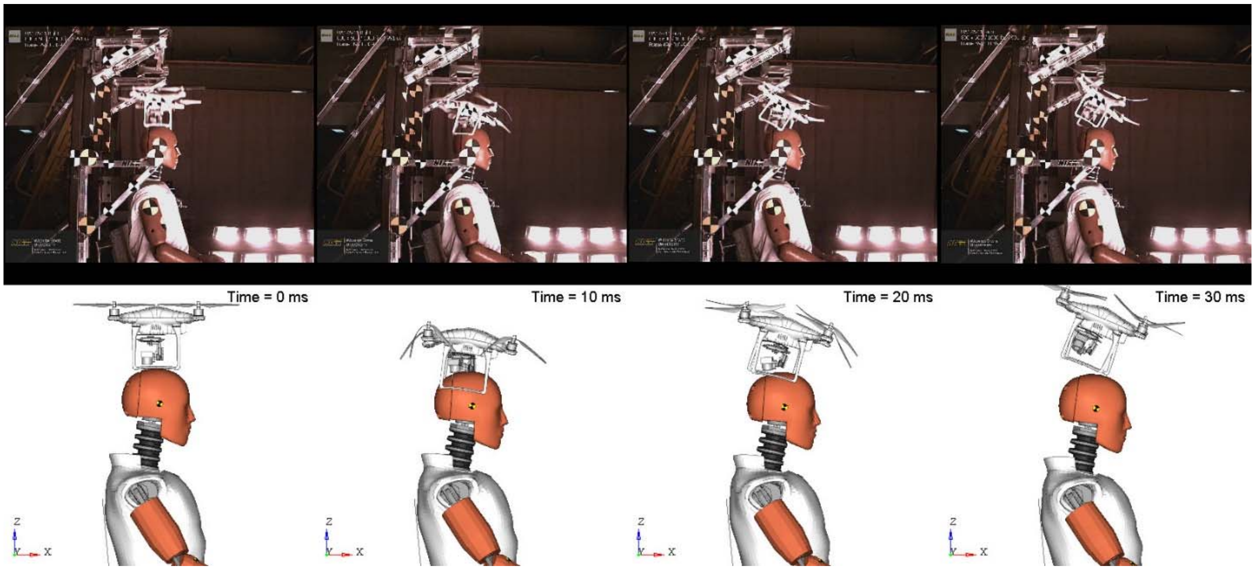

Figure 44. Test vs simulation comparison; DJI Phantom 3, 2.67 lb, bottom, 57 fps, vertical; A11 ATD test, top of the head; kinematics

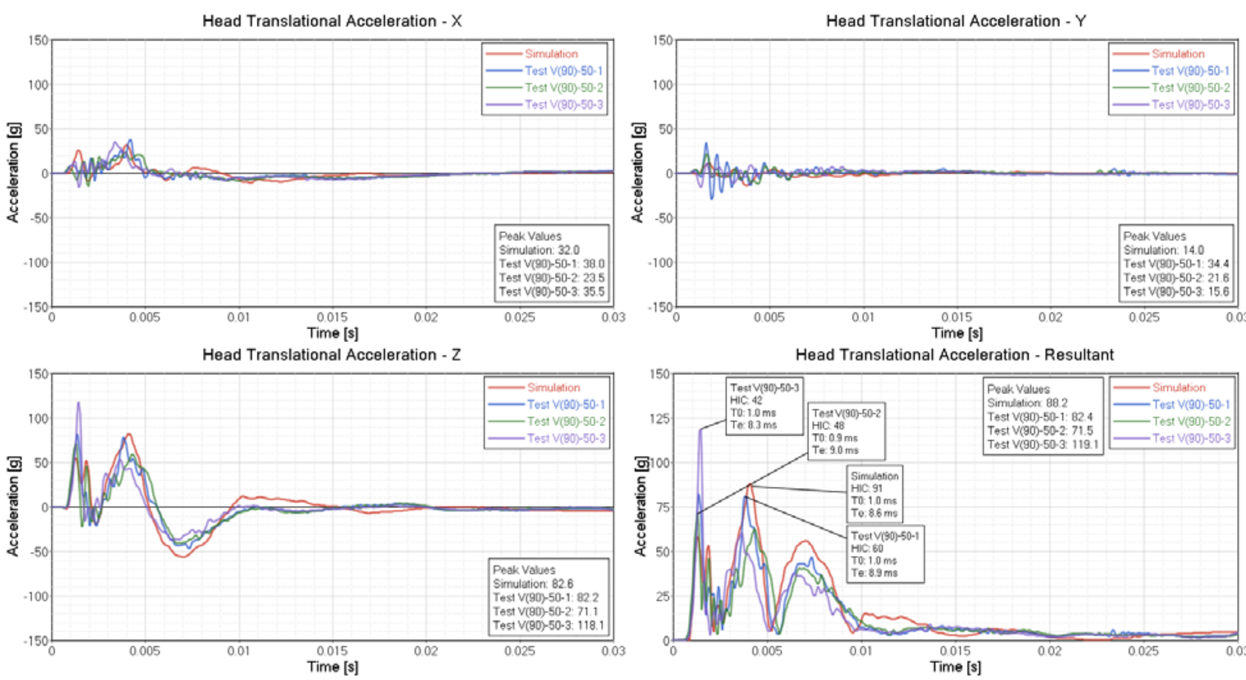

Figure 45. Test vs simulation comparison; DJI Phantom 3, 2.67 lb, bottom, 57 fps, vertical; A11 ATD test, top of the head; head CG acceleration

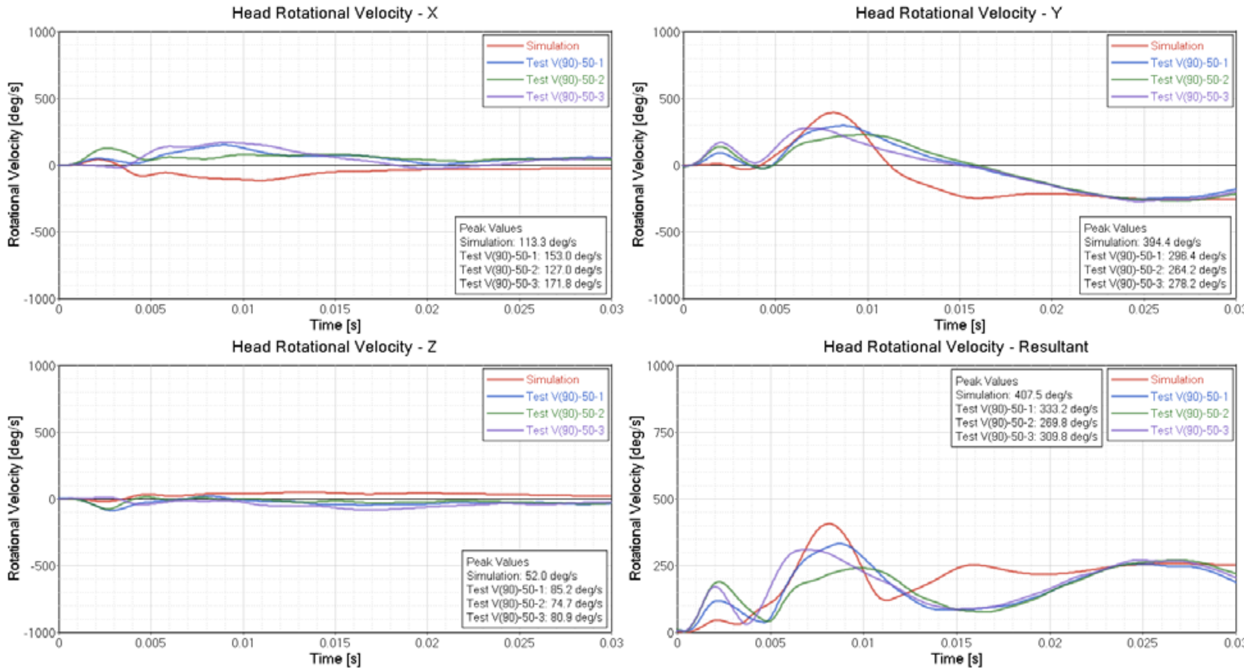

Figure 46. Test vs simulation comparison; DJI Phantom 3, 2.67 lb, bottom, 57 fps, vertical; A11 ATD test, top of the head; head angular rate

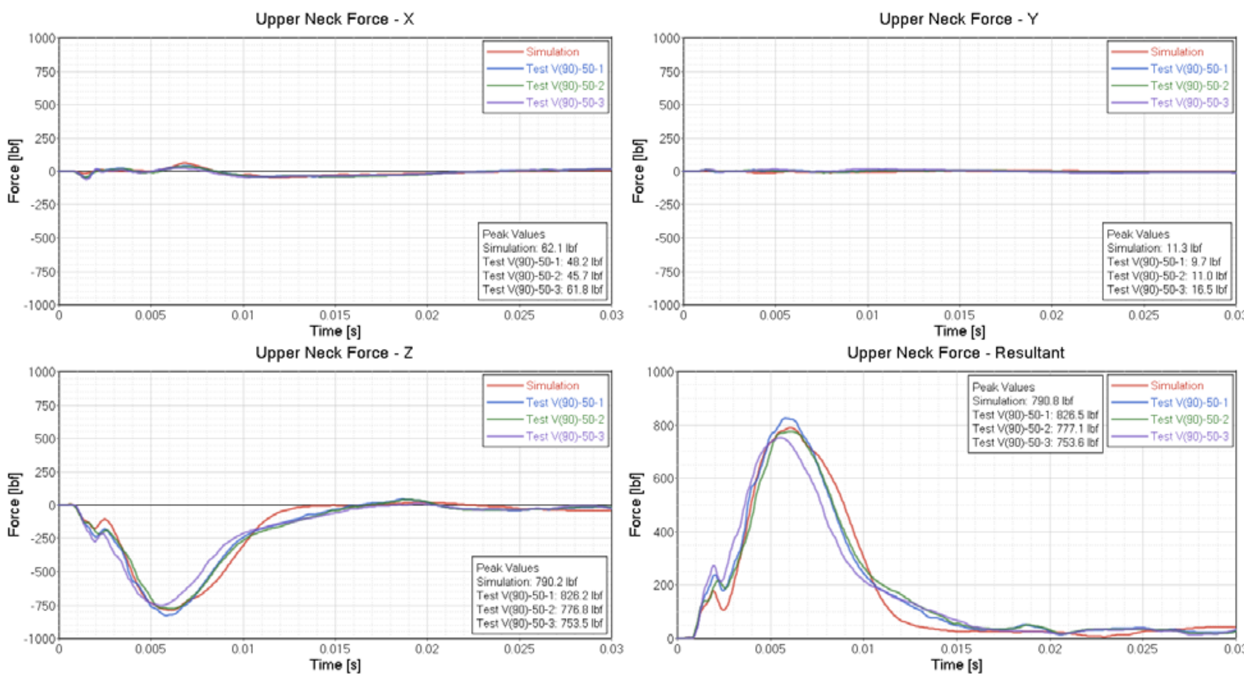

Figure 47. Test vs simulation comparison; DJI Phantom 3, 2.67 lb, bottom, 57 fps, vertical; A11 ATD test, top of the head; upper neck force

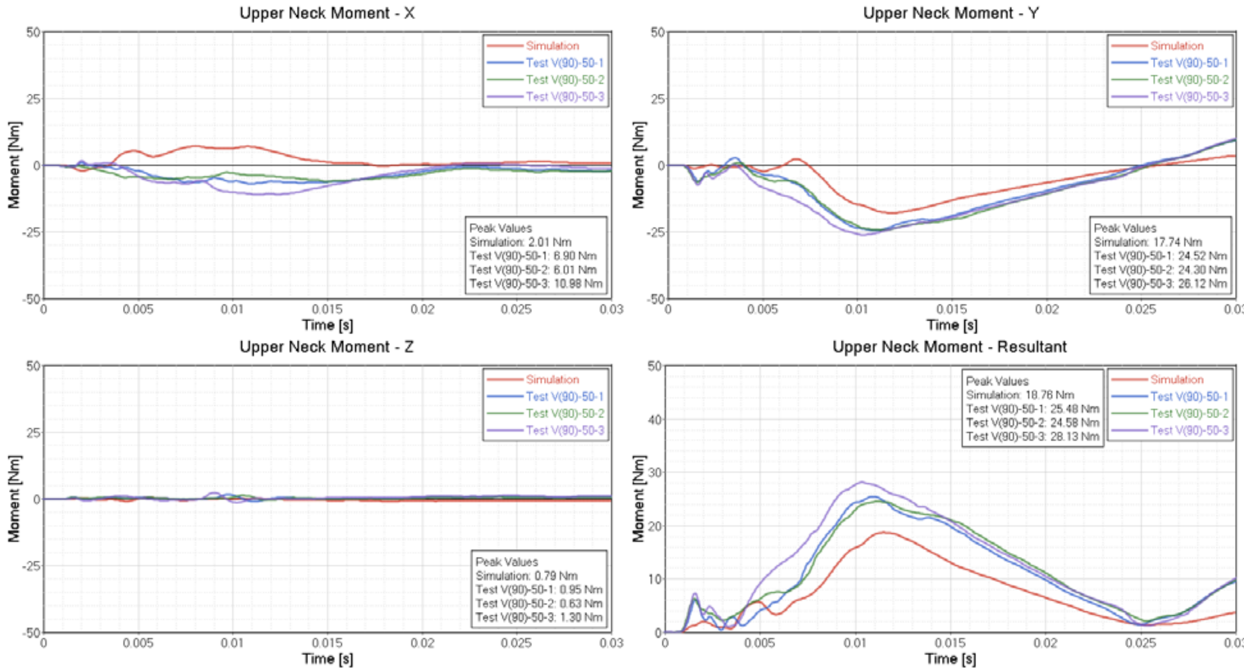

Figure 48. Test vs simulation comparison; DJI Phantom 3, 2.67 lb, bottom, 57 fps, vertical; A11 ATD test, top of the head; upper neck moment

4.2.2 A14 Worst-Case Orientation Study

This section introduces the parametric studies carried out to determine the worst-case orientation for the DJI Phantom III impact against the Humanetics model. NIAR used simulation to evaluate the Phantom worst impact orientation for each of the flying trajectories defined by UAH and used for Chapter 2 test matrix. These trajectories are:

- Side impact - Side head impact
- Vertical impact - Top head impact
- Front angled impact - UAS hits the head on the front at 55 degree
- Rear-angled impact - UAS hits the head on the back at 55 degree
- Side-angle impact - UAS hits the head on the side at 55 degree

The 55-degree angle was selected prior to the test matrix definition, based on preliminary studies carried out by UAH. Further work refined the test conditions, determining the angle of impact at 58-degrees. This later update does not compromise any of the work done for this section because the only variable of this analysis was the UAS orientation.

4.2.2.1 Side Impact

Figure 49 illustrates the four side-impact orientations simulated for this parametric study.

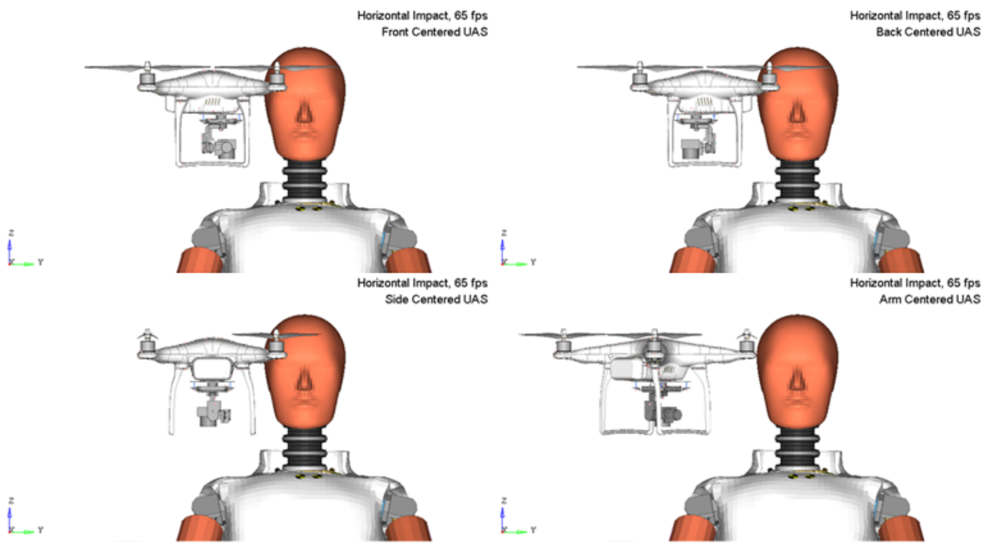

Figure 49. Worst-case ATD side impacts; simulation setup

Figure 50 summarizes the injury criteria values for the four side impact orientations. Two criteria limits were exceeded. The upper neck shear values were excessively high for all four cases, while in terms of HIC accelerations, Phantom impacts along the battery longitudinal direction seem to be more critical. Based on this information, the worst possible side-impact orientations are back and front orientation, respectively.

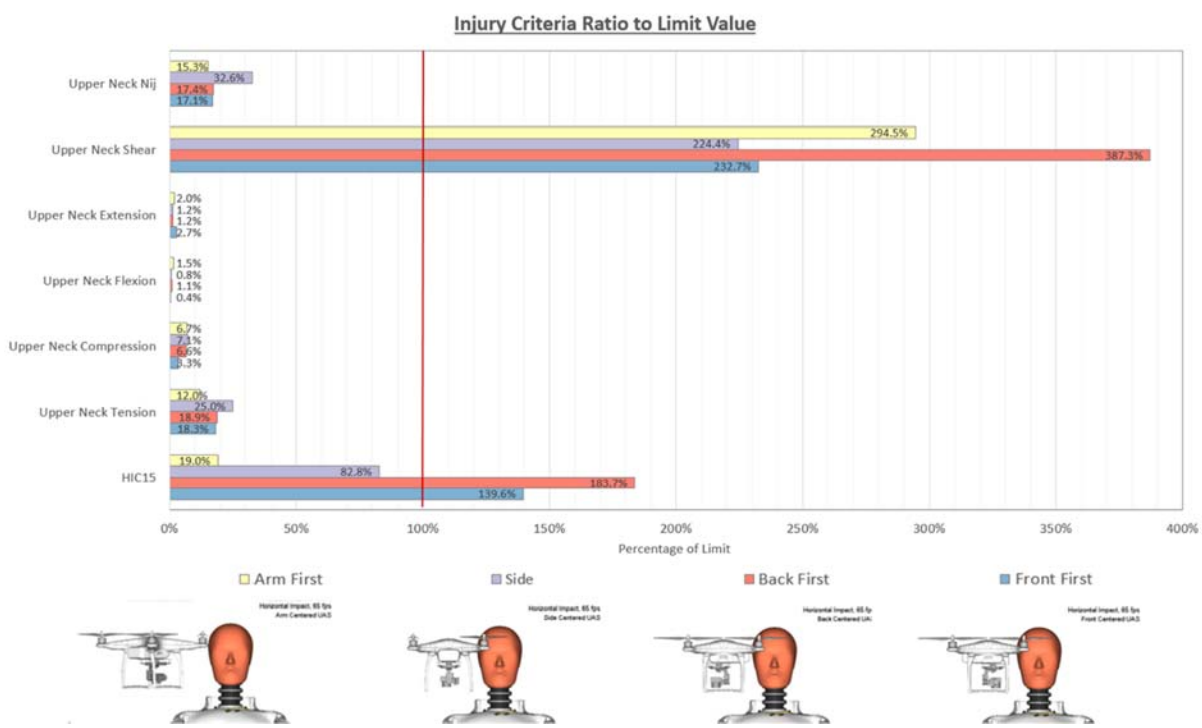

Figure 50. Worst-case ATD side impacts; injury criteria evaluation

4.2.2.2 Vertical Impact

Figure 51 illustrates the five vertical-impact orientations simulated for this parametric study.

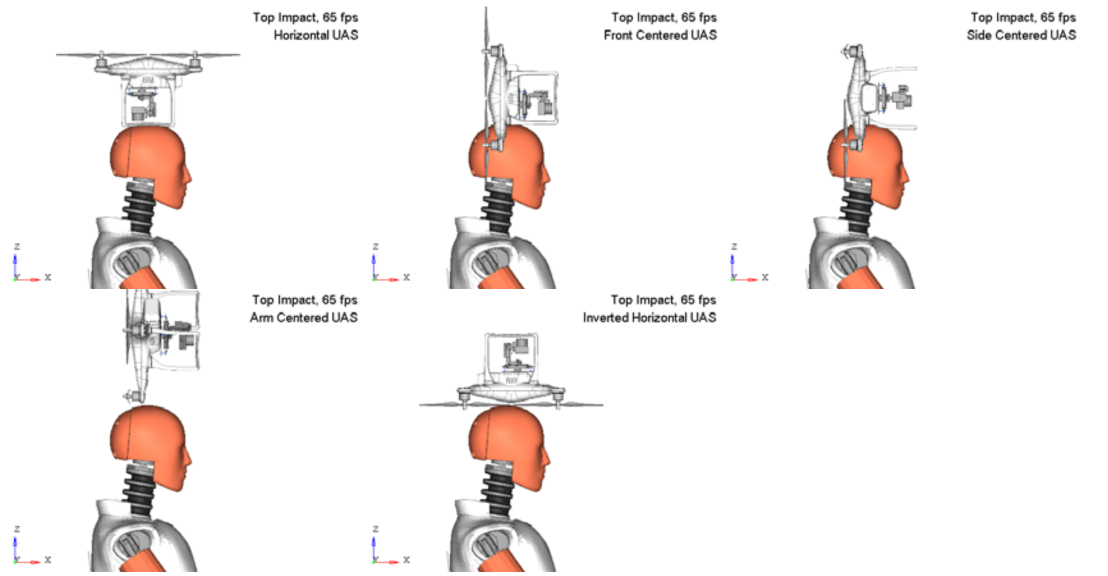

Figure 51. Worst-case ATD vertical impacts; simulation setup

Figure 52 collects the injury criteria values for the five vertical-impact orientations. The simulations did not comply with two of the criteria. Four of the five orientations did exceed the upper neck compression limit, while in terms of HIC accelerations, "front first" exceeded the acceleration levels.

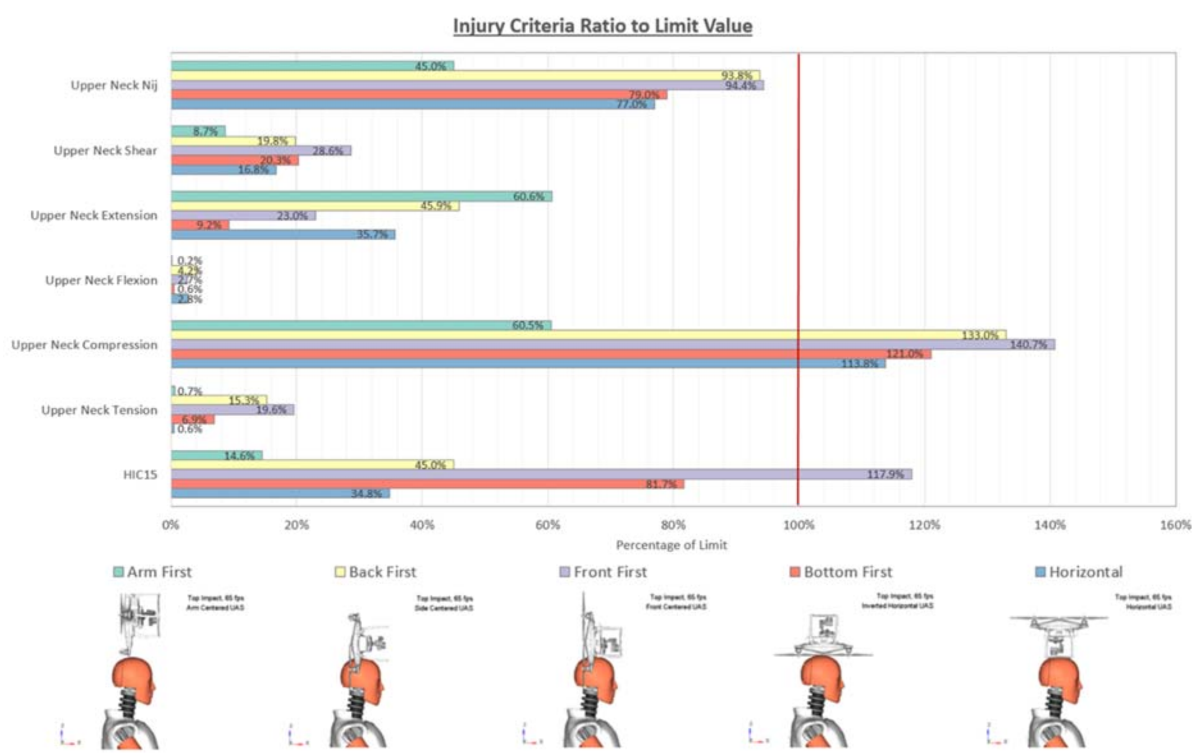

Figure 52. Worst-case ATD vertical impacts; injury criteria evaluation

4.2.2.3 Front-Angled Impact

Figure 53 illustrates the five front-angled impact orientations simulated for this parametric study.

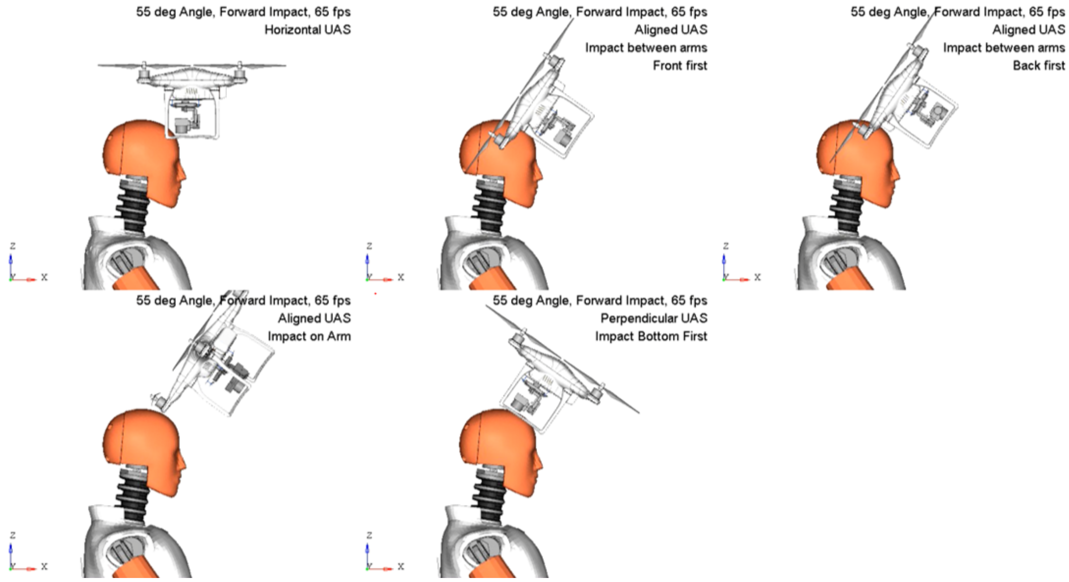

Figure 53. Worst-case ATD front-angled impacts; simulation setup

Figure 54 collects the injury criteria values for the five front-angled-impact orientations. The simulations did not conform with two of the criteria. Three of the five orientations did exceed the upper neck compression limit, while in terms of HIC accelerations, "front first" and "back first" exceeded the acceleration levels.

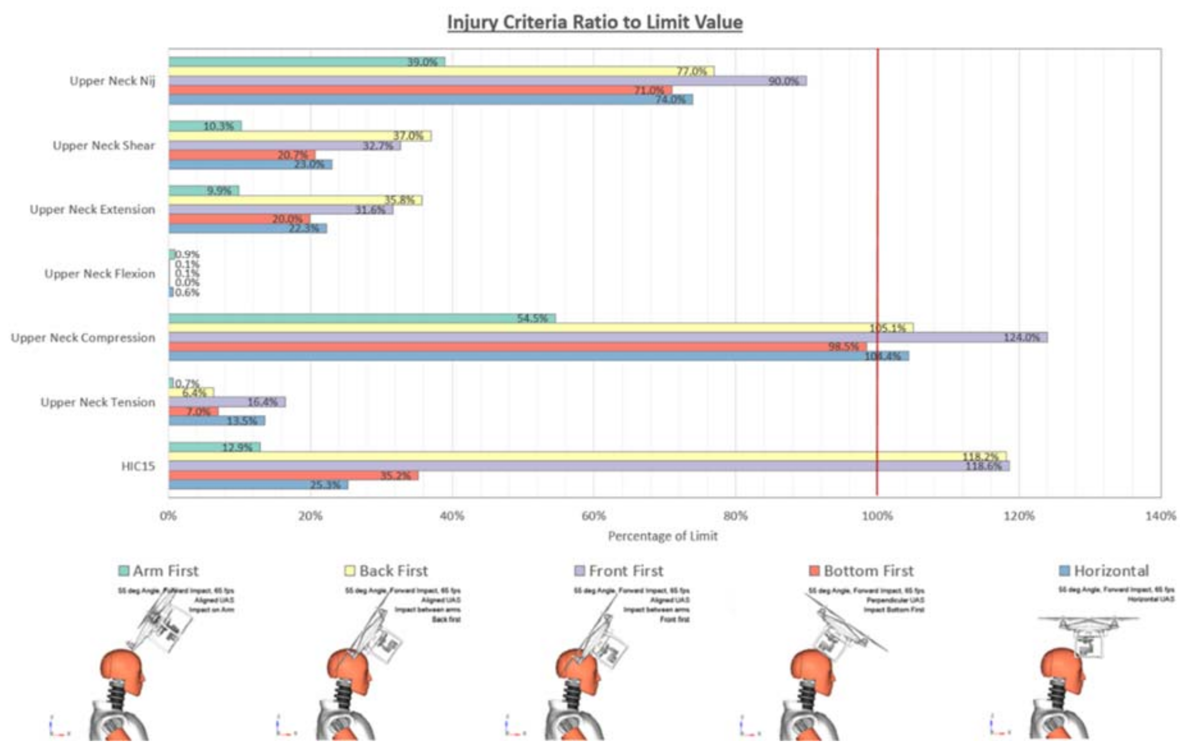

Figure 54. Worst-case ATD front-angled impacts; injury criteria evaluation

4.2.2.4 Rear-Angled Impact

Figure 55 illustrates the five rear-angled impact orientations simulated for this parametric study.

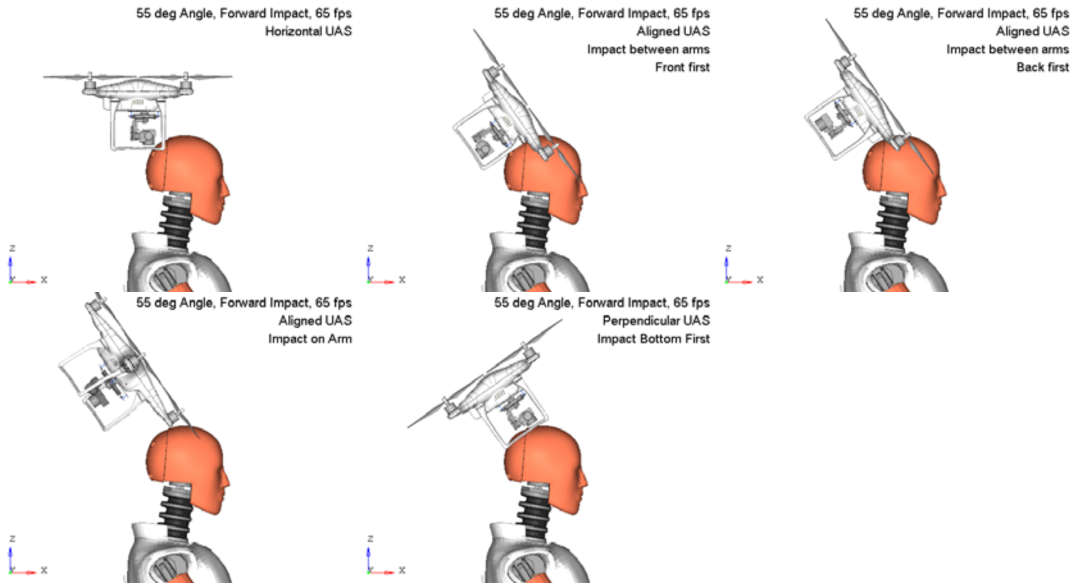

Figure 55. Worst-case ATD rear-angled impacts; simulation setup

Figure 56 collects the injury criteria values for the five rear-angled-impact orientations. HIC accelerations exceeded the limit for “front” and “back” first”, with “front first” being more severe.

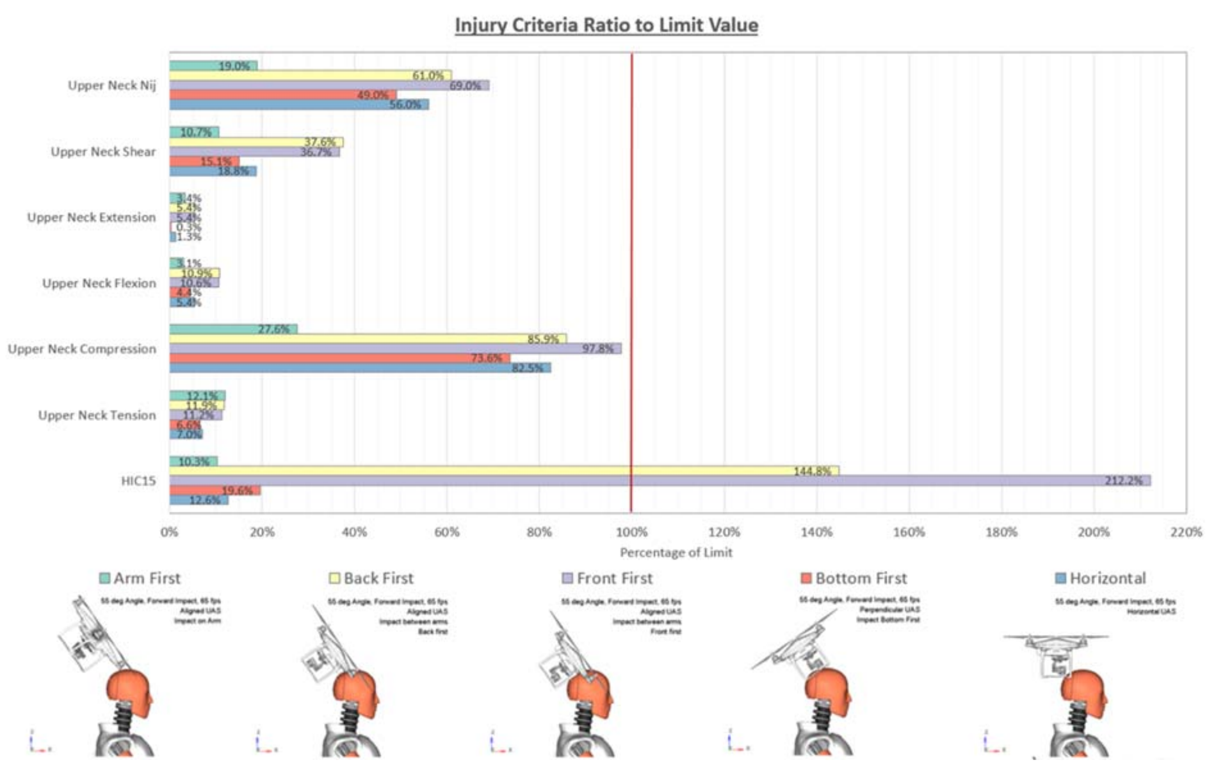

Figure 56. Worst-case ATD rear-angled impacts; injury criteria evaluation

4.2.2.5 Side-Angled Impact

Figure 57 illustrates the five side-angled impact orientations simulated for this parametric study.

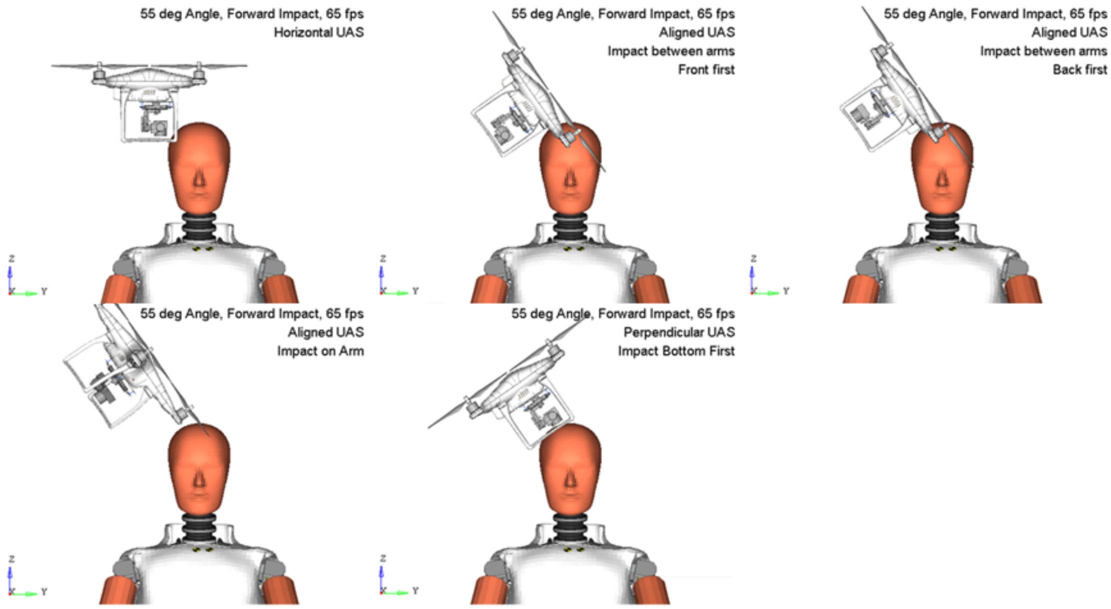

Figure 57. Worst-case ATD side-angled impacts; simulation setup

Figure 58 collects the injury criteria values for the five front-angled-impact orientations. The HIC limit was exceeded for the "back first" orientation.

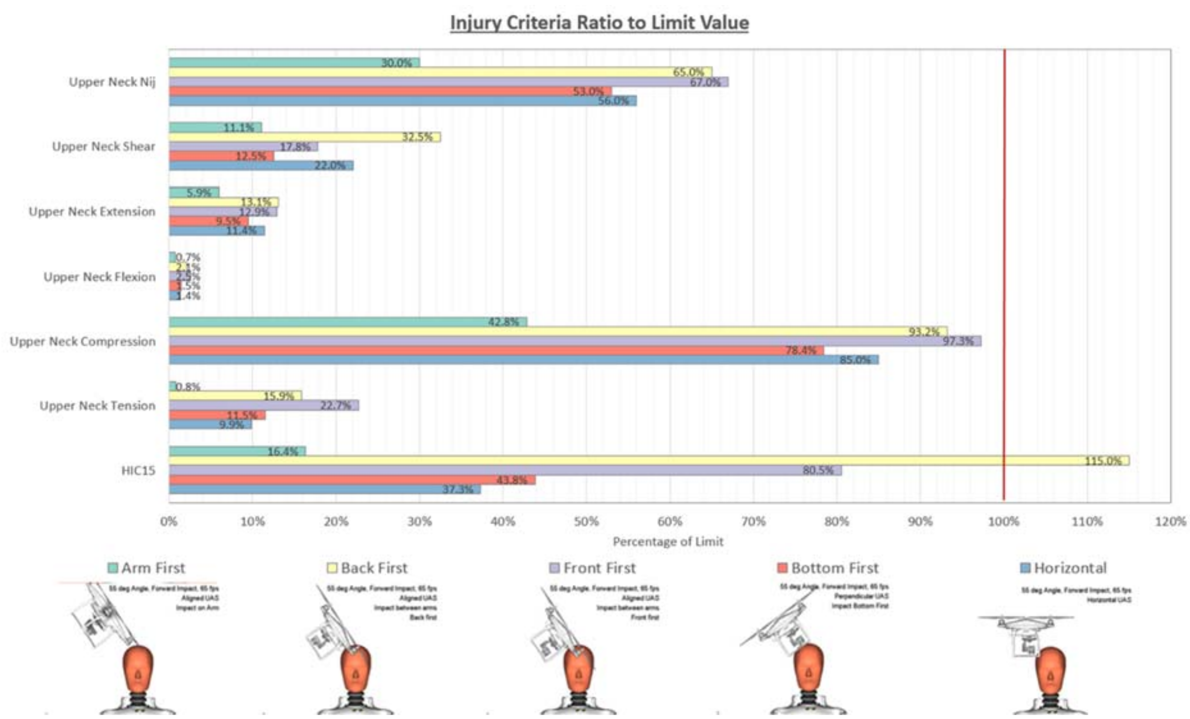

Figure 58. Worst-case ATD front-angled impacts; injury criteria evaluation

4.2.2.6 Worst-case Orientation

Table 23 summarizes the amount whereby criteria limits were exceeded for the most relevant orientations analyzed in this section. The superscript associated with each case indicates the number of worst cases per impact configuration.

Table 23. Injury criteria exceeded limits

		UAS orientation		
		Front first	Back first	Arm first
ATD impact configuration	Side impact	2	2^2	1
	Vertical impact	2^2	1	1
	Front-angled impact	2^2	2	0
	Rear-angled impact	1^1	1	0
	Side-angled impact	0	1^1	0
TOTAL		$\mathbf{7^5}$	$\mathbf{7^3}$	**2**

The simulation study determined that “front first” is the impact orientation with the largest number of severe cases per impact configuration. This conclusion was taken into account by UAH team and reflected in their efforts in elaborating the Chapter 2 test matrix.

4.2.3 A14 Conditions

The calibrated UAS finite element model in the impact simulations, which was introduced in Section 4.2.1, was used to predict worst-case impact scenarios against the ATD. The knowledge gained out of these predictions was used to plan the test conditions defined in Chapter 2. The present section compares test and simulation results for one of the twenty-four cases involving the DJI Phantom 3 in this project. The Phantom 3 FE model was frozen before performing the test campaign, so the results are pure predictions and no calibration was performed.

The test matrix, with the test conditions and results, can be found in Chapter 2. Table 24 collects a summary of the injury criteria results concerning the experimental and simulation data. A comparison of the kinematics and the time history from the sensors, processed to extract injury levels for each of the twenty-four cases, are presented in APPENDIX E—.

In general, the results show good agreement between simulation and test, especially for the most critical injury criteria. In contrast, it is noticeable that the UAS FE model correlates better for vertical and frontal conditions, rather than lateral and rear impacts.

Table 24. A14 Test and simulation result comparison

Injury Criteria	Test 1		Test 2		Test 3		Test 4	
	Test	Sim	Test	Sim	Test	Sim	Test	Sim
Head Acceleration (g)	52.96	79.32	65.24	73.84	42.58	44.28	81.87	132.75
HIC15	20.79	22.70	22.67	48.74	10.44	12.64	40.40	74.43
Head 3 ms (g)	26.17	26.74	25.43	38.15	17.94	19.70	33.58	37.15
BrIC	0.094	0.051	0.132	0.082	0.120	0.120	0.093	0.071
Probability of Concussion	0.003	0.005	0.022	0.009	0.011	0.002	0.021	0.240
Upper Neck Tension (lbf)	40.5	2.7	21.2	57.7	14.9	23.7	60.0	13.1
Upper Neck Compression (lbf)	575.9	465.5	575.6	509.1	436.4	367.5	702.2	638.4
Upper Neck Flexion (lbf-ft)	8.45	5.44	11.74	8.85	14.03	13.68	7.96	7.96
Upper Neck Extension (lbf-ft)	0.92	0.66	1.74	0.63	1.77	0.63	0.77	1.16
Upper Neck Shear (lbf)	42.58	41.10	54.93	42.20	53.94	40.16	44.27	68.44
Lateral Moment (lbf-ft)	2.39	2.44	3.44	4.42	1.87	1.67	9.34	4.83
Twisting Moment (lbf-ft)	0.40	0.12	0.92	0.43	0.58	0.25	1.40	0.56
Upper Neck Nij	0.45	0.34	0.46	0.38	0.36	0.28	0.54	0.48

Injury Criteria	Test 5		Test 6		Test 7		Test 8	
	Test	Sim	Test	Sim	Test	Sim	Test	Sim
Head Acceleration (g)	104.98	125.48	65.25	67.10	21.81	25.81	27.90	44.97
HIC15	102.03	108.71	22.50	24.54	4.83	4.49	7.92	12.59
Head 3 ms (g)	47.44	49.12	22.110	27.71	14.19	14.35	16.89	23.31
BrIC	0.123	0.111	0.099	0.106	0.136	0.058	0.236	0.082
Probability of Concussion	0.505	0.227	0.036	0.006	0.003	0.001	0.015	0.004
Upper Neck Tension (lbf)	44.4	48.9	12.9	16.9	34.8	8.1	34.2	13.2
Upper Neck Compression (lbf)	827.7	687.2	465.1	404.6	441.6	366.5	492.5	461.8
Upper Neck Flexion (lbf-ft)	9.66	9.35	8.92	12.62	4.57	4.94	16.73	8.56
Upper Neck Extension (lbf-ft)	2.34	0.63	2.46	0.63	1.54	1.38	1.70	1.48
Upper Neck Shear (lbf)	53.26	57.53	49.76	45.09	36.97	35.79	55.06	42.38
Lateral Moment (lbf-ft)	4.38	5.82	2.86	1.34	15.05	11.18	19.69	10.13
Twisting Moment (lbf-ft)	1.21	0.49	0.92	0.20	1.27	0.55	3.06	0.73
Upper Neck Nij	0.64	0.51	0.37	0.30	0.32	0.27	0.37	0.34

Injury Criteria	Test 9		Test 10		Test 11		Test 12	
	Test	Sim	Test	Sim	Test	Sim	Test	Sim
Head Acceleration (g)	52.37	84.91	114.09	155.16	145.32	187.44	146.38	190.45
HIC15	36.07	78.79	172.68	256.87	255.15	357.36	301.18	391.02
Head 3 ms (g)	30.13	34.75	50.28	45.25	52.84	42.03	48.81	41.61
BrIC	0.352	0.227	0.419	0.322	0.508	0.358	0.523	0.358
Probability of Concussion	0.086	0.301	0.562	0.997	0.562	1.000	0.957	1.000
Upper Neck Tension (lbf)	55.9	56.1	198.1	170.3	264.8	171.6	265.8	171.3
Upper Neck Compression (lbf)	13.6	24.8	27.0	62.5	9.7	18.6	9.4	35.8
Upper Neck Flexion (lbf-ft)	2.50	3.87	2.75	2.64	5.91	4.38	3.75	3.27
Upper Neck Extension (lbf-ft)	1.55	0.77	4.83	0.63	2.95	0.63	4.34	0.63
Upper Neck Shear (lbf)	148.27	184.53	233.10	267.04	239.23	305.47	263.25	342.92
Lateral Moment (lbf-ft)	31.38	30.65	48.02	48.83	41.49	39.49	49.55	55.85
Twisting Moment (lbf-ft)	5.76	3.74	5.63	4.94	12.13	6.33	11.37	5.38
Upper Neck Nij (modified)	0.04	0.04	0.17	0.11	0.18	0.12	0.18	0.12

Injury Criteria	Test 13		Test 14		Test 15		Test 16	
	Test	Sim	Test	Sim	Test	Sim	Test	Sim
Head Acceleration (g)	245.75	189.20	324.02	259.27	169.69	159.13	175.48	329.91
HIC15	420.73	409.80	736.20	883.99	291.06	229.98	346.77	180.73
Head 3 ms (g)	70.82	75.37	87.84	87.04	53.74	54.38	57.24	55.41
BrIC	0.141	0.110	0.159	0.094	0.293	0.227	0.306	0.245
Probability of Concussion	1.000	0.997	1.000	1.000	0.935	0.859	0.992	0.992
Upper Neck Tension (lbf)	53.2	53.7	52.6	63.9	57.9	44.9	57.6	56.2
Upper Neck Compression (lbf)	1192.7	1014.8	1377.1	1283.0	871.5	764.5	922.0	862.1
Upper Neck Flexion (lbf-ft)	9.82	8.04	4.89	8.17	28.35	13.37	33.15	14.31
Upper Neck Extension (lbf-ft)	2.28	0.63	8.38	1.28	12.45	12.86	13.95	14.28
Upper Neck Shear (lbf)	83.29	112.04	97.26	135.08	223.32	136.07	260.60	163.86
Lateral Moment (lbf-ft)	8.31	13.07	3.00	8.94	8.31	8.30	3.47	7.93
Twisting Moment (lbf-ft)	0.87	1.13	0.82	1.69	2.17	1.57	1.12	1.86
Upper Neck Nij	0.89	0.73	1.00	0.95	0.69	0.58	0.74	0.66

Injury Criteria	Test 17		Test 18		Test 19		Test 20	
	Test	Sim	Test	Sim	Test	Sim	Test	Sim
Head Acceleration (g)	191.06	190.52	232.21	151.37	233.81	153.07	250.80	183.98
HIC15	446.44	410.28	414.87	255.33	536.79	364.19	688.18	446.70
Head 3 ms (g)	58.80	59.36	69.05	69.77	73.49	71.64	78.14	73.18
BrIC	0.320	0.267	0.295	0.208	0.349	0.236	0.353	0.246
Probability of Concussion	0.997	0.950	1.000	0.776	1.000	0.884	1.000	0.950
Upper Neck Tension (lbf)	70.5	65.5	43.8	57.1	64.28	75.51	70.82	91.19
Upper Neck Compression (lbf)	957.6	882.9	991.3	793.3	1130.05	840.82	1166.06	883.26
Upper Neck Flexion (lbf-ft)	36.25	20.48	14.03	16.56	18.84	18.71	21.07	19.06
Upper Neck Extension (lbf-ft)	13.77	16.53	14.74	13.26	18.07	18.64	19.97	21.08
Upper Neck Shear (lbf)	280.17	183.47	231.19	118.23	245.24	166.64	284.75	197.93
Lateral Moment (lbf-ft)	4.64	4.06	9.22	3.64	8.50	6.40	7.56	8.37
Twisting Moment (lbf-ft)	1.73	1.11	1.81	1.01	2.30	1.46	1.76	1.63
Upper Neck Nij	0.77	0.68	0.81	0.61	0.97	0.68	1.00	0.72

Injury Criteria	Test 21		Test 22		Test 23		Test 24	
	Test	Sim	Test	Sim	Test	Sim	Test	Sim
Head Acceleration (g)	42.46	51.79	128.73	153.52	155.87	123.91	153.81	171.39
HIC15	18.76	34.49	149.70	179.70	189.54	199.75	233.49	268.86
Head 3 ms (g)	22.98	27.22	50.89	49.86	52.88	56.06	56.08	51.70
BrIC	0.297	0.178	0.310	0.229	0.393	0.265	0.392	0.260
Probability of Concussion	0.018	0.006	0.916	0.996	0.989	0.923	0.993	1.000
Upper Neck Tension (lbf)	19.82	59.81	80.84	102.03	102.91	117.89	47.77	155.96
Upper Neck Compression (lbf)	396.34	411.88	783.19	621.13	845.71	723.39	880.46	749.52
Upper Neck Flexion (lbf-ft)	8.25	4.51	9.68	6.48	11.14	7.44	11.73	8.92
Upper Neck Extension (lbf-ft)	8.65	3.13	8.36	2.31	8.16	2.66	9.44	2.58
Upper Neck Shear (lbf)	78.42	101.59	103.21	89.88	123.13	128.52	141.26	116.20
Lateral Moment (lbf-ft)	19.12	12.92	17.51	14.82	28.65	19.98	24.94	20.71
Twisting Moment (lbf-ft)	3.12	2.18	4.46	2.14	6.14	4.45	5.84	2.70
Upper Neck Nij (modified)	0.43	0.43	0.58	0.53	0.60	0.58	0.65	0.62

Figure 59 through Figure 62 present the injury values for all test repetitions and simulations in bar chart format. The values presented in Table 24 are normalized with its corresponding injury limit, previously specified in Chapter 2.

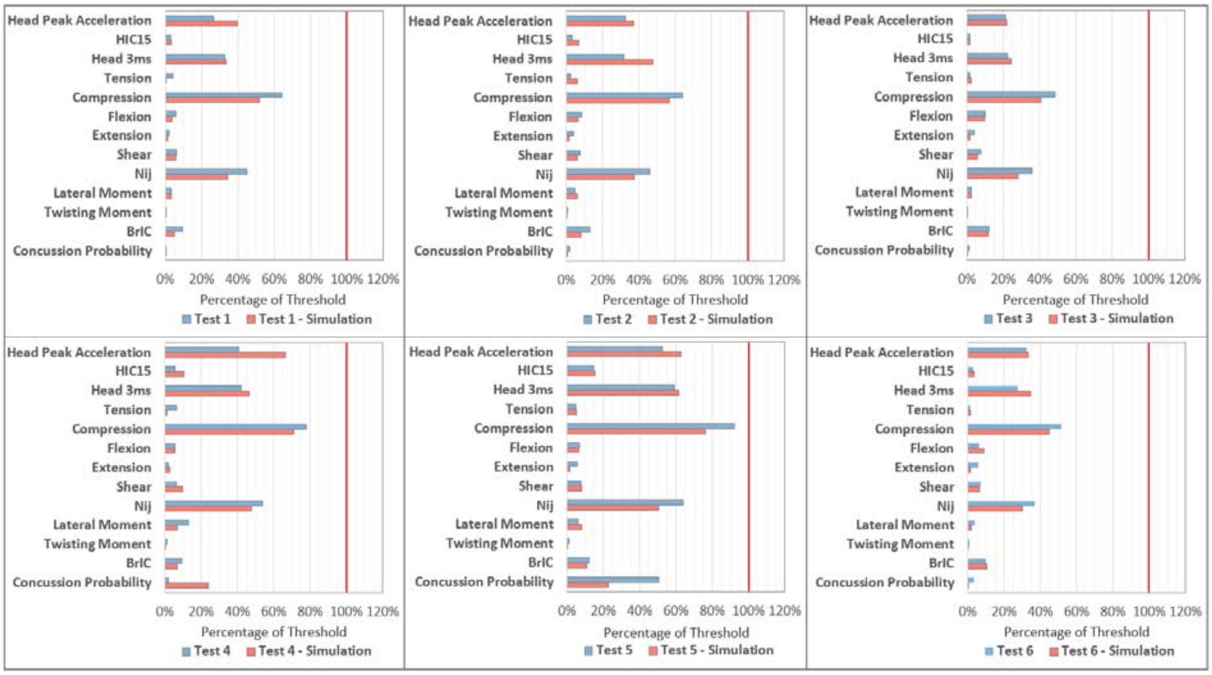

Figure 59. Bar chart with summary of injury criteria for A14 test vs simulation comparison. DJI Phantom 3 tests 1 through 6.

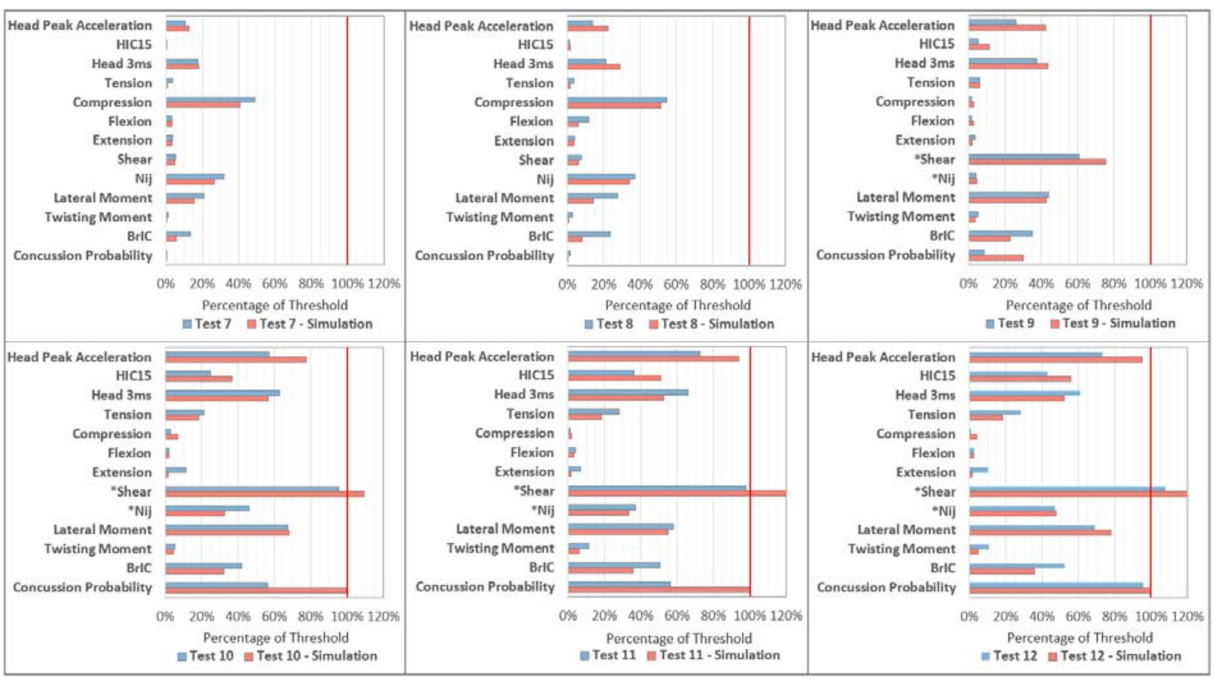

Figure 60. Bar chart with summary of injury criteria for A14 test vs simulation comparison. DJI Phantom 3 tests 7 through 12. The asterisk denotes the modified criteria that were used for side impact test scenarios.

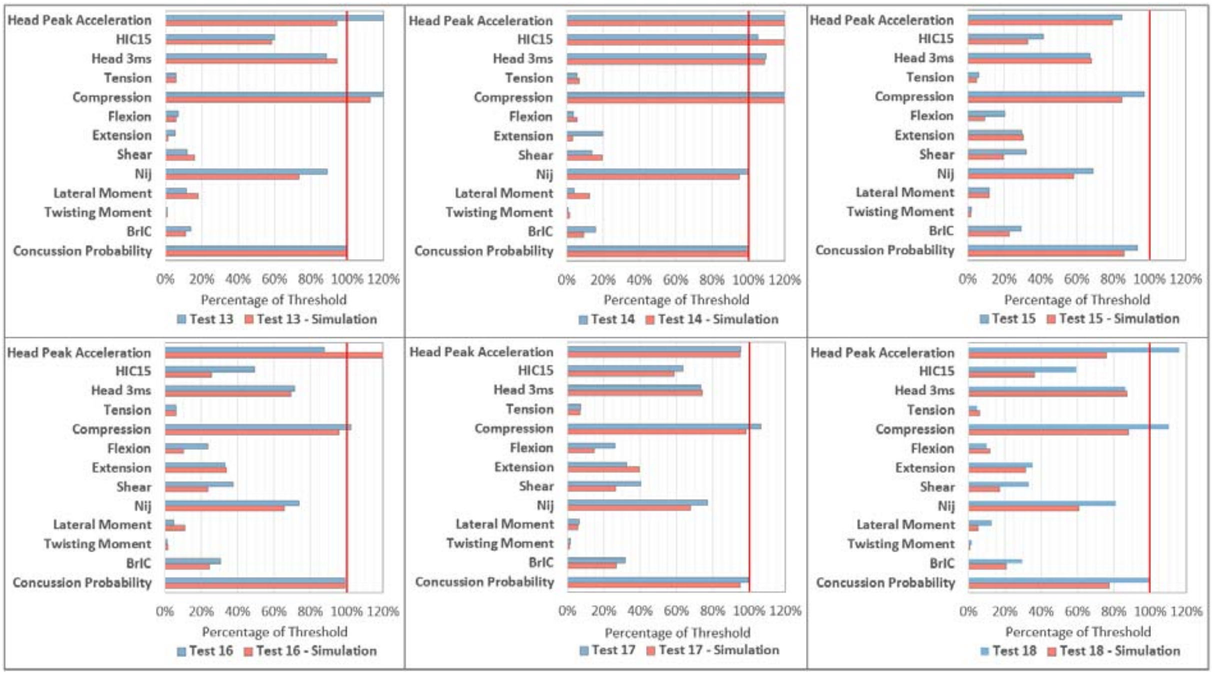

Figure 61. Bar chart with summary of injury criteria for A14 test vs simulation comparison. DJI Phantom 3 tests 13 through 18.

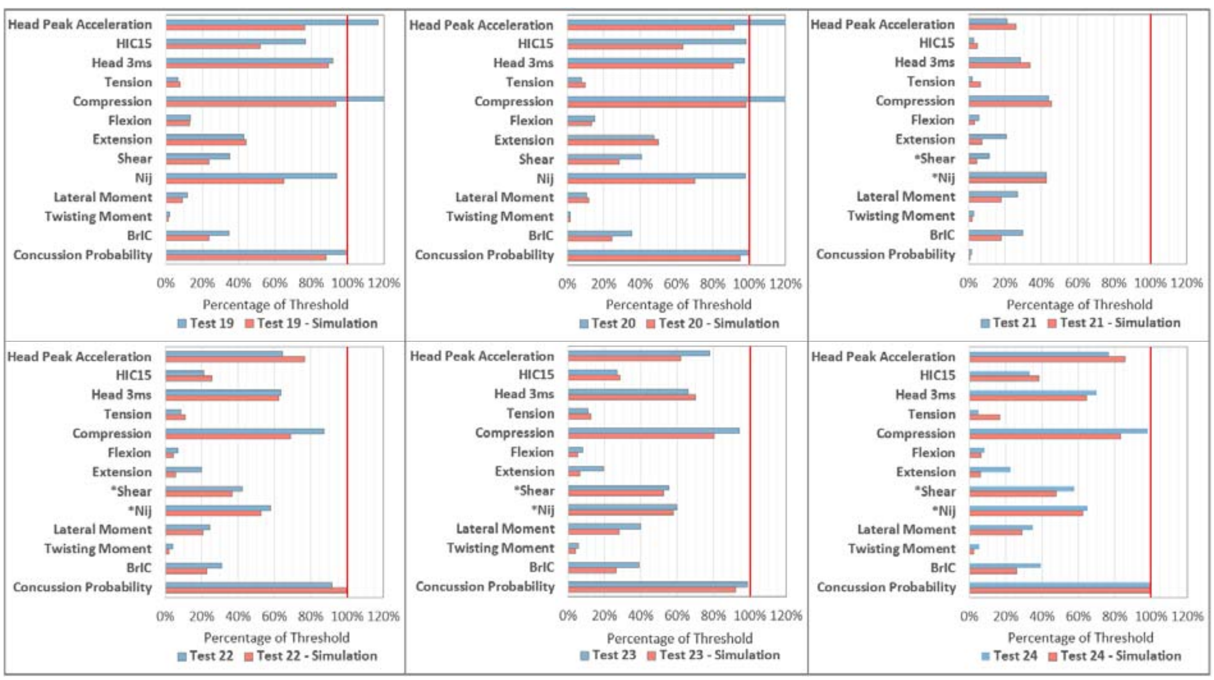

Figure 62. Bar chart with summary of injury criteria for A14 test vs simulation comparison. DJI Phantom 3 tests 19 through 24. The asterisk denotes the modified criteria that were used for side impact test scenarios.

4.3 SENSEFLY EBEE PLUS

4.3.1 A14 Conditions

This section presents a comparison of test and simulation results for the ten cases involving the eBeePlus in this project. After the calibration tests presented in Chapter 3, the FE model was frozen for these simulations. So the results are pure predictions, and no calibration was performed to better match the test results.

The test matrix, with the test conditions and results, was presented in Chapter 2. The following table summarizes the results for the injury criteria, both experimental and simulation. A comparison of the kinematics and the time history from the sensors were again processed to extract injury levels for each of the ten cases; the results are presented in APPENDIX F—.

Table 25. A14 Test and simulation result comparison

Injury Criteria	Test 25		Test 26		Test 27		Test 28	
	Test	Sim	Test	Sim	Test	Sim	Test	Sim
Head Acceleration (g)	33.00	18.85	51.02	24.73	15.12	19.42	17.16	26.44
HIC15	8.21	4.02	10.72	8.69	3.86	5.22	5.11	13.58
Head 3 ms (g)	16.93	12.27	15.49	15.22	13.56	15.73	14.68	18.60
BrIC	0.11	0.09	0.11	0.06	0.20	0.11	0.17	0.16
Probability of Concussion	0.00	0.00	0.00	0.00	0.00	0.00	0.00	0.00
Upper Neck Tension (lbf)	30.90	48.23	53.47	5.62	29.44	31.37	33.87	39.61
Upper Neck Compression (lbf)	495.14	435.78	586.16	544.88	3.57	22.55	4.09	22.04
Upper Neck Flexion (lbf-ft)	4.03	2.92	3.11	3.61	1.53	0.90	1.46	1.26
Upper Neck Extension (lbf-ft)	9.29	6.17	7.57	1.38	0.57	0.63	1.38	0.63
Upper Neck Shear (lbf)	26.07	23.13	26.67	27.82	56.51	39.32	61.38	72.64
Lateral Moment (lbf-ft)	2.67	0.51	6.39	1.22	14.15	8.83	15.21	12.17
Twisting Moment (lbf-ft)	0.21	0.19	0.75	0.30	2.03	0.77	3.55	1.59
Upper Neck Nij	0.38	0.33	0.43	0.41	-	-	-	-
Upper Neck Nij (modified)	-	-	-	-	0.11	0.05	0.14	0.06

Injury Criteria	Test 29		Test 30		Test 31		Test 32	
	Test	Sim	Test	Sim	Test	Sim	Test	Sim
Head Acceleration (g)	51.91	45.53	59.69	49.64	9.66	12.31	16.20	16.70
HIC15	24.73	49.88	39.00	60.95	1.41	2.35	3.53	5.10
Head 3 ms (g)	23.14	36.33	30.66	39.56	8.40	9.63	12.08	13.88
BrIC	0.35	0.26	0.43	0.27	0.12	0.07	0.12	0.09
Probability of Concussion	0.00	0.00	0.02	0.00	0.00	0.00	0.00	0.00
Upper Neck Tension (lbf)	40.49	49.96	57.74	51.32	5.90	11.35	7.52	36.58
Upper Neck Compression (lbf)	76.81	46.28	66.59	52.52	157.91	196.83	193.42	225.01
Upper Neck Flexion (lbf-ft)	2.39	2.59	2.63	2.73	2.44	3.68	3.79	4.21
Upper Neck Extension (lbf-ft)	0.99	0.63	1.22	0.63	0.40	0.63	0.67	0.63
Upper Neck Shear (lbf)	164.82	124.26	197.12	133.93	30.07	27.30	46.81	43.03
Lateral Moment (lbf-ft)	45.96	19.37	54.89	20.23	9.25	6.30	8.20	7.53
Twisting Moment (lbf-ft)	4.06	3.67	5.29	3.95	1.38	0.31	2.05	0.44
Upper Neck Nij (modified)	0.31	0.11	0.40	0.12	0.12	0.16	0.15	0.17

Injury Criteria	Test 33		Test 34	
	Test	Sim	Test	Sim
Head Acceleration (g)	76.86	30.59	106.22	35.54
HIC15	37.15	12.34	58.06	22.97
Head 3 ms (g)	25.68	19.75	28.93	28.31
BrIC	0.22	0.11	0.27	0.16
Probability of Concussion	0.12	0.00	0.42	0.00
Upper Neck Tension (lbf)	64.20	50.13	52.23	51.21
Upper Neck Compression (lbf)	510.88	383.94	569.84	483.19
Upper Neck Flexion (lbf-ft)	7.56	6.38	9.19	11.10
Upper Neck Extension (lbf-ft)	1.10	1.05	1.03	0.63
Upper Neck Shear (lbf)	67.88	61.62	70.21	62.31
Lateral Moment (lbf-ft)	12.63	10.43	13.50	10.74
Twisting Moment (lbf-ft)	2.47	0.69	3.58	2.21
Upper Neck Nij (modified)	0.41	0.30	0.45	0.37

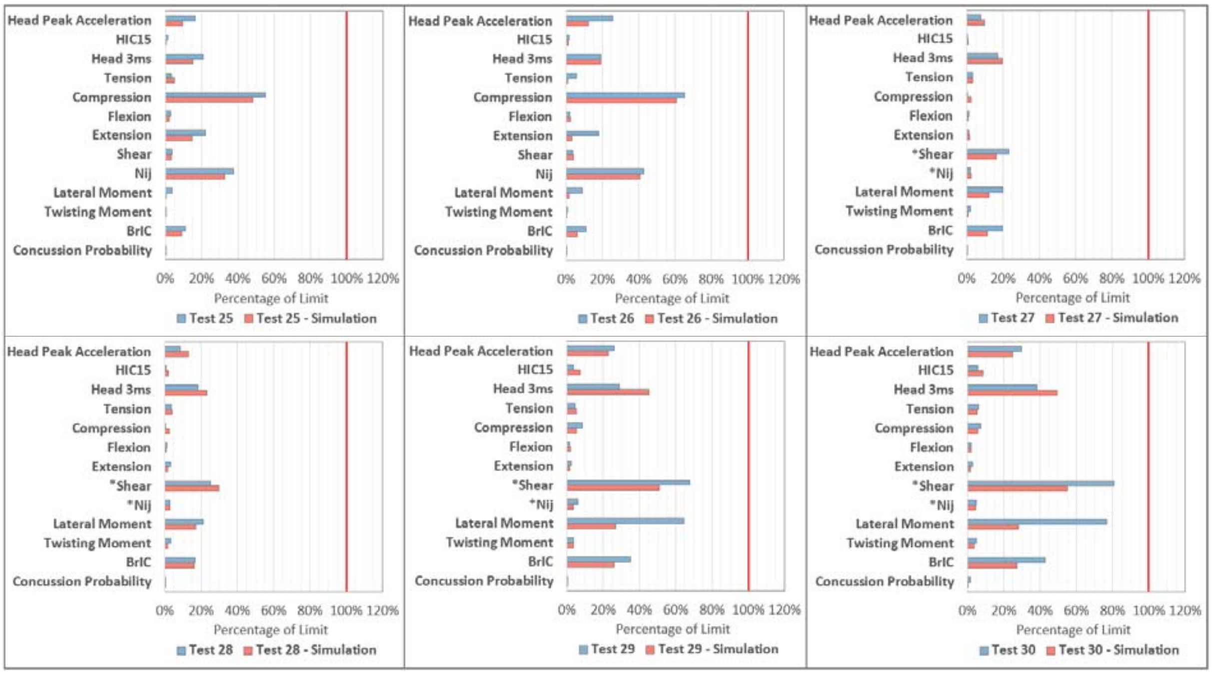

Figure 63. Bar chart with summary of injury criteria for A14 test vs simulation comparison. DJI Phantom 3 tests 25 through 30. The asterisk denotes the modified criteria that were used for side impact test scenarios.

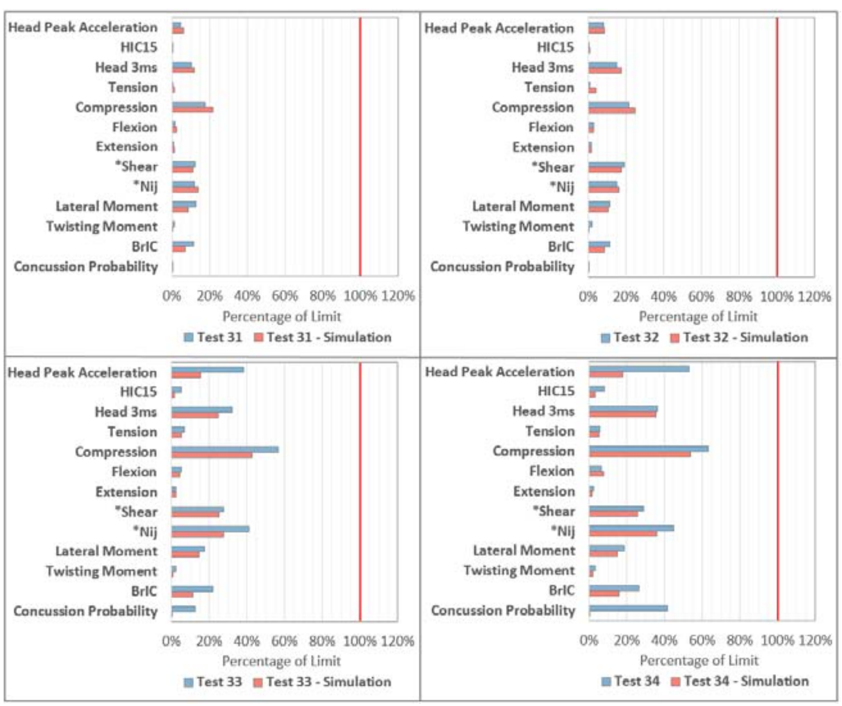

Figure 64. Bar chart with summary of injury criteria for A14 test vs simulation comparison. DJI Phantom 3 tests 31 through 34.

4.4 EVALUATION OF ADDITIONAL CONDITIONS – PRECISION HAWK MKIII

As an extension of the simulation work performed in this chapter, and with the aim of shedding light on how much higher is the injury risk associated with a fixed-wing pusher UAS impact in comparison to the Phantom 3 and the eBeePlus, NIAR carried out a series of simulation between the ATD virtual model and the Precision Hawk FEM.

The following impact conditions were defined by UAH, in accordance to their findings on likely Lancaster impact speed and orientations:

- Horizontal impact at 36 fps, in accordance to the Precision Hawk flare speed. The PMHS head was impacted frontally and sideward.
- Parachute vertical speed of 16 fps, based on a drop at a height of 20 ft.
- Parachute vertical drop of half the energy of the previous drop speed. This second case speed was estimated at 12 fps.

This section introduces the front impact case at 36 fps. The remaining three impact cases are attached in APPENDIX G—.

Figure 65 and Figure 66 present the kinematics and the neck loads, and head acceleration for the front impact at 36 fps, respectively.

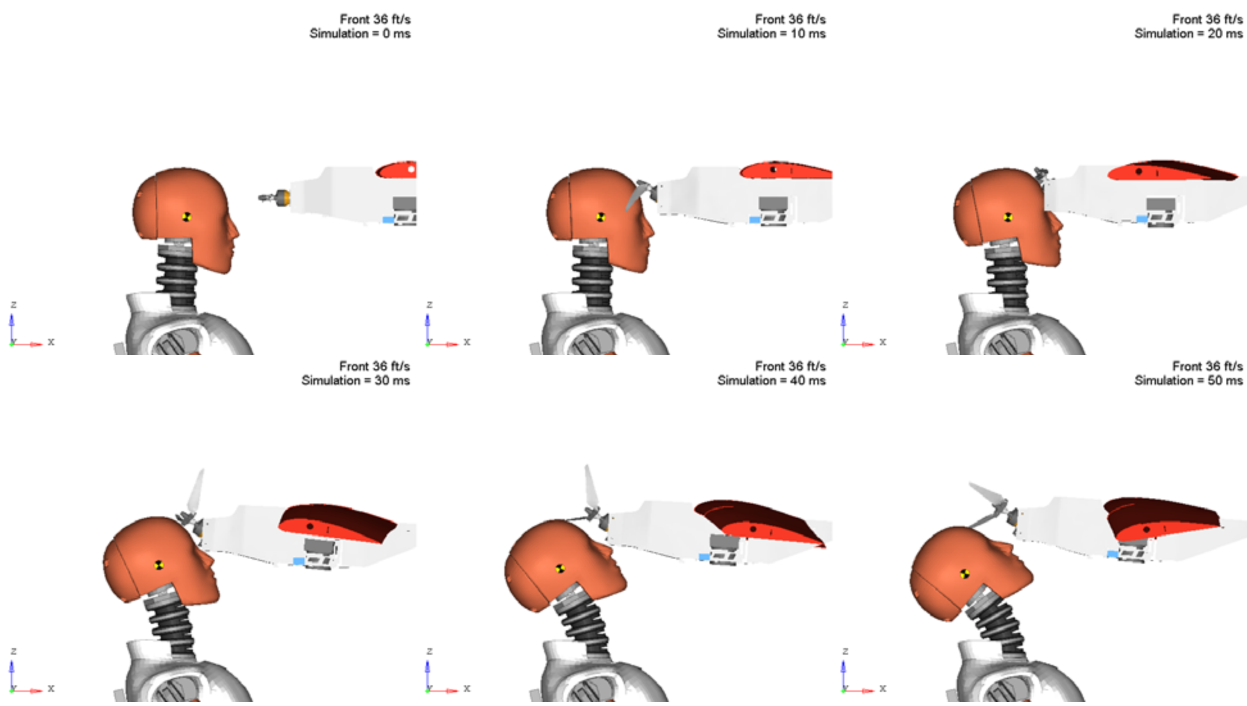

Figure 65. Precision Hawk, 4.4 lb, 36 fps, front; additional ATD simulations; kinematics

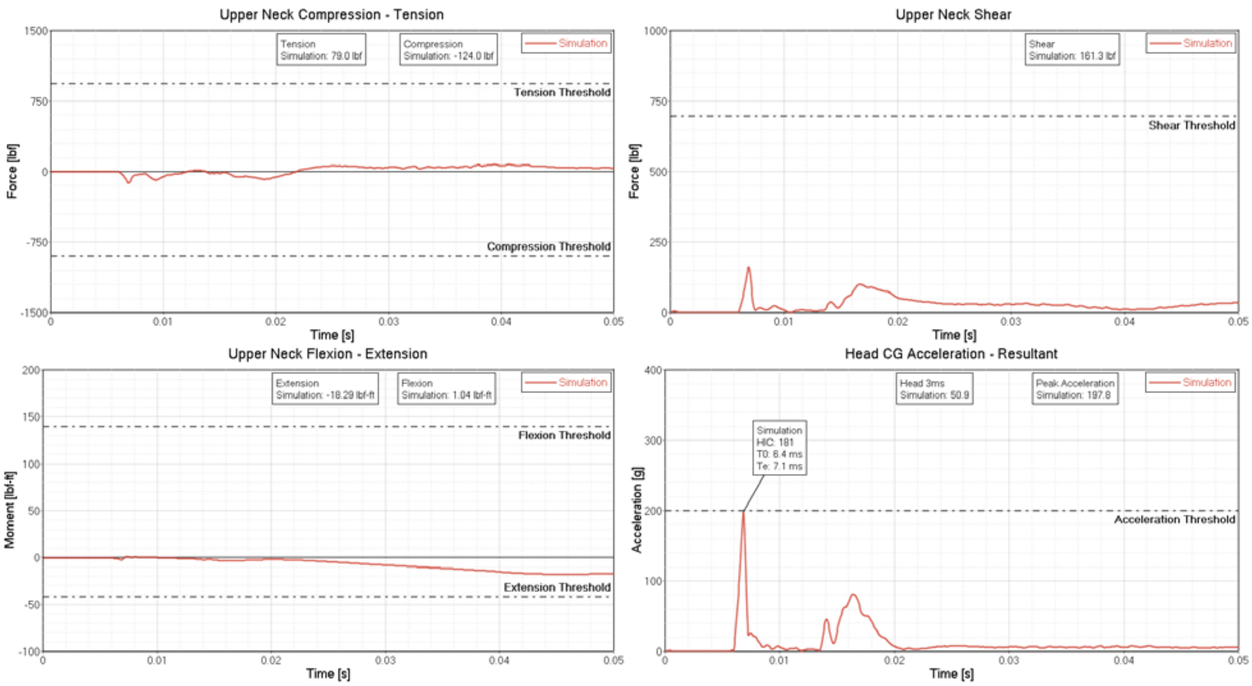

Figure 66. Precision Hawk, 4.4 lb, 36 fps, front; additional ATD simulations; neck loads, and head acceleration

Even though the load and acceleration values remain within the criteria thresholds, it must be noticed that the head acceleration value reached a 99% of the threshold limit.

4.5 CONCLUSIONS FROM UAS FE MODEL VERIFICATION AND MODEL LIMITATIONS

Three sUAS models were developed utilizing the building block approach with reverse engineered geometry, CAD models, and data from material coupon tests, component and system level tests described in Section 3. , as well as assembly level ATD impact testing during the A14 research (for Phantom3 and eBeePlus). These FE models have shown repeatable responses to simulated impact scenarios and have adequately characterized the physical outcomes of tested conditions. It is noted that the Phantom3 model showed a less accurate response to rearward impact conditions, implying that additional testing would be required to fully capture those impact dynamics. Further testing is recommended to improve the material model for the eBeePlus foam components so that material failure modes and post-damage load paths could be defined with better accuracy. Likewise, full-scale ATD testing of Precision Hawk articles would enhance the validity of the FE model for ground collision impact scenarios.

5. FINITE ELEMENT HUMAN BODY MODEL CALIBRATION

In this chapter, an introduction to the Total Human Model for Safety (THUMS) model is given, the numerical sensor modeling methodology is explained, and the results of the calibration impact simulations is presented and compared with those of the ATD.

The THUMS is a biofidelic finite element human body model representing a 50th percentile male. The model was jointly developed by Toyota Motor Corporation and Toyota Central R&D Labs., Inc. The significant human body parts are represented by FE meshes and their material properties are defined assuming constitutive laws.

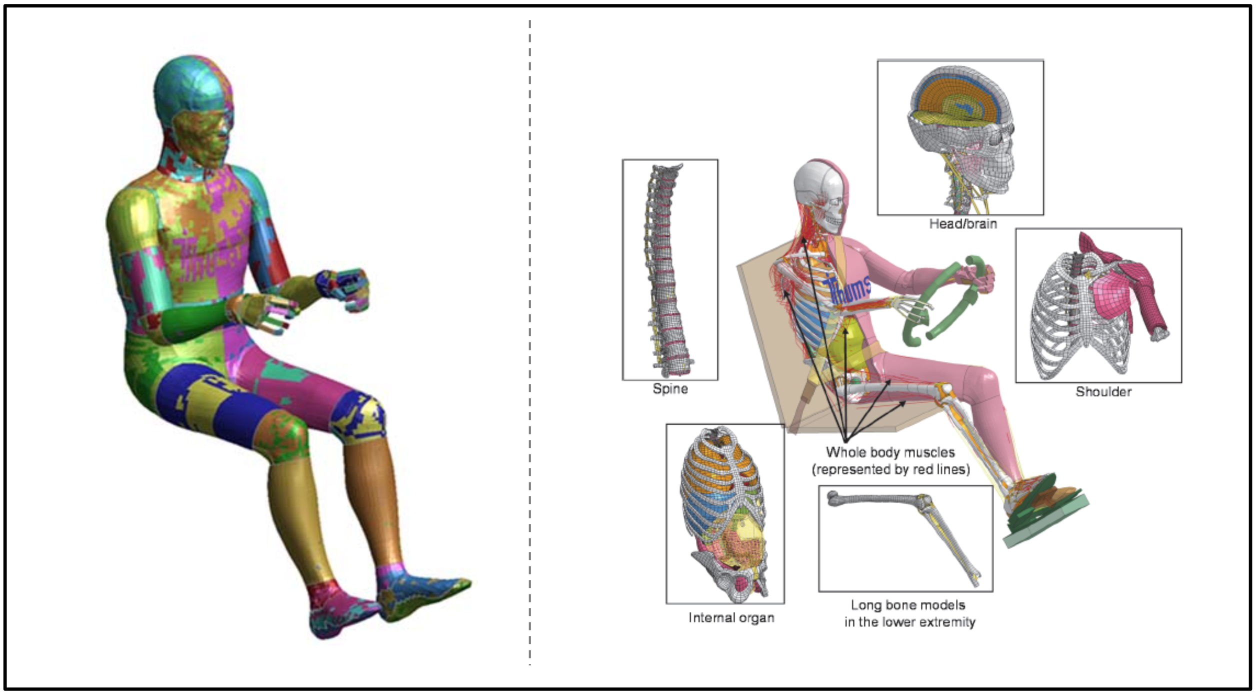

Figure 67. Total Human Model for Safety (THUMS) isometric view (left) and expanded cutaway views (right)

5.1 TOTAL HUMAN MODEL FOR SAFETY – THUMS

This section documents the FE status and usage of the THUMS model. This project used the THUMS V5.01AC AM50 seated version representing an occupant of a vehicle.

The following figures give an overview of the validation efforts that the THUMS developers provided as verification of the biofidelity and accuracy of the model. See [30] for additional details regarding validation against published literature, applications, and other supporting data.

Due to the automotive development environment, the sitting posture of the THUMS is reclined so as to fit a typical vehicle seat. This posture was modified to reflect the posture required for the PMHS tests as defined by OSU in [3]. This modification required simulations of the THUMS to be performed utilizing simulated accelerations and loads applied with FE strap models to guide the body parts into the final upright seated posture. VICON measurements and CMM data from PMHS testing were used to verify the THUMS posture represents that of the test subjects.

The THUMS model was evaluated to determine the appropriate numerical sensors to represent the instrumentation used in PMHS testing. The commercially available THUMS model does not include any load cells or accelerometers. Hence, different techniques and methods were investigated to determine the best way to capture the desired data output. Once the THUMS model was instrumented, the same test impact conditions analyzed with the ATD were evaluated with the THUMS model. Both simulation exercises were compared against one another to demonstrate the level of agreement between the outputs.

5.2 INSTRUMENTATION OF THE THUMS MODEL

Instrumentation consists of numerical entities that represent physical test instrumentation such as accelerometers, load cells, strain gages, and VICON markers. The following list gives the type of instrumentation and the numerical implementation methodology.

- Accelerometers
  - Element_Seatbelt_Accelerometer
    - Attached to nodes with a nodal rigid body (NRB)
  - Constrained_Interpolation
    - Attached to all nodes of a part
- Load cells
  - Database_Section
- VICON Markers
  - Database_History_Node

These numerical sensors used the same sign convention, where possible, as that of the related instrumentation in the ATD's and PMHS sensor arrays. When a sensor relies on the global coordinate system rather than a local coordinate system, the sign difference was corrected during post-processing of the simulation output.

5.2.1 ELEMENT_SEATBELT_ACCELEROMETER

The accelerometer element in LS-Dyna reports time-histories of linear and angular displacements, velocities, and accelerations. The element is attached to components within the FE model by means of a nodal rigid body or some other rigid entity that contains three or more nodes. The sampling rate of the accelerometer element can be adjusted to the same frequency as used in testing or some standard value as per user's convenience. The accelerometer element is rigidly connected to a tetrahedral instrumentation fixture representing the same dimensions and mass as the T6aw fixture used in PMHS testing, as discussed in [3]. This simulated fixture is attached to the Occipital bones of the THUMS skull with an EXTRA_NODES set, which is a rigid constraint type within LS-Dyna; the fixture and the connection nodes are assumed to be rigidly constrained, acting together as a single rigid body. The output from this instrumentation set is useful to compare against the data output from the PMHS tests at the equivalent sensor location.

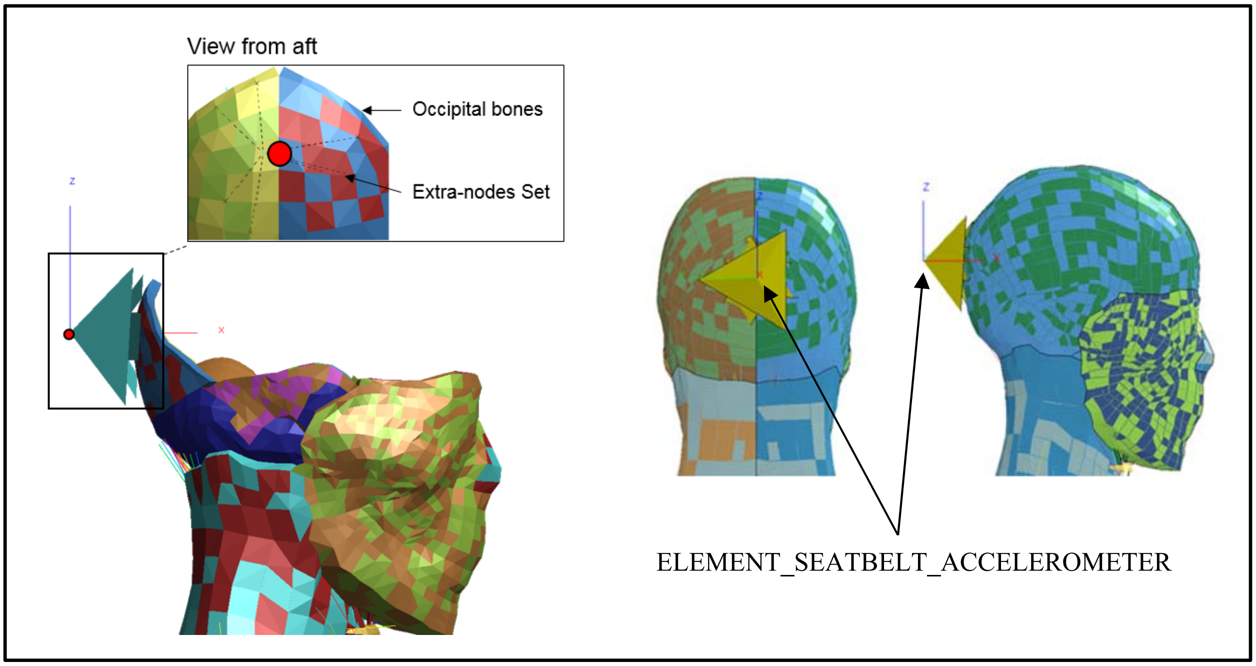

Figure 68. Numerical implementation of the T6aw tetrahedral instrumentation fixture shown attached to the Occipital bones of the THUMS model

5.2.2 CONSTRAINED_INTERPOLATION

The constrained interpolation element in LS-Dyna defines the motion of a dependent node or master node, based on the interpolated motion of a set of independent nodes or slave nodes. The application of this element type for the present study entails creating a dependent node, which is detached from the FE mesh at the location of the physical sensor in the test setup, and using the nodes of the representative FE components as the independent node set. For example, the PMHS head instrumentation output is simulated by defining a dependent node at the head CG and using the remaining nodes of the head as the independent nodes. This allows the motion of the independent nodes to be unaffected during the impact simulation because the dependent node is free to move in space without any influence from structural mass and stiffness. Consequently, the motion of the dependent node is similar to an averaged representation of the motion of the independent nodes. This preserves the overall body's motion but minimizes interference in the signal from local fluctuations and opposing contralateral kinematics. Figure 69 shows the head CG instrumentation used in THUMS simulations.

Figure 69. Wireframe depiction of the THUMS head with CONSTRAINED_INTERPOLATION element connecting the head CG node to the skull bones and intracranial contents

The sensitivity of the interpolation element to the boundary conditions was evaluated by performing a series of simulations in which the independent node set was altered for each iteration. The setup and simulation outputs are shown in Figure 70, Figure 71, and Figure 72.

- Configuration #1 – Included the cranial bones and all of the intracranial contents in the independent node set. This characterized the various parts of the head as a single entity.
- Configuration #2 – Included the cranial bones but excluded the intracranial contents from the independent node set. This characterized the response of the skull bones alone.
- Configuration #3 – Consisted of an independent node set containing only the nodes of the cranial bone elements under the footprint of the tetrahedral fixture. This allows the local attachment of the T6aw fixture to be evaluated against the output of the entire skull and against the entire skull with the brain matter.

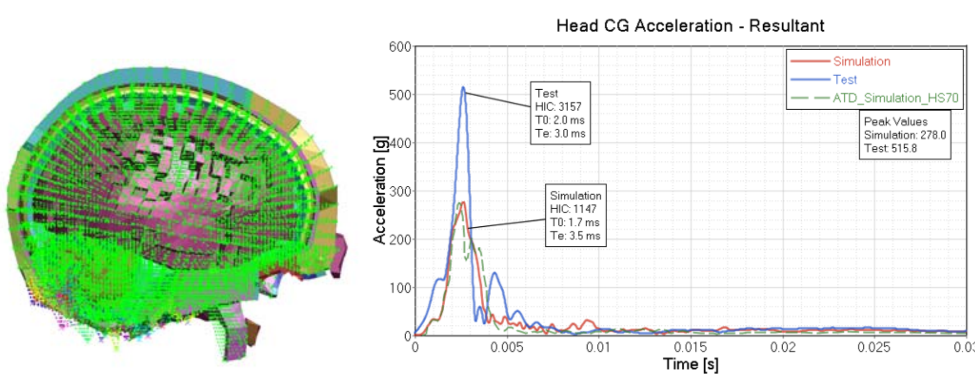

Figure 70. Cross-section view of the THUMS skull of Configuration #1 (left); resultant head CG acceleration output shown compared against PMHS test data (right)

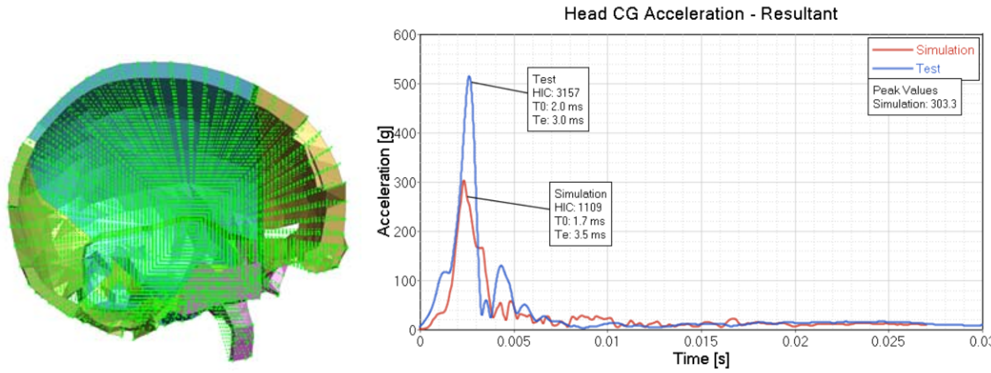

Figure 71. Cross-section view of the THUMS skull of Configuration #2 (left); resultant head CG acceleration output shown compared against PMHS test data (right)

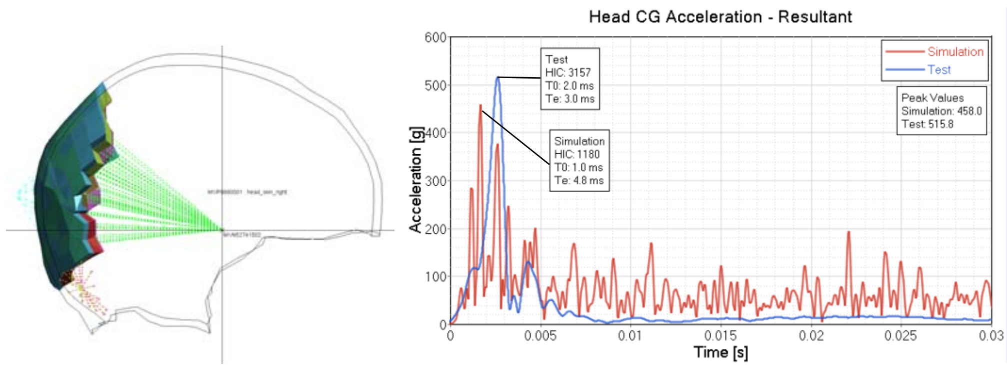

Figure 72. Wireframe view of the THUMS skull of Configuration #1 (left); resultant head CG acceleration output shown compared against PMHS test data (right)

It can be seen from this sensitivity study that the peak acceleration value increased when the intracranial contents were removed from the interpolation set and the HIC decreased. This is attributed to the brain matter causing a slight amount of damping to the displacement response, but extending the duration of the predominant accelerations. These two configuration are considered equally acceptable for characterizing head accelerations with the THUMS model since the injury criteria showed only slight differences when compared to the overall signal accuracy. Furthermore, the third configuration indicates that the skull nodes in a localized region of the head do not respond in the same way as the CG of the head. In order to characterize the head CG kinematics, the acceleration field of the entire head should be considered.

5.2.3 DATABASE_SECTION

The DATABASE_SECTION defines a section cutting plane corresponding to a set of parts. Cross-section loads can be reported as time-histories of total force and moment at the location of the cutting plane. This is convenient for assessing the loads passing through the neck of the THUMS during the impact simulations.

In order to confirm that the section cut taken at the occipital condyle (OC) is capable of determining the total neck force, three section cuts are defined such that the load-bearing components of the neck are identified by the simulation output. The first section cut, labeled OC_1, is defined at the OC with the least number of parts included in the section cut set, shown in Figure 73. This represents a section cut through the base of the skull without any connecting ligaments, muscles, or vertebrae. The second section cut, labeled OC_2, is located at the same plane but with an expanded set of parts along the section cut, accounting for the connecting tissue at the OC, as shown in Figure 74. The final section cut, labeled Upper_Neck3, shown in Figure 75, is defined near the C1-C2 vertebrae junction including all of the relevant neck components but excluding the face and jaw.

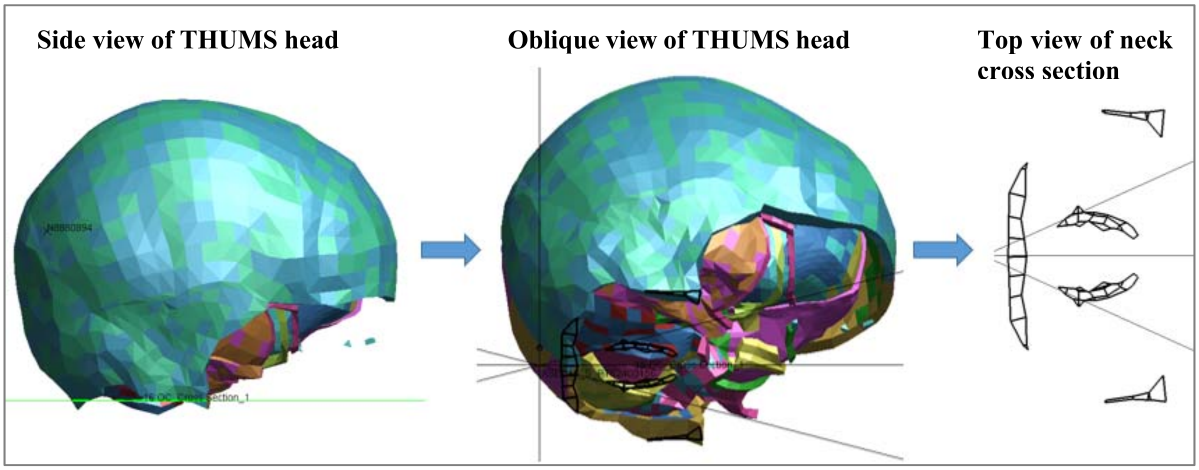

Figure 73. Location of OC_1 section cut and the associated elements in cross-section

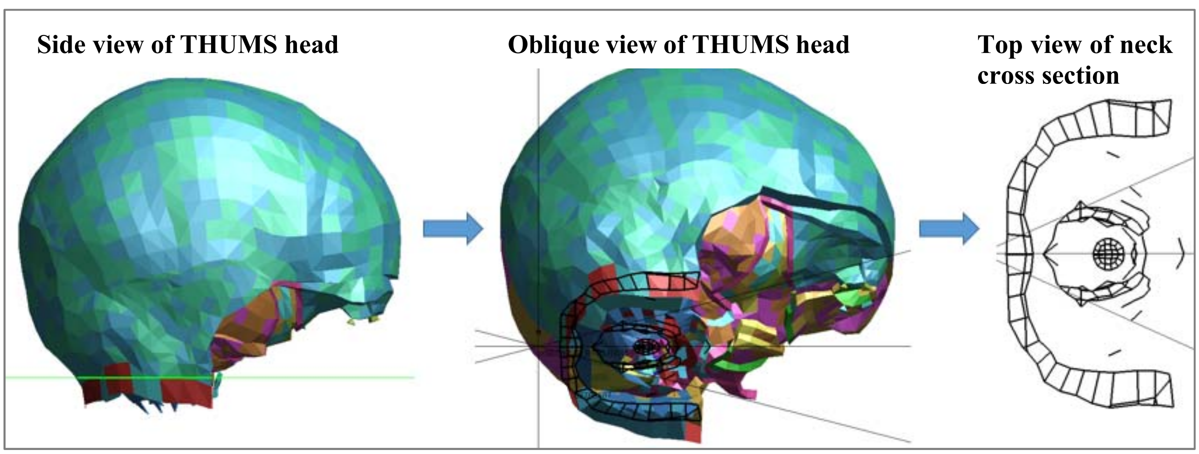

Figure 74. Location of OC_2 section cut and the associated elements in cross-section

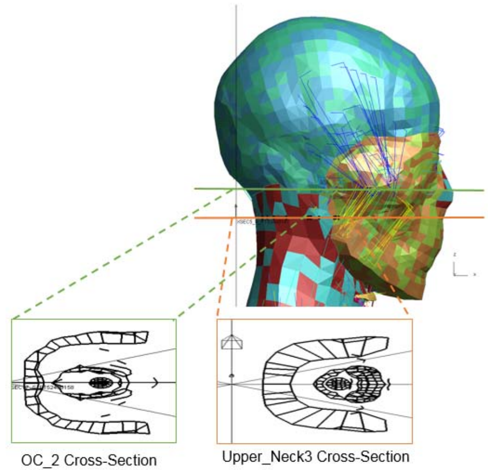

Figure 75. Section cut location for neck loads output; inset windows show element cross-sections for OC_2 and Upper_Neck3 section cuts

These section cut definitions were evaluated through simulation for a vertical impact with the DJI Phantom3 at 50 ft/s. This case is labeled V(90)-50 in post-processing plots. Figure 76 presents the post-processed data for this case. The general agreement of the OC_2 section and the and the Upper_Neck3 section cut indicates that the OC_2 section contains all of the load-bearing elements attached to the occipital condyle.

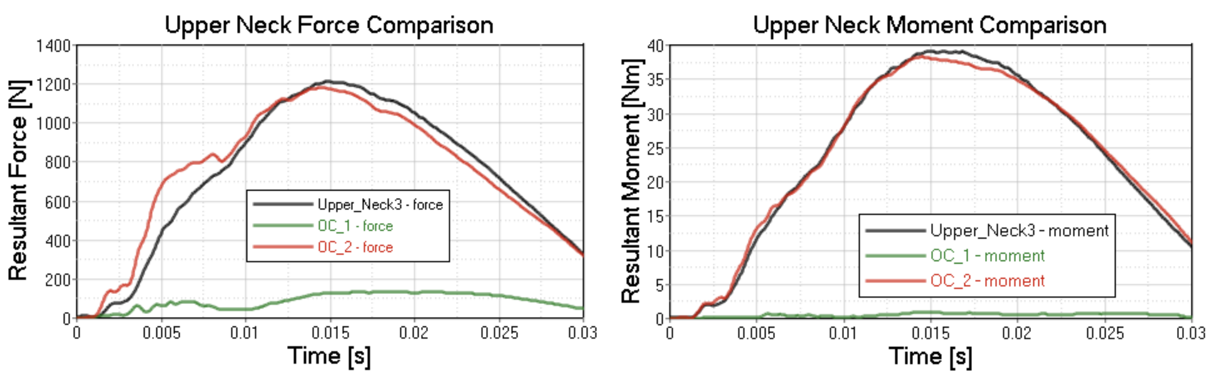

Figure 76. Correlation of neck loads between the upper neck section cut and the occipital condyle section #2; DJI Phantom3, 2.67 lb, bottom, 57 fps, vertical

To conclude the neck section cut validation efforts, the neck loads were integrated over the time of the impact event to determine the total impulse loading. The calculated impulse is used to understand the neck load outputs because the neck force time-histories show discrepant responses when comparing the THUMS model output to ATD test data. These load discrepancies are attributed to the mechanical response of the ATD as compared to the biofidelic response of the THUMS to similar impacts. The ATD has a column-like assembly representing the neck which allows more vertical loading to be sustained than the biofidelic layout having a complex curved form. Furthermore, the THUMS simulations show less neck loading than seen in ATD test outputs, as shown in Figure 77, likely due to the biological material models damping the magnitude of the force response and extending its duration, preserving the total impulse transfer, as shown in Figure 78.

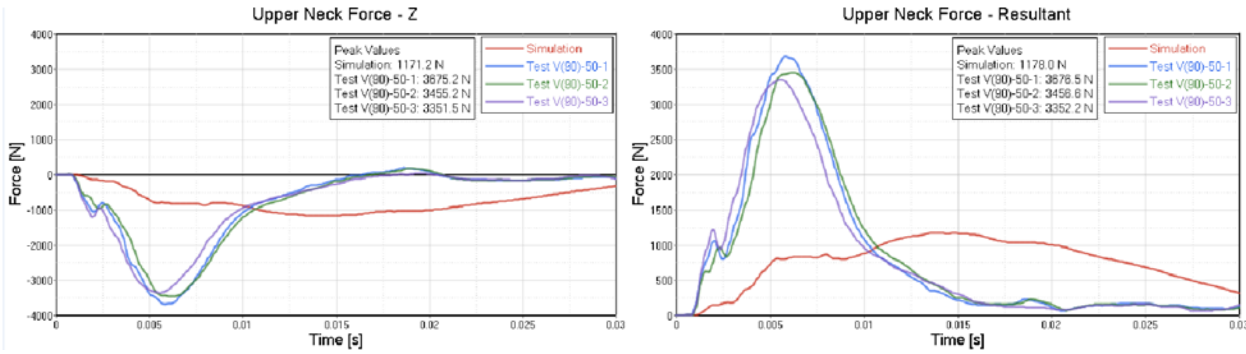

Figure 77. Upper neck force comparison, test and simulation, Z-axis (left) and resultant (right); DJI Phantom3, 2.67 lb, bottom, 50 fps, vertical

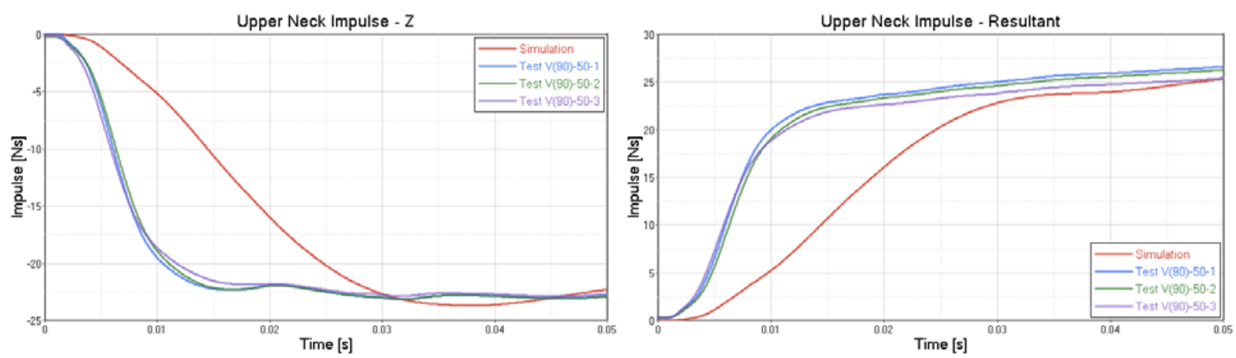

Figure 78. Upper neck impulse comparison, test and simulation, Z-axis (left) and resultant (right); DJI Phantom3, 2.67 lb, bottom, 57 fps, vertical

5.2.4 DATABASE_HISTORY_NODE

The VICON markers used in PMHS testing allow the kinematics of the test subject to be tracked during the impact. Node locations on the THUMS model corresponding to the sensor locations on the PMHS were included in the DATABASE_HISTORY_NODE output for node tracking purposes. This allows comparisons between THUMS simulations and the PMHS kinematics as needed for confirming test and model correlation. This data is not used in any injury metric or any ranking for the severity of the test conditions.

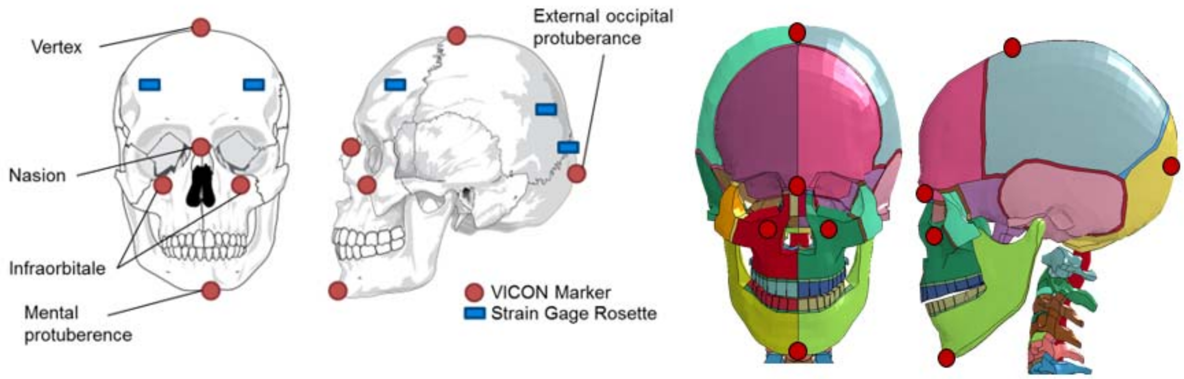

Figure 79. VICON marker locations used in PMHS testing (left) and the numerical implementation in the THUMS model (right)

5.2.5 Effective Plastic Strain Correlation Methodology

The THUMS bone material models allow for plastic deformations beyond a predetermined yield limit. These plastic deformations can be quantified with the Effective Plastic Strain (EPS) output given by LS-Dyna. EPS increases in value whenever the material is actively yielding [27]. Mapping the EPS output from THUMS to documented fracture limits was demonstrated by simulating an equivalent test setup used by Yoganandan (1995) and comparing the EPS values in the skull bones to the force versus deflection data from the impactor. Figure 80 shows the test setups used by Yoganandan and the model implementation of the skull vertex impact test conducted at 7.2 m/s with a 48mm radius rigid impactor.

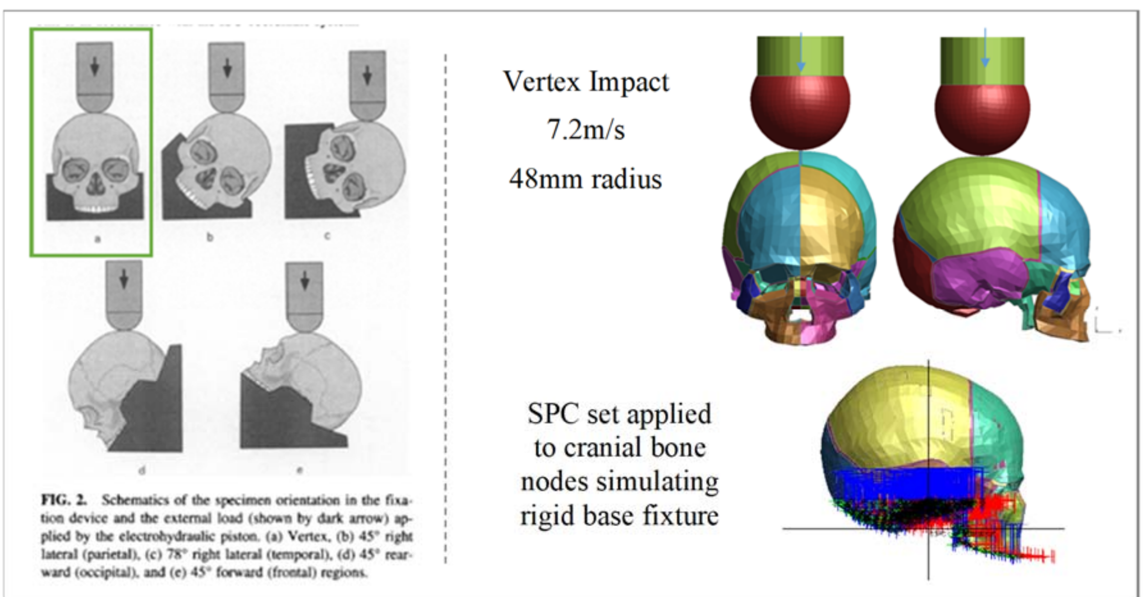

Figure 80. Test and simulation setup diagrams for skull fracture tests performed by Yoganandan (1995)

Figure 81 shows the simulated skull fracture test output. The simulation predicted an EPS value 0.0395 (3.95% strain) at the time when the force vs deflection curve crossed the tested lower deflection limit of approximately 5mm. This indicates that an EPS value of 3.95% or greater is associated with skull fractures in real impact testing conditions.

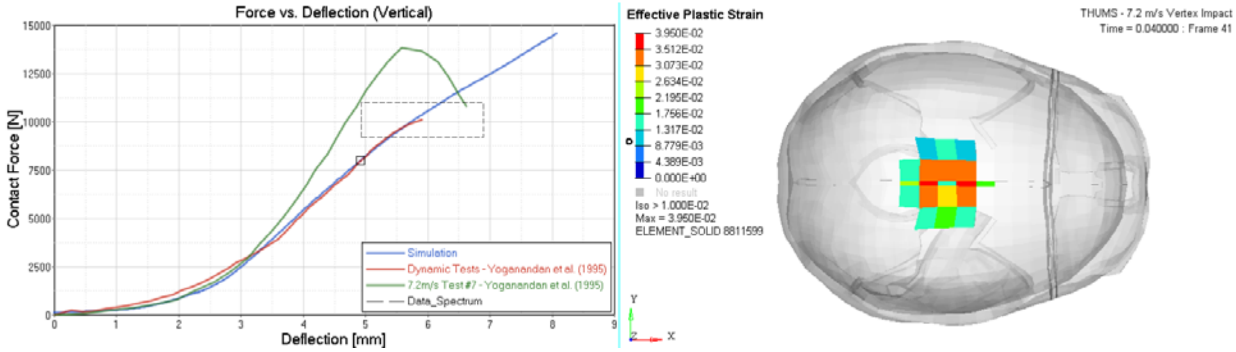

Figure 81. Simulation force vs. deflection output compared to test data (left) and EPS contours at skull vertex impact site, view looking down (right); simulated vertex impact test [28]

With the EPS output from the THUMS correlated to skull fracture conditions, simulations including the DJI Phantom3, SenseFly eBeePlus, and Lancaster Precision Hawk MKII were conducted with many different UAS impact orientations at differing impact locations on the THUMS head over a range of impact energies. Then, these simulations were ranked based on injury metric values from each case in order to determine the most critical impact conditions for the PMHS test program.

5.2.6 Intracranial Pressure Correlation Methodology

Brain injury thresholds can be assessed with THUMS simulations by means of pressure and strain outputs from the various parts representing layers of skin, bone, and the physiology of the brain.

Preliminary studies indicate that the pressure ranges reported by the THUMS model correspond to results from test conditions published in the literature [29]. However, due to the delicate nature of brain material, tested pressure readings may or may not be representative of brain matter in vivo since these tests have been performed on PMHS. The conclusions drawn from these simulations should be considered as contingent on further methodology validation efforts.

Nahum et al. (1977) Test Replication

This simulation effort utilized known test conditions from Nahum et al. (1977) [29] and the THUMS documentation [30]. A representative impactor and cushion model were developed and applied to the THUMS model at the test conditions shown in Figure 82.

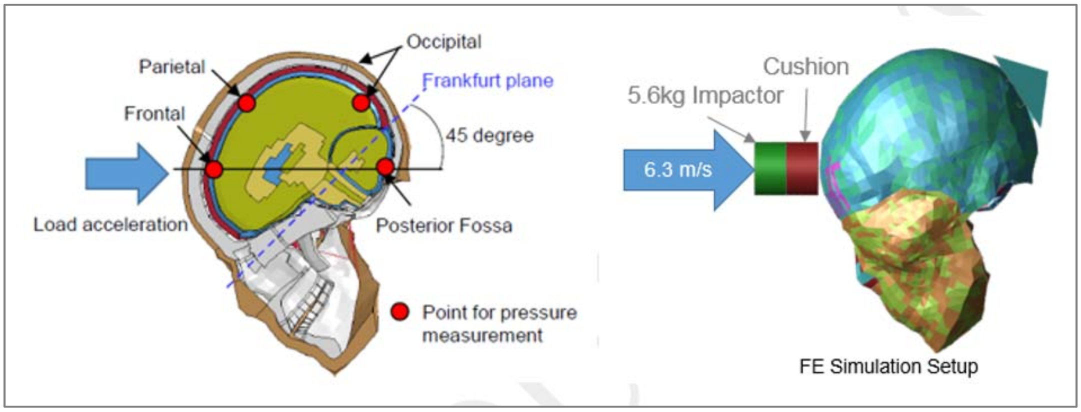

Figure 82. THUMS model documentation of Nahum test replication (left) and NIAR impact simulation of test conditions (right); 6.3 m/s impact test with a 5.6 kg impactor [29]

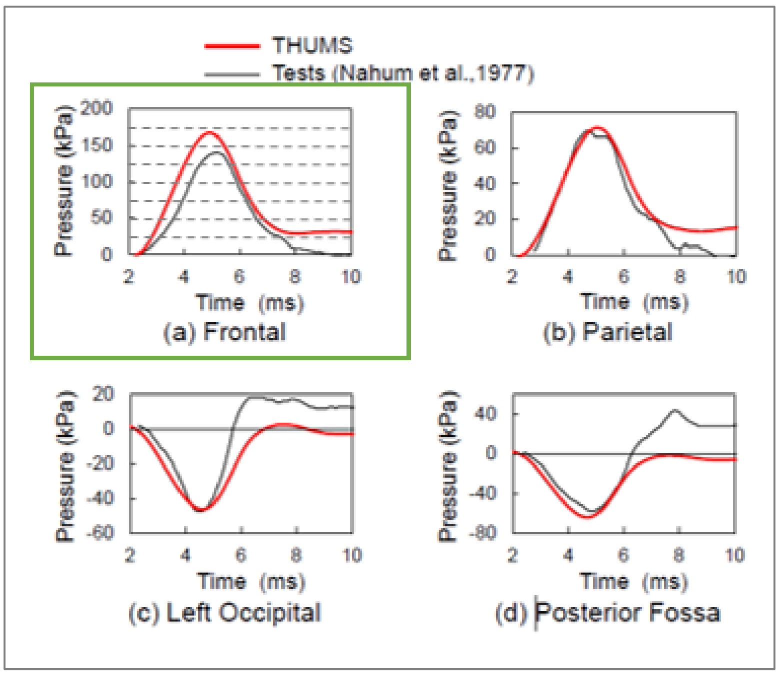

Figure 83. Comparison of pressure readings from Nahum et al (1977) with THUMS model outputs [30]

In order to confirm the post-processing methodology for this effort, contour plots of material stresses were given iso limits of 150 kPa and 170 kPa, as shown in Figure 84. This allows only the elements which exceed the iso limit to be displayed with color contours and all elements below the limit shaded gray. The results of this simulated impact test indicate that the frontal brain matter experienced pressure levels between 150 kPa and 170 kPa. These results are in agreement with the data given by the Nahum et al. (1977) and the data from the THUMS development work.

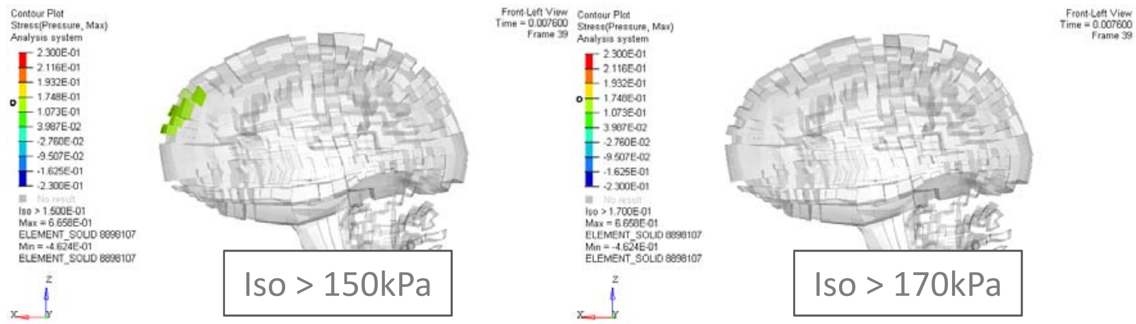

Figure 84. NIAR impact simulation output pressure contours showing elements exceeding 150 kPa (left) and elements exceeding 170 kPa (right)

5.3 EVALUATION OF IMPACT TEST CONDITIONS WITH DJI PHANTOM III

NIAR performed impact simulations of the DJI Phantom III quadcopter UAS against the THUMS model at various speeds and orientations. To maximize the efficient usage of the available test articles and to ensure the relative severity of the proposed test conditions discussed in SECTION 4.2.2 , preliminary simulations were performed and ranked based on the resulting head kinematics, neck loads, and skull strains for each case. The ranked list of critical conditions was expanded to allow for overlapping tests with the ATD impact test program and to cover the lower energy spectrum of the UAS flight envelope. Test conditions are evaluated using an ideal alignment between the sUAS CG and the THUMS head CG, as shown in Figure 85.

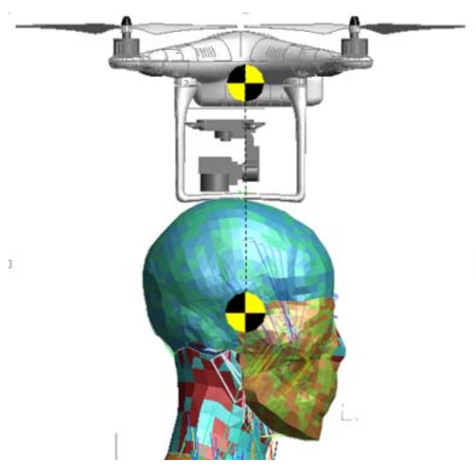

Figure 85. CG alignment of UAS and the THUMS head in the vertical impact direction with the sUAS shown in the bottom first orientation

5.3.1 A11 Conditions

During the A11 project [22], the DJI Phantom 3 was impacted against an FAA Hybrid III 50th ATD in eight different test scenarios (angle and speed). Three repetitions were completed for each impact scenario. Six of the eight conditions tested were simulated with the respective FE model. For A11, only UAS orientations with the bottom impacting first were investigated for the vertical and angled impacts. These tests were used to calibrate the UAS model, which originally was defined for airborne collision simulations, to better predict ground collision scenarios. The implementations in the UAS model, presented in Chapter 3, were defined based on the feedback obtained from comparing simulation and test results for all six tests of the A11 test campaign for the DJI Phantom 3, see Section 4.2.1 for more information. Table 26 presents a summary of the results for the injury criteria, both experimental and simulated.

Table 26. A11 Test and simulation result comparison

Injury Criteria	**V(90)-20**				**V(90)-50**			
	Test 1	Test 2	Test 3	Sim	Test 1	Test 2	Test 3	Sim
Head Acceleration (g)	54.3	56.7	49.2	61	82.4	71.5	119.1	99.4
HIC15	12.0	15.0	15.6	37	59.5	48.0	42.2	110.0
Upper Neck Tension (lbf)	75.9	76.8	74.8	20.3	43.9	42.2	25.8	36.9
Upper Neck Compression (lbf)	536.2	574.4	564.9	188.1	826.2	776.8	753.5	263.5
Upper Neck Flexion (lbf-ft)	7.16	6.95	6.45	20.31	6.99	7.68	7.60	28.36
Upper Neck Extension (lbf-ft)	11.40	10.87	14.24	4.79	15.76	15.45	16.71	8.18
Upper Neck Shear (lbf)	35.9	31.9	34.8	21.4	48.2	46.8	62.7	36.0
Upper Neck Nij	0.42	0.45	0.47	0.22	0.65	0.62	0.63	0.31

Injury Criteria	**H(0)-4.5**				**A(65)-36.5**			
	Test 1	Test 2	Test 3	Sim	Test 1	Test 2	Test 3	Sim
Head Acceleration (g)	25.1	60.7	43.2	47.4	60.1	60.9	55.6	92.0
HIC15	7.8	29.2	19.9	27.0	39.6	30.3	26.3	101.0
Upper Neck Tension (lbf)	12.4	27.3	20.6	2.1	68.1	54.6	49.2	64.3
Upper Neck Compression (lbf)	65.2	118.2	93.5	14.7	626.5	596.3	579.9	195.4
Upper Neck Flexion (lbf-ft)	4.02	4.00	4.14	2.07	23.50	29.17	28.65	32.88
Upper Neck Extension (lbf-ft)	5.45	6.12	6.22	0.34	5.96	6.14	5.22	12.66
Upper Neck Shear (lbf)	32.0	71.5	50.7	15.91	133.6	139.5	135.5	191.3
Upper Neck Nij	0.08	0.10	0.09	0.02	0.53	0.52	0.51	0.28

Injury Criteria	A(58)-46.1				A(58)-57.1			
	Test 1	Test 2	Test 3	Sim	Test 1	Test 2	Test 3	Sim
Head Acceleration (g)	112.7	120.5	130.5	171.5	119.8	139.2	126.6	131.0
HIC15	107.9	119.1	147.8	217	137.2	165.1	123.6	213
Upper Neck Tension (lbf)	49.7	62.9	65.1	24.0	57.6	92.0	82.9	24.5
Upper Neck Compression (lbf)	619.6	593.6	612.1	128.9	581.4	602.6	601.7	123.4
Upper Neck Flexion (lbf-ft)	34.05	28.74	33.22	24.18	22.54	27.96	25.57	23.48
Upper Neck Extension (lbf-ft)	7.92	8.63	9.93	12.44	9.63	10.07	9.80	11.78
Upper Neck Shear (lbf)	171.2	174.8	196.5	146.51	192.9	208.2	183.0	137.0
Upper Neck Nij	0.53	0.50	0.52	0.20	0.48	0.50	0.50	0.19

Figure 86 presents the injury values for the V(90)-50 impact case in bar chart format. The values, presented in Table 26, have been normalized with the injury limit introduced in Chapter 2. It can be seen that the THUMS HIC value is in agreement with the test data but that the neck injury metrics have a discrepant response. This is typical for the THUMS model due to the biofidelic nature of the model as compared to the mechanical nature of the ATD.

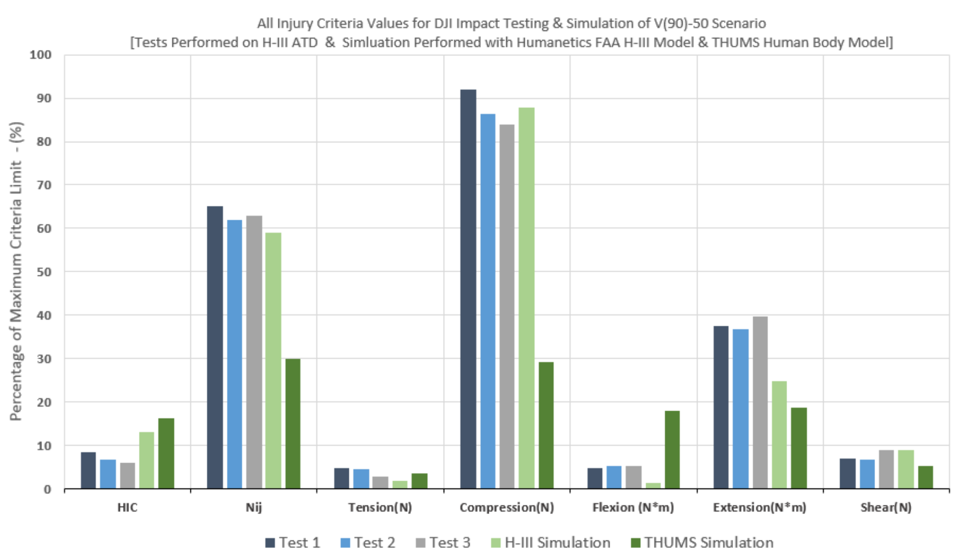

Figure 86. Bar chart with summary of injury criteria for A11 test vs simulation comparison; DJI Phantom 3, 2.67 lb, bottom, 57 fps, vertical

The difference in neck injury results is attributed to the mechanical response of the ATD as compared to the biological response of the PMHS and THUMS to similar impacts. The ATD has a straight column-like assembly representing the neck which could sustain more vertical loading than the biofidelic layout having a complex curved form. Furthermore, the THUMS simulations report consistently lower neck loads than seen in ATD test outputs, likely due to the biological material models damping the magnitude of the force response and extending the duration such that the total impulse transfer is conserved. Additional component and full scale testing, as well as simulation, of known injury-producing conditions are recommended in order to improve the ATD injury criteria thresholds and to better understand the biofidelic response to the tested conditions.

The images in Figure 87 through Figure 90 present the results of the comparison between test case V(90)-50 and the simulation. This case produced the highest level of injury values, and was selected to represent the level of accuracy achieved by the model. The remaining five cases are summarized in APPENDIX H—.

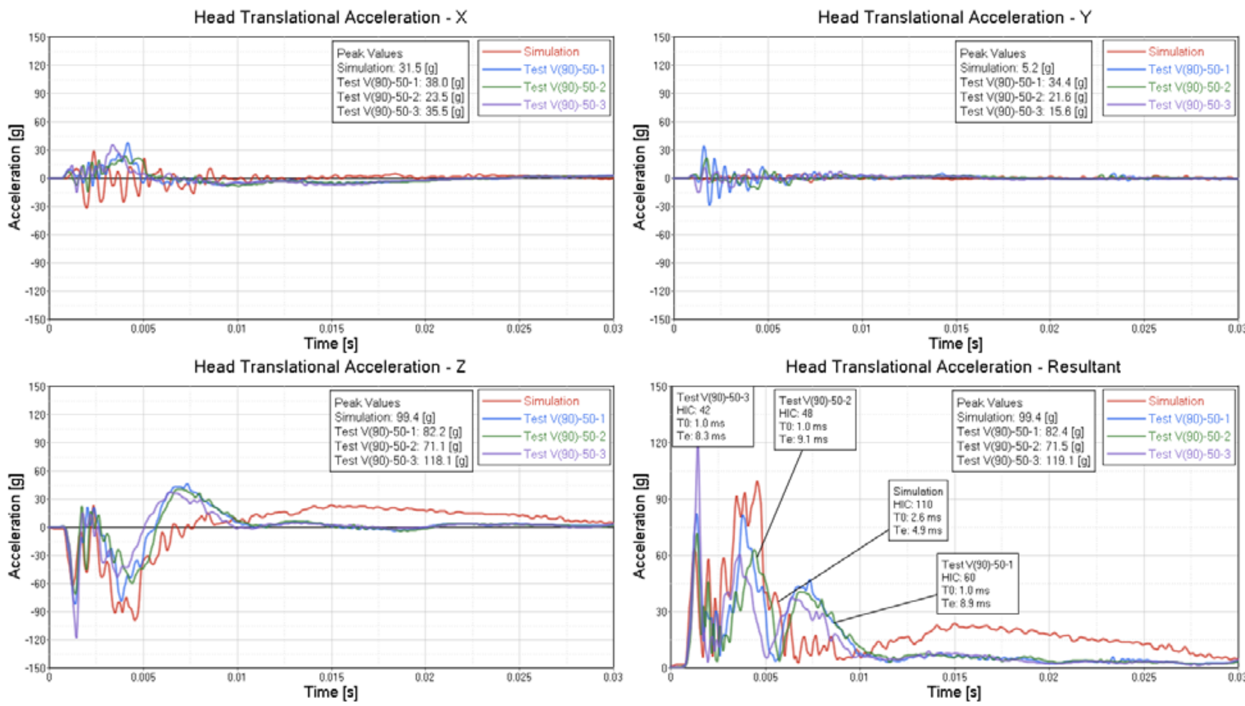

Figure 87. Test vs simulation comparison; DJI Phantom 3, 2.67 lb, bottom, 57 fps, vertical; A11 ATD test, top of the head; head CG acceleration

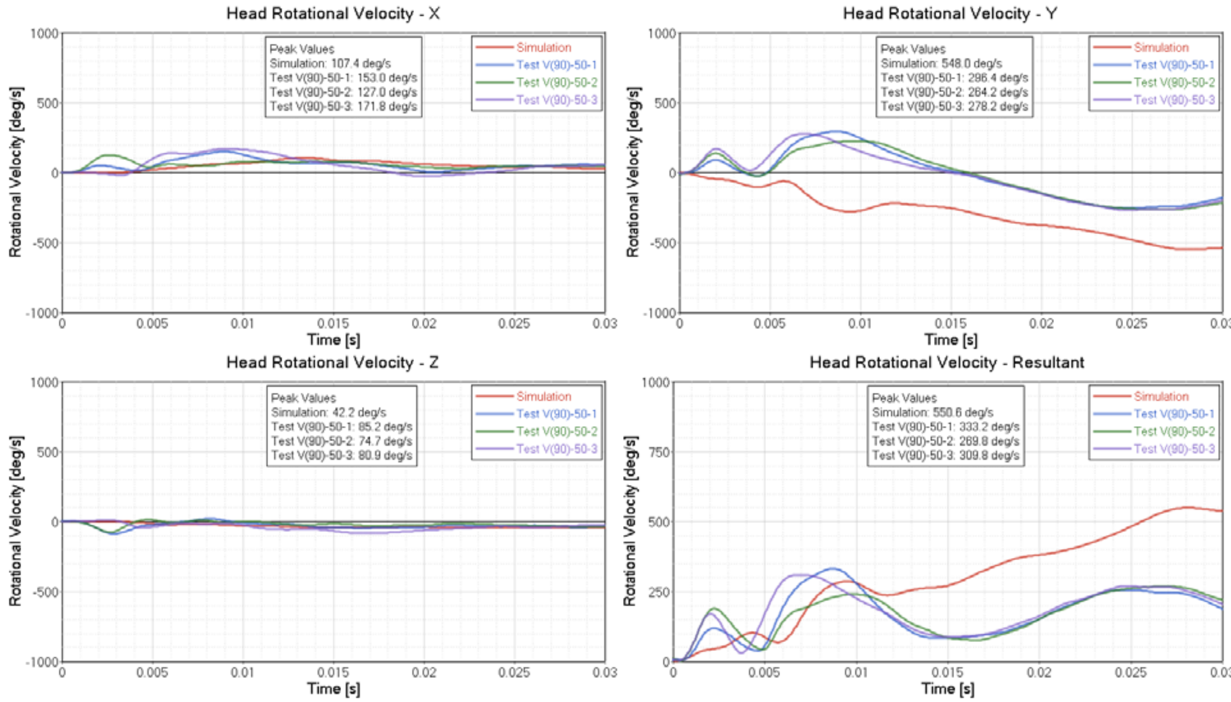

Figure 88. Test vs simulation comparison; DJI Phantom 3, 2.67 lb, bottom, 57 fps, vertical; A11 ATD test, top of the head; head angular rate

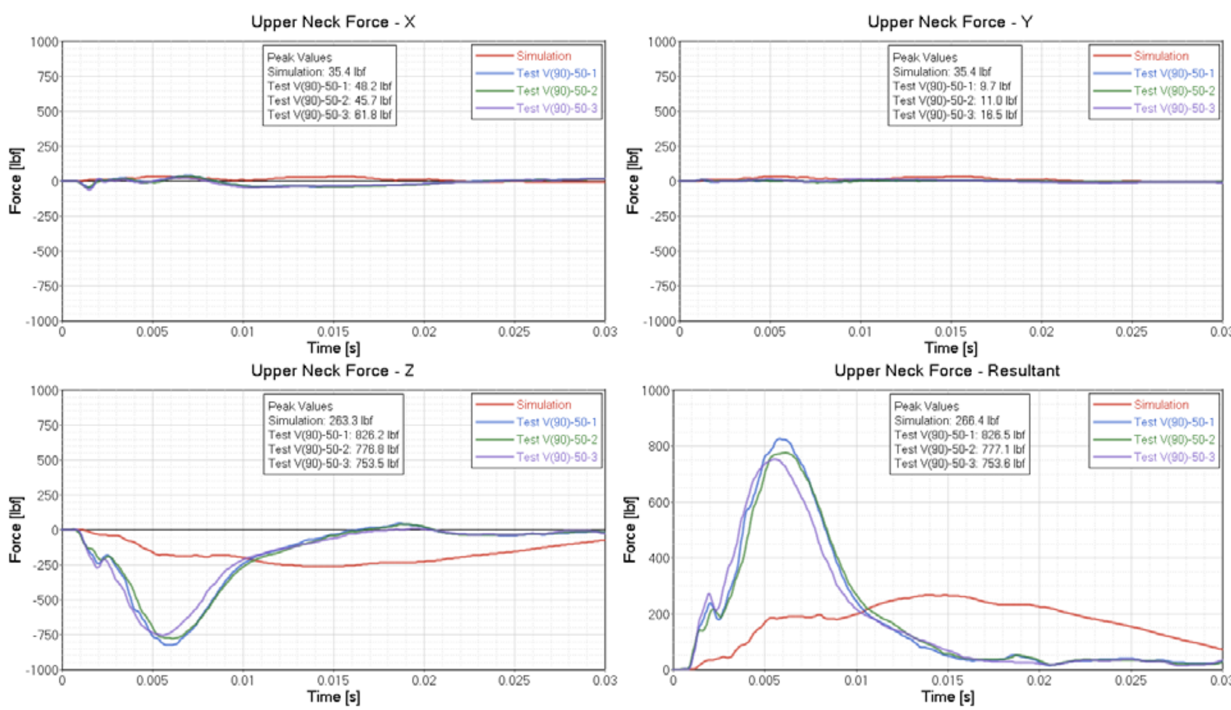

Figure 89. Test vs simulation comparison; DJI Phantom 3, 2.67 lb, bottom, 57 fps, vertical; A11 ATD test, top of the head; upper neck force

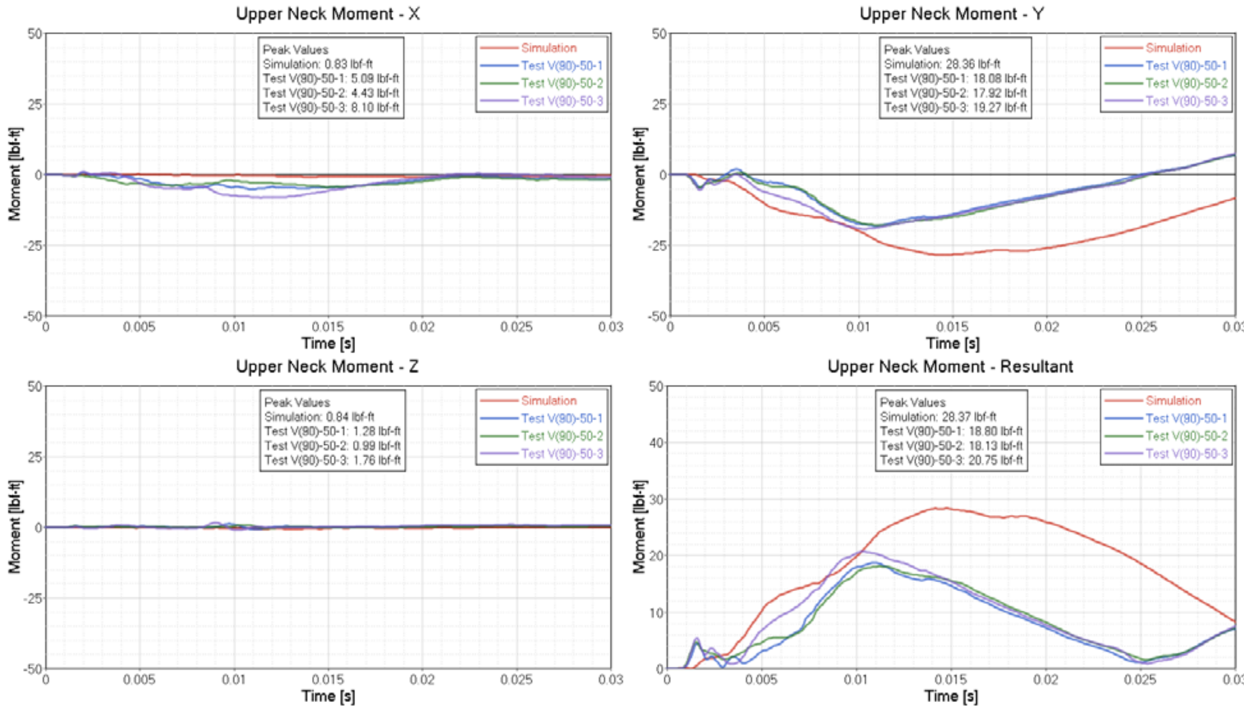

Figure 90. Test vs simulation comparison; DJI Phantom 3, 2.67 lb, bottom, 57 fps, vertical; A11 ATD test, top of the head; upper neck moment

5.3.2 Critical sUAS Orientation

The orientation of the sUAS at the time of impact can affect the amount of impact energy that is transferred during the collision. This effect is a product of the specific construction features and the distribution of mass near the impact contact site. The DJI Phantom3 model was verified as a valid predictor of the physical test outcomes during the A11 test and simulation comparison studies in Section 4.2.1 . Using the verified Phantom3 model, numerical ATD impact simulations determined the critical orientation of the sUAS to be the 'between the arms' impact orientation (also labeled 'Front First'), discussed in Section 5.3.2 . Impact simulations were also performed with the THUMS model to characterize the relative severity of the 'Front First', 'Rear First', and 'Arm First' orientations in terms of EPS, HIC15, Nij, neck shear, extension/flexion, and compression/tension.

Figure 91 shows an example case from the impact orientation study conducted with the THUMS and DJI Phantom3 models. The clear difference between impact orientations can be seen in Figure 92. The 'Front First' orientation leads to more severe injury predictions than the 'Arm First' orientation in all of the evaluated metrics.

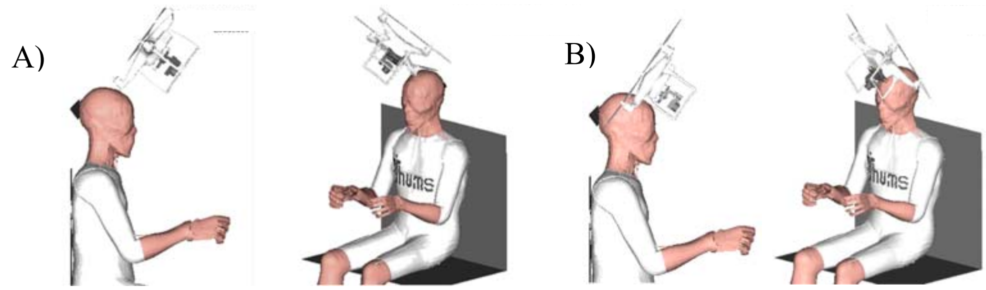

Figure 91. Critical sUAS orientations; DJI Phantom 3, 2.67 lb, 65 fps, angled 58 degrees forward - A) ‘Arm First’ and B) ‘Front First’ orientations

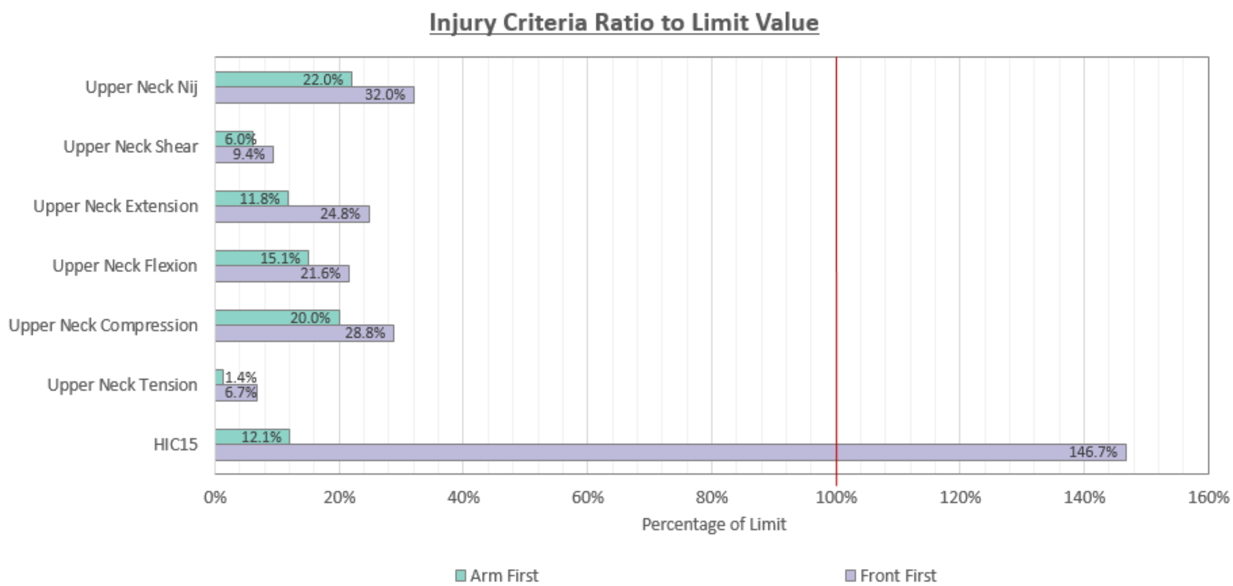

Figure 92. Critical sUAS orientation impact simulation comparison; DJI Phantom 3, 2.67 lb, 65 fps, angled 58 degrees forward

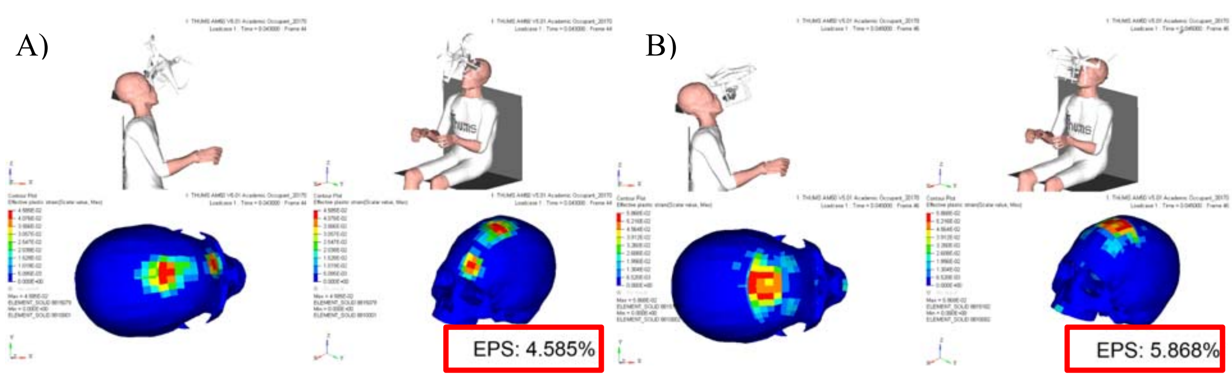

Figure 93. Critical sUAS orientation impact simulation comparison; DJI Phantom 3, 2.67 lb, 65 fps, angled 58 degrees forward - A) ‘Arm First’ and B) ‘Front First’ orientations

5.3.3 A14 Test Matrix Development

In order to define the A14 test matrix such that the limited number of sUAS articles could be used most effectively, two rounds of preparatory impact simulations were carried out. First, pre-test impact simulations were conducted at different impact directions and velocities with the critical sUAS orientation being common to all iterations. These simulations were subsequently compared with one another and ranked according to the severity of the injury criteria predictions, as shown in Figure 94 and Figure 95.

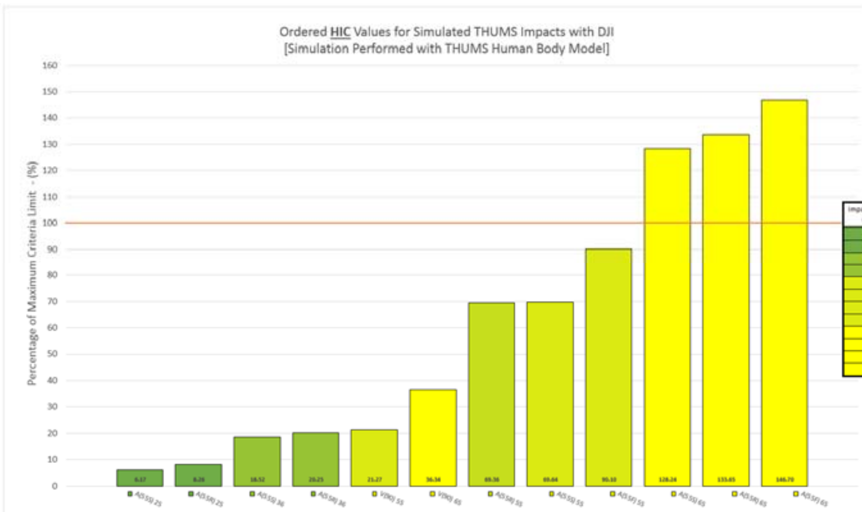

Figure 94. Pre-test impact simulations ranked by HIC output; DJI Phantom 3, 2.67 lb, 25 thru 65 fps, various orientations

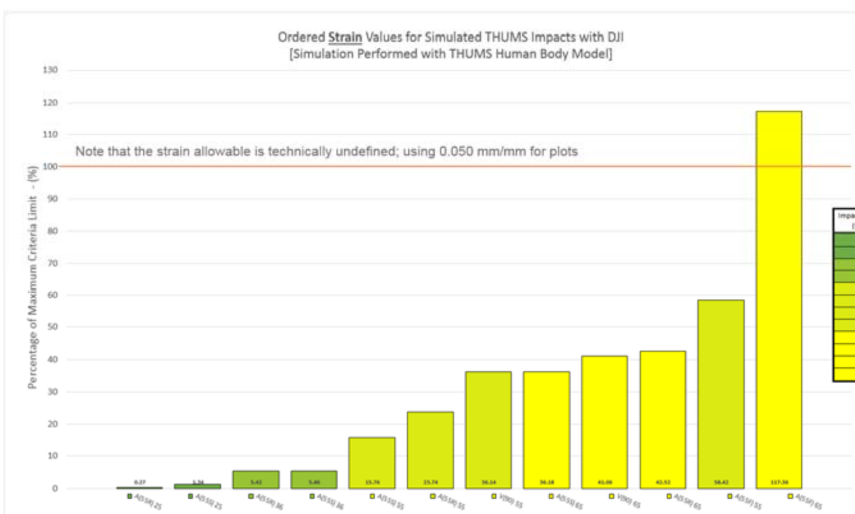

Figure 95. Pre-test impact simulations ranked by EPS output; DJI Phantom 3, 2.67 lb, 25 thru 65 fps, various orientations

The complete injury criteria data set is shown in Figure 96. Note that the color code begins with dark green representing lower velocity tests (25 fps), progresses through lighter green representing medium velocity tests (36 fps), and continues to shades of yellow for higher speed tests (55 fps and 65 fps). The order of the tests, increasing severity from left to right, is based on the respective injury criteria magnitude for each test. The scalar values in Figure 96 denote the percentage of the critical limit for each injury criteria. This chart shows that the THUMS model predicted the high speed angled frontal impact to be the worst case in more injury metrics than any other test condition.

HIC	A(55S) 25	A(55R) 25	A(55S) 36	A(55R) 36	V(90) 55	V(90) 65	A(55R) 55	A(55S) 55	A(55F) 55	A(55S) 65	A(55R) 65	A(55F) 65
	6.2	8.3	18.5	20.3	21.3	36.3	69.4	69.6	90.1	128.2	133.7	146.7
Nij	A(55R) 25	A(55R) 36	A(55R) 55	A(55F) 55	A(55R) 65	A(55F) 65	V(90) 55	V(90) 65	A(55S) 25	A(55S) 36	A(55S) 55	A(55S) 65
	14.0	18.0	26.0	28.0	29.0	32.0	33.0	35.0	41.9	57.1	81.6	90.4
Tension	A(55R) 25	V(90) 55	A(55S) 25	V(90) 65	A(55S) 36	A(55R) 36	A(55F) 55	A(55S) 55	A(55R) 55	A(55S) 65	A(55R) 65	A(55F) 65
	0.1	0.1	1.7	1.8	2.9	3.4	4.6	5.2	5.2	5.7	6.5	6.7
Compression	A(55S) 25	A(55R) 25	A(55R) 36	A(55S) 36	A(55R) 55	A(55F) 55	A(55S) 55	A(55S) 65	A(55F) 65	A(55R) 65	V(90) 55	V(90) 65
	13.1	13.5	17.6	17.7	25.2	25.2	25.2	27.9	28.8	30.2	31.9	34.8
Flexion	A(55R) 25	A(55S) 25	A(55R) 36	A(55S) 36	A(55R) 55	A(55S) 55	A(55R) 65	A(55F) 55	A(55S) 65	V(90) 55	A(55F) 65	V(90) 65
	7.8	8.2	10.5	11.3	15.2	16.3	17.3	18.0	18.1	19.6	20.6	21.6
Extension	A(55R) 25	V(90) 55	A(55S) 25	A(55R) 36	A(55S) 36	A(55F) 55	V(90) 65	A(55R) 55	A(55S) 55	A(55R) 65	A(55S) 65	A(55F) 65
	0.5	0.7	6.1	9.8	11.0	14.0	14.6	17.3	19.2	22.0	22.2	24.8
Shear	A(55S) 25	A(55S) 36	A(55R) 25	V(90) 55	A(55F) 55	V(90) 65	A(55R) 36	A(55R) 55	A(55S) 55	A(55F) 65	A(55S) 65	A(55R) 65
	3.2	4.9	5.7	6.1	6.6	7.0	8.0	12.5	47.8	52.1	58.9	81.9
Strain	A(55R) 25	A(55S) 25	A(55R) 36	A(55S) 36	A(55S) 55	A(55R) 55	V(90) 55	A(55S) 65	V(90) 65	A(55R) 65	A(55F) 55	A(55F) 65
	0.3	1.3	5.4	5.5	15.8	23.7	36.1	36.2	41.1	42.5	58.4	117.4

Note that the strain allowable is technically undefined; using 0.050 mm/mm for plots

Figure 96. Pre-test impact simulations ranked for multiple injury criteria; DJI Phantom 3, 2.67 lb, 25 thru 65 fps, various orientations

Following this first simulation set, researchers at UAH proposed a set of preliminary test conditions that were informed by the preceding studies. These proposed test conditions were evaluated with the THUMS model impact simulations. The THUMS model was impacted with the DJI Phantom3 sUAS model in simulations utilizing the critical orientation for each impact direction and covering a velocity range of 56 thru 71fps. Figure 97 presents the impact directions studied in this effort, which are: vertical, horizontal sideward, angled frontal, and angled rear. Note that these are not the final A14 test conditions, even though they are similar.

Test	PMHS	Aircraft	Impact Orientation with Respect to Head	Aircraft Impact Orientation	Impact Velocity/KE	Remark
1	#1	DJI Phantom 3 (2.69 lbs)	Vertical to top of Head	Forward - Impact Point Between Arms	56 ft/s (124 ft-lb)	
2	#1	DJI Phantom 3 (2.69 lbs)	Vertical to top of Head	Forward - Impact Point Between Arms	61 ft/s (150 ft-lb)	
3	#1	DJI Phantom 3 (2.69 lbs)	Vertical to top of Head	Forward - Impact Point Between Arms	71 ft/s (200 ft-lb)	
4	#1	DJI Phantom 3 (2.69 lbs)	Horizontal to Side of Head	Forward - Impact Point Between Arms	56 ft/s (124 ft/s)	Assess neck injury
5	#1	DJI Phantom 3 (2.69 lbs)	Horizontal to Side of Head	Forward - Impact Point Between Arms	61 ft/s (150 ft-lb)	Only complete if no injury on previous test
6	#2	DJI Phantom 3 (2.69 lbs)	58 Deg to Front of Skull	Forward - Impact Point Between Arms	61 ft/s (150 ft-lb)	Above Skull Fracture Limit; Objective is to Bracket Skull Fracture Limit
7	#2	DJI Phantom 3 (2.69 lbs)	58 Deg to Rear of Skull	Forward - Impact Point Between Arms	71 ft/s (200 ft-lb)	
8	#2	DJI Phantom 3 (2.69 lbs)	Horizontal to Side of Head	Forward - Impact Point Between Arms	71 ft/s (200 ft-lb)	

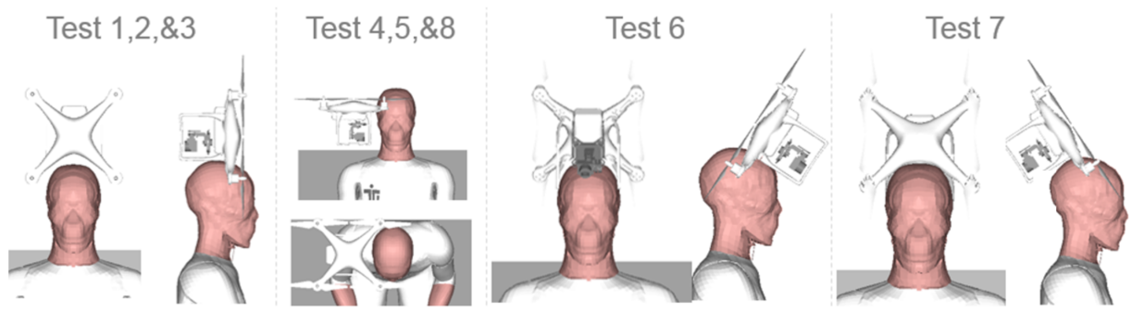

Figure 97. A14 test matrix development condition set; DJI Phantom 3, 2.67 lb, 56 fps thru 71 fps, vertical, sideward, angled frontal, and angled rear impact directions.

The results of this simulated test matrix gave the output shown in Figure 98. Note that the color codes classify the impact orientations as follows: shades of blue correspond to vertical tests, shades of green denote horizontal tests, yellow indicates the frontal angled test, and orange relates to the rearward angled impact.

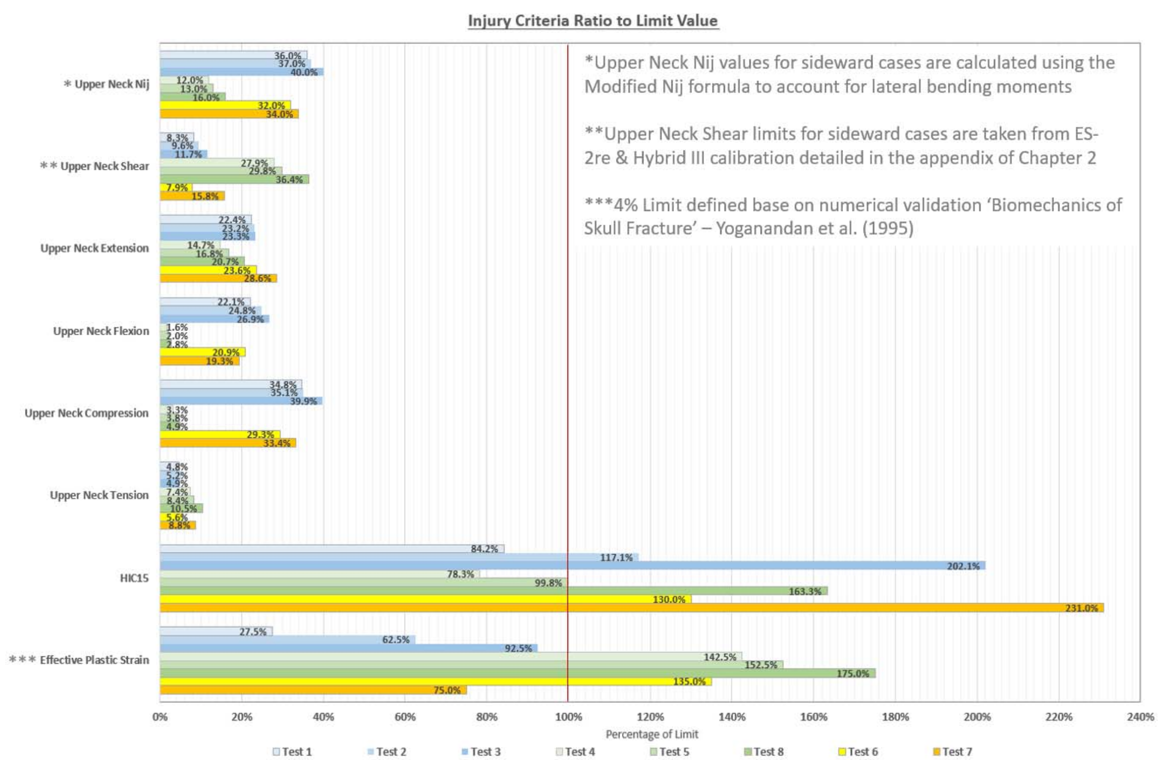

Figure 98. Simulation outputs for A14 test matrix development condition set; DJI Phantom 3, 2.67 lb, 56 fps thru 71 fps, vertical, sideward, angled frontal, and angled rear impact directions

The THUMS simulations used flat rigid panels for the seat base and backrest in the preceding model development work. In order to replicate the A14 PMHS test series with good fidelity, NIAR created a model of the seat assembly used by OSU, described in [3]. Following the seat model update, simulations were conducted using the conditions shown in Figure 97 to ensure that the response of the THUMS model would not be deteriorated. The seat model did not change the simulation output to a significant degree in these comparisons. This is attributed to the rather short duration of these sUAS impact events and the damped kinematic reactions of the biofidelic model. Inspecting the simulation kinematics showed that the significant reactions of the THUMS model had completed by the time the energy transfer propagated to the seat model. Therefore, the seat displacements are effectively inconsequential to the simulation output because they occur after the peak values in the various data channels.

6. HUMAN BODY MODEL ANALYSES

Once the THUMS model was evaluated and calibrated to the A11 test data, additional impact conditions were analyzed and documented. These numerical analyses are focused on validating the thresholds for head acceleration, head rotational velocity, and head rotational acceleration that will result in concussion and injuries at AIS level 3 and beyond for both UAS models.

6.1 A14 TEST EVALUATION - PHANTOM III

The level of accuracy achieved by the UAS finite element model and the THUMS human body model in the impact simulations presented in previous sections gave confidence to continue using the FE models to compare simulation outputs to the full PMHS test matrix, Table 27.

Table 27. A14 Test Conditions – Phantom 3

UAH Test #	Impact Trajectory	Model	Impact Speed (fps)	Impact Speed (kts)	Impact Location	Vehicle Orientation	Impact KE (ft-lbf)
2	Horizontal	DJI Phantom 3	56	33	Right Side of Head	Front First	125.9
3	Horizontal	DJI Phantom 3	61	36	Right Side of Head	Front First	149.8
4	Horizontal	DJI Phantom 3	71	42	Right Side of Head	Front First	198.5
6	Angled	DJI Phantom 3	56	33	58 deg to Front Side of Skull	Front First	136.1
7	Angled	DJI Phantom 3	61	36	58 deg to Front Side of Skull	Front First	156.3
8a	Angled	DJI Phantom 3	61	36	58 deg to Front Side of Skull	Front First	147.9
9	Angled	DJI Phantom 3	71	42	58 deg to Front Side of Skull	Front First	204.8
10	Angled	DJI Phantom 3	61	36	58 deg to Right Side of Skull	Front First	151.5
11a	Angled	DJI Phantom 3	71	42	58 deg to Right Side of Skull	Front First	205.3
13	Vertical	DJI Phantom 3	55	33	Vertical to Top of Head	Front First	117.5
14	Vertical	DJI Phantom 3	65	38	Vertical to Top of Head	Front First	161.0
15	Vertical	DJI Phantom 3	71	42	Vertical to Top of Head	Front First	195.6
16a	Angled	DJI Phantom 3	61	36	58 deg to Right Side of Skull	Front First	142.2
17	Angled	DJI Phantom 3	71	42	58 deg to Right Side of Skull	Front First	209.1
18	Angled	DJI Phantom 3	61	36	58 deg to Front Side of Skull	Front First	150.7
19	Angled	DJI Phantom 3	71	42	58 deg to Front Side of Skull	Front First	197.6
22	Vertical	DJI Phantom 3	65	38	Vertical to Top of Head	Front First	167.8
23	Vertical	DJI Phantom 3	71	42	Vertical to Top of Head	Front First	198.8

This section presents a comparison of test and simulation results for the eighteen A14 cases involving the DJI Phantom 3, see Table 28. The Phantom 3 FE model was frozen for these simulations, so the results are pure predictions, and no calibration was performed.

Table 28. A14 Test and simulation result comparison for Phantom3

Injury Criteria	Test 2		Test 3		Test 4		Test 6	
	Test	Sim	Test	Sim	Test	Sim	Test	Sim
Head Acceleration (g)	283.97	165.01	327.59	235.38	486.22	237.68	218.60	156.63
HIC15	865.66	342.73	1076.11	535.30	2892.49	570.33	521.88	296.01
Head 3 ms (g)	74.48	37.19	82.59	30.84	92.20	39.43	55.23	35.89
BrIC	0.38	0.36	0.45	0.35	0.50	0.39	0.30	0.37
Probability of Concussion	1.00	0.94	1.00	1.00	1.00	0.99	1.00	0.88
Upper Neck Tension (lbf)	-	72.03	-	65.57	-	90.84	-	87.78
Upper Neck Compression (lbf)	-	17.75	-	32.29	-	34.33	-	222.83
Upper Neck Flexion (lbf-ft)	-	1.12	-	2.29	-	2.24	-	31.07
Upper Neck Extension (lbf-ft)	-	7.00	-	6.23	-	8.64	-	14.97
Upper Neck Shear (lbf)	-	72.35	-	67.44	-	84.25	-	64.49
Lateral Moment (lbf-ft)	-	8.66	-	7.55	-	10.49	-	0.67
Twisting Moment (lbf-ft)	-	6.04	-	5.30	-	7.41	-	0.52
Upper Neck Nij	-	0.12	-	0.10	-	0.14	-	0.30

Injury Criteria	Test 7		Test 8		Test 9		Test 10	
	Test	Sim	Test	Sim	Test	Sim	Test	Sim
Head Acceleration (g)	241.24	188.33	159.82	194.13	175.40	218.91	239.19	145.06
HIC15	1303.76	382.32	379.62	386.66	538.76	512.74	500.28	294.36
Head 3 ms (g)	134.04	40.15	75.44	38.78	58.12	46.29	62.50	37.73
BrIC	0.35	0.39	0.51	0.39	0.56	0.42	0.26	0.30
Probability of Concussion	1.00	0.98	0.98	0.98	1.00	1.00	1.00	0.88
Upper Neck Tension (lbf)	-	94.68	-	92.35	-	102.71	-	49.31
Upper Neck Compression (lbf)	-	236.01	-	257.48	-	254.83	-	193.09
Upper Neck Flexion (lbf-ft)	-	31.93	-	33.67	-	33.77	-	22.22
Upper Neck Extension (lbf-ft)	-	15.95	-	15.81	-	16.87	-	8.40
Upper Neck Shear (lbf)	-	66.99	-	72.66	-	79.81	-	55.58
Lateral Moment (lbf-ft)	-	0.86	-	1.00	-	0.88	-	7.91
Twisting Moment (lbf-ft)	-	0.59	-	0.54	-	0.57	-	4.56
Upper Neck Nij	-	0.31	-	0.33	-	0.33	-	0.24

Injury Criteria	Test 11		Test 13		Test 14		Test 15	
	Test	Sim	Test	Sim	Test	Sim	Test	Sim
Head Acceleration (g)	302.63	182.40	393.40	155.47	467.89	201.86	551.15	264.15
HIC15	928.62	478.19	1848.20	319.04	2549.83	533.96	4197.13	836.25
Head 3 ms (g)	95.75	38.23	99.59	29.39	110.54	36.27	145.45	41.68
BrIC	0.34	0.33	0.35	0.19	0.35	0.21	0.26	0.23
Probability of Concussion	1.00	1.00	1.00	0.41	1.00	0.92	1.00	1.00
Upper Neck Tension (lbf)	-	52.98	-	39.33	-	48.08	-	46.98
Upper Neck Compression (lbf)	-	202.77	-	277.17	-	311.91	-	319.00
Upper Neck Flexion (lbf-ft)	-	22.94	-	30.71	-	34.08	-	37.57
Upper Neck Extension (lbf-ft)	-	9.69	-	9.67	-	10.85	-	10.93
Upper Neck Shear (lbf)	-	65.69	-	54.04	-	67.75	-	83.55
Lateral Moment (lbf-ft)	-	8.67	-	0.86	-	1.10	-	1.11
Twisting Moment (lbf-ft)	-	5.35	-	1.85	-	0.59	-	0.73
Upper Neck Nij	-	0.25	-	0.33	-	0.37	-	0.39

Injury Criteria	Test 16		Test 17		Test 18		Test 19	
	Test	Sim	Test	Sim	Test	Sim	Test	Sim
Head Acceleration (g)	216.15	218.91	377.56	237.20	385.27	226.61	643.59	300.72
HIC15	411.72	512.74	2527.15	649.91	1860.89	726.12	5473.40	1330.74
Head 3 ms (g)	64.69	46.29	123.85	35.08	67.76	33.38	112.38	42.61
BrIC	0.30	0.42	0.40	0.32	0.46	0.38	0.50	0.42
Probability of Concussion	1.00	1.00	1.00	1.00	1.00	1.00	1.00	1.00
Upper Neck Tension (lbf)	-	102.71	-	47.70	-	61.64	-	55.04
Upper Neck Compression (lbf)	-	254.83	-	220.56	-	249.39	-	285.13
Upper Neck Flexion (lbf-ft)	-	33.77	-	25.11	-	32.83	-	34.68
Upper Neck Extension (lbf-ft)	-	16.87	-	9.58	-	13.58	-	13.80
Upper Neck Shear (lbf)	-	79.81	-	66.16	-	58.75	-	63.29
Lateral Moment (lbf-ft)	-	0.88	-	8.16	-	0.90	-	1.54
Twisting Moment (lbf-ft)	-	0.57	-	6.14	-	1.01	-	1.55
Upper Neck Nij	-	0.33	-	0.27	-	0.32	-	0.35

Injury Criteria	Test 22		Test 23	
	Test	Sim	Test	Sim
Head Acceleration (g)	356.17	167.57	307.26	209.68
HIC15	1219.00	443.46	1747.90	554.55
Head 3 ms (g)	80.22	40.73	125.48	41.88
BrIC	0.34	0.23	0.35	0.25
Probability of Concussion	1.00	0.72	1.00	0.92
Upper Neck Tension (lbf)	-	50.43	-	50.98
Upper Neck Compression (lbf)	-	306.30	-	319.04
Upper Neck Flexion (lbf-ft)	-	34.29	-	37.02
Upper Neck Extension (lbf-ft)	-	11.11	-	11.27
Upper Neck Shear (lbf)	-	55.33	-	59.89
Lateral Moment (lbf-ft)	-	1.74	-	1.92
Twisting Moment (lbf-ft)	-	1.44	-	1.63
Upper Neck Nij	-	0.37	-	0.39

The A14 test data is also plotted in bar chart form in Figure 99, Figure 100 and Figure 101. Note that the injury metrics have been normalized according to their respective threshold values.

Figure 99. Bar charts with summary of injury criteria for A14 PMHS test vs THUMS simulation comparison. DJI Phantom 3 tests 2, 3, 4, 6, 7, and 8

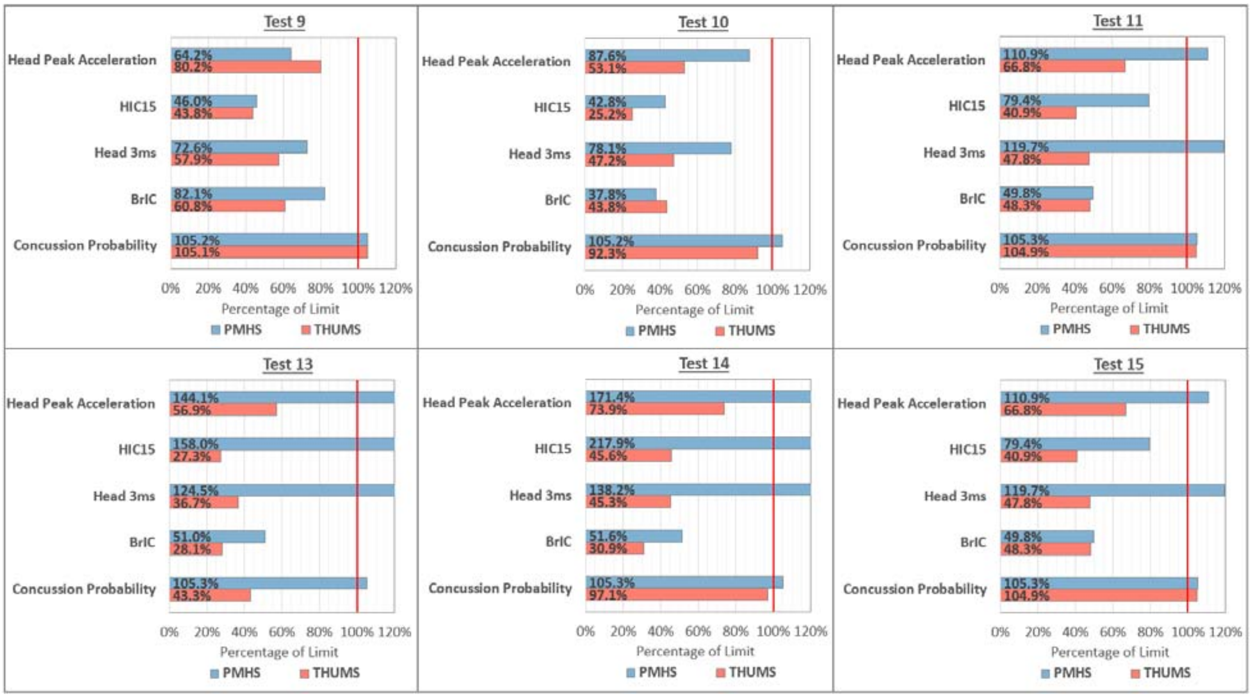

Figure 100. Bar charts with summary of injury criteria for A14 PMHS test vs THUMS simulation comparison. DJI Phantom 3 tests 9, 10, 11, 13, 14, and 15

Figure 101. Bar charts with summary of injury criteria for A14 PMHS test vs THUMS simulation comparison. DJI Phantom 3 tests 16, 17, 18, 19, 22, and 23

The following examples show the highest energy impact condition from each impact direction. The full test matrix documentation for the A14 Phantom3 impacts against the THUMS are contained in APPENDIX I—.

6.1.1 Vertical

PMHS Test 15 is shown in Figure 102; THUMS EPS contours are given in Figure 103; data outputs are summarized in Figure 104.

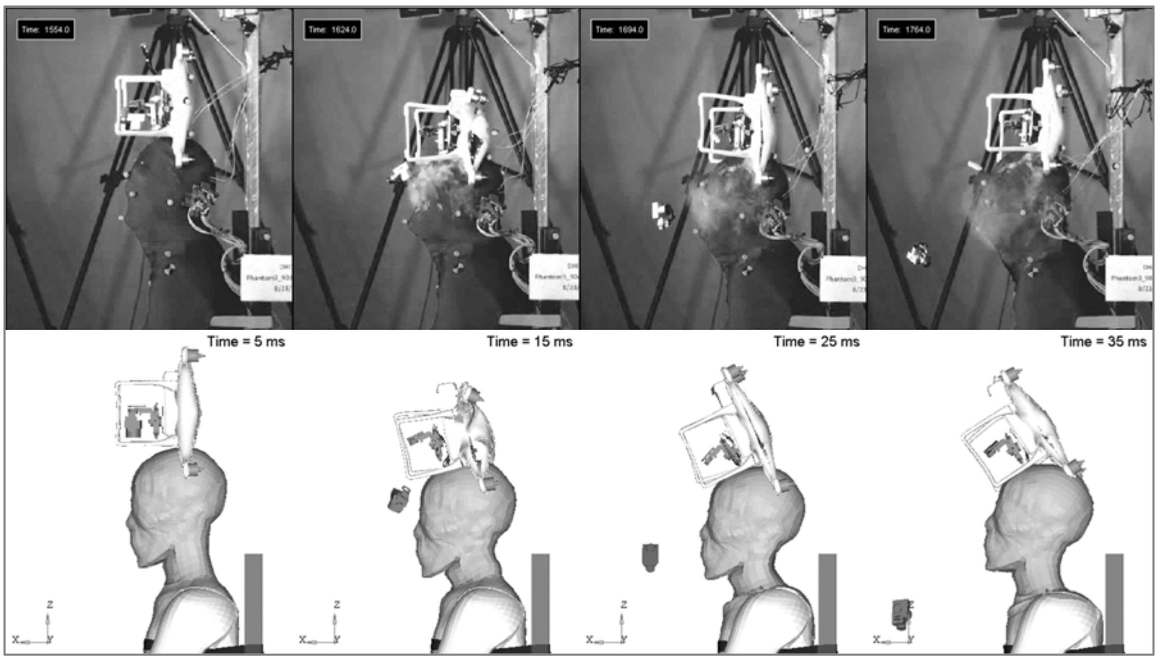

Figure 102. PMHS test 15 vs simulation comparison; DJI Phantom 3, 2.67 lb, bottom, 71 fps, vertical; subject #2; top of the head; kinematics

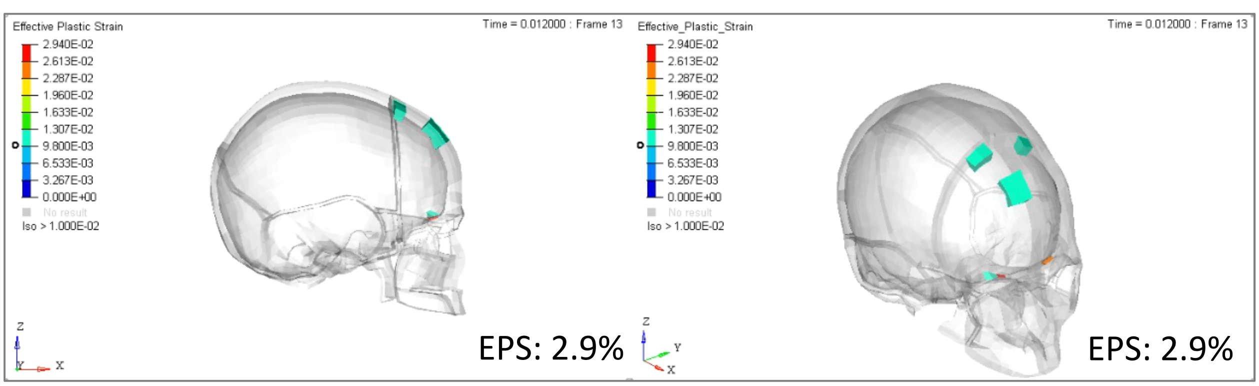

Figure 103. PMHS test 15 simulation; DJI Phantom 3, 2.67 lb, bottom, 71 fps, vertical; subject #2; top of the head; contour plot of skull strains

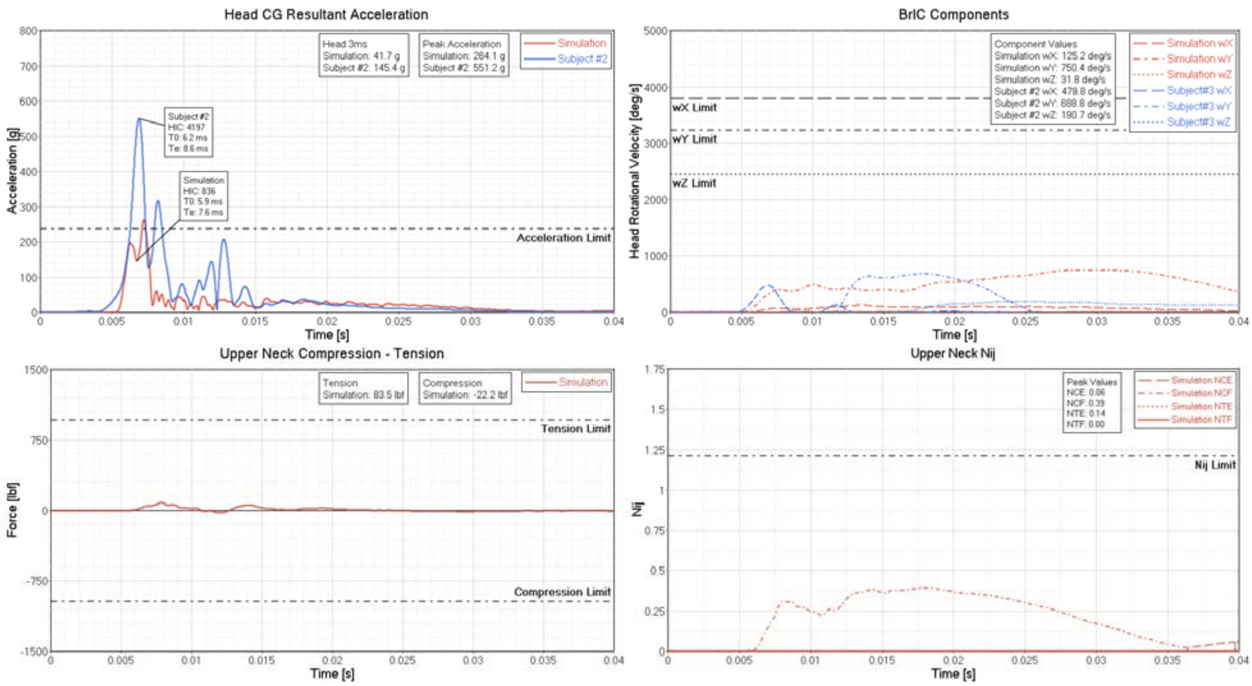

Figure 104. PMHS test 15 vs simulation comparison; DJI Phantom 3, 2.67 lb, bottom, 71 fps, vertical; subject #2; top of the head; time-history summary

6.1.2 Side

PMHS Test 4 is shown in Figure 105; THUMS EPS contours are given in Figure 106; data outputs are summarized in Figure 107.

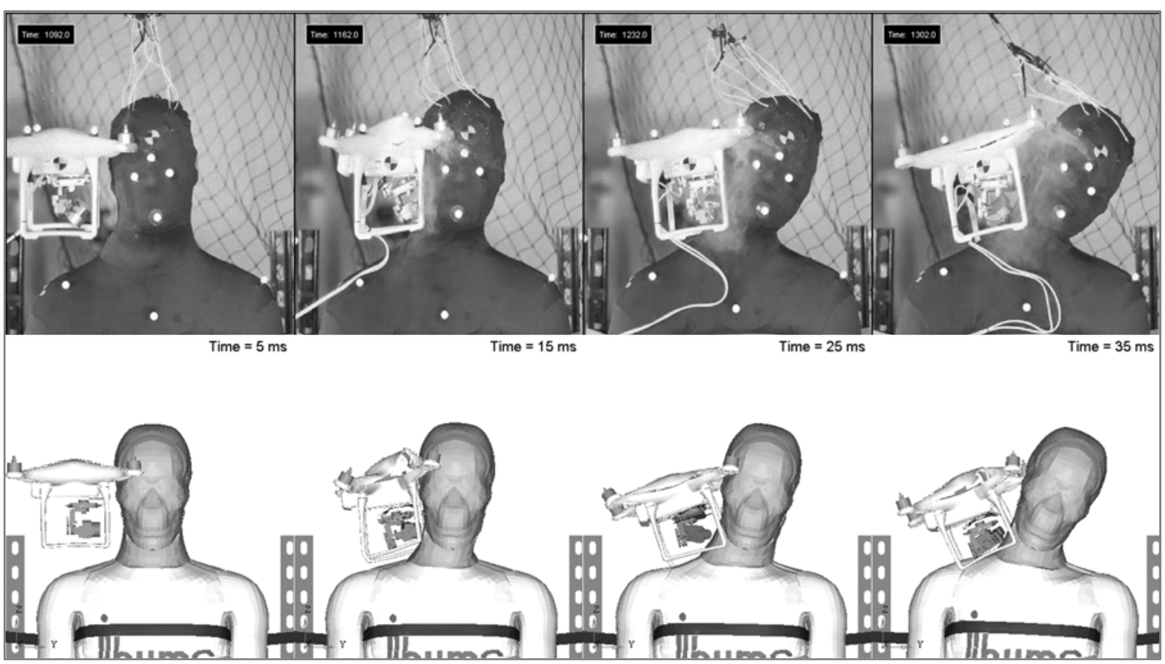

Figure 105. PMHS test 4 vs simulation comparison; DJI Phantom 3, 2.67 lb, between arms, 71 fps, sideward; subject #1; side of the head; kinematics

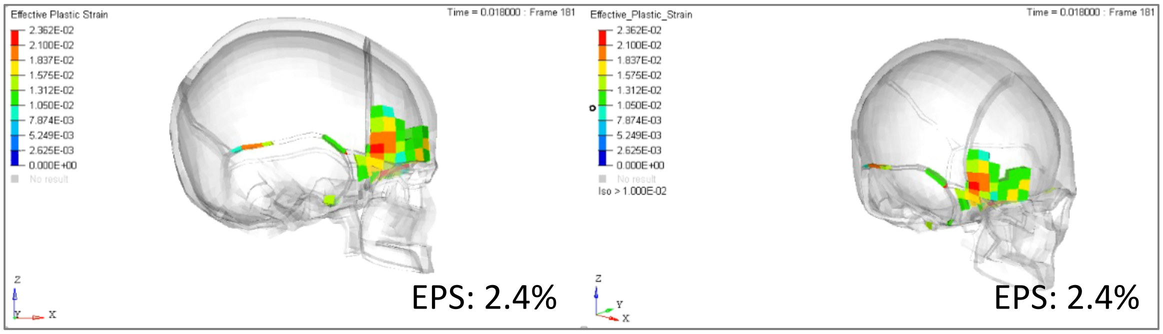

Figure 106. PMHS test 4 simulation; DJI Phantom 3, 2.67 lb, between arms, 71 fps, sideward; subject #1; side of the head; contour plot of skull strains

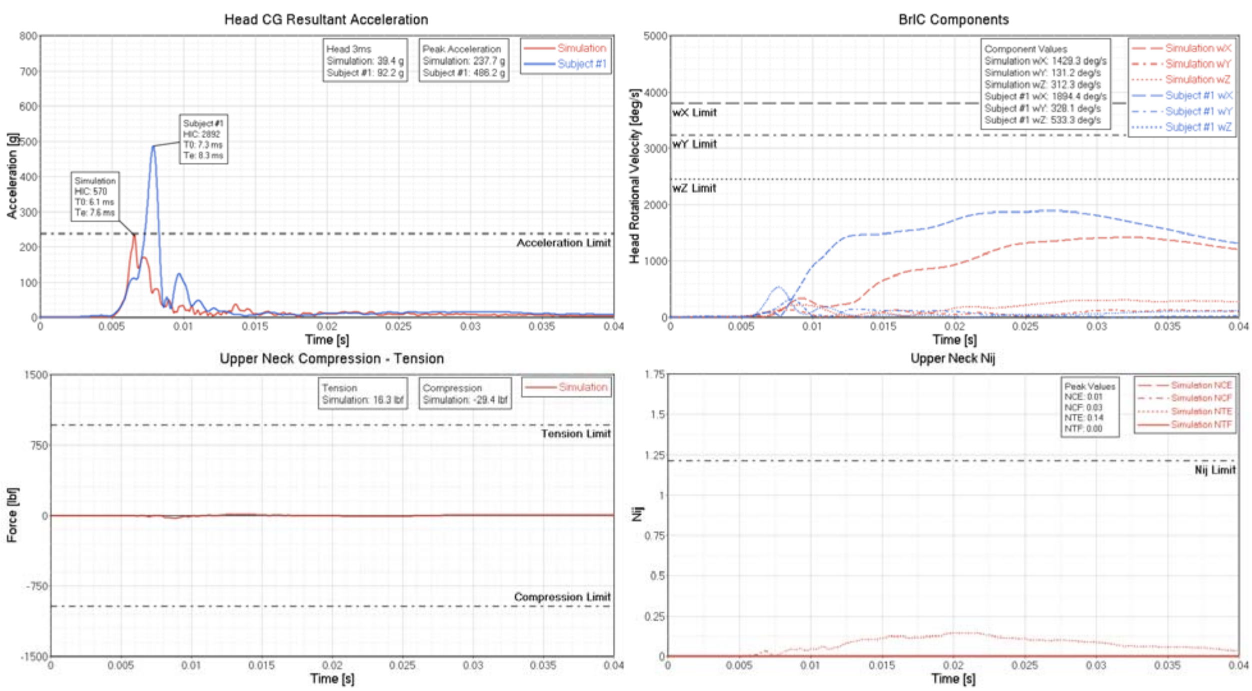

Figure 107. PMHS test 4 vs simulation comparison; DJI Phantom 3, 2.67 lb, between arms, 71 fps, sideward; subject #1; side of the head; time-history summary

6.1.3 Angle

PMHS Test 19 is shown in Figure 108; THUMS EPS contours are given in Figure 109; data outputs are summarized in Figure 110.

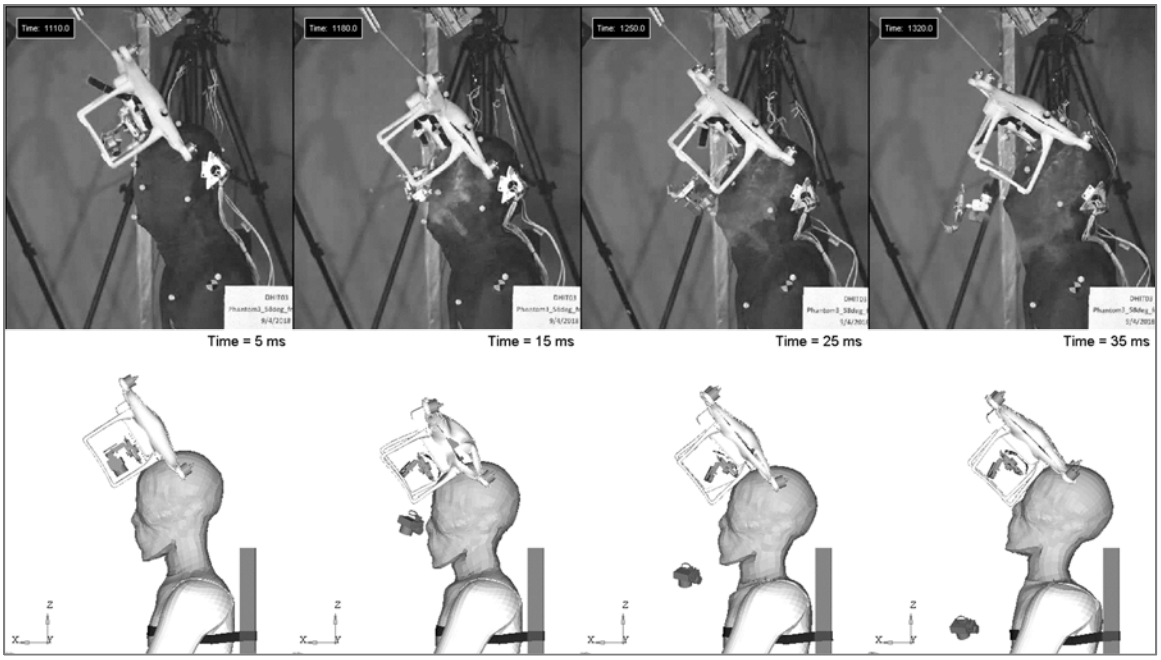

Figure 108. PMHS test 19 vs simulation comparison; DJI Phantom 3, 2.67 lb, between arms, 71 fps, 58 degree angled forward; subject #3; front of the head; kinematics

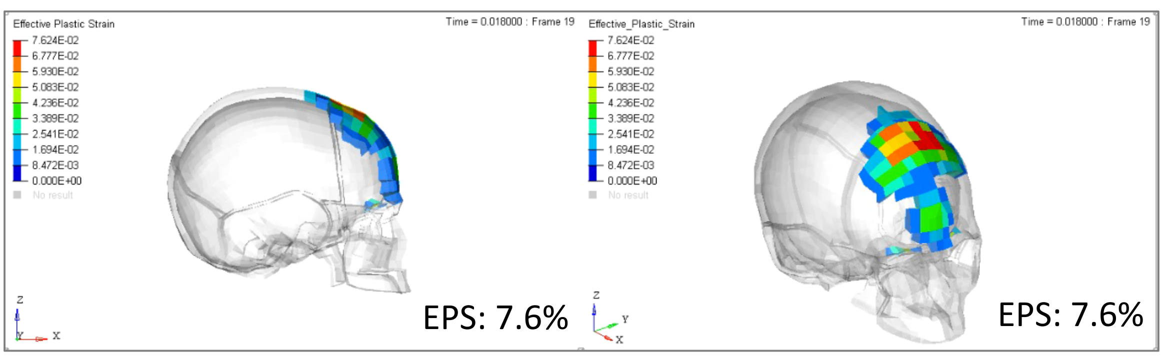

Figure 109. PMHS test 19 simulation EPS results; DJI Phantom 3, 2.67 lb, between arms, 71 fps, 58 degree angled forward; subject #3; front of the head; contour plot of skull strains

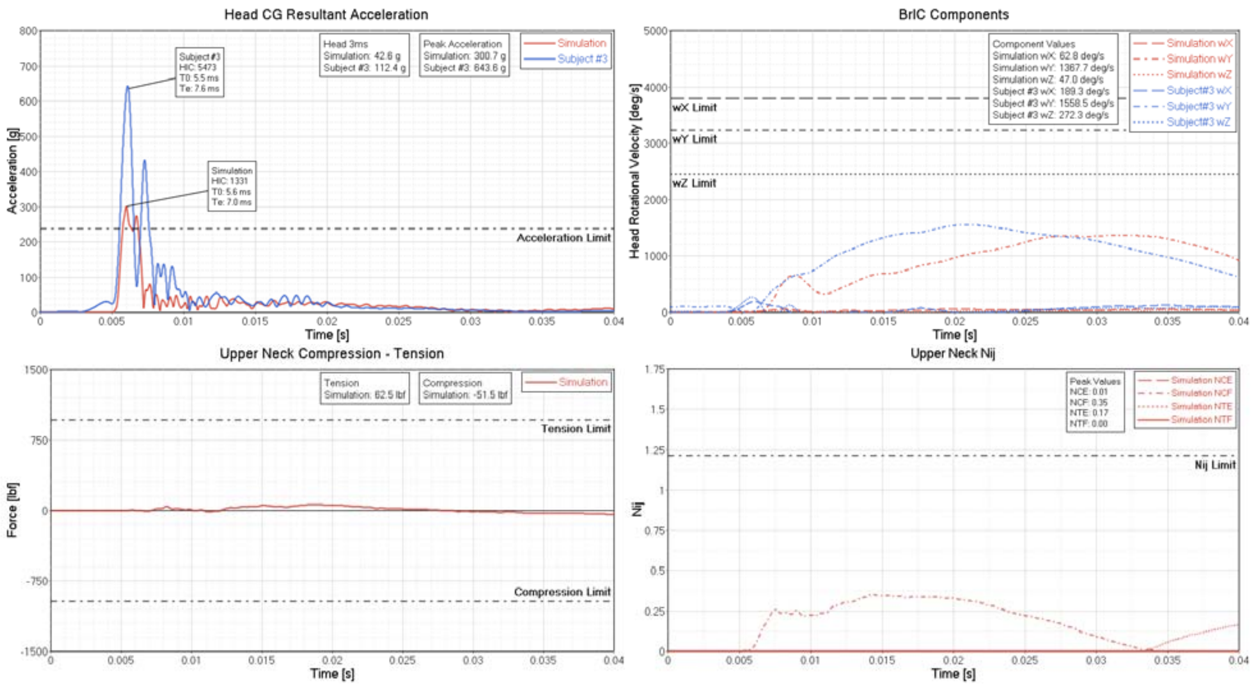

Figure 110. PMHS test 19 vs simulation comparison; DJI Phantom 3, 2.67 lb, between arms, 71 fps, 58 degree angled forward; subject #3; front of the head; time-history summary

Note that the peak magnitudes for angular velocity show a much better agreement between the PMHS test and THUMS simulation than the head acceleration values. The discrepancy in the PMHS head accelerations is discussed in Section 6.1.4.3 . The angular velocity outputs may show a better agreement due to the time that they occur relative to the beginning of the impact. The peak angular velocity values occur after the impact energy has been transferred from the UAS to the PMHS or THUMS head, whereas the head accelerations have their peak values during the transient phase of the impact, which could have been affected the instrumentation outputs, as discussed in Section 6.4.1.3 .

6.1.3.1 Critical PMHS Impact Test Replication with FAA Hybrid III ATD

The most critical impact test from the PMHS test series was the angled 58-degree frontal impact with the DJI Phantom3 impacting front-first at 71 fps. This designation is applied as a result of the test producing an AIS2 level skull fracture. This test also caused the largest value of head peak acceleration of any sUAS test.

A14 ATD testing did not initially include this test condition due to mechanical limitations of the sUAS launcher at the desired impact velocity. This limitation did not apply to the PMHS testing equipment as it utilized elastic tension forces rather than pneumatic pressure to achieve the launch velocity. At the end of the ATD testing program, NIAR determined that a small set of tests could be conducted in this higher energy range, despite the risk of damaging test equipment. These tests would give a comparable data set for the ATD response to the critical impact conditions. Test setup diagrams are shown in Figure 111.

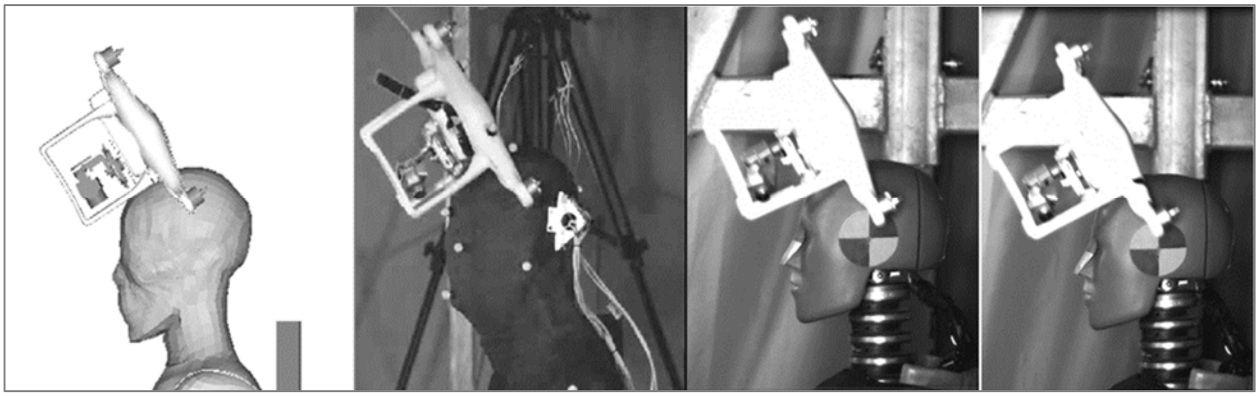

Figure 111. PMHS test 19 replication with FAA Hybrid-III ATD; DJI Phantom 3, 2.67 lb, front first, 71 fps, 58 degree angled forward; subject #3; front of the head; setup overview

This critical test replication effort utilized the VICON marker tracking data provided by OSU to ensure the same UAS orientation and impact angle were used in the ATD impacts. NIAR conducted two iterations of this test with the FAA Hybrid-III ATD. An impact location offset of approximately one-half inch (0.5 in) was observed between the two test iterations, shown in Figure 112. Given that the magnitude of the contact location offset was small, the data outputs for the two ATD tests show significant differences, plotted in Figure 113.

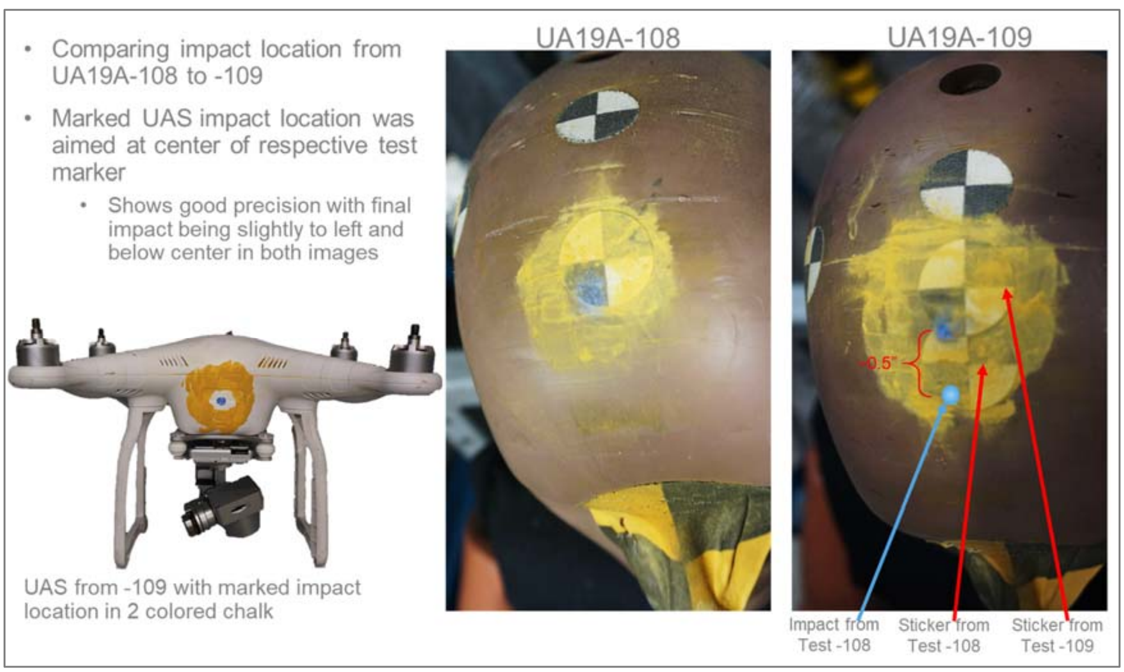

Figure 112. PMHS test 19 replication with FAA Hybrid-III ATD; DJI Phantom 3, 2.67 lb, front first, 71 fps, 58 degree angled forward; subject #3; front of the head; post-test inspection

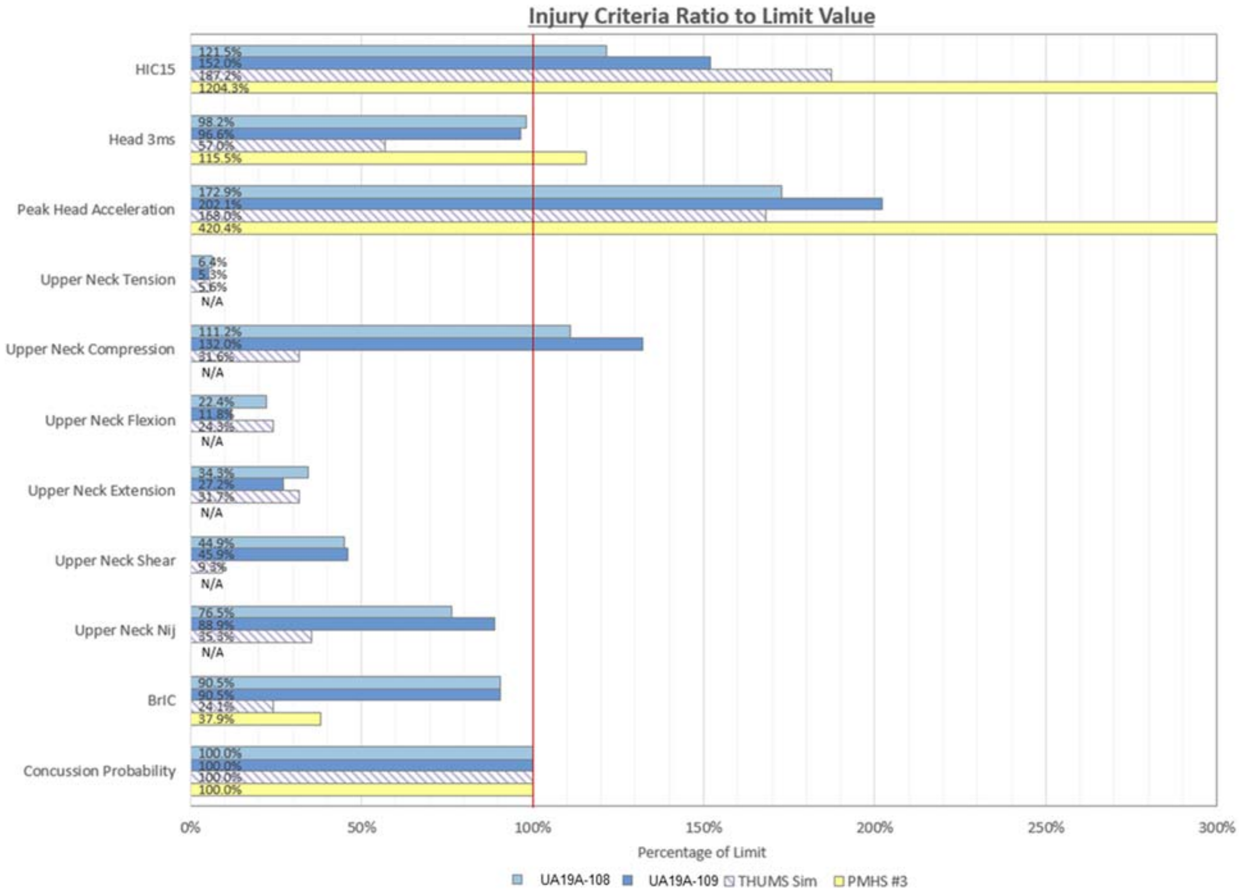

Figure 113. PMHS test 19 replication with FAA Hybrid-III ATD; DJI Phantom 3, 2.67 lb, front first, 71 fps, 58 degree angled forward; subject #3; front of the head; data output comparison

6.1.4 Post-test Analysis and Discussion

In support of the PMHS test and simulation comparison effort, NIAR conducted post-test analysis of the data output. This analysis provided insights into the mechanisms contributing to injury severity, trends regarding localized deformations of the THUMS skull model, and observations concerning pressure and strain values related to brain injury.

6.1.4.1 Injury Probability – 30% AIS3+

The probability of obtaining an injury from the A14 impact conditions is determined with respect to the threshold values corresponding to 30% for AIS3+ category injuries. Head peak acceleration is an exception to this rule, being compared against a 30% chance of receiving an AIS2+ level injury due to concerns about onset of skull fracture which occurs at this level.

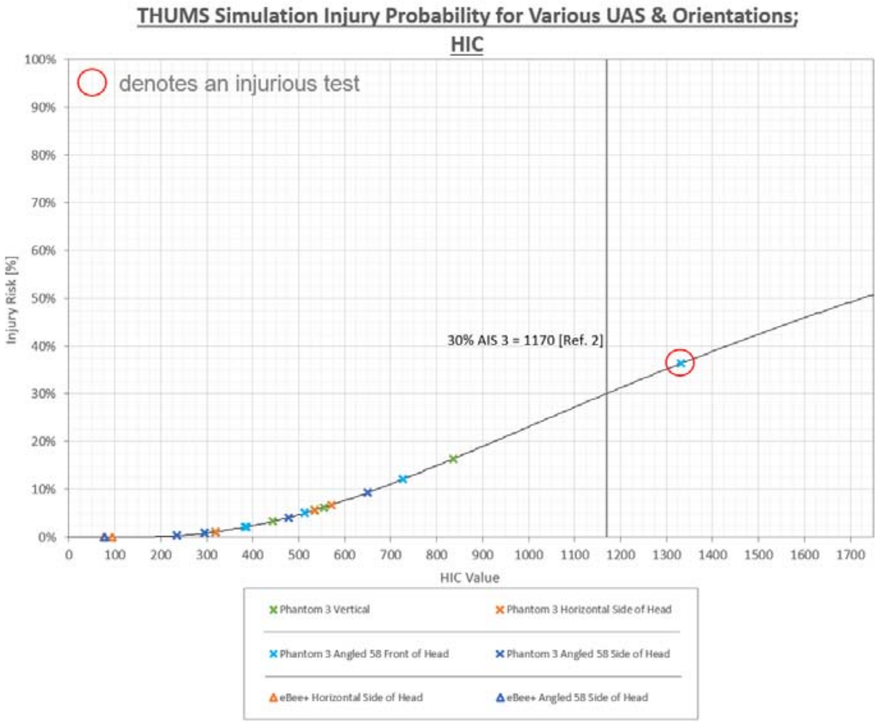

Figure 114. HIC injury probability for A14 THUMS simulations

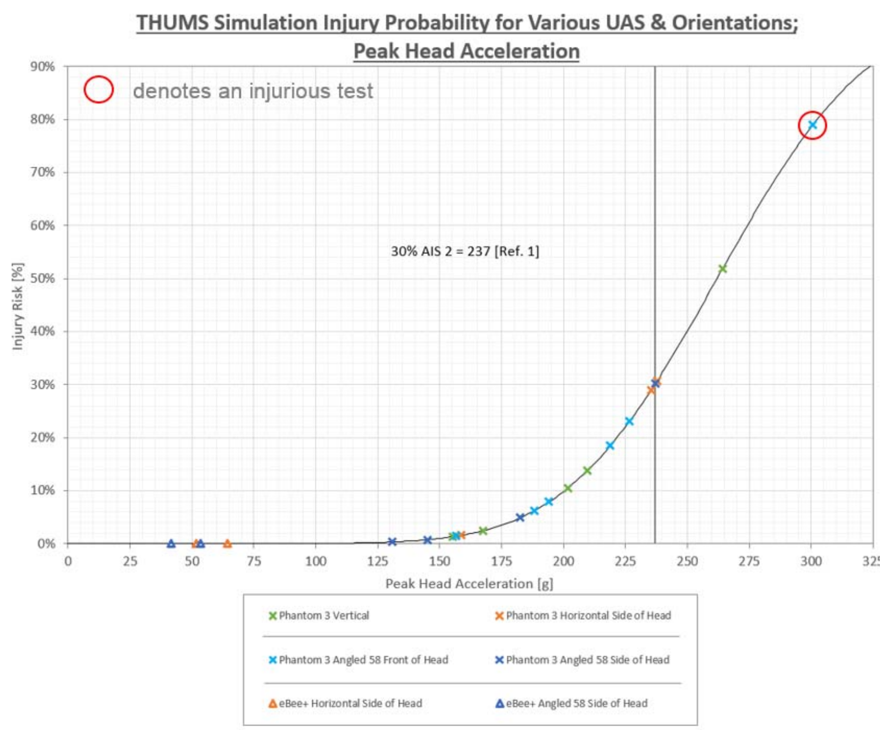

Figure 115. Head peak acceleration injury probability for A14 THUMS simulations

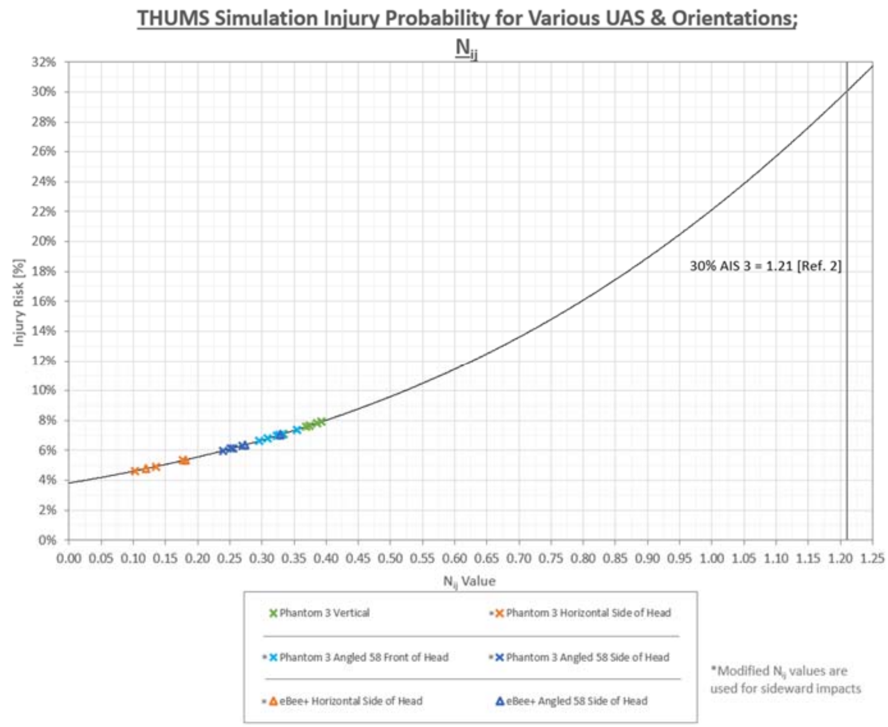

Figure 116. Nij injury probability for A14 THUMS simulations

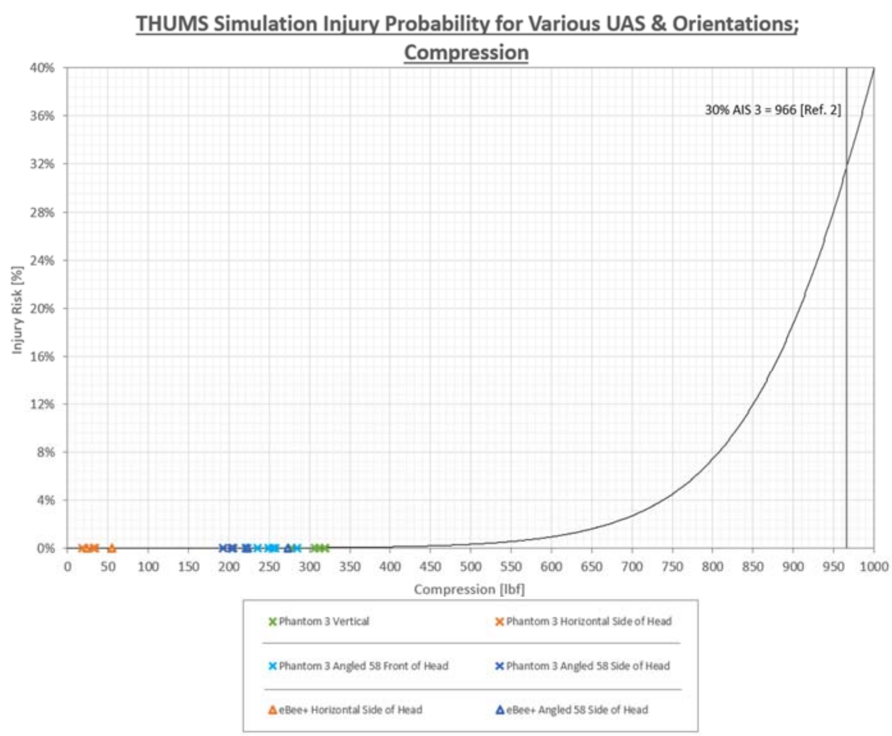

Figure 117. Neck compression injury probability for A14 THUMS simulations

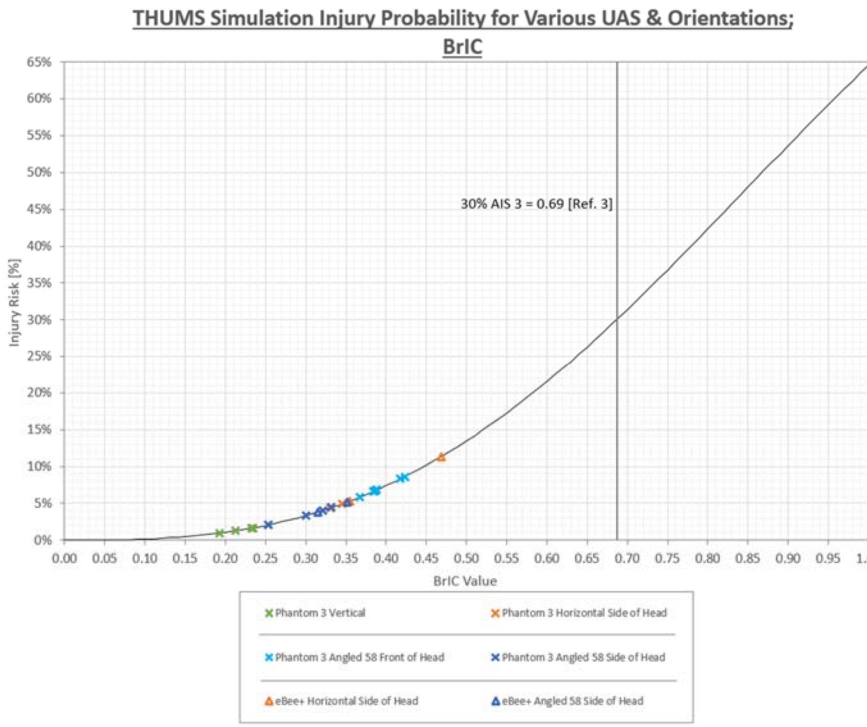

Figure 118. BrIC injury probability for A14 THUMS simulations

6.1.4.2 Mechanisms Contributing to Injury Severity

This section describes injury producing mechanisms that were determined with the cases discussed above.

THUMS model results showed that injury potential is related to the specific impact location and the direction of the impact relative to the test subject. This is consistent with trends seen in ATD testing as well, where sideward impacts typically produced lesser magnitude HIC values than vertical and angled impacts. Additionally, the front of the skull appears to be more susceptible to fracture due to the sinus cavities in that location being represented in the THUMS model as solid bones with reduced density and stiffness to reflect the porous and hollow anatomical structures. The model appears to allow greater strain values in the frontal bone as a reflection of the biofidelic vulnerability of that region on the actual human frontal bone. In terms of skull fracture probability, frontal angled impacts showed the greatest severity of the cases studied. The most critical frontal angled impact condition was replicated in ATD testing with two iterations to determine impact location sensitivity. The results of this test showed a 30% difference in HIC and peak acceleration, and a 20% difference in neck compression loading. Despite this significant difference from test-to-test, both tests resulted in HIC and peak acceleration values exceeding their respective limits. Measurements of the contact locations of both tests indicated an offset of approximately 0.5 in on the surface of the ATD head form. The significant discrepancy in acceleration and load magnitudes indicates a high dependence on the contact location, due to the relative impact angle at the contact surface and the alignment of the sUAS CG with that of the ATD's head form. Furthermore, the significance of the sUAS impact location is supported by the results from PMHS testing. PMHS #2 and #3 were both tested at the critical frontal angled condition, but the impact angle and the CG alignment was less precise for PMHS #2, resulting in no observable injury, while PMHS #3 had a more significant contact angle and CG alignment, which resulted in an AIS2 level injury.

The impact location sensitivity trend appears in all of the test and simulation environments and could be a general feature of projectile impacts to the head. The skull being roughly spherical implies that any deviation from a true CG-to-CG alignment could reduce the head translational acceleration and neck forces while increasing rotational accelerations and neck moments. The particular skull geometry of a test subject or HBM can lead to test output deviations when comparing various tests against one another but this study showed typically consistent trends relating the impact severity to the CG-to-CG alignment of the projectile and the target, despite the geometrical differences between test subjects and the THUMS model. Regarding the HBM outputs, it is possible that the model details can drive deviations in the model outputs compared to test results based on the material properties and biofidelic geometry but the extent to which this is significant depends on the validation status of the model. Physics based modeling has been demonstrated in preceding sections of this report and in other modeling and test comparisons [10] [30].

6.1.4.3 Localized Deformations

NIAR noted that the THUMS model can show deformation gradients propagating outward from the impact site, as shown in Figure 119. This means that the skull does not act as a purely rigid body and thus would not report the same acceleration in any two different locations.

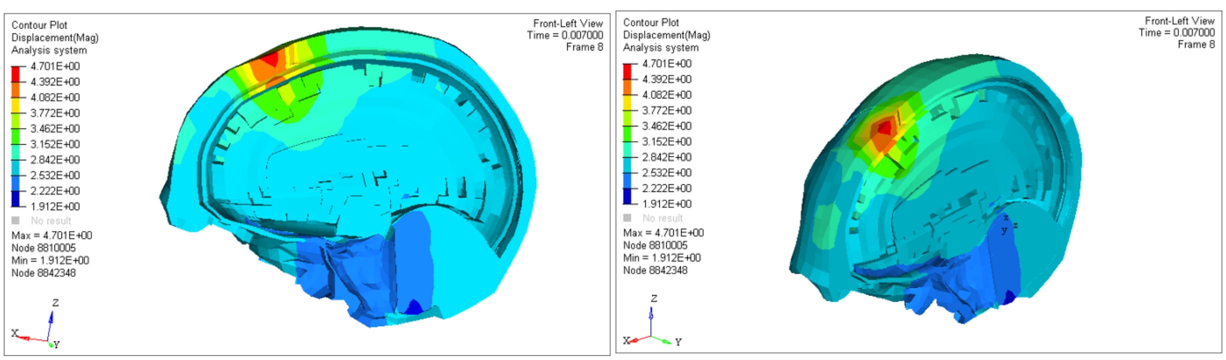

Figure 119. PMHS test 19 simulation; DJI Phantom 3, 2.67 lb, between arms, 71 fps, 58 degree angled forward; subject #3; front of the head; skull displacement contour plot

This observation is supported by the trends shown in Section 5.2.2 regarding the independent node set sensitivity study. Note that the material properties of the THUMS model allow local deformations to occur in a way that may not represent the skull kinematics of the PMHS test subjects, due to the lack of validation testing concerning this specific phenomenon. However, it is an unavoidable truth that the biological materials composing the head and neck are deformable materials that may allow similar relative deformations and thus differential acceleration values.

Note that these deformations depend on the amount of contact area between the external surfaces of the UAS and the head. This implies that for a given UAS shape, there is a corresponding location on the head that would obtain more severe injuries than other locations. For the Phantom3, that location is the front of the head due to the radius of the UAS body surface between the motor mount 'arms' and the shape of the frontal bones of the THUMS model.

NIAR performed the following post-processing examples to confirm that local deformations are present in the THUMS simulation and that these can affect the test data output based on the relative deformations present in vicinity of the test instrumentation. Figure 120 shows the simulation corresponding to the sideward impact performed in test #4 with PMHS #1. The displacement output from four nodes around the perimeter of the THUMS skull were evaluated in the X-axis direction (transverse to the Y-axis direction of the impact); two nodes are located on the side of the skull near the impact site, one node is located on the frontal bone, and one node is located on the occipital bone. These nodes are color coded on the diagram as well as on the plot. The time-history plot shows that the fwd-most and aft-most nodes move fore-and-aft in opposing directions at the start of the sideward contact with the UAS, and then move in synchrony after about 9 ms. This confirms that local deformations are present between the fwd and aft surfaces of the skull. Furthermore, it is inherent that the velocity and acceleration time-histories for these locations would differ as well.

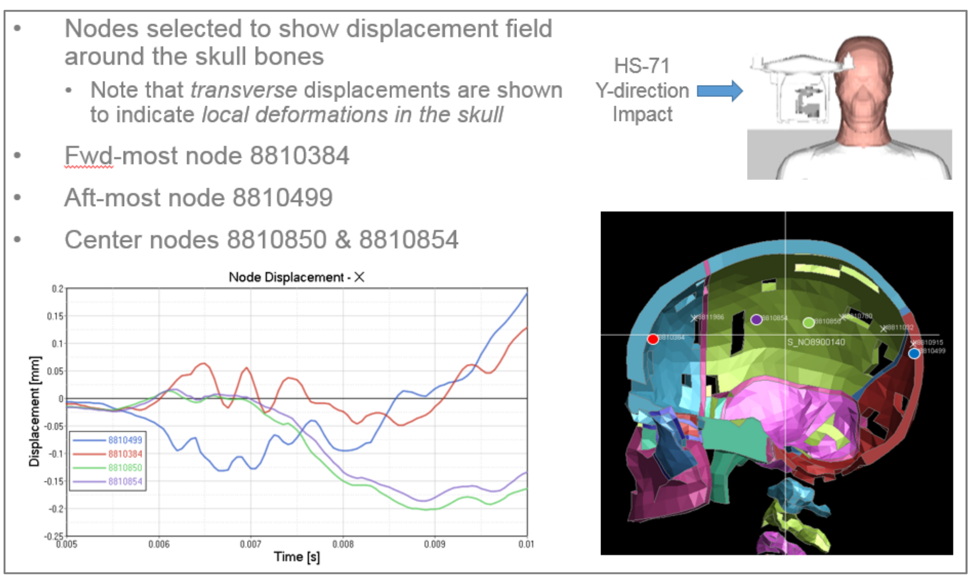

Figure 120. PMHS test 4 vs simulation comparison; DJI Phantom 3, 2.67 lb, between arms, 71 fps, sideward; subject #1; side of the head; node displacement time-history

Similar analysis was performed for Test 19, the critical angled impact condition. In this version of the analysis, fives nodes along the centerline of skull bones and one node from each side of the skull are selected to show displacements during the impact event, as shown in Figure 121. The nodes on the side of the skull are taken from opposite sides to show that they move in opposing directions due to the overall skull deformability. Note that the deformations in the visual representation have been scaled by a factor of 10x for clarity; this does not apply to the time-history plot. The impact contact begins at 5 ms from the start of the simulation. The maximum lateral displacement of the two sideward nodes occurs at T = 6 ms. The maximum impact deformation in the skull occurs at T = 7 ms (shown in the visual depiction, since these are not lateral displacements like those plotted in the time-history results). After 10 ms, all of the nodes move synchronously in the positive Y-direction, demonstrating that localized lateral displacements were associated with the critical angled frontal impact.

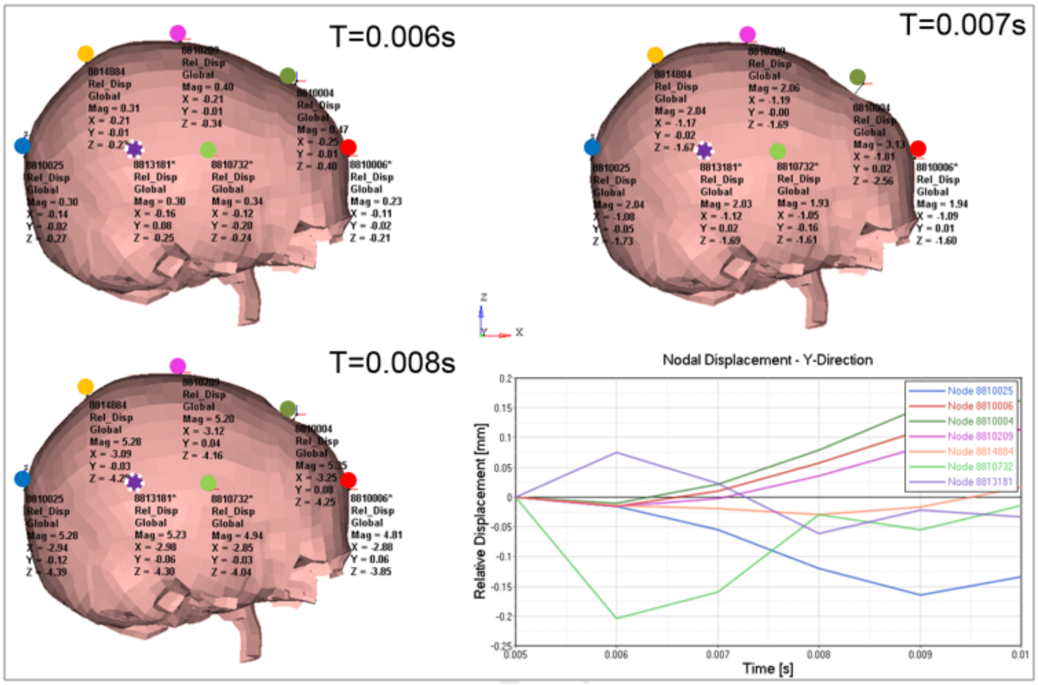

Figure 121. PMHS test 19 simulation; DJI Phantom 3, 2.67 lb, between arms, 71 fps, angled 58 degrees forward; subject #3; front of the head; node displacement time-history

<u>6.1.4.4 Brain Injury Assessment</u>

Brain injury is not identifiable from the PMHS tests performed during this research effort, but can be investigated with the THUMS simulations. The current understanding of brain injury mechanisms, and the parameters that are assumed to quantify injury potentials, are in somewhat preliminary stages of development for the present impact conditions. As such, the following assessments are provided as an example of the present state of the injury metrics as applied to the THUMS. Since these pressures and strains are validated against a limited set of test data, the results should not be considered in the same category as the HIC and Nij but should serve as an indication of the possible range of outcomes from these impact conditions. Figure 122 and Figure 123 present the brain pressures and principal strains for the most critical impact test: the Phantom 3, 58 degree angled forward, 71 fps case. The plots in Figure 124 and Figure 125 show the brain pressures and principal strains for the eBeePlus, 58 degree angled sideward, 71 fps case. Note that the eBeePlus pressure contour plot indicates a minimal number of elements above the injury threshold, while the Phantom3 example case shows a significant portion of the brain material exceeding the pressure limit. Preliminary results for TBI and DAI injury prediction are shown for the following cases:

- DJI Phantom 3 – Frontal Angled 58deg. Impact - 71 ft/s
- eBeePlus - Side Angled 58 deg. Impact – 71 ft/s

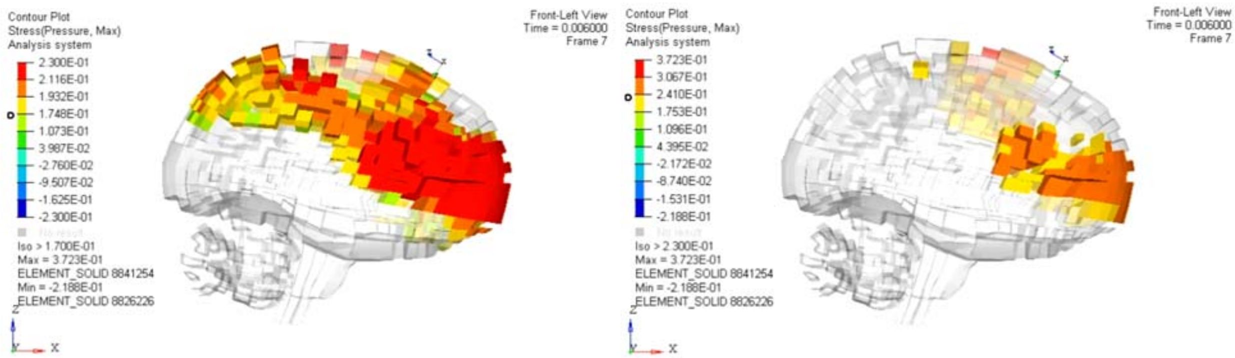

Figure 122. DJI Phantom 3, 2.67 lb, forward, 71 fps, angled 58 degree; A14 THUMS simulation, front of the head; brain pressure output

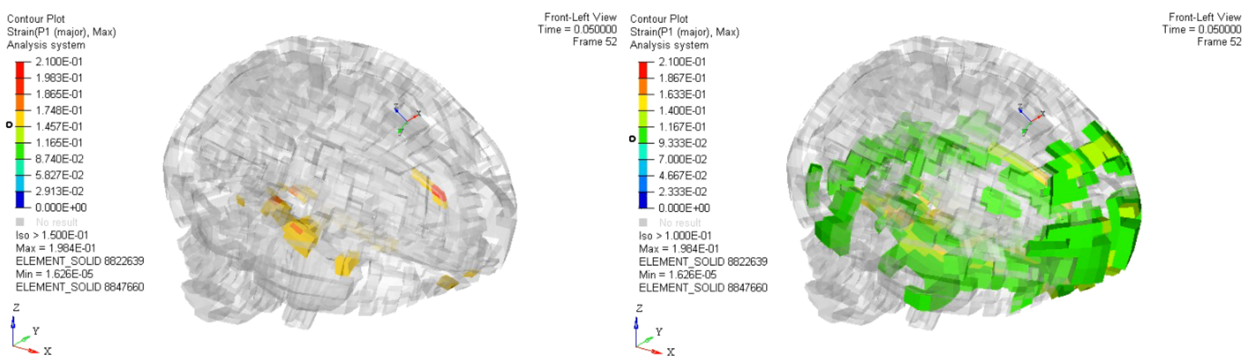

Figure 123. DJI Phantom 3, 2.67 lb, forward, 71 fps, angled 58 degree; A14 THUMS simulation, front of the head; brain maximum principal strain output

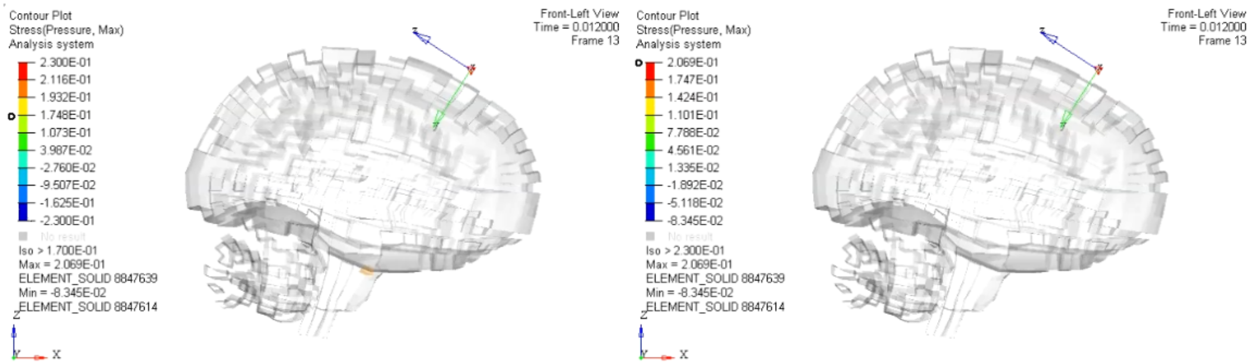

Figure 124. SenseFly eBeePlus, 2.4 lb, forward, 71 fps, angled 58 degree; A14 THUMS simulation, side of the head; brain pressure output

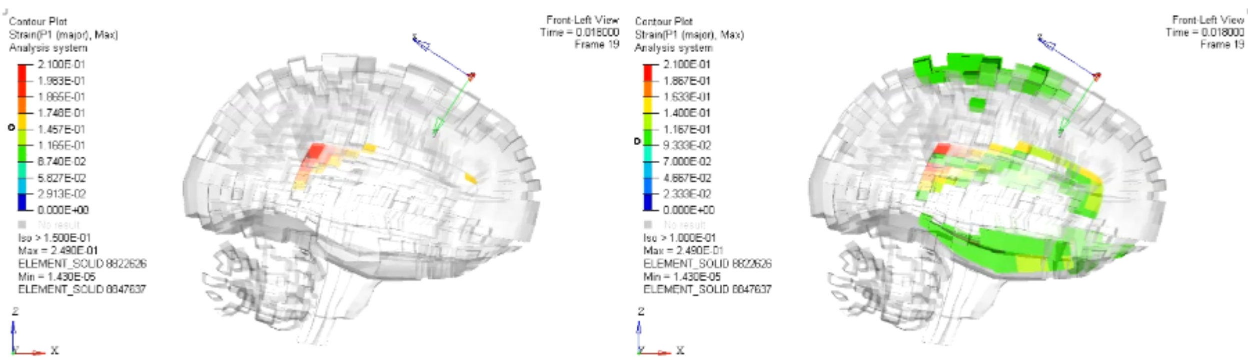

Figure 125. SenseFly eBeePlus, 2.4 lb, forward, 71 fps, angled 58 degree; A14 THUMS simulation, side of the head; brain maximum principal strain output

Time offsets are present between the occurrence of the maximum pressure condition and the maximum principal strain event, indicating that the brain may be affected by pressure and strain through different mechanisms. The current injury metrics find correlation with either pressure or strain or through head kinematic measurements. Numerical simulation has the capability to investigate all of these parameters and the combinations thereof which contribute to injury potential.

6.2 A14 TEST EVALUATION - EBEE PLUS

The eBeePlus was evaluated for the A14 test conditions shown in Table 29.

Table 29. A14 Test Conditions - eBeePlus

UAH Test #	Impact Trajectory	Model	Impact Speed (fps)	Impact Speed (kts)	Impact Location	Vehicle Orientation	Impact KE (ft-lbf)
24	Horizontal	eBeePlus	64	38	Right Side of Head	Nose into Head	152.6
25	Horizontal	eBeePlus	71	42	Right Side of Head	Nose into Head	187.8
26	Angled	eBeePlus	64	38	58 deg to Left Side of Skull	Nose into Head	152.6
27a	Angled	eBeePlus	71	42	58 deg to Left Side of Skull	Nose into Head	187.8

This section presents a comparison of test and simulation results for the four A14 cases involving the eBeePlus, see Table 30. The Phantom 3 FE model was frozen for these simulations, so the results are pure predictions, and no calibration was performed.

Table 30. A14 Test and simulation result comparison for eBeePlus

Injury Criteria	Test 24		Test 25		Test 26		Test 27	
	Test	Sim	Test	Sim	Test	Sim	Test	Sim
Head Acceleration (g)	72.61	44.34	141.72	62.81	90.65	41.46	53.42	53.42
HIC15	81.12	62.71	150.12	90.67	67.46	50.54	89.08	77.32
Head 3 ms (g)	42.42	40.31	40.89	47.71	31.59	37.54	33.54	46.35
BrIC	0.44	62.55	0.43	22.85	0.39	33.35	0.34	44.60
Probability of Concussion	0.39	27.75	0.99	7.59	0.17	223.36	0.16	272.76
Upper Neck Tension (lbf)	-	1.91	-	0.50	-	25.54	-	30.30
Upper Neck Compression (lbf)	-	7.93	-	2.09	-	8.44	-	10.73
Upper Neck Flexion (lbf-ft)	-	72.87	-	26.20	-	71.65	-	83.01
Upper Neck Extension (lbf-ft)	-	0.12	-	0.04	-	0.27	-	0.33
Upper Neck Shear (lbf)	-	72.87	-	26.20	-	71.65	-	83.01
Lateral Moment (lbf-ft)	-	0.13	-	0.04	-	0.27	-	0.33
Twisting Moment (lbf-ft)	-	4.17	-	2.12	-	6.70	-	7.77
Upper Neck Nij	-	7.46	-	1.46	-	7.22	-	8.60

The A14 test data is also plotted in bar chart form in Figure 126. Note that the injury metrics have been normalized according to their respective threshold values.

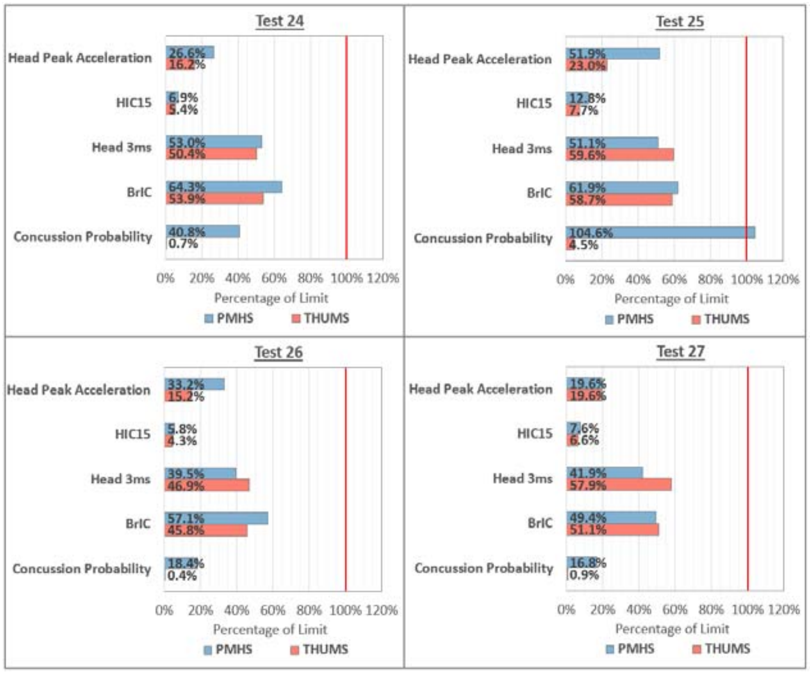

Figure 126. Bar charts with summary of injury criteria for A14 PMHS test vs THUMS simulation comparison. eBeePlus tests 24, 25, 26, and 27

6.2.1 Side

PMHS Test 24 is shown in Figure 127; THUMS EPS contours are given in Figure 128; data outputs are summarized in Figure 129.

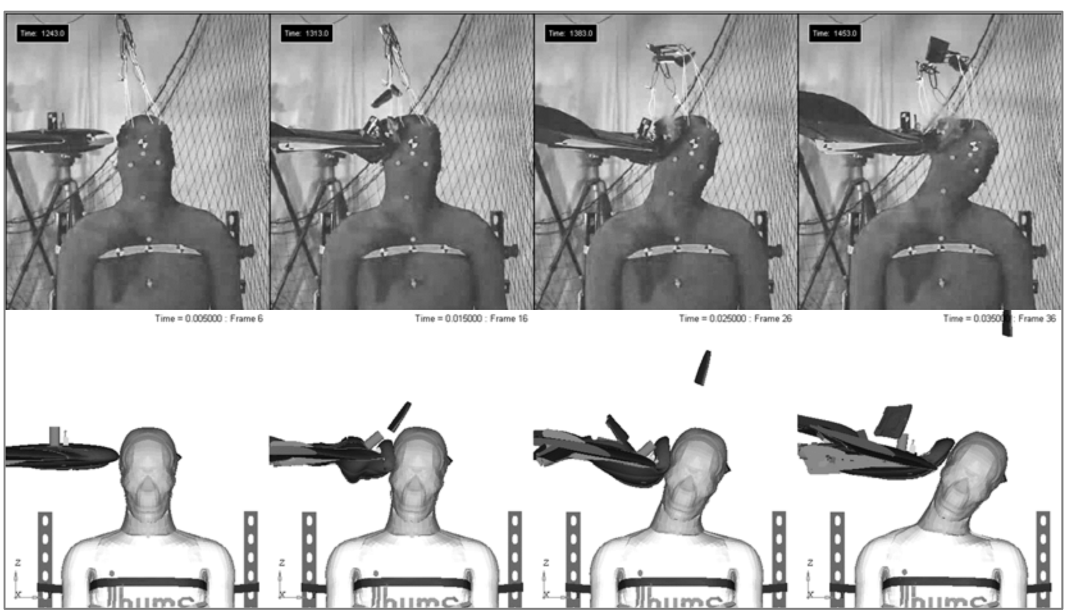

Figure 127. PMHS test 24 vs simulation comparison; eBeePlus, 2.4 lb, nose first, 64 fps, horizontal sideward; subject #4; side of the head; kinematics

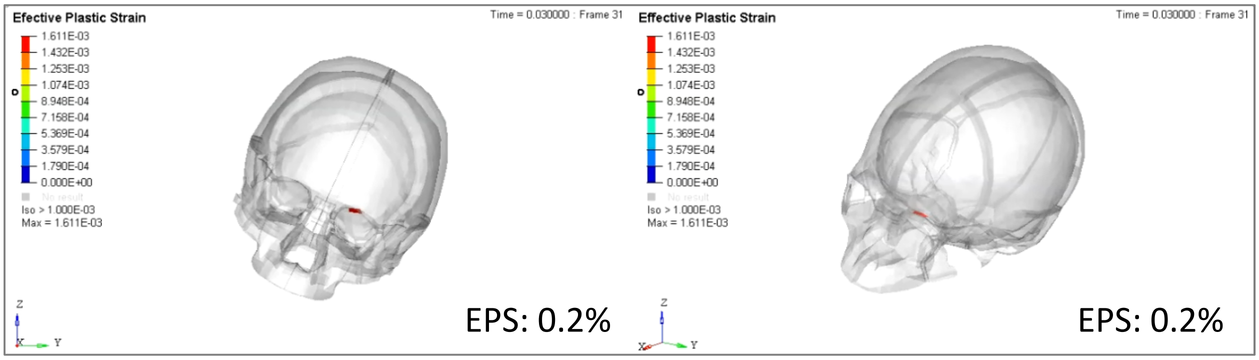

Figure 128. PMHS test 24 simulation; eBeePlus, 2.4 lb, nose first, 64 fps, horizontal sideward; subject #4; side of the head; contour plot of skull strains

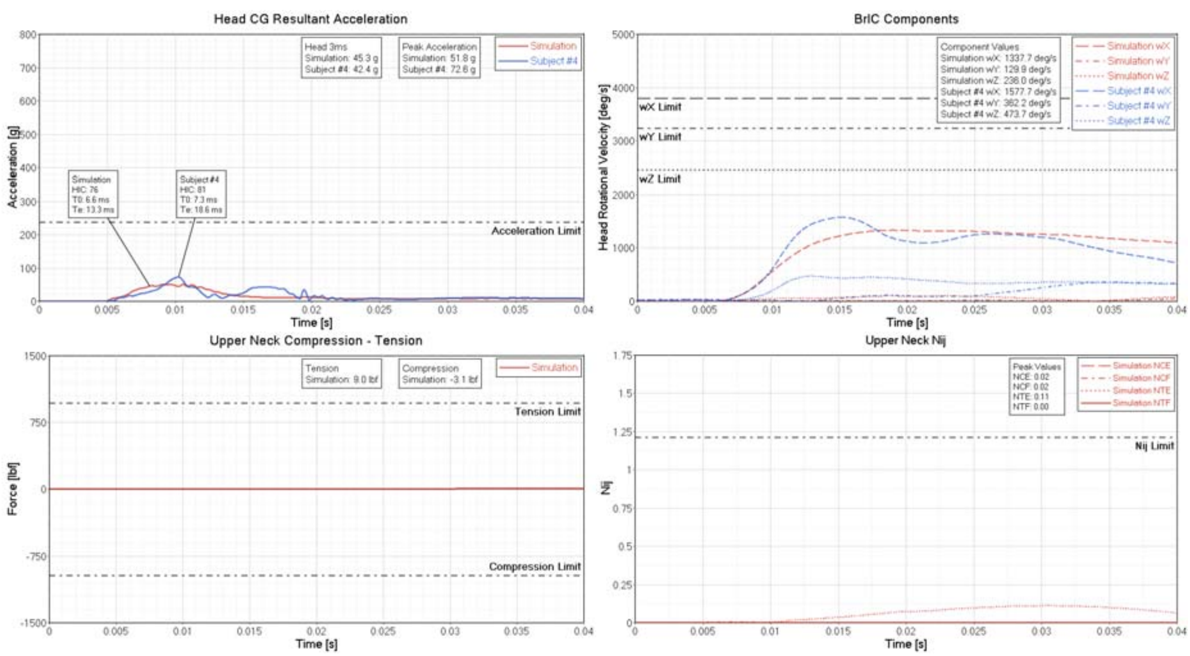

Figure 129. PMHS test 24 vs simulation comparison; eBeePlus, 2.4 lb, nose first, 64 fps, horizontal sideward; subject #4; side of the head; time-history summary

PMHS Test 25 is shown in Figure 130; THUMS EPS contours are given in Figure 131; data outputs are summarized in Figure 132.

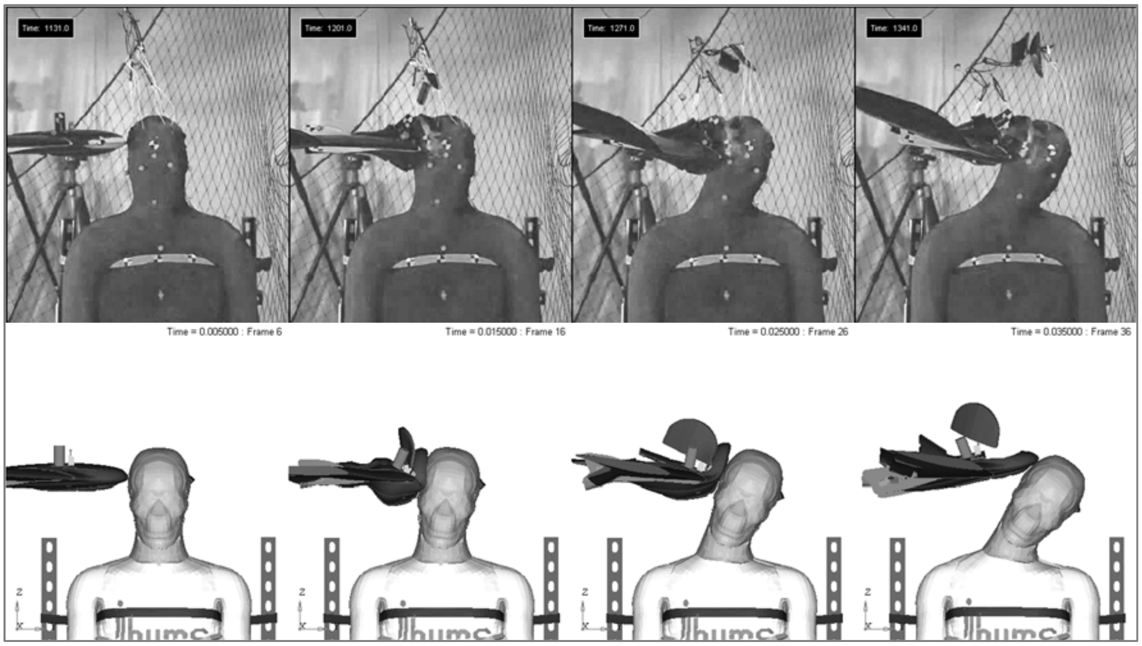

Figure 130. PMHS test 25 vs simulation comparison; eBeePlus, 2.4 lb, nose first, 71 fps, horizontal sideward; subject #4; side of the head; kinematics

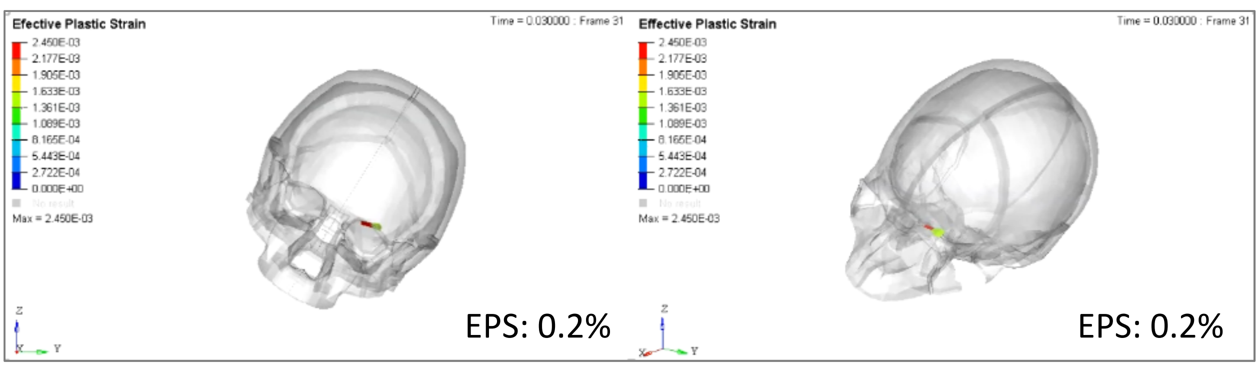

Figure 131. PMHS test 25 simulation; eBeePlus, 2.4 lb, nose first, 71 fps, horizontal sideward; subject #4; side of the head; contour plot of skull strains

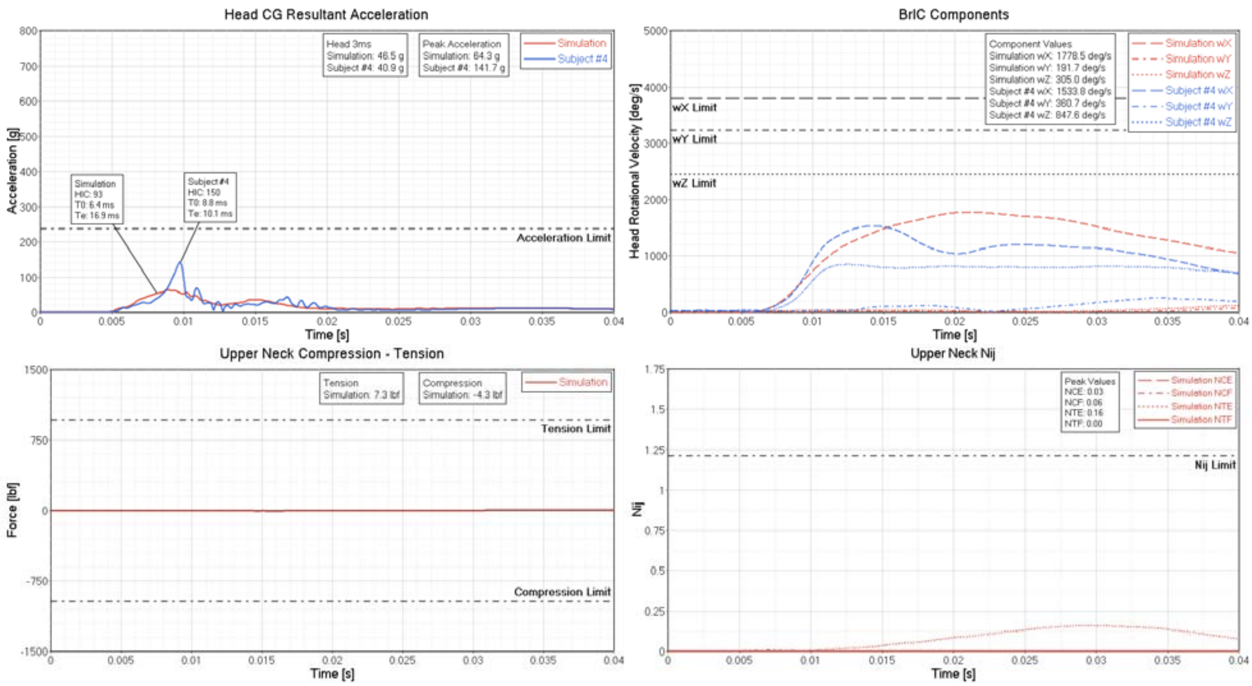

Figure 132. PMHS test 25 vs simulation comparison; eBeePlus, 2.4 lb, nose first, 71 fps, horizontal sideward; subject #4; side of the head; time-history summary

6.2.2 Angle

PMHS Test 25 is shown in Figure 133; THUMS EPS contours are given in Figure 134; data outputs are summarized in Figure 135.

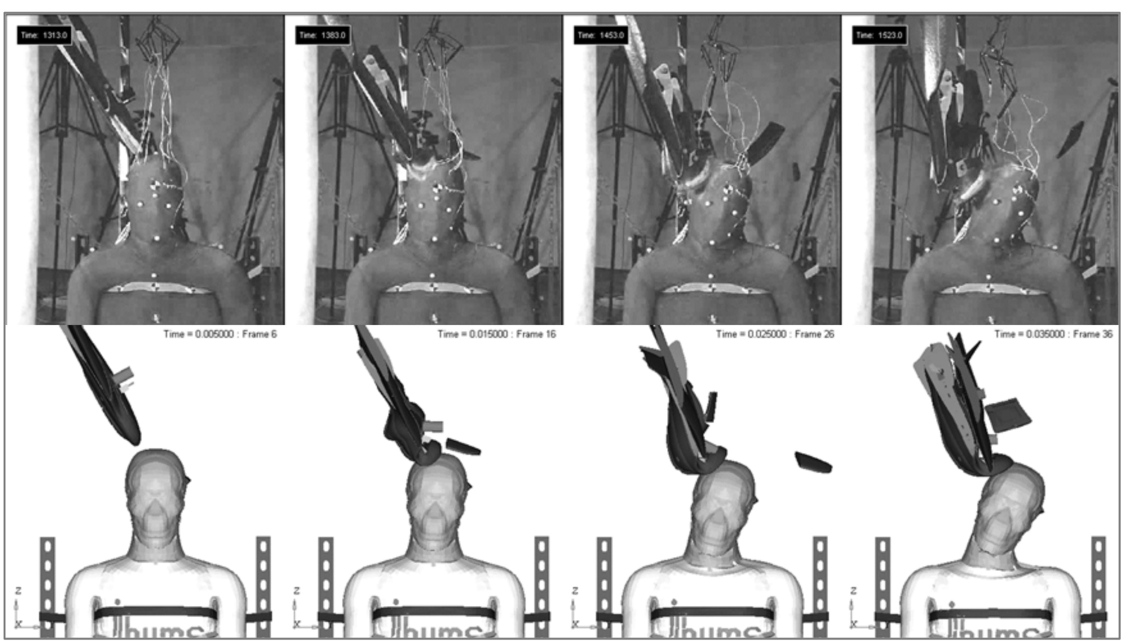

Figure 133. PMHS test 26 vs simulation comparison; eBeePlus, 2.4 lb, nose first, 64 fps, angled 58 degree sideward; subject #4; side of the head; kinematics

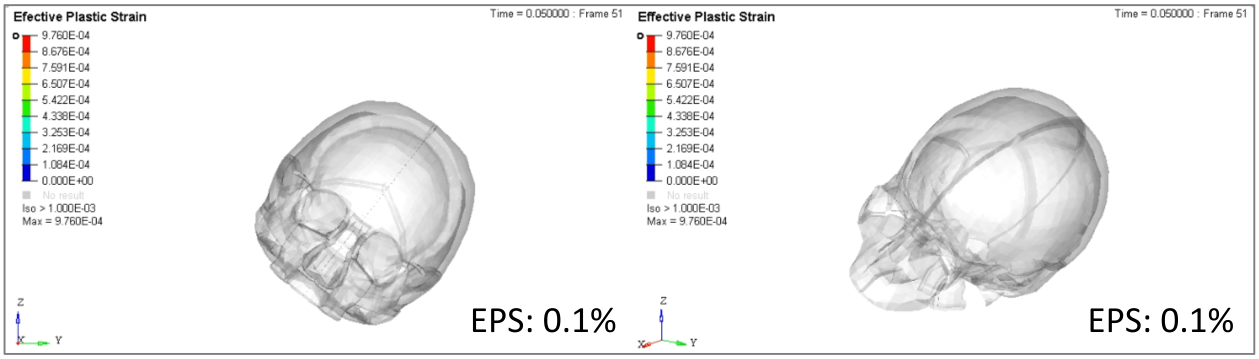

Figure 134. PMHS test 26 simulation; eBeePlus, 2.4 lb, nose first, 64 fps, angled 58 degree sideward; subject #4; side of the head; kinematics

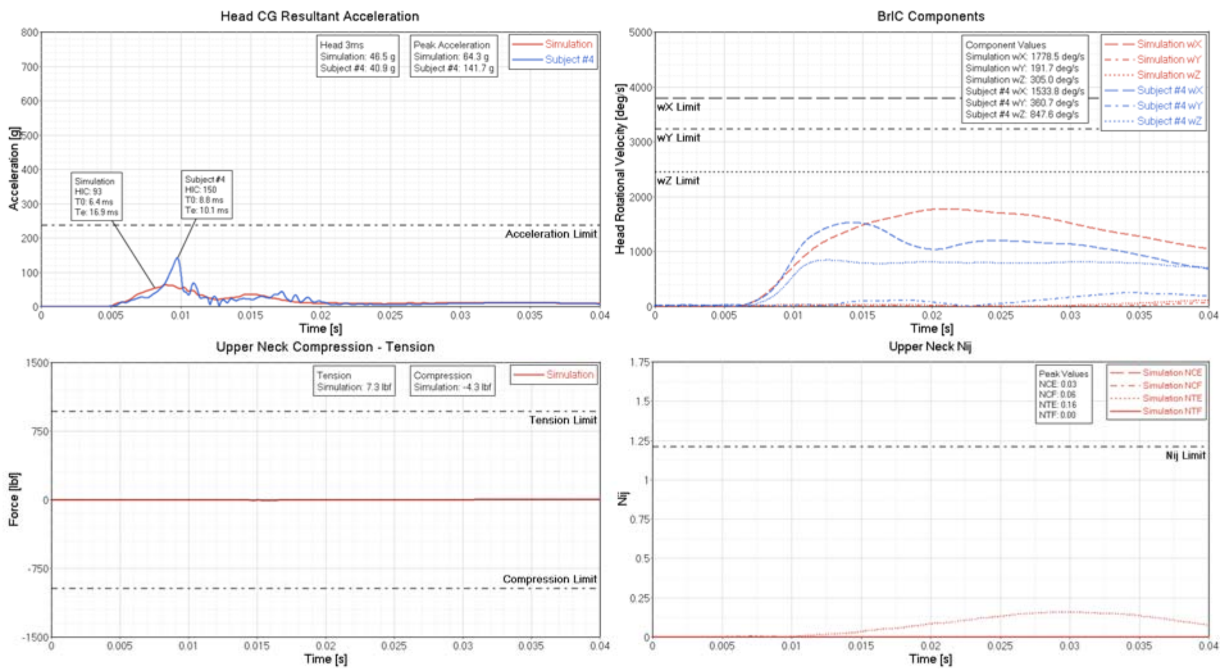

Figure 135. PMHS test 26 vs simulation comparison; eBeePlus, 2.4 lb, nose first, 64 fps, angled 58 degree sideward; subject #4; side of the head; time-history summary

PMHS Test 25 is shown in Figure 136; THUMS EPS contours are given in Figure 137; data outputs are summarized in Figure 138.

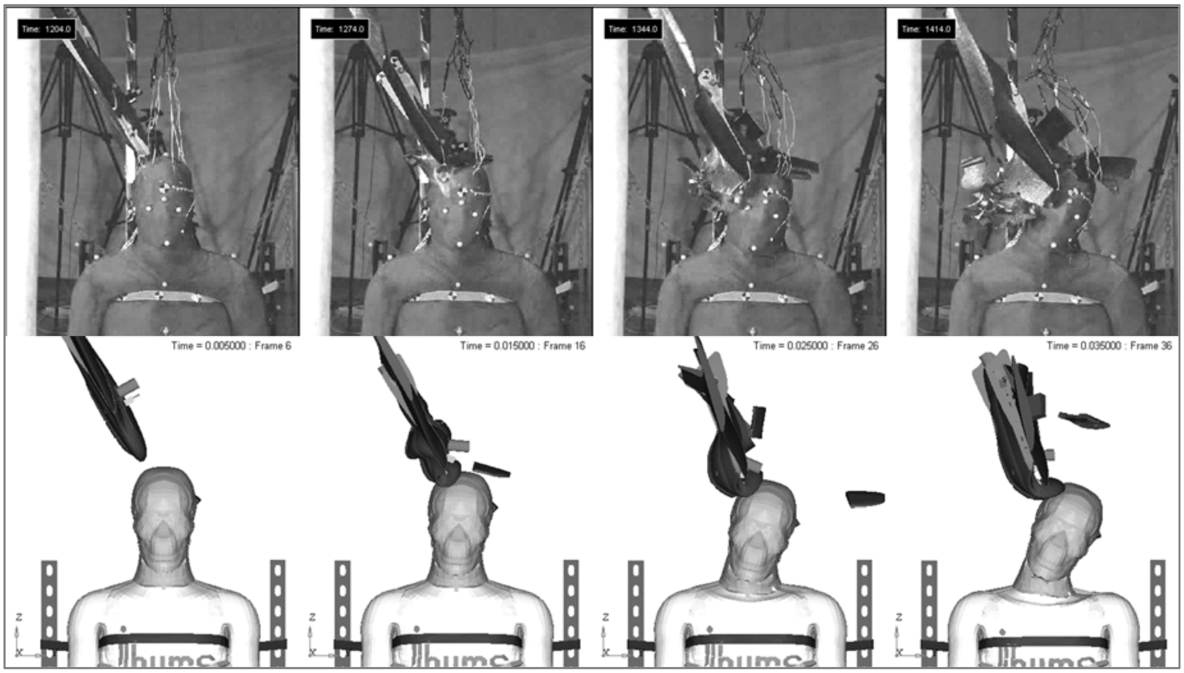

Figure 136. PMHS test 27 vs simulation comparison; eBeePlus, 2.4 lb, nose first, 71 fps, angled 58 degree sideward; subject #4; side of the head; kinematics

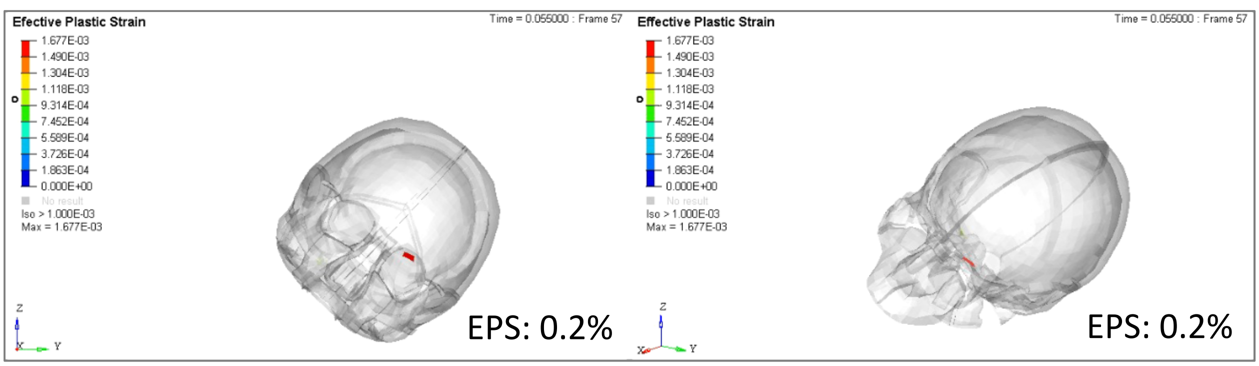

Figure 137. PMHS test 27 simulation; eBeePlus, 2.4 lb, nose first, 71 fps, angled 58 degree sideward; subject #4; side of the head; kinematics

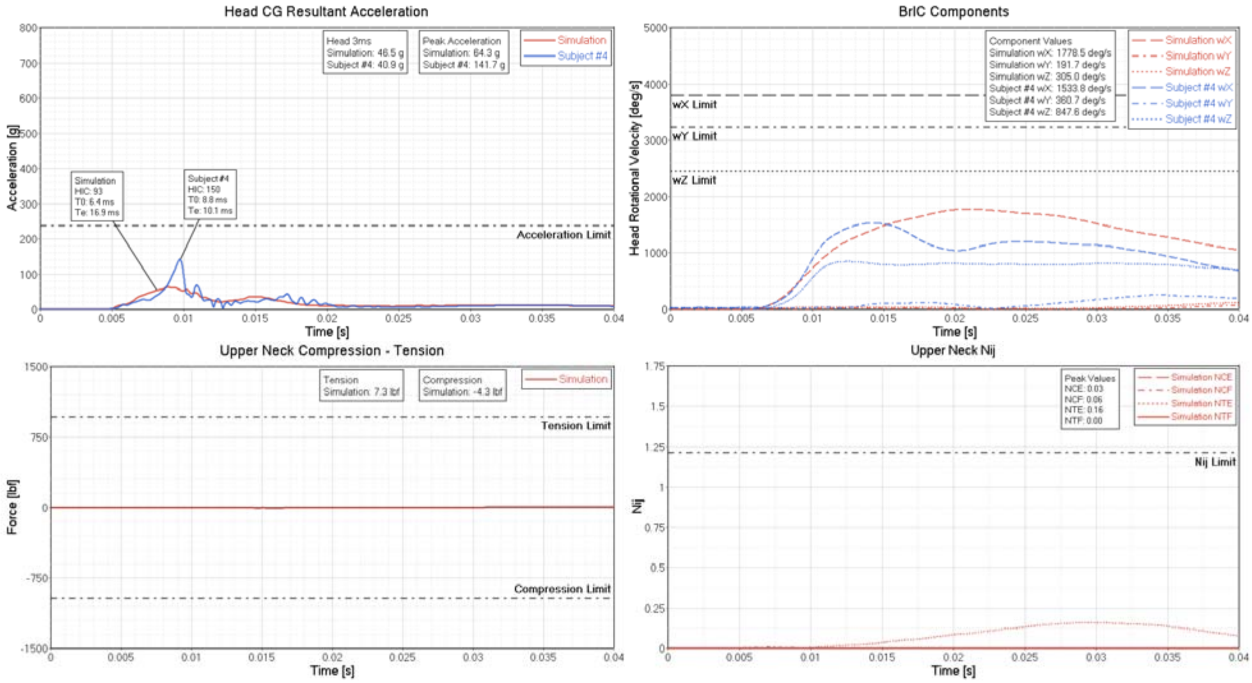

Figure 138. PMHS test 27 vs simulation comparison; eBeePlus, 2.4 lb, nose first, 71 fps, angled 58 degree sideward; subject #4; side of the head; time-history summary

6.3 EVALUATION OF ADDITIONAL CONDITIONS – PRECISION HAWK MKIII

As an extension of the simulation work performed in this chapter, and with the aim of shedding light on how much higher is the damage caused by a puller-prop UAS impact in comparison to the Phantom 3 and the eBeePlus, NIAR carried out a series of simulation between the PMHS virtual model and the Precision Hawk FEM.

The following impact conditions were defined by UAH, in accordance to their findings on likely Lancaster impact speed and orientations:

- Horizontal impact at 36 fps, in accordance to the Precision Hawk flare speed. The PMHS head was impacted frontally and sideward.
- Parachute vertical speed of 16 fps, based on a drop at a height of 20 ft.
- Parachute vertical drop of half the energy of the previous drop speed. This second case speed was estimated at 12 fps.

6.3.1 Frontal Impact at 36 fps

Figure 139 through Figure 141 present the kinematics, the effective plastic strain contour plots, and injury report of the 36 fps frontal impact, respectively.

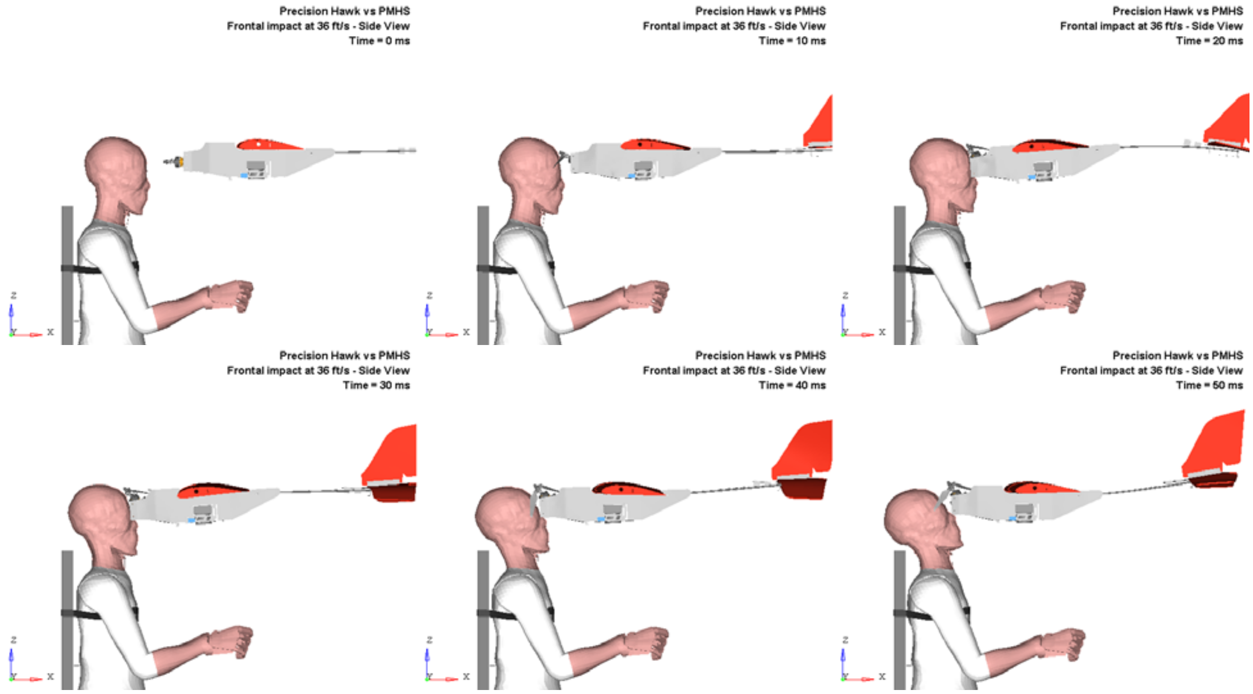

Figure 139. THUMS simulation; Precision Hawk frontal impact at 36 fps; kinematics

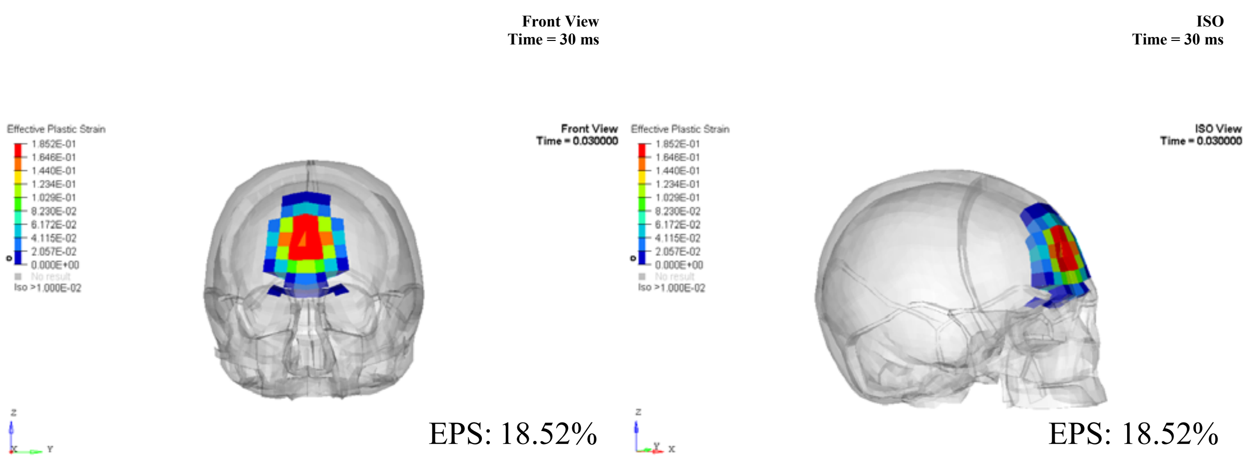

Figure 140. Lancaster vs THUMS simulation; Frontal impact at 36 fps; EPS contour plot of skull

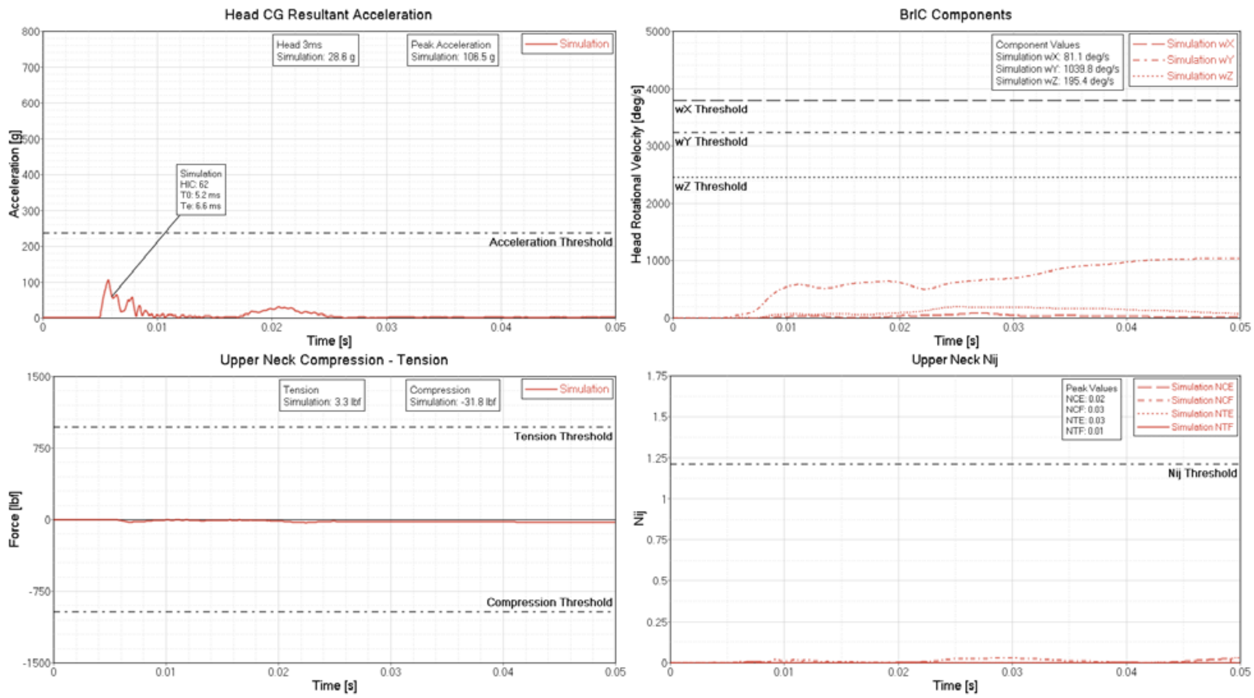

Figure 141. THUMS simulation; Precision Hawk frontal impact at 36 fps; time-history summary

6.3.2 Side Impact at 36 fps

Figure 142 through Figure 144 present the kinematics, the effective plastic strain contour plots, and injury report of the 36 fps side impact, respectively.

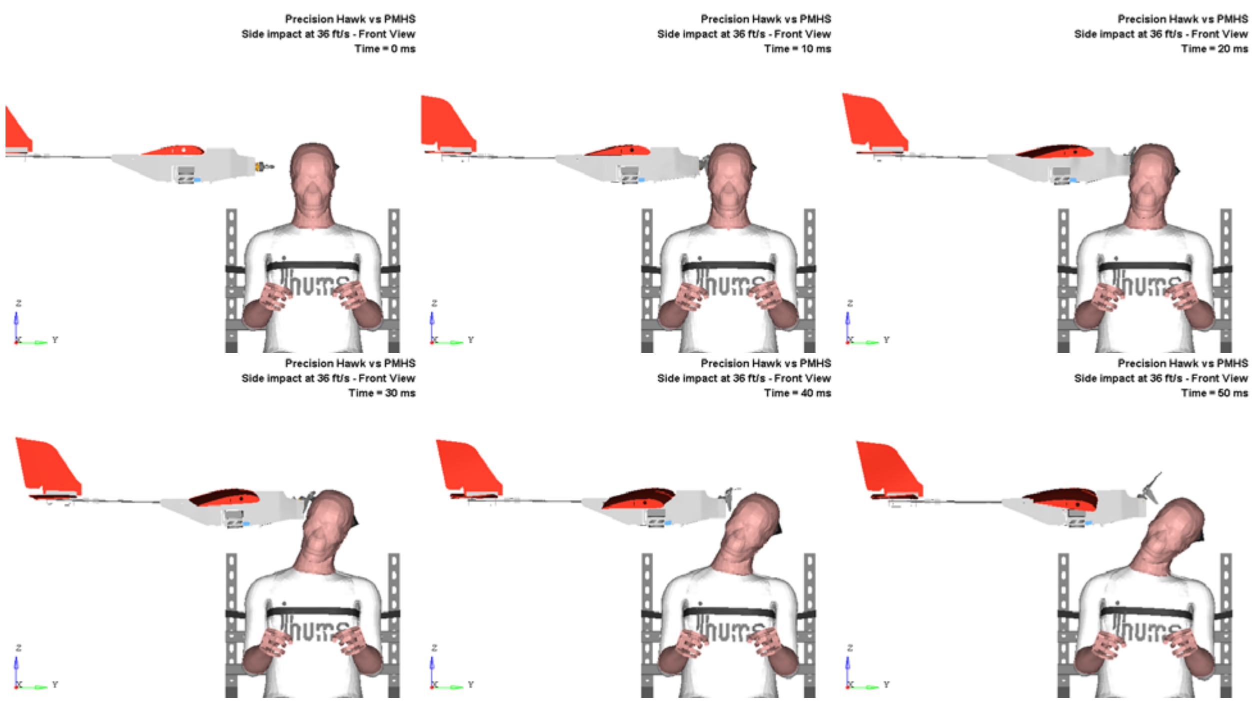

Figure 142. THUMS simulation; Precision Hawk side impact at 36 fps; kinematics

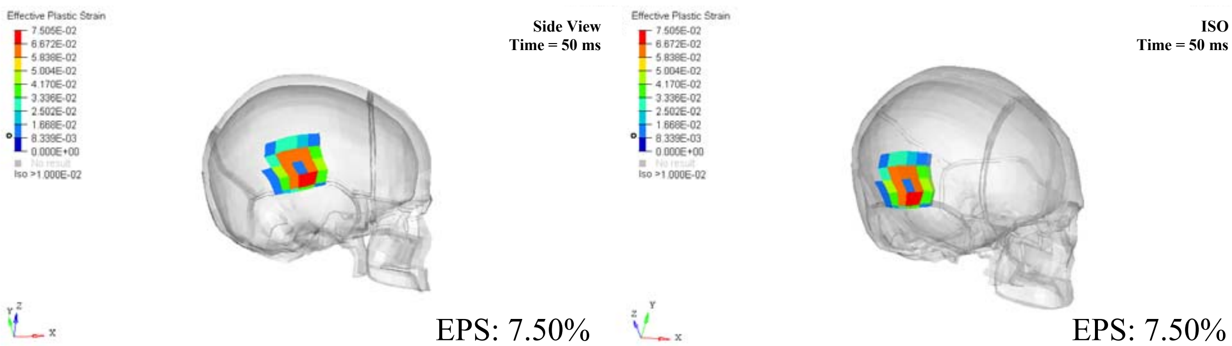

Figure 143. Lancaster vs THUMS simulation; Side impact at 36 fps; EPS contour plot of skull

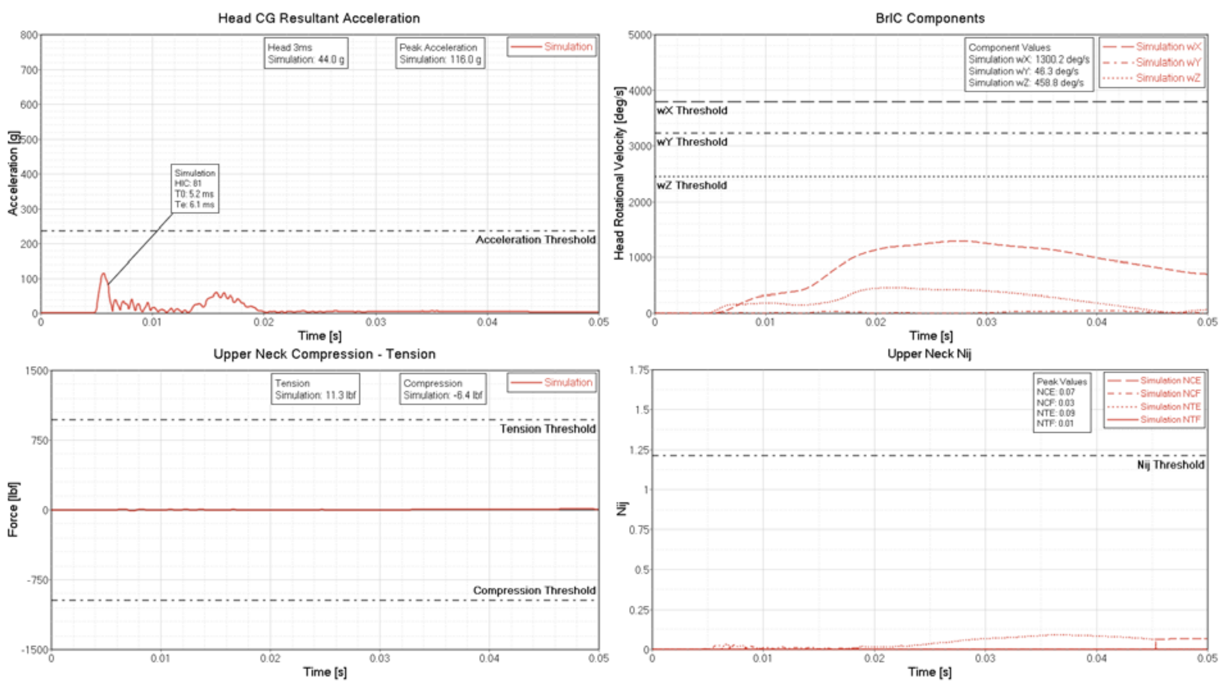

Figure 144. THUMS simulation; Precision Hawk side impact at 36 fps; time-history summary

6.3.3 Vertical Drop at 16 fps

Figure 145 through Figure 147 present the kinematics, the effective plastic strain contour plots, and injury report of the 16 fps vertical impact, respectively.

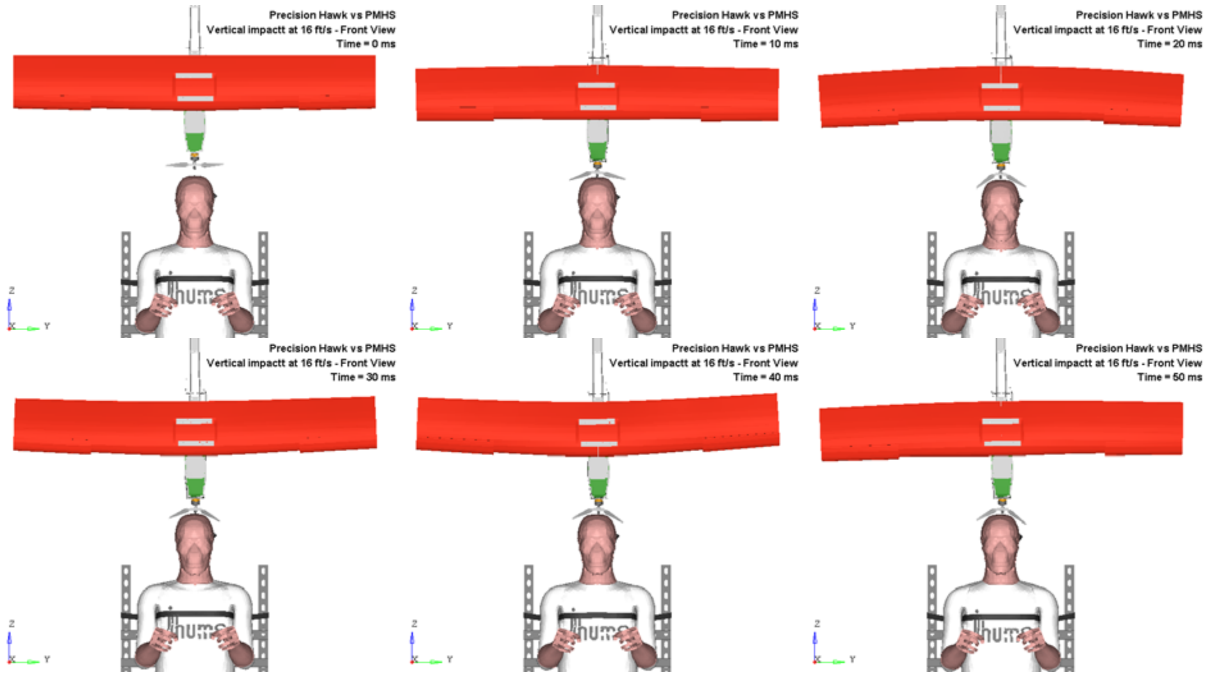

Figure 145. THUMS simulation; Precision Hawk vertical impact at 16 fps; kinematics

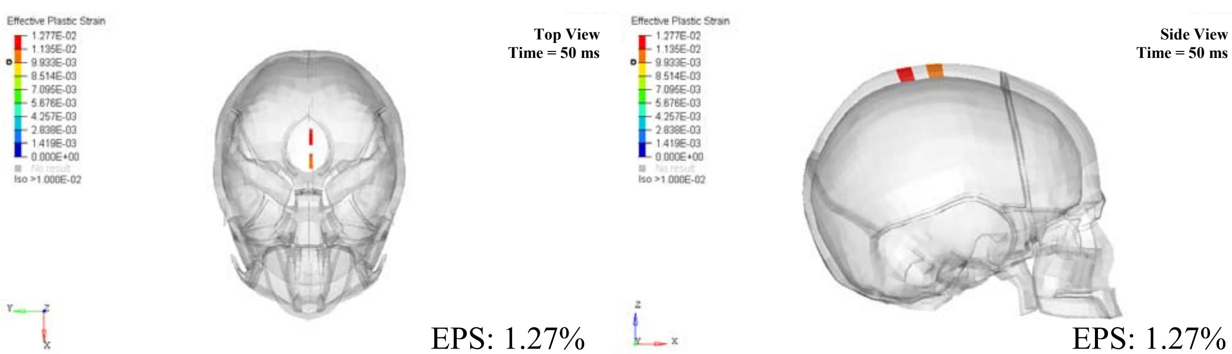

Figure 146. Lancaster vs THUMS simulation; Vertical drop at 16 fps; EPS contour plot of skull

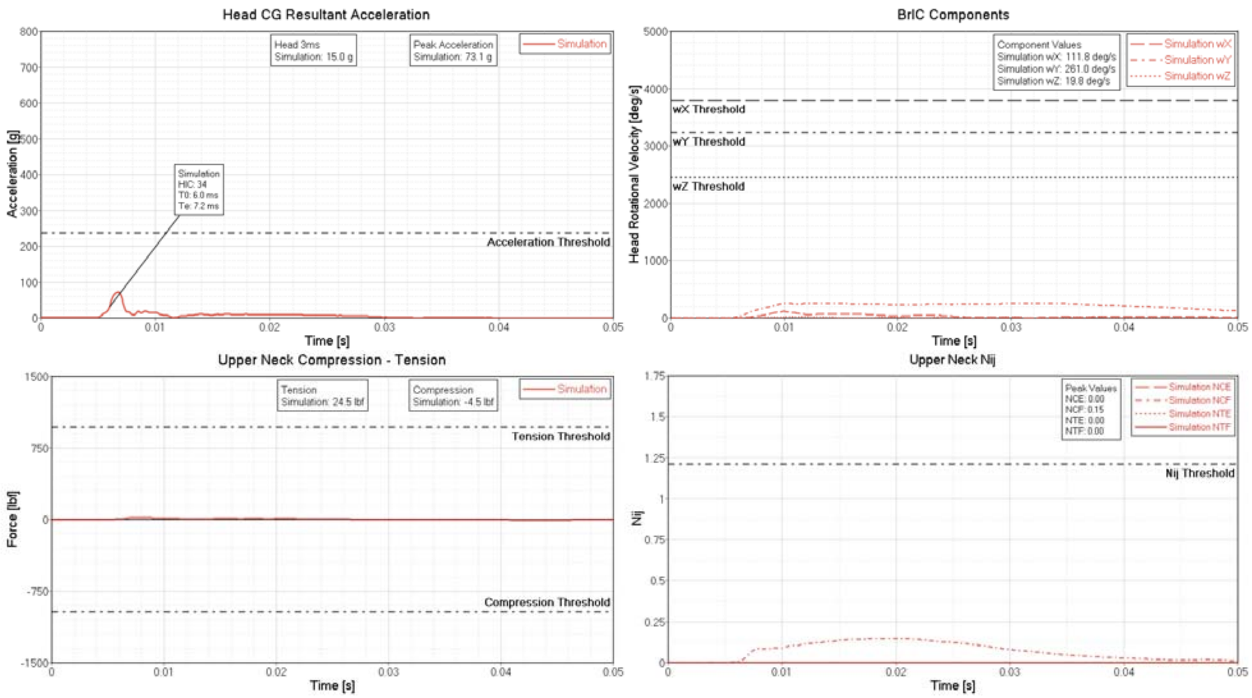

Figure 147. THUMS simulation; Precision Hawk vertical impact at 16 fps; time-history summary

6.3.4 Vertical Drop at 12 fps

Figure 148 through Figure 150 present the kinematics, the effective plastic strain contour plots, and injury report of the 12 fps vertical impact, respectively.

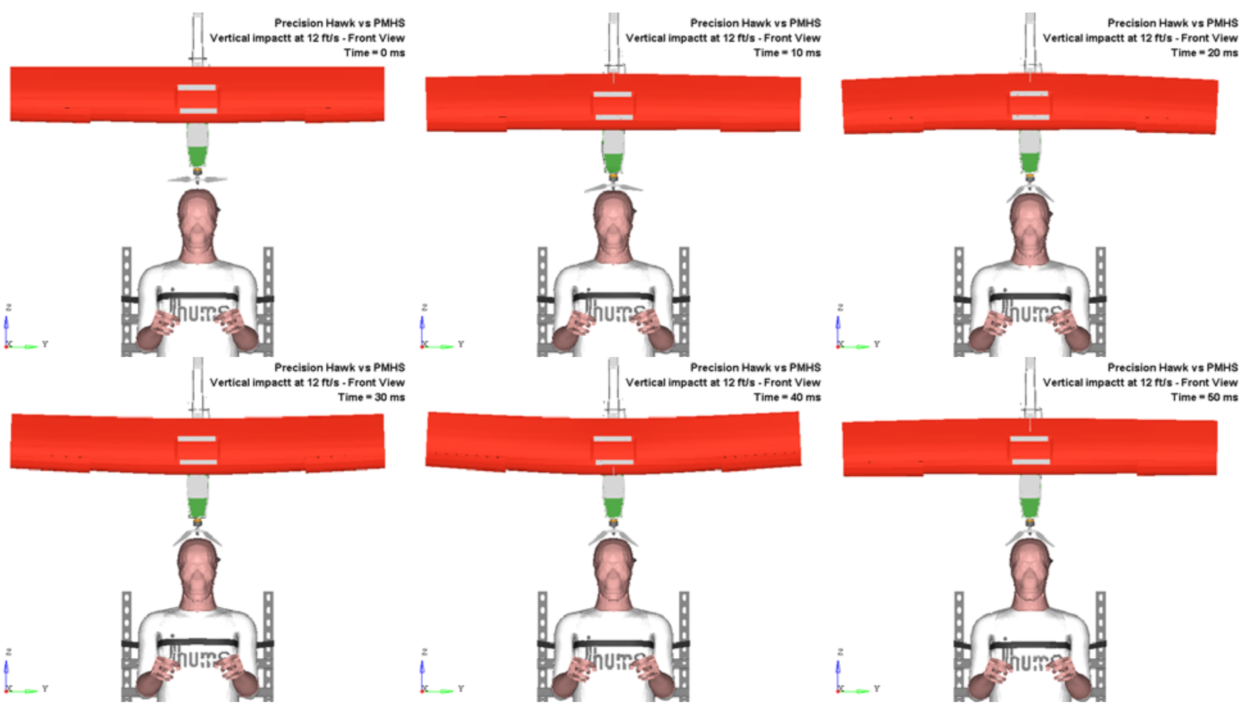

Figure 148. THUMS simulation; Precision Hawk vertical impact at 12 fps; kinematics

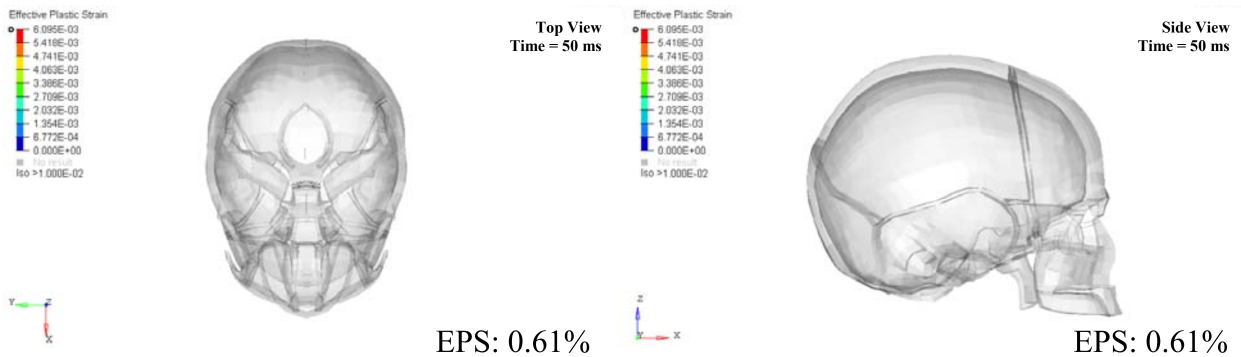

Figure 149. Lancaster vs THUMS simulation; Vertical drop at 12 fps; EPS contour plot of skull

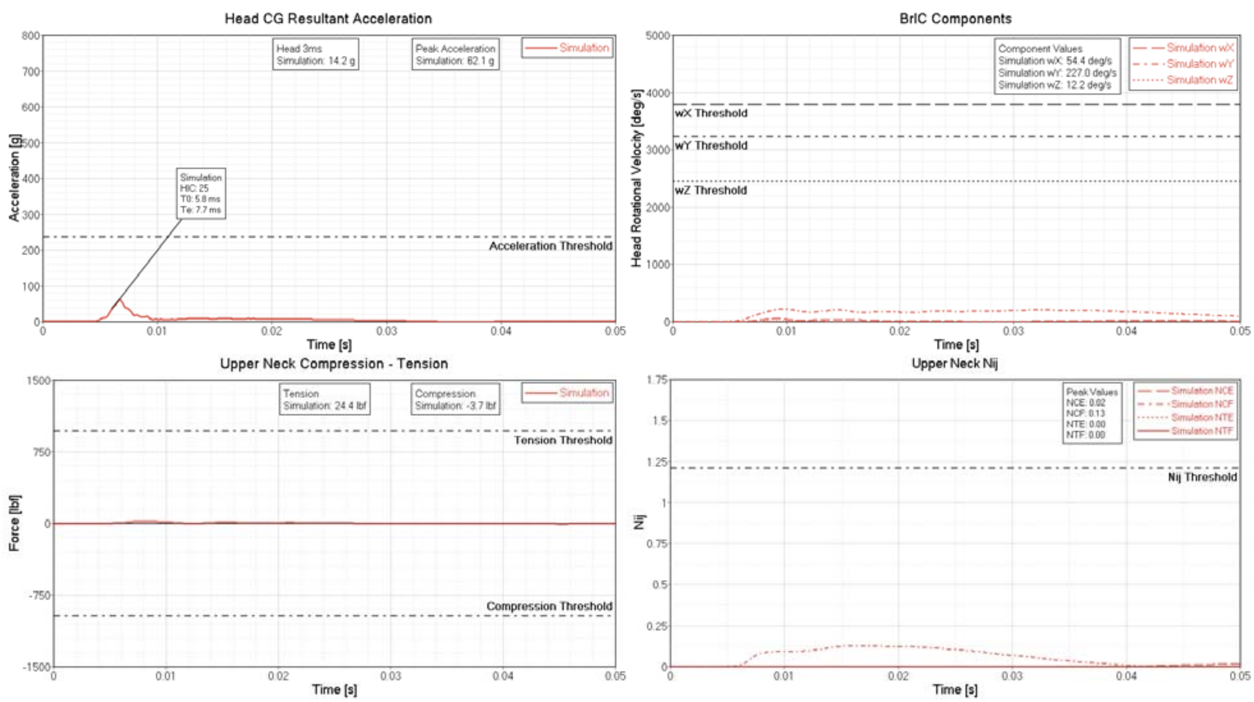

Figure 150. THUMS simulation; Precision Hawk vertical impact at 12 fps; time-history summary

To summarize, all four simulation remained within the criteria thresholds, indicating no injury to the PMHS model. This work is purely virtual in nature, meaning that none of these results have been validated by means of experimental data. Nevertheless, the calibration and correlation efforts done for the Phantom 3 and eBeePlus model concerning the PMHS give some confidence to accept these results as representative of the injury range for this specific type of UAS.

6.4 SUMMARY DISCUSSION

The conclusions from this set of tests are discussed as follows.

6.4.1.1 Impact Location and Direction

THUMS model results showed that injury potential is related to the specific impact location and the direction of the impact, relative to the test subject. In terms of skull fracture probability, frontal angled impacts showed the greatest severity of the cases studied. The most critical frontal angled impact condition was replicated in ATD testing, with two iterations to determine impact location sensitivity. The results of this test show a 30% difference in HIC and peak acceleration and a 20% difference in neck compression loading. Measurements of the contact locations of both tests indicate an offset of approximately 0.5 in on the surface of the ATD head form. The significant discrepancy in acceleration and load magnitudes indicates a high dependence on the contact location due to the relative impact angle at the contact surface, and the alignment of the sUAS CG with that of the ATD's head form. Furthermore, the significance of the sUAS impact location is supported by the results from PMHS testing. PMHS #2 and #3 were both tested at the critical frontal angled condition, but the impact angle and the CG alignment was less precise for PMHS #2, resulting in no observable injury, while PMHS #3 had a more significant contact angle and CG alignment which resulted in an AIS2 level injury. In order to confirm the impact conditions governing a worst case scenario designation, it is recommended to develop an injury severity heat map of the skull through further ATD testing and human body model simulations in which impact location and direction could be iterated until absolute maxima and minima are identified.

6.4.1.2 Individual Physiology

HBM simulations indicate that injury potential was related to the specific contact points that were present between the surface of the sUAS and the THUMS head, in combination with the bone thickness in those areas. This relationship is described in terms of effective plastic strain (EPS) output from the simulated PMHS test series. In the critical frontal angled impact condition with the DJI Phantom3, the local curvature of the sUAS shell and the shape of the frontal bone parts in the THUMS model allowed a more direct path for the energy transfer than in sideward angled impacts, in which the motor mount 'arms' of the sUAS can contact the front and rear of the THUMS head and absorb some energy through bending deformations, before the central mass of the sUAS contacts the side of the head. Bone strain output values showed approximately 50% less strain in the sideward condition. This trend is complicated, however, due to the observation that the biofidelic shape of the THUMS neck allowed more rotation in the sideward conditions than in the fore-aft impact simulations. It is not known to what extent this effect could be reducing the EPS readings in the sideward condition, but it is unlikely to be the sole factor in the difference between the frontal and sideward impact EPS readings; therefore the dependence on physiology is attributed primarily to differences in head shape. Note that the shape of the sUAS is a primary factor in determining the severity of the impact as well. In the preceding example, the shape of PMHS head and the surface curvature of the sUAS at the impact site combined to cause a skull fracture. A different shape or size of sUAS could potentially cause greater damage in the sideward condition than in the forward direction, if the hypothetical sUAS design were such that it could contact the side of the head with a more significant density and construction stiffness.

6.4.1.3 Dynamic Skull Bone Deformations

The numerical model allows detailed investigation into the relative displacement of each node in the skull and brain components (approximately 28,000 nodes) throughout the simulated impact event. These relative displacements demonstrate that the skull bones deform under sUAS impact conditions. For example, in the critical frontal angled impact simulation with the Phantom 3 sUAS, a localized indentation at the impact contact site was identified along with opposing transverse displacements on the temporal bones. These displacements appear to be transient, occurring within 1-3 ms after first contact with the sUAS, and dissipating within another 2 ms, for a total dynamic event lasting less than 5 ms. The repercussions of this deformation phenomenon are that the bones of the skull can deform relative to one another, and therefore cannot be considered as a rigid body during this transient phase of a projectile impact. Since the bones can have different localized displacements, it is inherent that the velocity and acceleration of these locations would also be different from one another. NIAR performed post-processing analysis to confirm that local deformations are present in other THUMS simulations, and that these could affect the test data output based on the relative deformations present in the vicinity of the test instrumentation used during PMHS testing. As a result of this assessment, NIAR also identified that there is a relationship between the severity of the bone deformations, the amount of difference between the PMHS test results and the simulation outputs, and the alignment of the head CG with the sUAS CG. The relationship between these three parameters appears to be that the alignment of the CGs allows the maximum impact energy transfer and induces the greatest amount of bone deformation, which subsequently causes the instrumentation to record the localized bone excitations during the impact event in addition to the overall head kinematics.

6.4.1.4 THUMS and PMHS Angular Metrics

THUMS angular velocity results have a better agreement with PMHS test outputs than the linear and angular acceleration outputs. Inspecting the time-history outputs for the THUMS simulations compared against the PMHS test results shows that the maximum angular velocity occurs after the impact contact has finished. During this phase of the impact event, the head of the subject has already been accelerated due to the energy transferred during the collision, and subsequently moves through a trajectory path defined by its inertia and the constraints at the neck and torso. The head trajectory typically showed a smooth time-history curve profile after the transient dynamics of the impact were finished. During the initial phase of the impact, the dynamic bone deformations noted in Section 6.4.1.3 could have affected the magnitudes of the acceleration readings, but would have dissipated by the time the sensors recorded the subsequent angular velocity measurements of the head's motion. This inference describes the correlation of the angular velocity results from the THUMS with the results from the PMHS tests.

6.4.1.5 Pressure and Strain-Based Injury Assessment

THUMS simulations indicate that intracranial pressure waves occur as a result of the initial acceleration of the head and the local impact site deformation, while the peak values of principal strains in the brain matter occur at a later time in the simulation as a result of the head kinematics after the initial energy transfer is finished. The pressure wave distribution appears to have a shorter duration than that of the maximum principal strains. Finally, the measured outputs from an impact test are used to quantify brain injury potential based on the peak values in the applicable data components, irrespective of the time at which the peaks occur. This implies that the metrics predict injuries based on measurable head kinematics but that these values may not be tied to the physical stresses and strains within the brain matter (the pressure and / or strain that would be associated with material damage are not completely characterized by external measurements of body kinematics). Accordingly, NIAR acknowledges that the current state of the technology is limited by practical testing difficulties, a lack of sensor equipment for measuring the mechanical properties of soft matter in situ, and that there is a general lack of understanding about concussion and brain injury as they relate to these impact scenarios. Therefore, it is concluded that brain injury thresholds can be assessed with THUMS simulations, contingent on further modeling methodology validation and confirmation of tested injury thresholds as applied to the THUMS. It is recommended to conduct further PMHS testing and human body model simulation work to verify pressure and strain thresholds for brain injury prediction.

7. CONCLUSIONS

This research effort aimed to characterize the injury severity of sUAS impacts with the non-participating public through testing and numerical simulation. Tests were conducted utilizing anthropomorphic test devices (ATDs) to quantify the head kinematics and neck loads associated with sUAS impacts. The research utilized FAA Hybrid-III 50th percentile ATDs representing an average adult male. Eleven sUAS articles were tested – quadcopter and fixed-wing configurations – with masses ranging from 0.73 lbm to 9.82 lbm. These articles represented a range of construction materials from composite and metal to plastic and foam. Impact velocities covered a spectrum from 10 fps to 71 fps; energy levels of 2.4 ft-lbf to 209 ft-lbf. This energy range encompasses parachute velocities for heavier sUAS as well as the general flight performance of middle and lower weight sUAS. Injury severity was quantified in terms of standard aerospace and automotive criteria: HIC, head peak acceleration, and Nij.

In support of the testing effort, NIAR developed and validated three sUAS FE models for use in impact simulations. The sUAS articles represent the DJI Phantom3 quadcopter, the SenseFly eBeePlus pusher prop, and the Lancaster PrecisionHawk MKIII fixed-wing puller UAS. These sUAS articles had masses of 2.67 lbm, 2.4 lbm, and 4.4 lbm, respectively. Model development activities followed the building block approach using reverse engineered geometry, CAD models, and data from material coupon tests, component and system level tests, as well as assembly level ATD impact testing done as part of the A11 research. In addition to the numerical sUAS and ATD simulations, NIAR utilized the A11 test data to develop and calibrate the THUMS numerical instrumentation methodology. With these calibrated models, ATD and THUMS simulations were used to determine the critical sUAS orientation and impact conditions for the PMHS test matrix, thus reducing the cost and efforts associated with physical testing. THUMS simulations predicted the most injurious sUAS impact test from the PMHS test matrix as the DJI Phantom3 angled frontal condition, impacting front-first, at 71 ft/s. This determination was confirmed by the test resulting in a skull fracture and the greatest magnitude of head acceleration of all the sUAS tests.

The A14 studies provided data from four perspectives: ATD testing, ATD simulation, HBM simulation, and PMHS testing. ATD testing provided head and neck injury metrics as well as high-speed video of the impact kinematics. ATD simulations provided head and neck injury metrics, detailed model kinematics, and the potential to quantify energy transfers. HBM simulations provided head and neck injury metrics, detailed model kinematics, potential to quantify energy transfers, and also material stress and strain results related to skull fracture and brain injury potentials. PMHS testing provided head injury metrics, high-speed video kinematics, VICON marker tracking, and physical injury observations.

These four perspectives allowed researchers to identify consistent trends in terms of head injury metrics across all environments, and to give complementary results from each specific data source. Since the means of compliance for demonstrating an acceptable level safety for a given sUAS is not predetermined, these various perspectives give insight into the methods that could be applied. This test and simulation comparison effort showed that verified and validated models can predict real-world physics and that simulations can leverage computing power to investigate a broader range of conditions than are typically available in a test program.

7.1 CONCLUSIONS

During the course of this research program, researchers identified that injury potential is primarily related to the parameters discussed in Section 7.1.1 , that ATD test results showed trends related to injury criteria thresholds as discussed in Section 7.1.2 , and that human injury prediction depends on understanding multiple variables as outlined in Section 7.1.3 . Further insights were gained that are not specific to the aforementioned topics but are given for use in future research efforts.

7.1.1 Injury Potential

The conclusions in this section are based on findings from ATD testing, ATD simulations, as well as from the human body modeling work with comparisons to PMHS test results.

7.1.1.1 Energy Transfer

One of the main variables related to injury potential is the amount of energy transferred from the sUAS to the impact target. As such, the parameters that govern this energy transfer are: the initial impact energy of the sUAS due to its mass and velocity, Figure 6; the energy absorbing characteristics of the materials (metals, composites, plastics, foams, and so forth) in combination with the sUAS architecture (fixed-wing pusher / puller, multirotor, or other configurations), Figure 7; and the impact orientation of the sUAS at the time of contact (contacting first with a motor, battery, camera, or the central mass of the sUAS body), Figure 52.

7.1.1.2 Impact Location and Direction

THUMS model results showed that injury potential is related to the specific impact location and the direction of the impact relative to the test subject. Of the many impact conditions studied, the frontal angled impact direction was identified as the most injurious in Figure 97. In ATD test replications of the worst case frontal angled impact from PMHS testing, an impact location offset of 0.5 inches on the surface of the ATD head form was shown to cause a 30% difference in HIC and peak acceleration, and a 20% difference in neck compression loading, see Figure 113.

7.1.1.3 Individual Physiology

Numerical simulations indicated that injury potential was related to the specific contact points that were present between the surface of the sUAS and the THUMS head in combination with the bone thickness in those areas. In the critical frontal angled impact condition with the DJI Phantom3, the local curvature of the sUAS shell and the shape of the frontal bone in the THUMS model allowed the most direct path for the energy transfer, as discussed in Section 6.1.4.3 .

7.1.2 ATD Test Results - Injury Metrics

Analysts reviewed the ATD responses to over 100 sUAS impacts and determined the following relationships between the impact conditions and the injury metrics.

7.1.2.1 Tabulated Injury Criteria Exceedances

The greatest number of current automotive and aerospace injury criteria exceedances based on ATD testing correspond to head peak acceleration, HIC, neck compression, the modified shear criterion, and combined probability of concussion (CP) as shown in Section 2.3.3 .

7.1.2.2 Acceleration Based Criteria Thresholds

The HIC and peak acceleration metrics show conservative thresholds when applied to ATD tests with sUAS impacts. ATD tests, based on HIC and peak acceleration metrics, indicated more cases of skull fracture than found in PMHS testing.

Of the 109 ATD test cases, 16 exceeded the HIC15 threshold of 700. Of those cases, 12 were wood and foam block tests, and 4 were sUAS tests. Those 4 sUAS impact cases each have a 30% chance of achieving an AIS2+ skull fracture based on the current HIC15 limit, or 1 to 2 sUAS tests have a likelihood of producing conditions that could result in skull fracture. These ATD tests were done at energy levels lower than that of the PMHS testing program; 175 ft-lbs and 209 ft-lbs, respectively. If ATD testing had been capable of achieving comparable energy levels, NIAR believes that these tests would have exceeded the HIC15 values of the present maximum energy tests. It is noted that some of the sUAS configurations pose a lesser risk of injury, such as the eBeePlus, shown in Figure 6. Of the configurations that pose a notable injury risk like the Phantom 3, an impact energy increase of 34 ft*lbs is likely to increase the instances of HIC exceedance. This is particularly relevant to vertical impacts with the Phantom 3 in which ATD results showed HIC15 exceedances at 61 ft/s and a consistent relationship between increasing impact energy and HIC output. In PMHS testing, four Phantom 3 vertical impact conditions were tested above 61 ft/s but no fracture injuries were observed. It is also noted that the vertical impacts showed less test-to-test impact location variability than the angled frontal cases, implying that the PMHS test output for vertical cases is robust enough to derive such conclusions, with the caveat that more statistically significant testing is advised for future research. The low incidence of skull fracture injury seen from PMHS testing is not accurately represented by the probabilities predicted by ATD tests, when compared against the current injury threshold level. We therefore recommend to use a threshold value of 1170 for HIC15, corresponding to 30% of AIS3+, to better represent the PMHS observed injuries.

Of the 35 tests exceeding 200 g's peak head acceleration, 16 were sUAS cases, each associated with a 10% or greater chance of causing skull fracture, based on the current injury threshold values. As with the HIC15 criteria, these tests were conducted up to an energy level of 175 ft-lbs, while PMHS testing achieved 209 ft-lbs for many tests. Therefore, the ATD testing indicates that the occurrence of skull fracture injury should be greater than 1 to 2 for sUAS impacts, and more than 3 to 4 for the test matrix including the wood and foam block impacts. Since the PMHS test results showed lower injury rates, the threshold of 200 g appears to be conservative.

7.1.2.3 Neck Loading Criteria

Compression and modified shear criteria have conservative thresholds when applied to ATD test output. No significant neck injuries were attributed to the PMHS impact cases tested by OSU.

7.1.3 Human Body Modeling Assessment

The human body modeling effort utilized the THUMS model, in order to investigate the biofidelic response of a simulated PMHS to sUAS impacts.

7.1.3.1 Dynamic Skull Bone Deformations

THUMS simulations showed small yet measurable dynamic skull bone deformations that may have been present on test subjects and could have affected test output; Section 6.4.1.3 .

7.1.3.2 THUMS and PMHS Angular Metrics

THUMS angular velocity results have a better agreement with PMHS test outputs than the linear and angular acceleration outputs, Section 6.4.1.4 . This is due to the head rebound kinematics having a longer duration than the transient accelerations of the impact.

7.1.3.3 Pressure and Strain-Based Injury Assessment

Numerical simulation has the capability to investigate brain injury during sUAS impact events using three methodologies: measurement of global head kinematics (discussed in preceding sections); characterization of intracranial pressures; and determination of maximum principal strains. Section 6.4.1.5 .

7.2 FUTURE WORK:

As a result of the preceding conclusions and recommendations, NIAR identified the following topics as the most important next steps in characterizing injury potential as a result of sUAS ground collisions:

- **Evaluate injury potential for a larger population:** The present research effort focused on testing with 50th percentile male ATDs and PMHSs. However, injury potential was shown to be related to individual physiology and greater differences exist across the population than were present in the test subjects researched herein. It is therefore necessary to conduct a spectrum of analyses to evaluate a larger population including infants, 5th percentiles, and the elderly, using numerical analysis. Injury criteria limits could be developed for the entire population rather than just for the 50th percentile male.
- **Develop an injury severity heat map of the skull:** Due to the observation that impact location can have a significant effect on the resulting injury severity, it is recommended to develop a skull heat map based on worst-case impact location, direction, and sUAS orientation by means of numerical analysis.
- **sUAS rotation effects:** Linear translational impacts have been characterized and documented in this report. However, it is possible for these impact cases to have additional kinetic energy due to rotational kinematics of the sUAS upon impact. This additional kinetic energy could alter both the potential for injury and the occurrence of specific injury patterns. Due to realistic testing limitations, it is recommended that future research consider sUAS rotation effects with ATD and human body model simulations.
- **Parametric analysis of sUAS construction stiffness:** The energy transferred during an impact showed a significant dependence on the construction stiffness of the sUAS. The present research has characterized the major sUAS architectures and some of the

representative construction materials. Due to the high level of dependence on these parameters, NIAR recommends to conduct a parametric analysis with simulation and testing to better understand stiffness and construction effects in terms of injury potential.

- **Define representative neck injury thresholds:** Neck injuries were not identified to any significant degree in the present research data set. In order to maintain an equivalent level safety with ground collision conditions, it is recommended to perform further testing and analysis to better understand and define representative neck injury thresholds.
- **Improve brain injury prediction metrics:** Conduct further PMHS testing and human body model simulation work to verify pressure and strain thresholds as well as head rotational measurements for brain injury prediction.
- **Detailed analysis and testing of fixed-wing pusher vs puller configurations:** Injury potential associated with fixed-wing sUAS pusher and puller configurations have been studied with a small sample of the existing sUAS population. Therefore, detailed analysis and testing is recommended for fixed-wing pusher and puller configurations so that distinctions and applications can be defined for a broader selection of vehicles.

8. REFERENCES

1. "The Economic Impact if Unmanned Aircraft Systems Integration in the United States", AUVSI's, URL: https://www.auvsi.org/our-impact/economic-report
2. Arterburn, D., Duling, C., Goli, N., Sallis, C., "Annex A. UAH Final Report. Task A14: UAS Ground Collision Severity Evaluation 2017-2018", Federal Aviation Administration, Draft Report DOT/FAA/AR-XX/XX (to be published).
3. Bolte, J., Stark, D., Kang, S., McCrink, M., Gregory, J., "Annex C. OSU Final Report. Task A14: UAS Ground Collision Severity Evaluation 2017-2018", Federal Aviation Administration, Draft Report DOT/FAA/AR-XX/XX (to be published).
4. "Micro Unmanned Aircraft Systems Aviation Rulemaking Committee (ARC). ARC Recommendations Final Report", Federal Aviation Administration, URL: https://www.faa.gov/uas/resources/public_records/media/micro-uas-arc-final-report.pdf
5. Duma, S.M., Crandall, J.R., Rudd, Rodney W., and Kent., R.W., "Small female head and neck interaction with a deploying side airbag", *Accident Analysis & Prevention 35, no. 5* ,2003, pp. 811-816.
6. Lund, A. K. "Recommended procedures for evaluating occupant injury risk from deploying side airbags" TWG Report, First Revision, Insurance Institute for Highway Safety, 2003.
7. Takhounts, E.G., Craig, M.J., Moorhouse, K., McFadden, J., and Hasija, V., "Development of brain injury criteria (BrIC)", *Stapp Car Crash Journal*, Vol. 57, 2013, pp. 243-266.
8. Rowson, S., and Duma, S.M., "Brain injury prediction: assessing the combined probability of concussion using linear and rotational head acceleration", *Annals of biomedical engineering*, Vol 41, no. 5, 2013, pp. 873-882.
9. Kang, Y., Moorhouse, K., and Bolte, J.H., "Measurement of six degrees of freedom head kinematics in impact conditions employing six accelerometers and three angular rate sensors (6aω configuration)." *Journal of biomechanical engineering*, Vol 133, no. 11, 2011, pp. 111007-1 - 111007-11
10. Olivares, G., Gomez, L., Espinosa de los Monteros, J., Baldridge, R.J., Zinzuwadia, C., and Aldag, T., "Volume II–UAS Airborne Collision Severity Evaluation–Quadcopter.", 2017.
11. Olivares, G., Lacy, T., Gomez, L., Espinosa de los Monteros, J., Baldridge, R.J., Zinzuwadia, C., Aldag, T., Raj Kota, K., Ricks, T., and Jayakody, N., "Volume III–UAS Airborne Collision Severity Evaluation–Fixed-Wing.", 2017.
12. Ajmer, D., Bradley, J., Casem, D., "Mechanical response of polycarbonate with strength model fits", *Dynamic Science Inc Aberdeen MD*, 2012.
13. "Properties and Selection: Nonferrous Alloys and Special Purpose Materials", *ASM Handbook*, Vol. 2, ASM International, 1990.
14. "LS-DYNA Keywords User's Manual – Material Models", *LS-DYNA R8.0 User's Manual Vol. II*, Livermore Software Technology Corporation, 2017.
15. MMPDS-09, *Metallic Material Properties Development and Standardization (MMPDS)*, Chapter 9, Ed. 7, Battelle Memorial Institute, 2014.
16. Ravi-Chandar, K., and Satapathy, S., "Mechanical Properties of G-10 Glass-Epoxy Composite", Technical Report IAT.R0466, Institute for Advanced Technology, The University of Texas Austin, 2007.

17. Sahraei, E., Meier, J., and Wierzbicki, T., “Characterizing and Modeling Mechanical Properties and Onset of Short Circuit for Three Types of Lithium-Ion Pouch Cells”, *Journal of Power Sources*, Vol. 247, 2014, pp. 503-516.
18. Stander, N., Roux, W., Basudhar, A., Eggleston, T., Goel, T., and Craig, K., *LS-OPT User's Manual, Ver. 5.1*, Livermore Software Technology Corporation, 2014.
19. Huculak, R., “NIAR UAS Drop Testing Report. Support of UAH Part 107 Waiver Case Study”, NIAR-Wichita State University, Doc. CDL-TR-17-2163-UA01, 2016.
20. SenseFly, URL: https://www.sensefly.com/drones/
21. “LS-DYNA Keywords User's Manual”, *LS-DYNA R8.0 User's Manual Vol. I*, Livermore Software Technology Corporation, 2017.
22. Arterburn, D., “Task A11 - Part 107 Waiver Request Case Study”, UAH Rotorcraft Systems Engineering and Simulation Center, Revision 1, 2016.
23. Guha, S., “LSTC_NCAC Hybrid III 50th Dummy. Positioning & Post-Processing”, LSTC Michigan, 2014.
24. “User's Manual FAA Hybrid III 50th Percentile Male Dummy”, LS-Dyna Model Version 1.2.2, Humanetics Innovative Solutions, 2017.
25. “Humanetics Hybrid III 50th Application Example” HUMANETICS Innovative Solutions URL: http://www.humaneticsatd.com/sites/default/files/file/H350%20Application%20Example%20HIS%20Website.pdf
26. “Evaluation of Humanetics Hybrid III 50th Model” HUMANETICS Innovative Solutions URL: http://www.humaneticsatd.com/sites/default/files/file/NASA%20for%20HIS%20website.pdf
27. “LS-DYNA Theory Manual”, LS-DYNA R8.0 User Manual, Livermore Software Technology Corporation, 2017.
28. Yoganandan, N., Pintar, F., Sances, A.Jr, Walsh, P., Ewing, C., Thomas, D., Snyder, R., "Biomechanics of skull fracture", *Journal of neurotrauma*, Vol. 12, no. 4, 1995, pp. 659-668.
29. Nahum, A., Smith, R., and Ward, C., “Intracranial pressure dynamics during head impact”, *SAE Technical Paper*, No. 770922, 1977.
30. Documentation Total Human Model for Safety (THUMS)”, AM50 Occupant Model Academic Version 5.0_20150527, Toyota Motor Corporation, 2015.
31. “Addendum A – NIAR A14 ATD Testing”, National Institute for Aviation Research, 2019.

APPENDIX A—TEST REPORTS

This section contains a summary of the A14 ATD test results in Table 31. For complete documentation of the ATD tests conducted by NIAR, see the addendum to this appendix [31].

Table 31. A14 sUAS-ATD Impact Test Results

Test N.	Impact Trajectory to Head	Head Impact Location	Model	Article mass [lb]	Achieved Velocity (ft/s)	Test KE (ft.lbs)	Head Resultant (g)	HIC	Head 3ms (g)	Tension (lbf)	Compression (lbf)	Flexion (lbf-ft)	Extension (lbf-ft)	Shear (lbf)	Nij	Modified Nij	Modified Shear (lbf)	Lateral Moment (lbf-ft)	Twisting Moment (lbf-ft)	BrIC	CP
1	Vertical	Top	Phantom 3	2.546	25.48	25.69	52.96	20.79	26.17	40.49	575.85	8.45	0.92	42.58	0.45	N/A	N/A	2.39	0.40	0.09	0.003
2	Vertical	Top	Phantom 3	2.592	25.18	25.54	65.24	22.67	25.43	21.18	575.58	11.74	1.74	54.93	0.46	N/A	N/A	3.44	0.92	0.13	0.022
3	Vertical	Top	Phantom 3	2.55	25.33	25.43	42.58	10.44	17.94	14.87	436.39	14.03	1.77	53.94	0.36	N/A	N/A	1.87	0.58	0.12	0.011
4	Vertical	Top	Phantom 3	2.452	36.02	49.44	81.87	40.40	33.58	60.01	702.15	7.96	0.77	44.27	0.54	N/A	N/A	9.34	1.40	0.09	0.021
5	Vertical	Top	Phantom 3	2.582	36.32	52.93	104.98	102.03	47.44	44.48	827.67	9.66	2.34	53.26	0.64	N/A	N/A	4.38	1.21	0.12	0.505
6	Vertical	Top	Phantom 3	2.55	35.41	49.69	65.25	22.50	22.11	12.93	465.06	8.92	2.46	49.76	0.37	N/A	N/A	2.86	0.92	0.10	0.036
7	Vertical	Top	Phantom 3	2.478	25.17	24.40	21.81	4.83	14.19	34.77	441.60	4.57	1.54	36.97	0.32	N/A	N/A	15.05	1.27	0.13	0.003
8	Vertical	Top	Phantom 3	2.482	36.31	50.85	27.90	7.92	16.89	34.20	492.45	16.73	1.70	55.06	0.37	N/A	N/A	19.69	3.06	0.24	0.015
9	Horizontal	Side	Phantom 3	2.474	35.96	49.72	52.37	36.07	30.13	55.92	13.64	2.50	1.55	N/A	N/A	0.22	148.27	31.38	5.76	0.35	0.086
10	Horizontal	Side	Phantom 3	2.518	57.00	127.14	114.09	172.68	50.28	198.11	27.03	2.75	4.83	N/A	N/A	0.46	233.10	48.02	5.63	0.42	0.562
11	Horizontal	Side	Phantom 3	2.552	61.92	152.06	145.32	255.15	52.84	264.84	9.66	5.91	2.95	N/A	N/A	0.37	239.23	41.49	12.13	0.51	0.918
12	Horizontal	Side	Phantom 3	2.55	64.28	163.74	146.38	301.18	48.81	265.84	9.43	3.75	4.34	N/A	N/A	0.47	263.25	49.55	11.37	0.52	0.957
13	Vertical	Top	Phantom 3	2.502	55.03	117.75	245.75	420.73	70.82	53.19	1192.71	9.82	2.28	83.28	0.89	N/A	N/A	8.31	0.87	0.14	1.000
14	Vertical	Top	Phantom 3	2.582	65.59	172.62	324.02	736.20	87.84	52.63	1377.07	4.89	8.38	97.26	1.00	N/A	N/A	3.00	0.82	0.16	1.000
15	Angled	58° - Front	Phantom 3	2.556	55.70	123.24	169.69	291.06	53.74	57.90	871.51	28.35	12.45	223.32	0.69	N/A	N/A	8.31	2.17	0.29	0.935
16	Angled	58° - Front	Phantom 3	2.562	61.51	150.64	175.48	346.77	57.24	57.63	921.99	33.15	12.95	260.60	0.74	N/A	N/A	3.47	1.12	0.31	0.992
17	Angled	58° - Front	Professional	2.56	64.43	165.15	191.06	446.44	58.80	70.50	957.62	36.25	13.77	280.17	0.77	N/A	N/A	4.64	1.73	0.32	0.997
18	Angled	58° - Rear	Professional	2.544	55.81	123.14	232.21	414.87	69.05	43.78	991.32	14.03	14.74	231.19	0.81	N/A	N/A	9.22	1.81	0.29	1.000
19	Angled	58° - Rear	Phantom 3	2.558	61.54	150.55	233.81	536.79	73.49	64.28	1130.05	18.84	18.07	245.24	0.94	N/A	N/A	8.50	2.30	0.35	1.000
20	Angled	58° - Rear	Phantom 3	2.55	65.31	169.03	250.80	688.18	78.14	70.82	1166.06	21.07	19.97	284.75	0.98	N/A	N/A	7.56	1.76	0.35	1.000
21	Angled	58° - Side	Professional	2.508	36.65	52.35	42.46	18.76	22.98	19.82	396.34	8.25	8.65	N/A	N/A	0.43	78.42	19.12	3.12	0.30	0.018
22	Angled	58° - Side	Professional	2.526	55.73	121.92	128.73	149.70	50.89	80.84	783.19	9.68	8.36	N/A	N/A	0.58	103.21	17.51	4.46	0.31	0.916
23	Angled	58° - Side	Phantom 3	2.548	61.50	149.77	105.67	88.67	0.17	39.99	585.41	11.01	6.49	N/A	N/A	0.62	135.25	28.65	6.14	0.39	0.989
23B	Angled	58° - Side	Phantom 3	2.552	61.51	150.87	155.87	189.54	52.88	102.91	845.71	11.14	8.16	N/A	N/A	0.62	123.13	22.80	4.60	0.33	0.989
24	Angled	58° - Side	Phantom 3	2.548	66.41	174.64	153.81	233.49	56.08	47.77	880.46	11.73	9.44	N/A	N/A	0.65	141.26	24.94	5.84	0.39	0.993
25	Vertical	Top	eBee+	2.546	50.64	101.46	33.00	8.21	16.93	30.90	495.14	4.03	9.29	26.07	0.38	N/A	N/A	2.67	0.21	0.11	0.001
26	Vertical	Top	eBee+	2.51	60.84	144.38	51.02	10.72	15.49	53.47	586.16	3.11	7.57	26.67	0.43	N/A	N/A	6.39	0.75	0.11	0.003
27	Horizontal	Side	eBee+	2.548	25.51	25.77	15.12	3.86	13.56	29.44	3.57	1.53	0.57	N/A	N/A	0.11	56.51	14.15	2.03	0.20	0.000
28	Horizontal	Side	eBee+	2.548	35.57	50.10	17.16	5.11	14.68	33.87	4.09	1.46	1.38	N/A	N/A	0.14	61.38	15.21	3.55	0.17	0.000
29	Horizontal	Side	eBee+	2.532	59.64	139.96	51.91	24.73	23.14	40.49	76.81	2.39	0.99	N/A	N/A	0.31	164.82	45.96	4.06	0.35	0.003
30	Horizontal	Side	eBee+	2.546	64.25	163.33	59.69	39.00	30.66	57.74	66.59	2.63	1.22	N/A	N/A	0.40	197.12	54.89	5.29	0.43	0.015
31	Angled	58° - Side	eBee+	2.532	24.42	23.46	9.66	1.41	8.40	5.90	157.91	2.44	0.40	N/A	N/A	0.12	30.07	9.25	1.38	0.12	0.000
32	Angled	58° - Side	eBee+	2.53	36.35	51.95	16.20	3.53	12.08	7.52	193.42	3.79	0.67	N/A	N/A	0.15	46.81	8.20	2.05	0.13	0.000
33	Angled	58° - Side	eBee+	2.544	58.65	135.99	76.86	37.15	25.68	64.20	510.88	7.56	1.10	N/A	N/A	0.41	67.88	12.63	2.47	0.22	0.124
34	Angled	58° - Side	eBee+	2.516	64.35	161.91	106.22	58.06	28.93	52.23	569.84	9.19	1.03	N/A	N/A	0.45	70.21	13.50	3.58	0.25	0.415
35	Vertical	Top	Vendor1	0.71	25.55	7.20	16.61	0.99	6.00	43.11	161.51	2.39	0.61	23.33	0.12	N/A	N/A	1.03	0.12	0.04	0.000
36	Vertical	Top	Vendor1	0.71	25.54	7.20	28.68	2.93	9.54	27.79	184.42	2.15	0.52	28.10	0.13	N/A	N/A	0.67	0.14	0.07	0.001
37	Vertical	Top	Vendor1	0.714	25.88	7.43	11.80	0.67	6.65	53.88	161.53	0.78	0.92	9.08	0.12	N/A	N/A	0.48	0.18	0.07	0.000
38	Vertical	Top	Vendor1	0.71	35.68	14.05	23.63	1.62	8.87	52.08	136.13	2.61	0.69	15.07	0.11	N/A	N/A	1.02	0.32	0.07	0.000
39	Vertical	Top	Vendor1	0.712	35.66	14.07	52.45	9.02	15.00	4.47	260.30	2.77	0.67	42.53	0.19	N/A	N/A	1.10	0.15	0.04	0.005
40	Vertical	Top	Vendor1	0.708	36.35	14.54	15.62	2.33	11.23	36.56	236.41	4.55	0.81	29.32	0.18	N/A	N/A	0.63	0.22	0.05	0.000
41	Vertical	Top	Vendor1	0.71	25.54	7.20	9.68	0.68	6.72	53.28	113.96	0.92	0.31	15.73	0.08	N/A	N/A	1.75	0.21	0.05	0.000

Test N.	Impact Trajectory to Head	Head Impact Location	Model	Article mass [lb]	Achieved Velocity (ft/s)	Test KE (ft.lbs)	Head Resultant (g)	HIC	Head 3ms (g)	Tension (lbf)	Compression (lbf)	Flexion (lbf-ft)	Extension (lbf-ft)	Shear (lbf)	Nij	Modified Nij	Modified Shear (lbf)	Lateral Moment (lbf-ft)	Twisting Moment (lbf-ft)	BrIC	CP
42	Vertical	Top	Vendor1	0.712	36.55	14.78	14.89	1.06	7.85	24.16	123.48	3.77	0.82	17.10	0.10	N/A	N/A	0.87	0.20	0.03	0.000
43	Vertical	Top	Vendor1	0.714	24.17	6.48	37.40	3.89	11.39	41.19	177.10	1.75	0.56	28.09	0.13	N/A	N/A	1.09	0.21	0.06	0.001
44	Vertical	Top	Vendor1	0.708	35.89	14.17	75.27	13.10	17.37	19.29	279.45	3.08	0.67	44.72	0.21	N/A	N/A	1.43	0.18	0.07	0.009
45	Vertical	Top	Vendor1	0.712	24.57	6.68	39.39	4.28	11.25	51.63	186.10	2.00	0.48	29.51	0.14	N/A	N/A	0.85	0.19	0.08	0.001
46	Vertical	Top	Vendor1	0.712	35.89	14.25	67.87	12.66	16.79	19.15	274.66	2.98	1.02	41.86	0.21	N/A	N/A	1.63	0.20	0.08	0.011
47	Vertical	Top	Vendor1	0.712	45.02	22.43	101.82	23.85	19.86	2.98	366.62	2.03	2.48	43.73	0.28	N/A	N/A	1.75	0.52	0.04	0.370
48	Vertical	Top	Vendor1	0.714	54.99	33.55	145.20	47.58	26.62	16.30	438.72	1.80	2.79	44.05	0.34	N/A	N/A	2.13	0.25	0.06	0.680
49	Angled	80° - Front	Vendor1	0.708	45.20	22.48	98.88	22.35	18.12	5.52	291.42	5.43	0.82	76.27	0.21	N/A	N/A	1.61	0.33	0.04	0.045
50	Angled	80° - Front	Vendor1	0.712	54.83	33.26	138.09	44.18	24.23	7.00	353.04	7.05	1.45	97.94	0.26	N/A	N/A	1.97	0.47	0.10	0.672
51	Angled	80° - Side	Vendor1	0.71	45.16	22.50	109.49	34.33	20.97	5.24	306.05	3.70	0.57	N/A	N/A	0.24	45.61	1.56	0.41	0.14	0.559
52	Angled	80° - Side	Vendor1	0.712	55.71	34.34	127.68	45.80	22.70	5.87	363.23	3.75	0.74	N/A	N/A	0.28	51.67	1.98	0.34	0.06	0.812
53	Vertical	Top	Wood Block	2.728	9.65	3.95	146.61	123.37	35.80	33.40	704.78	5.93	0.78	67.88	0.51	N/A	N/A	4.08	0.38	0.13	0.966
54	Vertical	Top	Wood Block	2.722	19.56	16.18	311.19	594.93	50.26	50.19	1187.95	8.33	0.82	71.31	0.86	N/A	N/A	6.15	1.23	0.07	1.000
55	Vertical	Top	Wood Block	2.72	28.66	34.72	537.79	1790.01	58.03	56.08	1725.66	11.45	1.76	83.85	1.25	N/A	N/A	5.29	4.06	0.13	1.000
56	Horizontal	Front	Wood Block	2.692	19.32	15.62	60.76	28.41	16.77	26.99	22.01	19.37	9.84	138.88	0.11	N/A	N/A	1.08	2.16	0.25	0.003
57	Horizontal	Front	Wood Block	2.694	30.12	37.98	126.91	138.70	19.47	39.55	119.15	48.23	13.63	324.32	0.25	N/A	N/A	2.53	1.96	0.37	1.000
58	Horizontal	Front	Wood Block	2.692	39.32	64.68	317.09	978.41	19.20	51.95	207.11	51.52	16.86	597.76	0.26	N/A	N/A	2.09	3.12	0.43	1.000
59	Horizontal	Side	Wood Block	2.708	20.51	17.70	203.80	198.22	10.39	96.13	7.61	1.48	1.25	N/A	N/A	0.12	224.05	14.00	2.48	0.18	1.000
60	Horizontal	Side	Wood Block	2.706	28.57	34.33	411.18	921.50	18.89	198.86	14.31	2.34	1.99	N/A	N/A	0.16	444.37	19.19	3.84	0.24	1.000
61	Horizontal	Side	Wood Block	2.706	38.90	63.63	662.12	3169.97	22.93	263.67	36.05	3.41	2.53	N/A	N/A	0.21	606.42	25.67	5.34	0.31	1.000
62	Angled	58° - Front	Wood Block	2.71	21.42	19.32	250.51	504.79	43.37	18.10	901.66	9.94	5.54	279.67	0.68	N/A	N/A	3.11	2.54	0.12	1.000
63	Angled	58° - Front	Wood Block	2.71	32.78	45.25	552.20	2189.40	60.89	23.07	1493.36	14.82	7.58	435.03	1.11	N/A	N/A	4.08	3.84	0.16	1.000
64	Angled	58° - Front	Wood Block	2.71	39.84	66.85	762.10	3901.16	71.26	38.19	1901.96	14.52	8.11	504.97	1.40	N/A	N/A	2.78	3.22	0.20	1.000
65	Angled	58° - Side	Wood Block	2.718	20.63	17.98	210.01	220.67	28.25	25.10	619.80	4.55	0.52	N/A	N/A	0.47	100.27	9.44	1.19	0.20	1.000
66	Angled	58° - Side	Wood Block	2.718	31.26	41.28	392.81	1102.49	40.07	35.01	1064.29	1.75	7.57	N/A	N/A	0.84	301.48	11.08	3.55	0.32	1.000
67	Angled	58° - Side	Wood Block	2.718	39.82	66.98	701.94	3893.65	57.08	65.51	1620.55	2.42	6.79	N/A	N/A	1.29	387.39	12.93	3.27	0.45	1.000
68	Vertical	Top	Foam Block	2.748	10.17	4.42	14.45	1.81	9.77	26.98	326.83	1.36	1.02	21.67	0.24	N/A	N/A	3.91	0.30	0.09	0.000
69	Vertical	Top	Foam Block	2.752	19.69	16.58	19.52	3.50	13.00	48.76	444.14	1.93	1.51	26.19	0.33	N/A	N/A	5.21	0.39	0.11	0.000
70	Vertical	Top	Foam Block	2.752	28.39	34.47	41.57	16.67	23.34	58.22	617.60	8.09	1.86	41.30	0.48	N/A	N/A	3.81	0.53	0.10	0.002
71	Horizontal	Front	Foam Block	2.758	20.63	18.24	21.79	7.60	0.00	41.35	55.89	34.85	9.31	107.63	0.18	N/A	N/A	4.97	2.65	0.26	0.001
72	Horizontal	Front	Foam Block	2.758	39.36	66.40	126.51	185.69	45.74	66.19	111.20	35.23	17.74	233.47	0.22	N/A	N/A	3.33	0.65	0.46	0.122
73	Horizontal	Front	Foam Block	2.758	59.63	152.40	651.92	3990.04	19.86	116.67	174.35	31.07	25.06	776.61	0.33	N/A	N/A	3.98	1.29	0.71	1.000
74	Horizontal	Side	Foam Block	2.756	20.63	18.23	23.98	8.52	18.65	70.33	10.14	1.64	3.03	N/A	N/A	0.29	86.30	29.99	6.05	0.27	0.001
75	Horizontal	Side	Foam Block	2.758	38.94	64.99	98.18	174.97	55.35	351.79	9.89	2.72	5.95	N/A	N/A	0.39	167.25	28.96	7.26	0.44	0.037
76	Horizontal	Side	Foam Block	2.756	59.83	153.31	573.48	3005.39	0.56	737.95	16.74	2.14	5.30	N/A	N/A	0.76	751.87	57.67	6.02	0.55	1.000
77	Angled	58° - Front	Foam Block	2.75	21.03	18.90	28.10	11.83	18.11	15.65	396.05	17.51	6.98	83.66	0.34	N/A	N/A	2.55	0.53	0.19	0.001
78	Angled	58° - Front	Foam Block	2.75	39.33	66.11	307.91	666.22	59.86	28.67	1054.63	20.97	10.64	282.27	0.81	N/A	N/A	10.24	2.81	0.29	1.000
79	Angled	58° - Front	Foam Block	2.748	59.73	152.36	737.84	5038.77	97.53	112.43	1977.28	25.08	13.91	522.28	1.46	N/A	N/A	8.16	4.43	0.25	1.000
80	Angled	58° - Side	Foam Block	2.748	20.40	17.77	25.22	10.70	20.24	45.85	182.25	2.01	1.29	N/A	N/A	0.15	43.94	10.21	1.24	0.13	0.001
81	Angled	58° - Side	Foam Block	2.748	38.86	64.49	153.01	190.75	48.55	76.06	766.14	5.29	1.72	N/A	N/A	0.58	140.35	16.42	1.93	0.27	0.891
82	Angled	58° - Side	Foam Block	2.75	59.67	152.16	577.88	2826.09	65.41	109.81	1269.12	6.93	2.86	N/A	N/A	1.05	288.97	19.60	2.37	0.52	1.000
93	Vertical	Top	MavicPro	1.568	51.18	63.83	285.72	325.35	48.33	44.45	801.00	9.54	3.79	92.35	0.58	N/A	N/A	3.17	0.37	0.08	1.000
94	Vertical	Top	MavicPro	1.542	59.67	85.32	241.54	298.15	51.10	45.68	802.54	11.99	3.68	120.12	0.59	N/A	N/A	1.93	0.52	0.13	1.000
95	Angled	58° - Front	MavicPro	1.544	40.26	38.89	111.58	49.31	27.04	21.66	402.36	8.82	8.24	135.64	0.31	N/A	N/A	1.73	0.58	0.15	0.234
96	Angled	58° - Front	MavicPro	1.548	51.13	62.89	156.70	120.62	31.28	41.81	543.32	8.08	6.51	169.94	0.41	N/A	N/A	1.96	1.44	0.17	0.898
97	Angled	58° - Front	MavicPro	1.556	59.63	85.98	264.09	280.61	36.96	53.90	730.96	9.05	6.34	200.84	0.54	N/A	N/A	3.15	1.29	0.13	0.999
98	Angled	58° - Side	MavicPro	1.58	39.78	38.86	145.42	71.90	24.73	25.69	422.23	5.32	0.64	N/A	N/A	0.33	59.44	7.99	1.49	0.19	0.880
98B	Angled	58° - Side	MavicPro	1.58	41.26	42.03	66.66	17.73	18.35	13.62	216.80	1.68	0.96	N/A	N/A	0.19	49.52	16.30	2.37	0.22	0.464
99	Angled	58° - Side	MavicPro	1.556	50.16	60.84	164.53	114.05	31.48	36.38	529.90	6.07	1.10	N/A	N/A	0.41	54.24	9.78	1.63	0.21	0.995

Test N.	Impact Trajectory to Head	Head Impact Location	Model	Article mass [lb]	Achieved Velocity (ft/s)	Test KE (ft.lbs)	Head Resultant (g)	HIC	Head 3ms (g)	Tension (lbf)	Compression (lbf)	Flexion (lbf-ft)	Extension (lbf-ft)	Shear (lbf)	Nij	Modified Nij	Modified Shear (lbf)	Lateral Moment (lbf-ft)	Twisting Moment (lbf-ft)	BrIC	CP
100	Angled	58° - Side	MavicPro	1.548	59.87	86.23	200.60	186.89	32.19	29.43	610.56	7.79	0.72	N/A	N/A	0.48	60.80	12.33	3.41	0.26	1.000
109	Vertical	Top	Karma	4.162	38.42	95.47	146.01	212.51	60.64	19.54	1011.00	9.33	2.13	60.28	0.76	N/A	N/A	24.39	1.56	0.24	0.782
110	Vertical	Top	Karma	4.13	50.16	161.48	217.56	602.85	74.27	43.07	1205.44	7.73	1.96	62.17	0.90	N/A	N/A	12.17	2.25	0.25	1.000
111	Angled	58° - Front	Karma	4.138	40.28	104.34	163.79	266.07	46.94	25.47	866.02	28.18	9.19	232.47	0.68	N/A	N/A	5.47	3.08	0.29	0.984
112	Angled	58° - Front	Karma	4.138	50.21	162.12	267.33	560.32	52.52	31.72	1037.66	33.10	10.61	255.68	0.80	N/A	N/A	12.87	2.95	0.29	1.000
112B	Angled	58° - Front	Karma	4.138	50.14	161.67	238.97	479.36	58.06	50.79	1002.16	35.60	13.54	303.38	0.80	N/A	N/A	27.28	6.56	0.40	1.000
113	Angled	58° - Side	Karma	4.152	39.81	102.26	217.86	441.44	72.84	45.08	1056.10	3.35	10.00	N/A	N/A	0.87	144.48	13.09	4.57	0.35	1.000
114	Angled	58° - Side	Karma	4.166	50.17	162.96	372.05	983.44	69.09	77.13	1204.00	11.03	15.31	N/A	N/A	0.98	192.55	18.59	5.73	0.40	1.000
115	Vertical	Top	Vendor3	4.238	40.27	106.80	173.20	423.94	77.80	65.75	1364.05	8.89	1.92	74.74	1.01	N/A	N/A	7.24	0.90	0.35	0.982
116	Vertical	Top	Vendor3	4.166	51.15	169.39	320.42	669.54	79.31	70.39	1663.58	6.49	5.49	115.34	1.21	N/A	N/A	3.83	0.97	0.19	1.000
117	Angled	58° - Side	Vendor3	4.076	40.29	102.82	138.19	152.16	34.44	45.81	671.58	9.69	13.56	N/A	N/A	0.68	237.18	28.47	6.40	0.38	0.998
118	Angled	58° - Side	Vendor3	4.32	50.64	172.16	144.45	230.55	37.08	66.61	844.09	10.35	16.94	N/A	N/A	0.95	232.29	45.77	7.00	0.49	1.000
119	Vertical	Top	Phantom 3 Battery	0.774	40.79	20.01	124.00	72.50	30.17	18.07	473.26	3.39	1.30	42.14	0.35	N/A	N/A	1.38	1.26	0.05	0.237
120	Vertical	Top	Phantom 3 Battery	0.762	61.25	44.43	231.51	209.27	36.15	25.25	697.29	3.99	3.21	64.29	0.52	N/A	N/A	2.78	1.25	0.10	0.997
121	Horizontal	Front	Phantom 3 Battery	0.762	37.15	16.34	51.10	14.80	8.16	20.36	34.18	17.75	7.68	138.68	0.09	N/A	N/A	1.79	1.79	0.18	0.035
122	Horizontal	Side	Phantom 3 Battery	0.76	59.67	42.05	233.56	265.73	8.63	80.56	5.47	1.16	0.69	N/A	N/A	0.07	283.28	13.58	1.65	0.17	0.999
129	Vertical	Top	Inspire 2	9.15	9.44	12.67	22.14	4.18	12.75	11.68	315.87	17.61	2.40	42.27	0.27	N/A	N/A	6.99	1.88	0.16	0.001
130	Vertical	Top	Inspire 2	9.106	14.79	30.95	32.70	13.22	20.56	20.18	448.43	28.28	2.03	55.23	0.37	N/A	N/A	5.81	1.56	0.28	0.008
131	Angled	20° - Side	Inspire 2	9.092	27.39	106.00	84.42	112.15	49.31	42.28	255.94	13.92	5.25	N/A	N/A	0.38	206.97	50.02	8.85	0.49	0.048
132	Angled	58° - Front	Phantom 3	2.53	71.83	202.86	363.70	1063.81	77.28	49.73	1186.91	16.56	11.44	319.12	0.89	N/A	N/A	5.70	1.49	0.30	1.000
133	Angled	58° - Front	Phantom 3	2.53	71.71	202.18	311.27	850.20	78.54	60.26	999.53	31.29	14.42	312.42	0.76	N/A	N/A	3.46	0.81	0.34	1.000

APPENDIX B—FAA H3 50TH AND ES-2RE UPPER NECK COMPARISON

Introduction

The sUAS impact testing for Task A14 is conducted with a FAA Hybrid 3 50th percentile ATD. This ATD will utilized a modified head (78051-61X-1846-H) to accommodate the 6aω instrumentation array (6 linear accelerometers and 3 angular rate sensors). This instrumentation is needed to calculate the angular acceleration of the ATD head during impacts which will be used to determine concussion risk by calculating the Combined Probability (CP) of Concussion [Rowson]. Since the FAA H3 head and neck were not designed for evaluating loads in the lateral direction, a preliminary comparison study was conducted in an attempt to correlate lateral impacts on an ES-2re head and neck to the FAA H3 50th. The experimental comparison study evaluates the FAA Hybrid 3 50th percentile ATD compared the to the ES-2re Upper Neck injury limits, from PS-ANM-25-03-R1, and kinematics. From the FAA research on side facing seats, it was determined that injury solely due to bending moment (Mx) is unlikely; most injuries occur from combined bending moment with tension or compression [DOT/FAA/AM-12/18]. The mechanics of the UAS impact are generally not expected to be able to induce the combined loading on the ATD neck. Therefore, the comparison testing will focus on the upper neck shear force (Fxy) injury limit as well as the overall head kinematics.

Table 32. FAA Side-Facing Seat ES-2re Neck Injury Criteria

FAA Side-Facing Seat ES-2re Neck Injury Criteria [PS-ANM-25-03-R1]	Limit
Peak Axial Tension (Fz)	405 lbf
Peak Axial Compression (Fz)	405 lbf
Peak Bending Moment (Mx)	1,018 in-lbf
Peak Resultant Shear (Fxy)	186 lbf

Methodology

A wood block, similar in weight to a Phantom 3 UAS, impacts the ES-2re head CG laterally at various velocities. The linear head accelerations (Ax, Ay, Az), head angular velocities (Wx, Wy, Wz) and upper neck forces and moments (Fx, Fy, Fz, Mx, My, Mz) are recorded with the data acquisition system and the head kinematics are recorded with high speed video. The impacts of the wood block are repeated on the FAA H3 50th ATD.

The upper neck shear forces of the two ATDs are compared to determine if there is a scaling factor that can be applied to correlate forces and moments from the ES-2re upper neck load cell to that of the FAA H3 50th in order transfer the lateral injury values determined for the ES-2re to the FAA H3. The head angular velocity and displacements are evaluated from the angular rate sensors to compare the two ATD head kinematics; auxiliary accelerometers are not able to be mounted in the ES-2re head and, therefore, angular accelerations are not compared.

Results

The ES-2re head was impacted with the wood block at various impact velocities, from approximately 10 ft/s up to 35 ft/s. An additional test was conducted at 23 ft/s to achieve a test point closer to the Upper Neck Shear Resultant limit of 186 lbf.

As expected in this impact condition and velocities, the Upper Neck Shear Resultant was the only upper neck injury criteria that exceeded its limit. The upper neck shear resultant limit of 186 lbf was exceed during the test that reached an impact velocity of 23.44 ft/s (22.56 ft-lbf). The highest upper neck tension achieved was only 111.24 lbf, 27.4% of the injury limit (405 lbf). The highest upper neck bending moment about the x-axis was 197.91 in-lbf, 19.4% of the injury limit (1,018 in-lbf). Using a linear interpolation, the HIC injury limit of 1,000 is exceeded at 28.1 ft/s (32.4 ft-lbf).

Table 33. ES-2re Test Results

ES-2re																		
Desired Impact Velocity	Achieved Impact Velocity	Achieved Impact KE	**Upper Neck Shear Resultant Fxy**		Upper Neck Tension		Upper Neck Bending Moment Mxoc		Head Angular Velocity Rx		Head Rotational Displacement X		Head Resultant		HIC			
(ft/s)	(ft/s)	(ft-lbf)	**Max (lbf)**	**Time (sec)**	Max (lbf)	Time (sec)	Max (in-lbf)	Time (sec)	Min (deg/s)	Time (sec)	Min (deg)	Time (sec)	Max (g)	Time (sec)		t1 (ms)	t2 (ms)	dt
10	9.89	4.02	60.40	0.11835	23.06	0.12085	53.18	0.16025	-378.45	0.11975	-13.80	0.17700	84.80	0.11830	35.85	117.85	118.80	0.95
15	16.42	11.07	133.04	0.08275	50.02	0.08565	122.67	0.11925	-608.45	0.10570	-20.86	0.13330	195.35	0.08275	189.84	82.40	83.05	0.65
20	21.32	18.66	160.46	0.05890	71.30	0.06310	157.19	0.09495	-809.93	0.08045	-26.63	0.11395	260.02	0.05885	324.96	58.55	59.10	0.55
23	23.44	22.56	**189.94**	0.05665	70.95	0.05610	150.31	0.09335	-802.86	0.07930	-28.55	0.11120	314.83	0.05665	532.48	56.35	56.90	0.55
25	25.49	26.68	**205.89**	0.05085	88.53	0.05465	155.79	0.08640	-863.74	0.07130	-29.32	0.10595	352.01	0.05080	668.40	50.55	51.05	0.50
30	29.81	36.48	**279.49**	0.04190	111.24	0.04575	173.25	0.07515	-1024.23	0.06110	-30.94	0.09525	482.46	0.04190	1308.01	41.65	42.10	0.45
35	34.95	50.15	**397.57**	0.03875	99.37	0.03880	197.91	0.06615	-1151.13	0.05800	-33.08	0.08755	655.51	0.03870	3031.46	38.45	38.90	0.45

The FAA H3 50th head was impacted at the same velocities as the ES-2re, ranging from approximately 10 ft/s up to 35 ft/s. Similar to the ES-2re, the upper neck resultant shear was the only upper neck injury criteria that exceeded its limit. Using linear interpolation, the upper neck shear resultant exceeds the limit at 19.3 ft/s (15.28 ft-lbf). The highest upper neck tension achieved was 145.04 lbf, 35.8% of the injury limit (405 lbf). The highest upper neck bending moment about the x-axis was 199.22 in-lbf, 19.6% of the injury limit (1,018 in-lbf). Using the third order best fit curve, the HIC injury limit is exceeded at approximately 29.59 ft/s (35.9 ft-lbf).

Table 34. FAA HIII Test Results

FAA Hybrid 3 50th																		
Desired Impact Velocity	Achieved Impact Velocity	Achieved Impact KE	**Upper Neck Shear Resultant Fxy**		Upper Neck Tension		Upper Neck Bending Moment Mxoc		Head Angular Velocity Rx		Head Rotational Displacement X		Head Resultant		HIC			
(ft/s)	(ft/s)	(ft-lbf)	**Max (lbf)**	**Time (sec)**	Max (lbf)	Time (sec)	Max (in-lbf)	Time (sec)	Min (deg/s)	Time (sec)	Min (deg)	Time (sec)	Max (g)	Time (sec)		t1 (ms)	t2 (ms)	dt
10	9.81	3.95	71.44	0.12930	34.37	0.13495	81.47	0.20700	-415.87	0.13035	-5.92	0.16015	70.33	0.12905	23.17	128.60	129.60	1.00
15	16.42	11.07	131.54	0.08415	60.33	0.08600	119.21	0.10585	-670.78	0.08565	-11.09	0.12020	159.64	0.08420	152.48	83.65	86.20	2.55
20	21.47	18.93	**233.13**	0.06130	80.59	0.06300	135.28	0.06130	-882.92	0.06250	-14.75	0.10065	236.14	0.06135	431.99	60.85	62.85	2.00
23	23.63	22.92	**237.54**	0.05745	87.89	0.05900	141.69	0.07880	-648.91	0.06030	-13.42	0.09790	298.14	0.05750	641.07	57.00	58.95	1.95
25	25.55	26.80	**317.20**	0.05940	116.91	0.06145	148.15	0.07970	-1066.37	0.06100	-17.08	0.10070	277.39	0.05940	877.67	59.00	60.75	1.75
30	29.59	35.95	**354.82**	0.04690	120.76	0.04835	171.13	0.06655	-1048.02	0.04885	-18.27	0.08945	411.08	0.04695	976.89	46.55	47.15	0.60
35	34.67	49.35	**431.65**	0.04045	145.04	0.04235	199.22	0.06005	-1087.73	0.04360	-17.98	0.08280	533.02	0.04075	1958.20	40.20	41.70	1.50

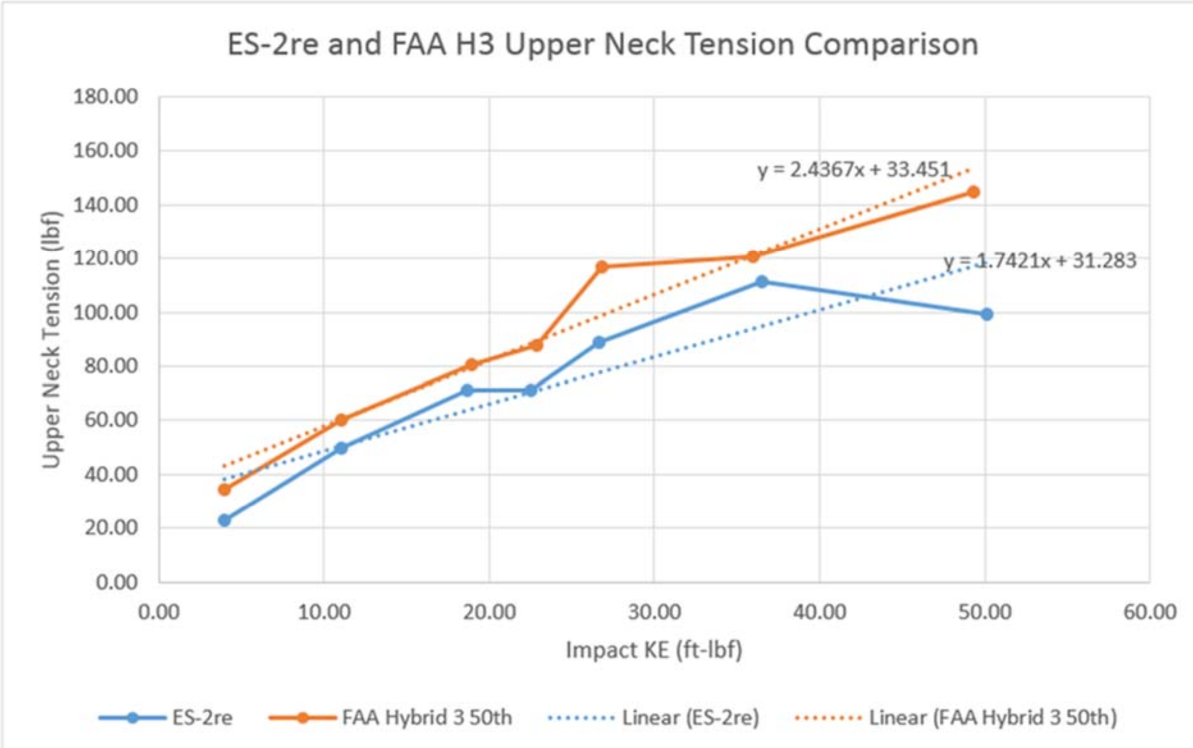

Figure 151. ES-2re vs. FAA HIII Upper Neck Tension

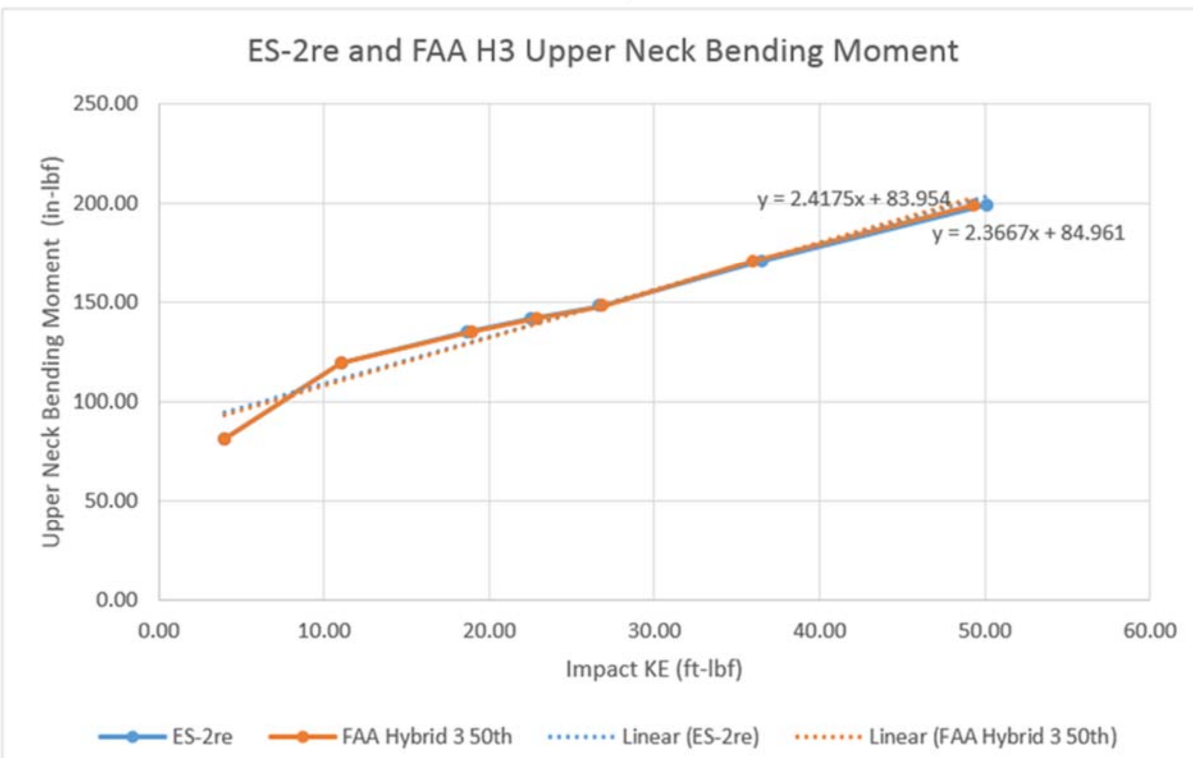

Figure 152. ES-2re vs. FAA HIII Upper Neck Bending Moment

The FAA H3 has approximately a 40% increase in the upper neck tension at the same impact energy levels for the ES-2re. The upper neck bending moment is almost identical for both the ES-2re and the FAA H3. The head resultant acceleration for the FAA H3 is approximately 20% lower than the ES-2re. The HIC values for the FAA H3 and the ES-2re are very similar for the velocities between 10 ft/s and 25 ft/s; however, they start to diverge at higher velocities. The HIC values for the ES-2re increase at a higher rate than the FAA H3. The peak angular velocity values for the FAA H3 and the ES-2re are very similar; however, the head rotational displacement for the ES-2re is approximately 50% higher than the FAA H3.

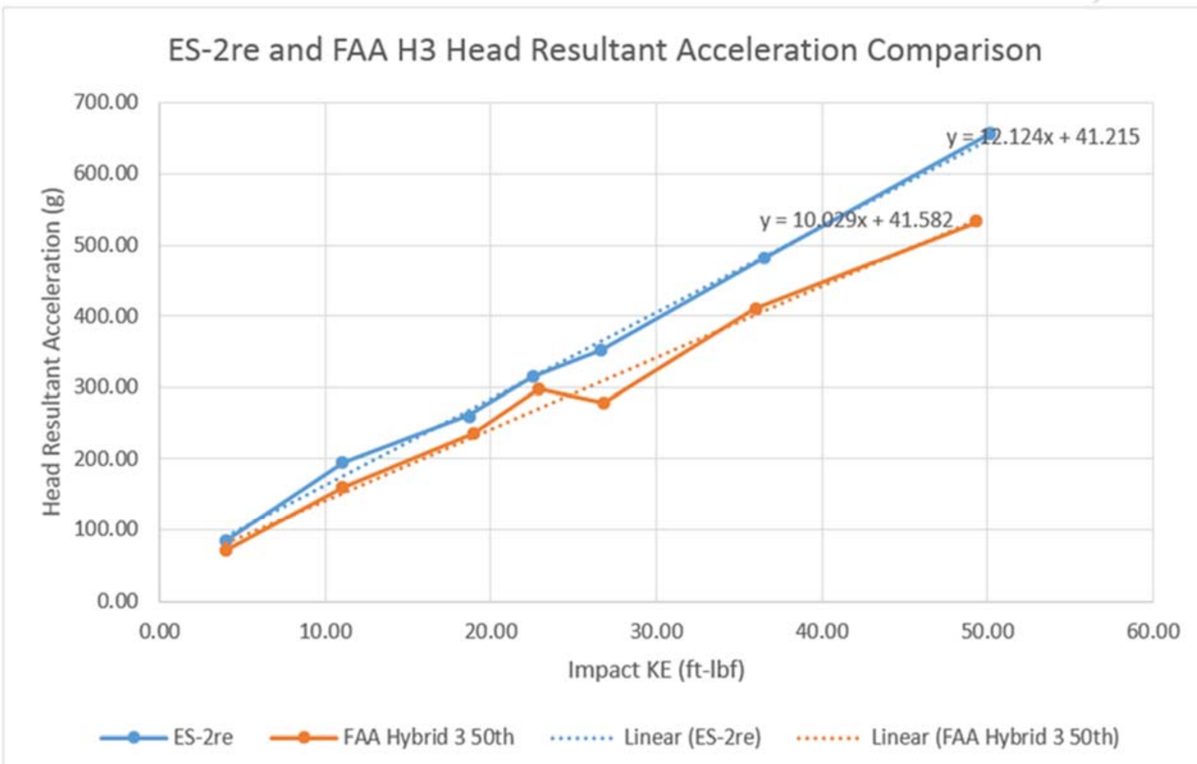

Figure 153. ES-2re vs. FAA HIII Head Resultant Acceleration

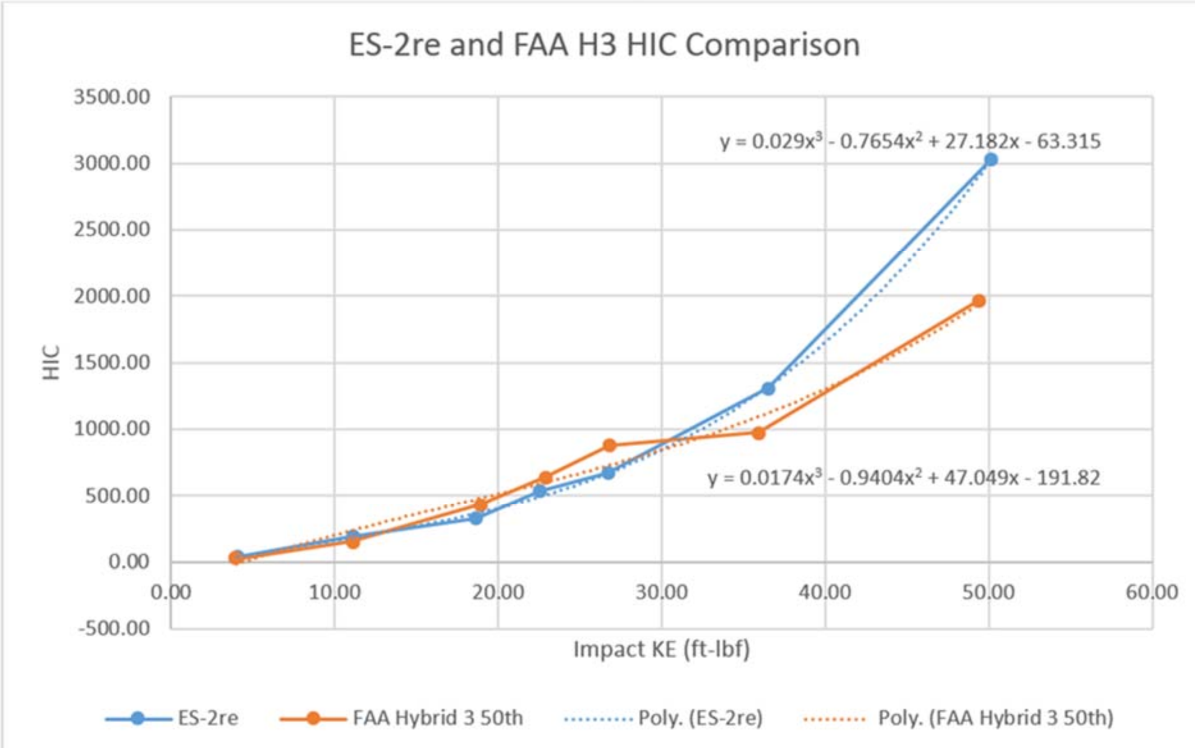

Figure 154. ES-2re vs. FAA HIII HIC

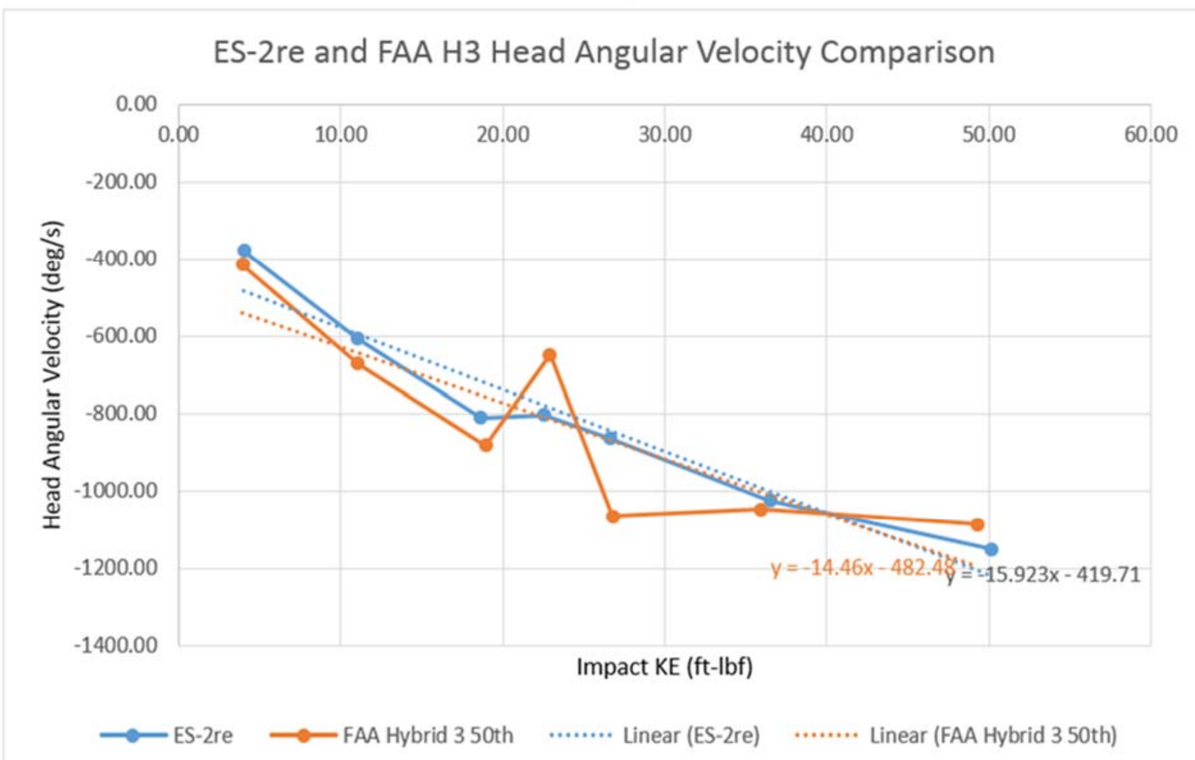

Figure 155. ES-2re vs. FAA HIII Head Angular Velocity

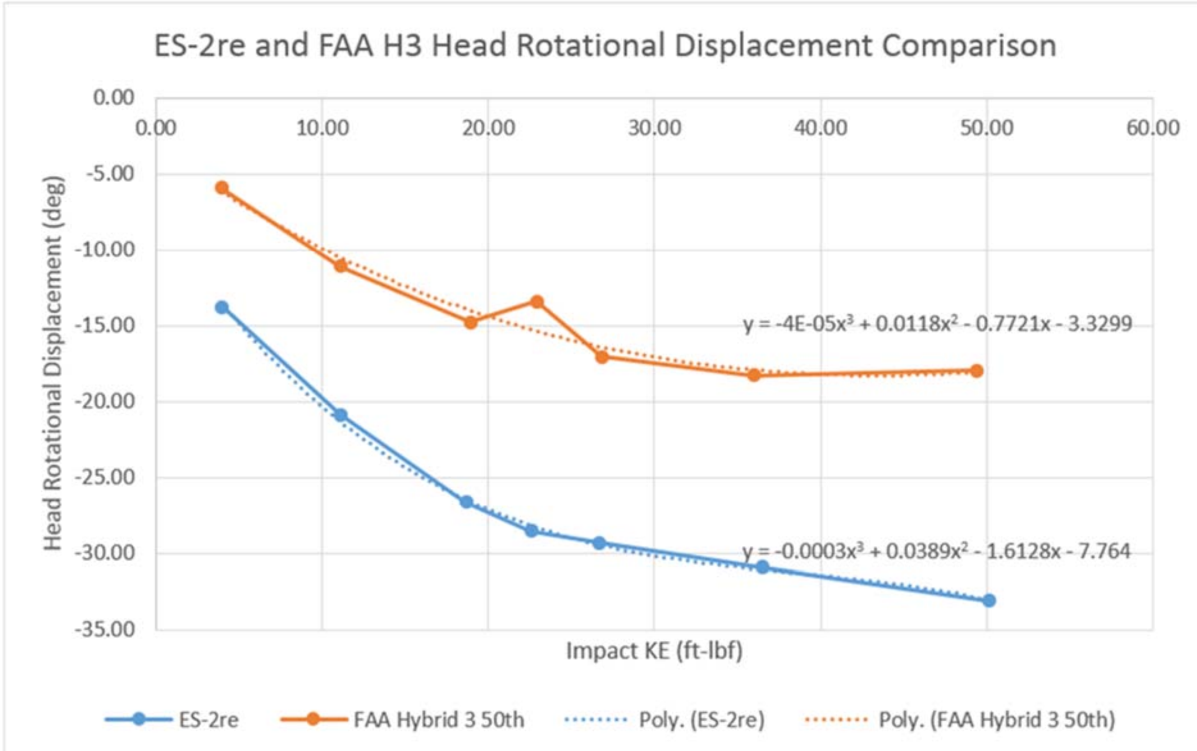

Figure 156. ES-2re vs. FAA HIII Head Rotational Displacement

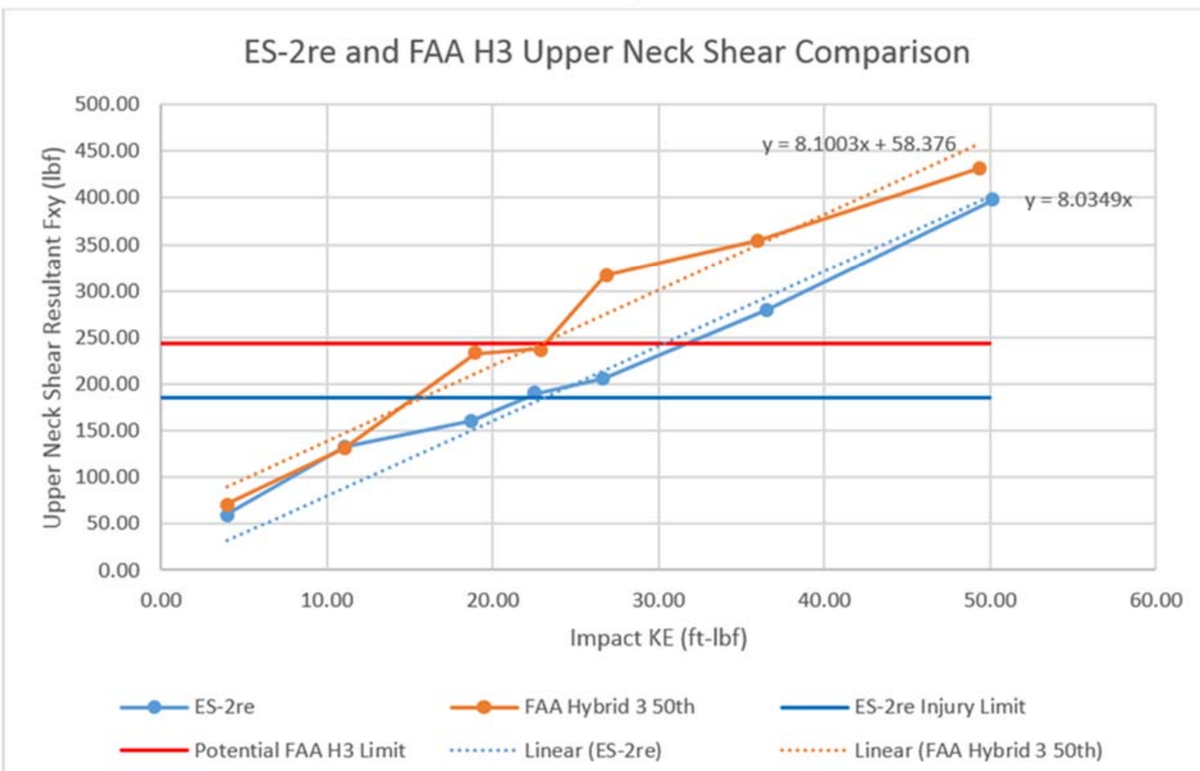

Figure 157. ES-2re vs. FAA HIII Upper Neck Shear

Conclusions

Overall, between the two ATD types, the results are similar for all categories. As was initially anticipated, the upper neck shear resultant was the only upper neck injury criteria that exceeded the limit. The upper neck tension/compression and the upper neck bending moment did not come close to reaching their respective injury limit values. Therefore, only an upper neck shear resultant temporary injury value is necessary for evaluating the sUAS impacts with the FAA H3 50th instead of the ES-2re for side impact test orientations.

Comparing the results of the upper neck shear resultant between the FAA H3 and the ES-2re for the various velocities, there does appear to be a linear trend between the two. While the shear resultant values are very similar at 10 ft/s (~4 ft-lbf) and 15 ft/s (~11 ft-lbf), the higher impact energies result in a higher upper neck shear resultant for the FAA H3 compared to the ES-2re. Fitting a linear trend line on the ES-2re results, and setting the y-intercept to zero, results in a slope of 8.0349. For the FAA H3, the trend line slope is 8.1 and the y-intercept is 58.4. From this, we can conclude that in the area of interest, around 186 lbf of the ES-2re upper neck shear resultant, with similar slopes for both ATDs, the FAA H3 has an equivalent shear resultant for the same impact energy 58 lbf higher than that of the ES-2re. This results in an upper neck shear resultant limit of 244 lbf for the FAA H3 50th ATD.

APPENDIX C—A14 ATD TEST DATA COMPARISON

Vertical Tests

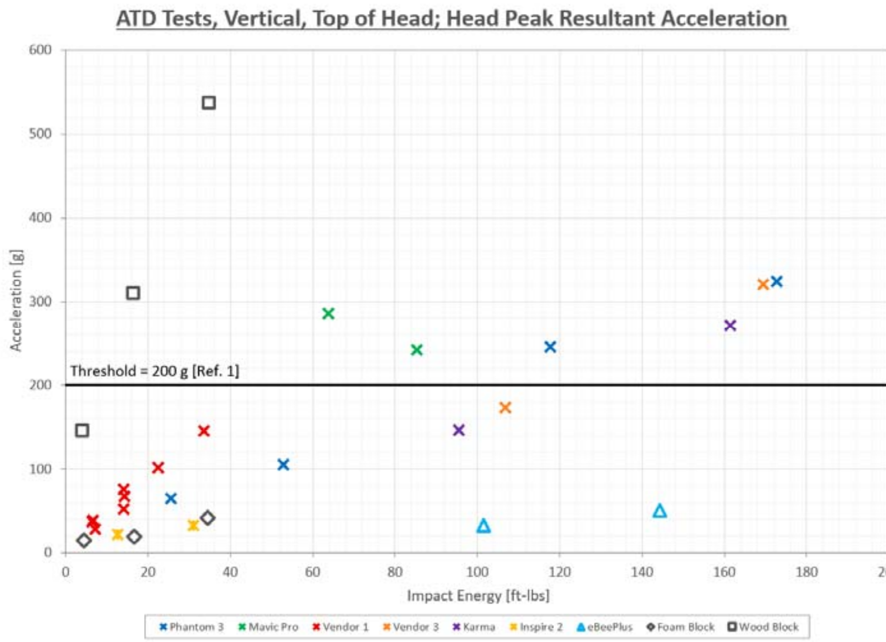

Figure 158. A14 ATD test comparison; multiple projectiles; vertical; top of the head; peak resultant head acceleration

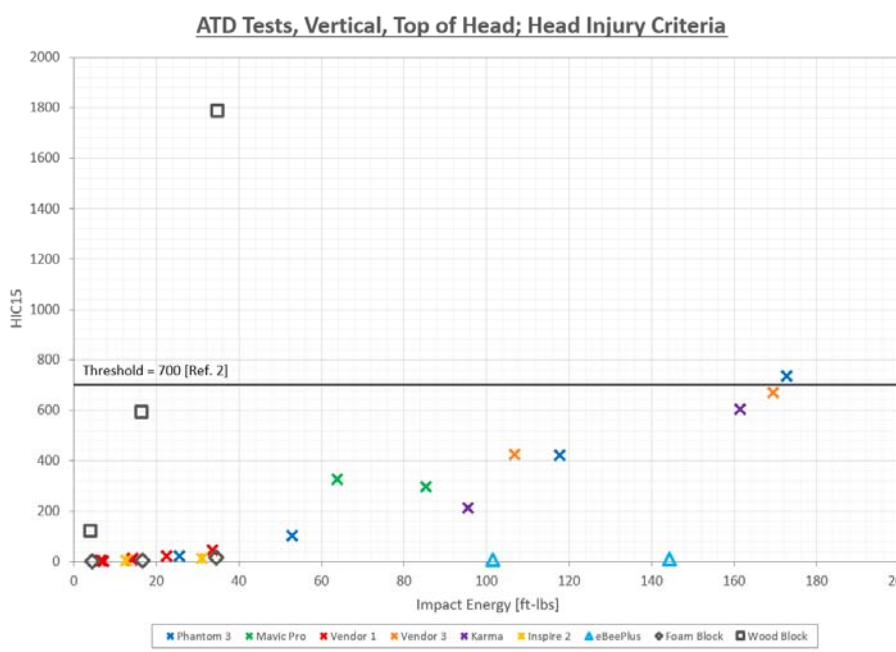

Figure 159. A14 ATD test comparison; multiple projectiles; vertical; top of the head; HIC15

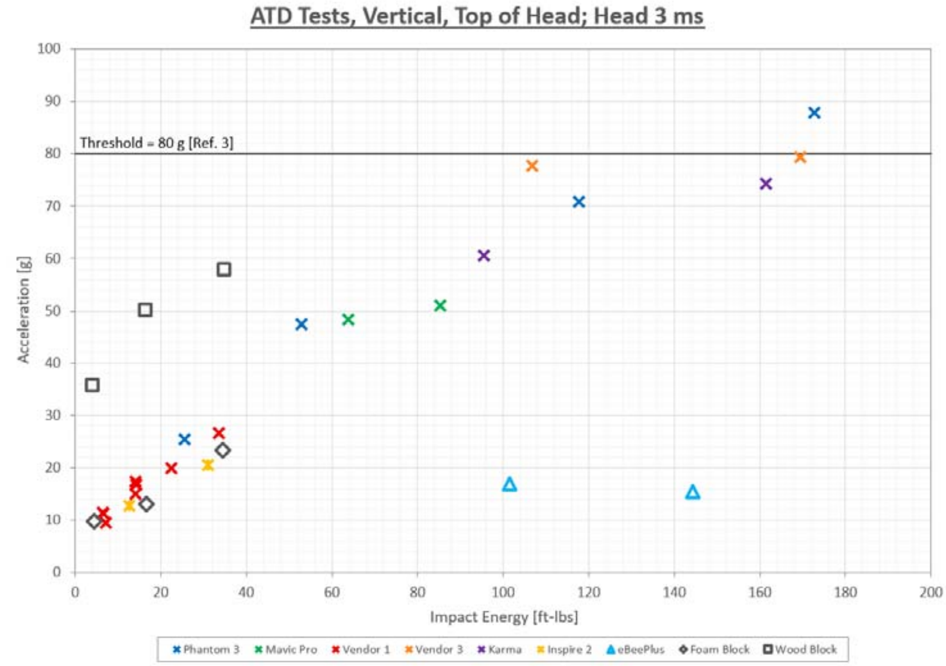

Figure 160. A14 ATD test comparison; multiple projectiles; vertical; top of the head; head 3ms acceleration

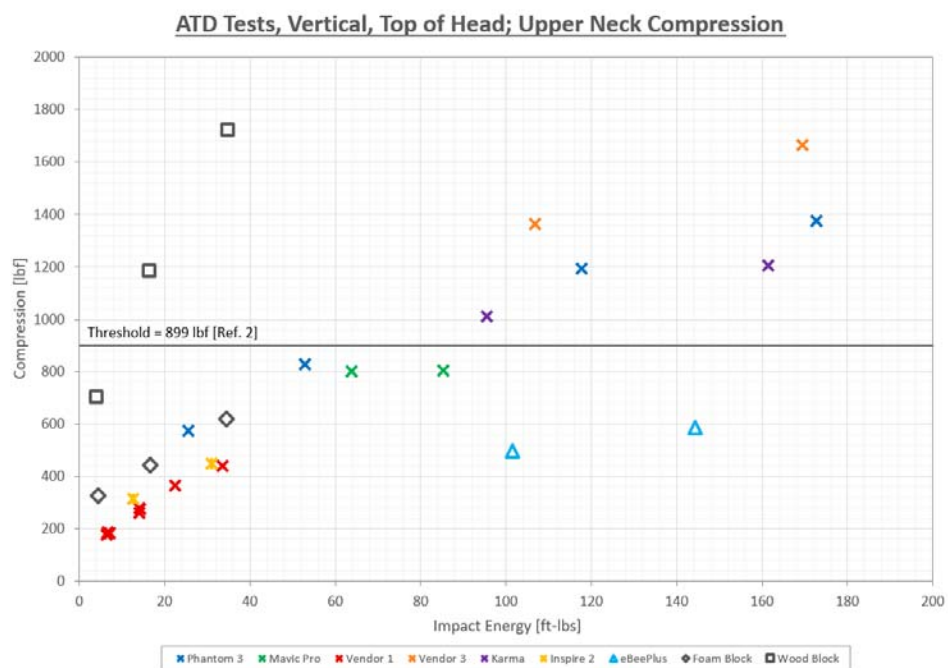

Figure 161. A14 ATD test comparison; multiple projectiles; vertical; top of the head; upper neck compression

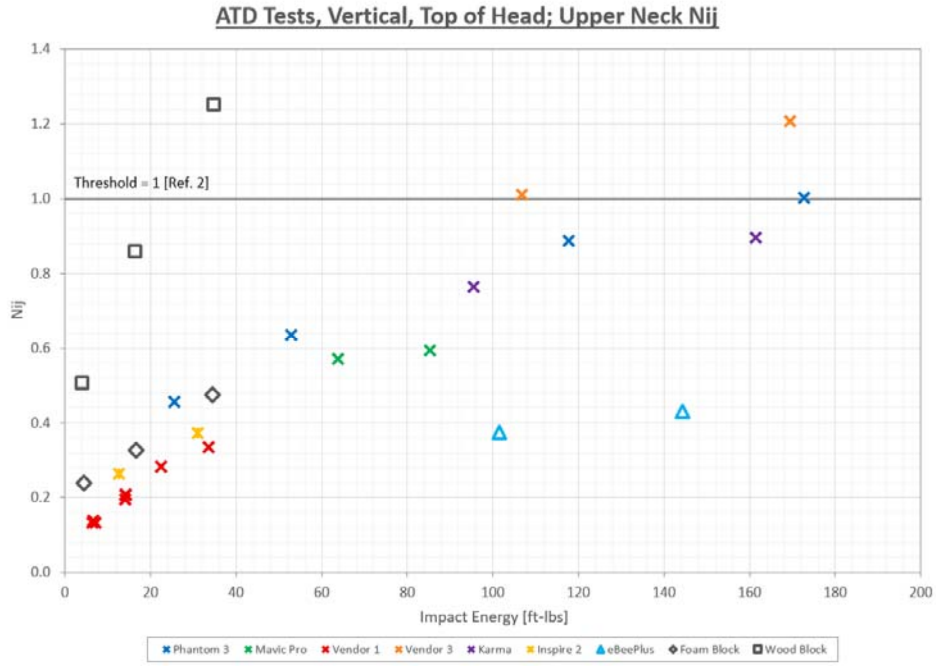

Figure 162. A14 ATD test comparison; multiple projectiles; vertical; top of the head; Nij

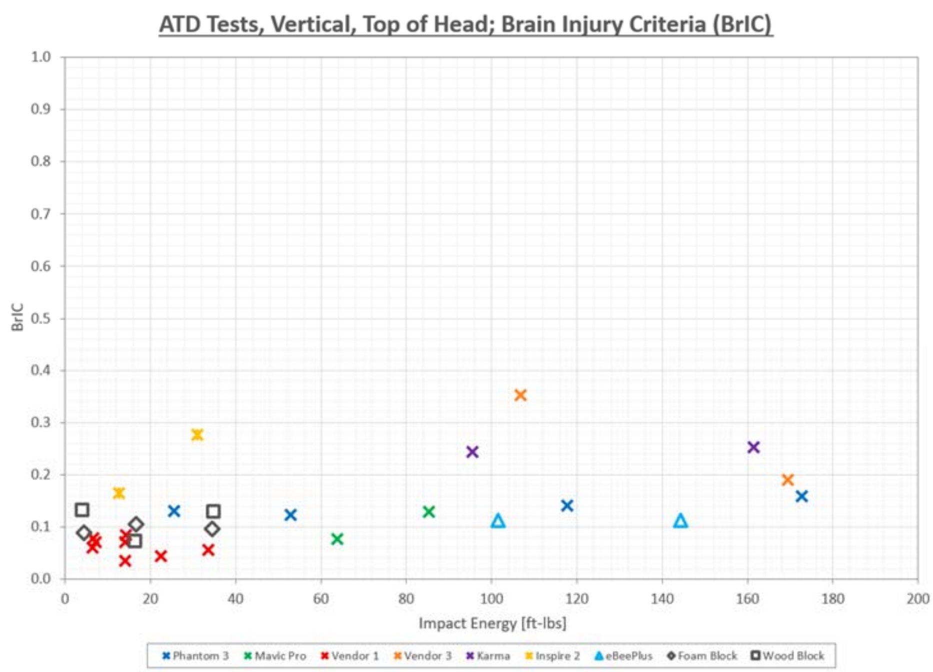

Figure 163. A14 ATD test comparison; multiple projectiles; vertical; top of the head; BrIC

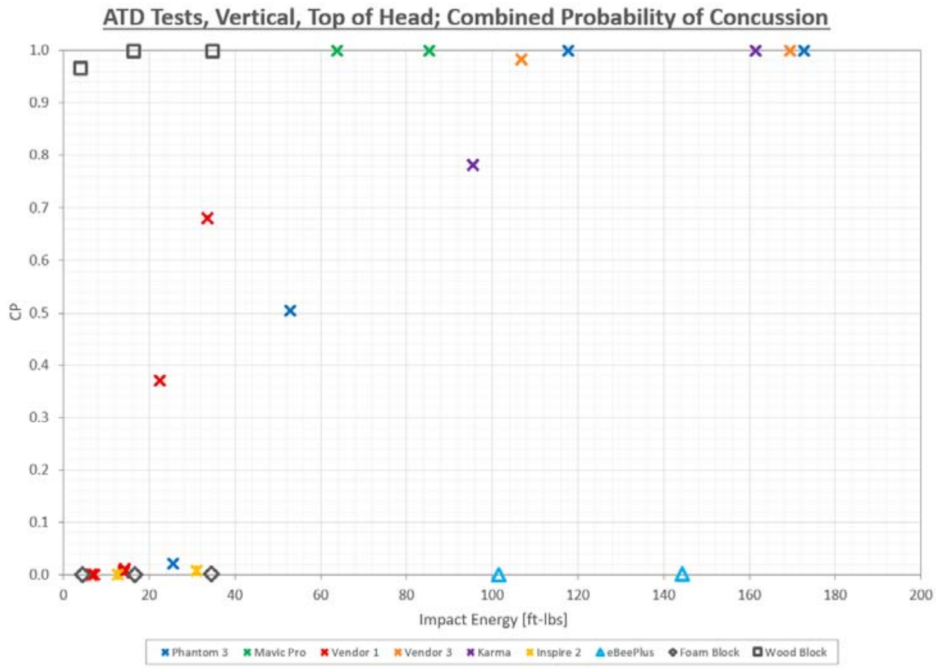

Figure 164. A14 ATD test comparison; multiple projectiles; vertical; top of the head; VT CP

Angled 58 Degree Frontal Tests

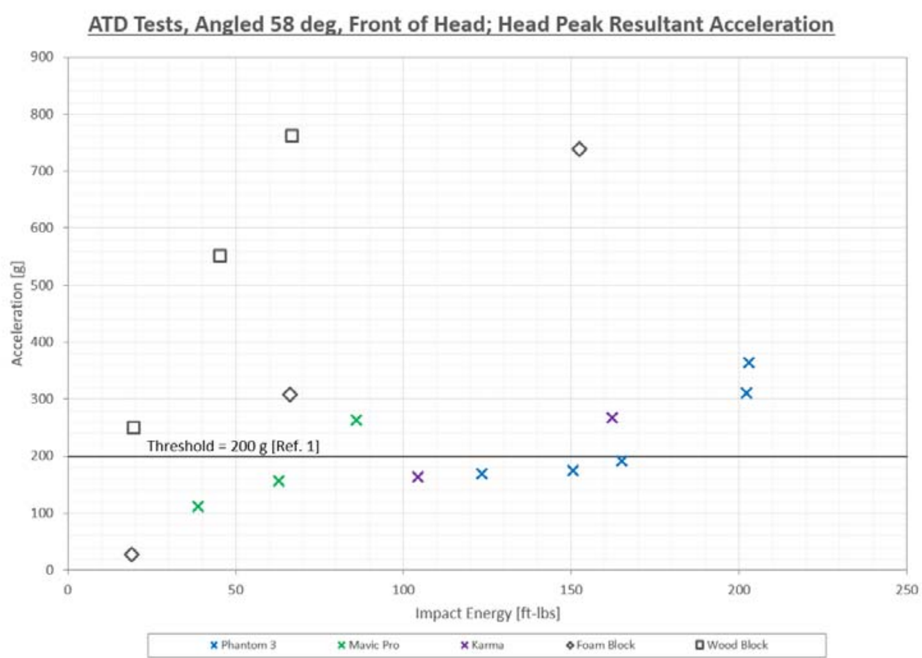

Figure 165. A14 ATD test comparison; multiple projectiles; angled frontal; front of the head; peak resultant head acceleration

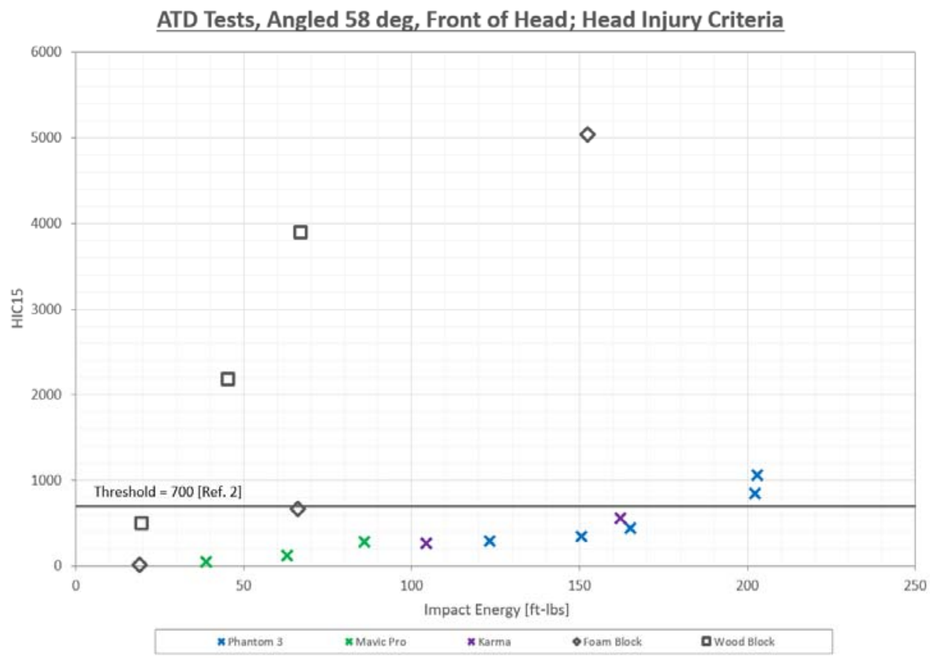

Figure 166. A14 ATD test comparison; multiple projectiles; angled frontal; front of the head; HIC15

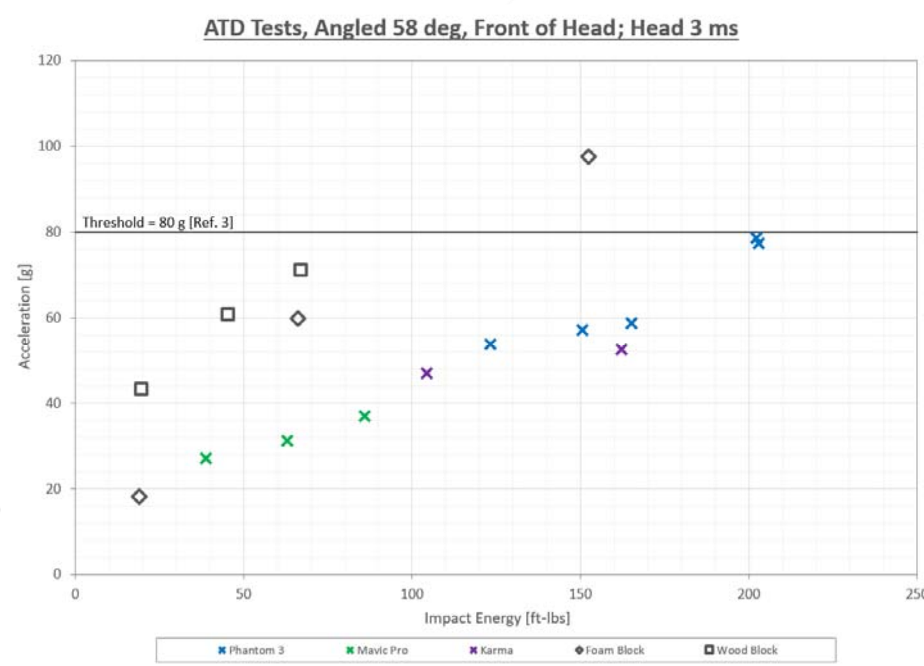

Figure 167. A14 ATD test comparison; multiple projectiles; angled frontal; front of the head; head 3ms acceleration

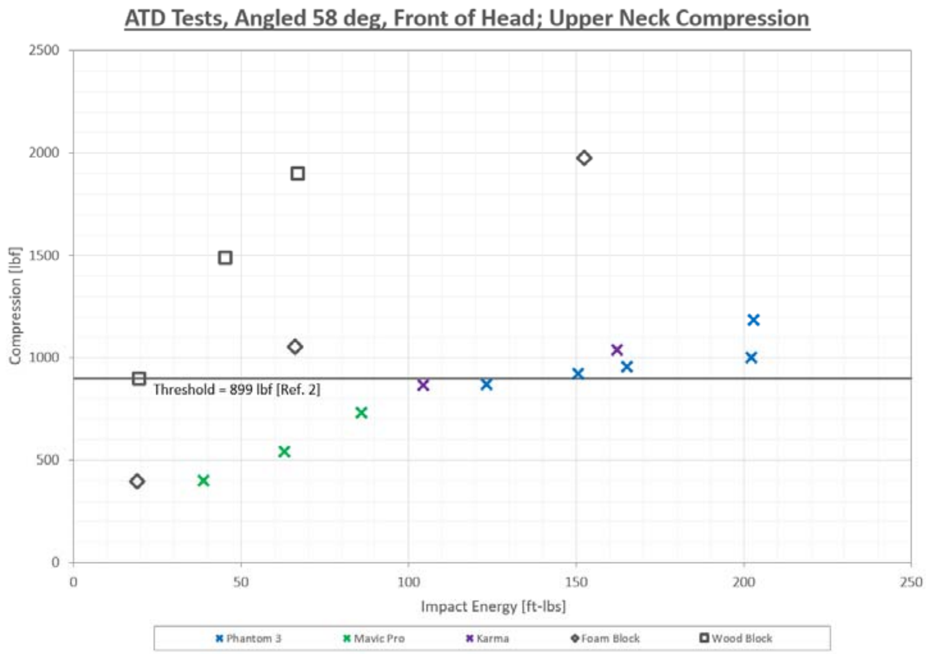

Figure 168. A14 ATD test comparison; multiple projectiles; angled frontal; front of the head; upper neck compression

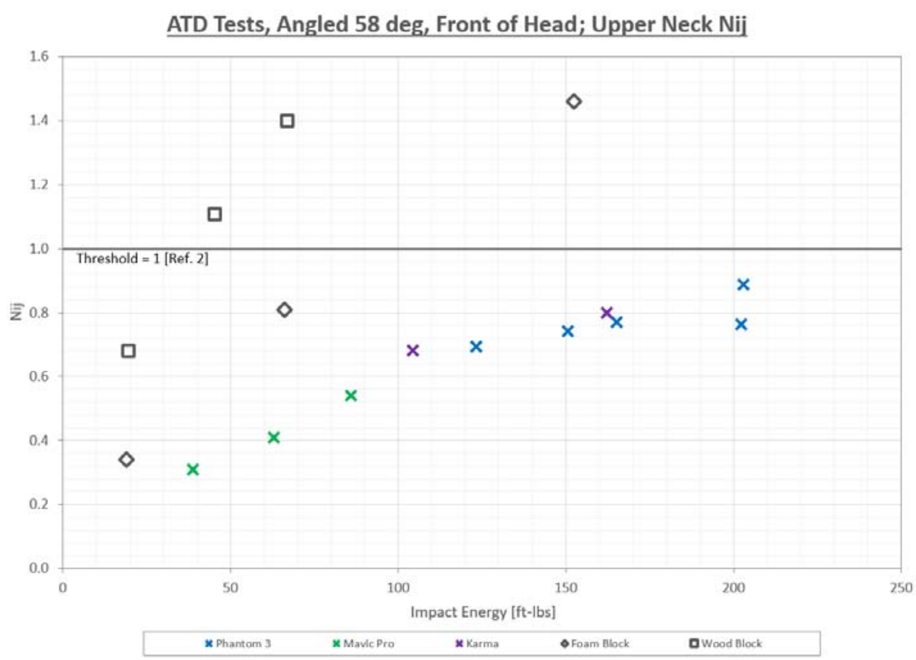

Figure 169. A14 ATD test comparison; multiple projectiles; angled frontal; front of the head; Nij

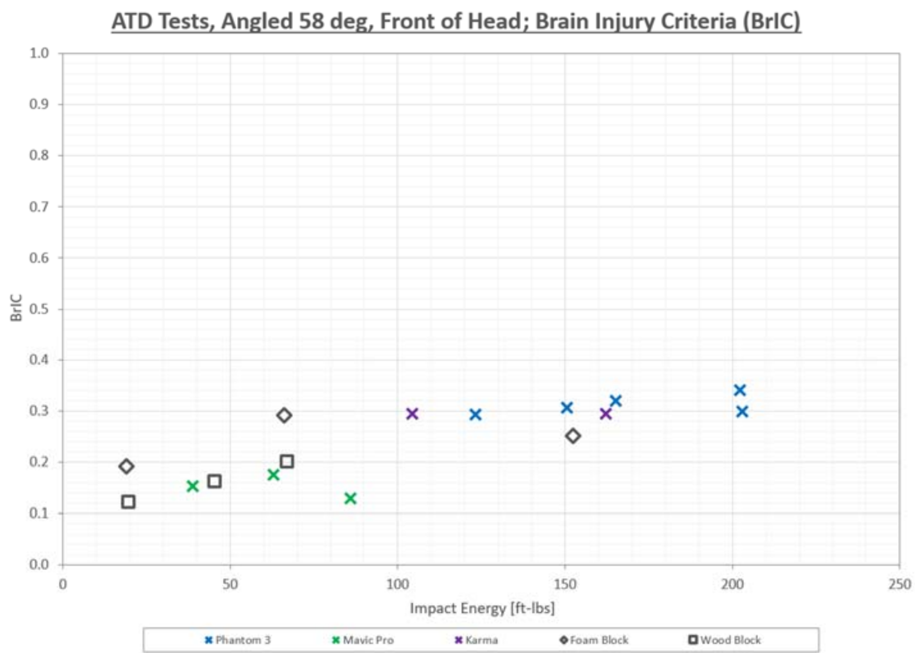

Figure 170. A14 ATD test comparison; multiple projectiles; angled frontal; front of the head; BrIC

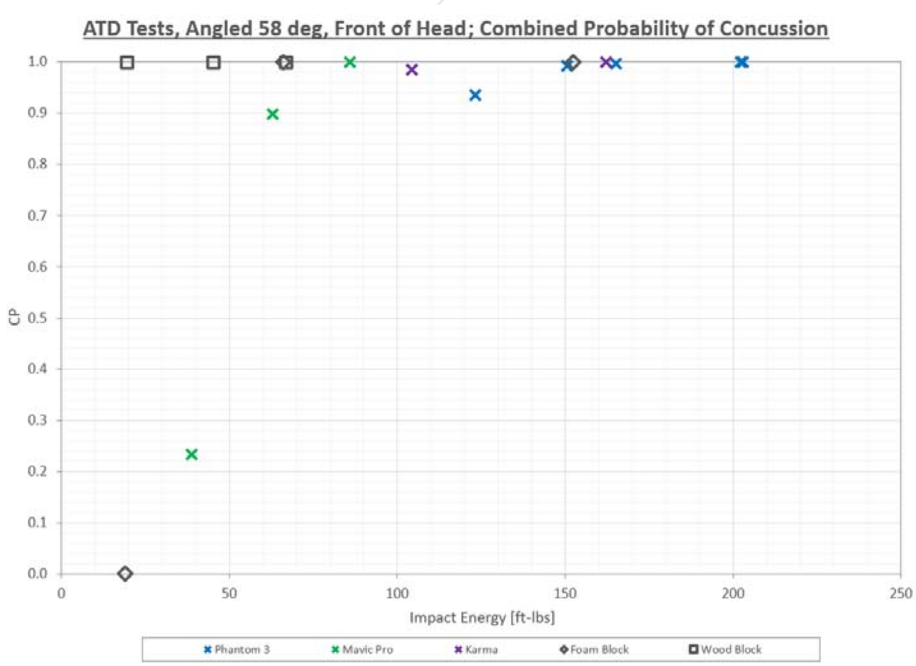

Figure 171. A14 ATD test comparison; multiple projectiles; angled frontal; front of the head; VT CP

Angled 58 Degree Sideward Tests

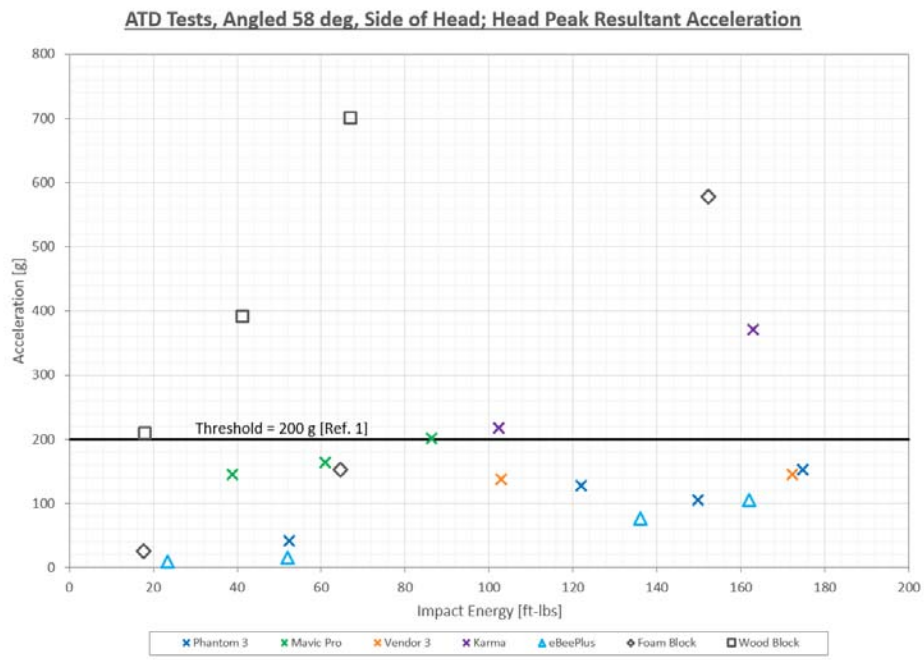

Figure 172. A14 ATD test comparison; multiple projectiles; angled sideward; side of the head; peak resultant head acceleration

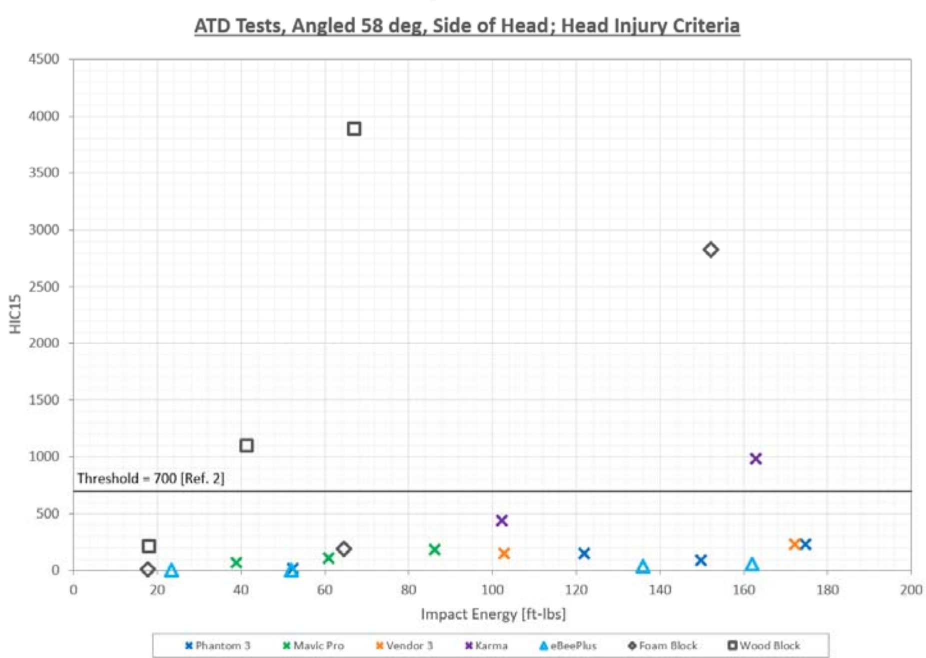

Figure 173. A14 ATD test comparison; multiple projectiles; angled sideward; side of the head; HIC15

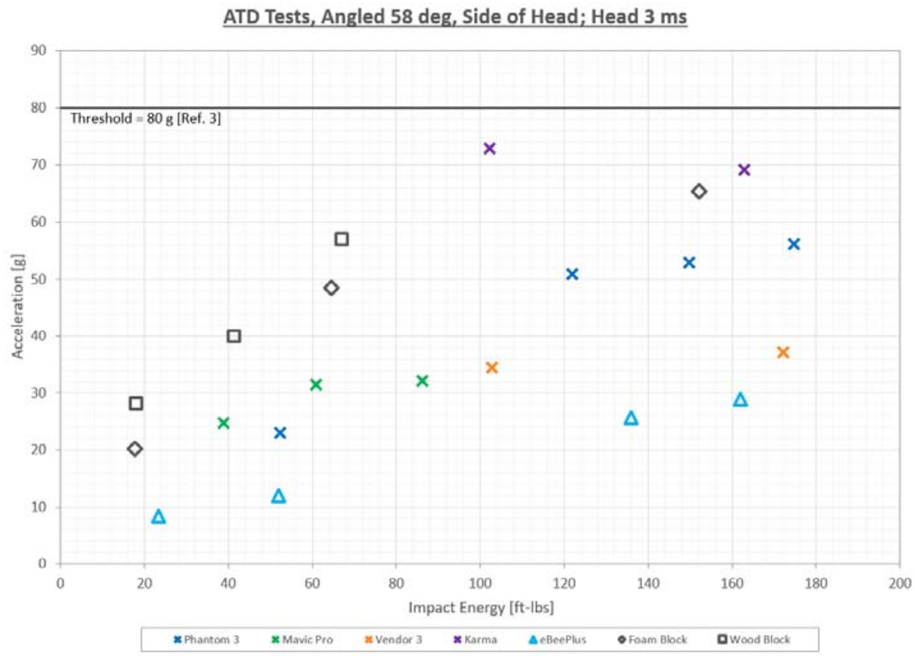

Figure 174. A14 ATD test comparison; multiple projectiles; angled sideward; side of the head; head 3ms acceleration

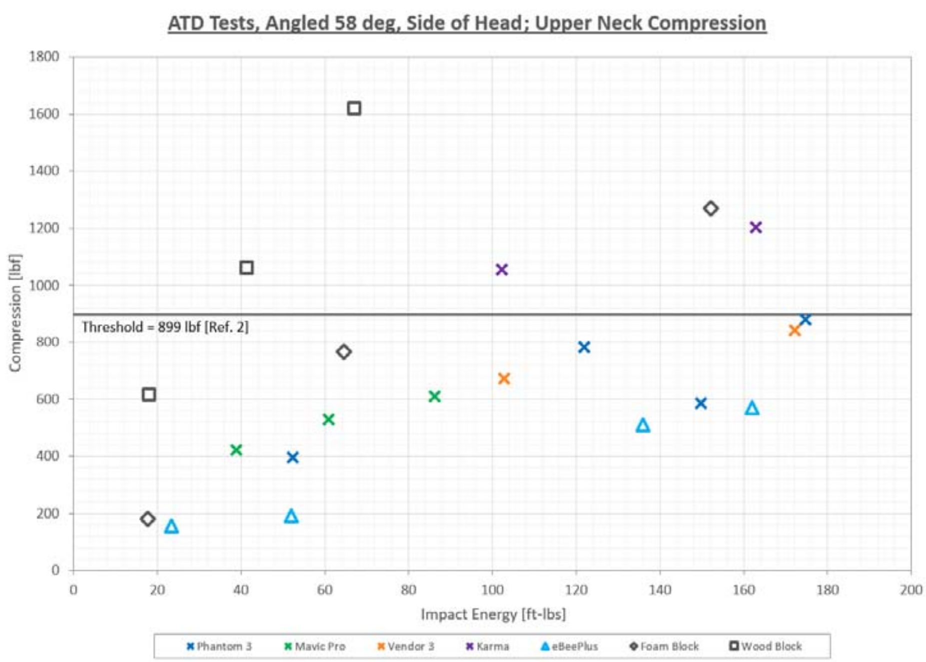

Figure 175. A14 ATD test comparison; multiple projectiles; angled sideward; side of the head; upper neck compression

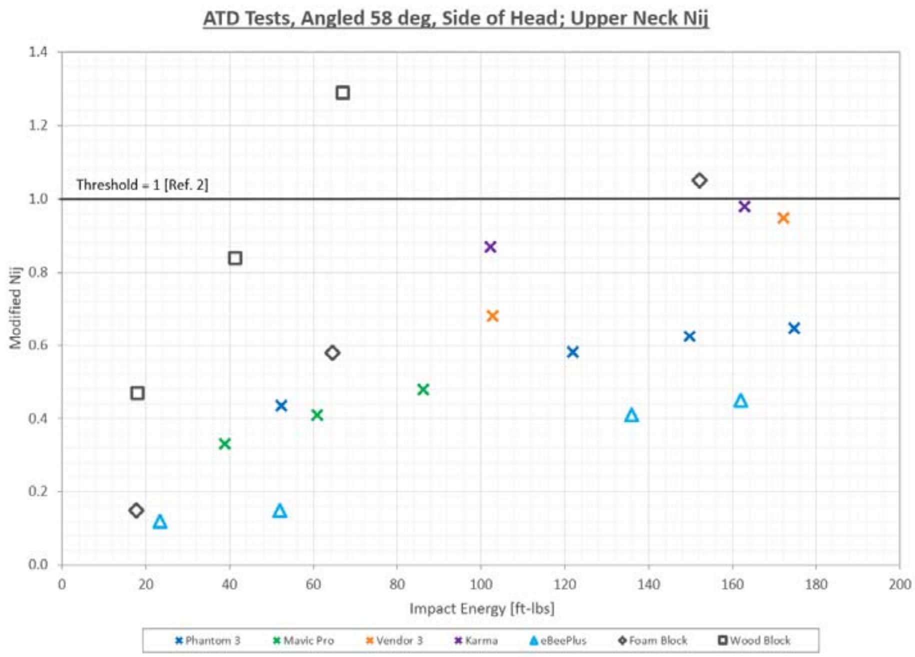

Figure 176. A14 ATD test comparison; multiple projectiles; angled sideward; side of the head; Nij

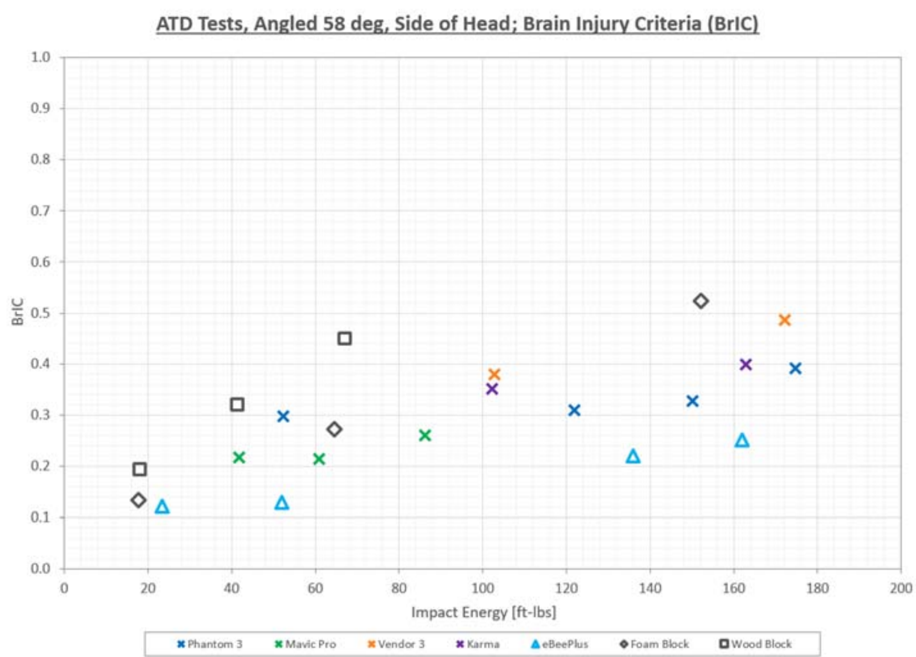

Figure 177. A14 ATD test comparison; multiple projectiles; angled sideward; side of the head; BrIC

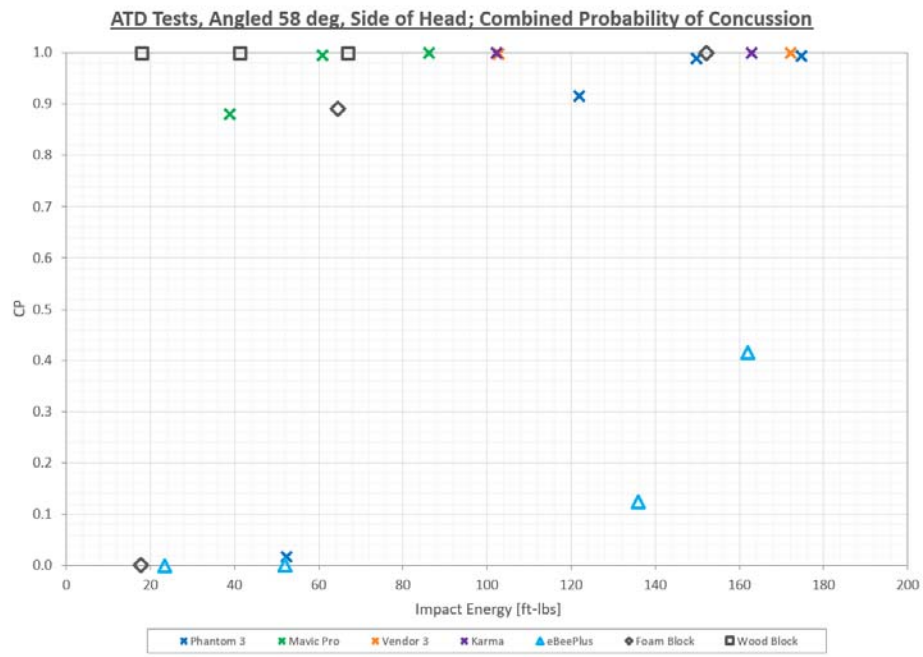

Figure 178. A14 ATD test comparison; multiple projectiles; angled sideward; side of the head; VT CP

Horizontal Sideward Tests

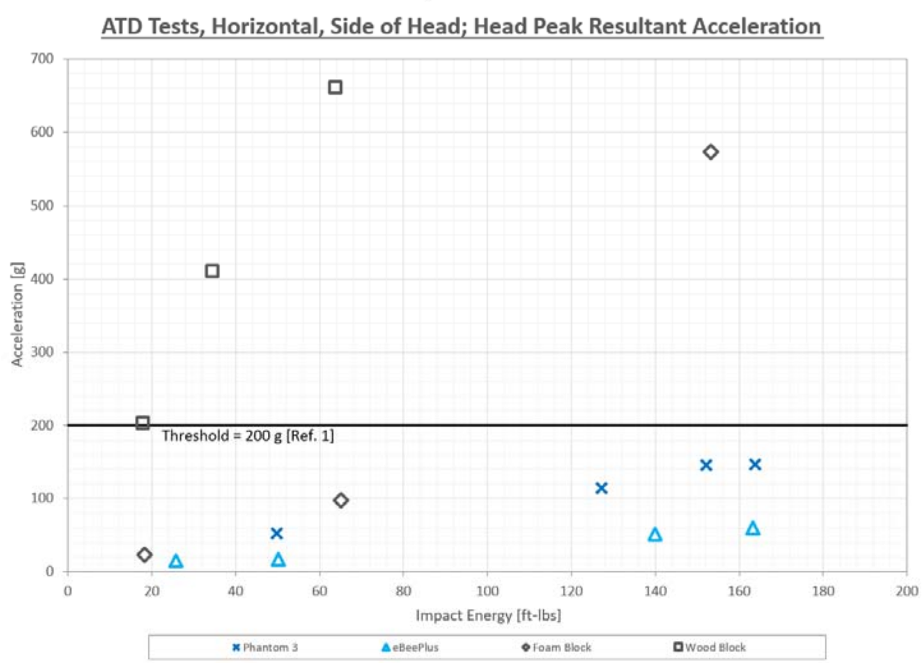

Figure 179. A14 ATD test comparison; multiple projectiles; sideward; side of the head; peak resultant head acceleration

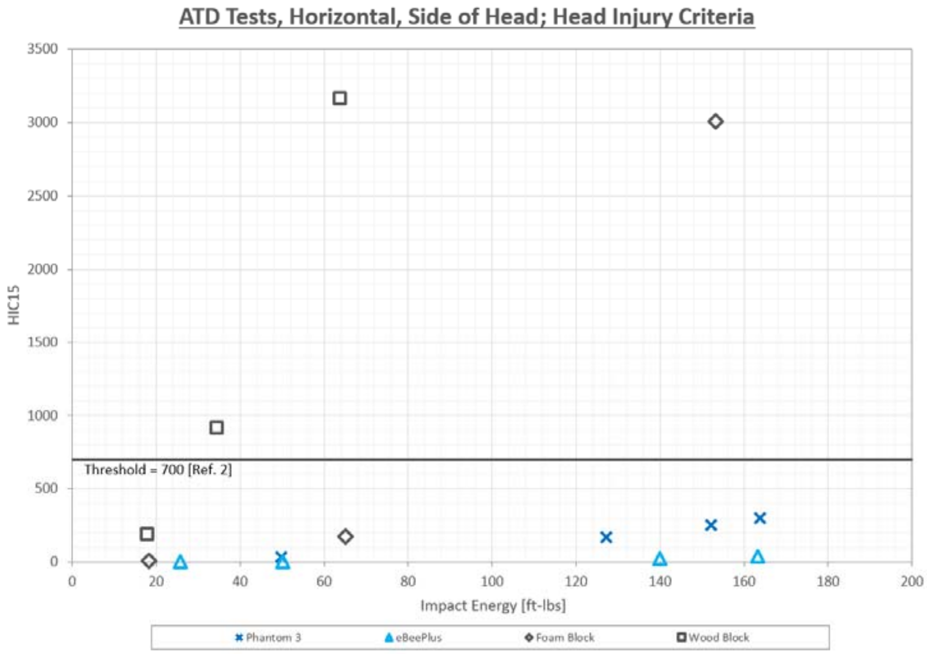

Figure 180. A14 ATD test comparison; multiple projectiles; sideward; side of the head; HIC15

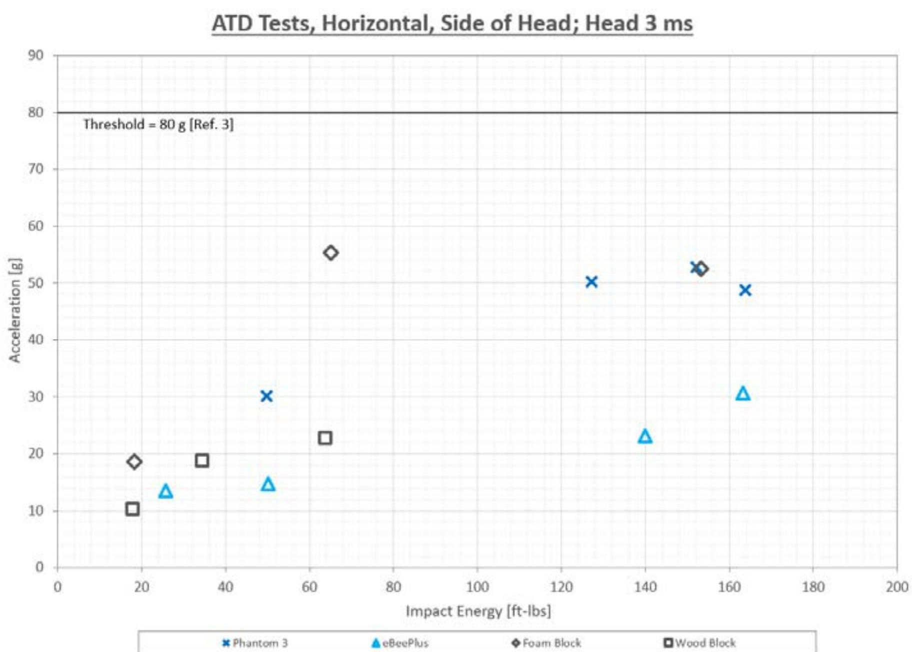

Figure 181. A14 ATD test comparison; multiple projectiles; sideward; side of the head; head 3ms acceleration

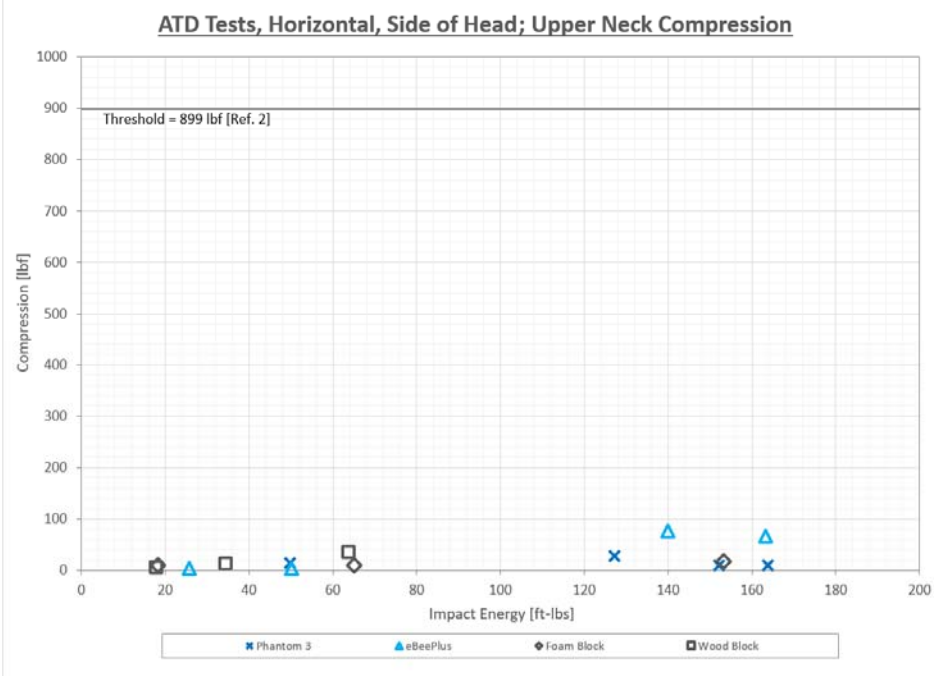

Figure 182. A14 ATD test comparison; multiple projectiles; sideward; side of the head; upper neck compression

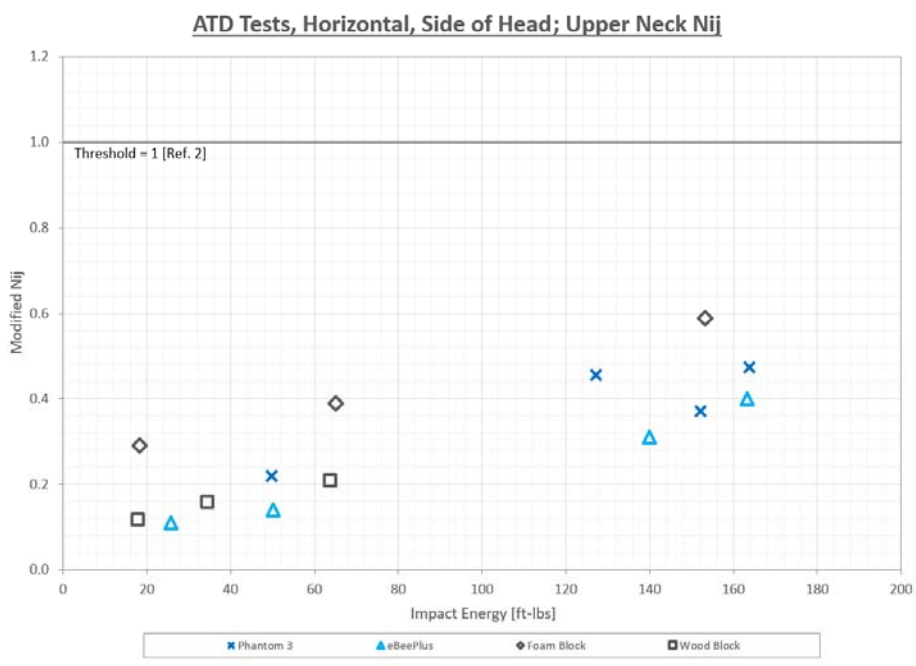

Figure 183. A14 ATD test comparison; multiple projectiles; sideward; side of the head; Nij

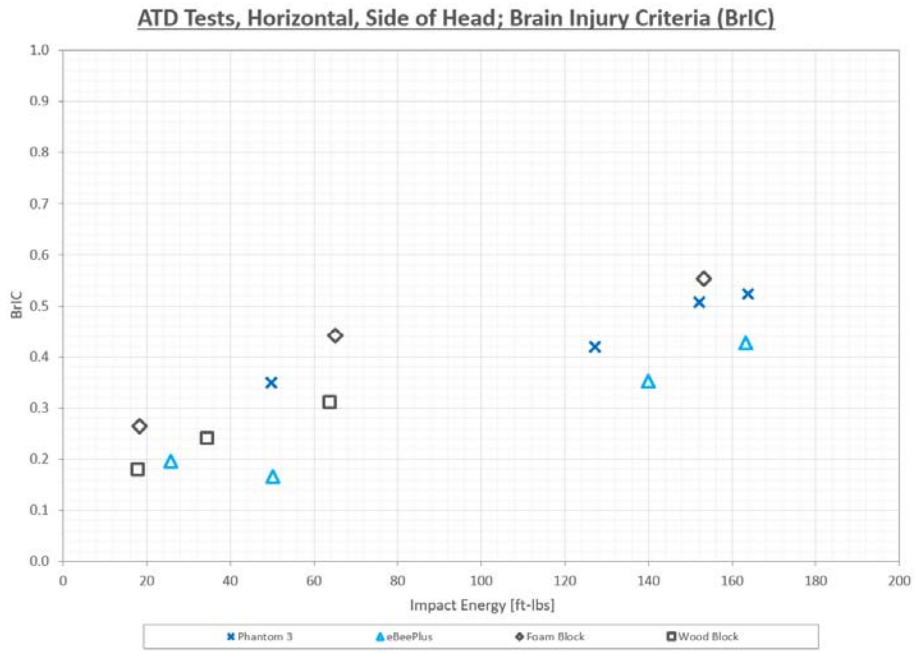

Figure 184. A14 ATD test comparison; multiple projectiles; sideward; side of the head; BrIC

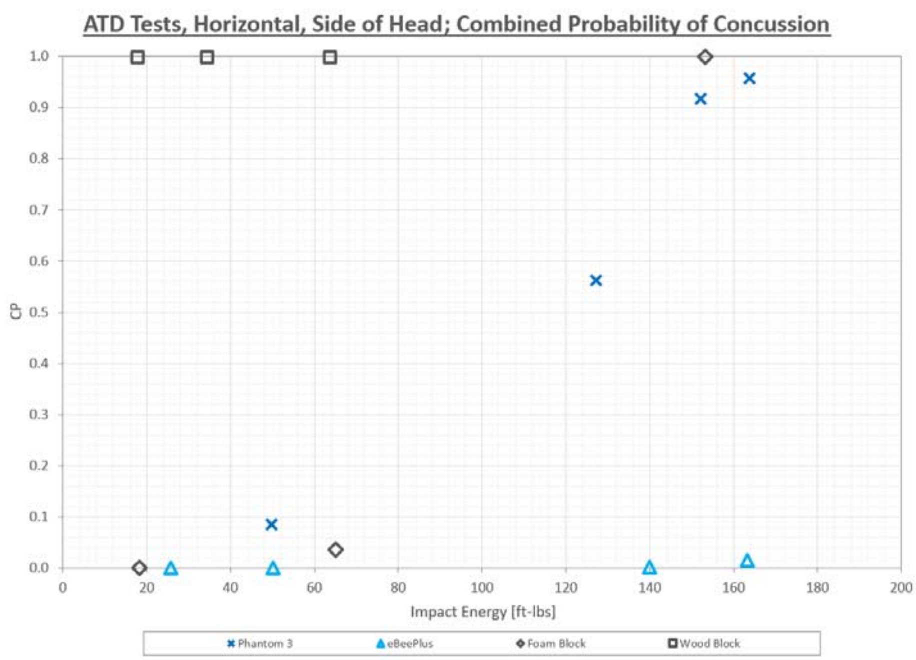

Figure 185. A14 ATD test comparison; multiple projectiles; sideward; side of the head; VT CP

Horizontal Frontal Tests

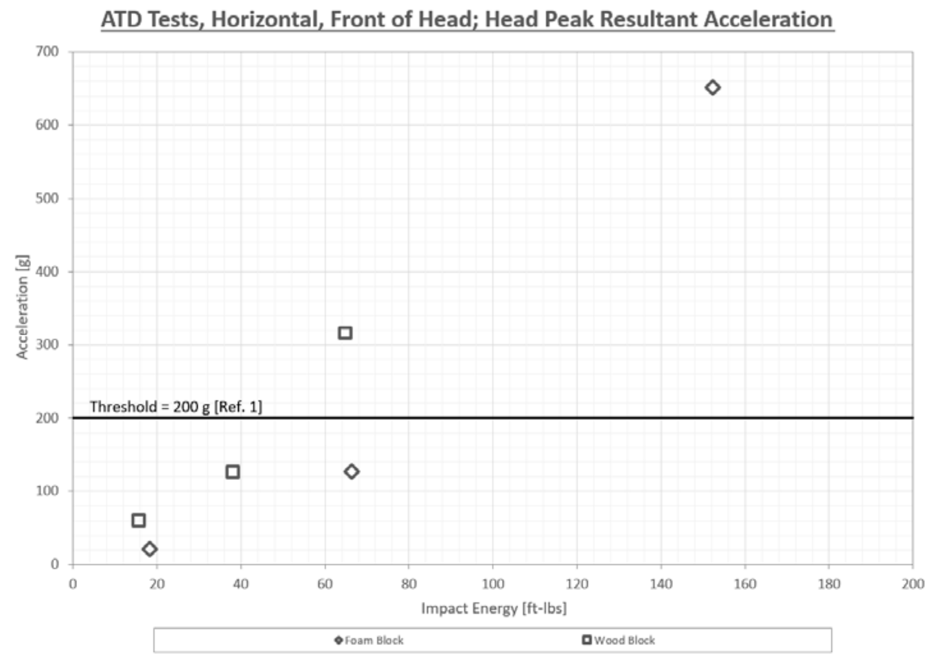

Figure 186. A14 ATD test comparison; multiple projectiles; frontal; front of the head; peak resultant head acceleration

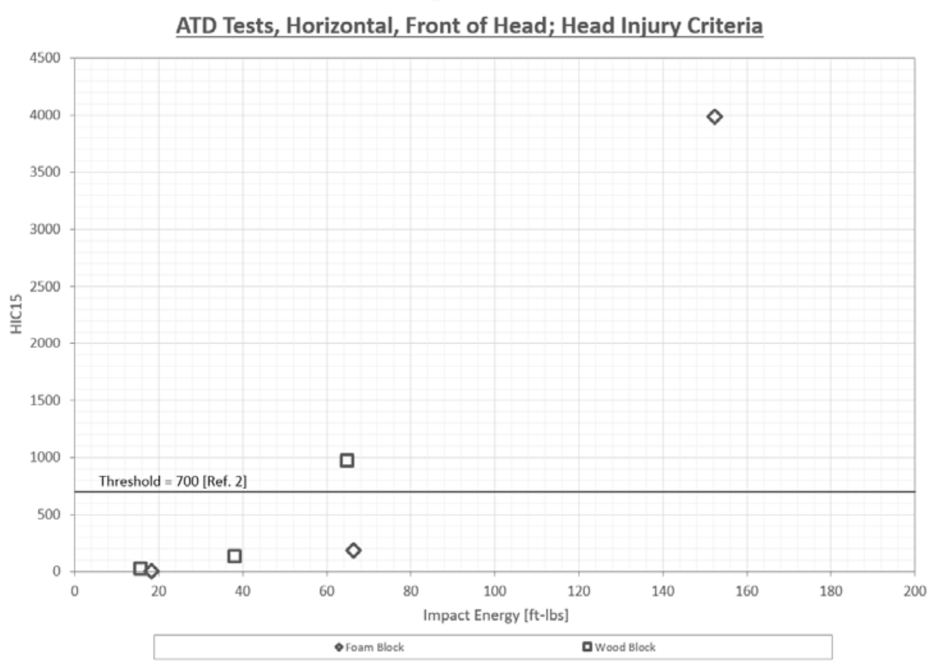

Figure 187. A14 ATD test comparison; multiple projectiles; frontal; front of the head; HIC15

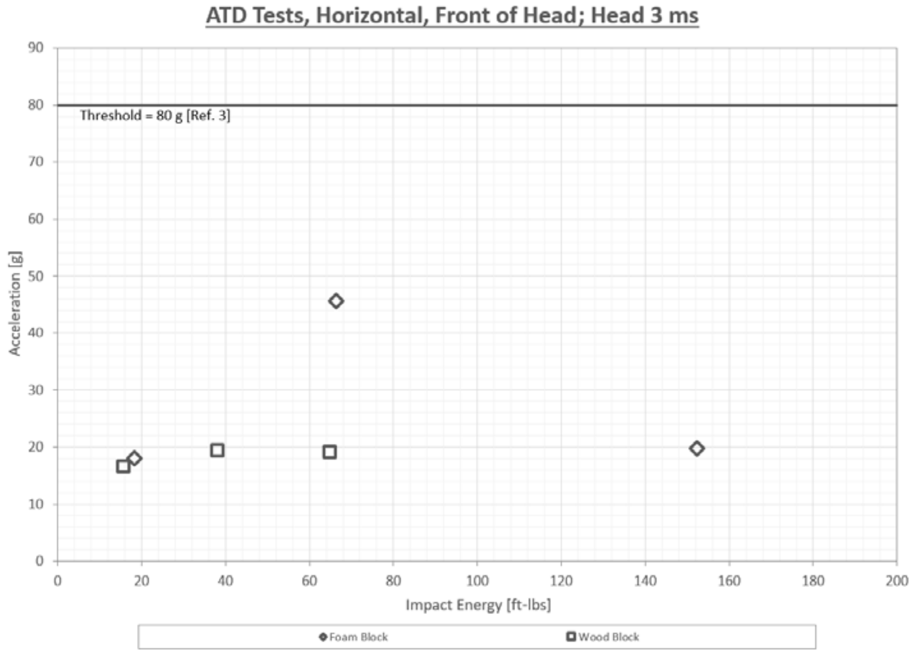

Figure 188. A14 ATD test comparison; multiple projectiles; frontal; front of the head; head 3ms acceleration

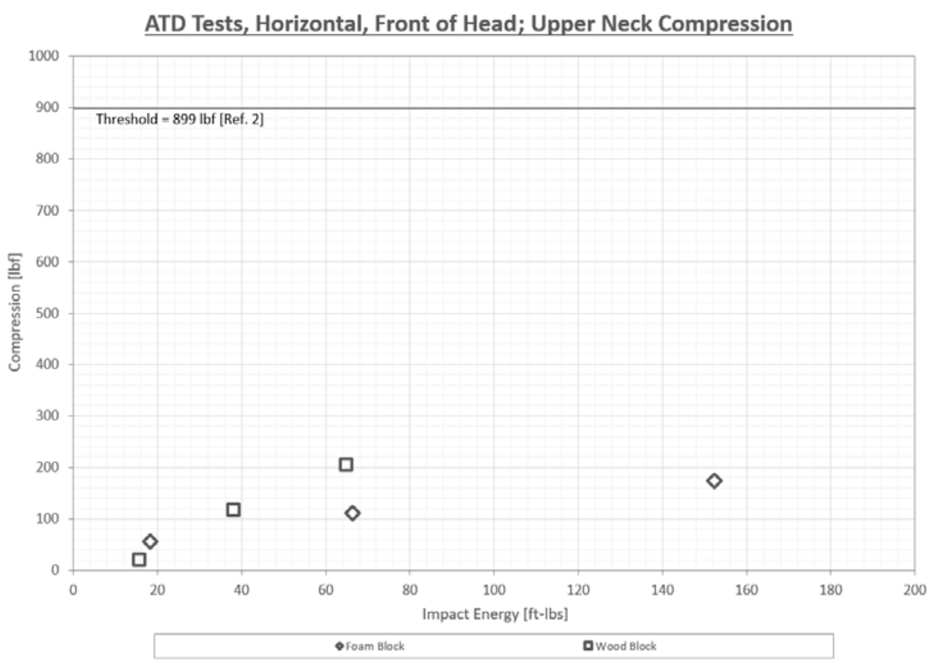

Figure 189. A14 ATD test comparison; multiple projectiles; frontal; front of the head; upper neck compression

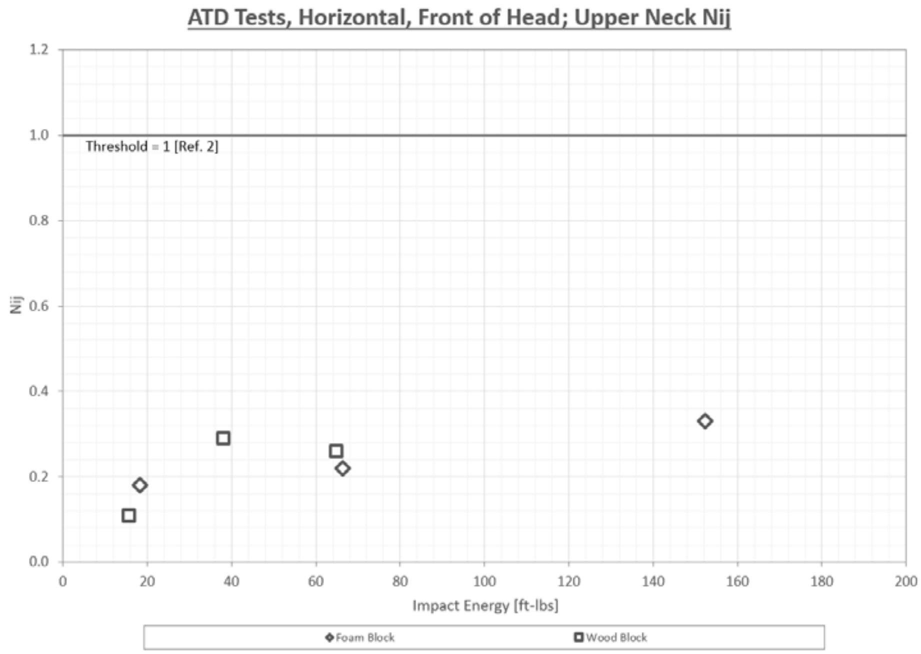

Figure 190. A14 ATD test comparison; multiple projectiles; frontal; front of the head; Nij

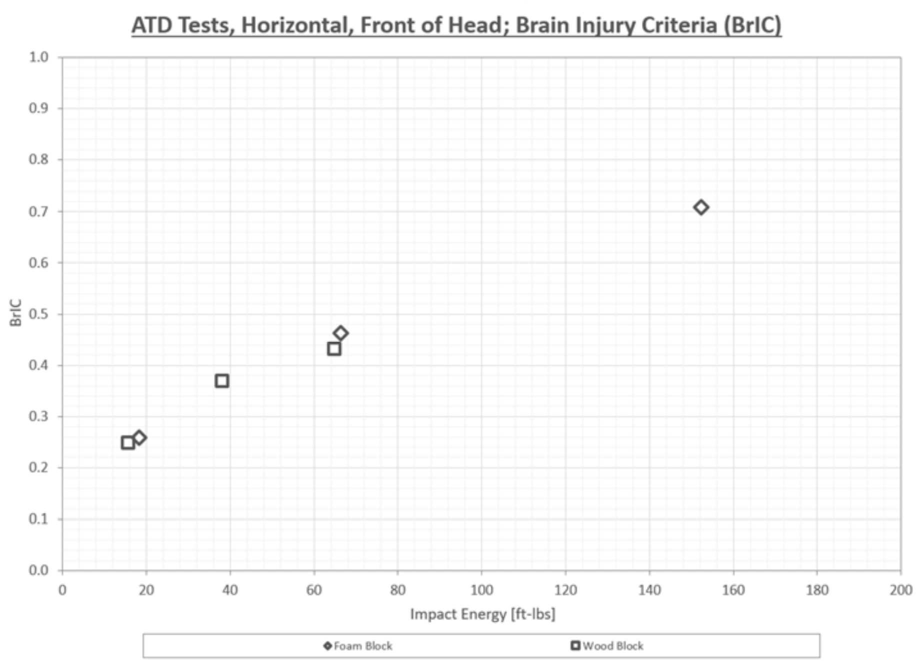

Figure 191. A14 ATD test comparison; multiple projectiles; frontal; front of the head; BrIC

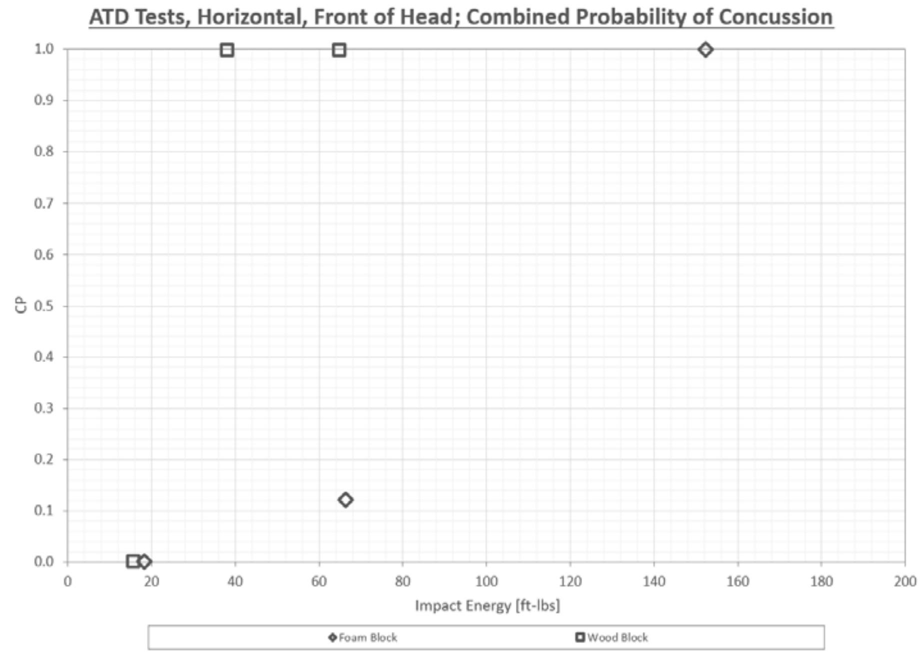

Figure 192. A14 ATD test comparison; multiple projectiles; frontal; front of the head; VT CP

Angled 58 Degree Rearward Tests

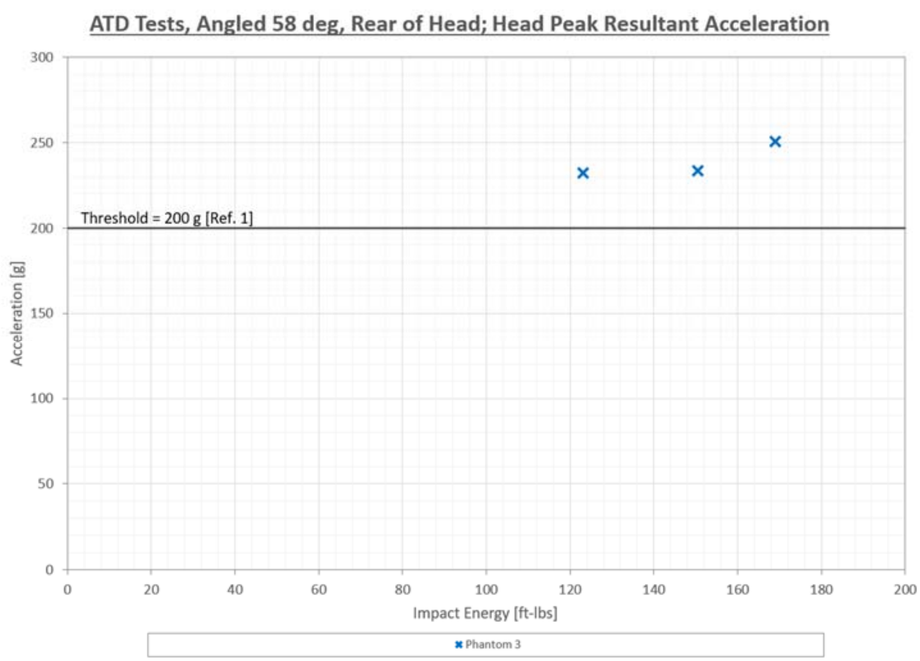

Figure 193. A14 ATD test comparison; multiple projectiles; angled rearward; rear of the head; peak resultant head acceleration

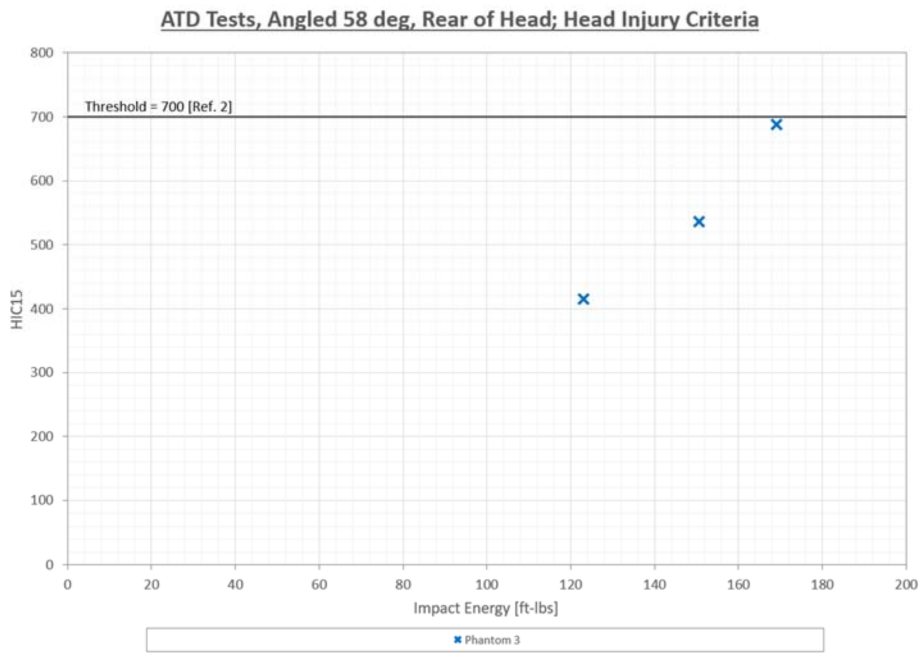

Figure 194. A14 ATD test comparison; multiple projectiles; angled rearward; rear of the head; HIC15

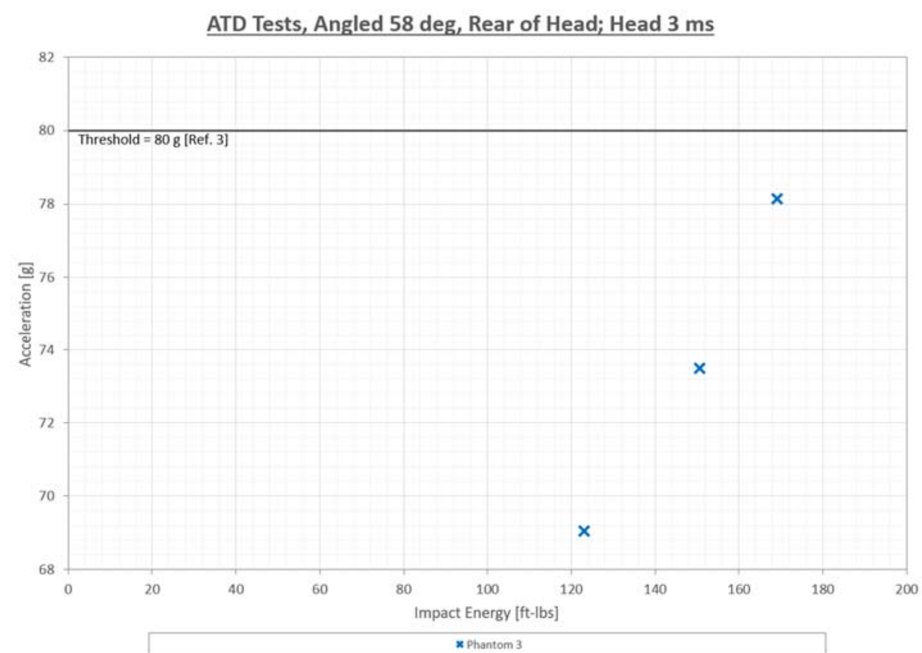

Figure 195. A14 ATD test comparison; multiple projectiles; angled rearward; rear of the head; head 3ms acceleration

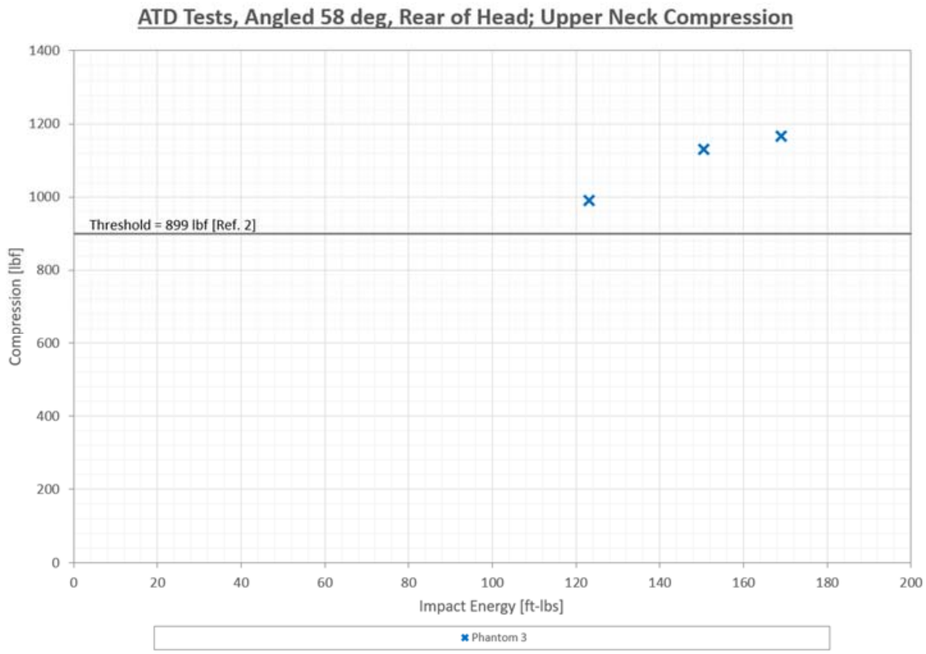

Figure 196. A14 ATD test comparison; multiple projectiles; angled rearward; rear of the head; upper neck compression

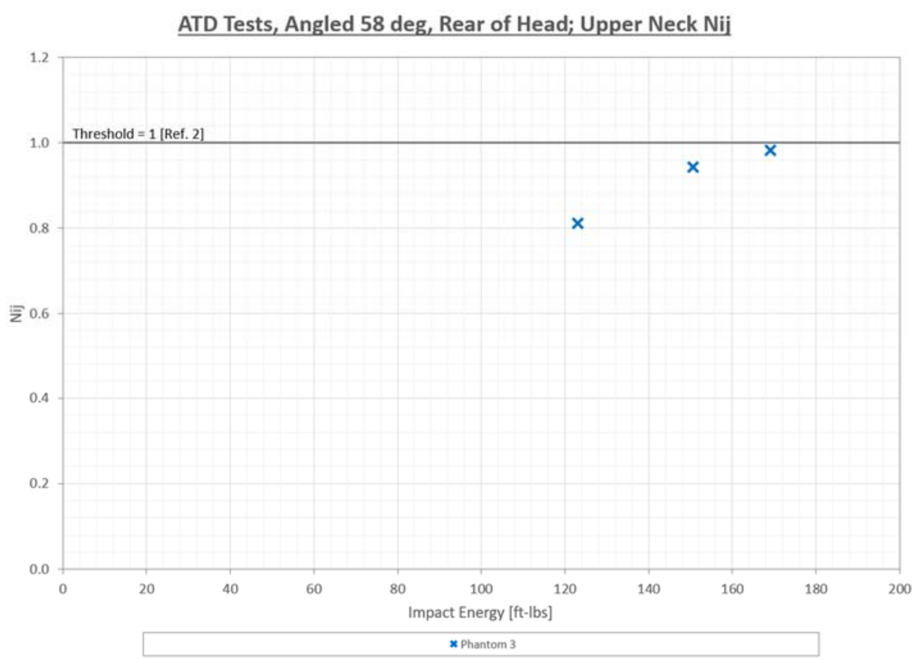

Figure 197. A14 ATD test comparison; multiple projectiles; angled rearward; rear of the head; Nij

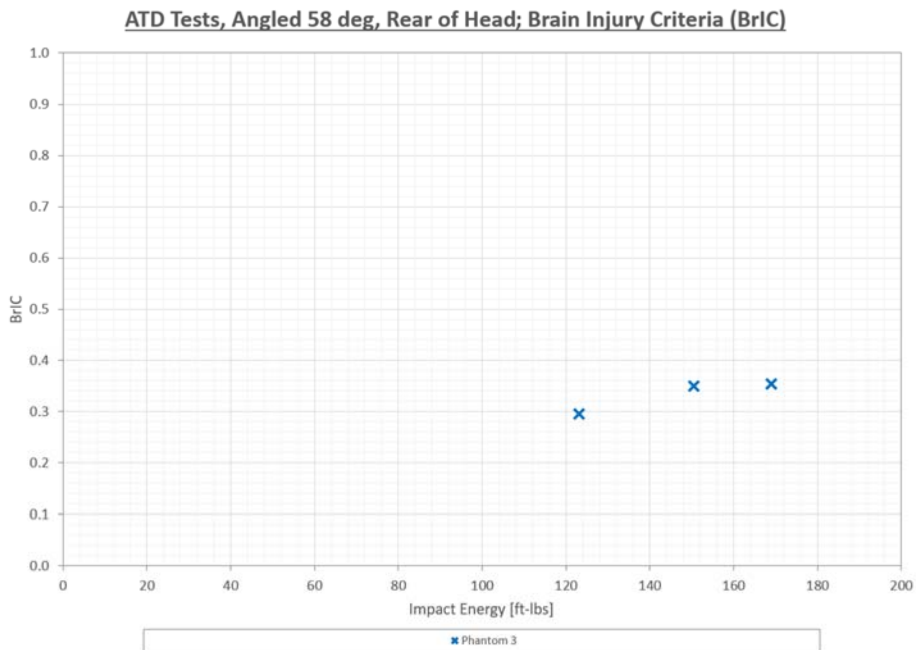

Figure 198. A14 ATD test comparison; multiple projectiles; angled rearward; rear of the head; BrIC

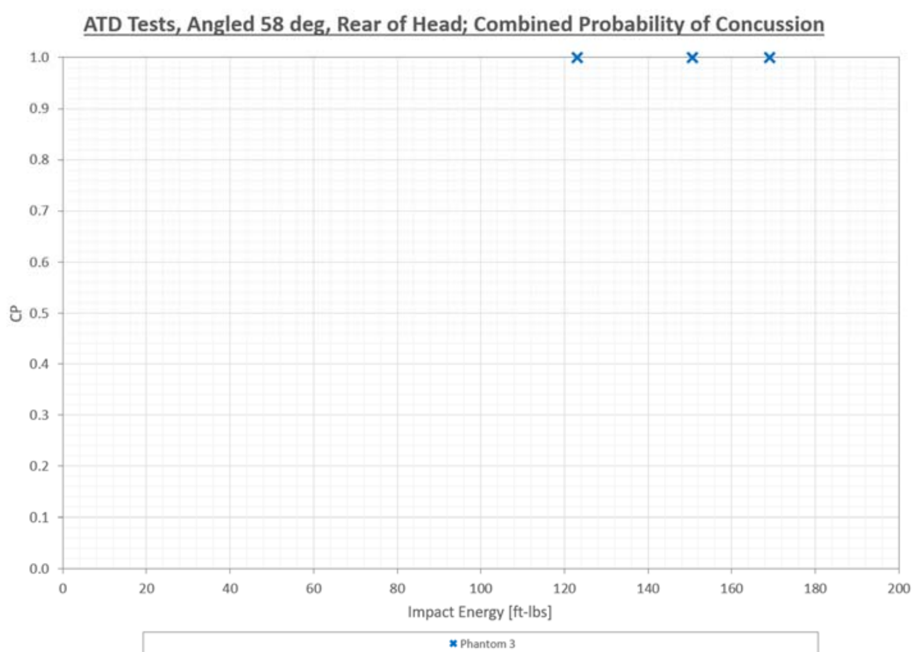

Figure 199. A14 ATD test comparison; multiple projectiles; angled rearward; rear of the head; VT CP

APPENDIX D—DJI PHANTOM III MODEL EVALUATION WITH A11 ATD TESTS

Vertical Maximum Velocity Test – V(90)-50

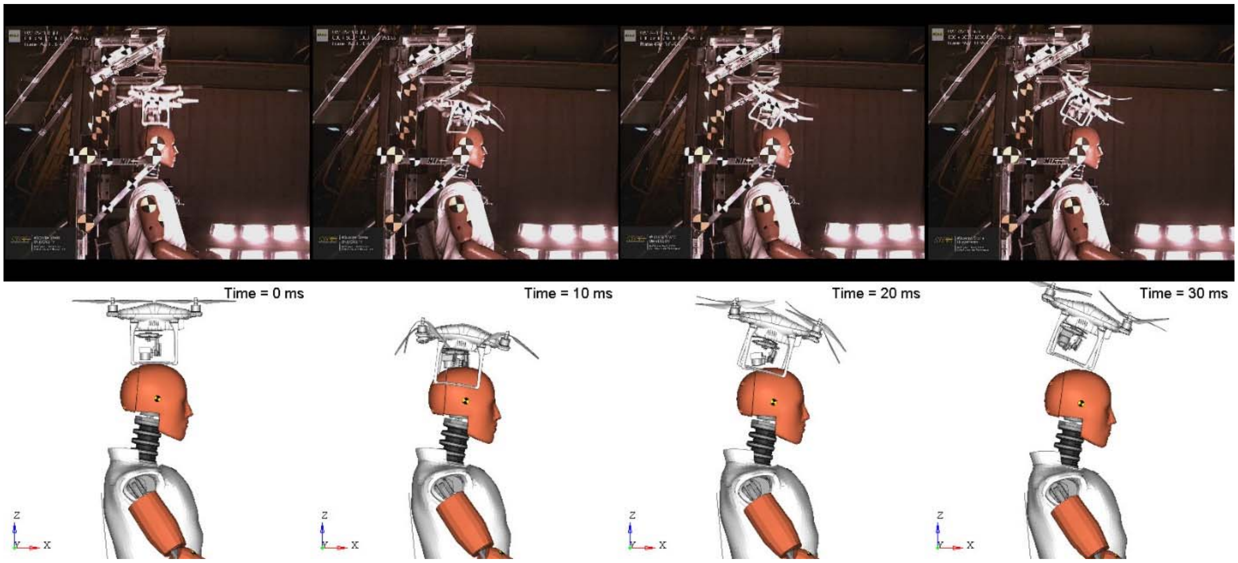

Figure 200. Test vs simulation comparison; DJI Phantom 3, 2.67 lb, bottom, 57 fps, vertical; A11 ATD test, top of the head; kinematics

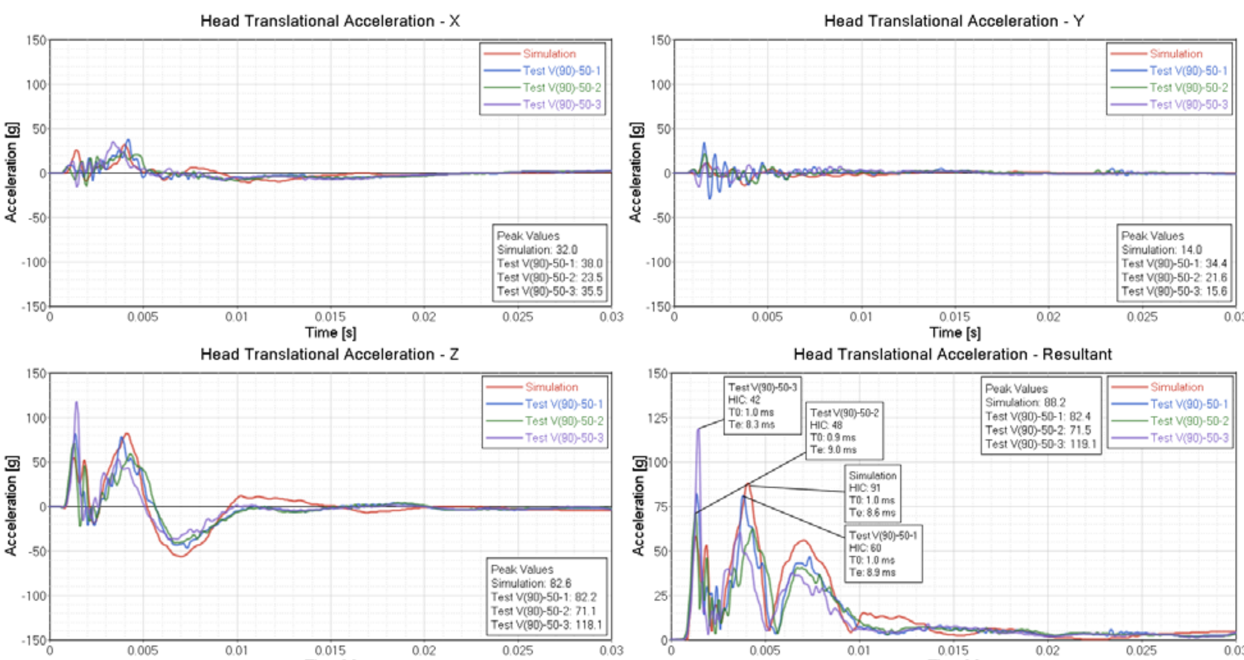

Figure 201. Test vs simulation comparison; DJI Phantom 3, 2.67 lb, bottom, 57 fps, vertical; A11 ATD test, top of the head; head CG acceleration

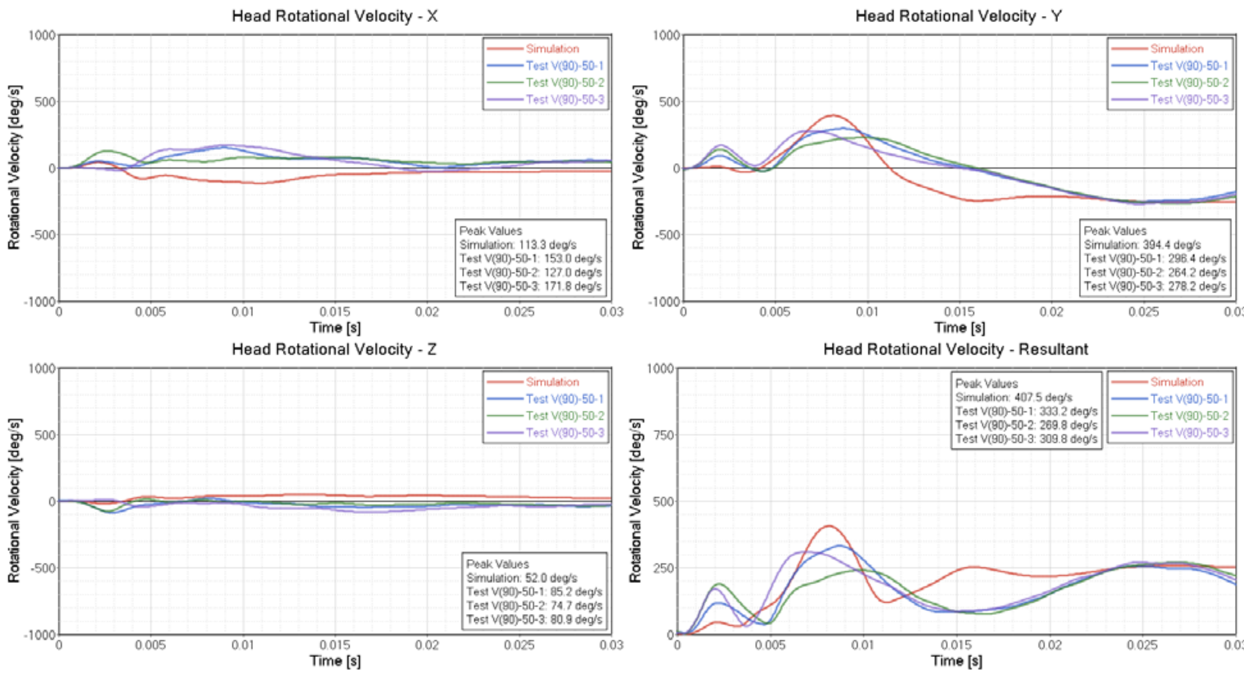

Figure 202. Test vs simulation comparison; DJI Phantom 3, 2.67 lb, bottom, 57 fps, vertical; A11 ATD test, top of the head; head angular rate

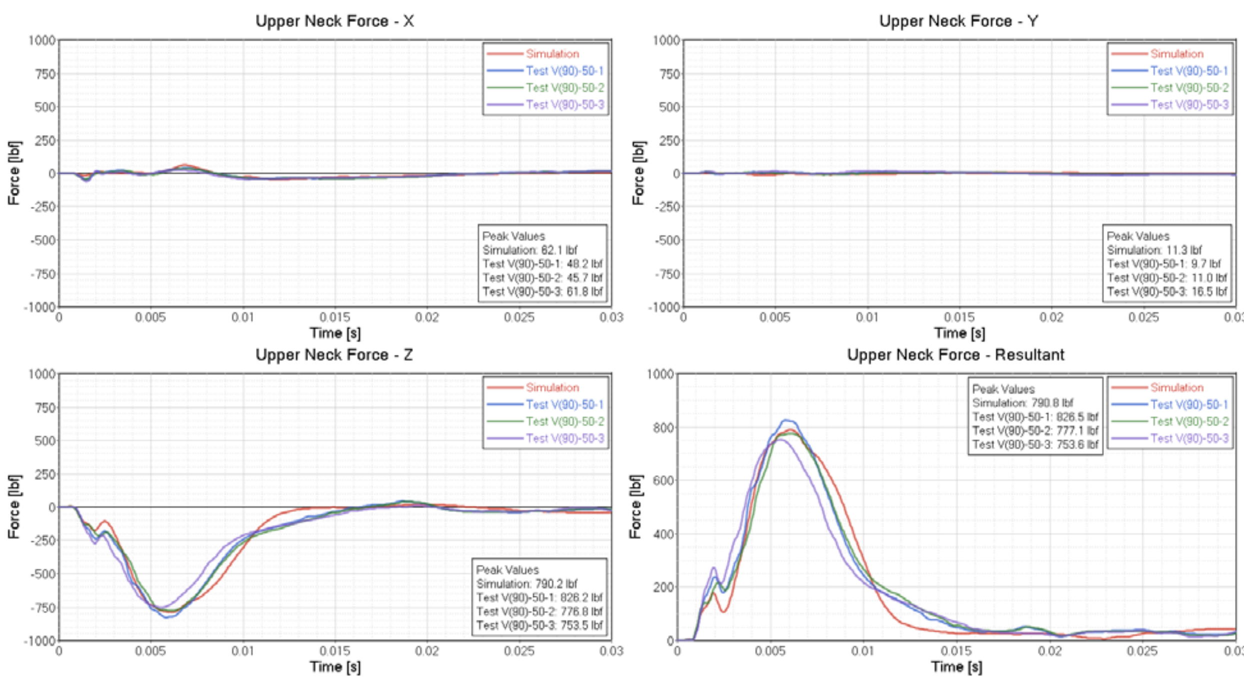

Figure 203. Test vs simulation comparison; DJI Phantom 3, 2.67 lb, bottom, 57 fps, vertical; A11 ATD test, top of the head; upper neck force

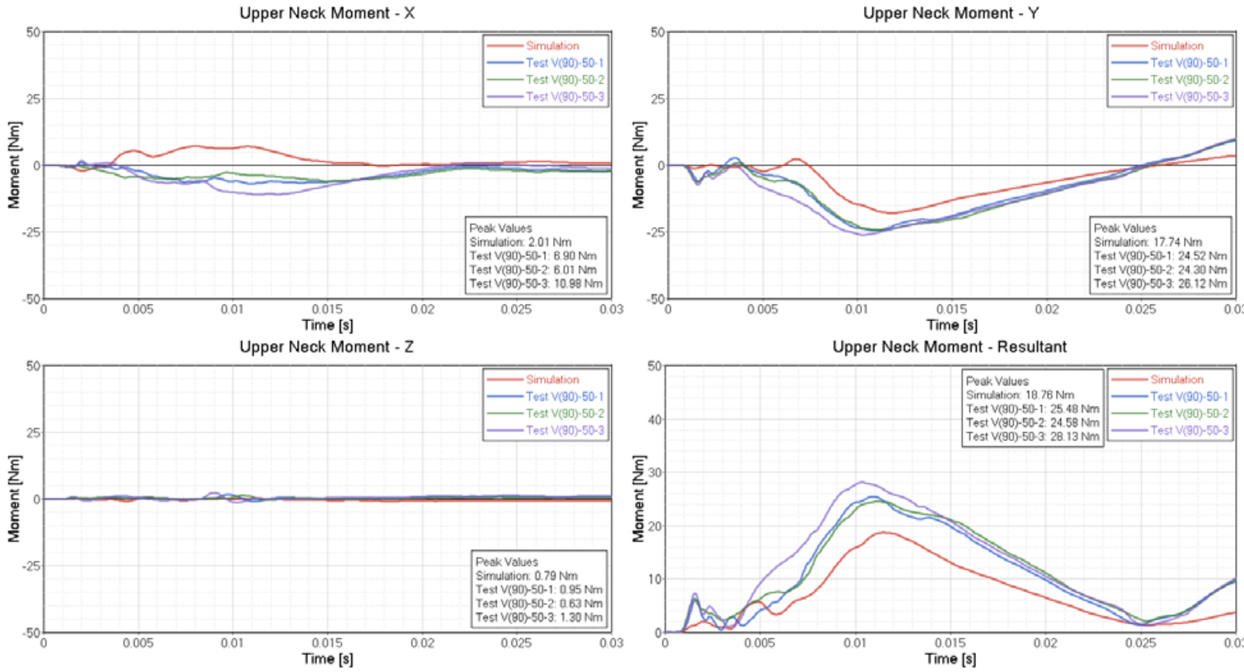

Figure 204. Test vs simulation comparison; DJI Phantom 3, 2.67 lb, bottom, 57 fps, vertical; A11 ATD test, top of the head; upper neck moment

<u>Vertical Minimum Velocity Test – V(90)-20</u>

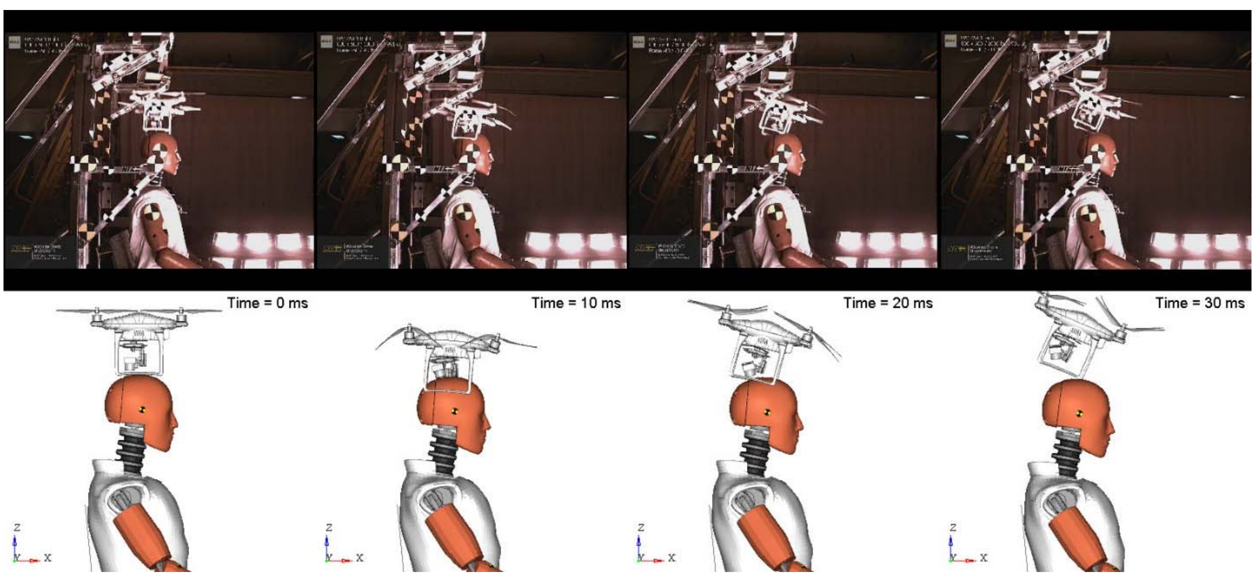

Figure 205. Test vs simulation comparison; DJI Phantom 3, 2.67 lb, bottom, 36 fps, vertical; A11 ATD test, top of the head; kinematics

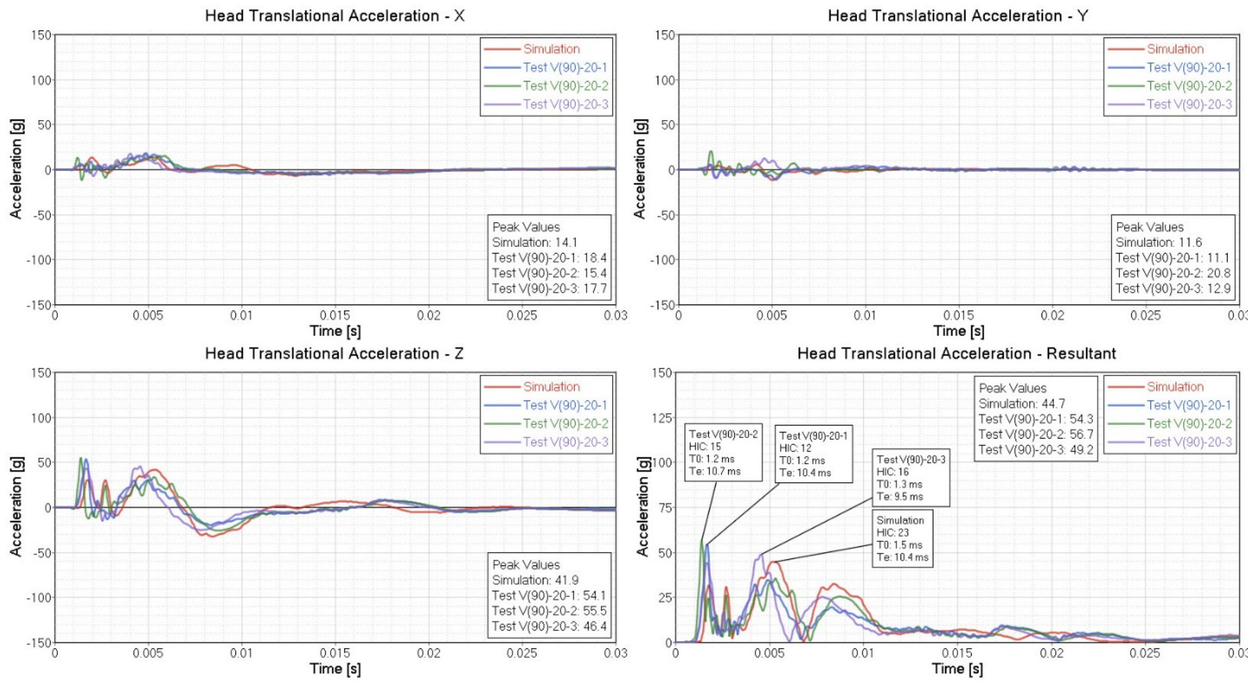

Figure 206. Test vs simulation comparison; DJI Phantom 3, 2.67 lb, bottom, 36 fps, vertical; A11 ATD test, top of the head; head CG acceleration

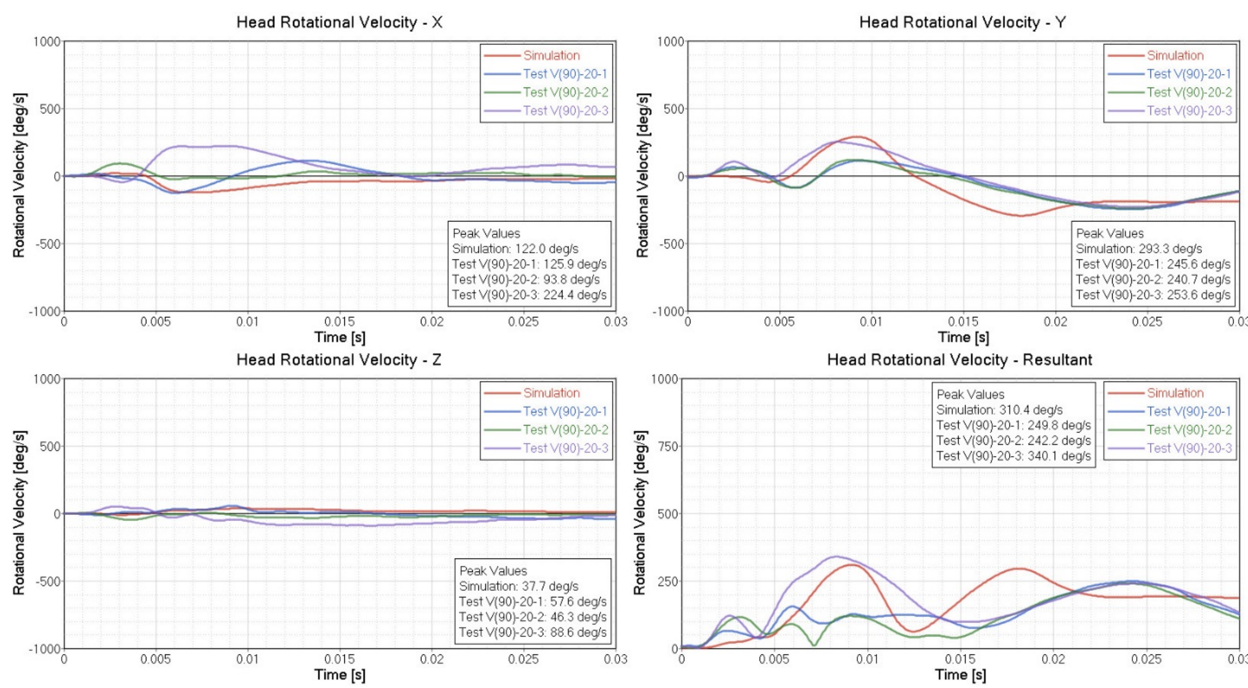

Figure 207. Test vs simulation comparison; DJI Phantom 3, 2.67 lb, bottom, 36 fps, vertical; A11 ATD test, top of the head; head angular rate

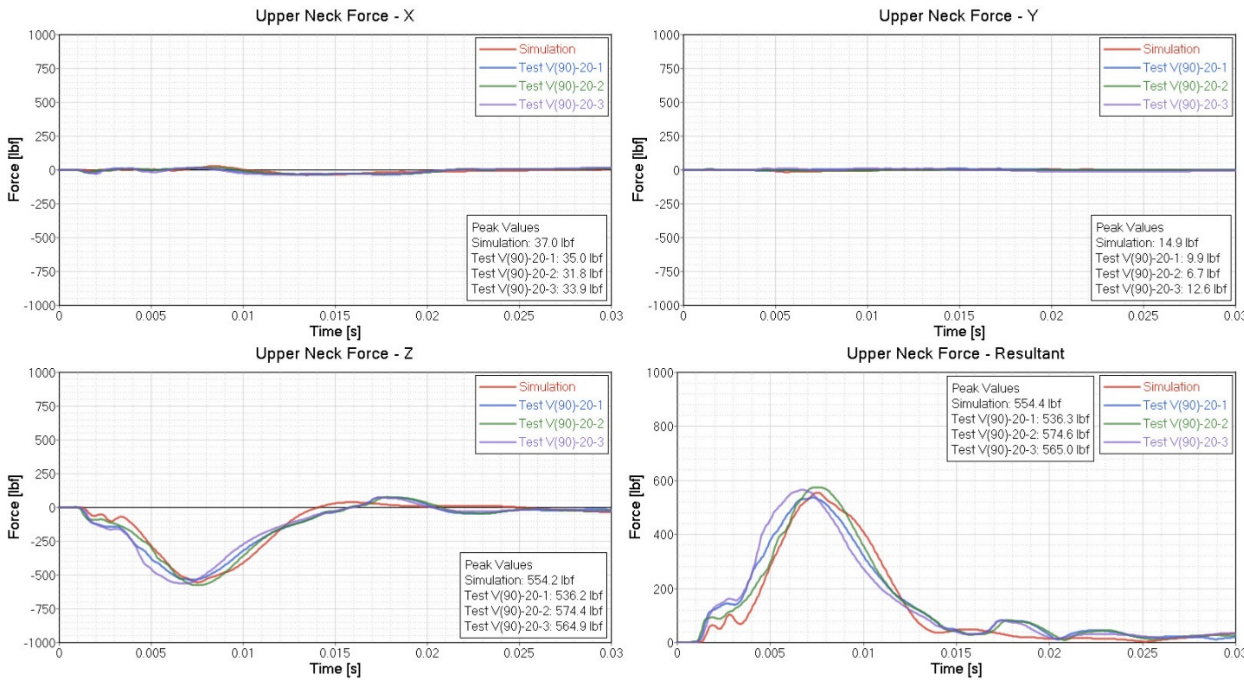

Figure 208. Test vs simulation comparison; DJI Phantom 3, 2.67 lb, bottom, 36 fps, vertical; A11 ATD test, top of the head; upper neck force

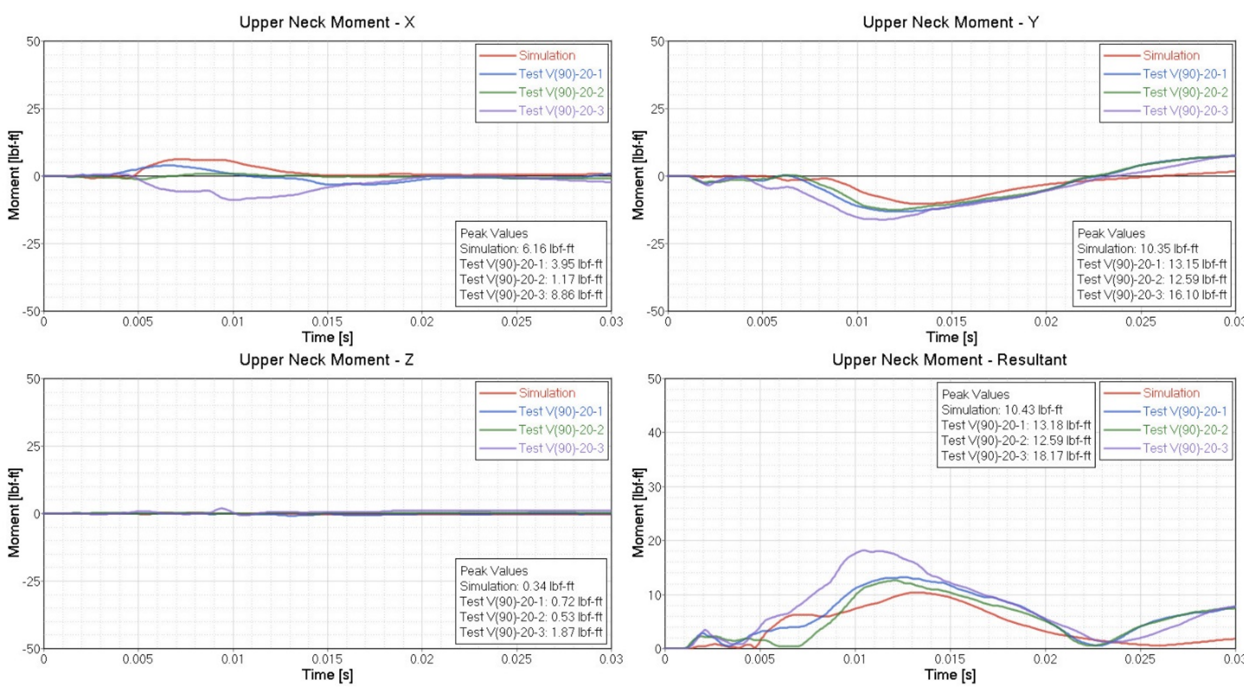

Figure 209. Test vs simulation comparison; DJI Phantom 3, 2.67 lb, bottom, 36 fps, vertical; A11 ATD test, top of the head; upper neck moment

<u>Horizontal Test H(0)-4.5</u>

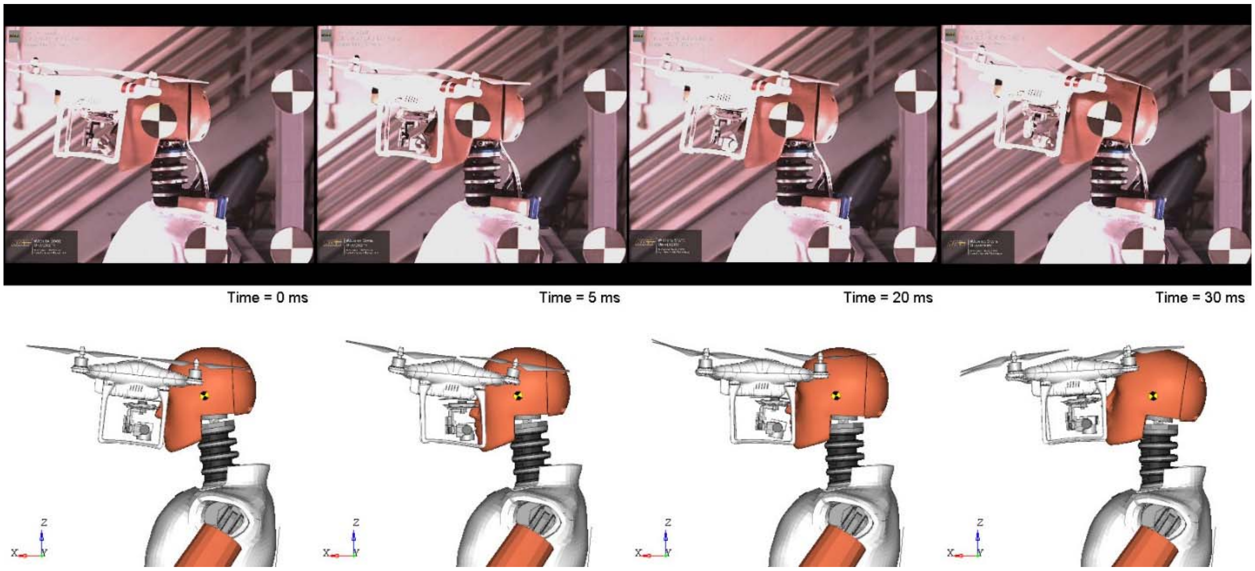

Figure 210. Test vs simulation comparison; DJI Phantom 3, 2.67 lb, between arms, 17 fps, horizontal; A11 ATD test, front of the head; kinematics

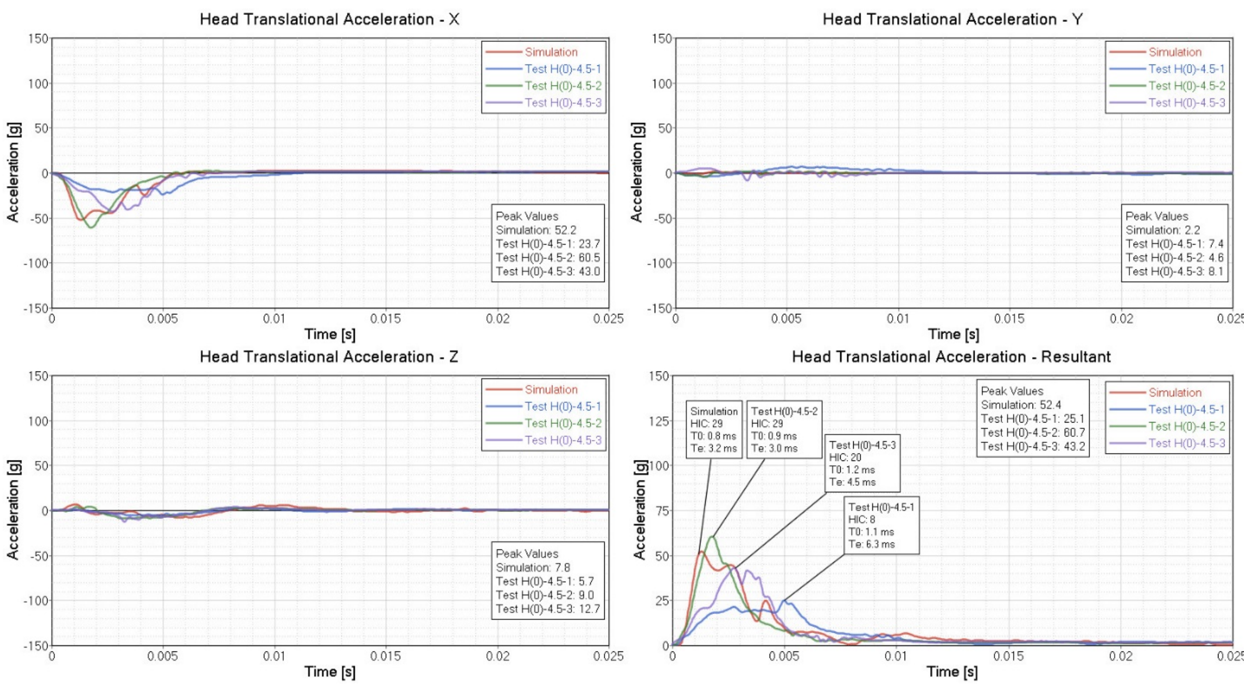

Figure 211. Test vs simulation comparison; DJI Phantom 3, 2.67 lb, between arms, 17 fps, horizontal; A11 ATD test, front of the head; head CG acceleration

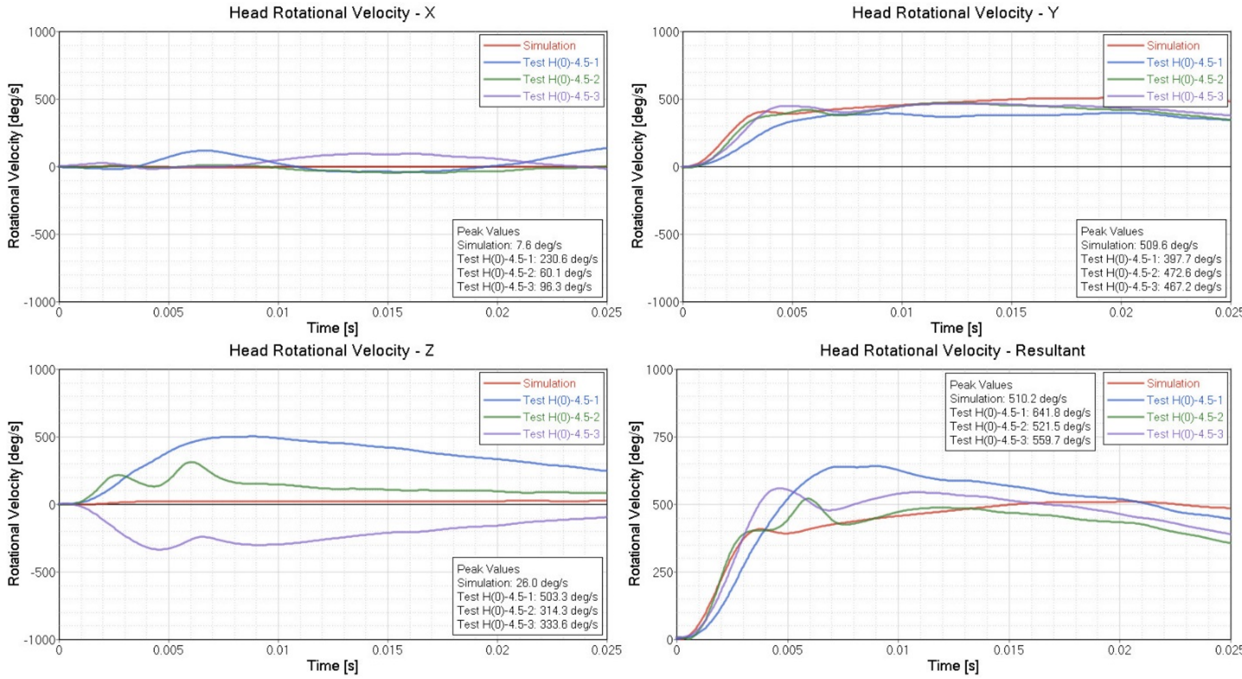

Figure 212. Test vs simulation comparison; DJI Phantom 3, 2.67 lb, between arms, 17 fps, horizontal; A11 ATD test, front of the head; head angular rate

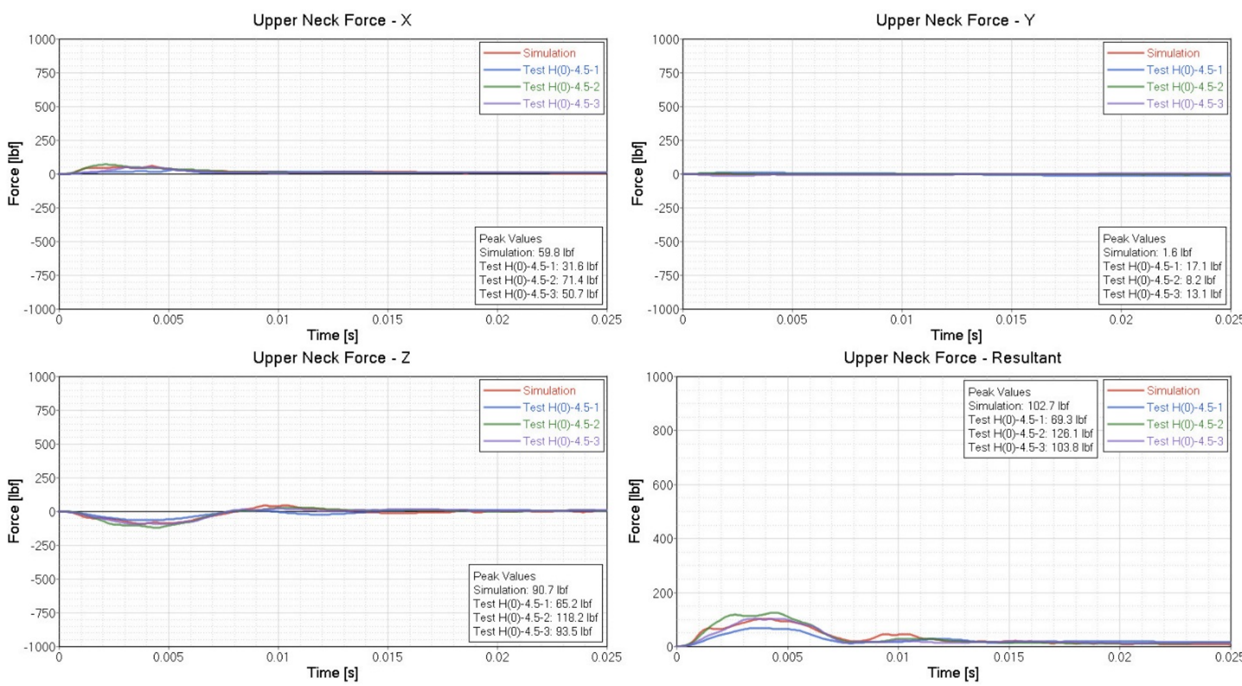

Figure 213. Test vs simulation comparison; DJI Phantom 3, 2.67 lb, between arms, 17 fps, horizontal; A11 ATD test, front of the head; upper neck force

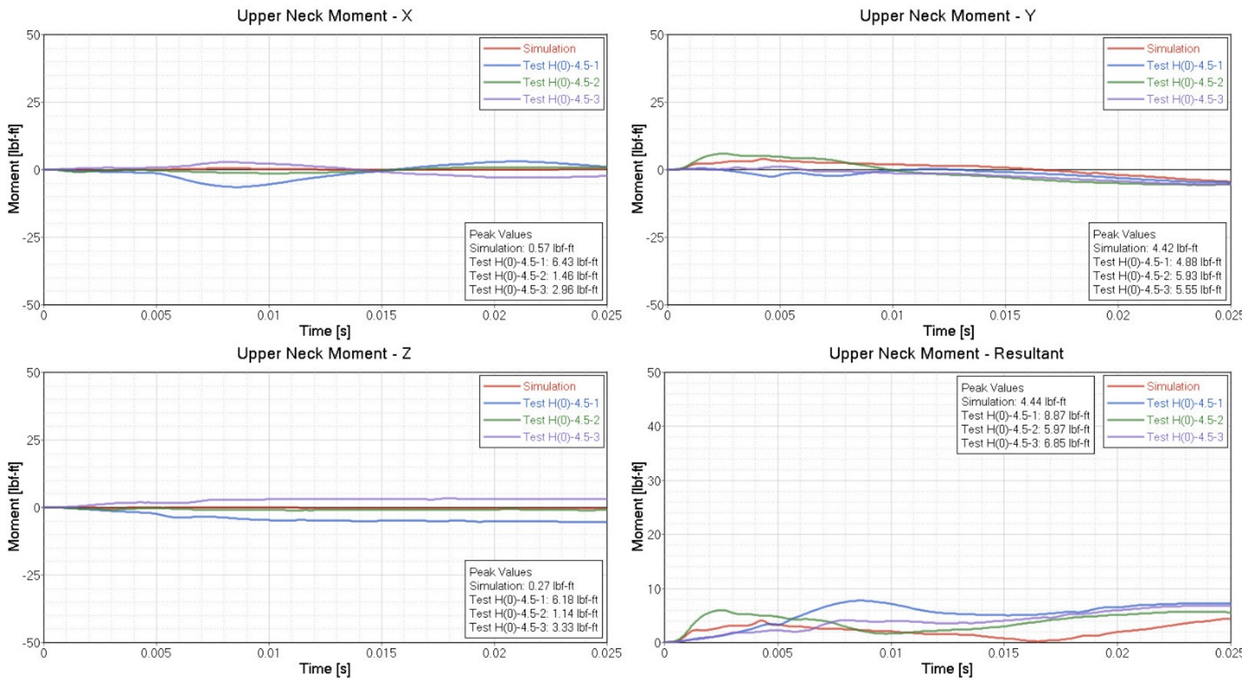

Figure 214. Test vs simulation comparison; DJI Phantom 3, 2.67 lb, between arms, 17 fps, horizontal; A11 ATD test, front of the head; upper neck moment

<u>Combined Impact 65 deg Angle Test – A(65)-36.5</u>

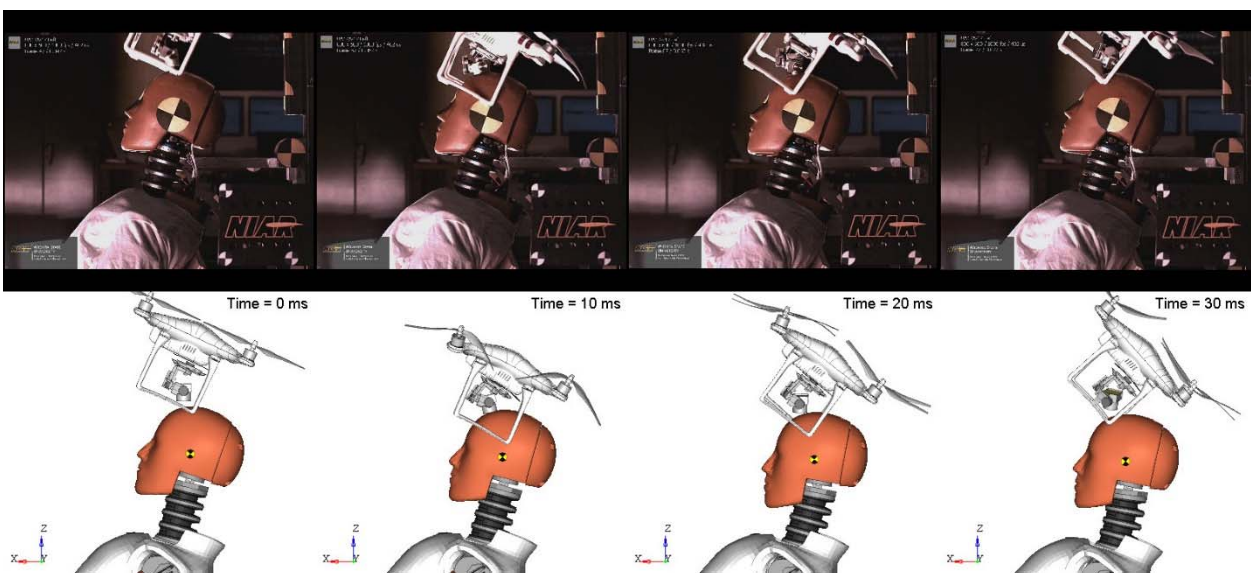

Figure 215. Test vs simulation comparison; DJI Phantom 3, 2.67 lb, bottom, 36 fps, 65 deg. angle; A11 ATD test, forward; kinematics

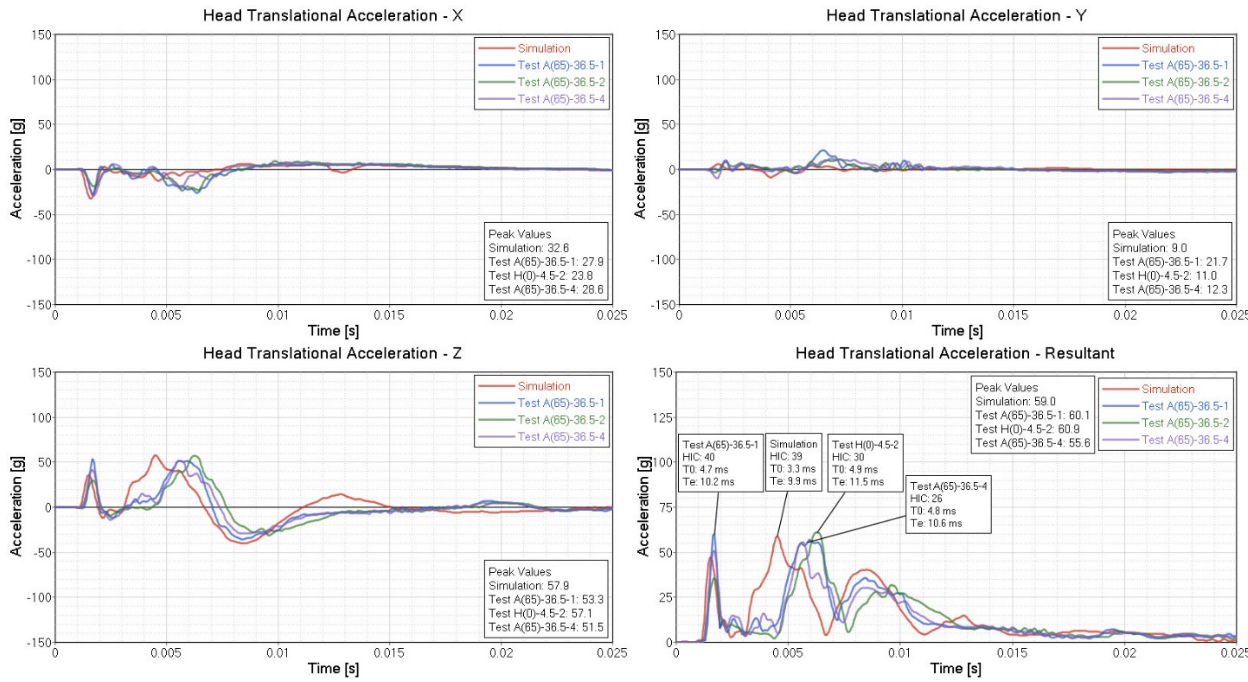

Figure 216. Test vs simulation comparison; DJI Phantom 3, 2.67 lb, bottom, 36 fps, 65 deg. angle; A11 ATD test, forward; head CG acceleration

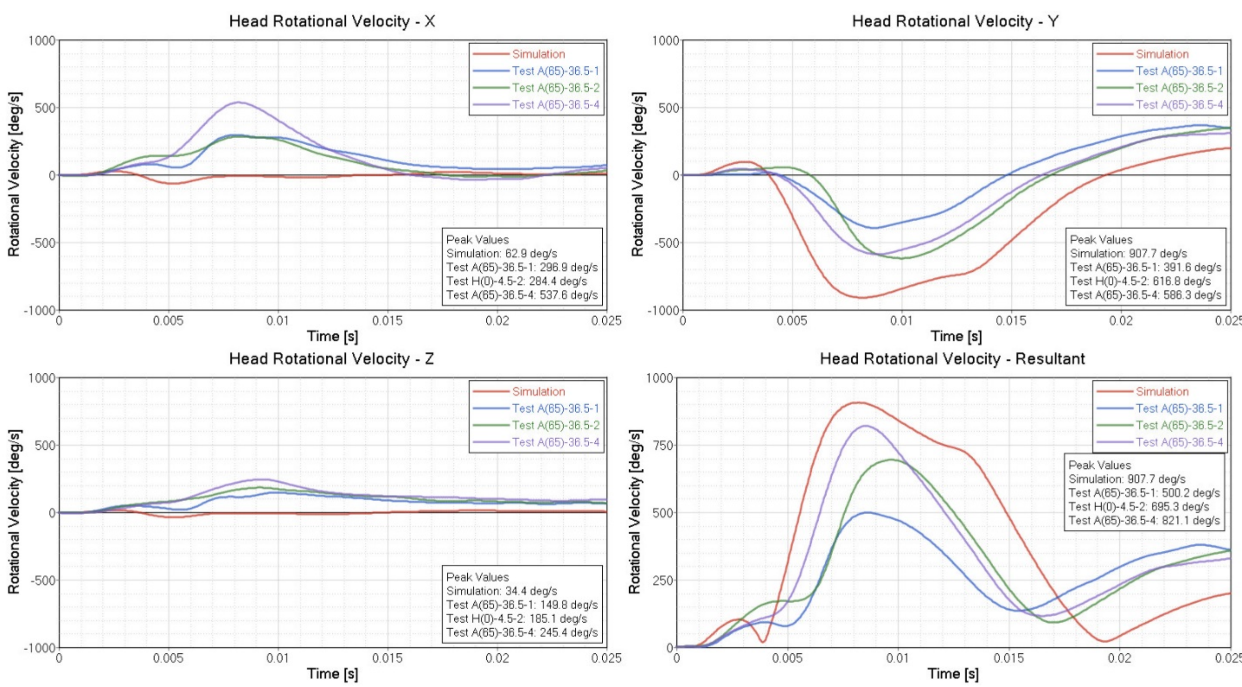

Figure 217. Test vs simulation comparison; DJI Phantom 3, 2.67 lb, bottom, 36 fps, 65 deg. angle; A11 ATD test, forward; head angular rate

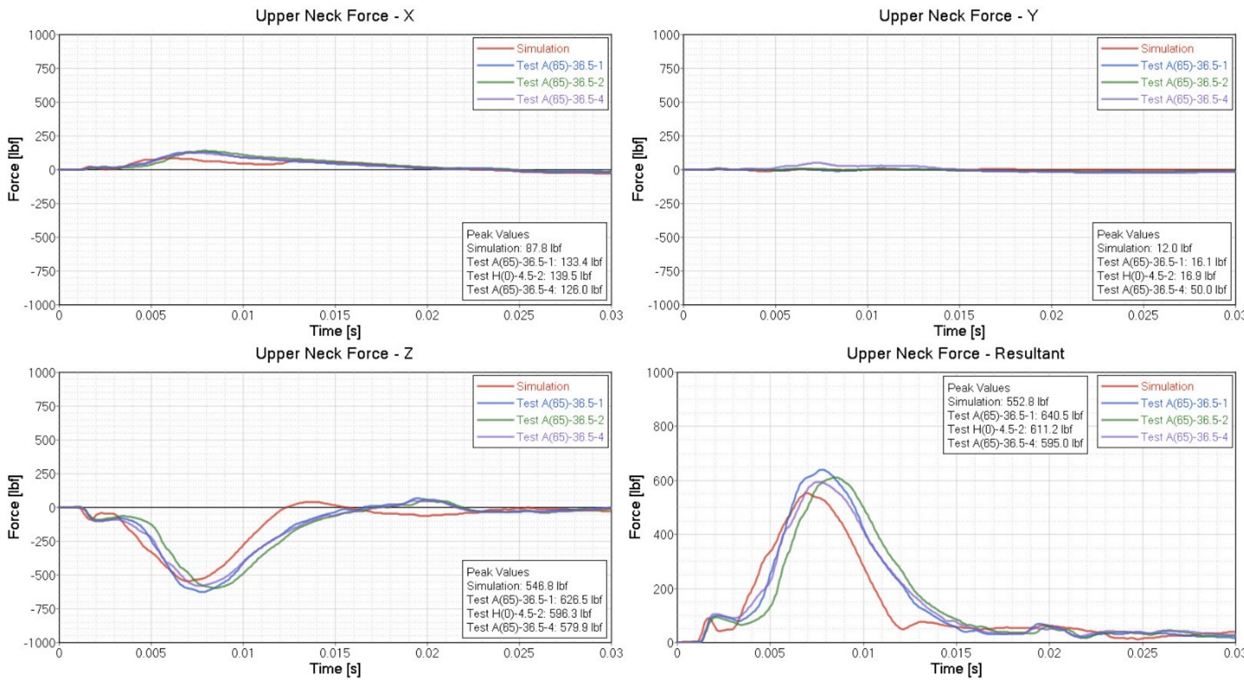

Figure 218. Test vs simulation comparison; DJI Phantom 3, 2.67 lb, bottom, 36 fps, 65 deg. angle; A11 ATD test, forward; upper neck force

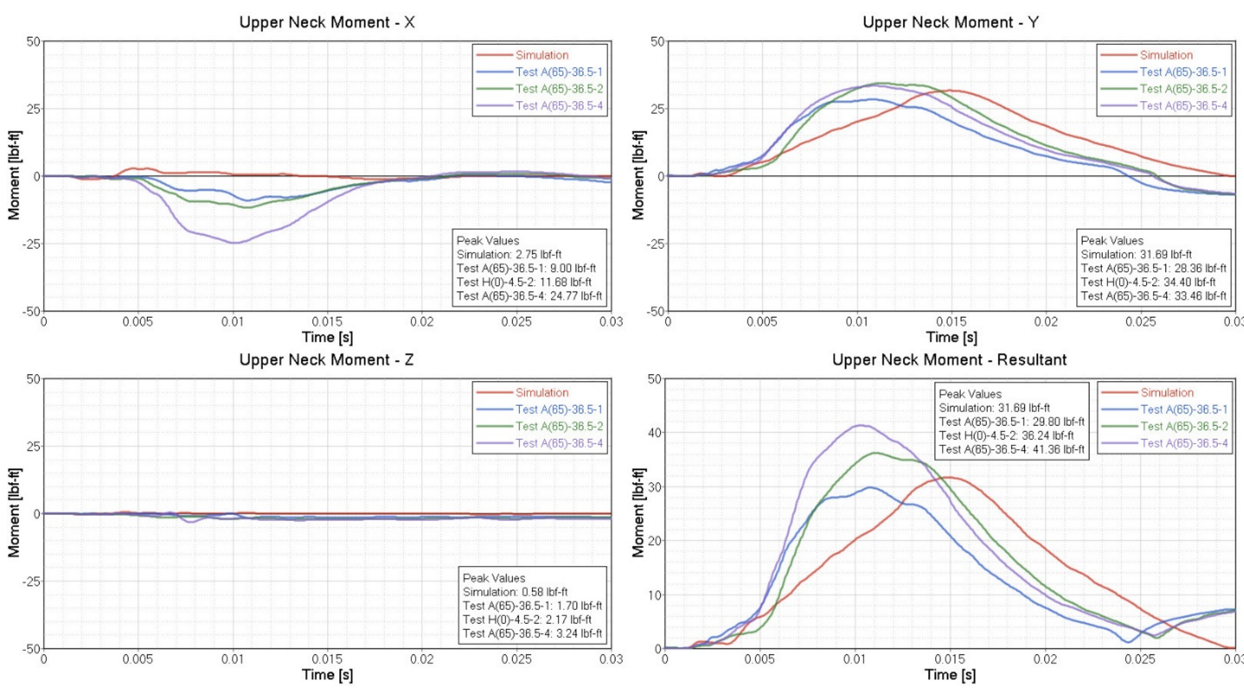

Figure 219. Test vs simulation comparison; DJI Phantom 3, 2.67 lb, bottom, 36 fps, 65 deg. angle; A11 ATD test, forward; upper neck moment

Combined Impact 58 deg Angle Maximum Velocity Test – A(58)-51.7

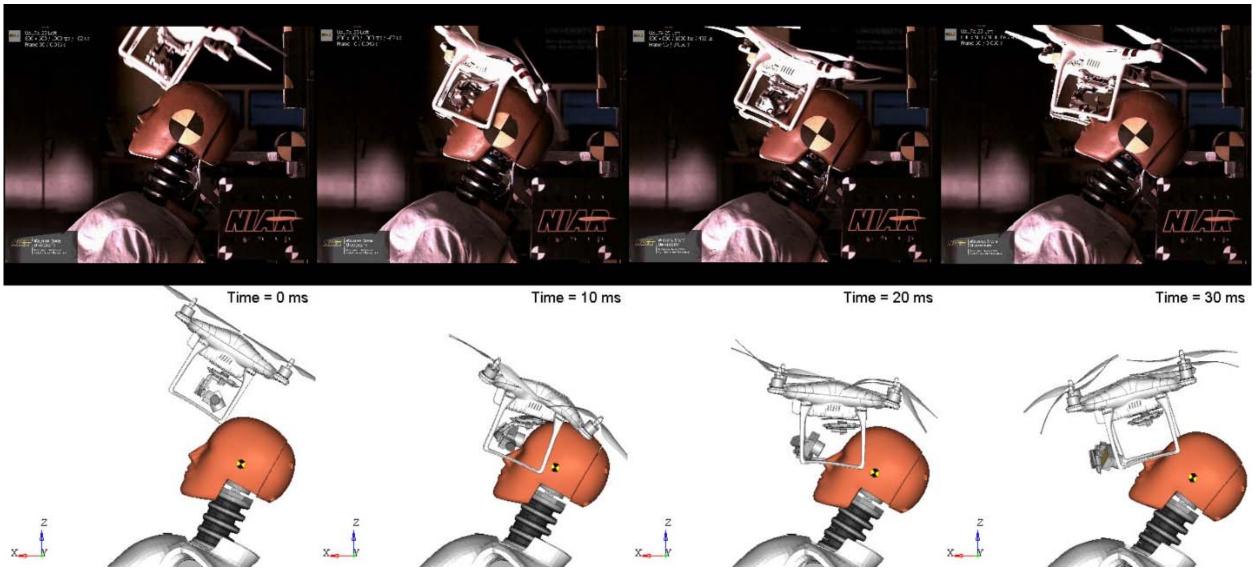

Figure 220. Test vs simulation comparison; DJI Phantom 3, 2.67 lb, bottom, 52 fps, 58 deg. angle; A11 ATD test, forward; kinematics

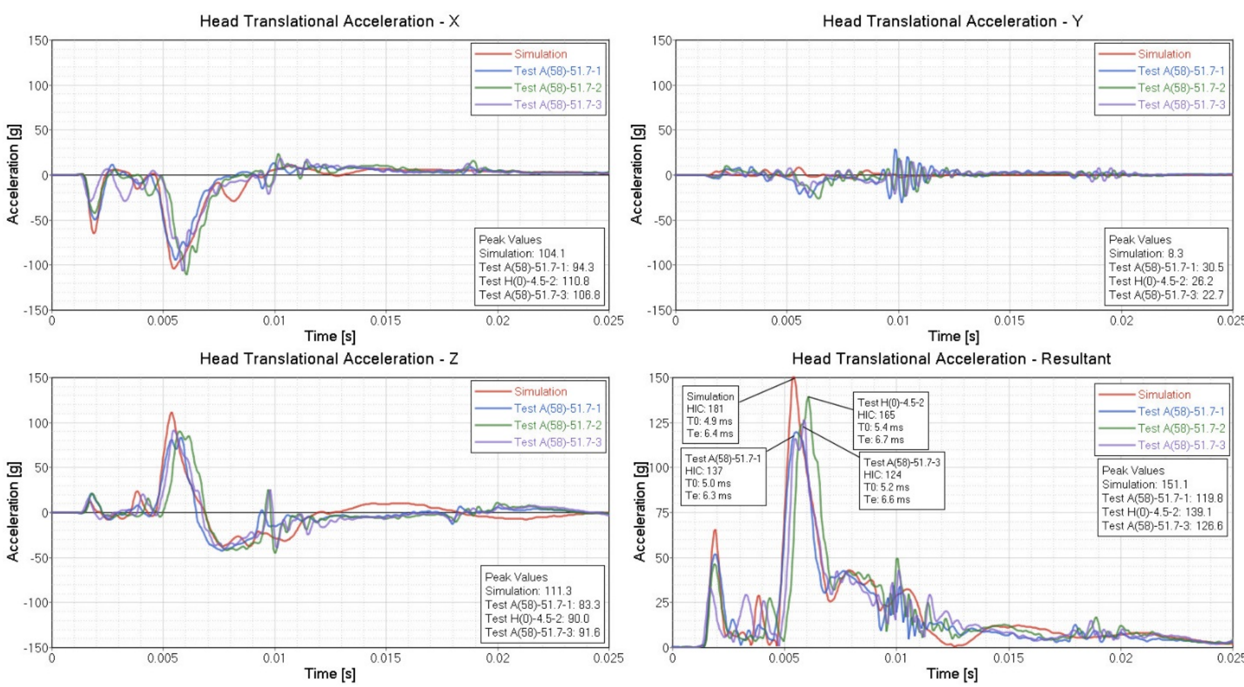

Figure 221. Test vs simulation comparison; DJI Phantom 3, 2.67 lb, bottom, 52 fps, 58 deg. angle; A11 ATD test, forward; head CG acceleration

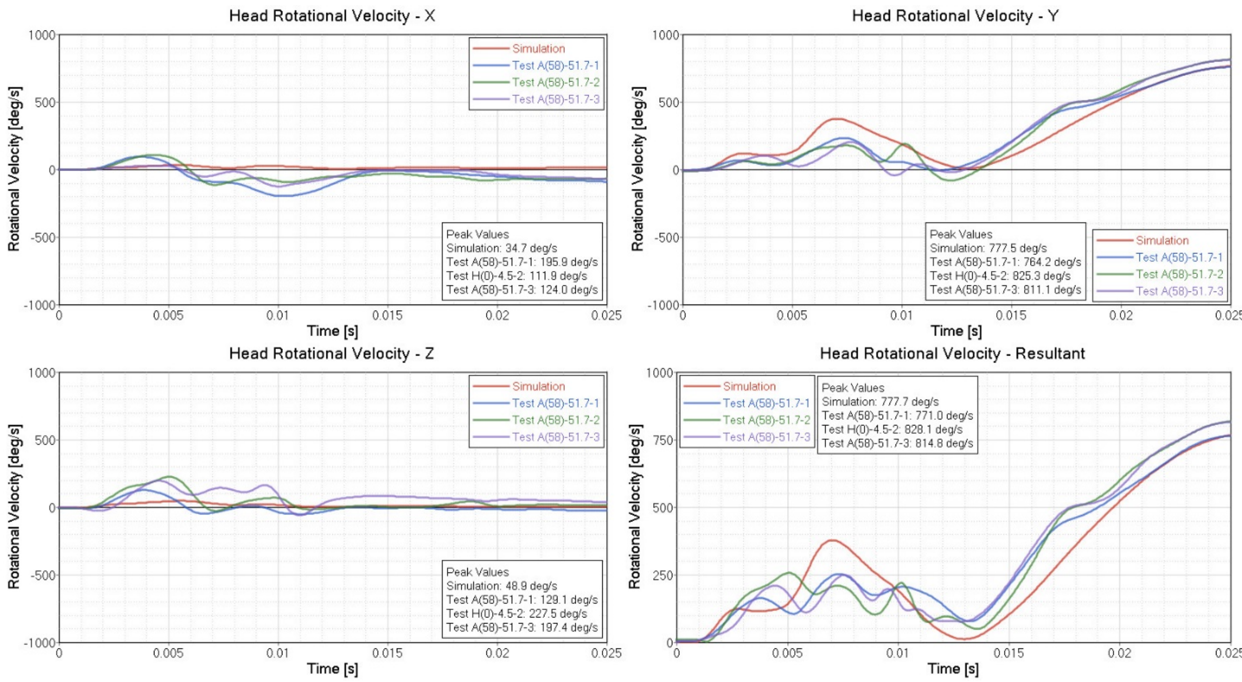

Figure 222. Test vs simulation comparison; DJI Phantom 3, 2.67 lb, bottom, 52 fps, 58 deg. angle; A11 ATD test, forward; head angular rate

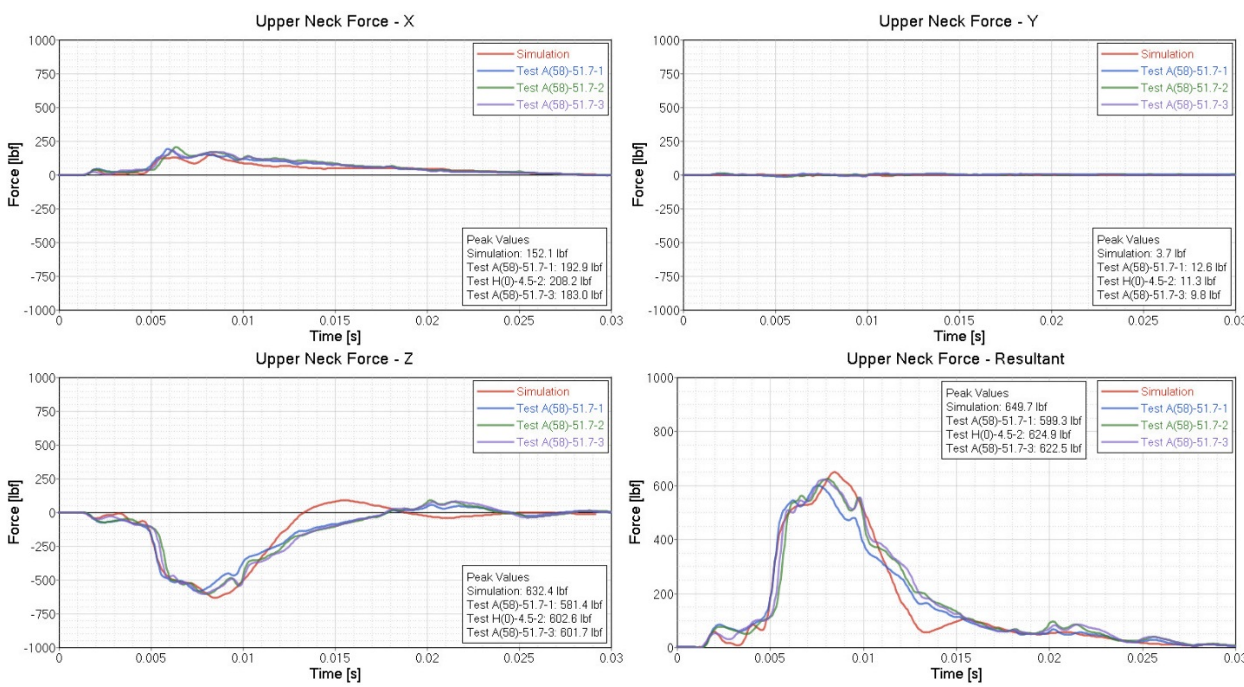

Figure 223. Test vs simulation comparison; DJI Phantom 3, 2.67 lb, bottom, 52 fps, 58 deg. angle; A11 ATD test, forward; upper neck force

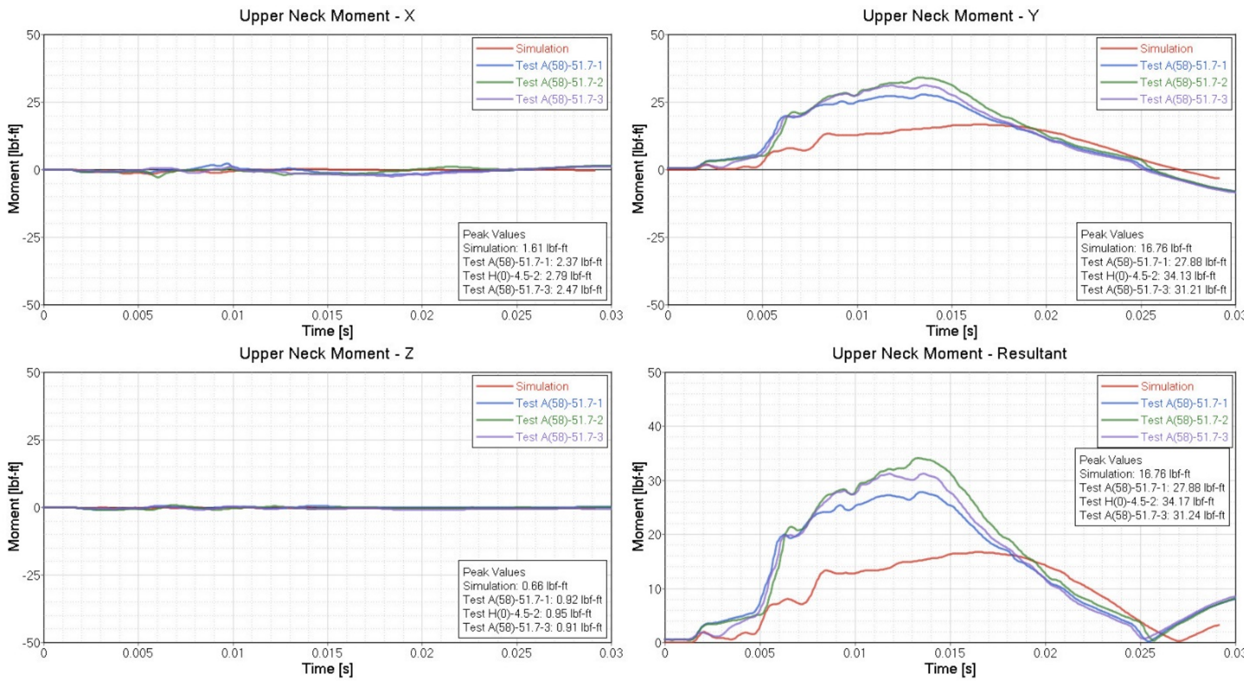

Figure 224. Test vs simulation comparison; DJI Phantom 3, 2.67 lb, bottom, 52 fps, 58 deg. angle; A11 ATD test, forward; upper neck moment

Combined Impact 58 deg Angle Minimum Velocity Test – A (58)-46.1

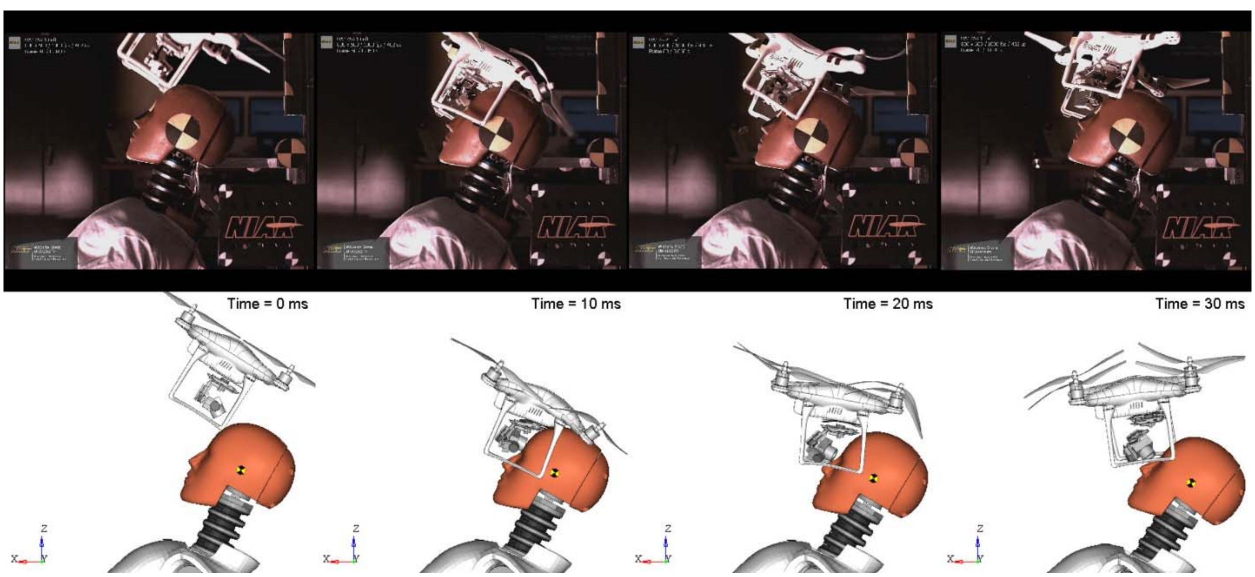

Figure 225. Test vs simulation comparison; DJI Phantom 3, 2.67 lb, bottom, 46 fps, 58 deg. angle; A11 ATD test, forward; kinematics

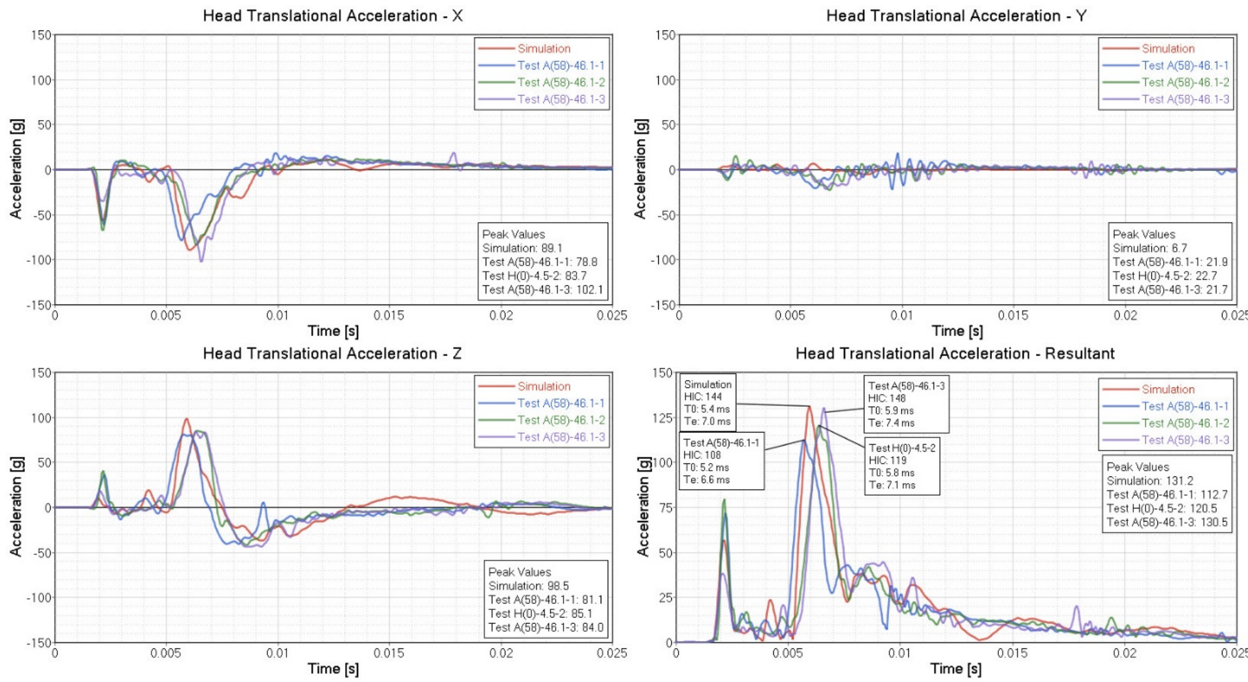

Figure 226. Test vs simulation comparison; DJI Phantom 3, 2.67 lb, bottom, 46 fps, 58 deg. angle; A11 ATD test, forward; head CG acceleration

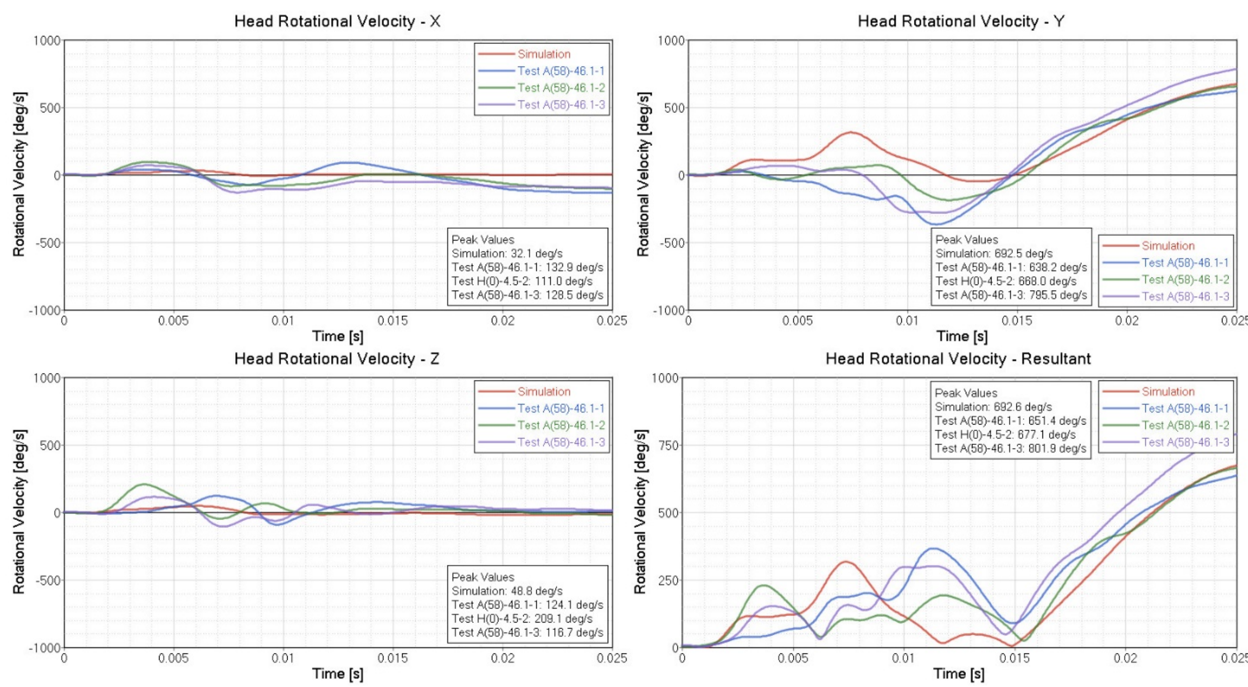

Figure 227. Test vs simulation comparison; DJI Phantom 3, 2.67 lb, bottom, 46 fps, 58 deg. angle; A11 ATD test, forward; head angular rate

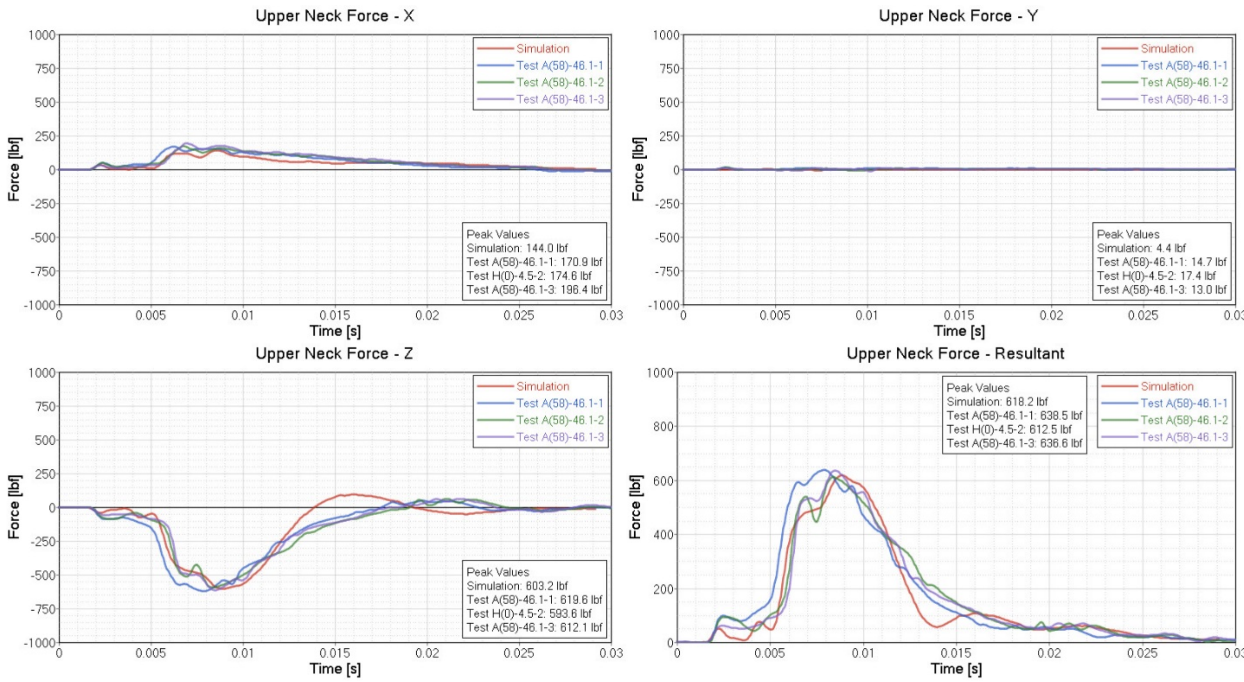

Figure 228. Test vs simulation comparison; DJI Phantom 3, 2.67 lb, bottom, 46 fps, 58 deg. angle; A11 ATD test, forward; upper neck force

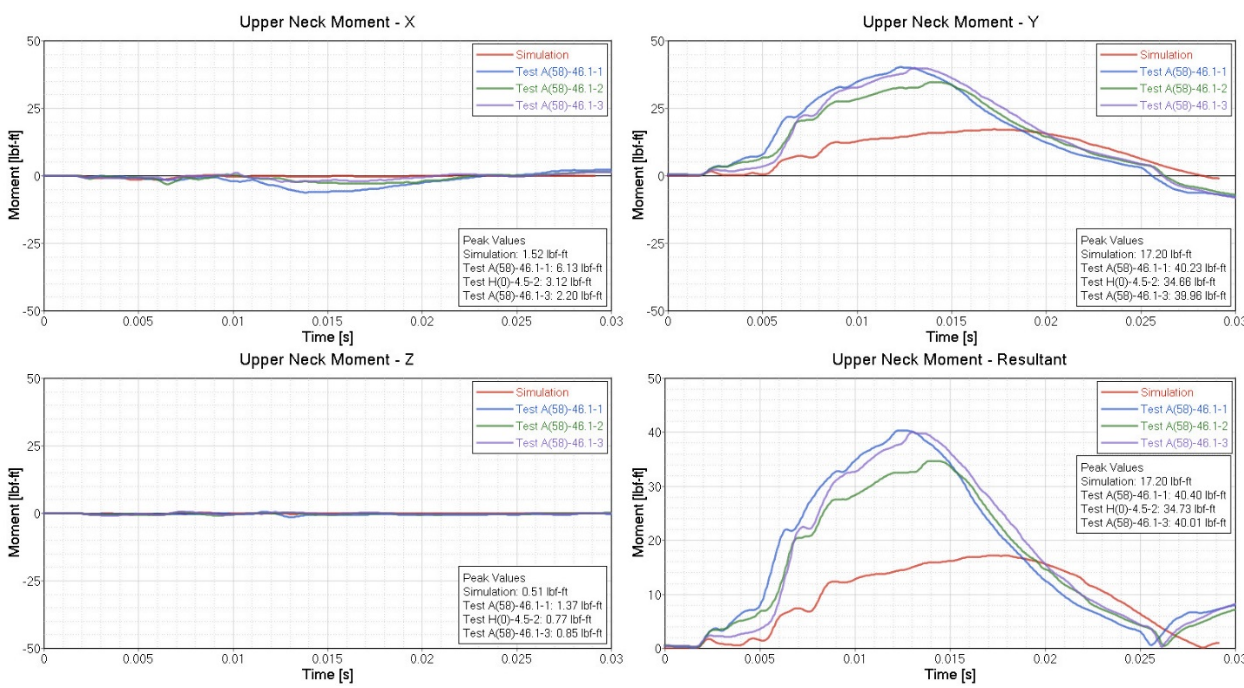

Figure 229. Test vs simulation comparison; DJI Phantom 3, 2.67 lb, bottom, 46 fps, 58 deg. angle; A11 ATD test, forward; upper neck moment

APPENDIX E—DJI PHANTOM III MODEL EVALUATION WITH A14 ATD TESTS

<u>Test 1: DJI Phantom 3, 2.54 lb, top, 25 fps, vertical; A14 ATD, top of the head</u>

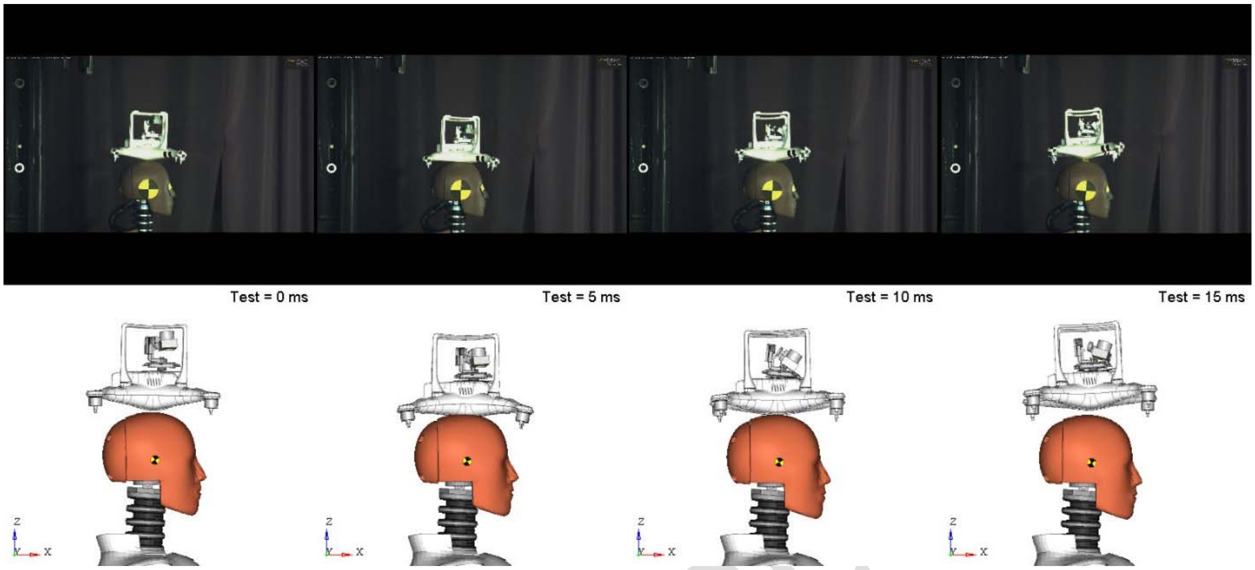

Figure 230. Test vs simulation comparison; DJI Phantom 3, 2.54 lb, top, 25 fps, vertical; A14 ATD test #1, top of the head; kinematics

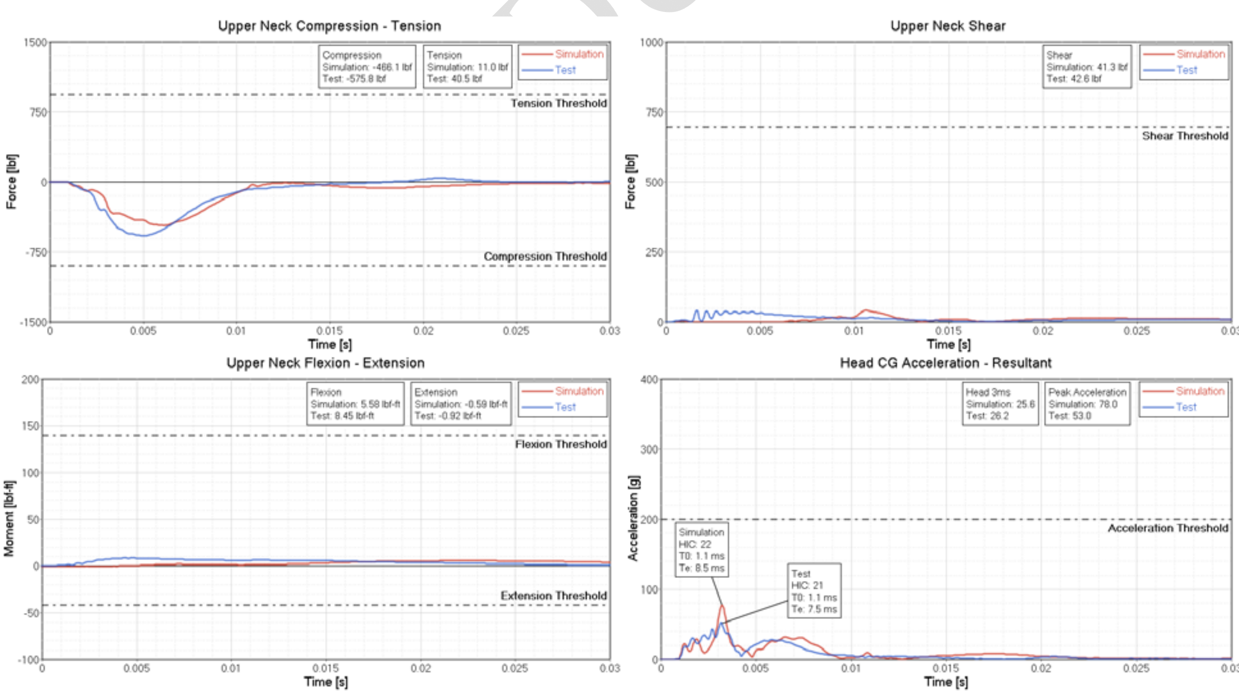

Figure 231. Test vs simulation comparison; DJI Phantom 3, 2.54 lb, top, 25 fps, vertical; A14 ATD test #1, top of the head; neck loads, and head acceleration

<u>Test 2: DJI Phantom 3, 2.54 lb, side, 25 fps, vertical; A14 ATD, top of the head</u>

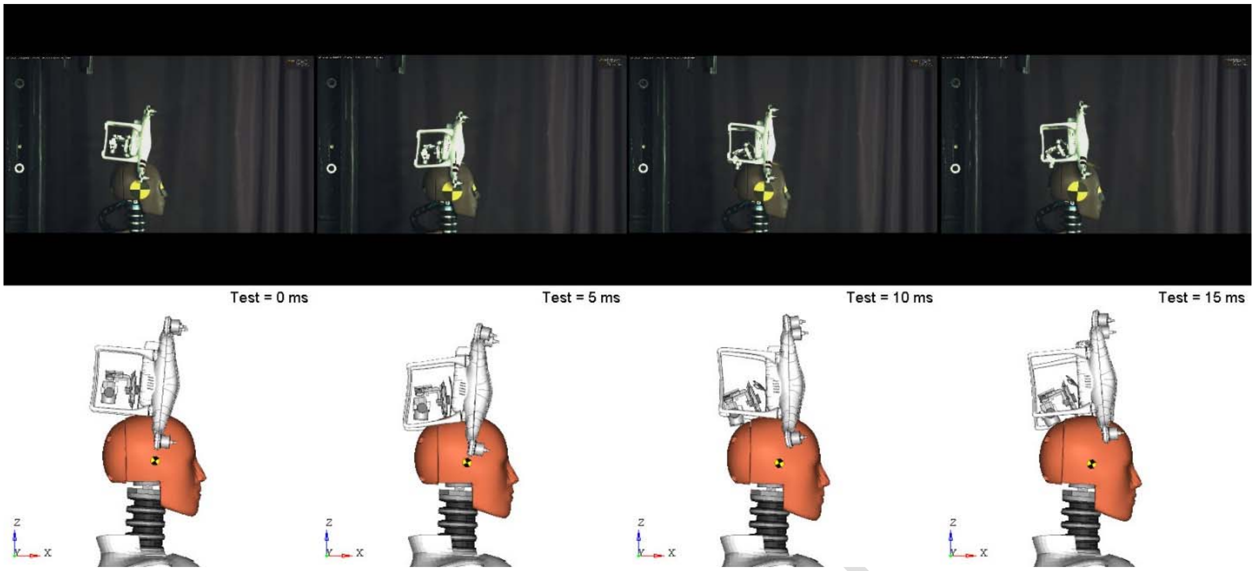

Figure 232. Test vs simulation comparison; DJI Phantom 3, 2.54 lb, side, 25 fps, vertical; A14 ATD test #2, top of the head; kinematics

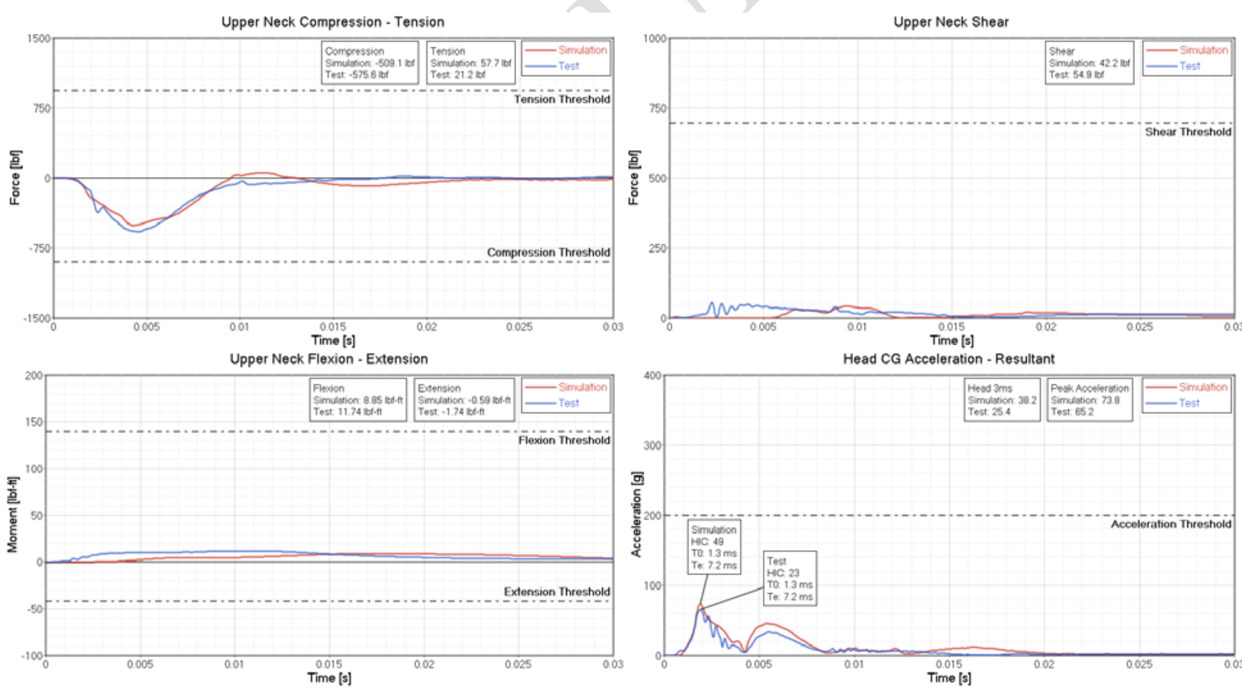

Figure 233. Test vs simulation comparison; DJI Phantom 3, 2.54 lb, side, 25 fps, vertical; A14 ATD test #2, top of the head; neck loads, and head acceleration

<u>Test 3: DJI Phantom 3, 2.54 lb, arm, 25 fps, vertical; A14 ATD, top of the head</u>

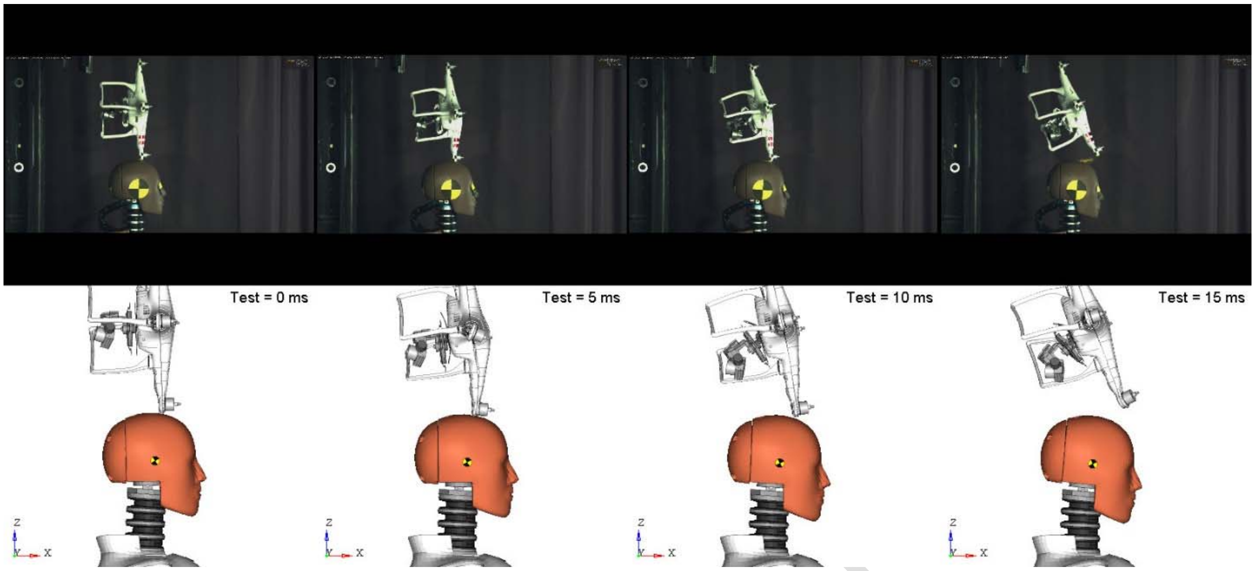

Figure 234. Test vs simulation comparison; DJI Phantom 3, 2.54 lb, arm, 25 fps, vertical; A14 ATD test #3, top of the head; kinematics

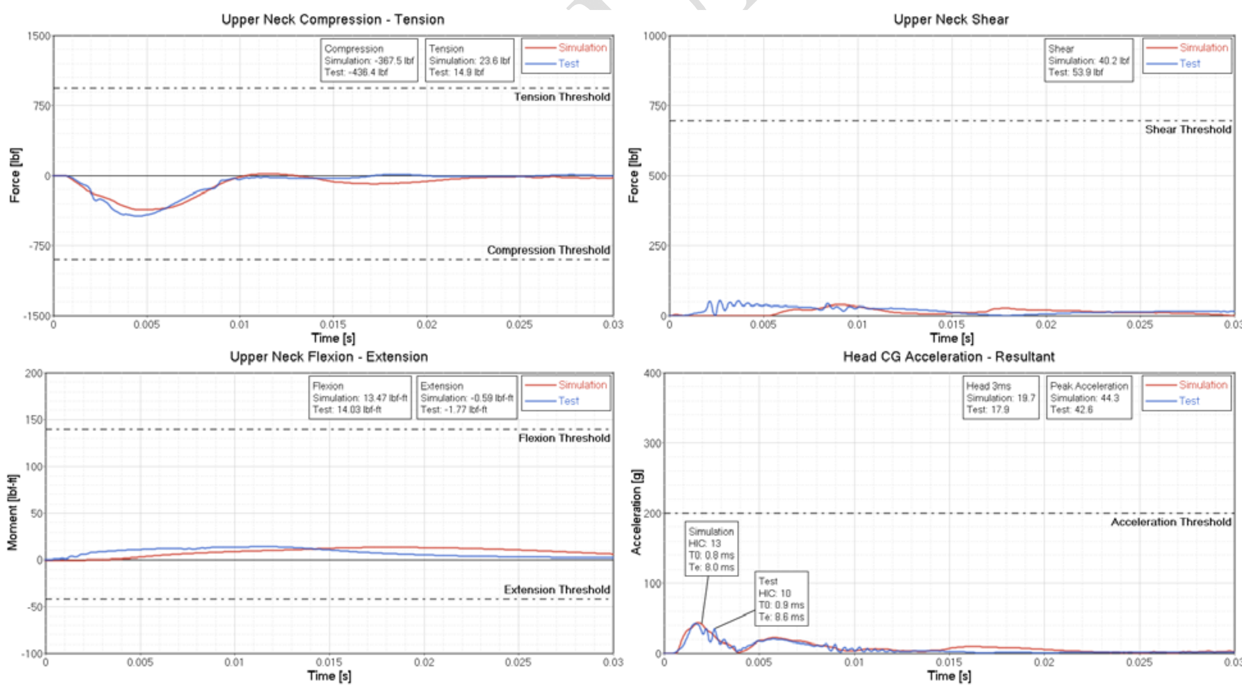

Figure 235. Test vs simulation comparison; DJI Phantom 3, 2.54 lb, arm, 25 fps, vertical; A14 ATD test #3, top of the head; neck loads, and head acceleration

Test 4: DJI Phantom 3, 2.54 lb, top, 36 fps, vertical; A14 ATD, top of the head

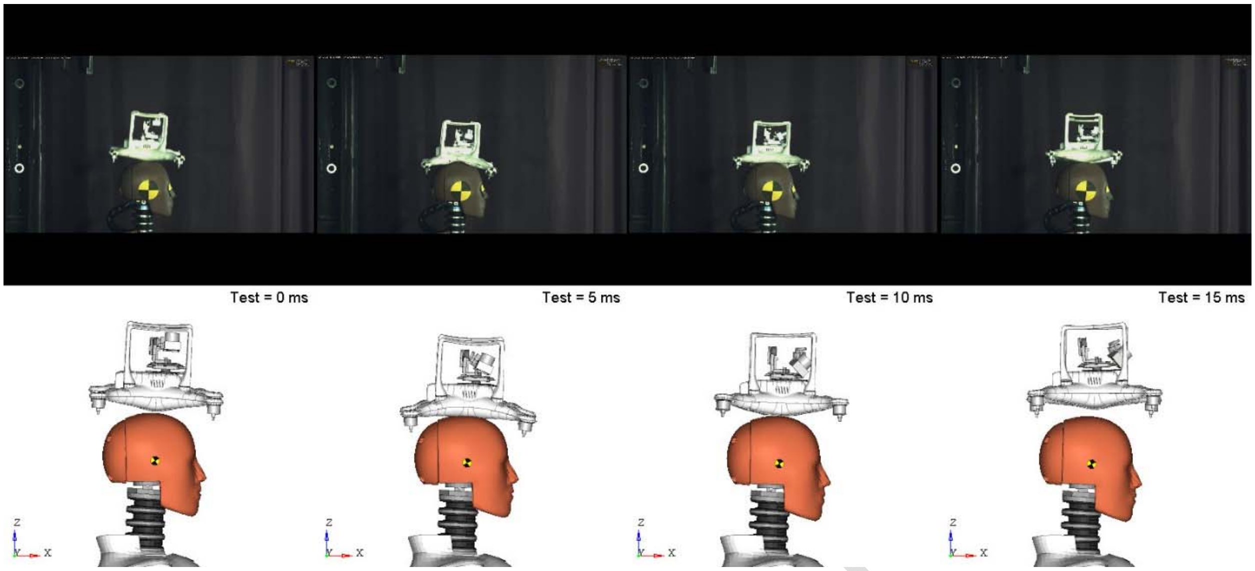

Figure 236. Test vs simulation comparison; DJI Phantom 3, 2.54 lb, top, 36 fps, vertical; A14 ATD test #4, top of the head; kinematics

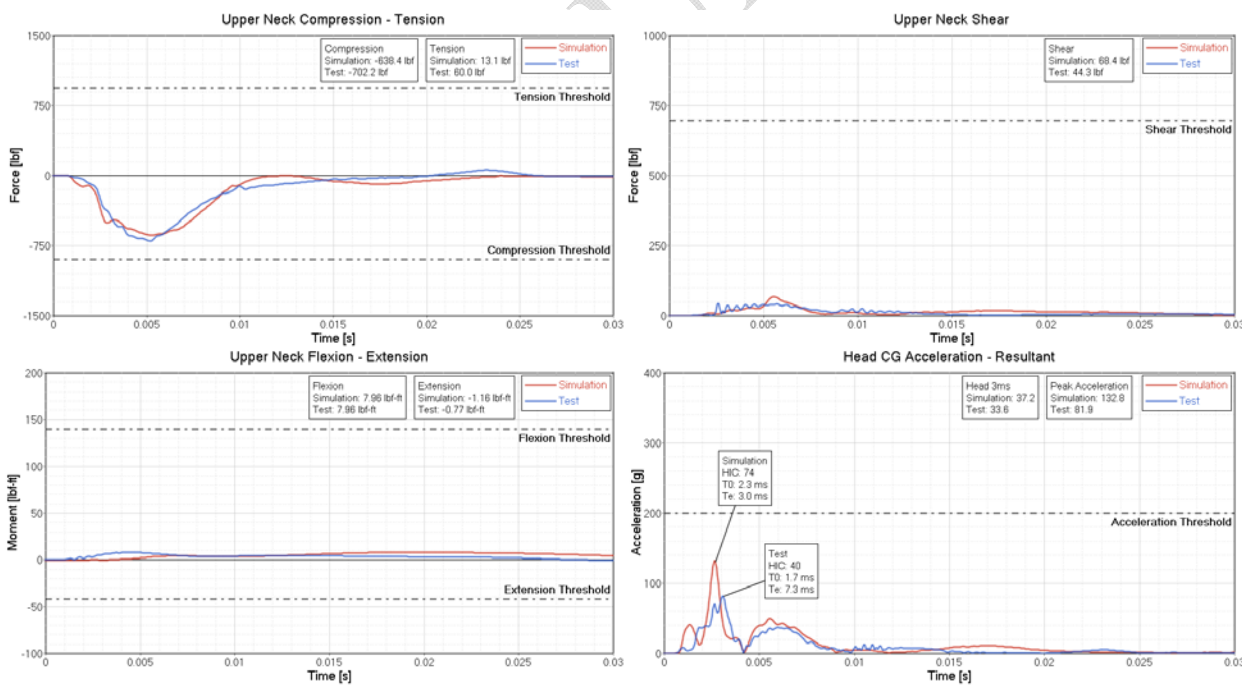

Figure 237. Test vs simulation comparison; DJI Phantom 3, 2.54 lb, top, 36 fps, vertical; A14 ATD test #4, top of the head; neck loads, and head acceleration

Test 5: DJI Phantom 3, 2.54 lb, side, 36 fps, vertical; A14 ATD, top of the head

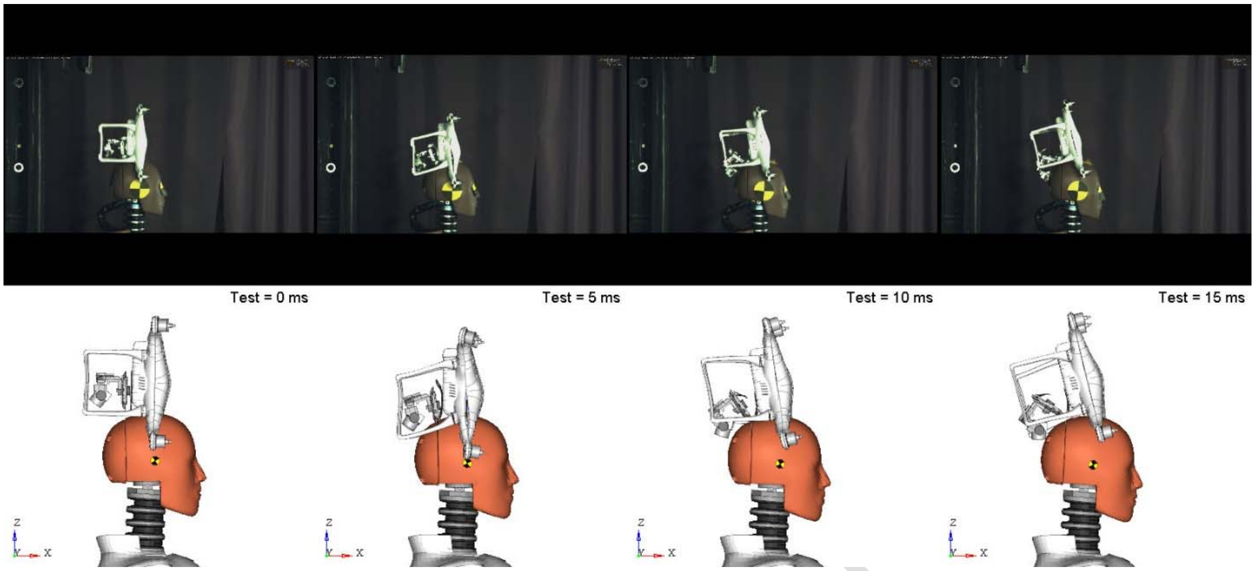

Figure 238. Test vs simulation comparison; DJI Phantom 3, 2.54 lb, side, 36 fps, vertical; A14 ATD test #5, top of the head; kinematics

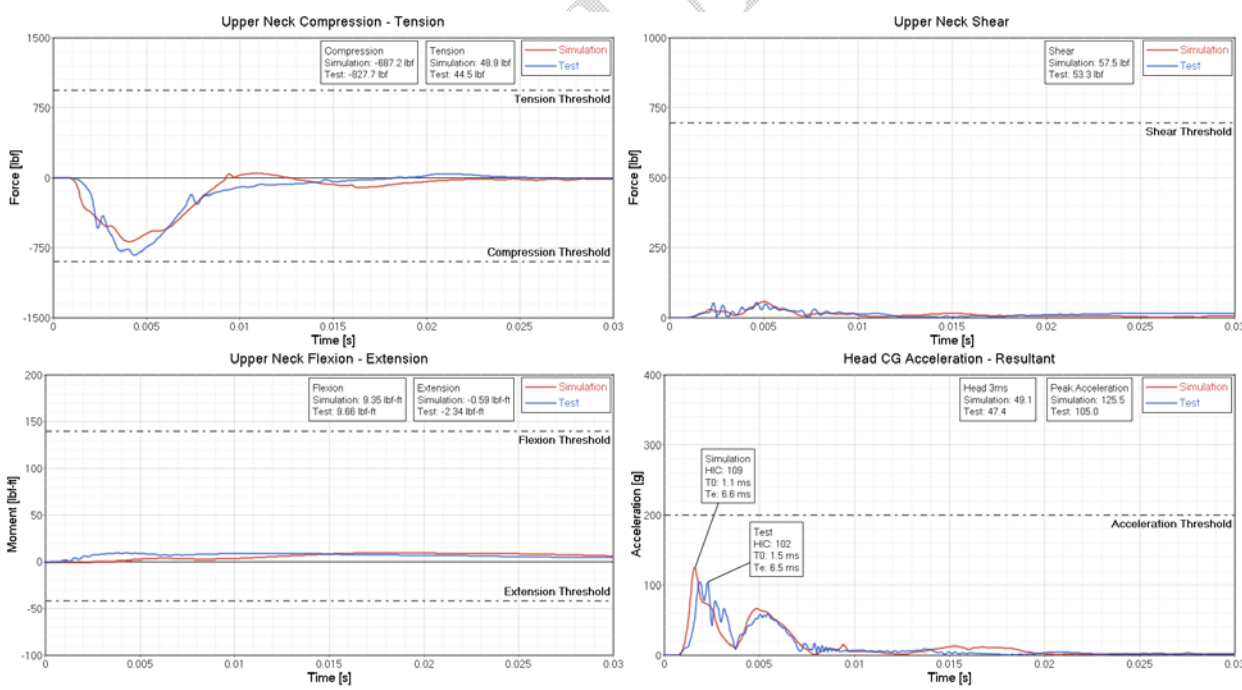

Figure 239. Test vs simulation comparison; DJI Phantom 3, 2.54 lb, side, 36 fps, vertical; A14 ATD test #5, top of the head; neck loads, and head acceleration

Test 6: DJI Phantom 3, 2.54 lb, arm, 36 fps, vertical; A14 ATD, top of the head

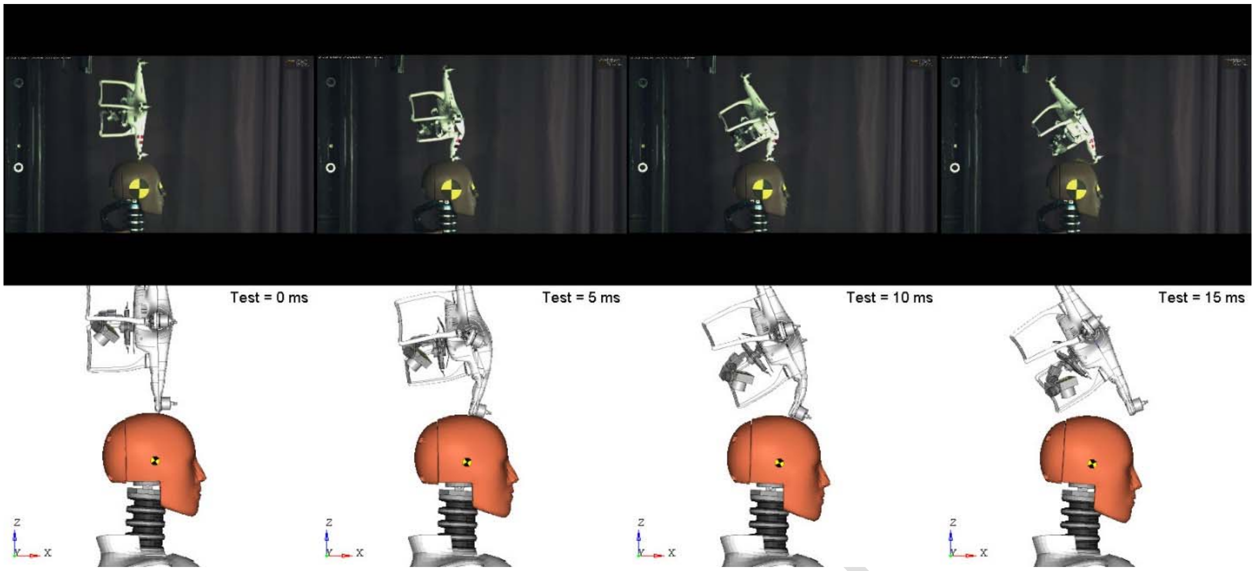

Figure 240. Test vs simulation comparison; DJI Phantom 3, 2.54 lb, arm, 36 fps, vertical; A14 ATD test #6, top of the head; kinematics

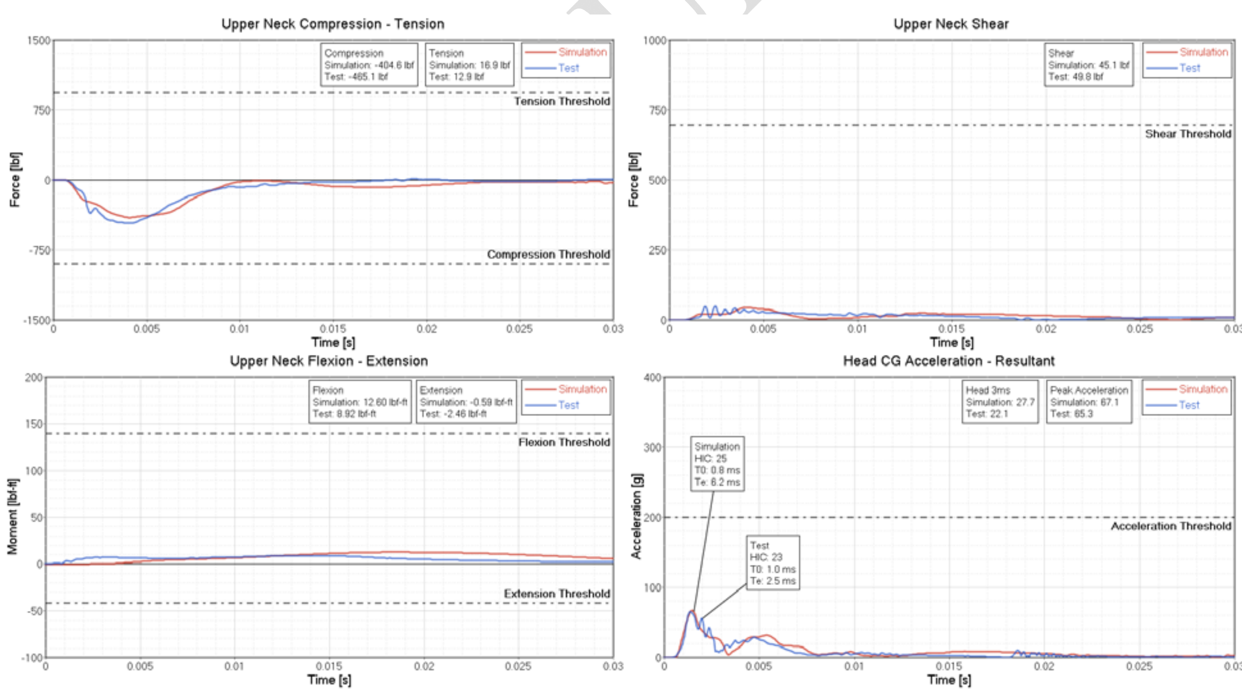

Figure 241. Test vs simulation comparison; DJI Phantom 3, 2.54 lb, arm, 36 fps, vertical; A14 ATD test #6, top of the head; neck loads, and head acceleration

Test 7: DJI Phantom 3, 2.54 lb, bottom, 25 fps, vertical; A14 ATD, top of the head

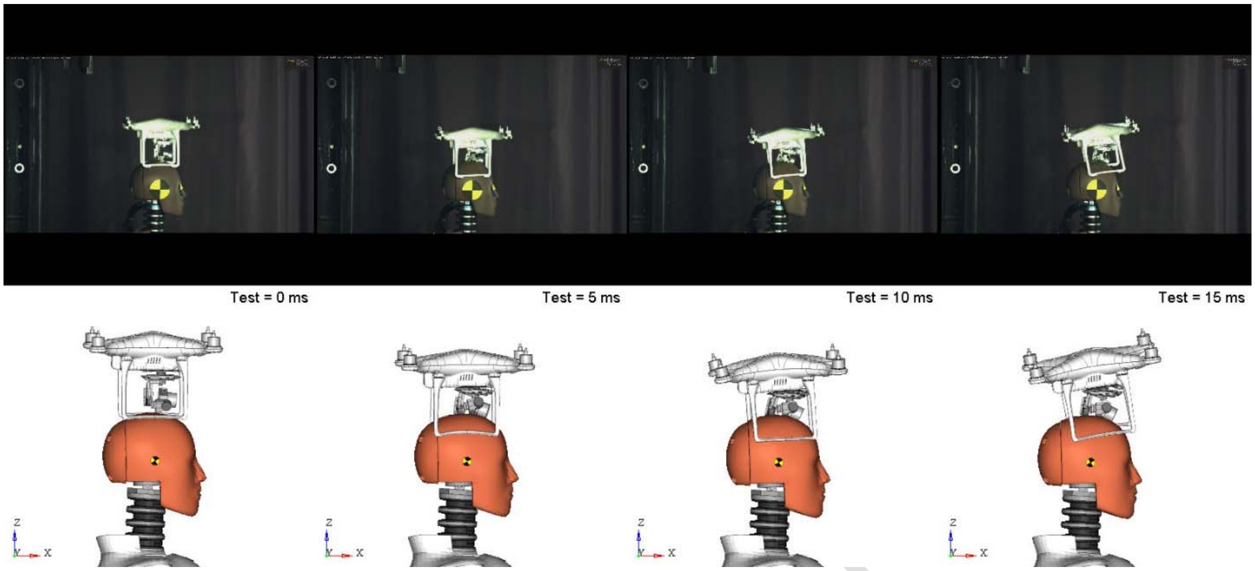

Figure 242. Test vs simulation comparison; DJI Phantom 3, 2.54 lb, bottom, 25 fps, vertical; A14 ATD test #7, top of the head; kinematics

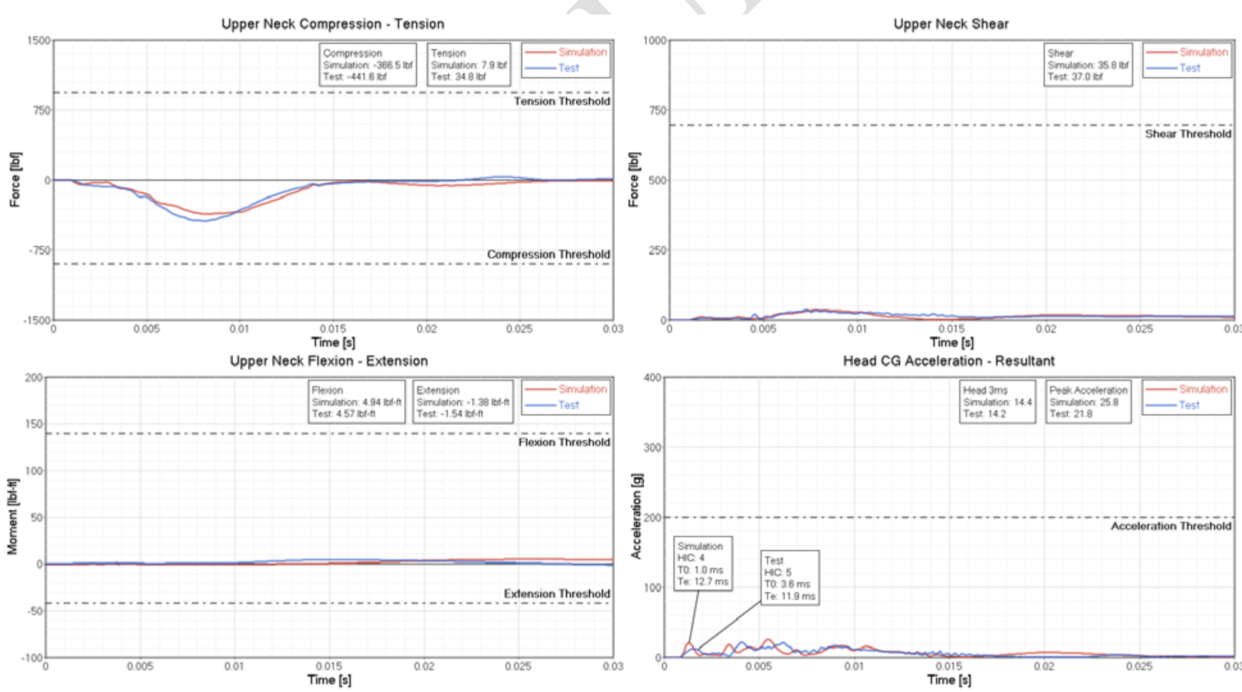

Figure 243. Test vs simulation comparison; DJI Phantom 3, 2.54 lb, bottom, 25 fps, vertical; A14 ATD test #7, top of the head; neck loads, and head acceleration

<u>Test 8: DJI Phantom 3, 2.54 lb, bottom, 36 fps, vertical; A14 ATD, top of the head</u>

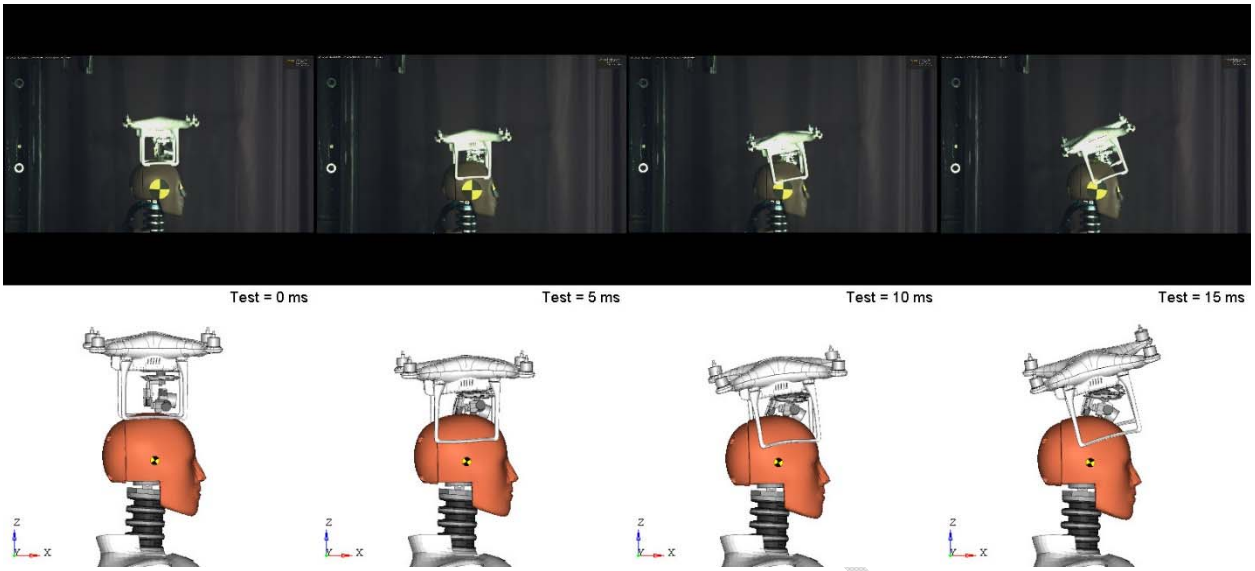

Figure 244. Test vs simulation comparison; DJI Phantom 3, 2.54 lb, bottom, 36 fps, vertical; A14 ATD test #8, top of the head; kinematics

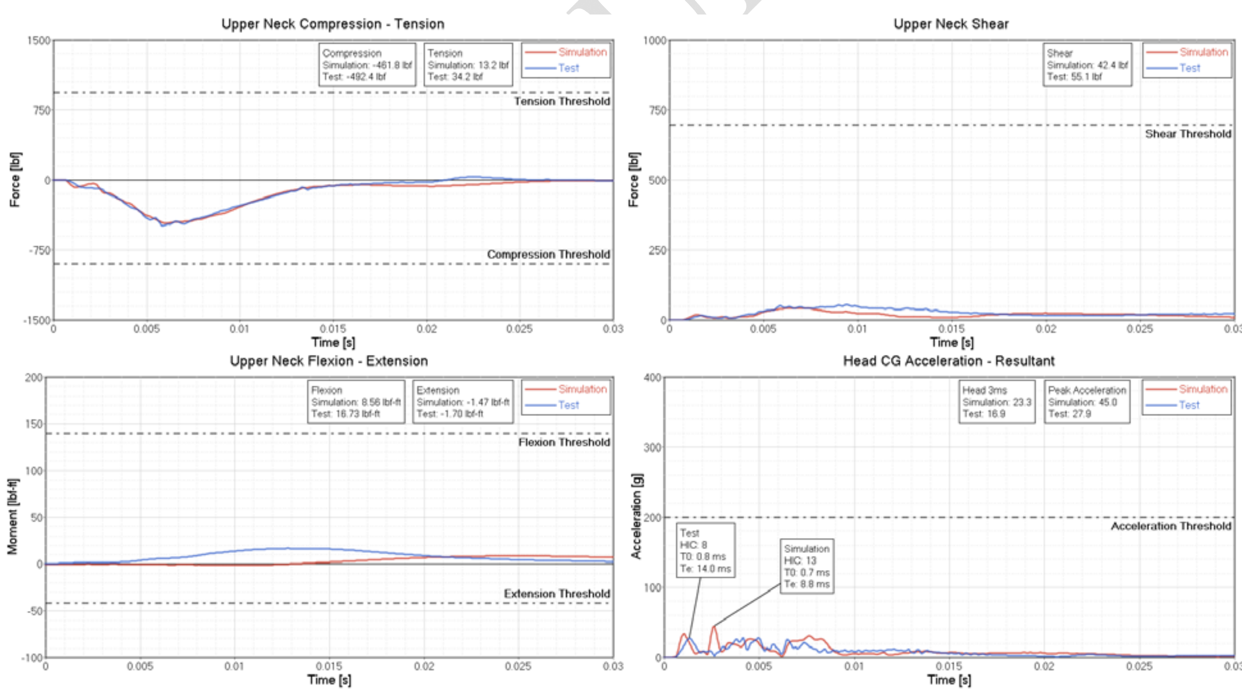

Figure 245. Test vs simulation comparison; DJI Phantom 3, 2.54 lb, bottom, 36 fps, vertical; A14 ATD test #8, top of the head; neck loads, and head acceleration

Test 9: DJI Phantom 3, 2.54 lb, side, 36 fps, horizontal; A14 ATD, side of the head

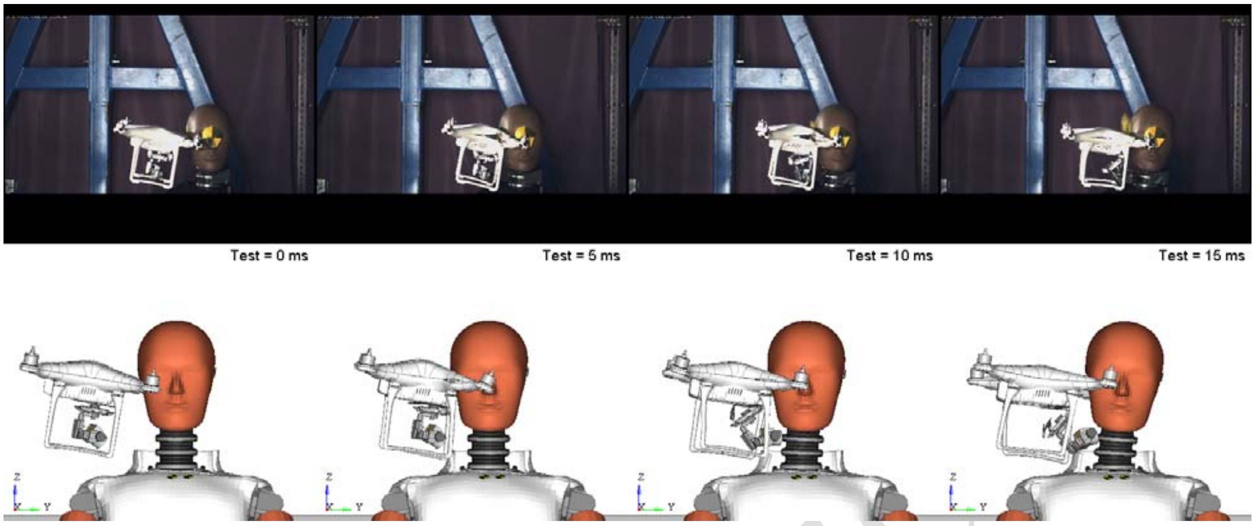

Figure 246. Test vs simulation comparison; DJI Phantom 3, 2.54 lb, side, 36 fps, horizontal; A14 ATD test #9, side of the head; kinematics

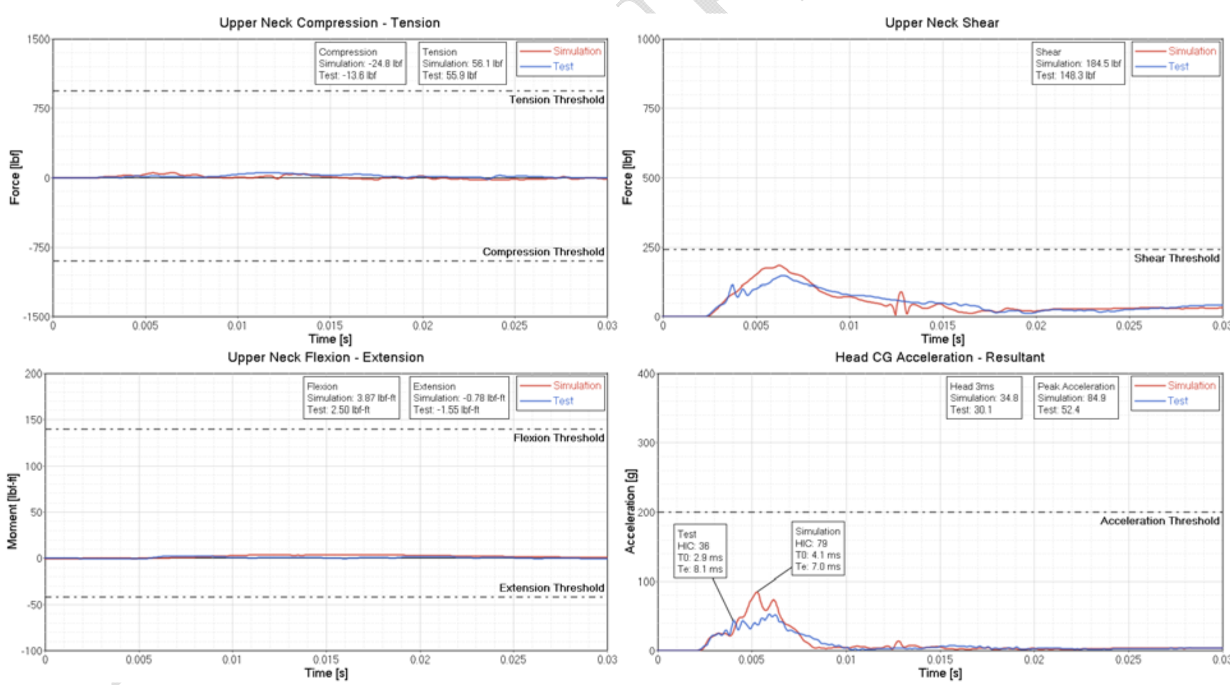

Figure 247. Test vs simulation comparison; DJI Phantom 3, 2.54 lb, side, 36 fps, horizontal; A14 ATD test #9, side of the head; neck loads, and head acceleration

<u>Test 10: DJI Phantom 3, 2.54 lb, side, 55 fps, horizontal; A14 ATD, side of the head</u>

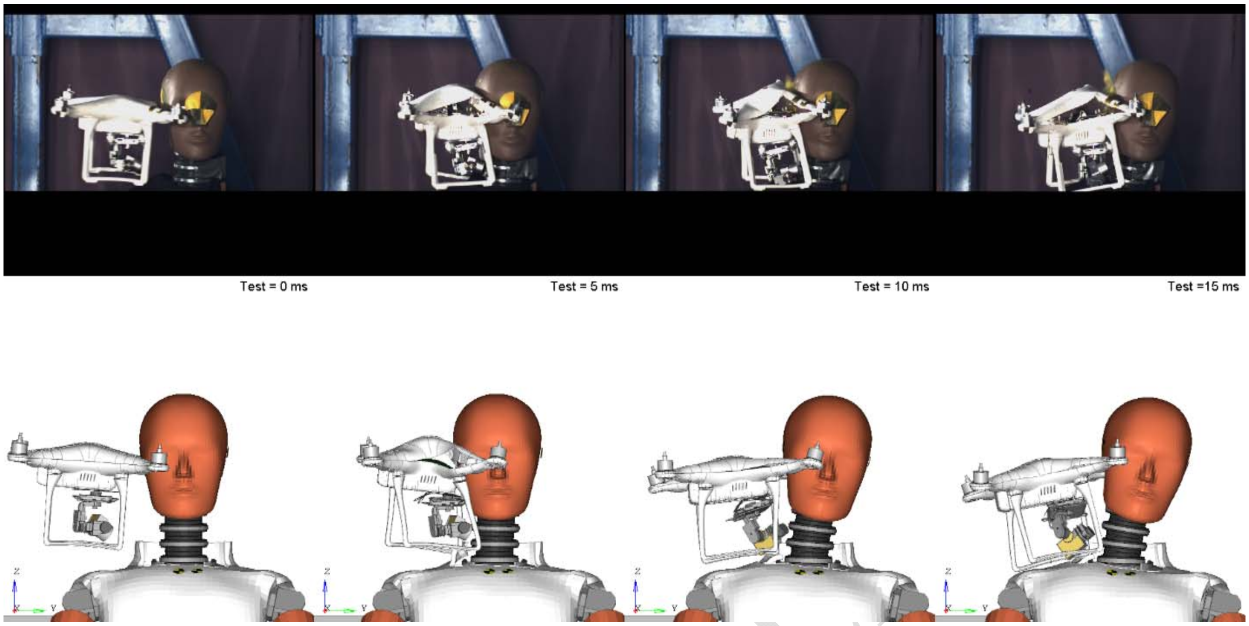

Figure 248. Test vs simulation comparison; DJI Phantom 3, 2.54 lb, side, 55 fps, horizontal; A14 ATD test #10, side of the head; kinematics

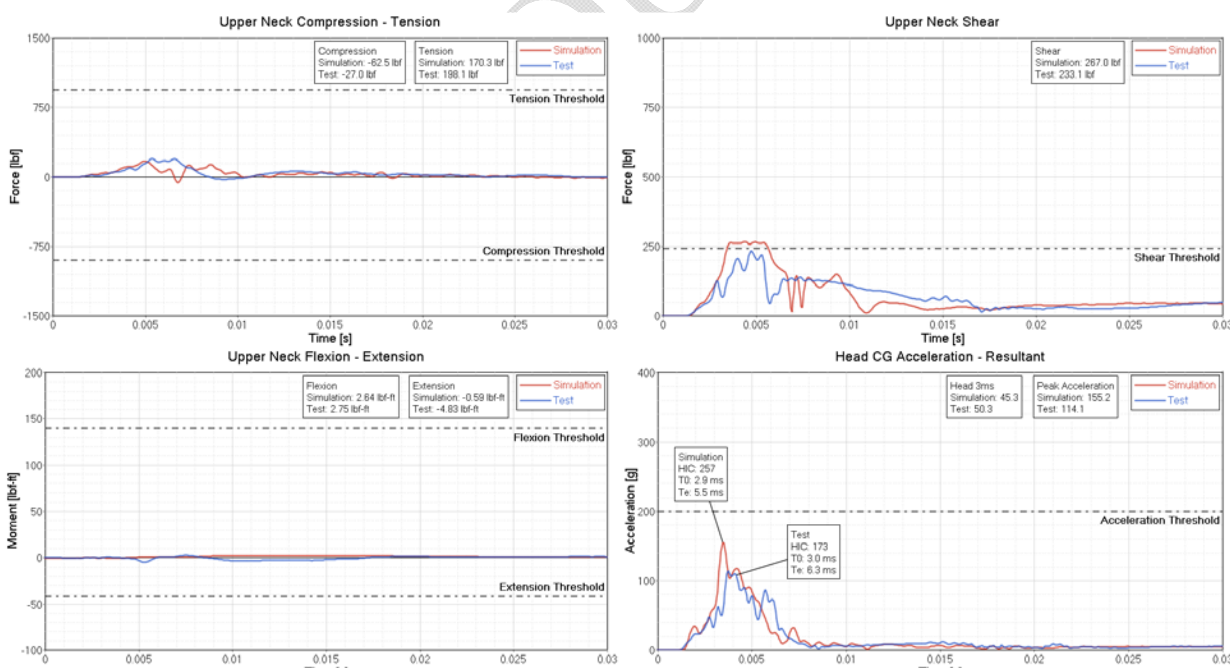

Figure 249. Test vs simulation comparison; DJI Phantom 3, 2.54 lb, side, 55 fps, horizontal; A14 ATD test #10, side of the head; neck loads, and head acceleration

Test 11: DJI Phantom 3, 2.54 lb, side, 61 fps, horizontal; A14 ATD, side of the head

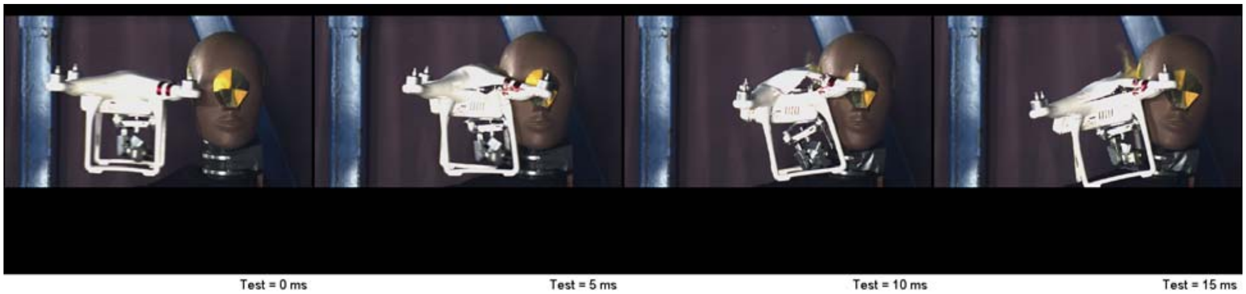

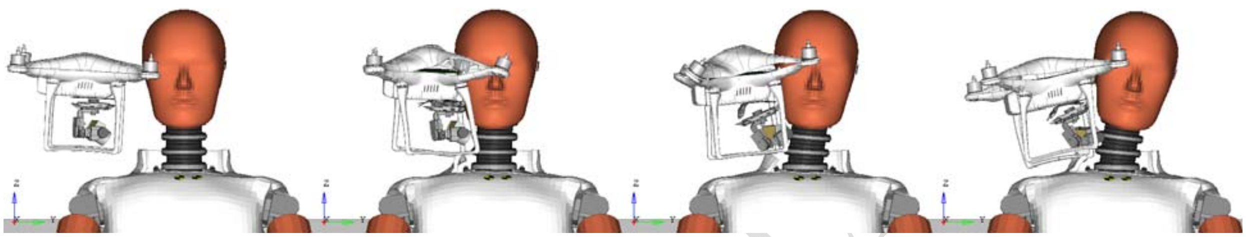

Figure 250. Test vs simulation comparison; DJI Phantom 3, 2.54 lb, side, 61 fps, horizontal; A14 ATD test #11, side of the head; kinematics

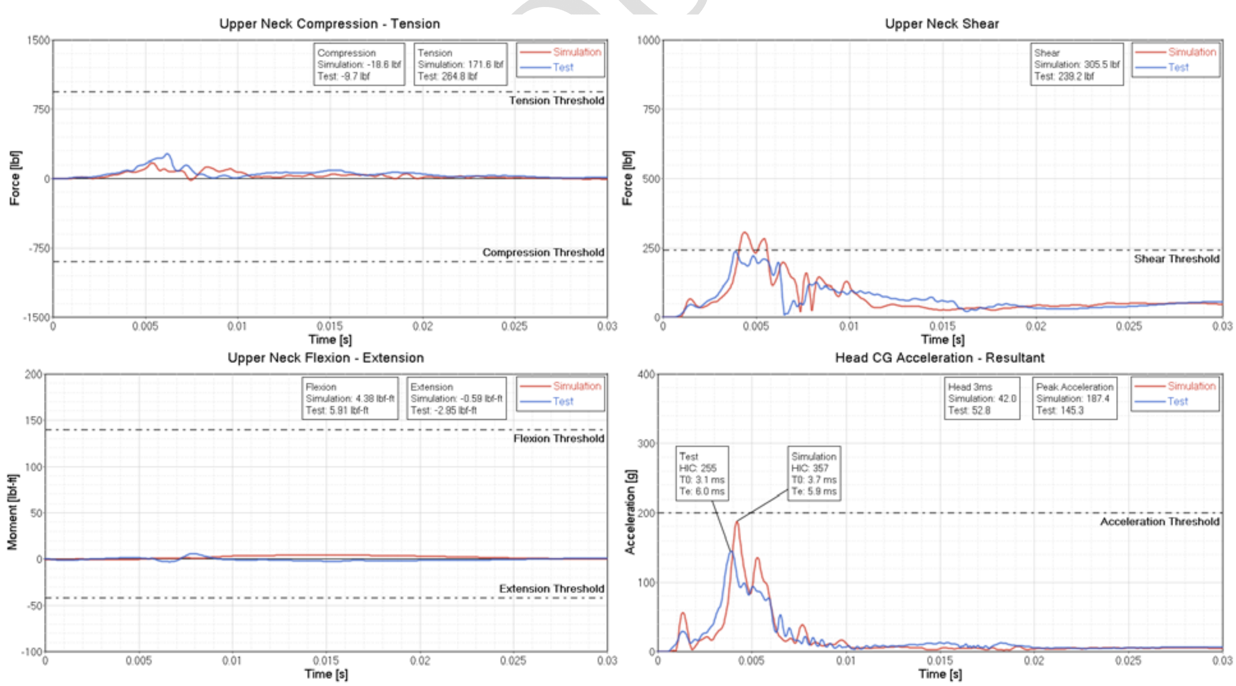

Figure 251. Test vs simulation comparison; DJI Phantom 3, 2.54 lb, side, 61 fps, horizontal; A14 ATD test #11, side of the head; neck loads, and head acceleration

Test 12: DJI Phantom 3, 2.54 lb, side, 65 fps, horizontal; A14 ATD, side of the head

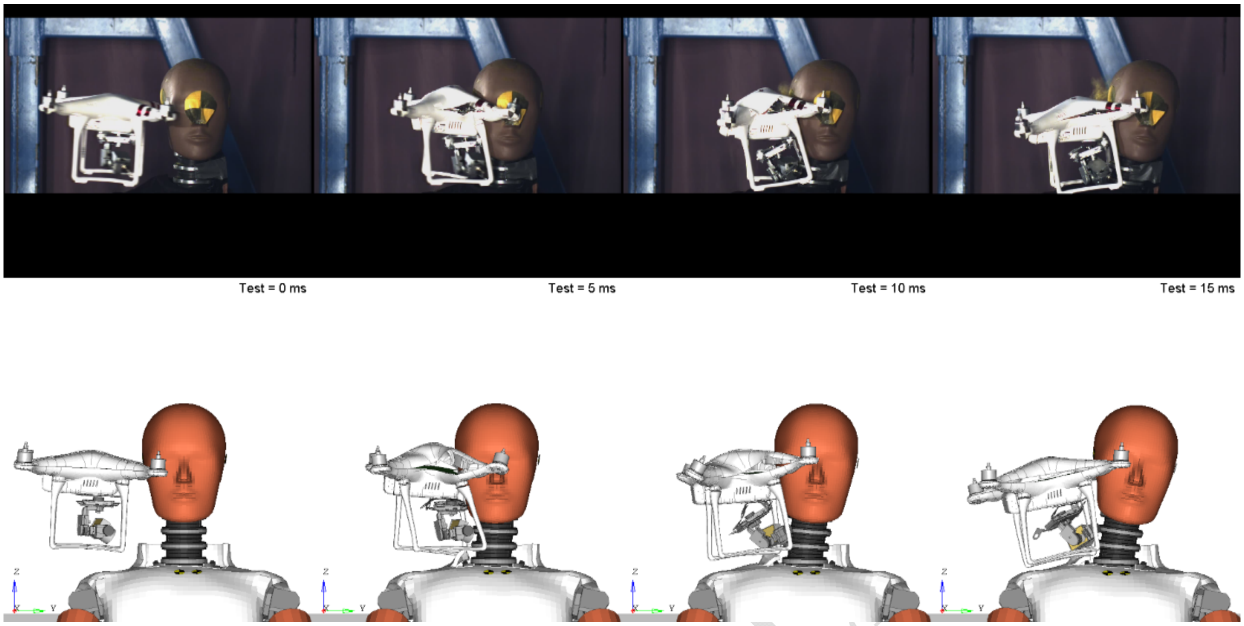

Figure 252. Test vs simulation comparison; DJI Phantom 3, 2.54 lb, side, 65 fps, horizontal; A14 ATD test #12, side of the head; kinematics

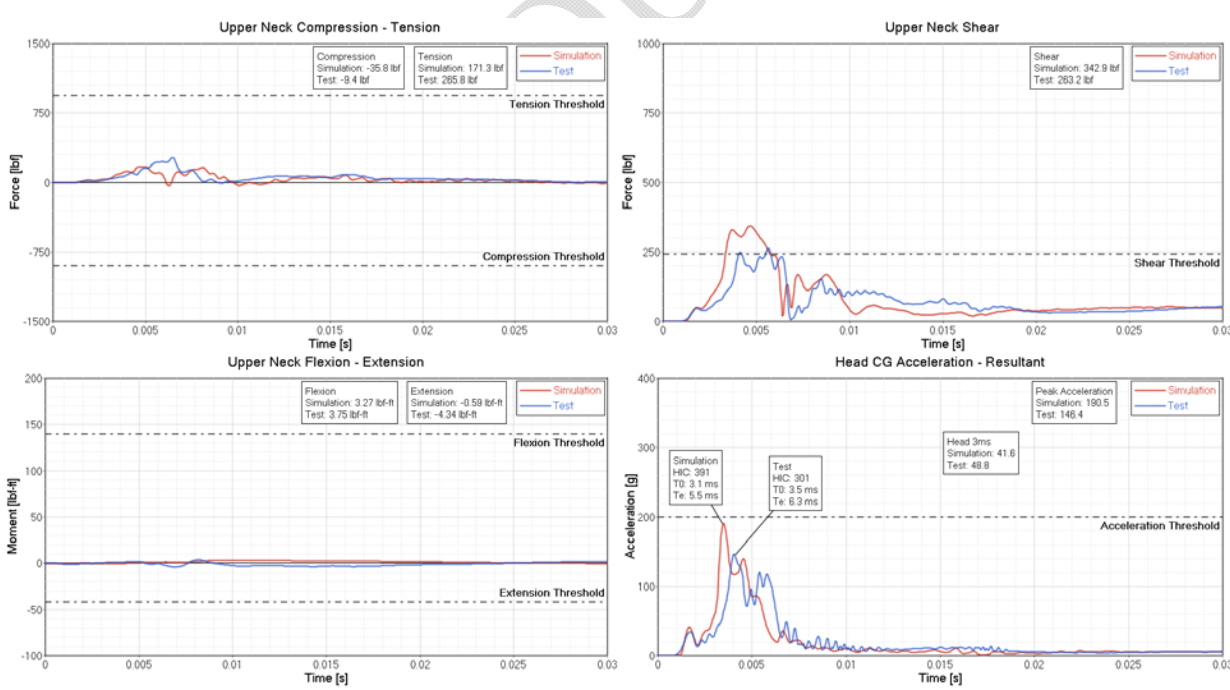

Figure 253. Test vs simulation comparison; DJI Phantom 3, 2.54 lb, side, 65 fps, horizontal; A14 ATD test #12, side of the head; neck loads, and head acceleration

Test 13: DJI Phantom 3, 2.54 lb, side, 55 fps, vertical; A14 ATD, top of the head

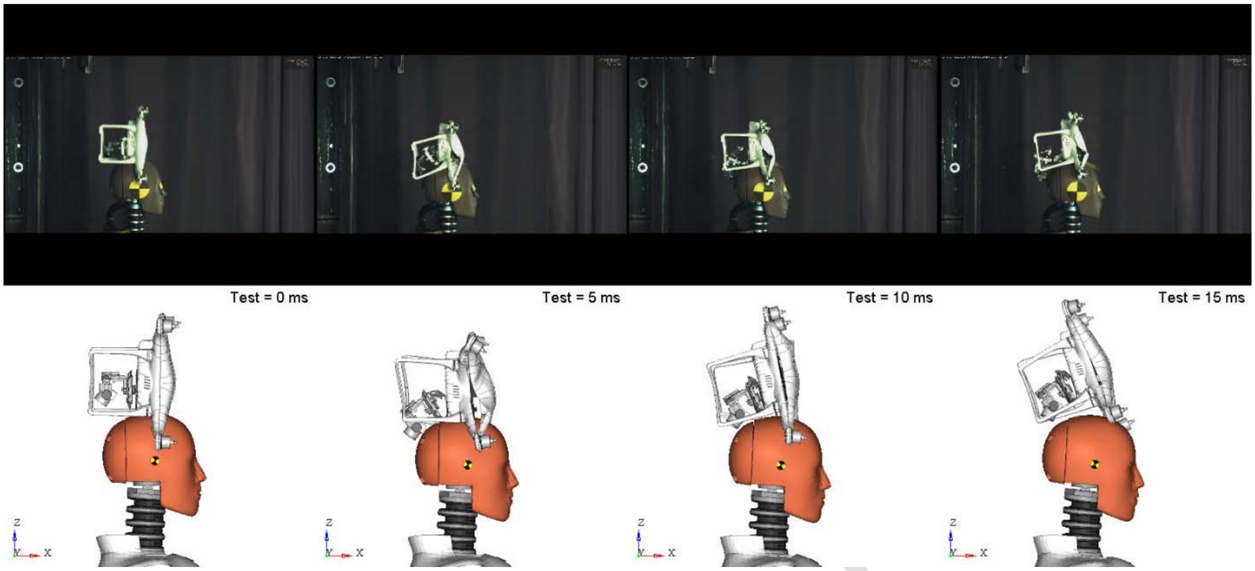

Figure 254. Test vs simulation comparison; DJI Phantom 3, 2.54 lb, side, 55 fps, vertical; A14 ATD test #13, top of the head; kinematics

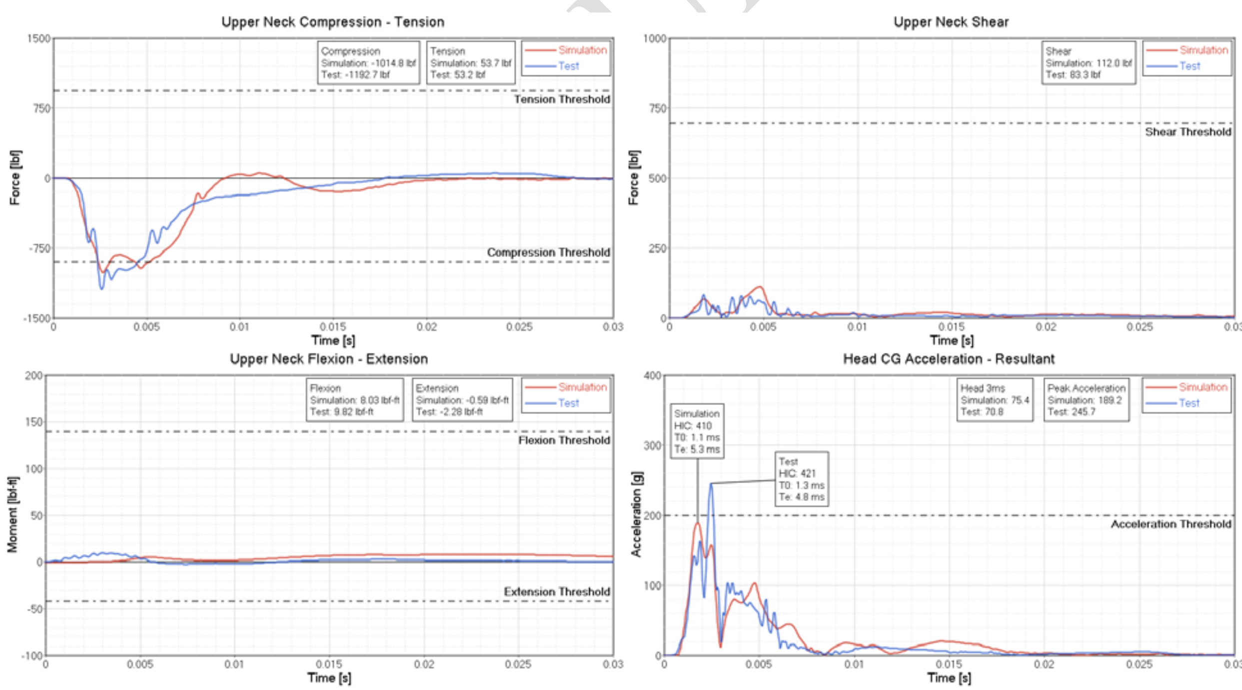

Figure 255. Test vs simulation comparison; DJI Phantom 3, 2.54 lb, side, 55 fps, vertical; A14 ATD test #13, top of the head; neck loads, and head acceleration

Test 14: DJI Phantom 3, 2.54 lb, side, 65 fps, vertical; A14 ATD, top of the head

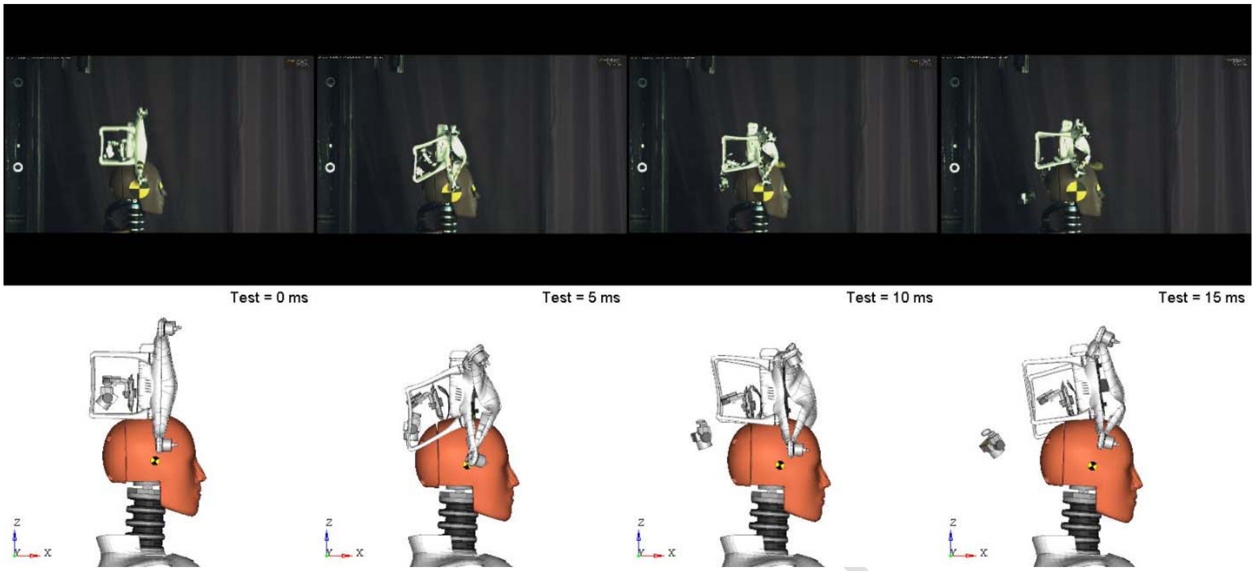

Figure 256. Test vs simulation comparison; DJI Phantom 3, 2.54 lb, side, 65 fps, vertical; A14 ATD test #14, top of the head; kinematics

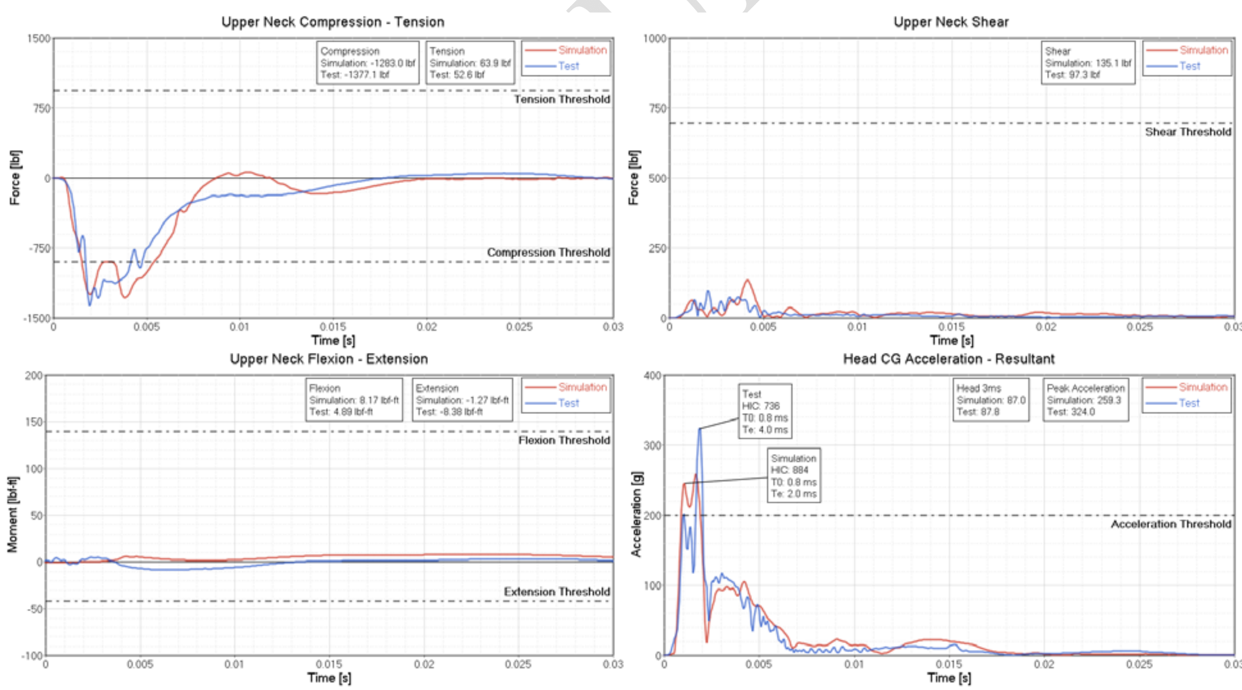

Figure 257. Test vs simulation comparison; DJI Phantom 3, 2.54 lb, side, 65 fps, vertical; A14 ATD test #14, top of the head; neck loads, and head acceleration

Test 15: DJI Phantom 3, 2.54 lb, side, 56 fps, 58 deg angle; A14 ATD, front of the head

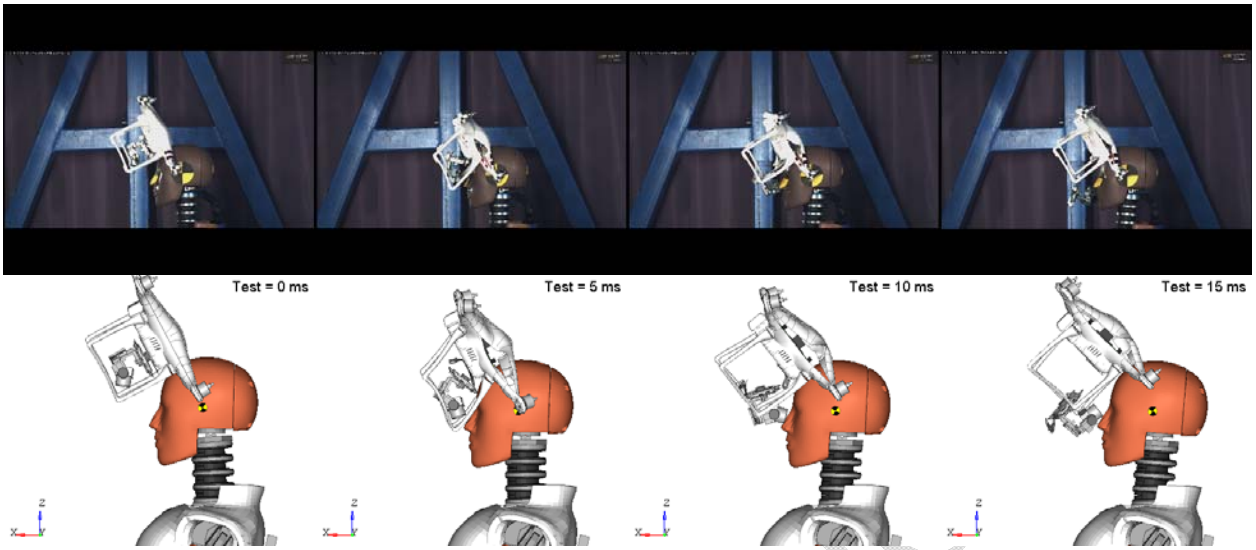

Figure 258. Test vs simulation comparison; DJI Phantom 3, 2.54 lb, side, 56 fps, 58 deg; A14 ATD test #15, front of the head; kinematics

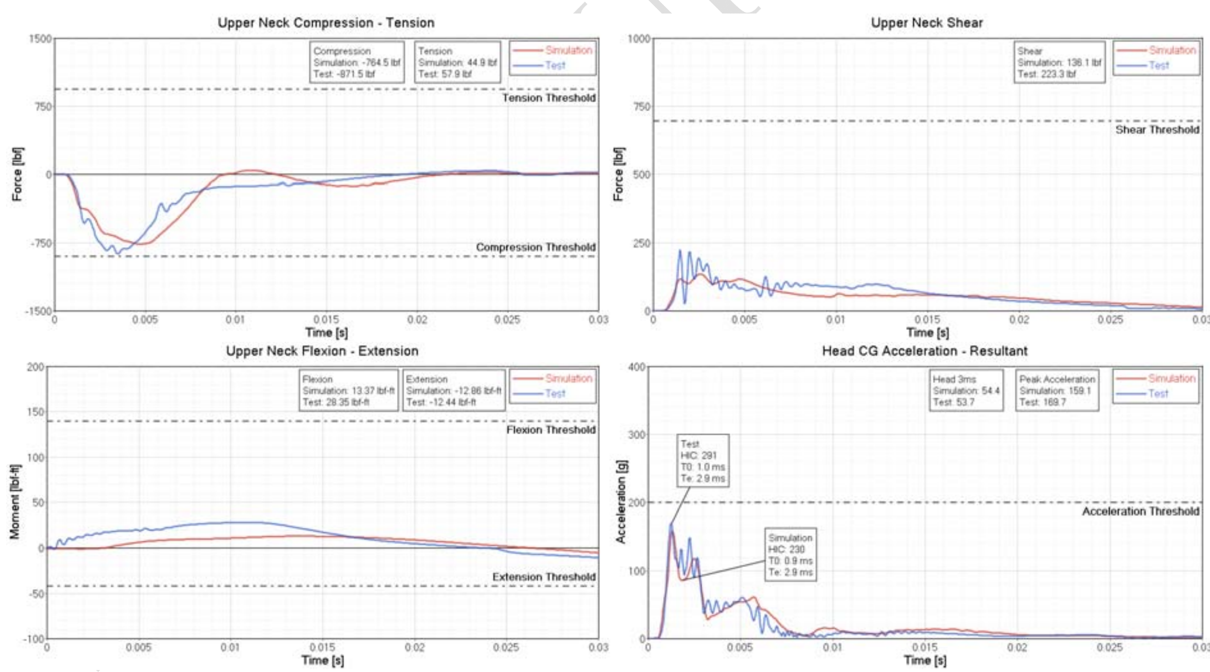

Figure 259. Test vs simulation comparison; DJI Phantom 3, 2.54 lb, side, 56 fps, 58 deg; A14 ATD test #15, front of the head; neck loads, and head acceleration

Test 16: DJI Phantom 3, 2.54 lb, side, 61 fps, 58 deg angle; A14 ATD, front of the head

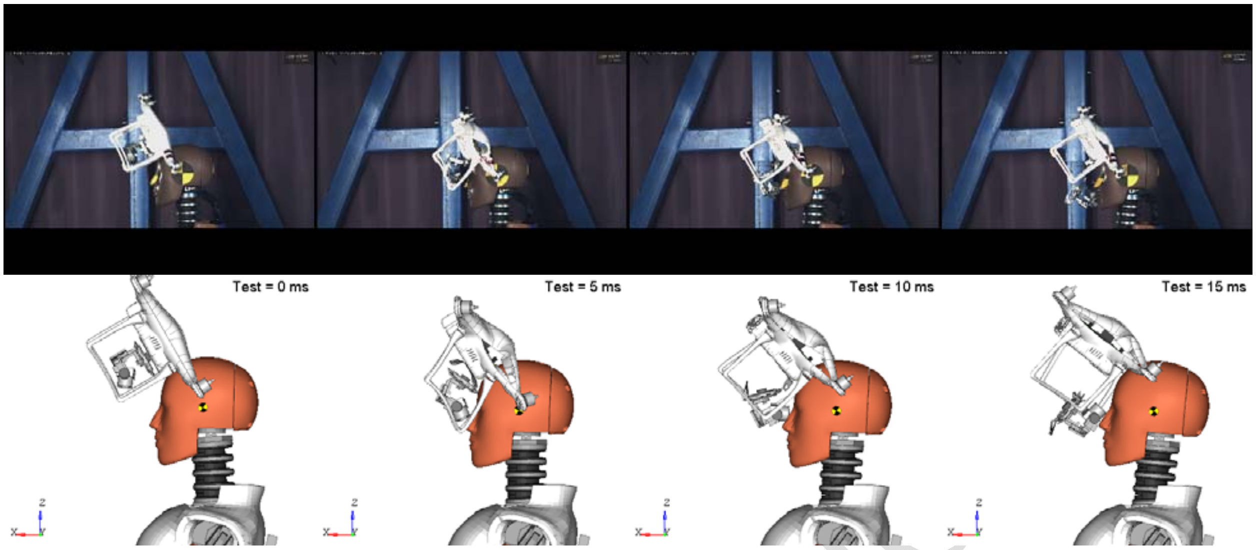

Figure 260. Test vs simulation comparison; DJI Phantom 3, 2.54 lb, side, 61 fps, 58 deg; A14 ATD test #16, front of the head; kinematics

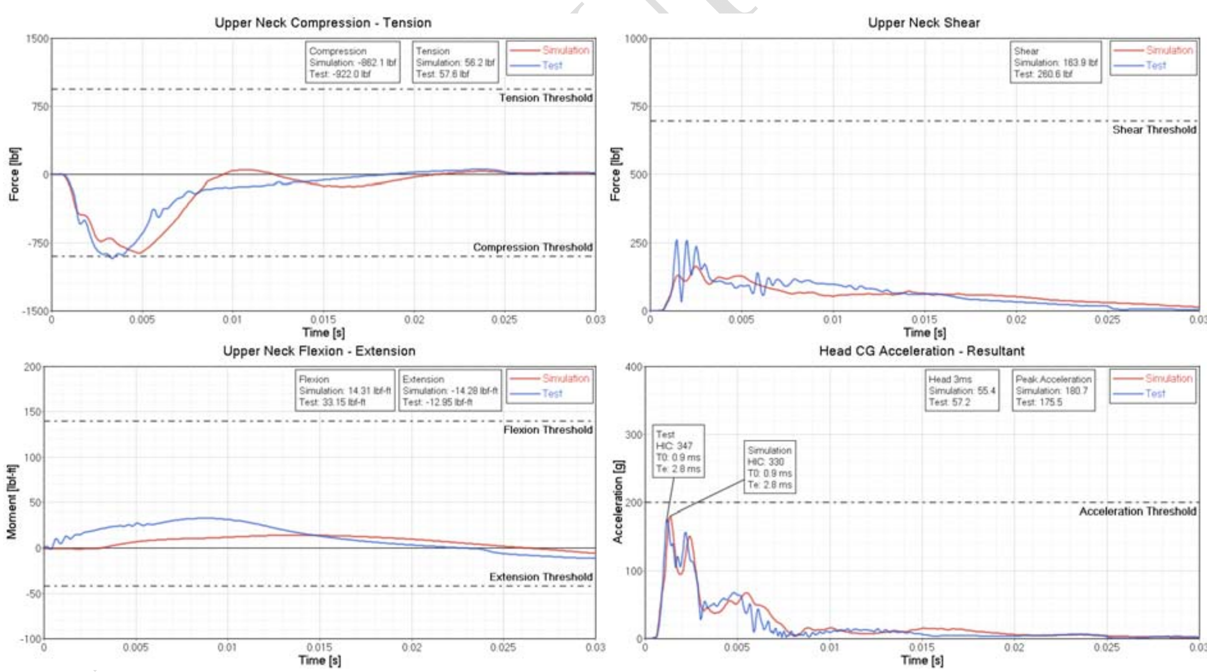

Figure 261. Test vs simulation comparison; DJI Phantom 3, 2.54 lb, side, 61 fps, 58 deg; A14 ATD test #16, front of the head; neck loads, and head acceleration

<u>Test 17: DJI Phantom 3, 2.54 lb, side, 65 fps, 58 deg angle; A14 ATD, front of the head</u>

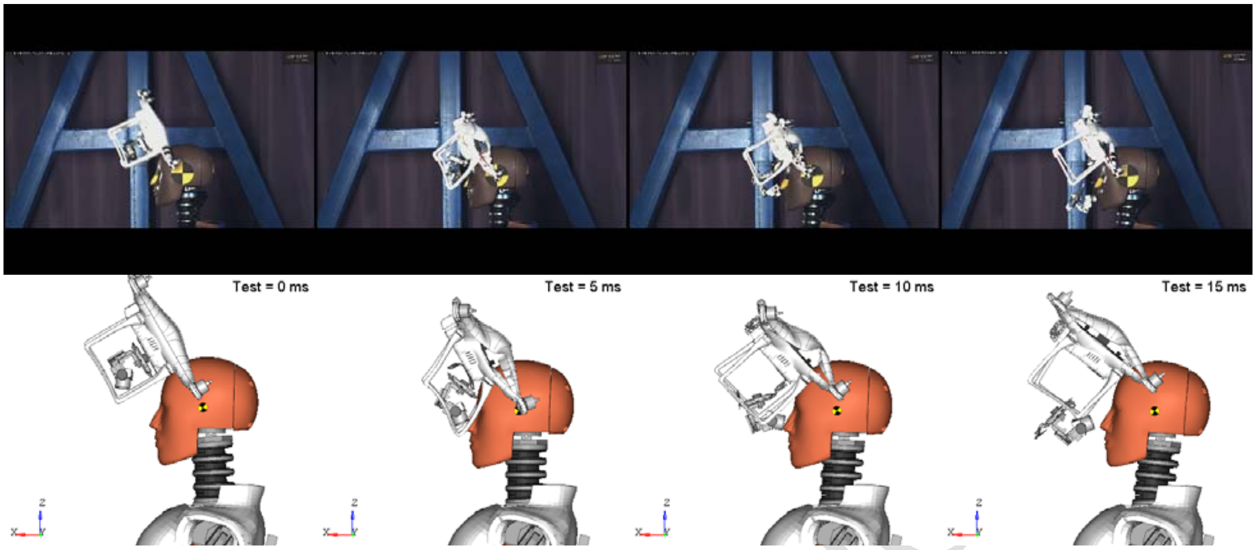

Figure 262. Test vs simulation comparison; DJI Phantom 3, 2.54 lb, side, 65 fps, 58 deg; A14 ATD test #17, front of the head; kinematics

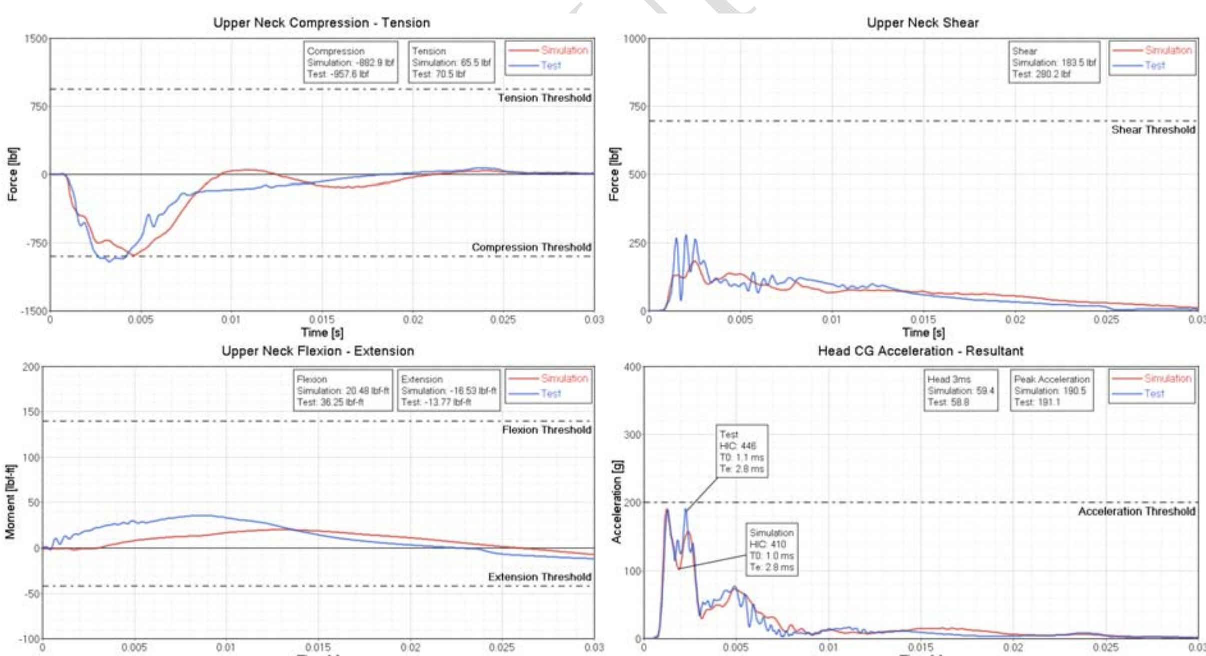

Figure 263. Test vs simulation comparison; DJI Phantom 3, 2.54 lb, side, 65 fps, 58 deg; A14 ATD test #17, front of the head; neck loads, and head acceleration

Test 18: DJI Phantom 3, 2.54 lb, side, 56 fps, 58 deg angle; A14 ATD, back of the head

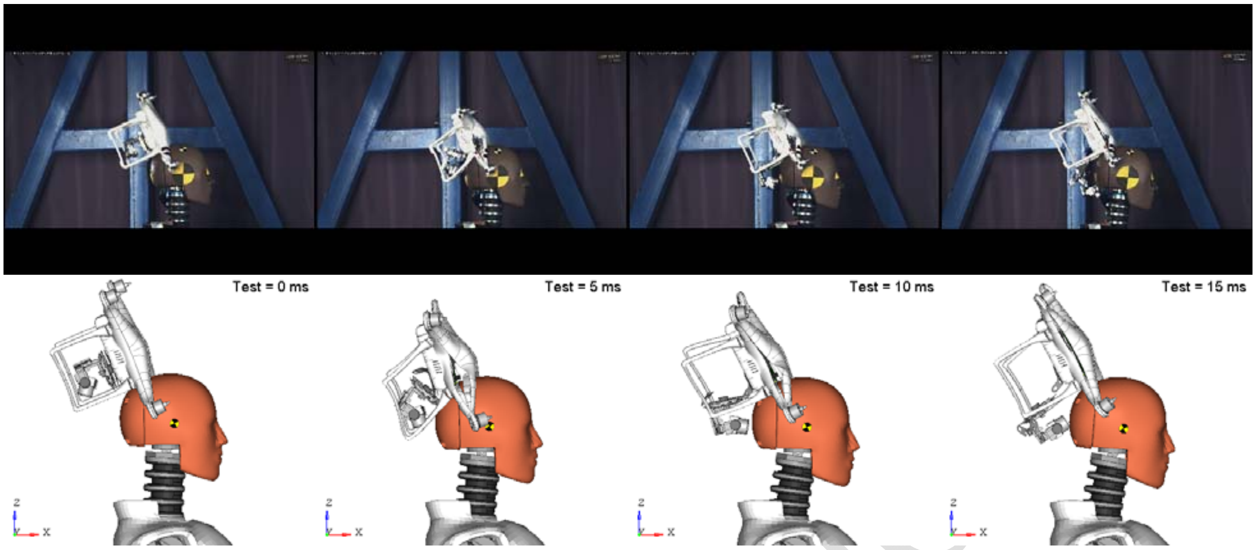

Figure 264. Test vs simulation comparison; DJI Phantom 3, 2.54 lb, side, 56 fps, 58 deg; A14 ATD test #18, back of the head; kinematics

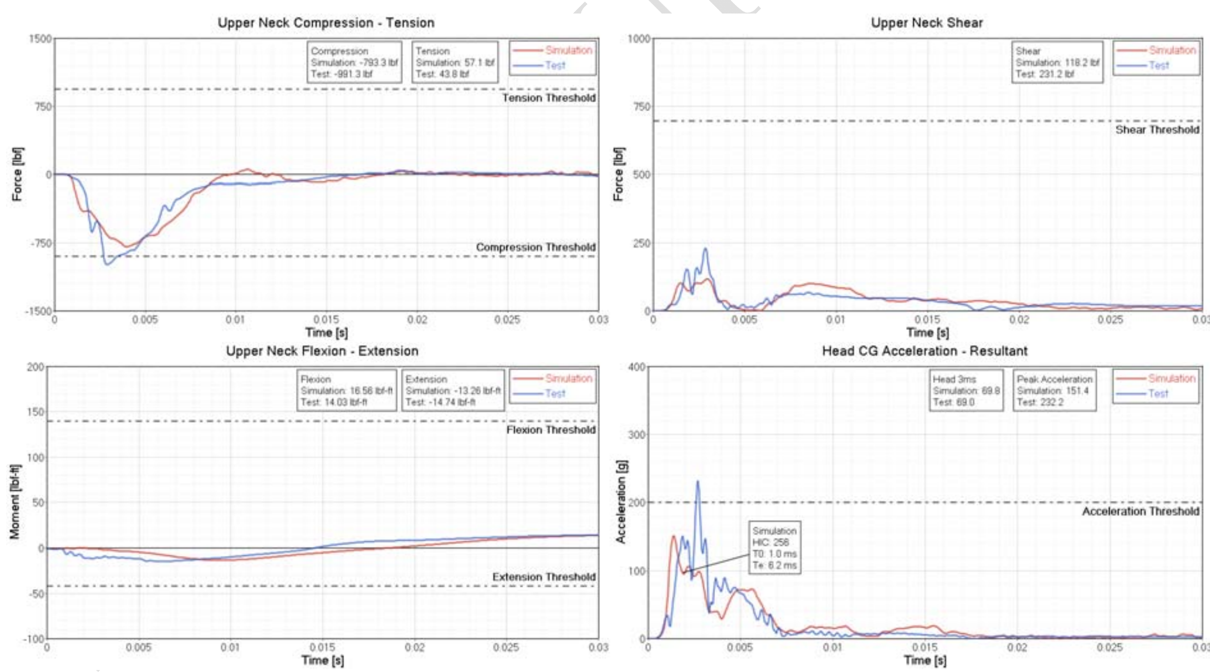

Figure 265. Test vs simulation comparison; DJI Phantom 3, 2.54 lb, side, 56 fps, 58 deg; A14 ATD test #18, back of the head; neck loads, and head acceleration

Test 19: DJI Phantom 3, 2.54 lb, side, 61 fps, 58 deg angle; A14 ATD, back of the head

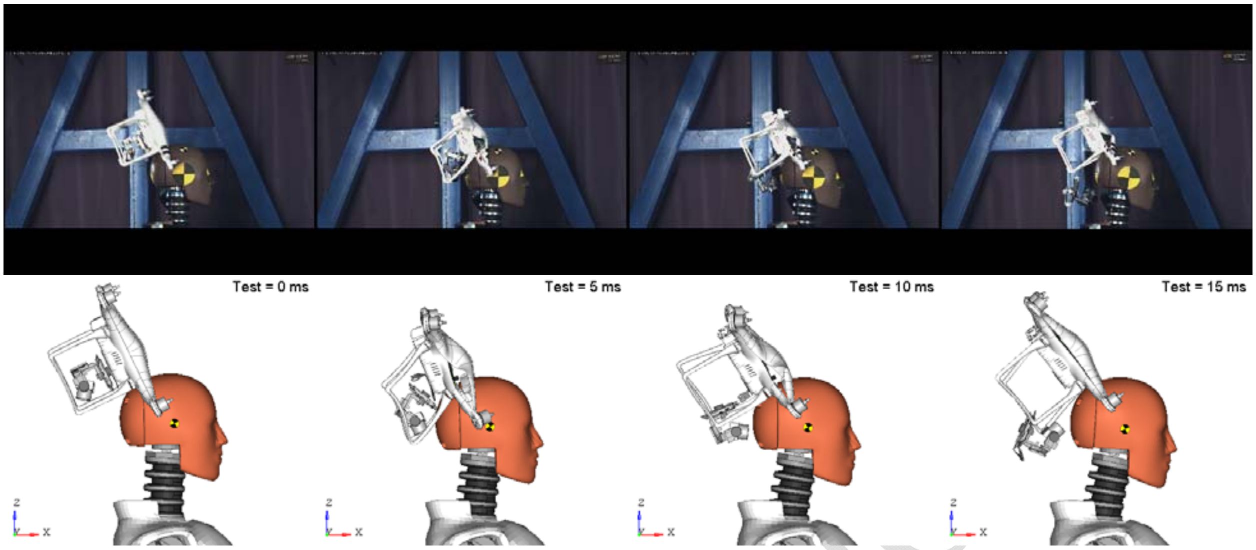

Figure 266. Test vs simulation comparison; DJI Phantom 3, 2.54 lb, side, 61 fps, 58 deg; A14 ATD test #19, back of the head; kinematics

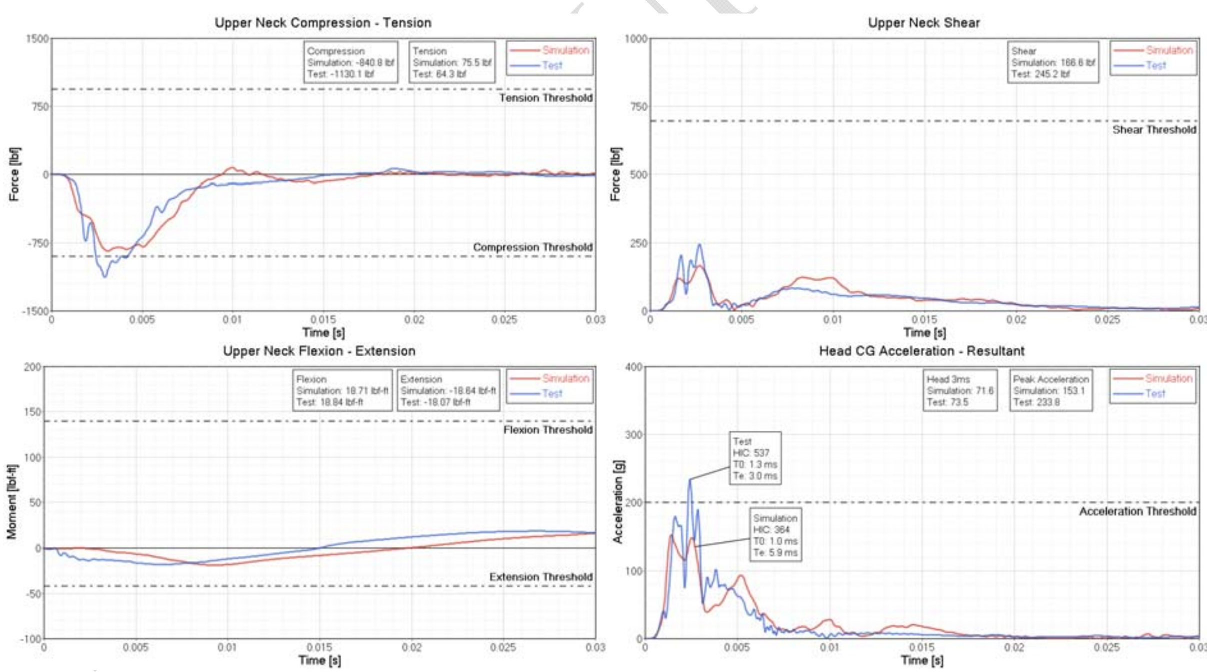

Figure 267. Test vs simulation comparison; DJI Phantom 3, 2.54 lb, side, 61 fps, 58 deg; A14 ATD test #19, back of the head; neck loads, and head acceleration

Test 20: DJI Phantom 3, 2.54 lb, side, 65 fps, 58 deg angle; A14 ATD, back of the head

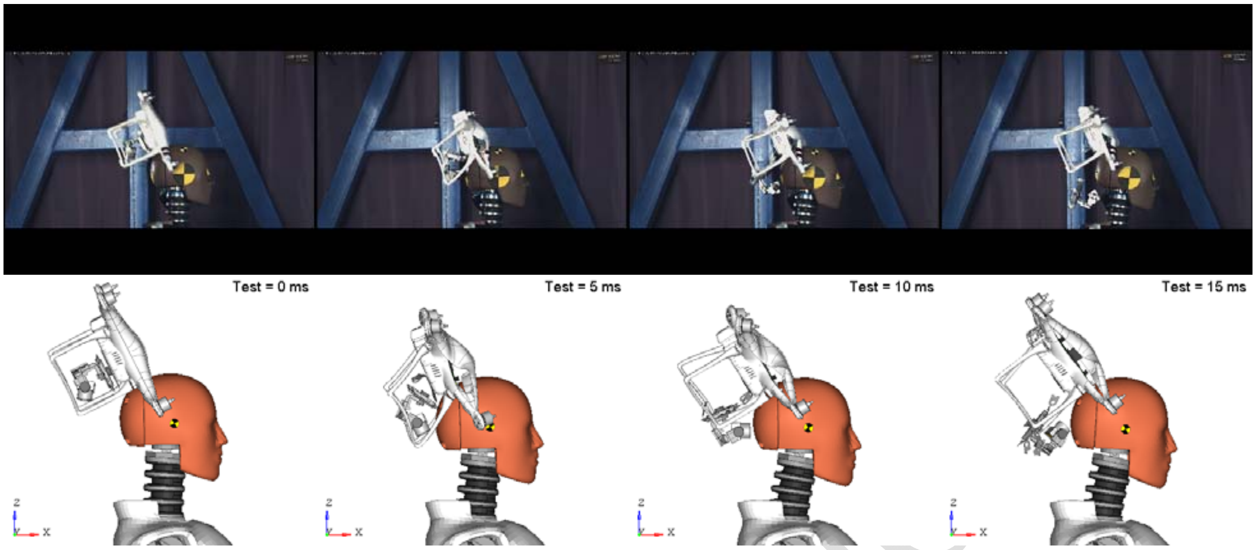

Figure 268. Test vs simulation comparison; DJI Phantom 3, 2.54 lb, side, 65 fps, 58 deg; A14 ATD test #20, back of the head; kinematics

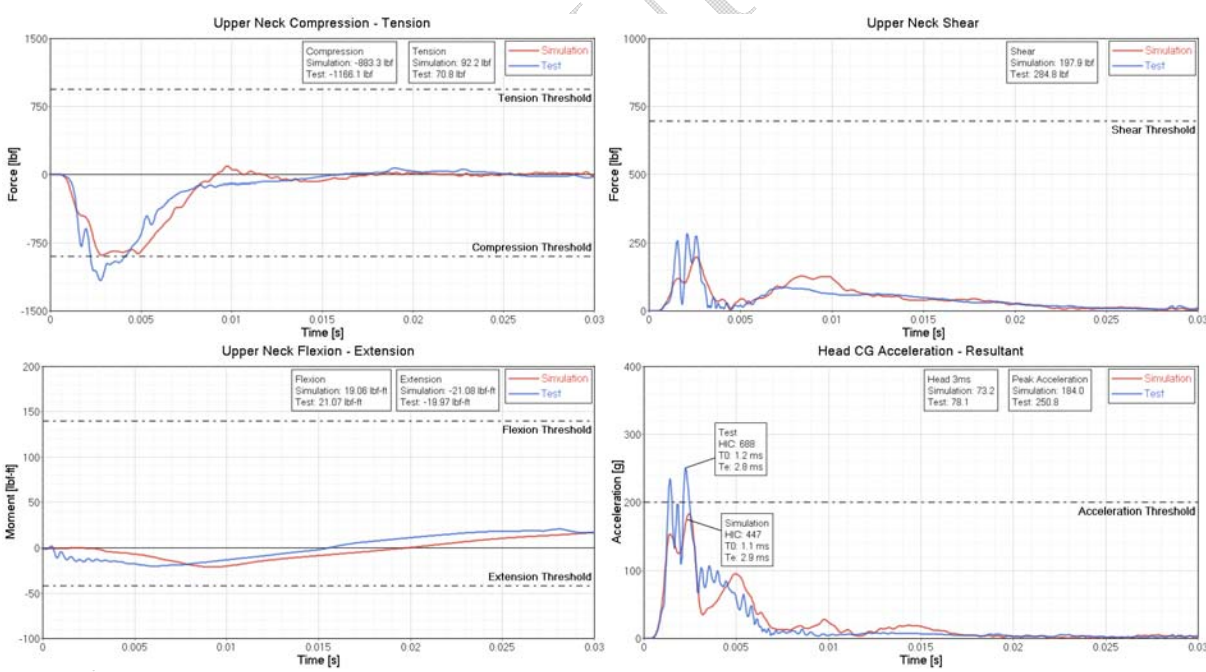

Figure 269. Test vs simulation comparison; DJI Phantom 3, 2.54 lb, side, 65 fps, 58 deg; A14 ATD test #20, back of the head; neck loads, and head acceleration

Test 21: DJI Phantom 3, 2.54 lb, side, 36 fps, 58 deg angle; A14 ATD, side of the head

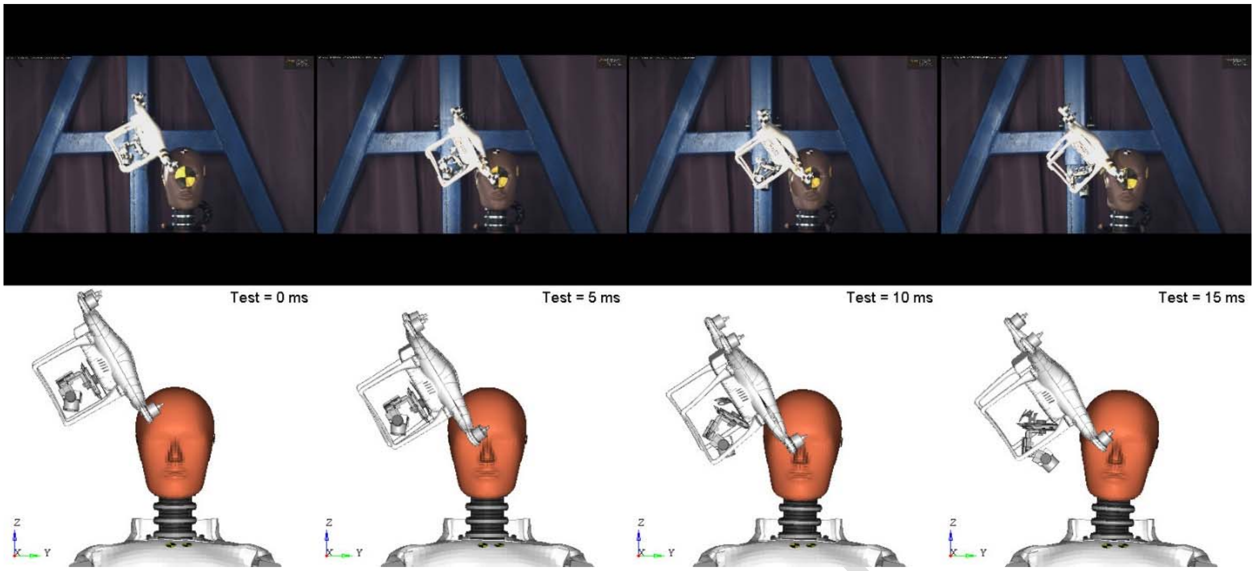

Figure 270. Test vs simulation comparison; DJI Phantom 3, 2.54 lb, side, 36 fps, 58 deg; A14 ATD test #21, side of the head; kinematics

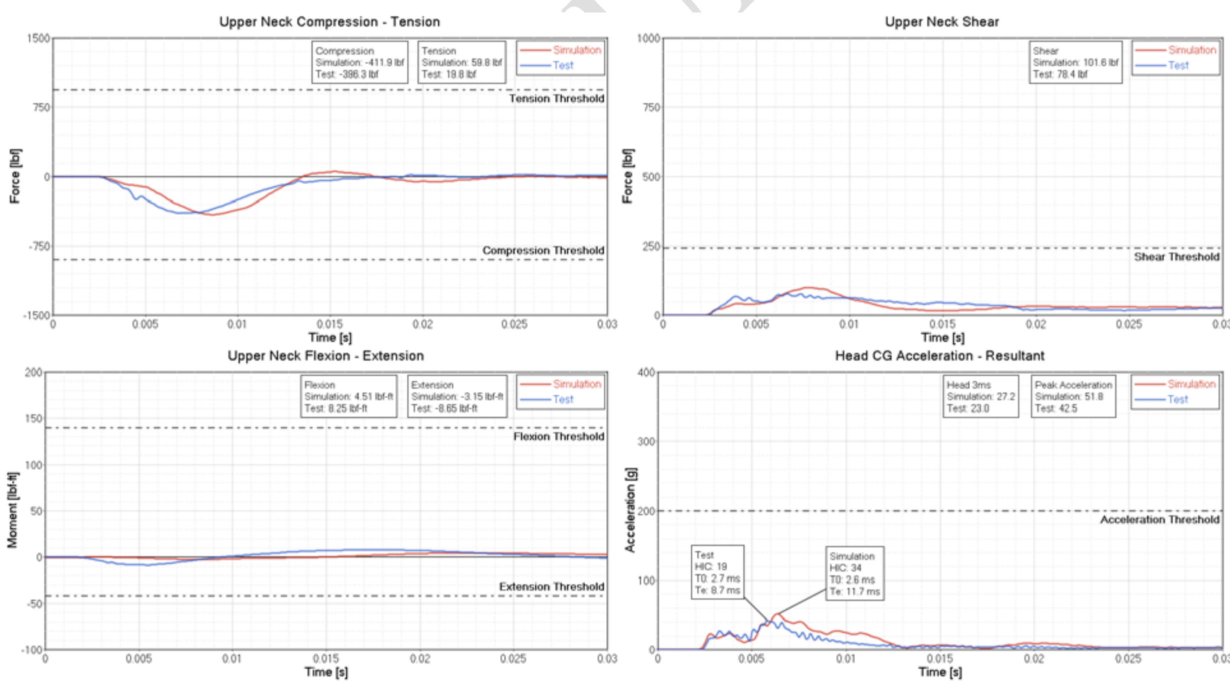

Figure 271. Test vs simulation comparison; DJI Phantom 3, 2.54 lb, side, 36 fps, 58 deg; A14 ATD test #21, side of the head; neck loads, and head acceleration

Test 22: DJI Phantom 3, 2.54 lb, side, 56 fps, 58 deg angle; A14 ATD, side of the head

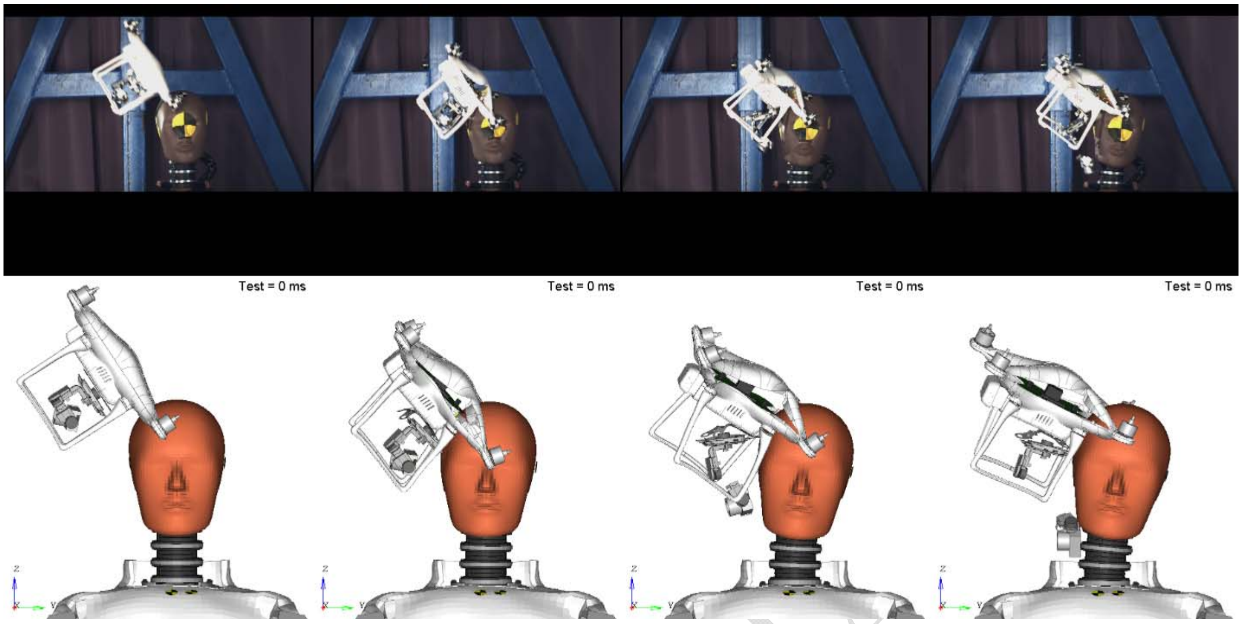

Figure 272. Test vs simulation comparison; DJI Phantom 3, 2.54 lb, side, 56 fps, 58 deg; A14 ATD test #22, side of the head; kinematics

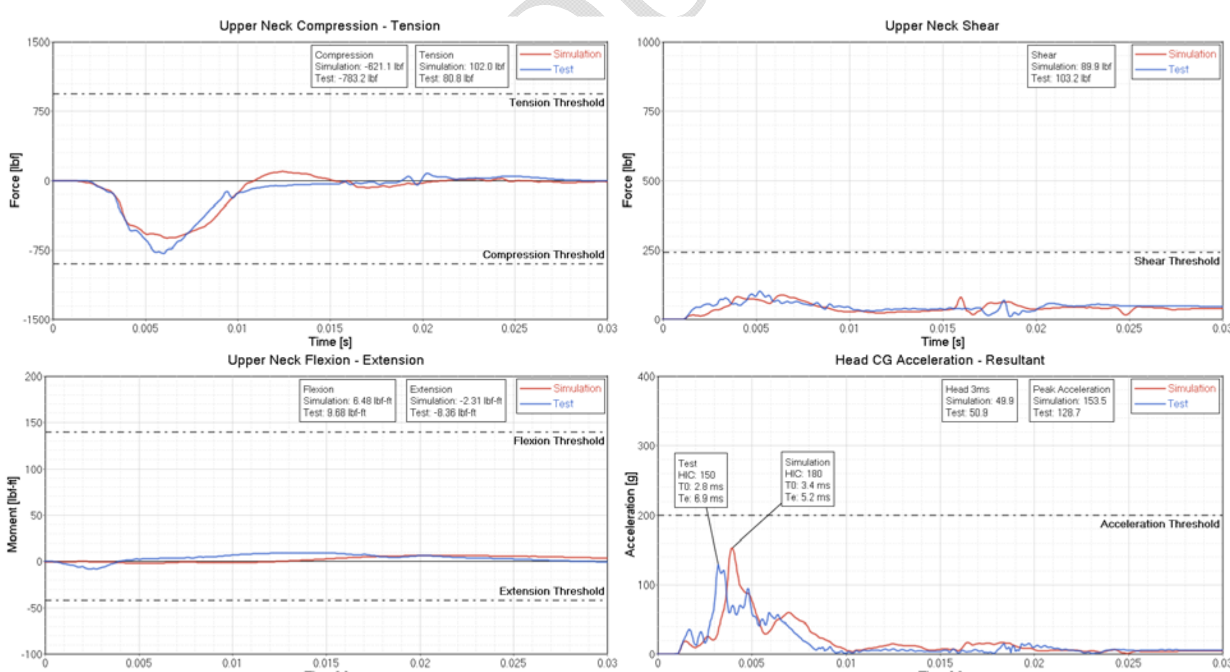

Figure 273. Test vs simulation comparison; DJI Phantom 3, 2.54 lb, side, 56 fps, 58 deg; A14 ATD test #22, side of the head; neck loads, and head acceleration

Test 23: DJI Phantom 3, 2.54 lb, side, 61 fps, 58 deg angle; A14 ATD, side of the head

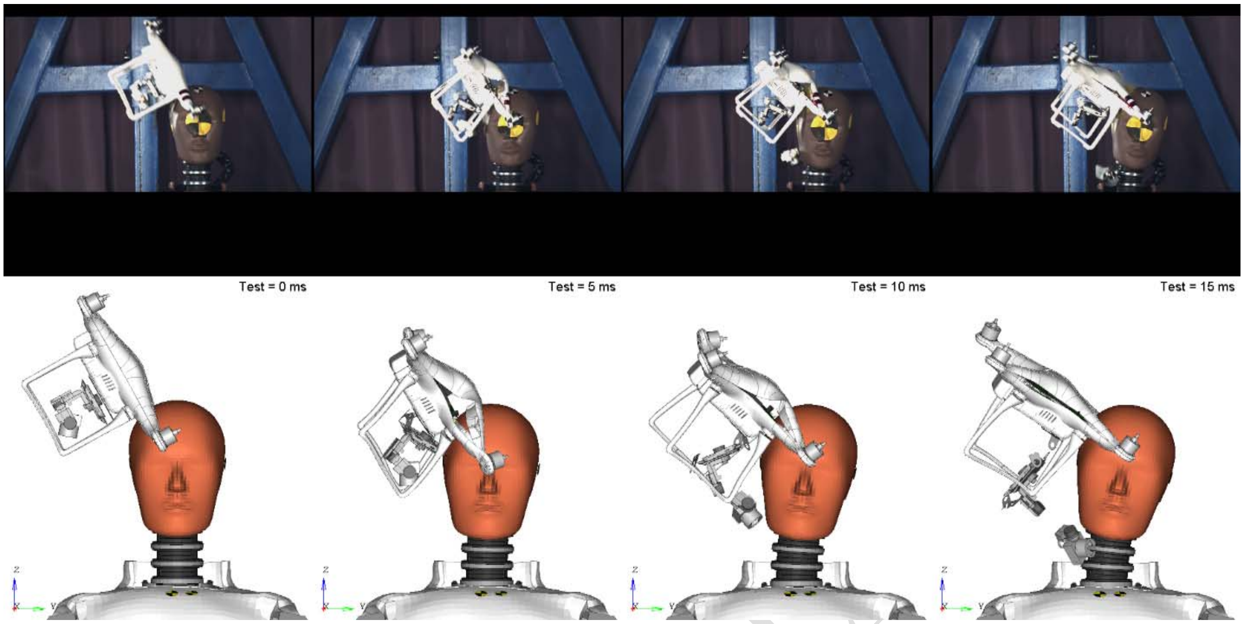

Figure 274. Test vs simulation comparison; DJI Phantom 3, 2.54 lb, side, 61 fps, 58 deg; A14 ATD test #23, side of the head; kinematics

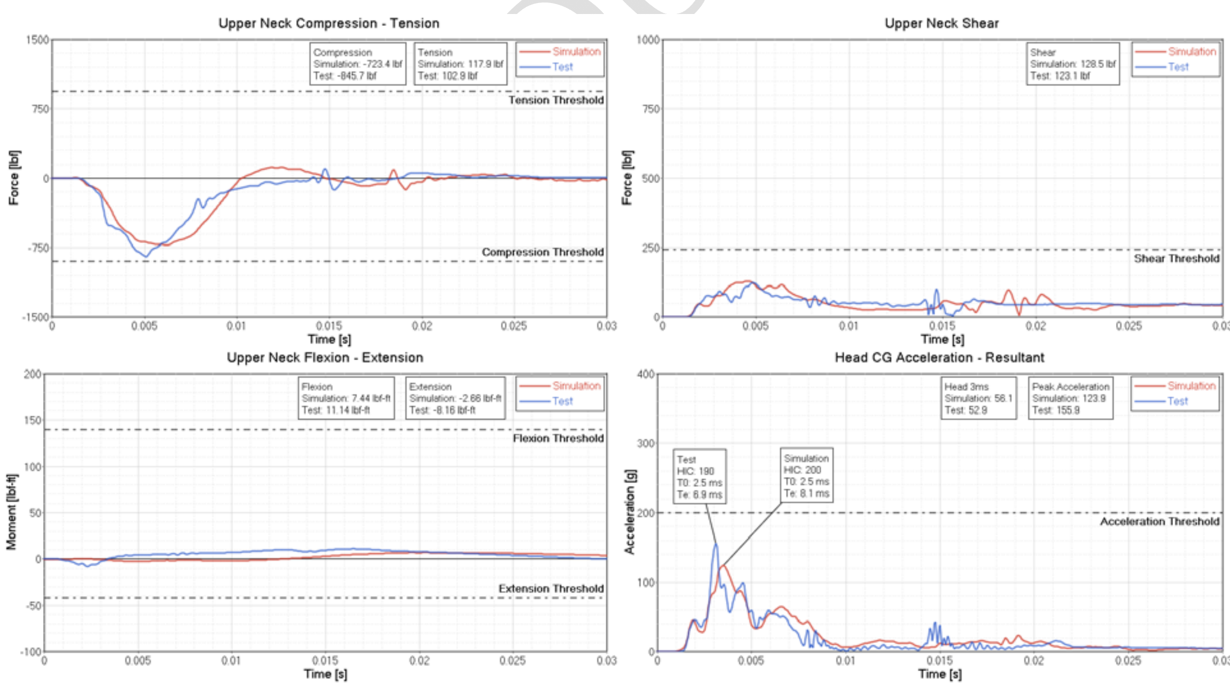

Figure 275. Test vs simulation comparison; DJI Phantom 3, 2.54 lb, side, 61 fps, 58 deg; A14 ATD test #23, side of the head; neck loads, and head acceleration

Test 24: DJI Phantom 3, 2.54 lb, side, 65 fps, 58 deg angle; A14 ATD, side of the head

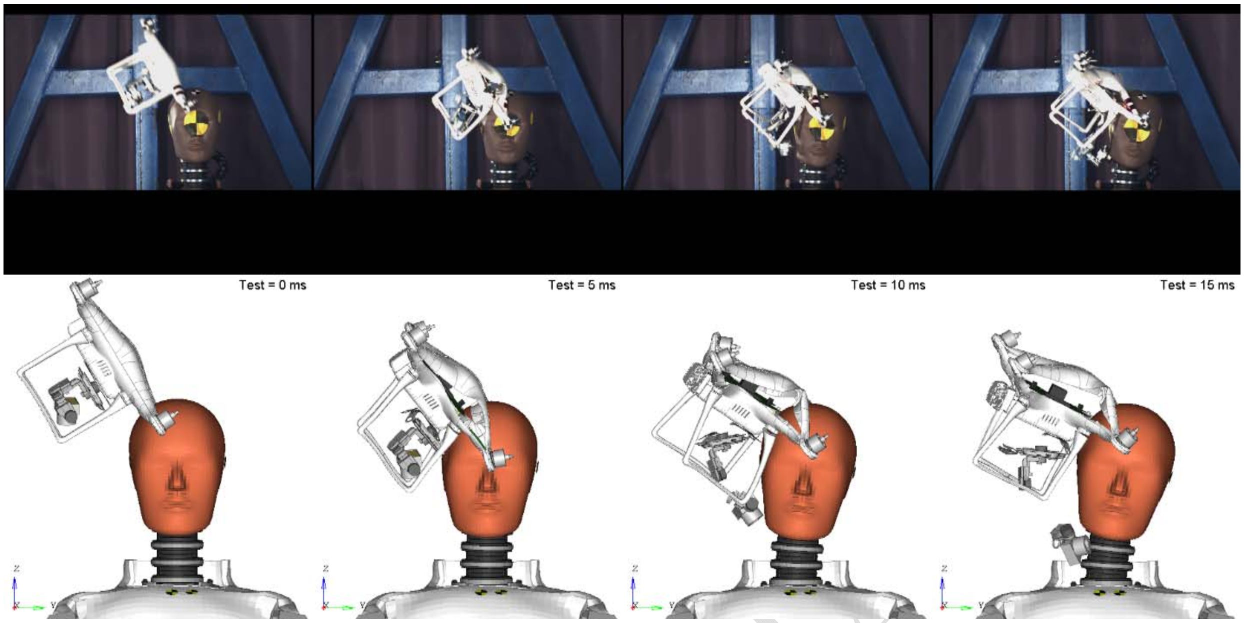

Figure 276. Test vs simulation comparison; DJI Phantom 3, 2.54 lb, side, 65 fps, 58 deg; A14 ATD test #24, side of the head; kinematics

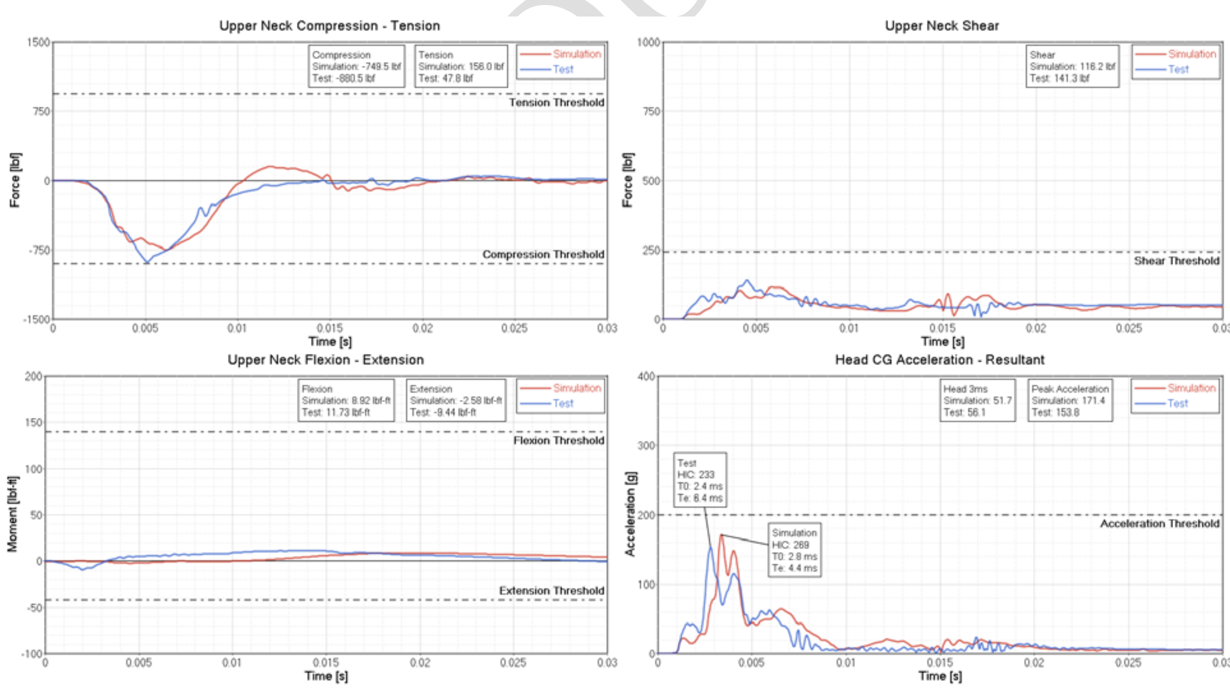

Figure 277. Test vs simulation comparison; DJI Phantom 3, 2.54 lb, side, 65 fps, 58 deg; A14 ATD test #24, side of the head; neck loads, and head acceleration

APPENDIX F—EBEE PLUS MODEL EVALUATION WITH ATD TESTS

Test 25: eBeePlus, 2.4 lb, nose, 50 fps, vertical; A14 ATD, top of the head

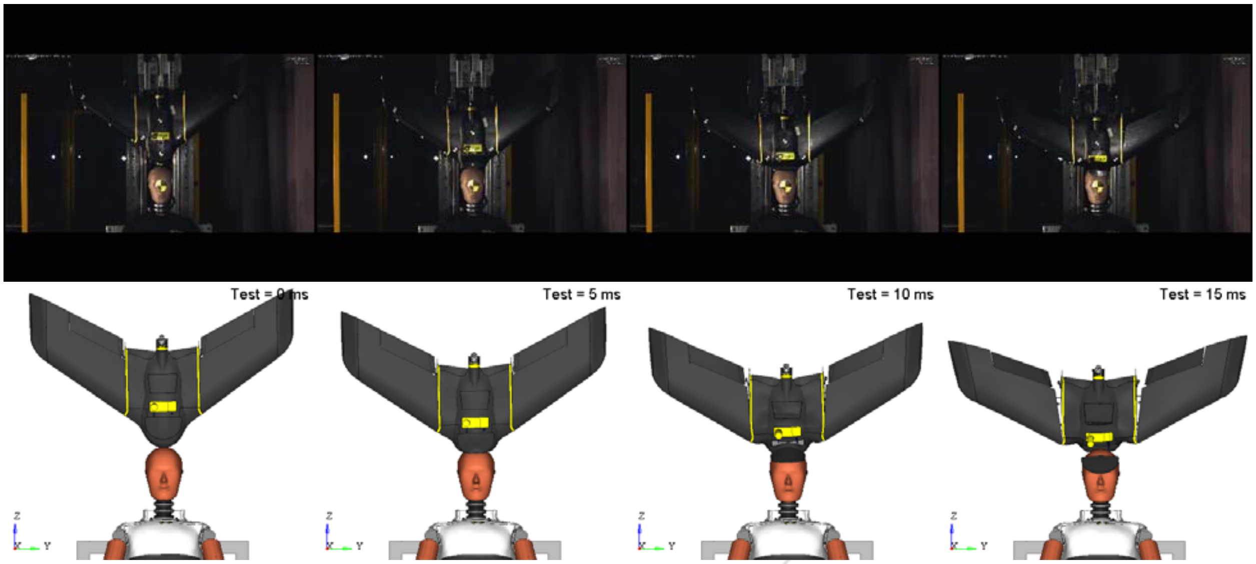

Figure 278. Test vs simulation comparison; eBeePlus, 2.4 lb, nose, 50 fps, vertical; A14 ATD test #25, top of the head; kinematics

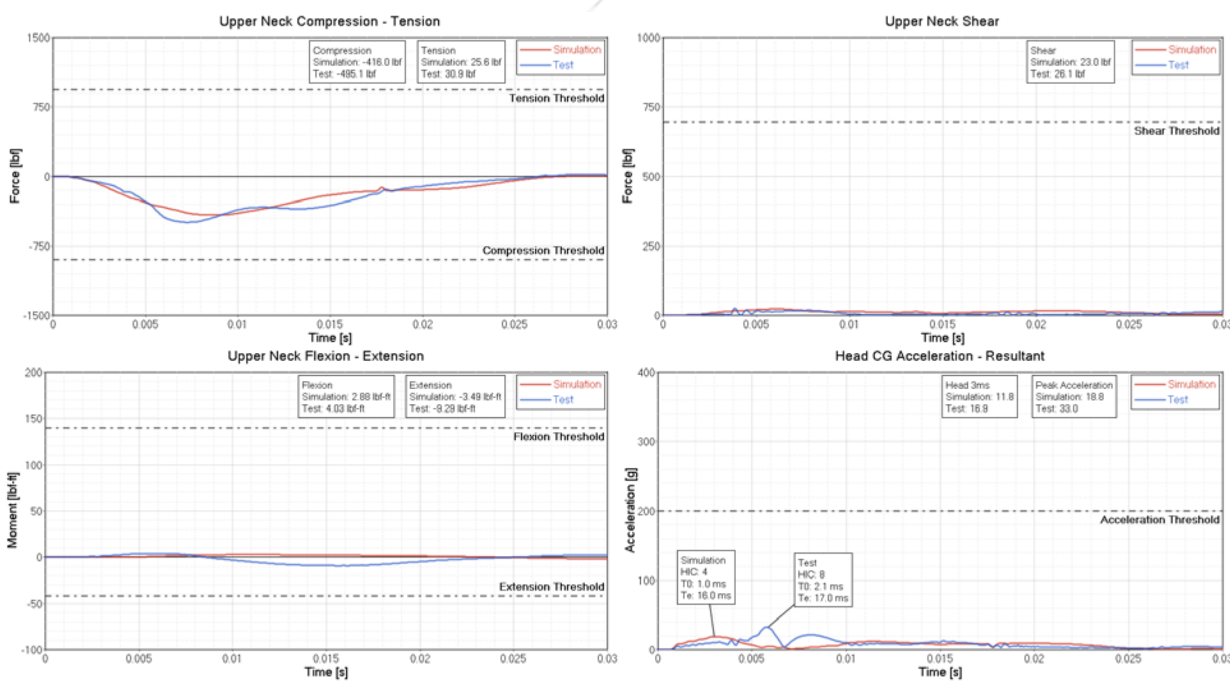

Figure 279. Test vs simulation comparison; eBeePlus, 2.4 lb, nose, 50 fps, vertical; A14 ATD test #25, top of the head; neck loads, and head acceleration

Test 26: eBeePlus, 2.4 lb, nose, 60 fps, vertical; A14 ATD, top of the head

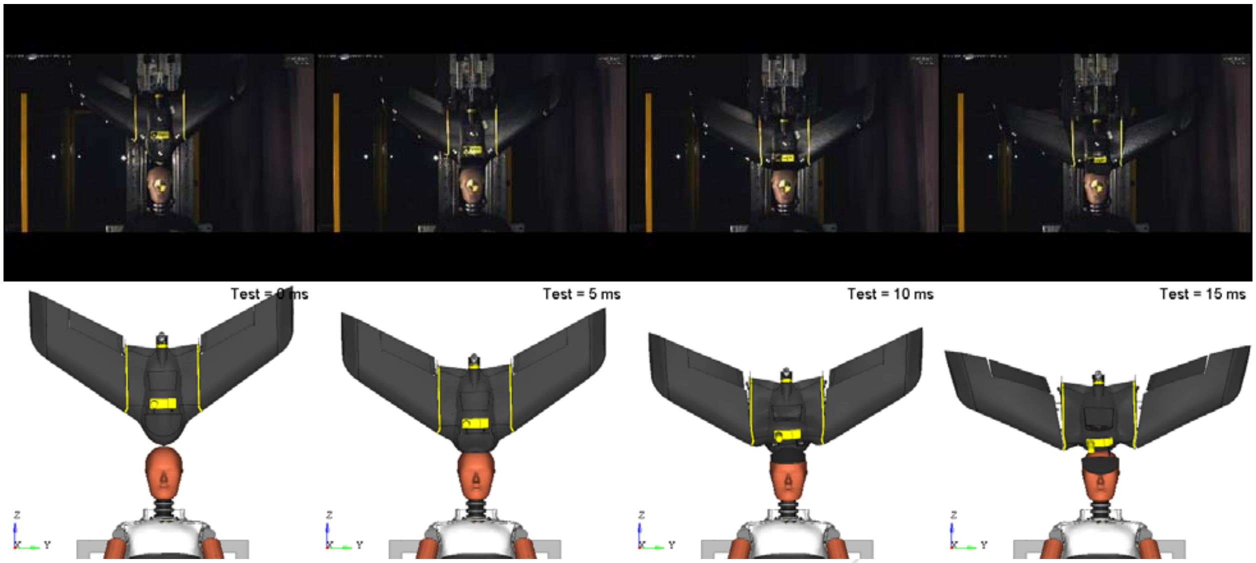

Figure 280. Test vs simulation comparison; eBeePlus, 2.4 lb, nose, 60 fps, vertical; A14 ATD test #26, top of the head; kinematics

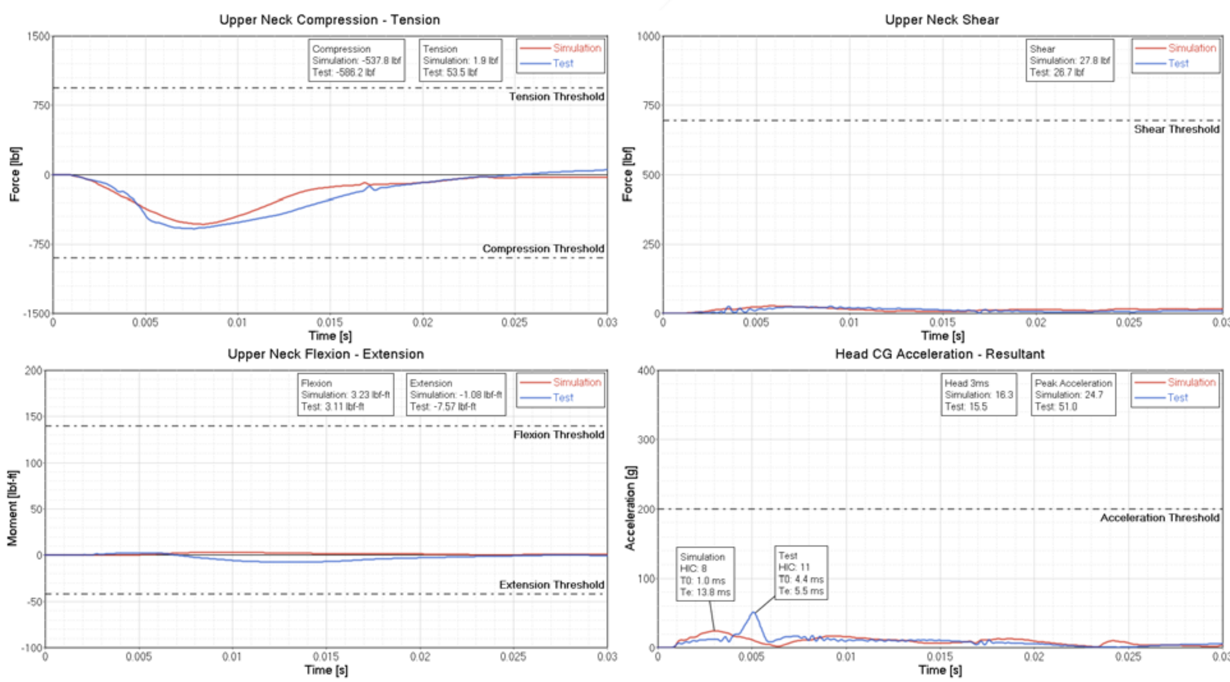

Figure 281. Test vs simulation comparison; eBeePlus, 2.4 lb, nose, 60 fps, vertical; A14 ATD test #26, top of the head; neck loads, and head acceleration

Test 27: eBeePlus, 2.4 lb, nose, 25 fps, horizontal; A14 ATD, side of the head

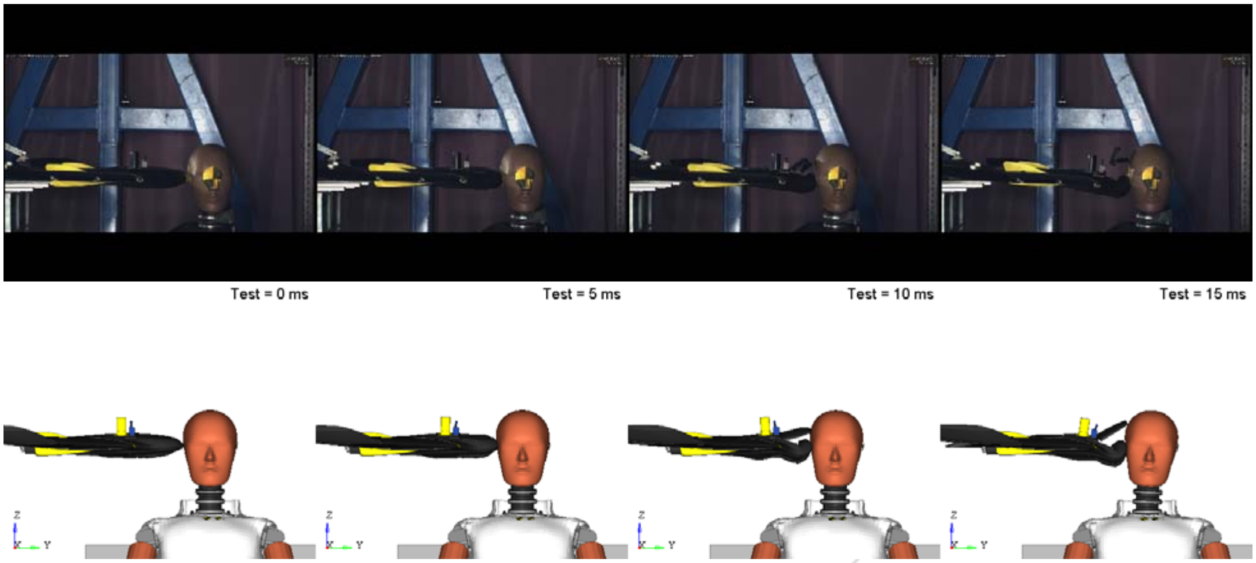

Figure 282. Test vs simulation comparison; eBeePlus, 2.4 lb, nose, 25 fps, horizontal; A14 ATD test #27, side of the head; kinematics

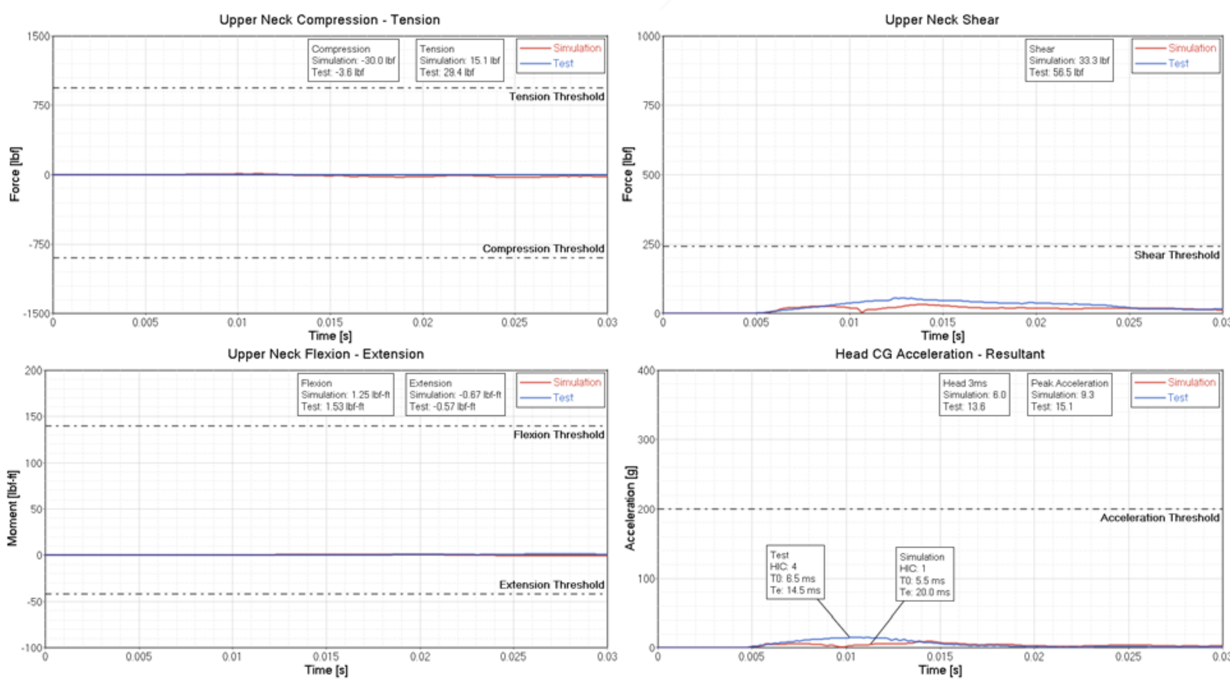

Figure 283. Test vs simulation comparison; eBeePlus, 2.4 lb, nose, 25 fps, horizontal; A14 ATD test #27, side of the head; neck loads, and head acceleration

Test 28: eBeePlus, 2.4 lb, nose, 36 fps, horizontal; A14 ATD, side of the head

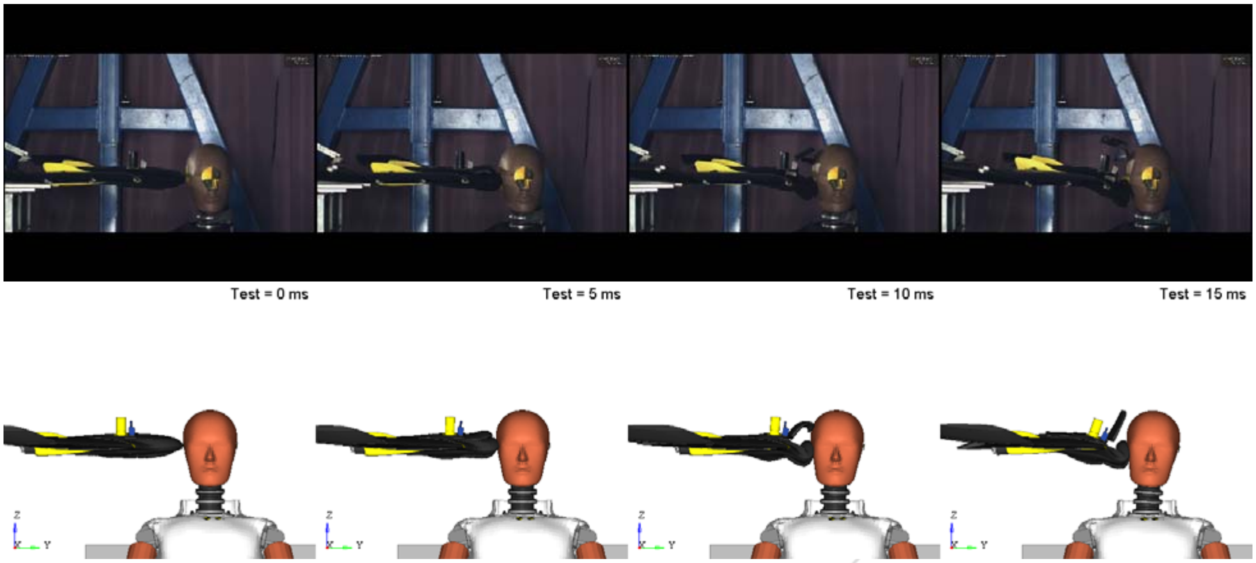

Figure 284. Test vs simulation comparison; eBeePlus, 2.4 lb, nose, 36 fps, horizontal; A14 ATD test #28, side of the head; kinematics

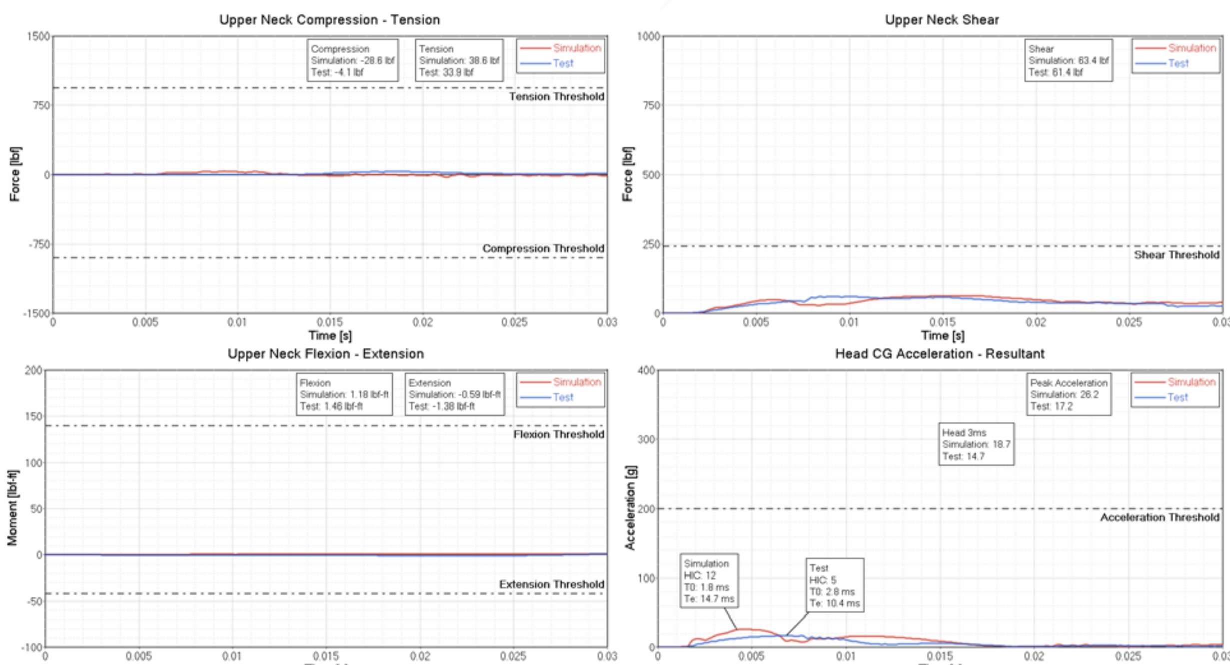

Figure 285. Test vs simulation comparison; eBeePlus, 2.4 lb, nose, 36 fps, horizontal; A14 ATD test #28, side of the head; neck loads, and head acceleration

<u>Test 29: eBeePlus, 2.4 lb, nose, 59 fps, horizontal; A14 ATD, side of the head</u>

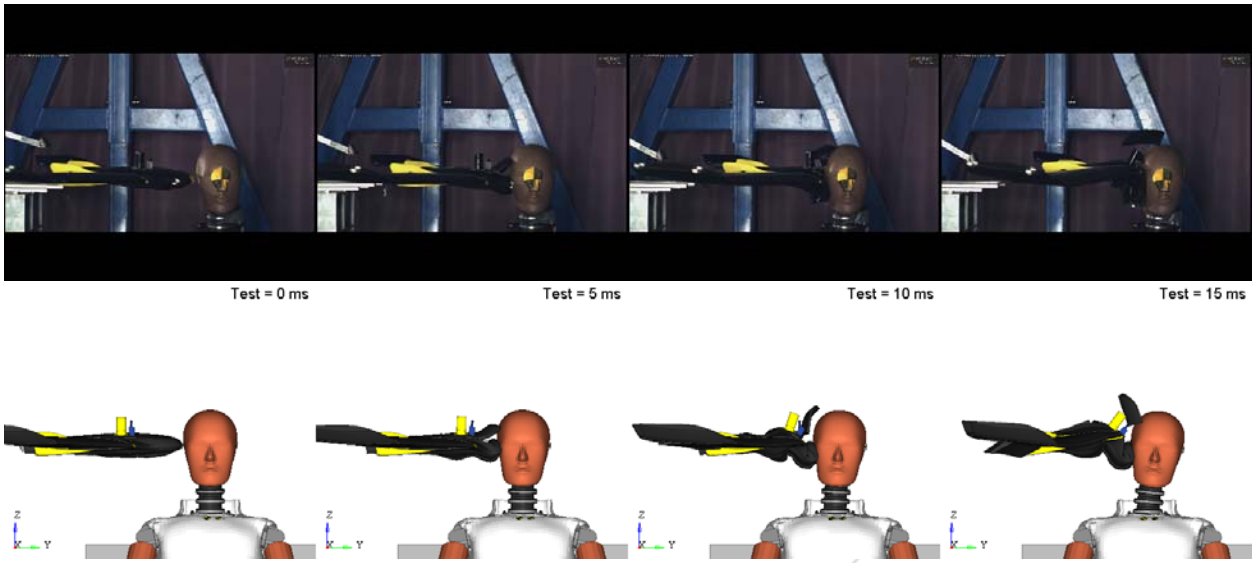

Figure 286. Test vs simulation comparison; eBeePlus, 2.4 lb, nose, 59 fps, horizontal; A14 ATD test #29, side of the head; kinematics

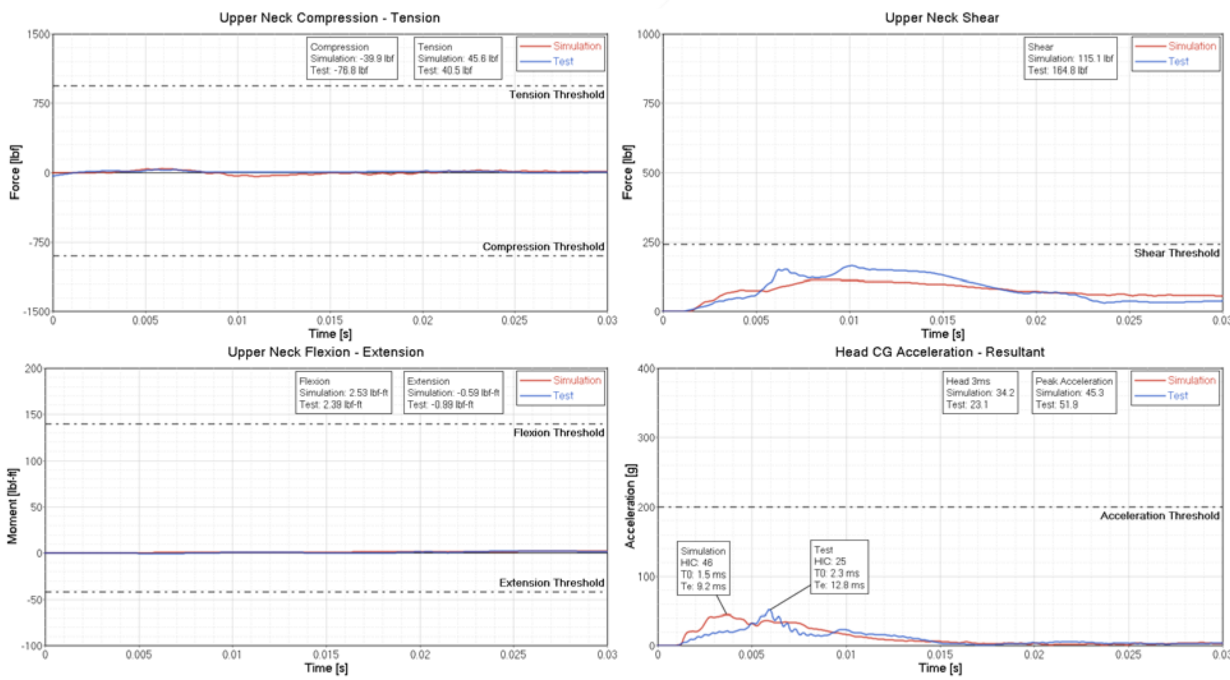

Figure 287. Test vs simulation comparison; eBeePlus, 2.4 lb, nose, 59 fps, horizontal; A14 ATD test #29, side of the head; neck loads, and head acceleration

<u>Test 30: eBeePlus, 2.4 lb, nose, 64 fps, horizontal; A14 ATD, side of the head</u>

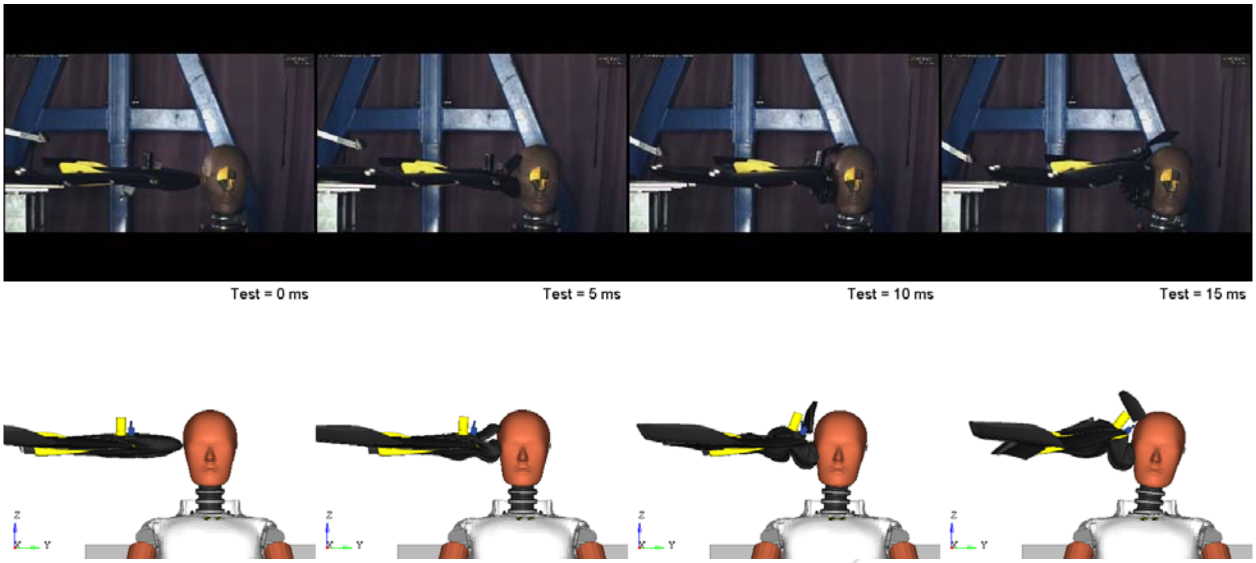

Figure 288. Test vs simulation comparison; eBeePlus, 2.4 lb, nose, 64 fps, horizontal; A14 ATD test #30, side of the head; kinematics

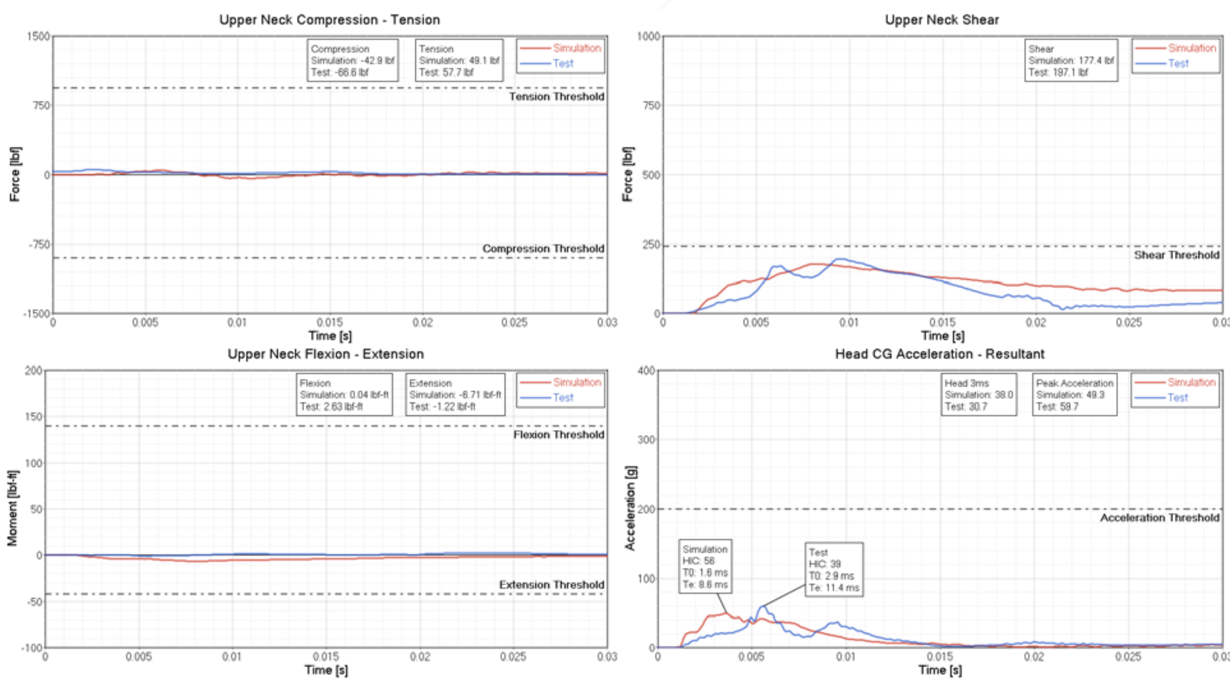

Figure 289. Test vs simulation comparison; eBeePlus, 2.4 lb, nose, 64 fps, horizontal; A14 ATD test #30, side of the head; neck loads, and head acceleration

Test 31: eBeePlus, 2.4 lb, nose, 25 fps, 58 deg angle; A14 ATD, side of the head

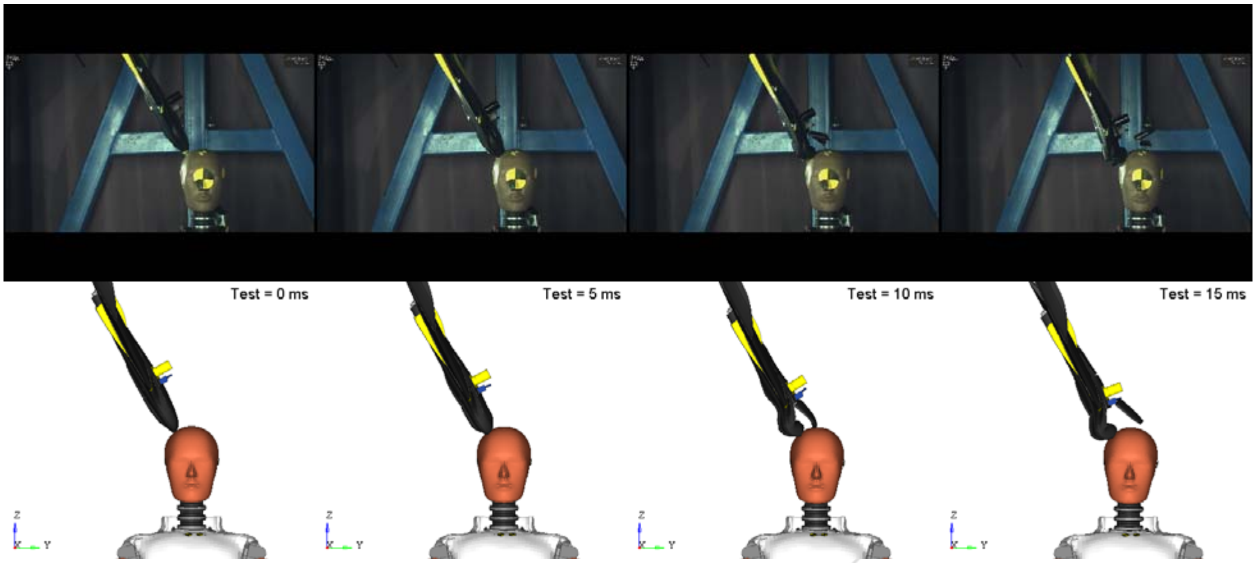

Figure 290. Test vs simulation comparison; eBeePlus, 2.4 lb, nose, 25 fps, 58 deg; A14 ATD test #31, side of the head; kinematics

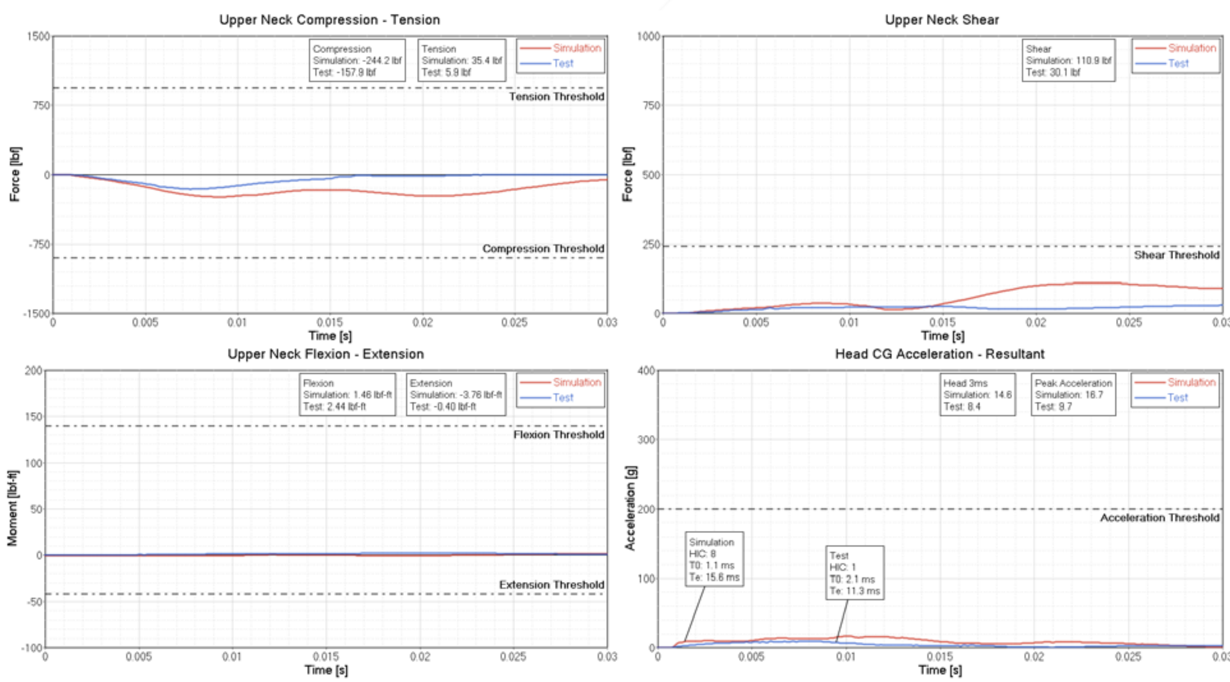

Figure 291. Test vs simulation comparison; eBeePlus, 2.4 lb, nose, 25 fps, 58 deg; A14 ATD test #31, side of the head; neck loads, and head acceleration

Test 32: eBeePlus, 2.4 lb, nose, 36 fps, 58 deg angle; A14 ATD, side of the head

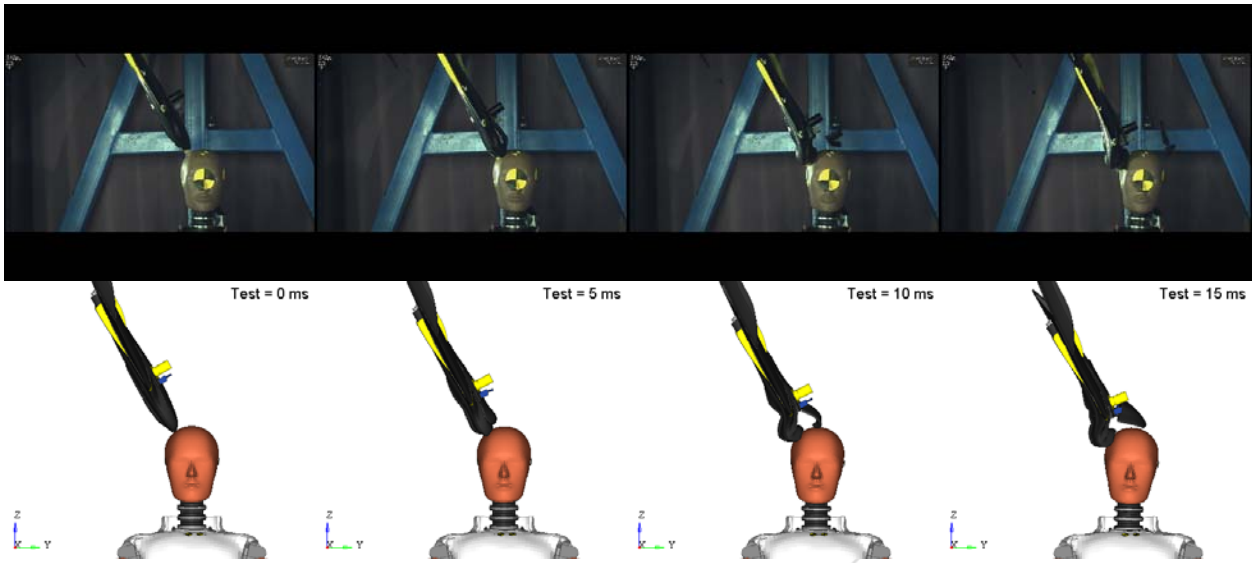

Figure 292. Test vs simulation comparison; eBeePlus, 2.4 lb, nose, 36 fps, 58 deg; A14 ATD test #32, side of the head; kinematics

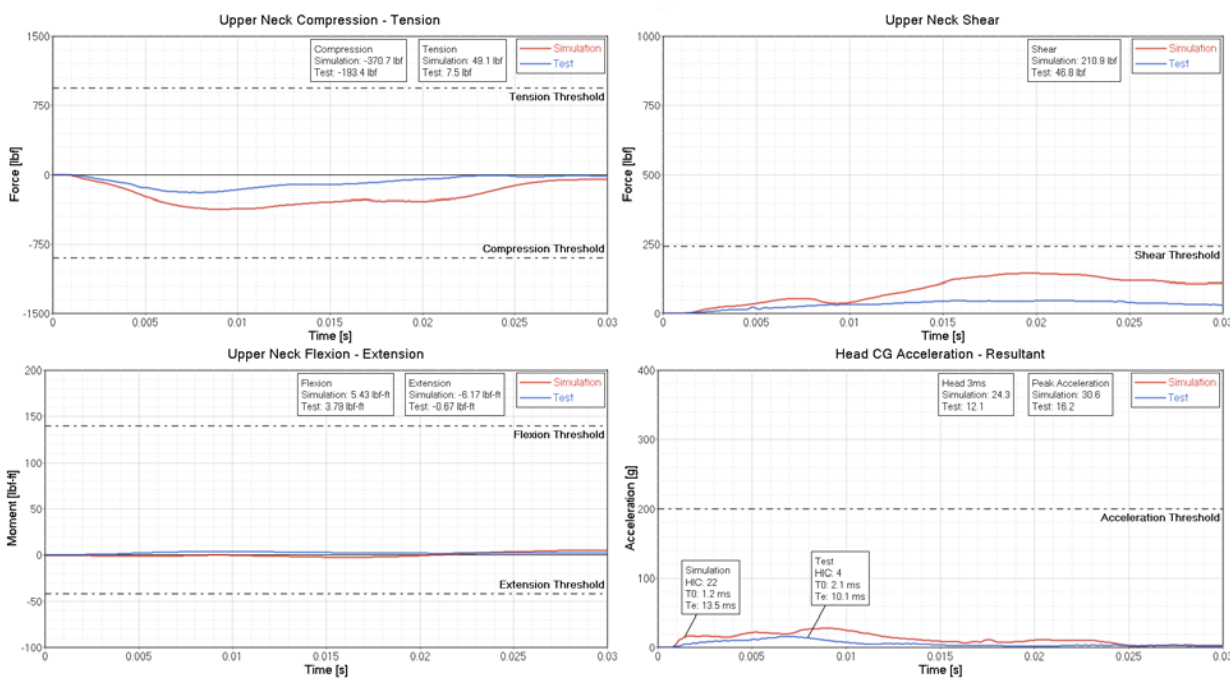

Figure 293. Test vs simulation comparison; eBeePlus, 2.4 lb, nose, 36 fps, 58 deg; A14 ATD test #32, side of the head; neck loads, and head acceleration

Test 33: eBeePlus, 2.4 lb, nose, 59 fps, 58 deg angle; A14 ATD, side of the head

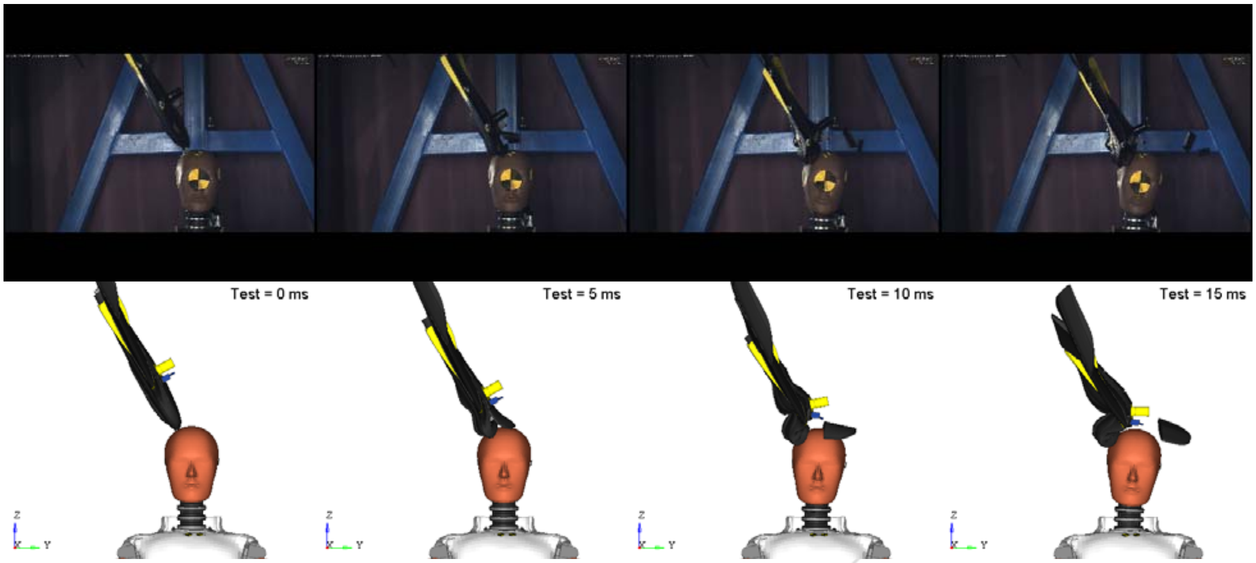

Figure 294. Test vs simulation comparison; eBeePlus, 2.4 lb, nose, 59 fps, 58 deg; A14 ATD test #33, side of the head; kinematics

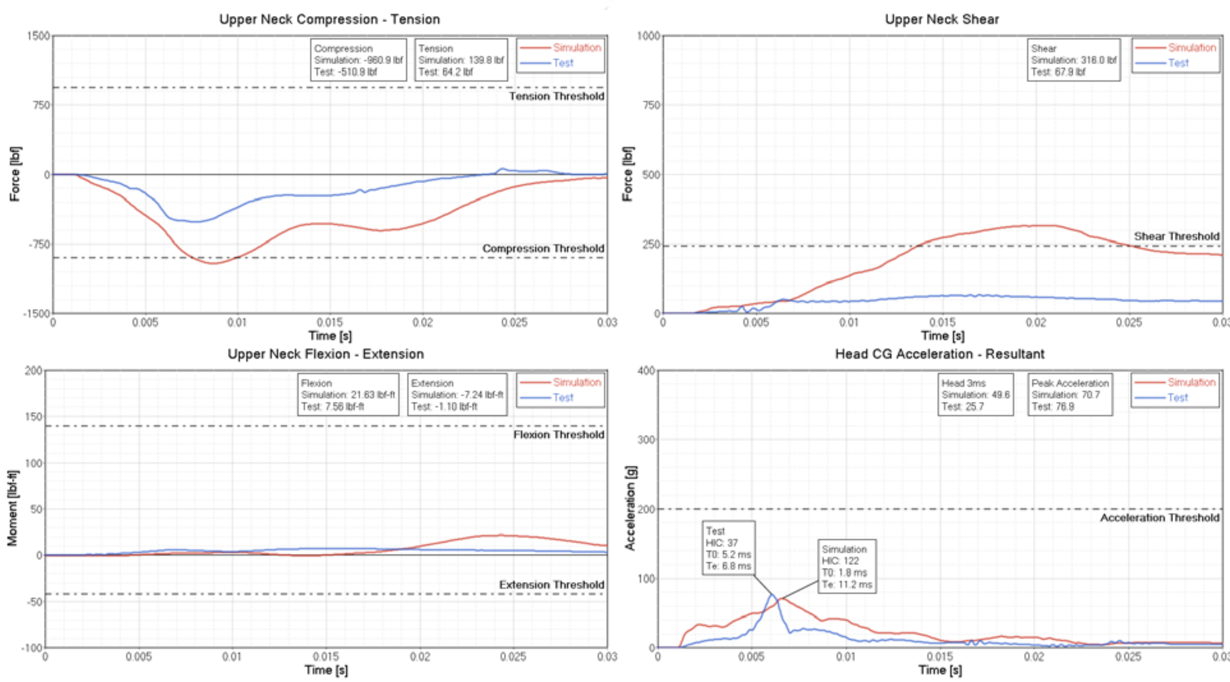

Figure 295. Test vs simulation comparison; eBeePlus, 2.4 lb, nose, 59 fps, 58 deg; A14 ATD test #33, side of the head; neck loads, and head acceleration

Test 34: eBeePlus, 2.4 lb, nose, 64 fps, 58 deg angle; A14 ATD, side of the head

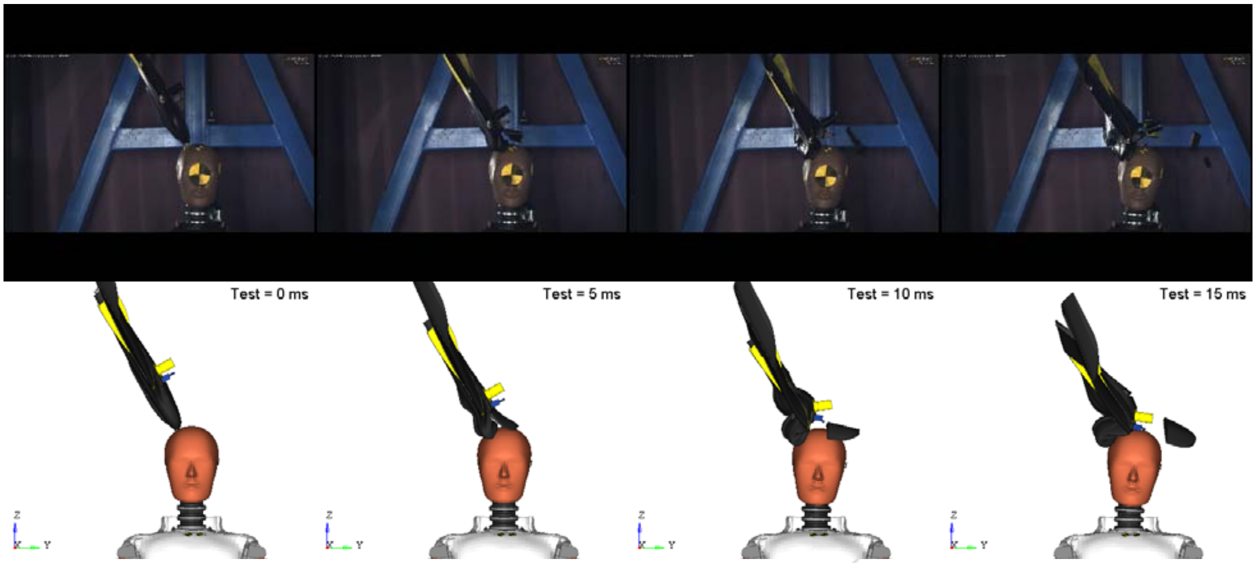

Figure 296. Test vs simulation comparison; eBeePlus, 2.4 lb, nose, 64 fps, 58 deg; A14 ATD test #34, side of the head; kinematics

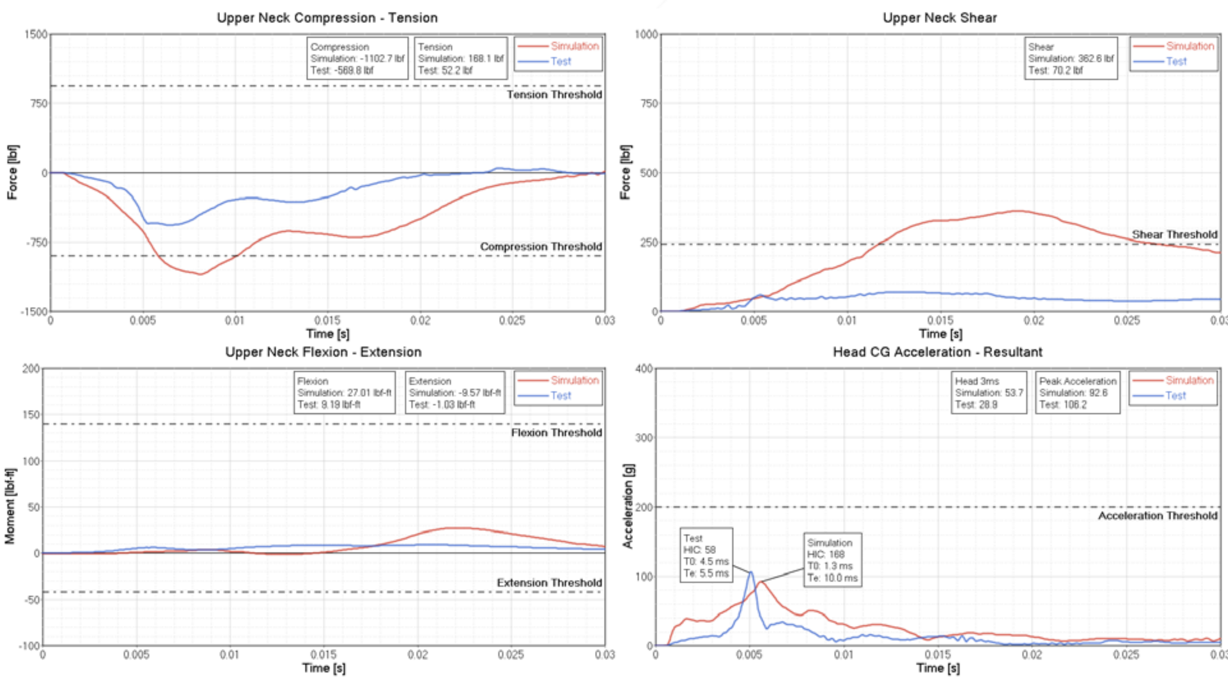

Figure 297. Test vs simulation comparison; eBeePlus, 2.4 lb, nose, 64 fps, 58 deg; A14 ATD test #34, side of the head; neck loads, and head acceleration

APPENDIX G—PRECISION HAWK MKIII SIMULATIONS WITH ATD

Side 36: Precision Hawk, 4.4 lb, 36 fps, side of the head; additional ATD simulations

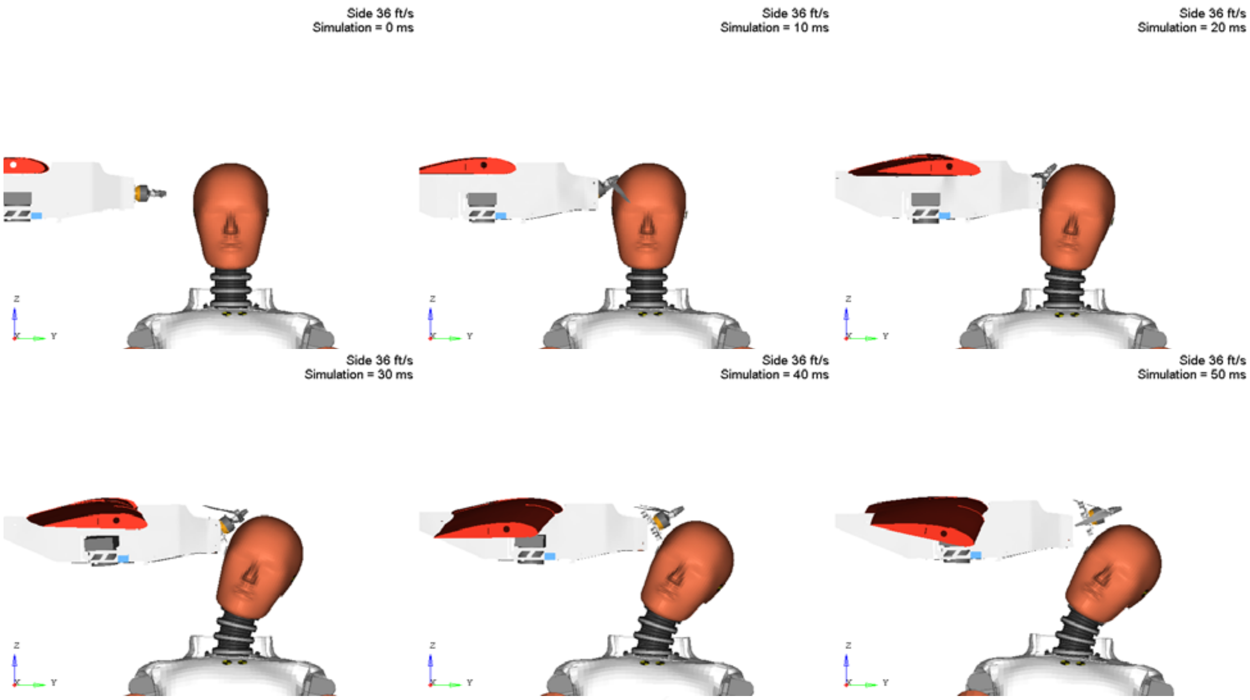

Figure 298. Precision Hawk, 4.4 lb, 36 fps, side; additional ATD simulations; kinematics

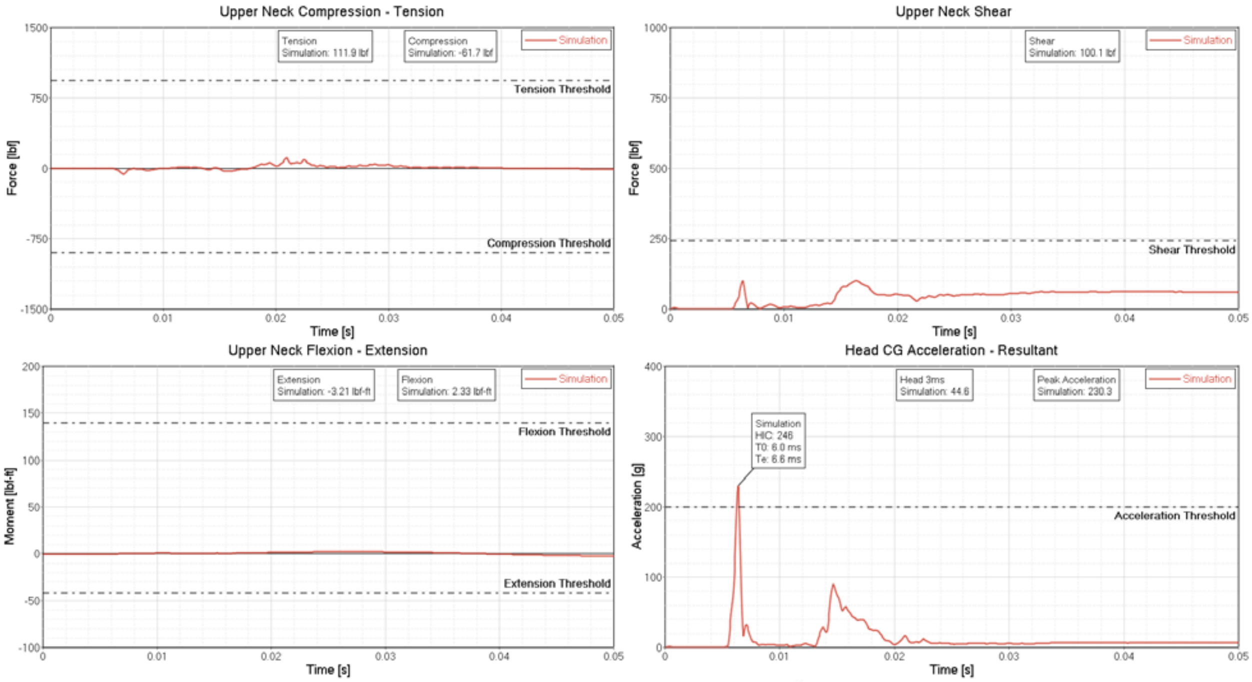

Figure 299. Precision Hawk, 4.4 lb, 36 fps, side; additional ATD simulations; neck loads, and head acceleration

<u>Vertical 16: Precision Hawk, 4.4 lb, 16 fps-parachute, top of the head; additional ATD simulations</u>

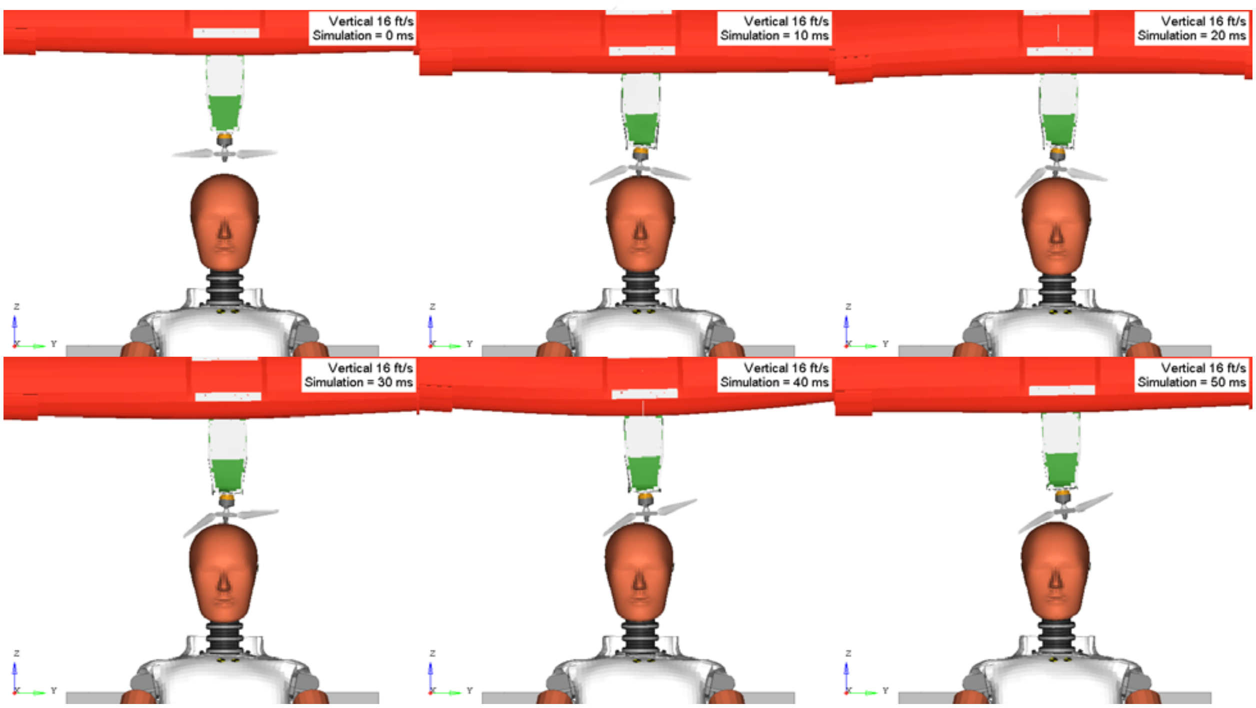

Figure 300. Precision Hawk, 4.4 lb, 16 fps, vertical; additional ATD simulations; kinematics

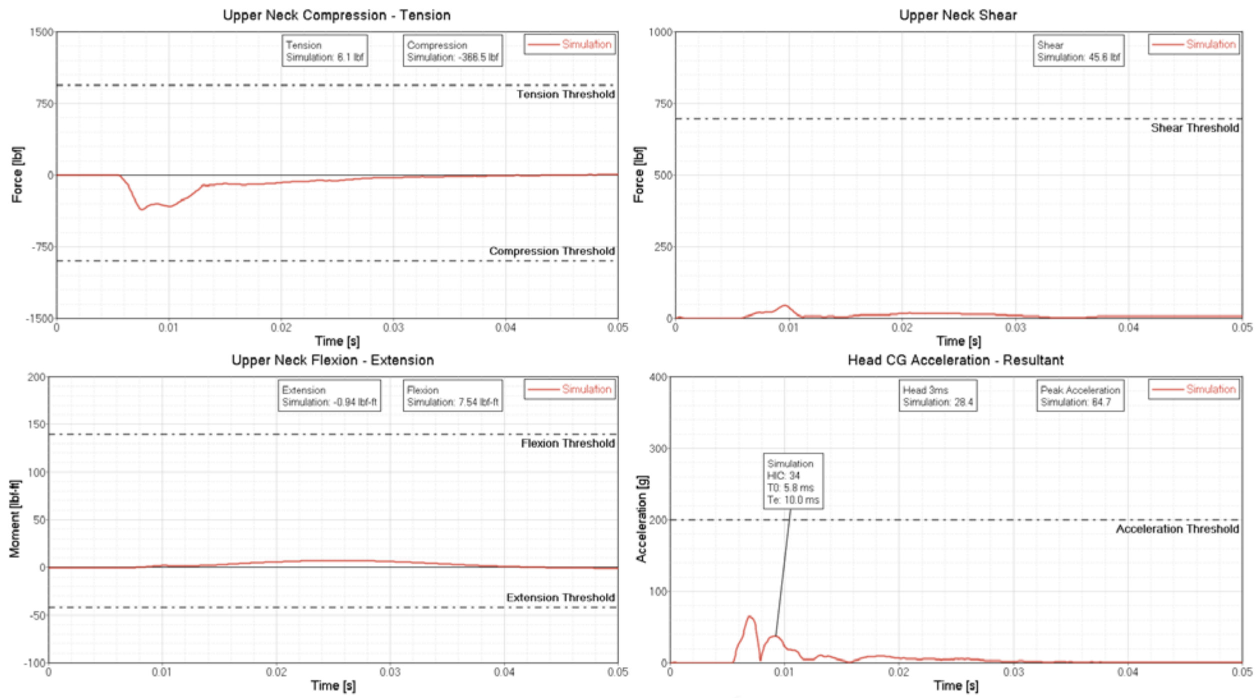

Figure 301. Precision Hawk, 4.4 lb, 16 fps, vertical; additional ATD simulations; neck loads, and head acceleration

<u>Vertical 12: Precision Hawk, 4.4 lb, 12 fps-parachute, top of the head; additional ATD simulations</u>

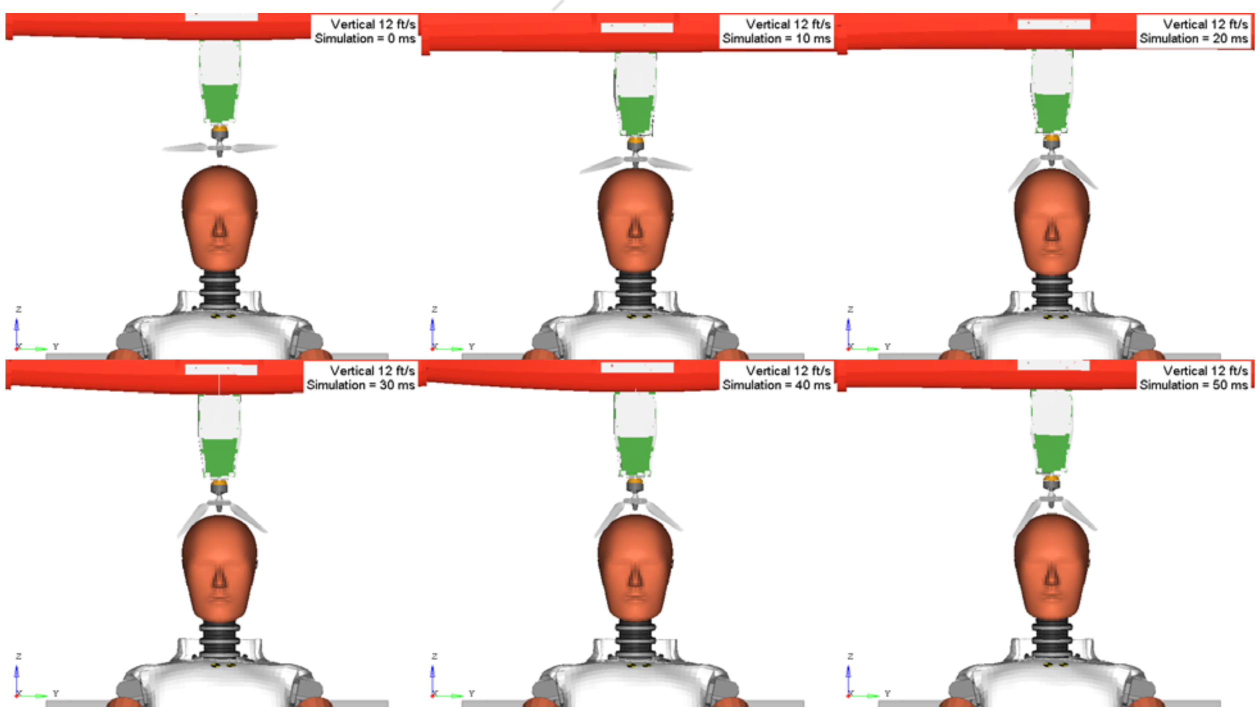

Figure 302. Precision Hawk, 4.4 lb, 12 fps, vertical; additional ATD simulations; kinematics

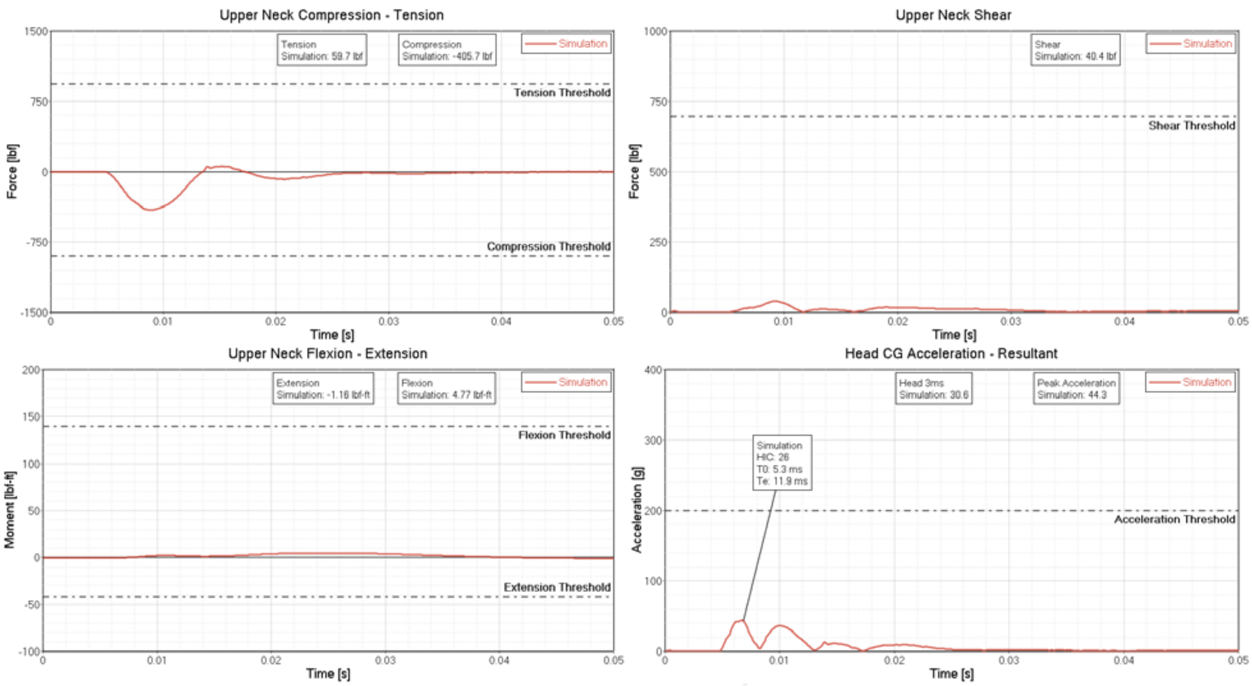

Figure 303. Precision Hawk, 4.4 lb, 12 fps, vertical; additional ATD simulations; neck loads, and head acceleration

APPENDIX H—DJI PHANTOM III MODEL EVALUATION WITH A11 ATD TESTS – THUMS SIMULATIONS

V(90)-20 Test and Simulation Comparison

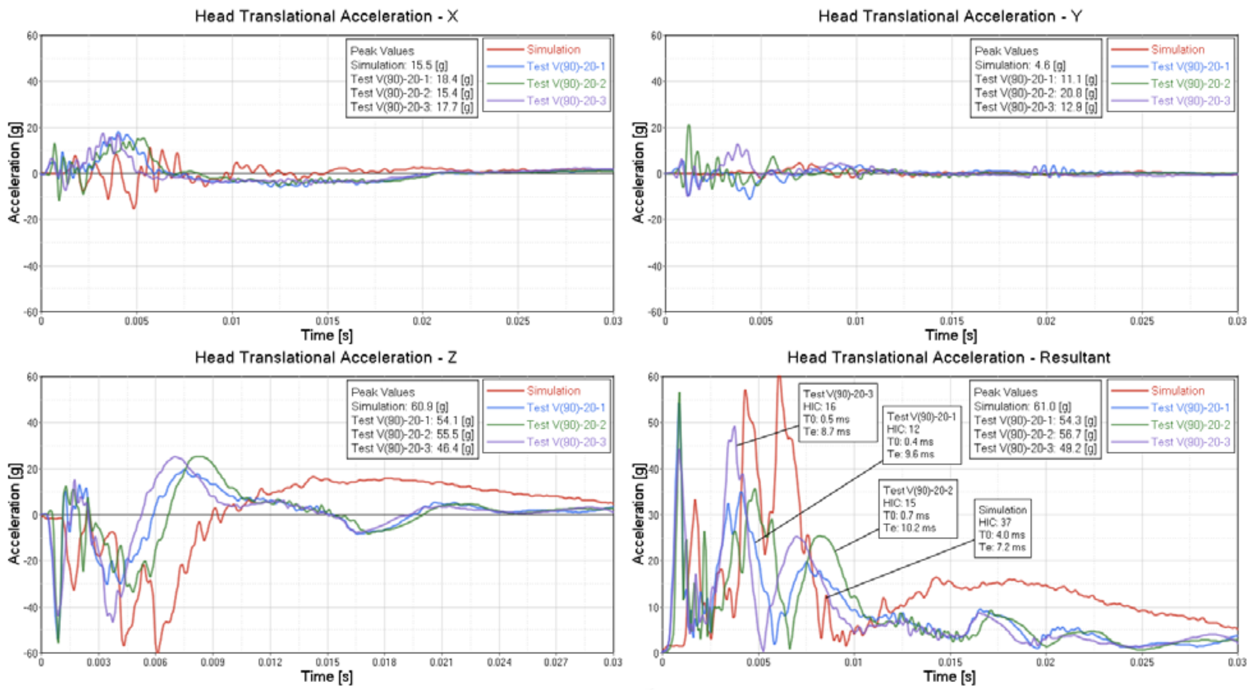

Figure 304. Test vs simulation comparison; DJI Phantom 3, 2.67 lb, bottom, 20 fps, vertical; A11 ATD test, top of the head; head CG acceleration

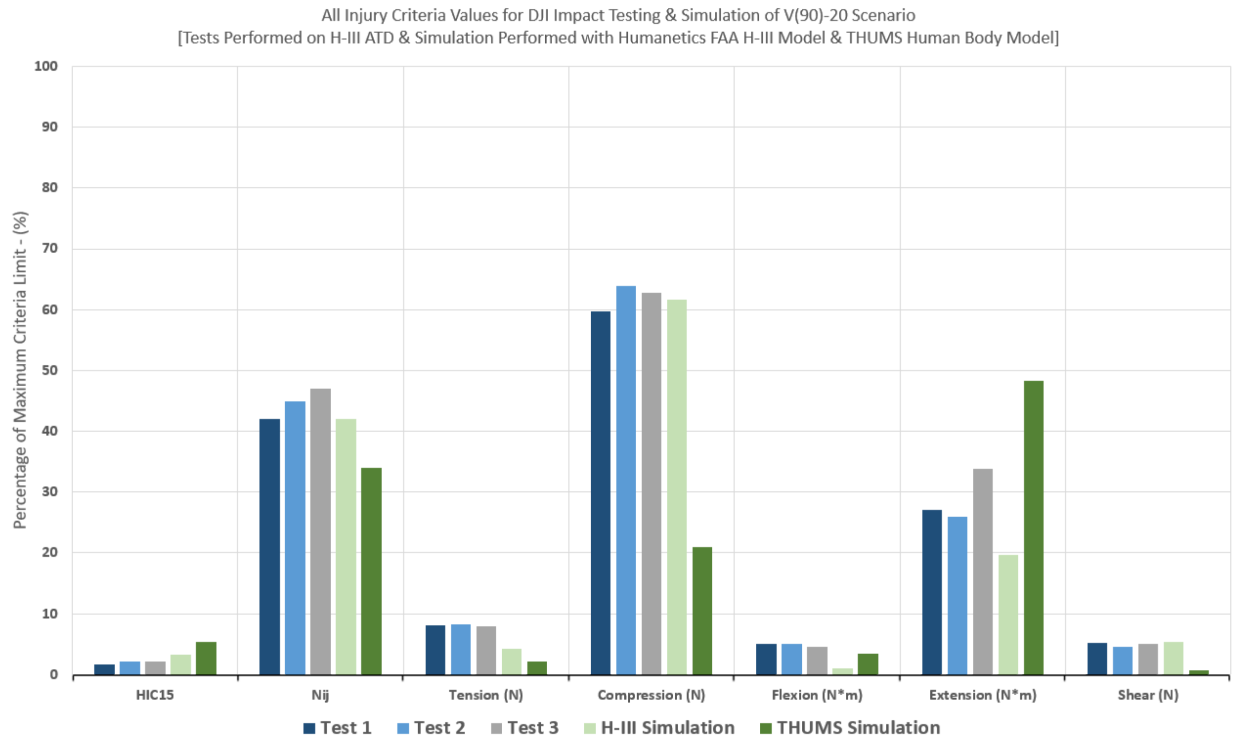

Figure 305. Bar chart with summary of injury criteria for A11 test vs simulation comparison.

V(90)-50 Test and Simulation Comparison

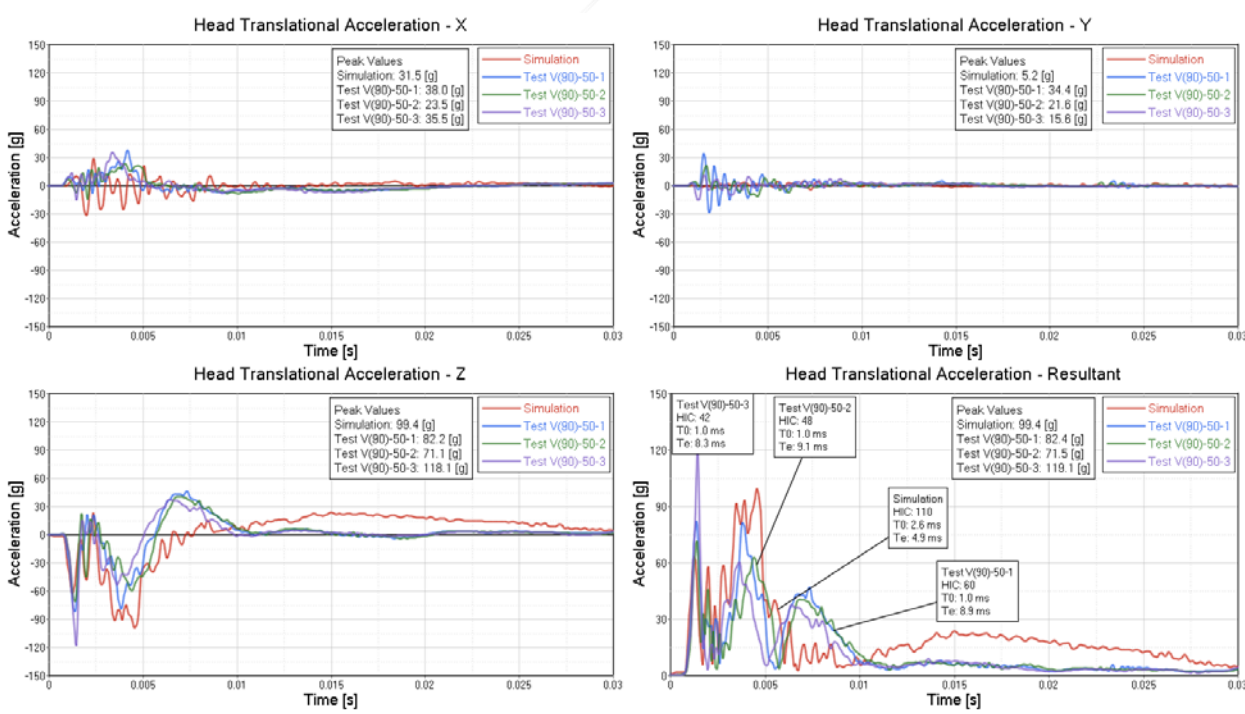

Figure 306. Test vs simulation comparison; DJI Phantom 3, 2.67 lb, bottom, 50 fps, vertical; A11 ATD test, top of the head; head CG acceleration

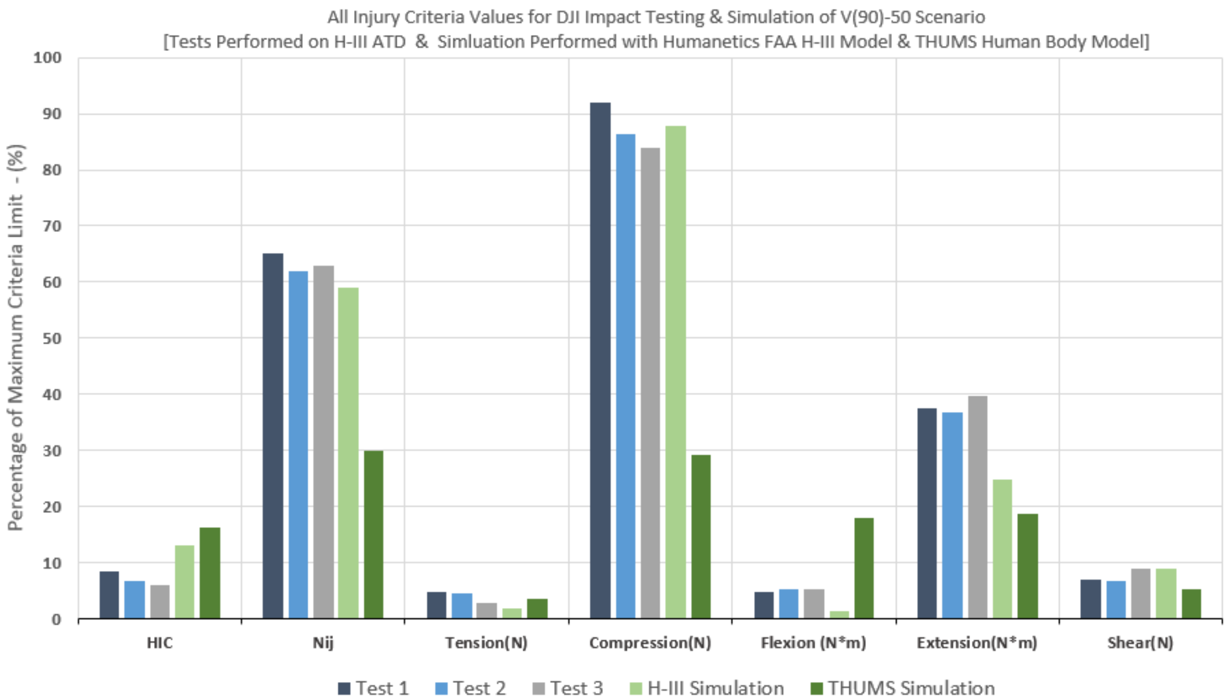

Figure 307. Bar chart with summary of injury criteria for A11 test vs simulation comparison.

H(0)-4.5 Test and Simulation Comparison

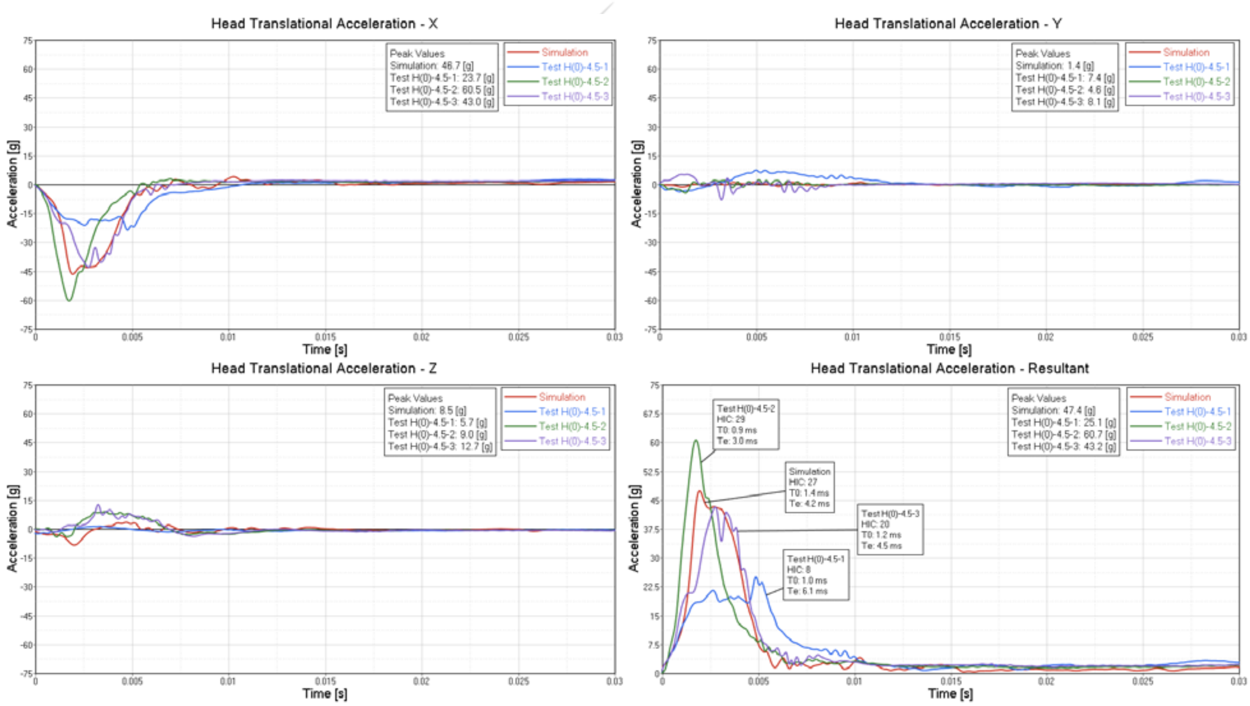

Figure 308. Test vs simulation comparison; DJI Phantom 3, 2.67 lb, front first, 4.5 fps, horizontal; A11 ATD test, side of the head; head CG acceleration

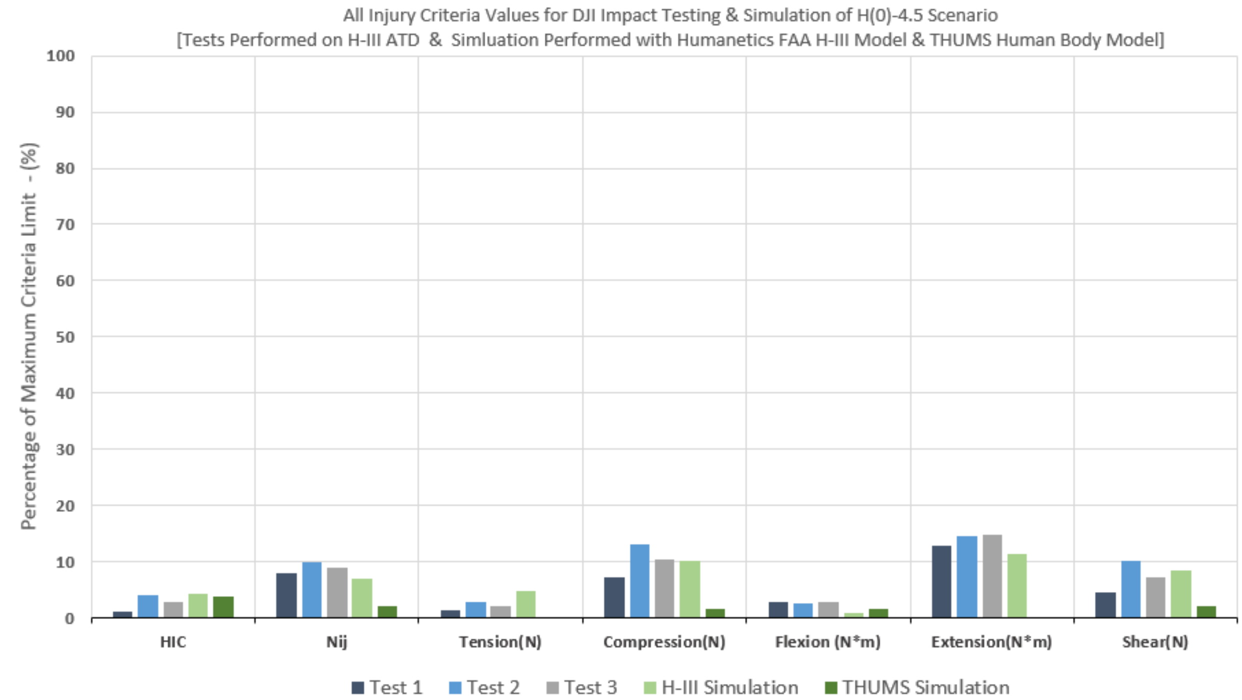

Figure 309. Bar chart with summary of injury criteria for A11 test vs simulation comparison.

A(58)-46.1 Test and Simulation Comparison

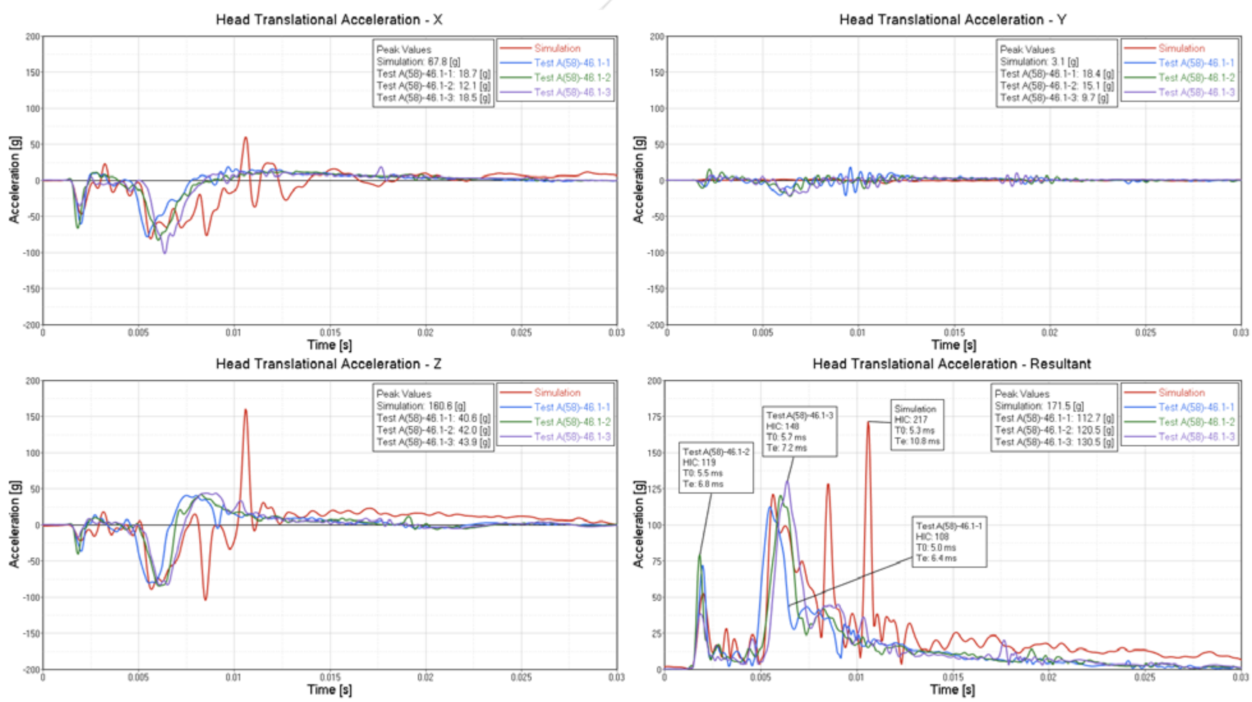

Figure 310. Test vs simulation comparison; DJI Phantom 3, 2.67 lb, bottom, 46.1 fps, angled frontal; A11 ATD test, front of the head; head CG acceleration

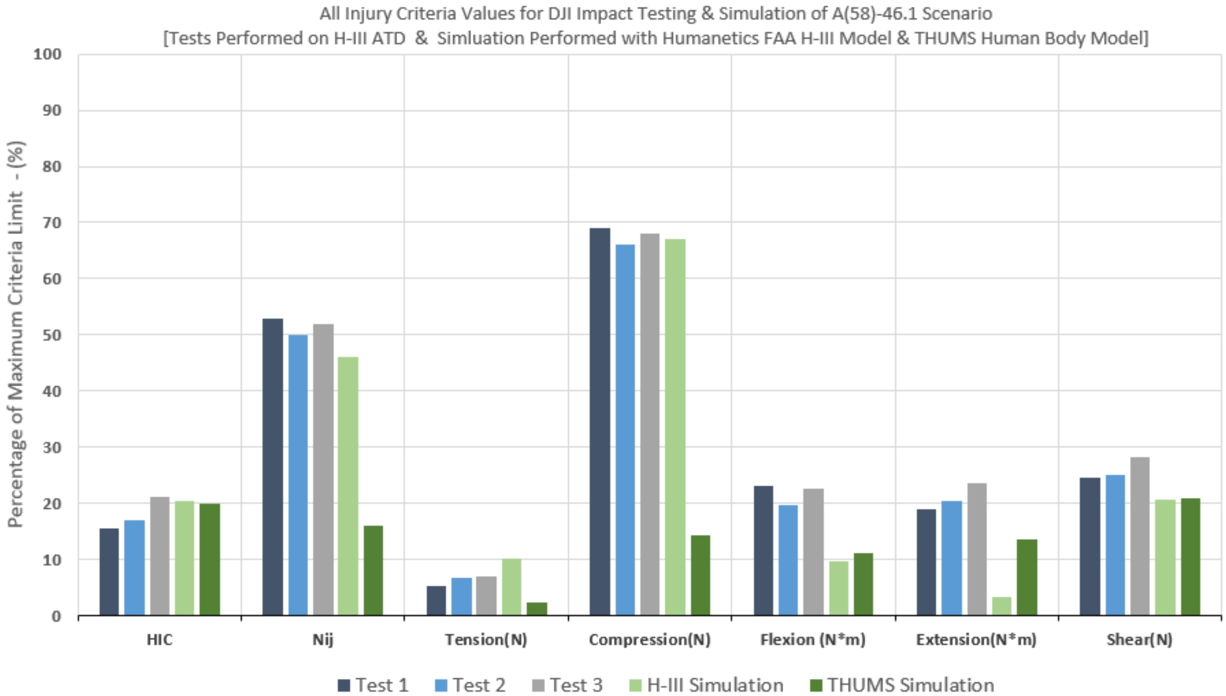

Figure 311. Bar chart with summary of injury criteria for A11 test vs simulation comparison.

A(58)-57.1 Test and Simulation Comparison

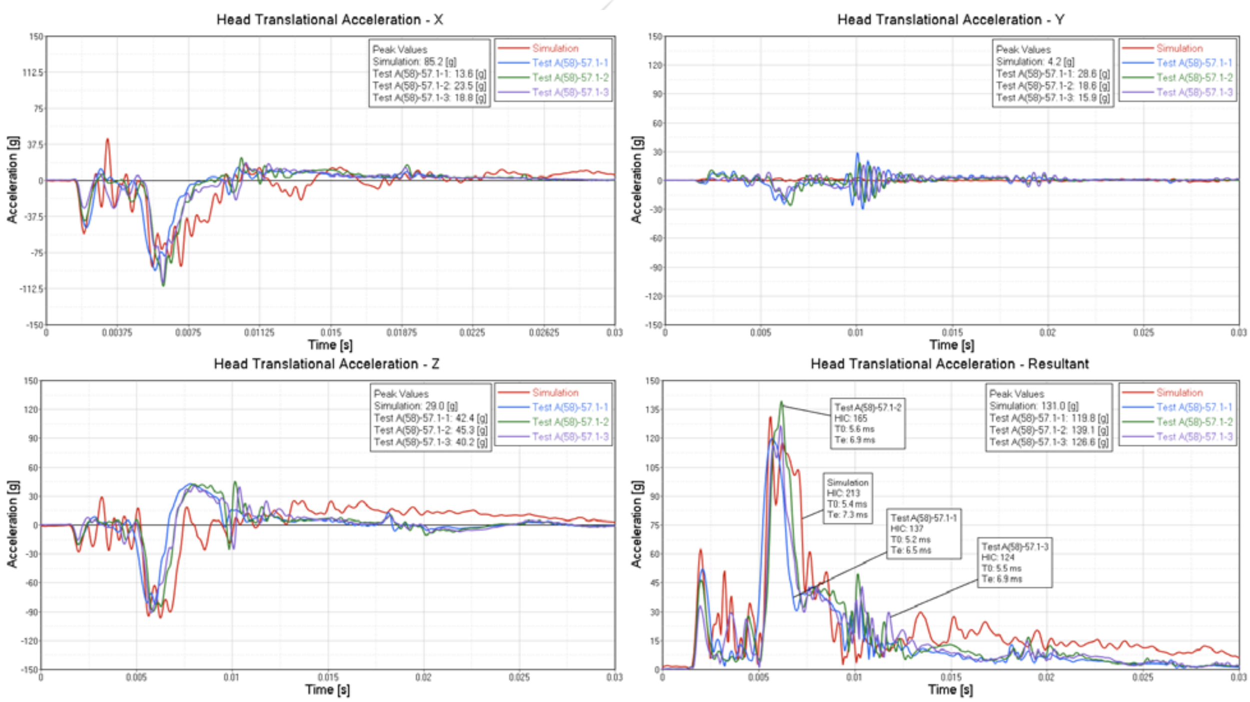

Figure 312. Test vs simulation comparison; DJI Phantom 3, 2.67 lb, bottom, 57.1 fps, angled frontal; A11 ATD test, front of the head; head CG acceleration

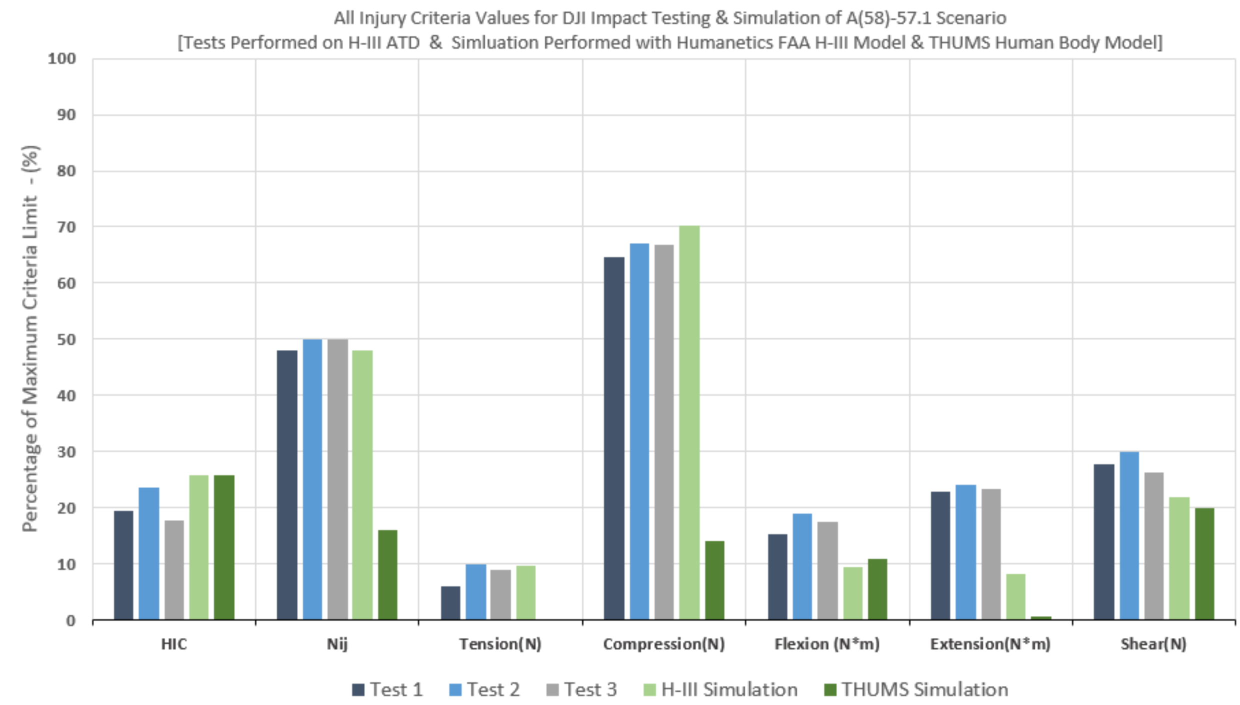

Figure 313. Bar chart with summary of injury criteria for A11 test vs simulation comparison.

A(65)-36.5 Test and Simulation Comparison

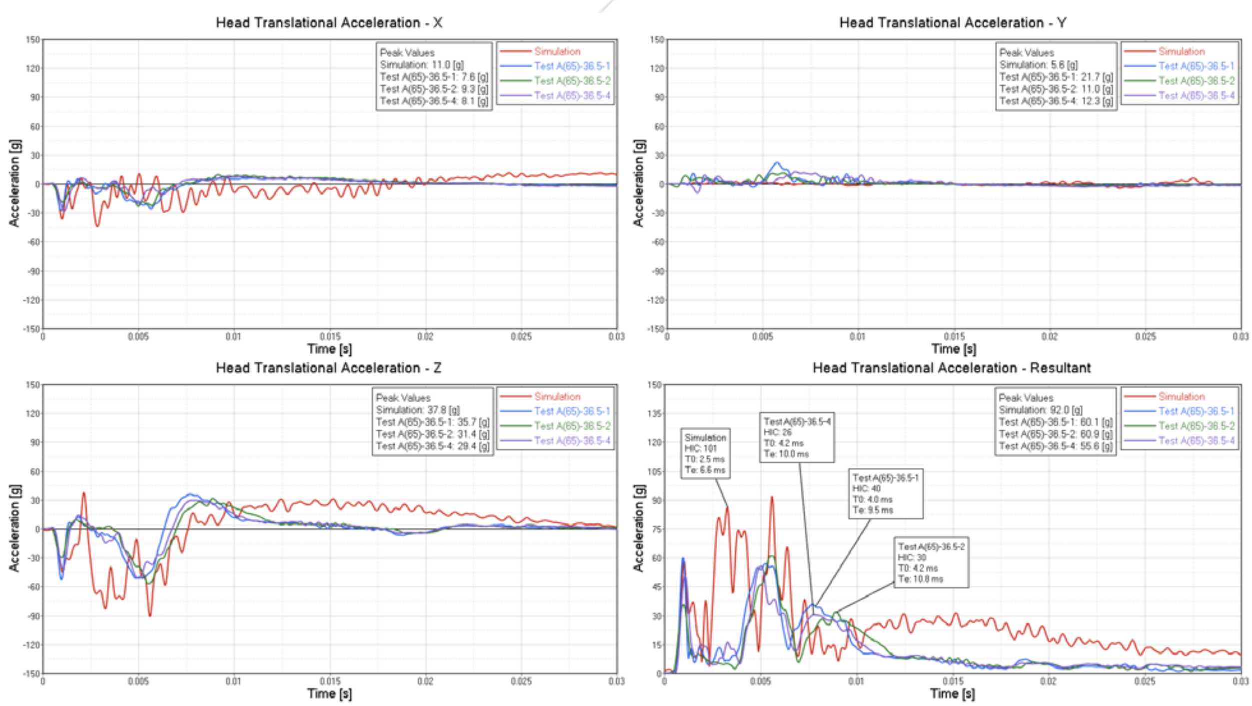

Figure 314. Test vs simulation comparison; DJI Phantom 3, 2.67 lb, bottom, 36.5 fps, angled frontal; A11 ATD test, front of the head; head CG acceleration

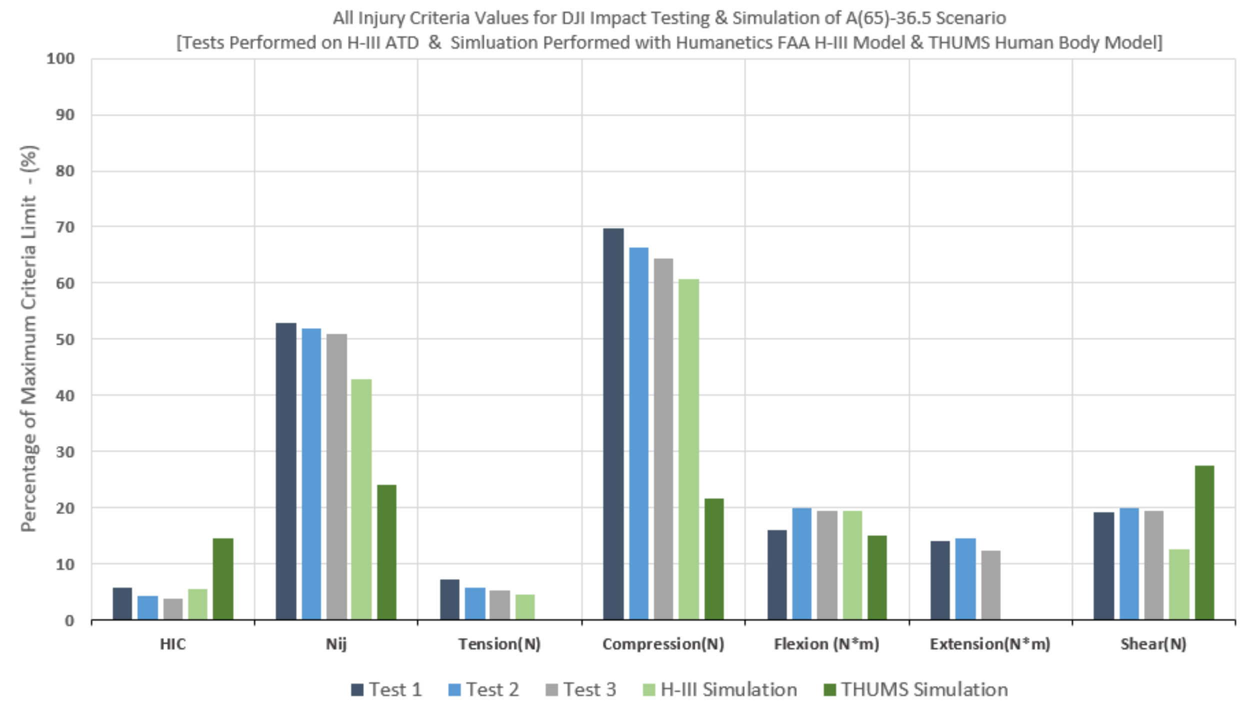

Figure 315. Bar chart with summary of injury criteria for A11 test vs simulation comparison.

APPENDIX I—DJI PHANTOM III MODEL EVALUATION WITH A14 PMHS TESTS

Test 2 – H(0S)-56

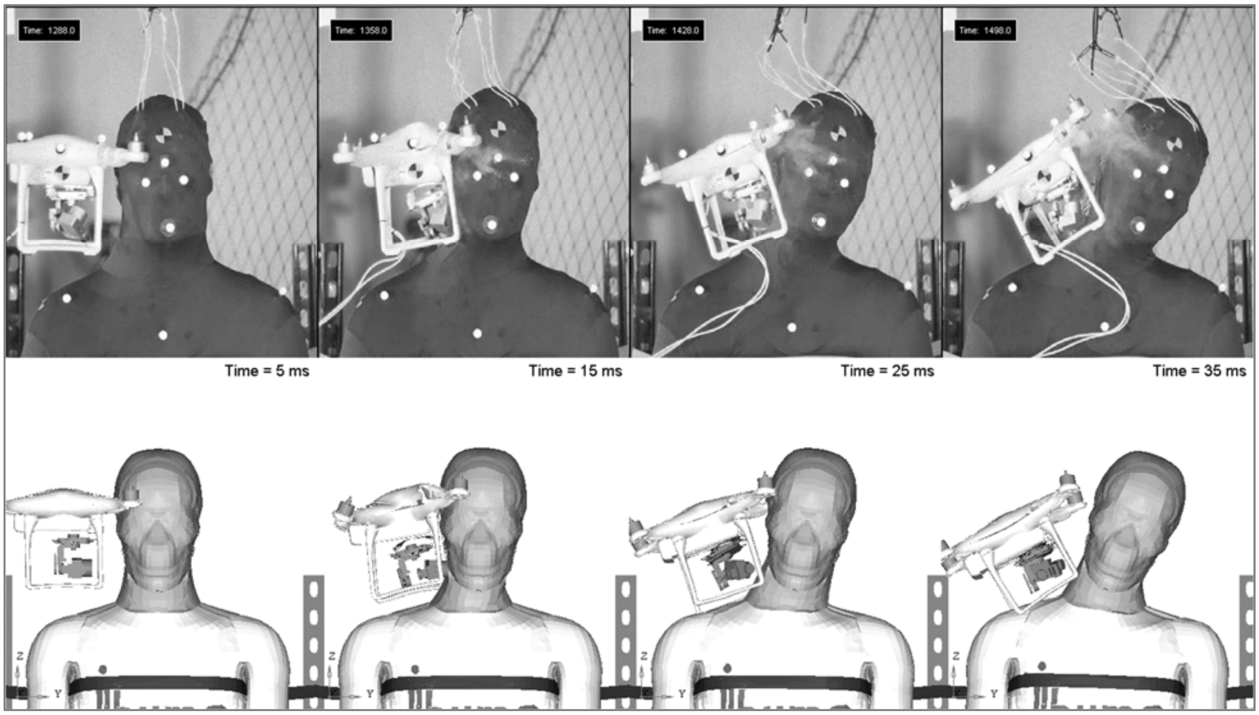

Figure 316. PMHS test 2 vs simulation comparison; DJI Phantom 3, 2.67 lb, between arms, 56 fps, sideward; subject #1; side of the head; kinematics

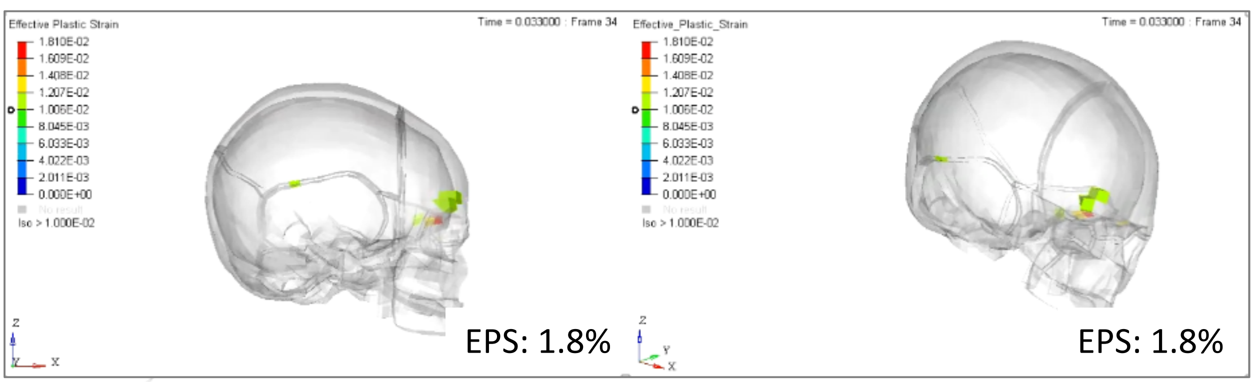

Figure 317. PMHS test 2 vs simulation comparison; DJI Phantom 3, 2.67 lb, between arms, 56 fps, sideward; subject #1; side of the head; EPS contour plot of skull

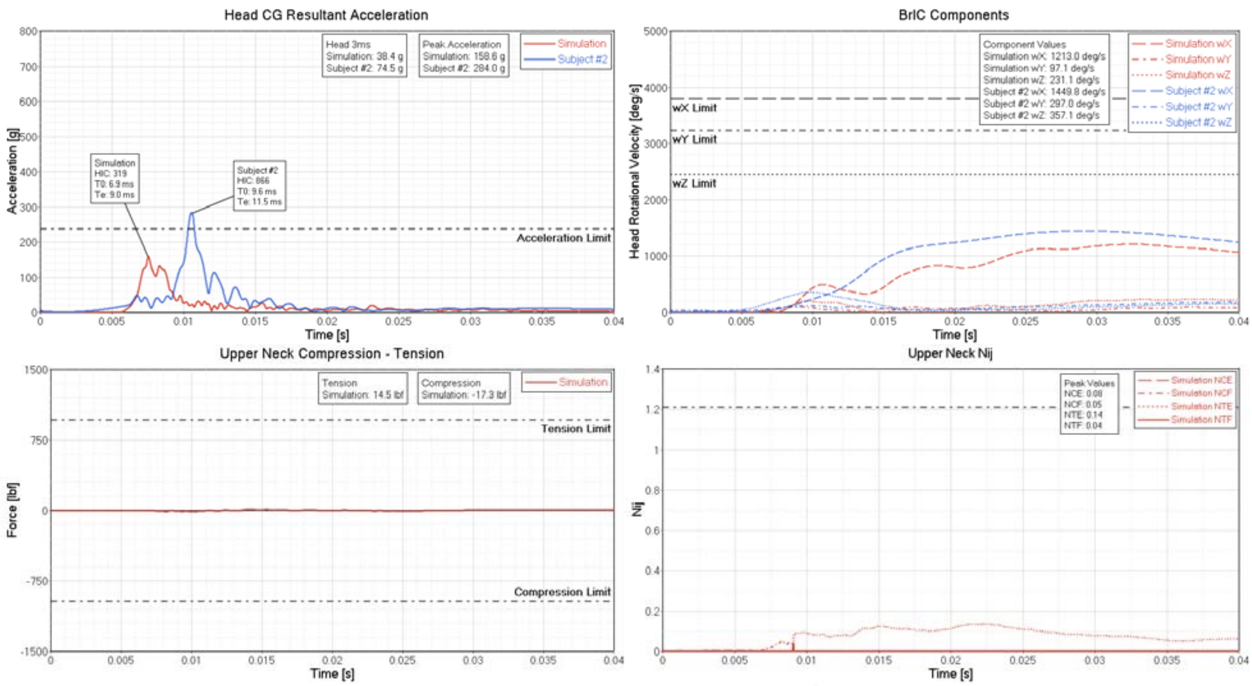

Figure 318. PMHS test 2 vs simulation comparison; DJI Phantom 3, 2.67 lb, between arms, 56 fps, sideward; subject #1; side of the head; time-history summary

Test 3 – H(0S)-61

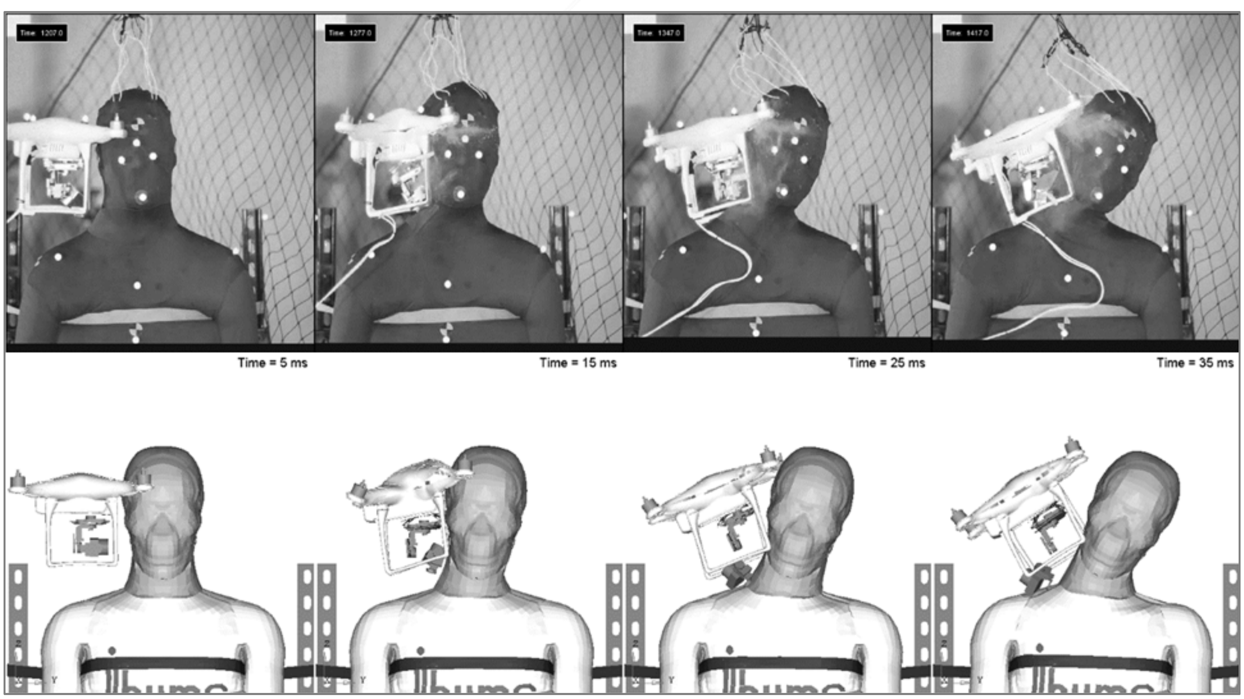

Figure 319. PMHS test 3 vs simulation comparison; DJI Phantom 3, 2.67 lb, between arms, 61 fps, sideward; subject #1; side of the head; kinematics

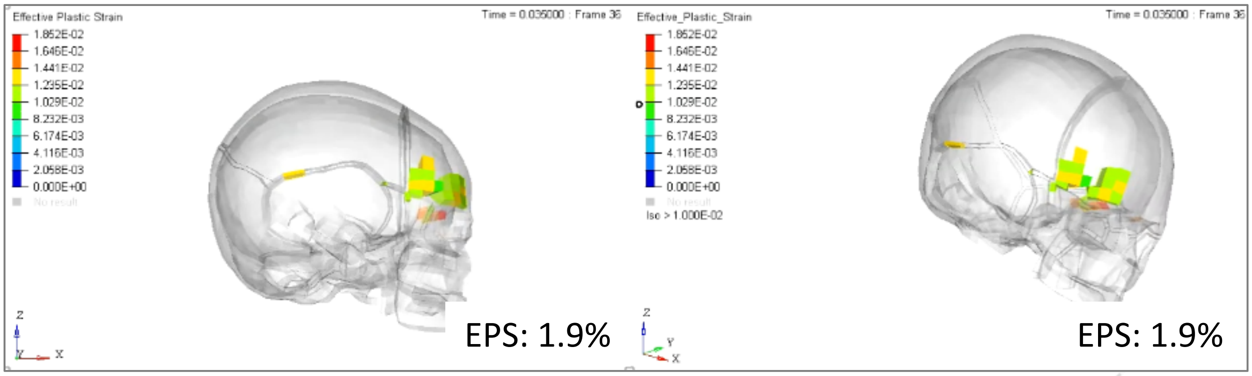

Figure 320. PMHS test 3 vs simulation comparison; DJI Phantom 3, 2.67 lb, between arms, 61 fps, sideward; subject #1; side of the head; EPS contour plot of skull

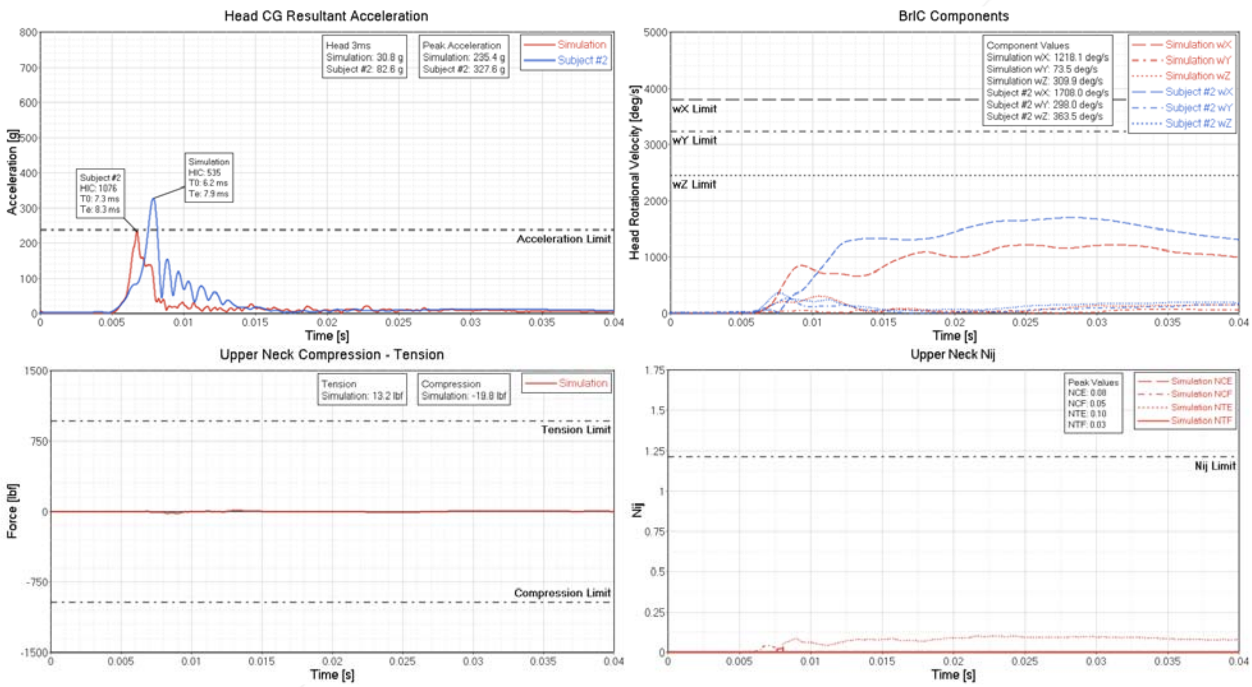

Figure 321. PMHS test 3 vs simulation comparison; DJI Phantom 3, 2.67 lb, between arms, 61 fps, sideward; subject #1; side of the head; time-history summary

Test 4 – H(0S)-71

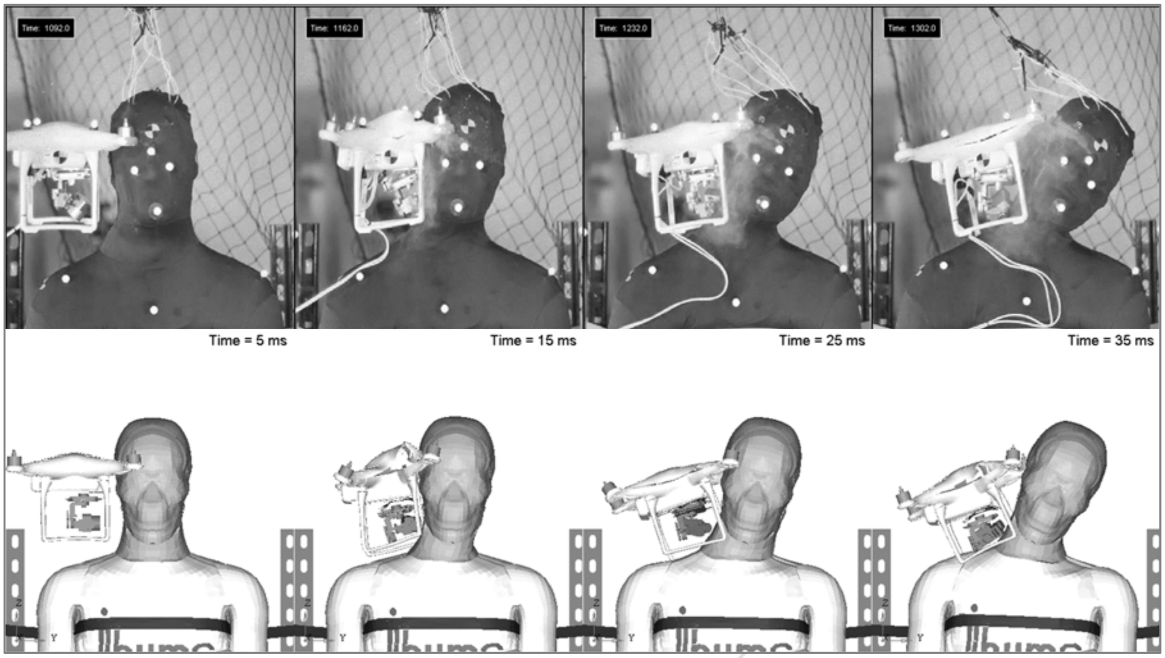

Figure 322. PMHS test 4 vs simulation comparison; DJI Phantom 3, 2.67 lb, between arms, 71 fps, sideward; subject #1; side of the head; kinematics

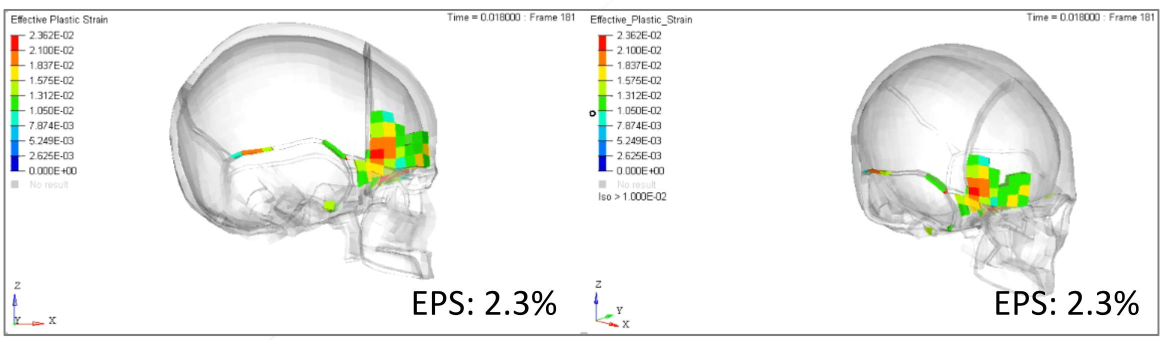

Figure 323. PMHS test 4 vs simulation comparison; DJI Phantom 3, 2.67 lb, between arms, 71 fps, sideward; subject #1; side of the head; EPS contour plot of skull

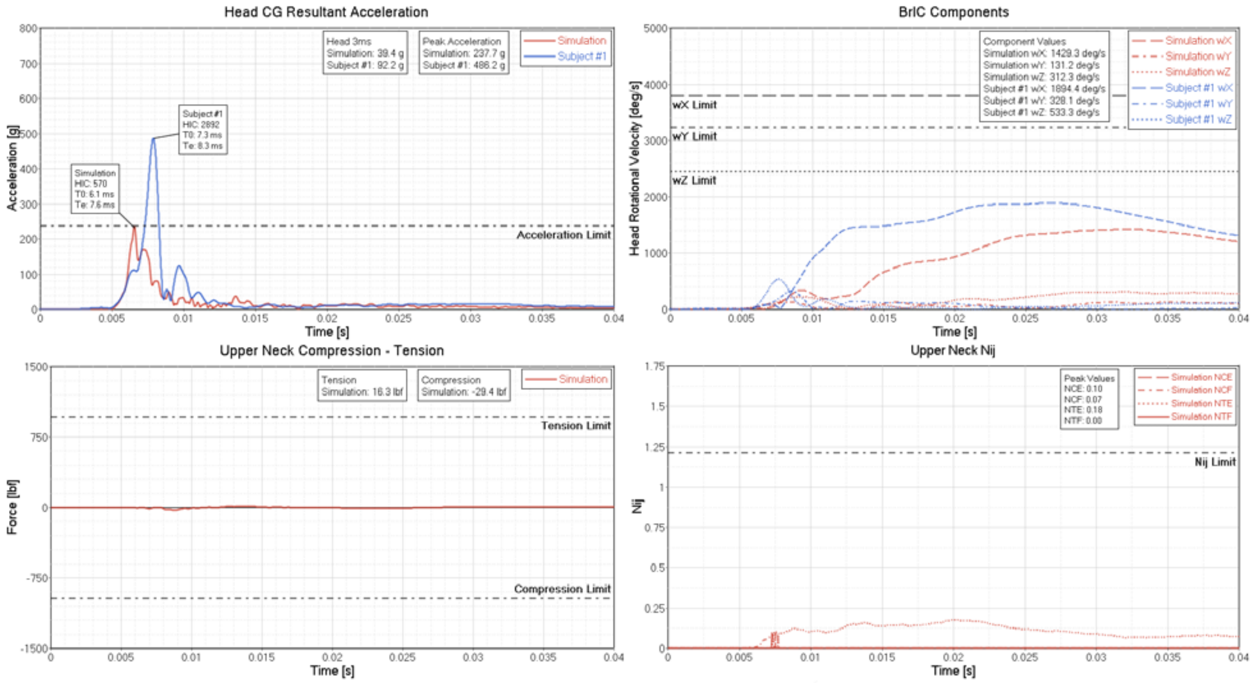

Figure 324. PMHS test 4 vs simulation comparison; DJI Phantom 3, 2.67 lb, between arms, 71 fps, sideward; subject #1; side of the head; time-history summary

<u>Test 6 – A(58F)-56</u>

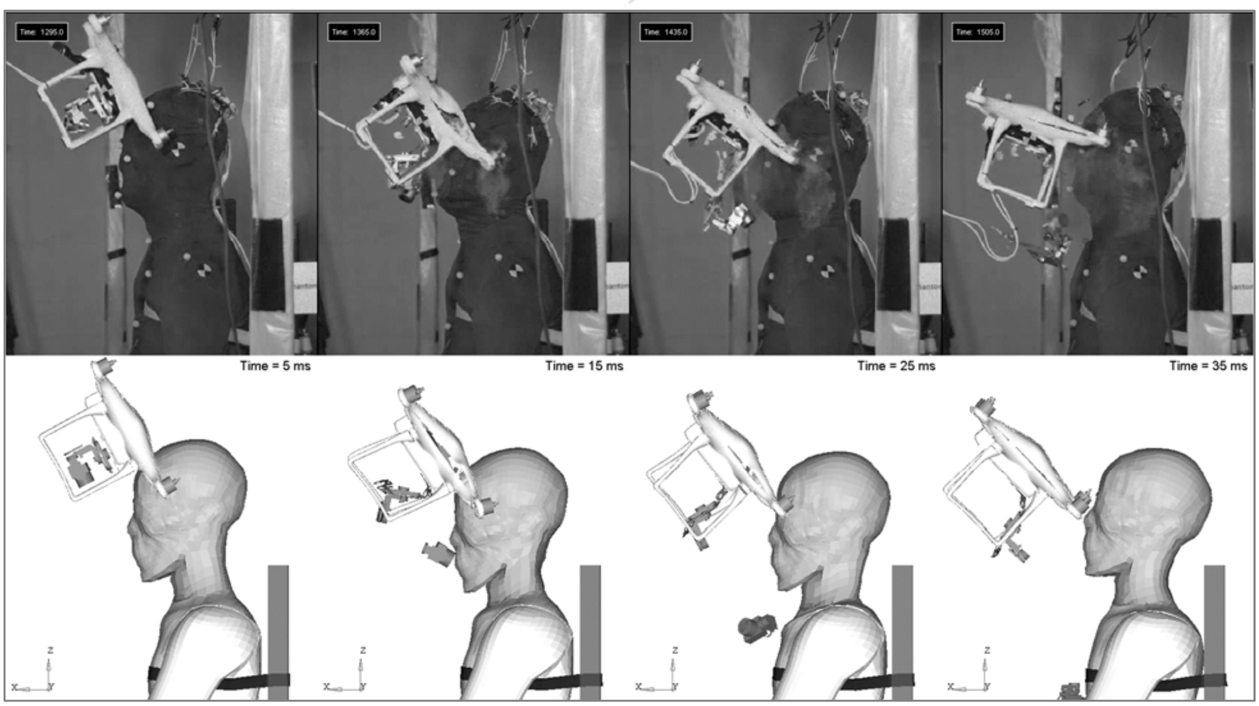

Figure 325. PMHS test 6 vs simulation comparison; DJI Phantom 3, 2.67 lb, between arms, 56 fps, angled frontal; subject #1; front of the head; kinematics

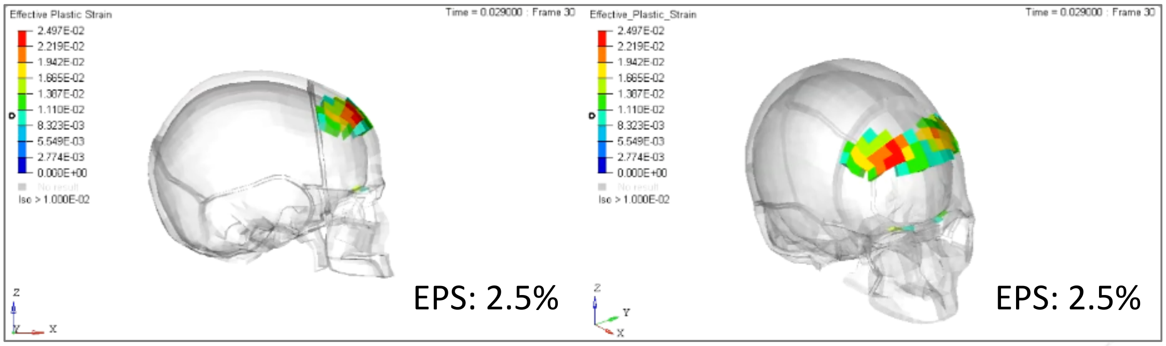

Figure 326. PMHS test 6 vs simulation comparison; DJI Phantom 3, 2.67 lb, between arms, 56 fps, angled frontal; subject #1; front of the head; EPS contour plot of skull

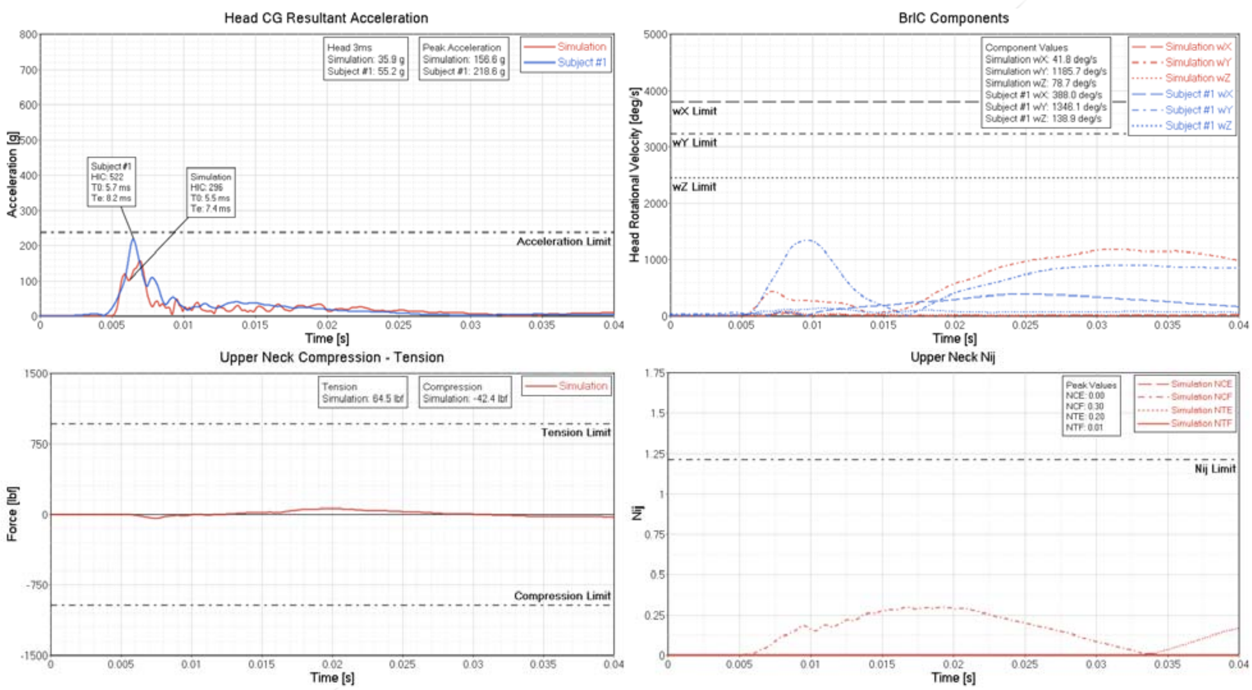

Figure 327. PMHS test 6 vs simulation comparison; DJI Phantom 3, 2.67 lb, between arms, 56 fps, angled frontal; subject #1; front of the head; time-history summary

Test 7 – A(58F)-61

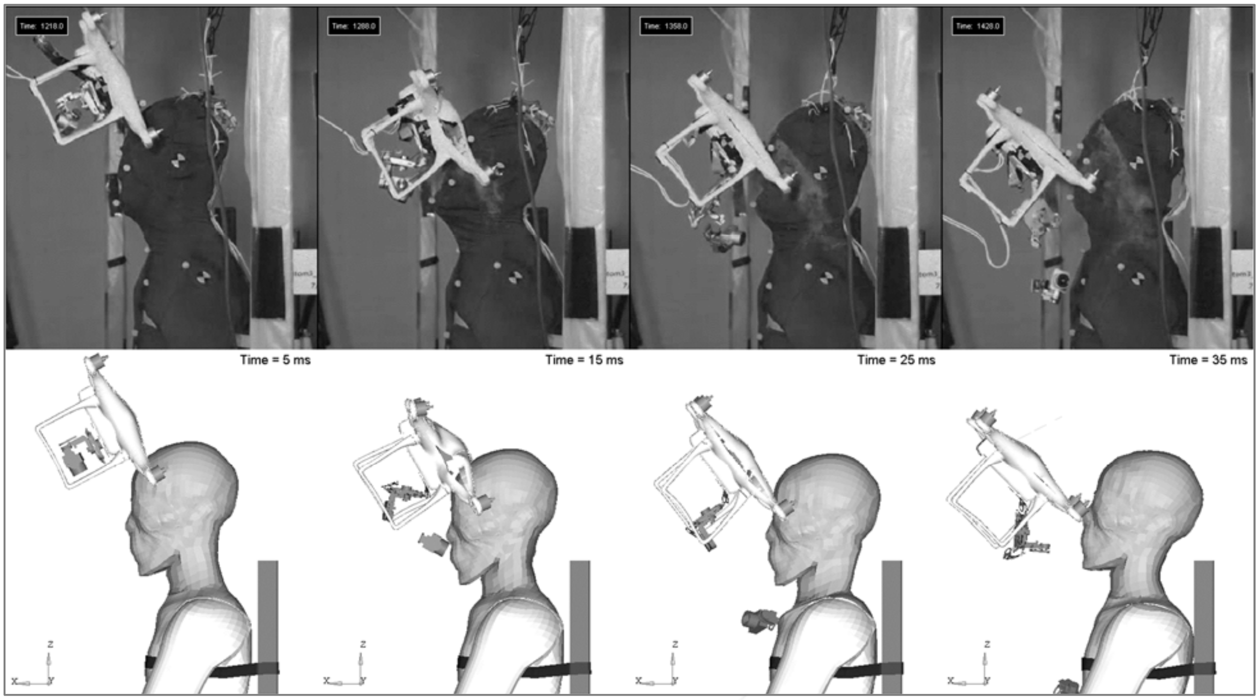

Figure 328. PMHS test 7 vs simulation comparison; DJI Phantom 3, 2.67 lb, between arms, 61 fps, angled frontal; subject #1; front of the head; kinematics

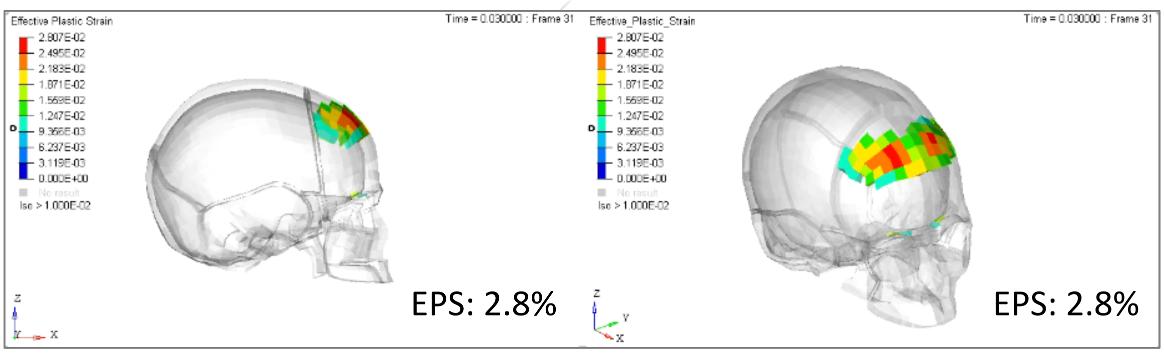

Figure 329. PMHS test 7 vs simulation comparison; DJI Phantom 3, 2.67 lb, between arms, 61 fps, angled frontal; subject #1; front of the head; EPS contour plot of skull

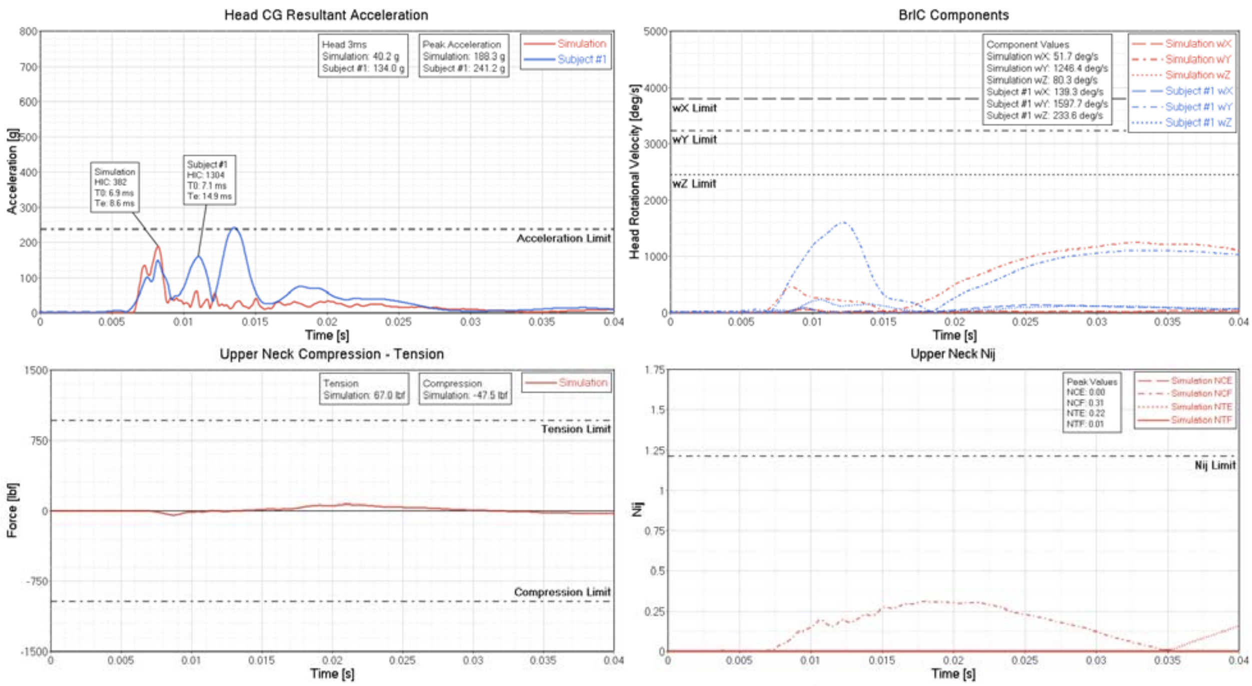

Figure 330. PMHS test 7 vs simulation comparison; DJI Phantom 3, 2.67 lb, between arms, 61 fps, angled frontal; subject #1; front of the head; time-history summary

Test 8a – A(58F)-61

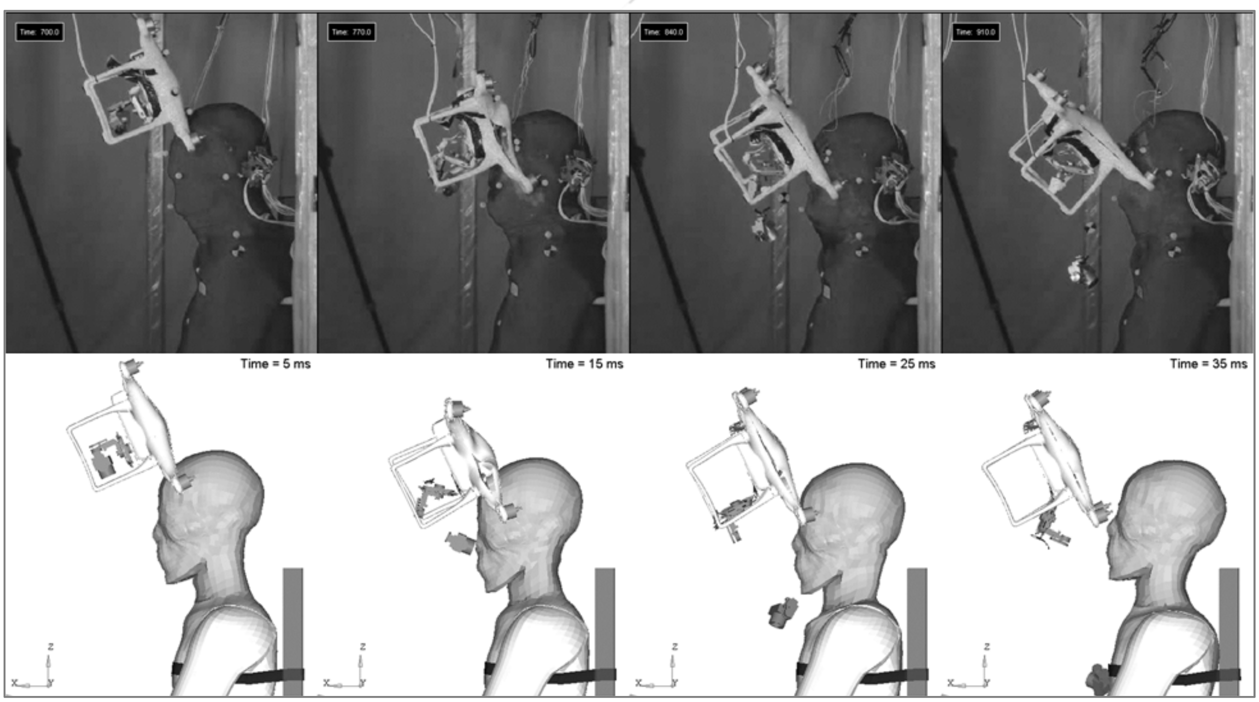

Figure 331. PMHS test 8a vs simulation comparison; DJI Phantom 3, 2.67 lb, between arms, 61 fps, angled frontal; subject #2; front of the head; kinematics

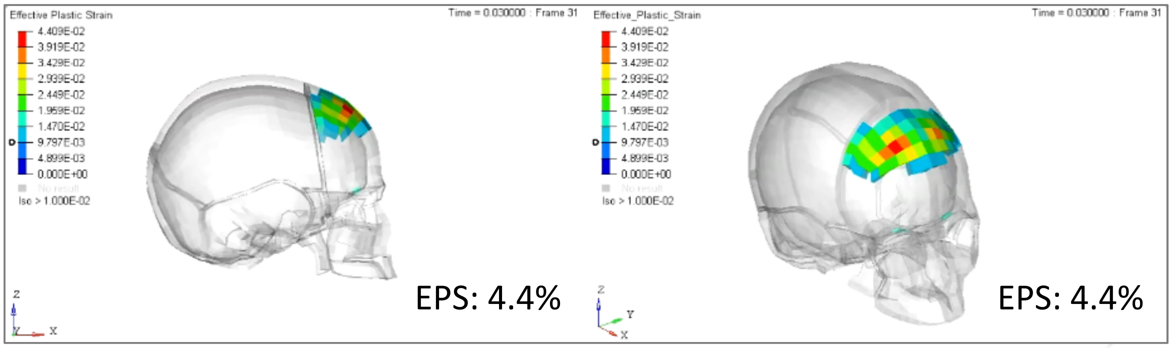

Figure 332. PMHS test 8a vs simulation comparison; DJI Phantom 3, 2.67 lb, between arms, 61 fps, angled frontal; subject #2; front of the head; EPS contour plot of skull

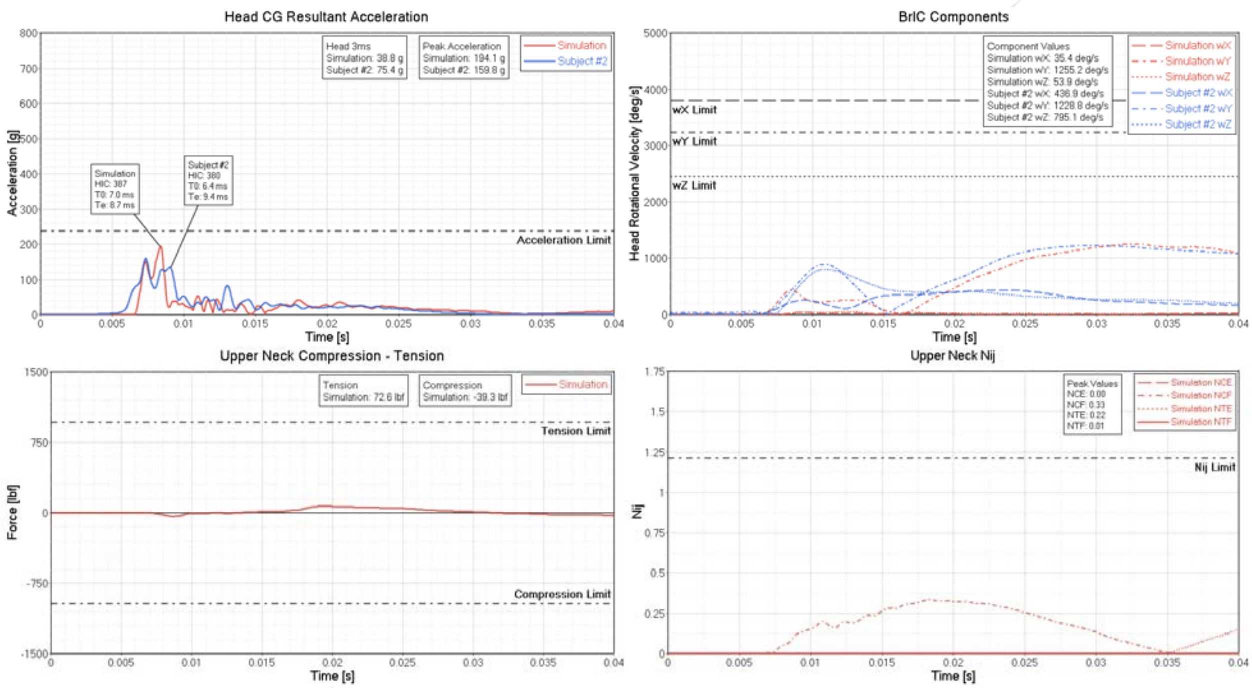

Figure 333. PMHS test 8a vs simulation comparison; DJI Phantom 3, 2.67 lb, between arms, 61 fps, angled frontal; subject #2; front of the head; time-history summary

<u>Test 9 – A(58F)-71</u>

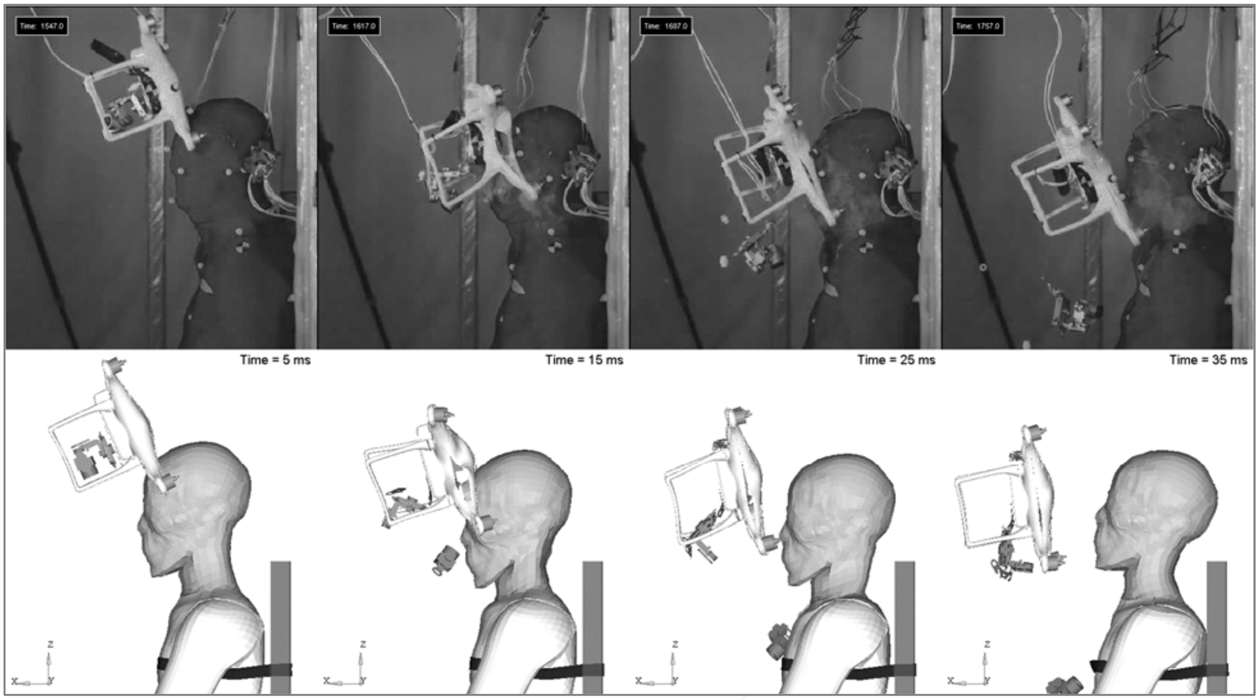

Figure 334. PMHS test 9 vs simulation comparison; DJI Phantom 3, 2.67 lb, between arms, 71 fps, angled frontal; subject #2; front of the head; kinematics

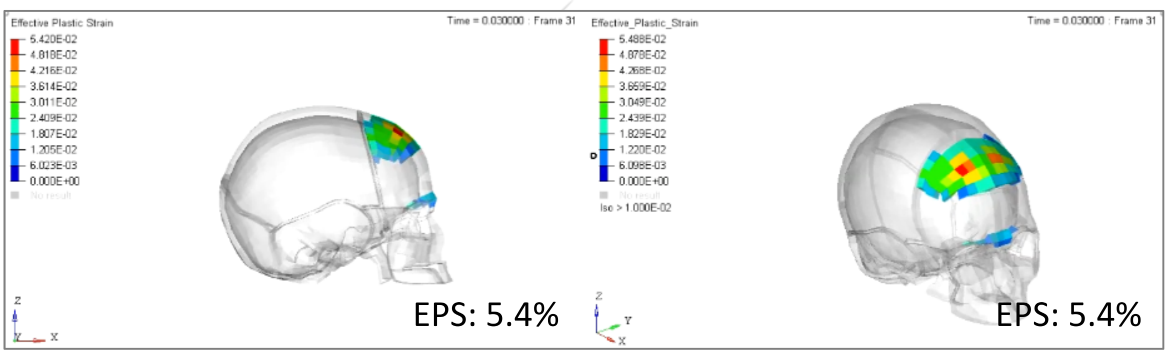

Figure 335. PMHS test 9 vs simulation comparison; DJI Phantom 3, 2.67 lb, between arms, 71 fps, angled frontal; subject #2; EPS contour plot of skull

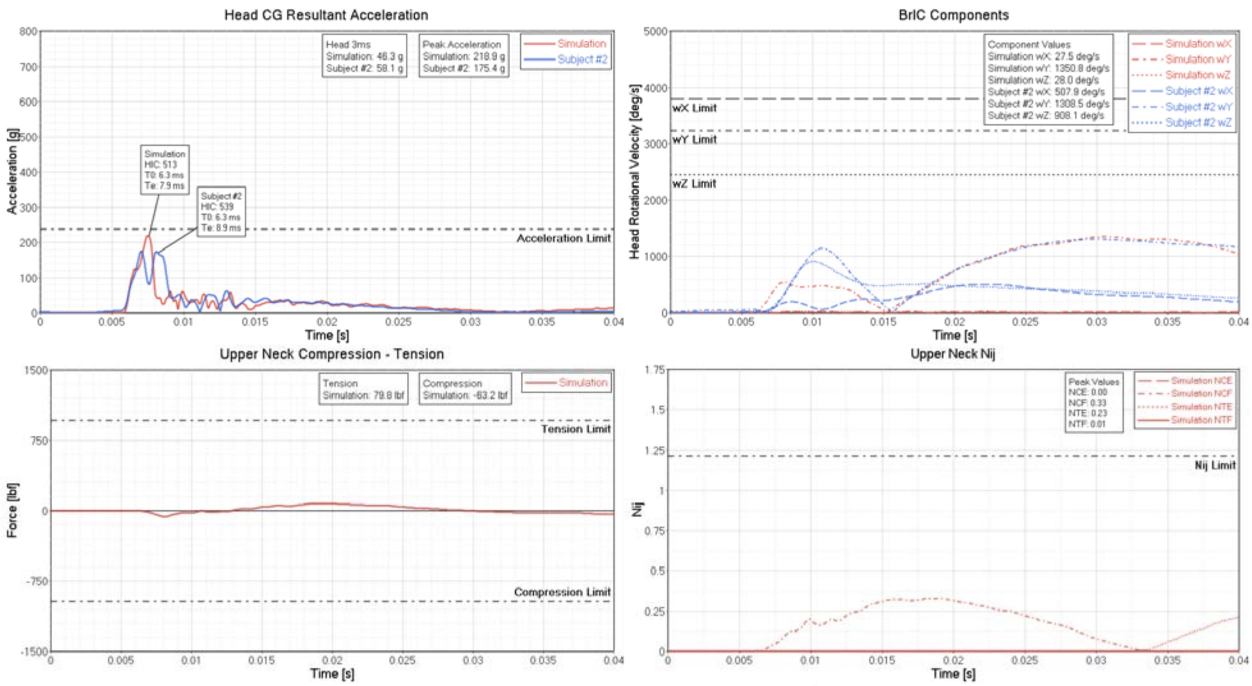

Figure 336. PMHS test 9 vs simulation comparison; DJI Phantom 3, 2.67 lb, between arms, 71 fps, angled frontal; subject #2; time-history summary

Test 10 – A(58S)-61

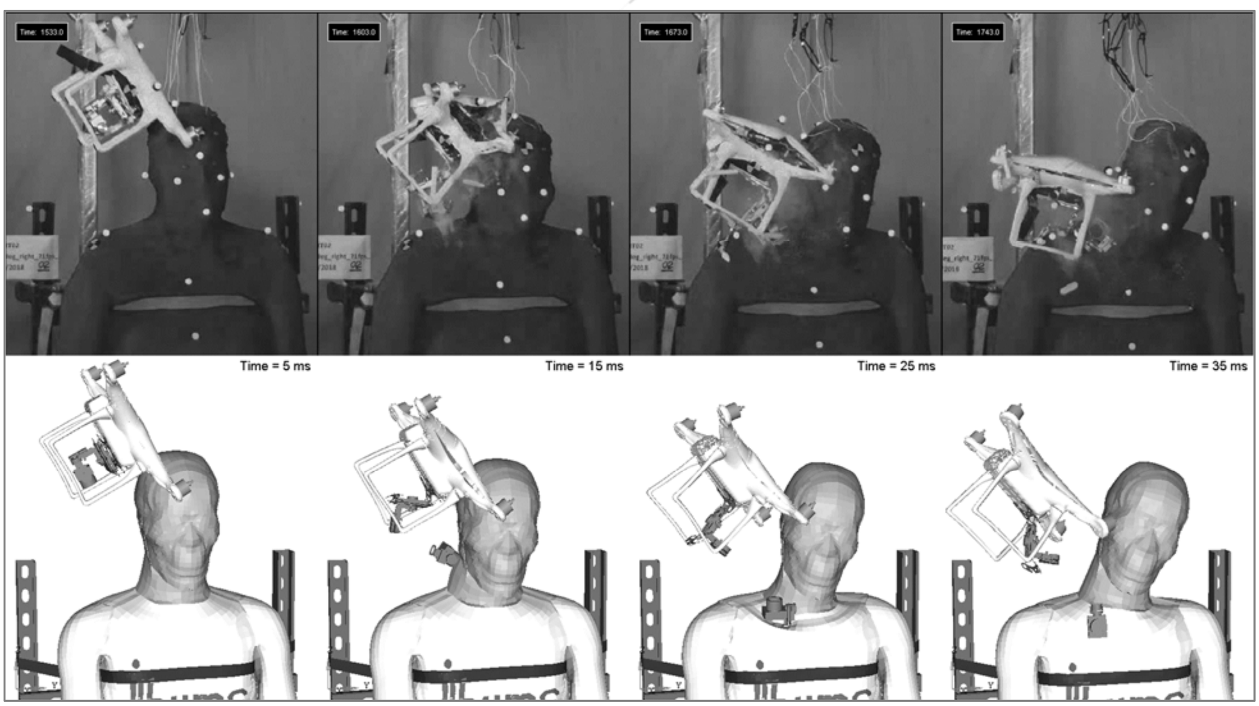

Figure 337. PMHS test 10 vs simulation comparison; DJI Phantom 3, 2.67 lb, between arms, 61 fps, angled frontal; subject #2; front of the head; kinematics

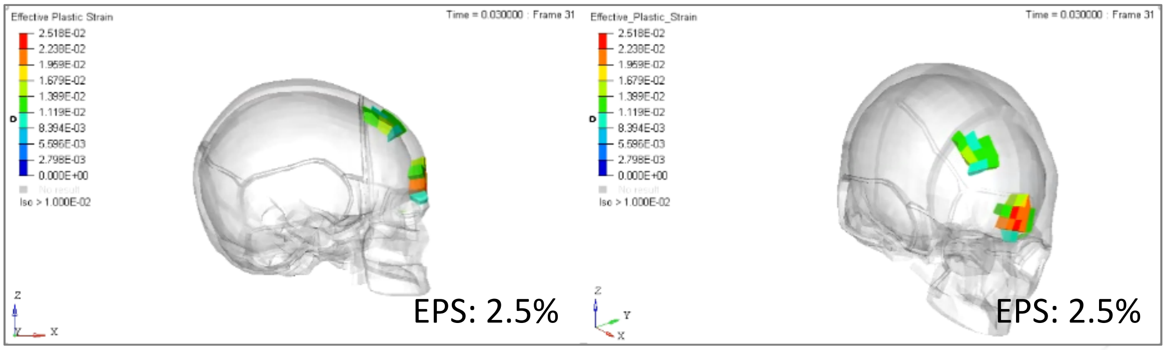

Figure 338. PMHS test 10 vs simulation comparison; DJI Phantom 3, 2.67 lb, between arms, 61 fps, angled frontal; subject #2; front of the head; EPS contour plot of skull

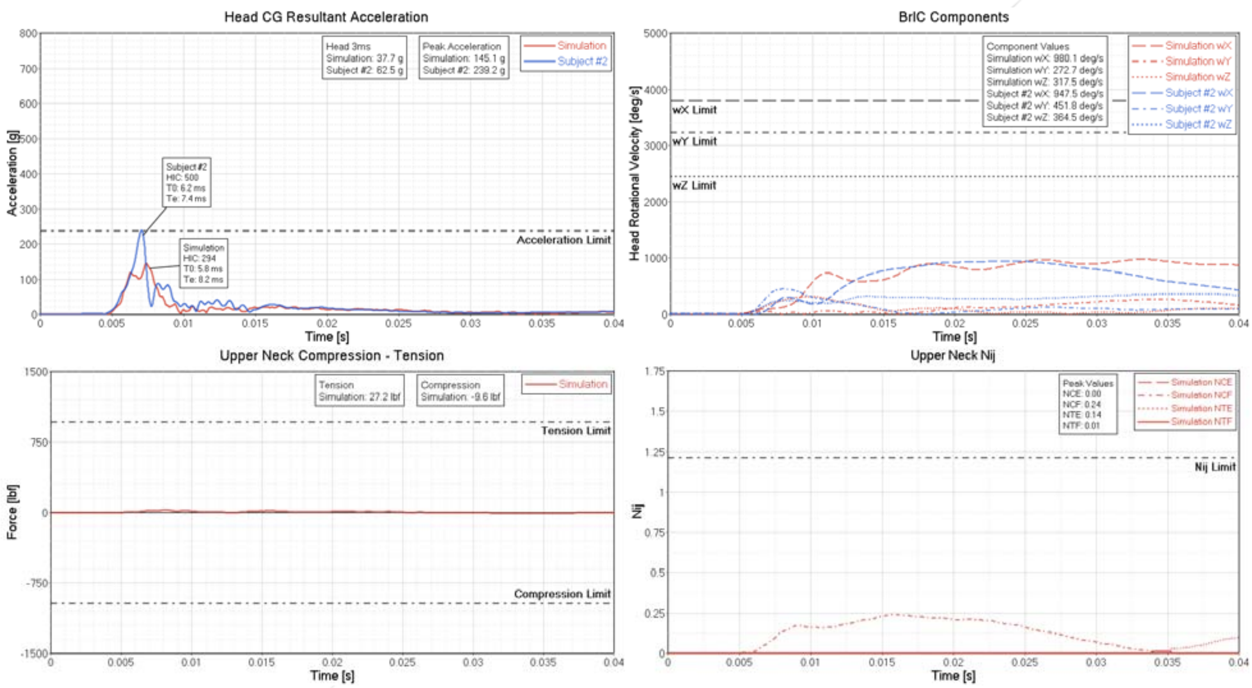

Figure 339. PMHS test 10 vs simulation comparison; DJI Phantom 3, 2.67 lb, between arms, 61 fps, angled frontal; subject #2; front of the head; time-history summary

Test 11a – A(58S)-71

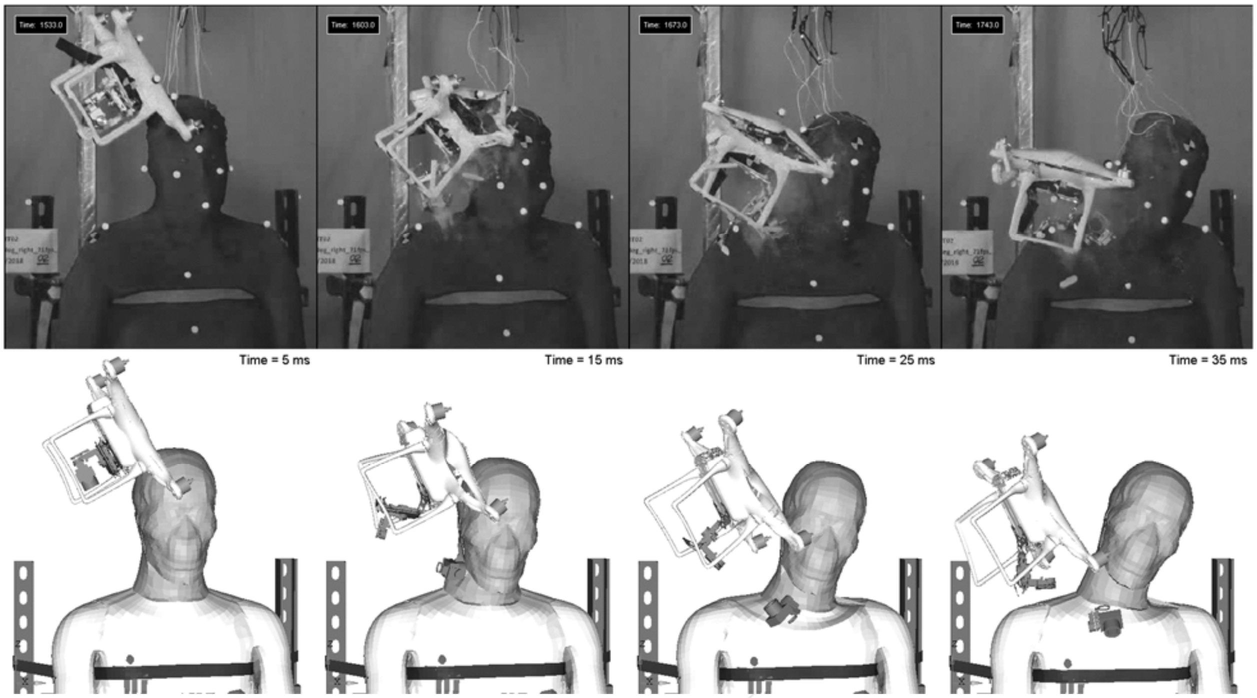

Figure 340. PMHS test 11 vs simulation comparison; DJI Phantom 3, 2.67 lb, between arms, 71 fps, angled frontal; subject #2; front of the head; kinematics

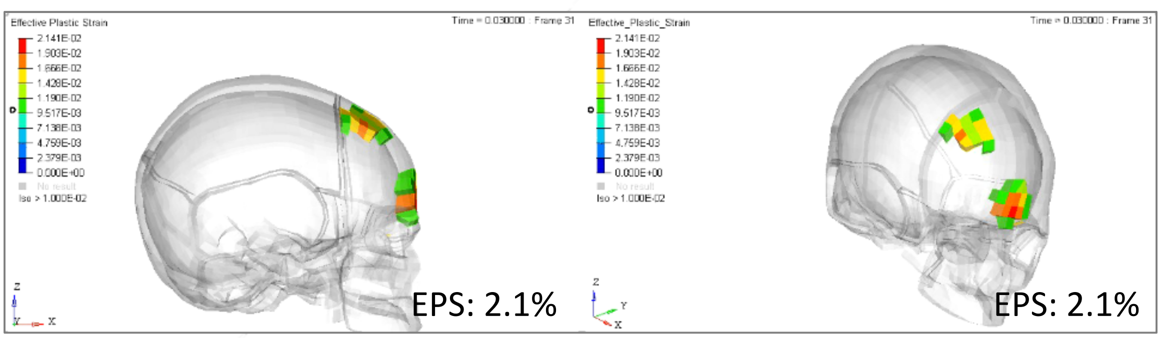

Figure 341. PMHS test 11 vs simulation comparison; DJI Phantom 3, 2.67 lb, between arms, 71 fps, angled frontal; subject #2; front of the head; EPS contour plot of skull

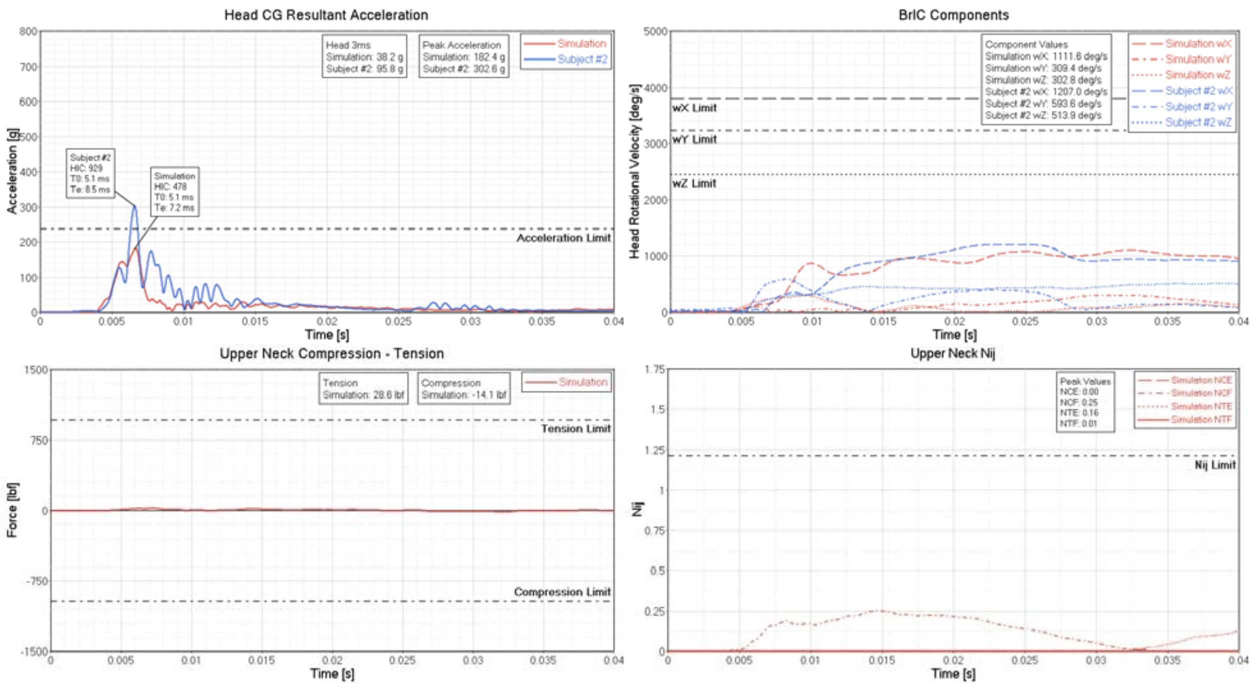

Figure 342. PMHS test 11 vs simulation comparison; DJI Phantom 3, 2.67 lb, between arms, 71 fps, angled frontal; subject #2; front of the head; time-history summary

Test 13 – V(90)-55

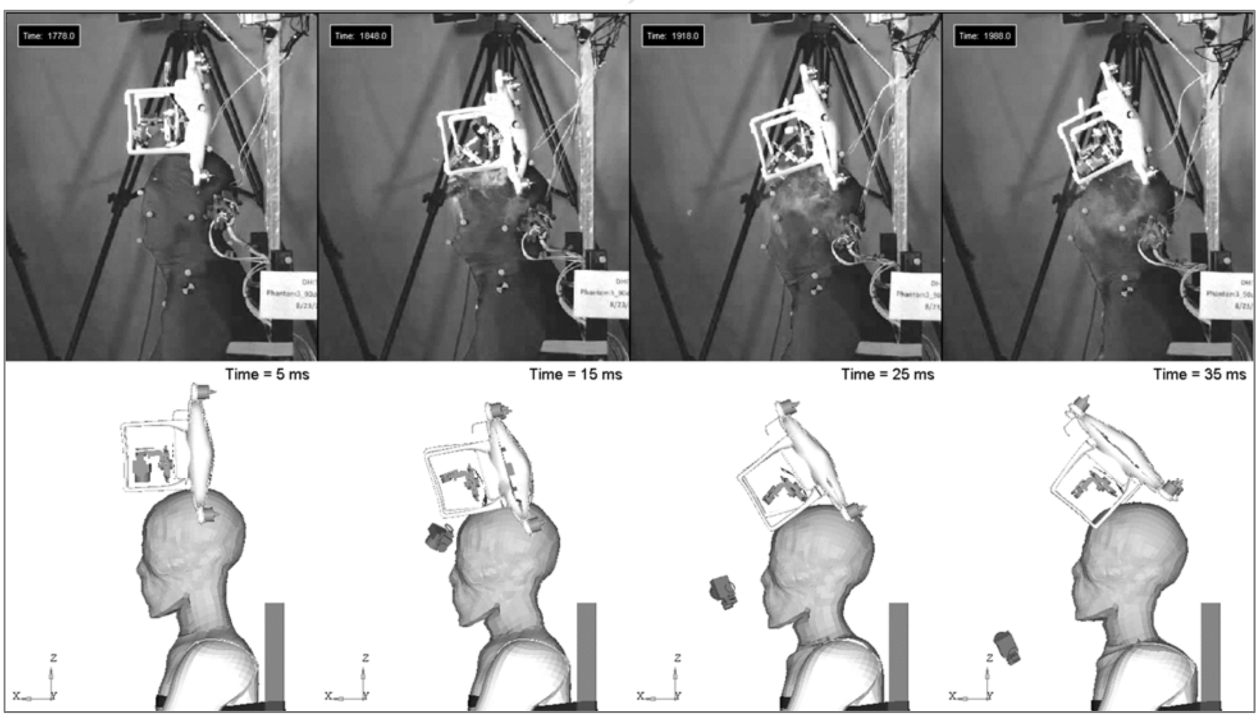

Figure 343. PMHS test 13 vs simulation comparison; DJI Phantom 3, 2.67 lb, bottom, 55 fps, vertical; subject #2; top of the head; kinematics

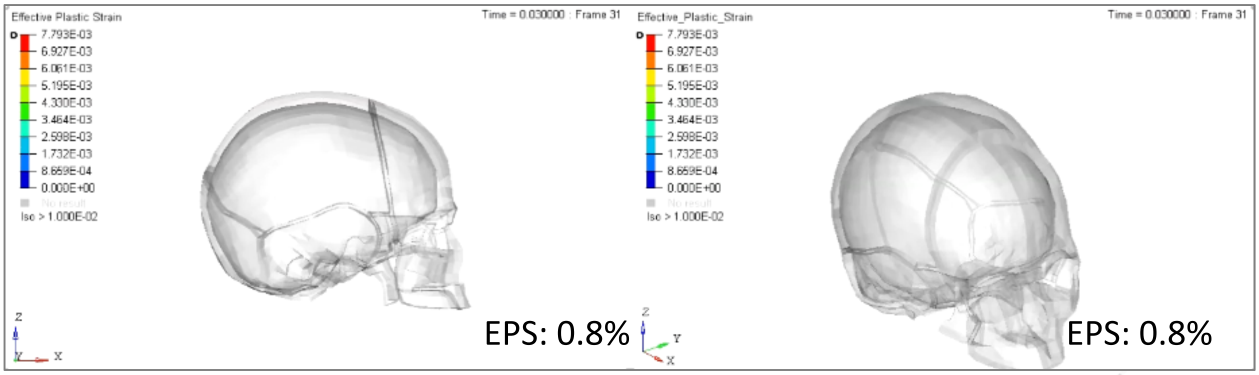

Figure 344. PMHS test 13 vs simulation comparison; DJI Phantom 3, 2.67 lb, bottom, 55 fps, vertical; subject #2; top of the head; EPS contour plot of skull

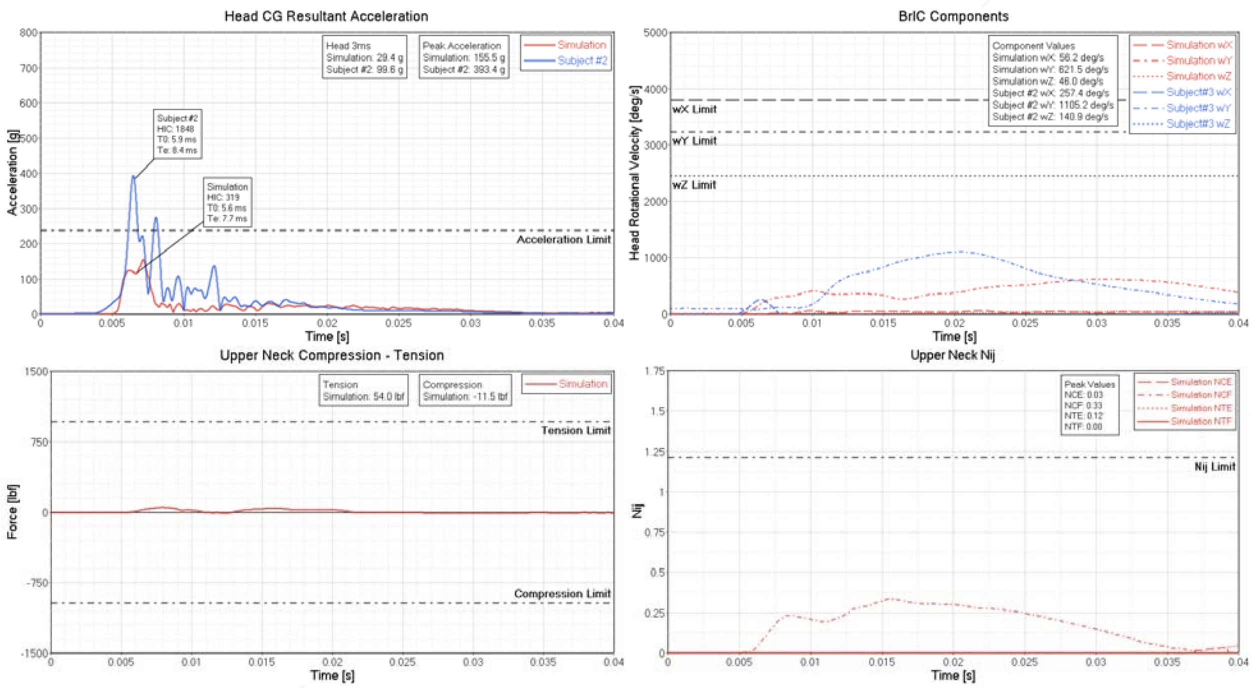

Figure 345. PMHS test 13 vs simulation comparison; DJI Phantom 3, 2.67 lb, bottom, 55 fps, vertical; subject #2; top of the head; time-history summary

Test 14 – V(90)-65

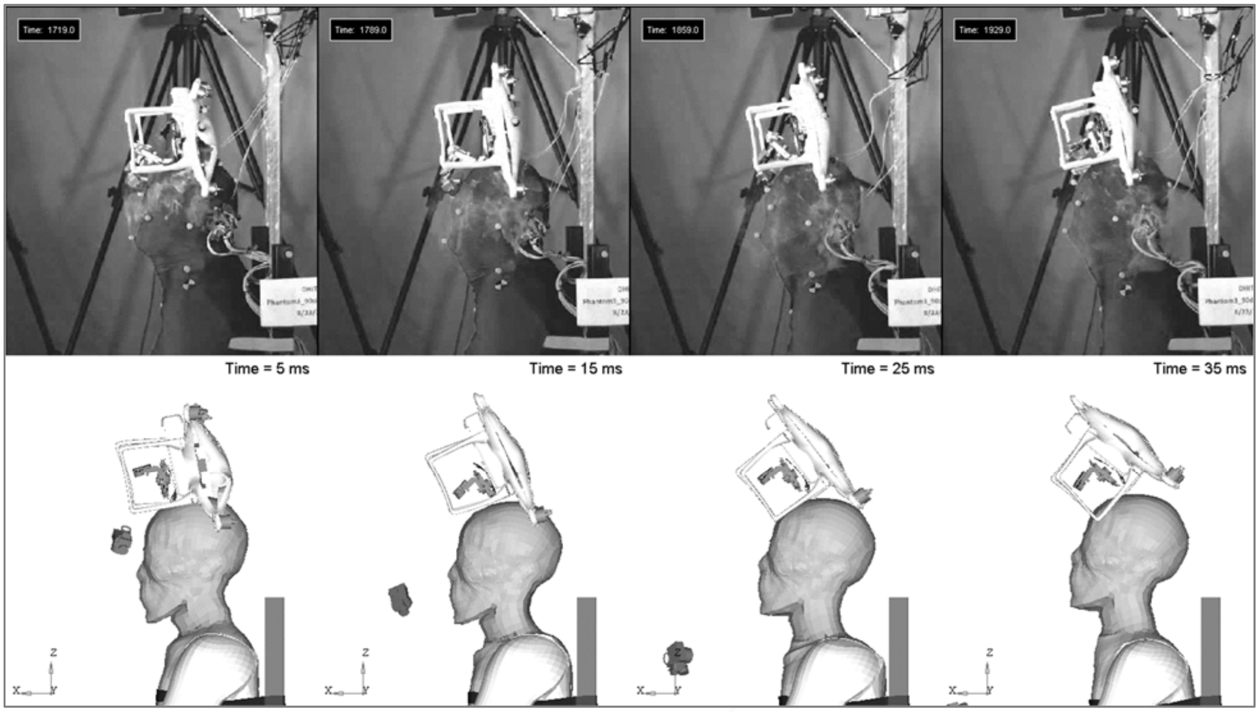

Figure 346. PMHS test 14 vs simulation comparison; DJI Phantom 3, 2.67 lb, bottom, 65 fps, vertical; subject #2; top of the head; kinematics

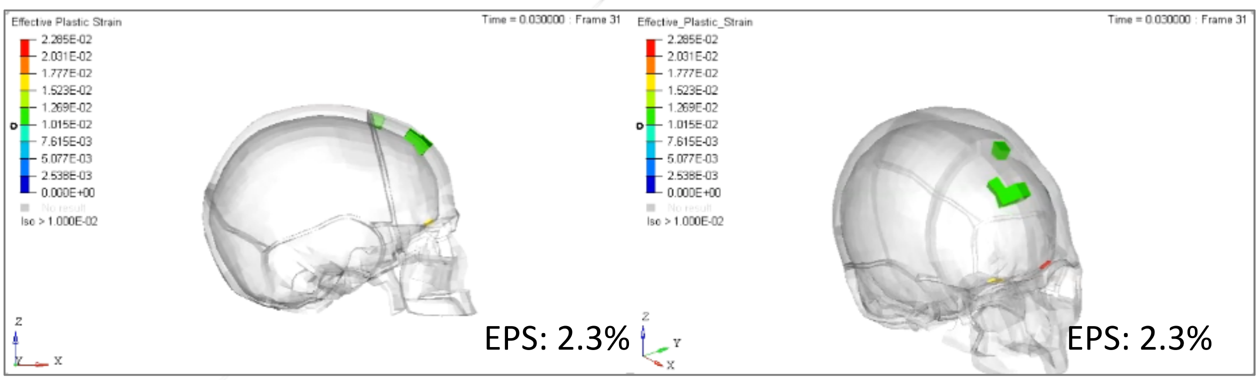

Figure 347. PMHS test 14 vs simulation comparison; DJI Phantom 3, 2.67 lb, bottom, 65 fps, vertical; subject #2; top of the head; EPS contour plot of skull

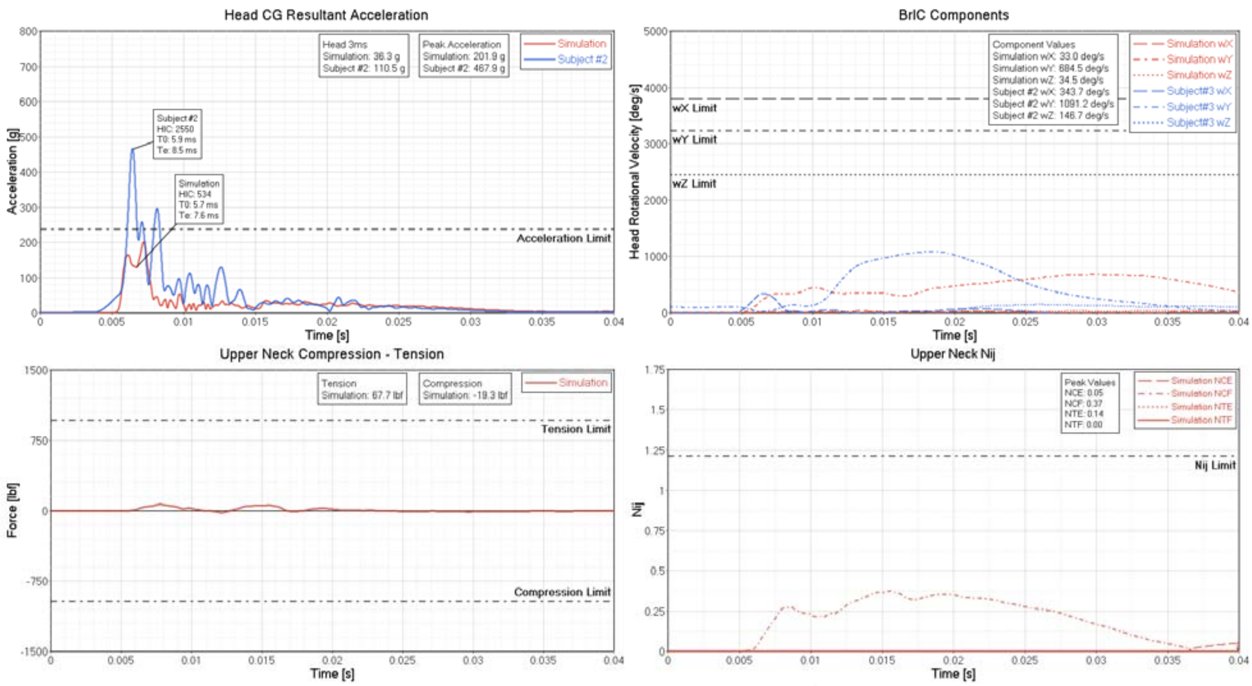

Figure 348. PMHS test 14 vs simulation comparison; DJI Phantom 3, 2.67 lb, bottom, 65 fps, vertical; subject #2; top of the head; time-history summary

<u>Test 15 – V(90)-71</u>

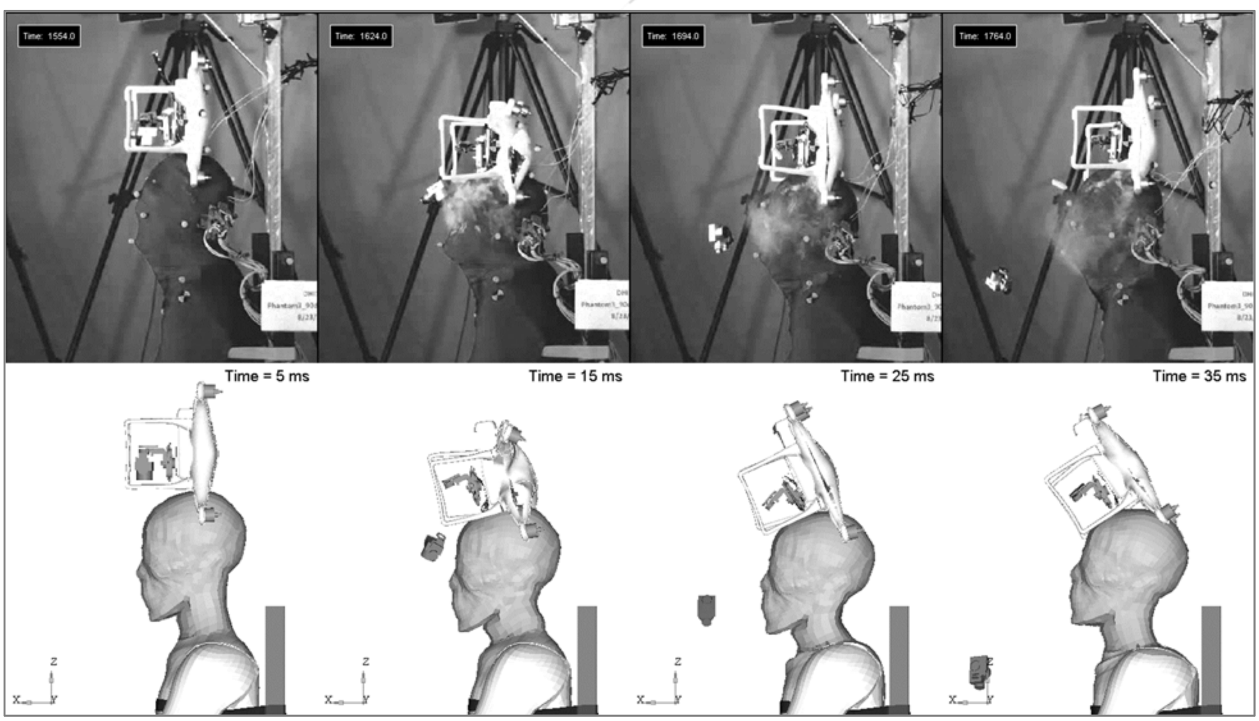

Figure 349. PMHS test 15 vs simulation comparison; DJI Phantom 3, 2.67 lb, bottom, 71 fps, vertical; subject #2; top of the head; kinematics

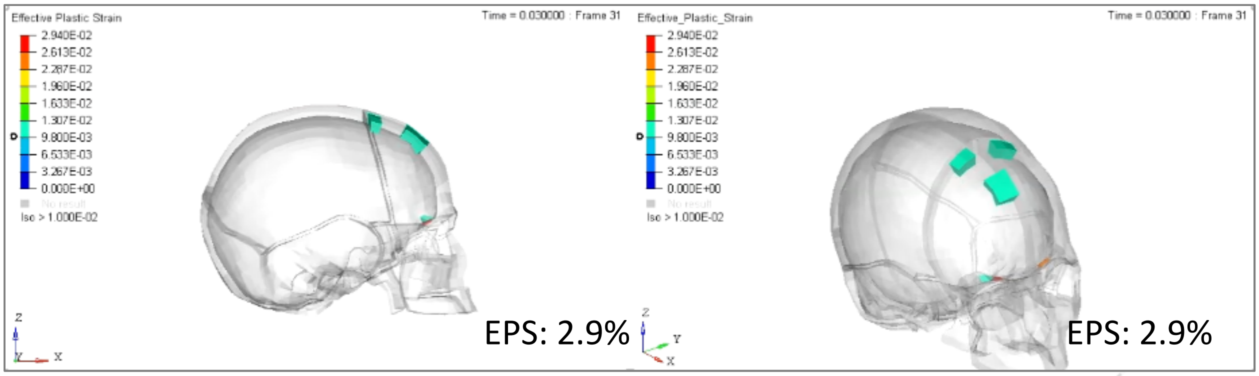

Figure 350. PMHS test 15 vs simulation comparison; DJI Phantom 3, 2.67 lb, bottom, 71 fps, vertical; subject #2; top of the head; EPS contour plot of skull

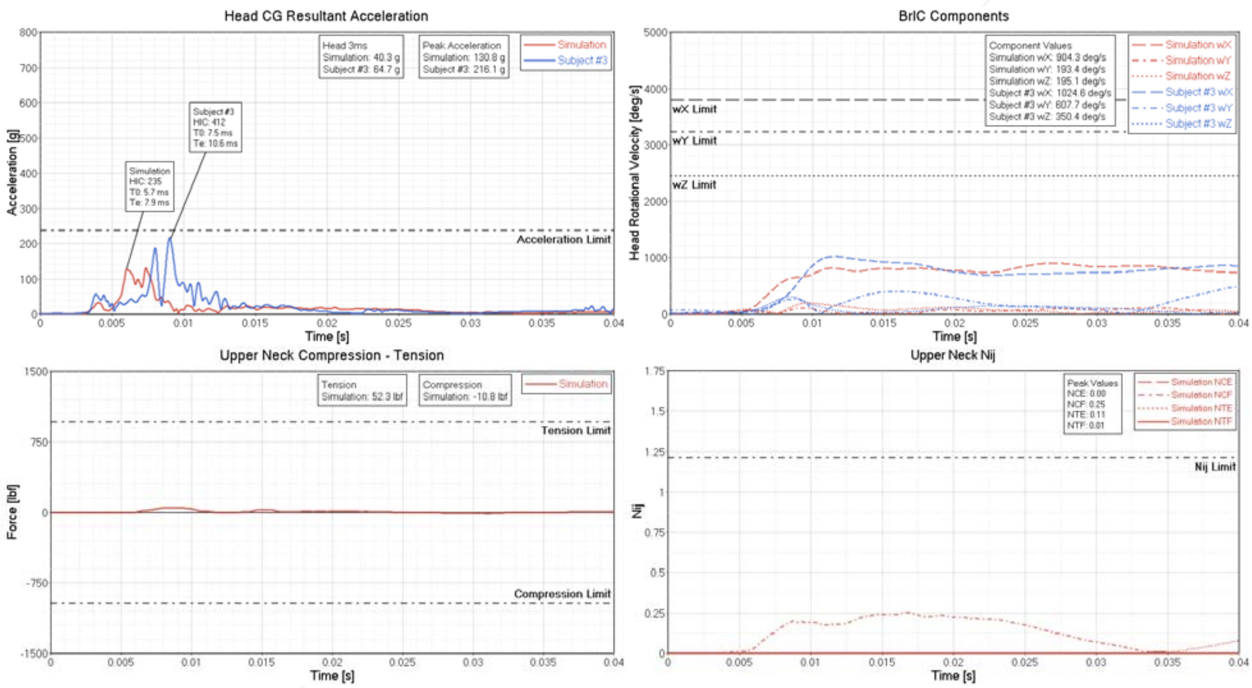

Figure 351. PMHS test 15 vs simulation comparison; DJI Phantom 3, 2.67 lb, bottom, 71 fps, vertical; subject #2; top of the head; time-history summary

Test 16 – A(58S)-61

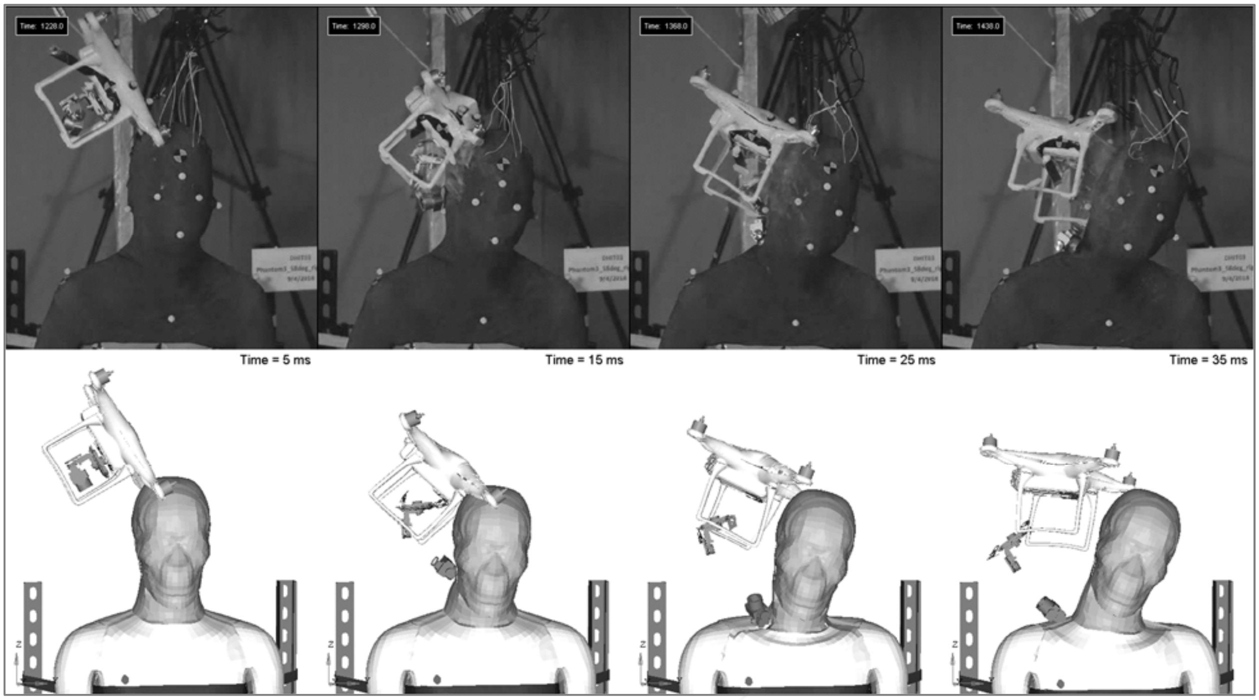

Figure 352. PMHS test 16 vs simulation comparison; DJI Phantom 3, 2.67 lb, between arms, 61 fps, angled sideward; subject #3; side of the head; kinematics

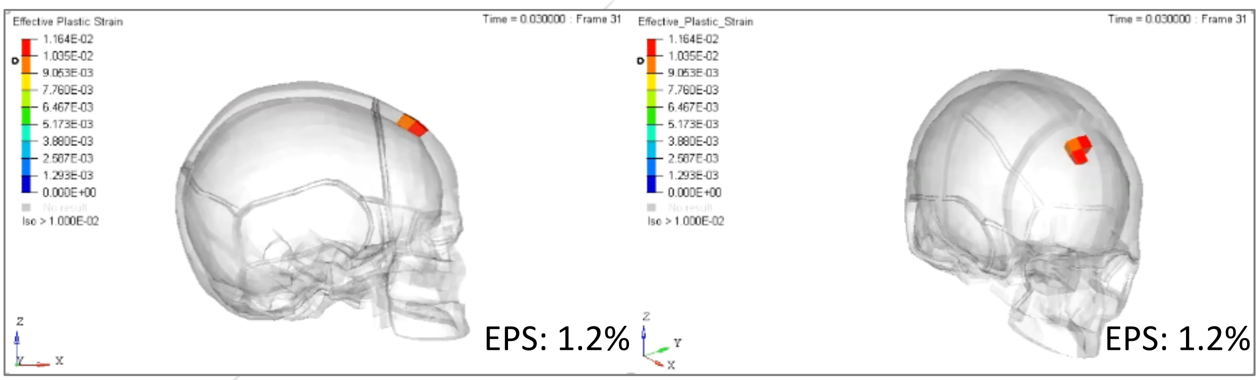

Figure 353. PMHS test 16 vs simulation comparison; DJI Phantom 3, 2.67 lb, between arms, 61 fps, angled sideward; subject #3; side of the head; EPS contour plot of skull

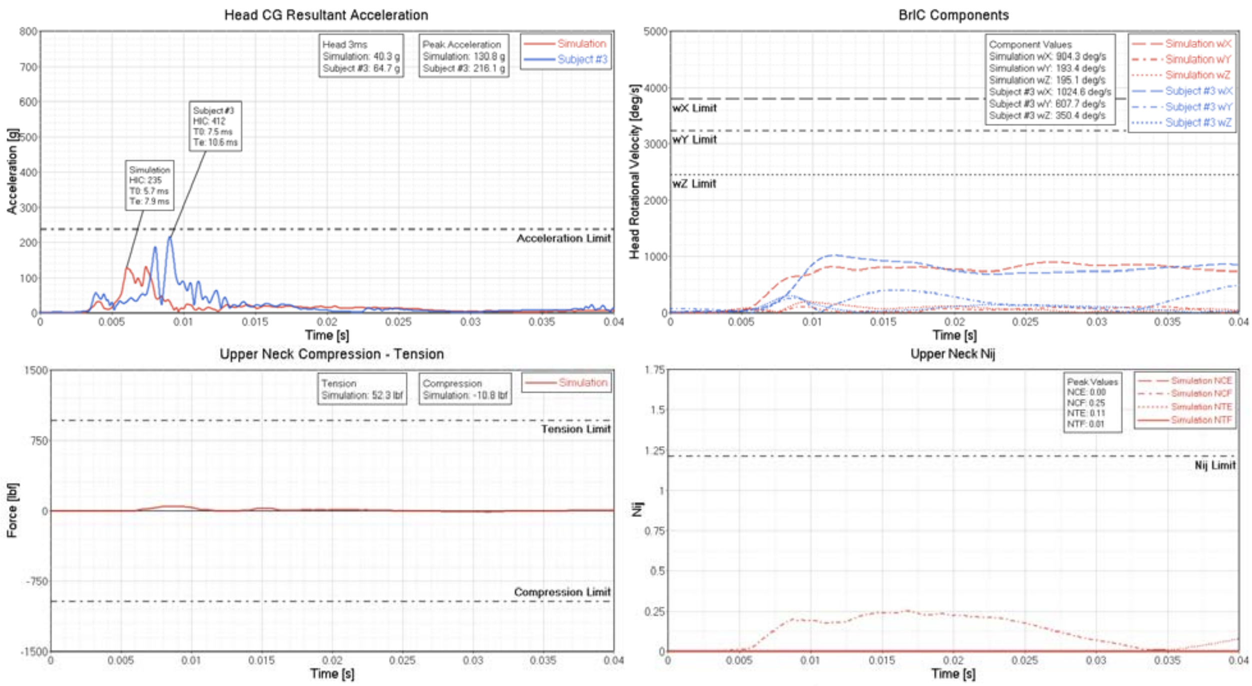

Figure 354. PMHS test 16 vs simulation comparison; DJI Phantom 3, 2.67 lb, between arms, 61 fps, angled sideward; subject #3; side of the head; time-history summary

<u>Test 17 – A(58S)-71</u>

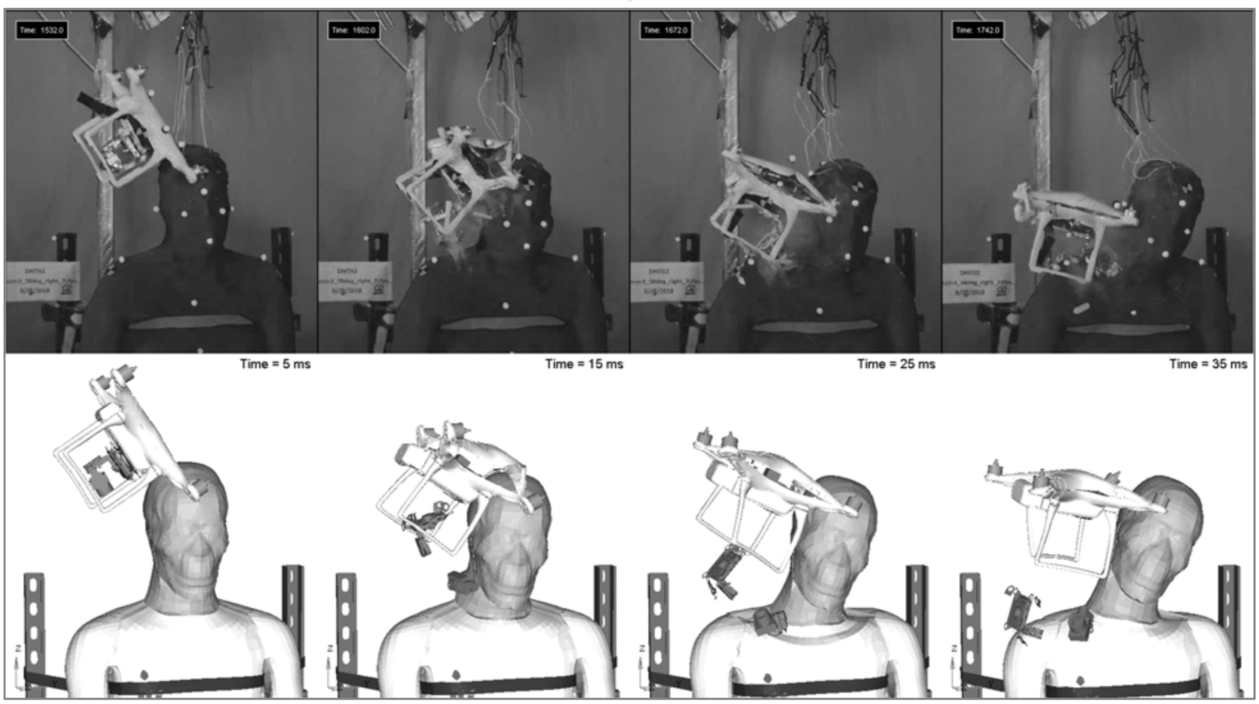

Figure 355. PMHS test 17 vs simulation comparison; DJI Phantom 3, 2.67 lb, between arms, 71 fps, angled sideward; subject #3; side of the head; kinematics

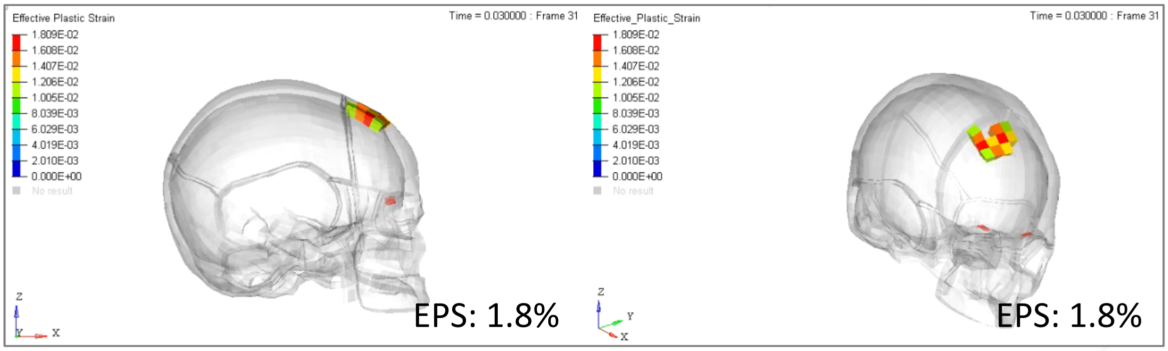

Figure 356. PMHS test 17 vs simulation comparison; DJI Phantom 3, 2.67 lb, between arms, 71 fps, angled sideward; subject #3; side of the head; EPS contour plot of skull

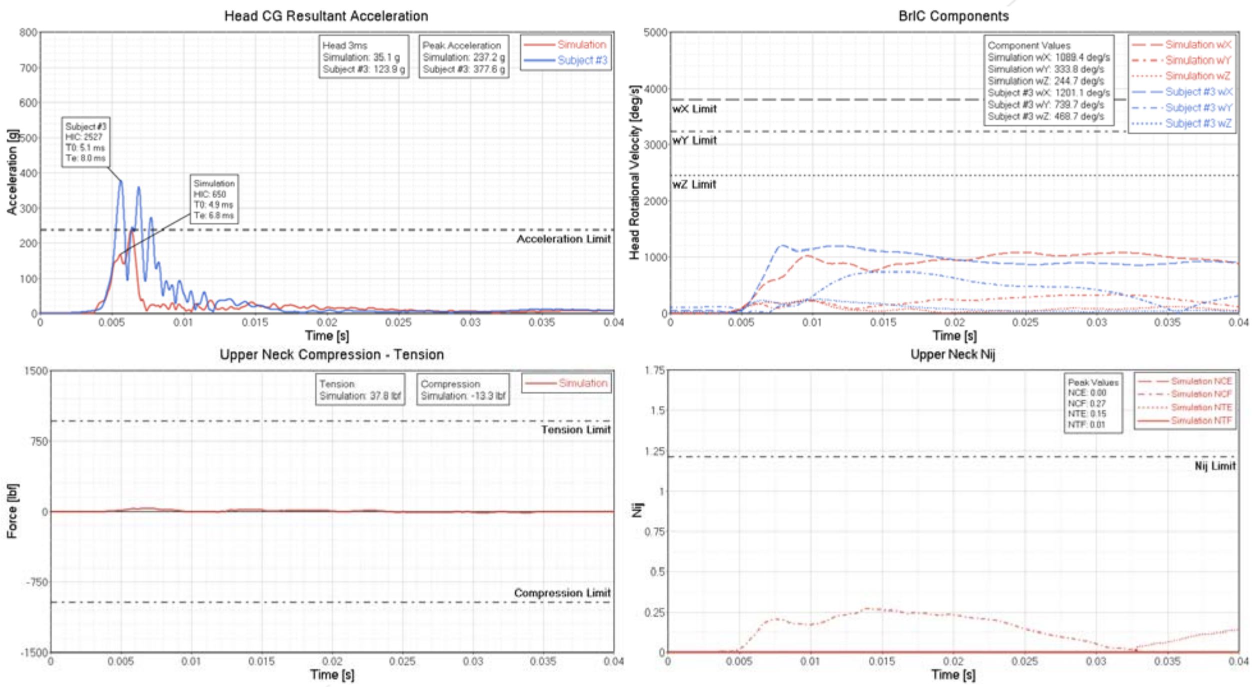

Figure 357. PMHS test 17 vs simulation comparison; DJI Phantom 3, 2.67 lb, between arms, 71 fps, angled sideward; subject #3; side of the head; time-history summary

Test 18 – A(58F)-61

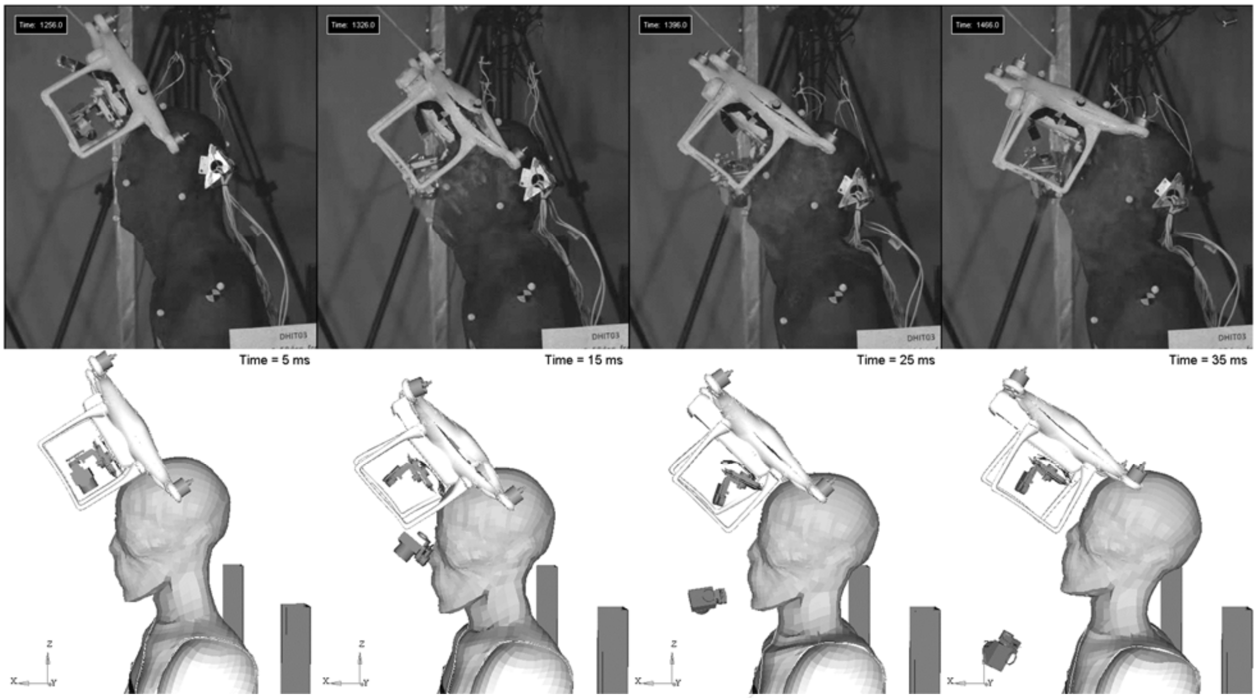

Figure 358. PMHS test 18 vs simulation comparison; DJI Phantom 3, 2.67 lb, between arms, 61 fps, angled frontal; subject #3; front of the head; kinematics

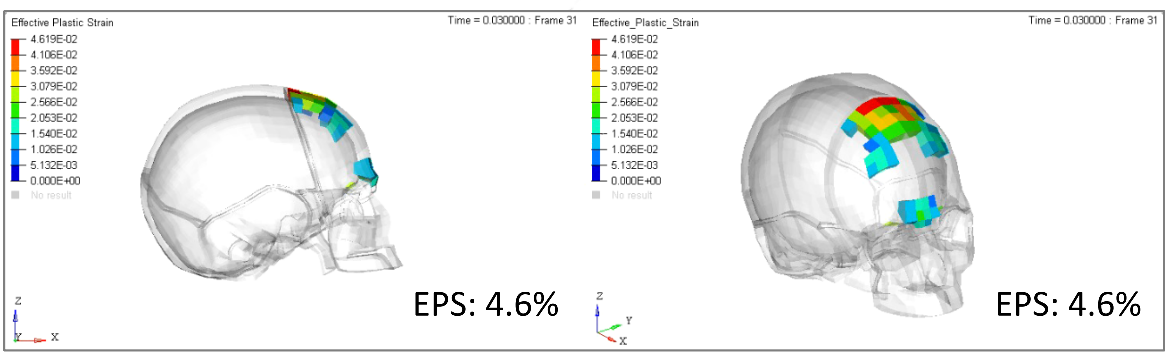

Figure 359. PMHS test 18 vs simulation comparison; DJI Phantom 3, 2.67 lb, between arms, 61 fps, angled frontal; subject #3; front of the head; EPS contour plot of skull

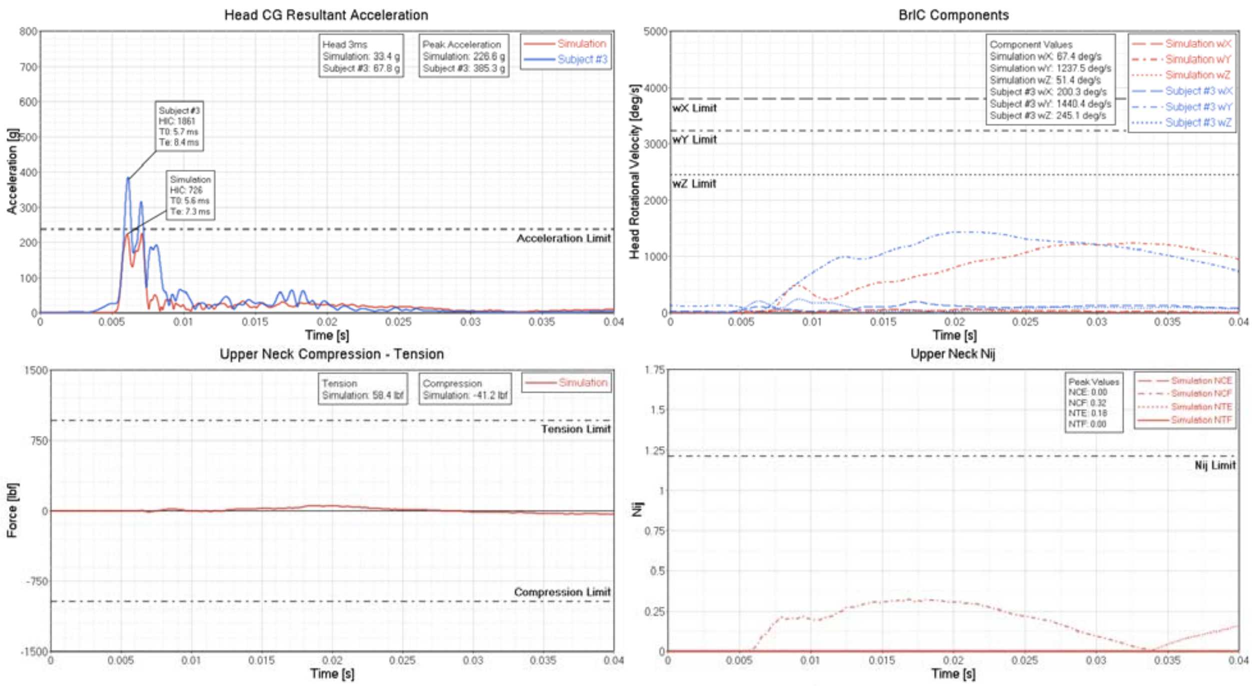

Figure 360. PMHS test 18 vs simulation comparison; DJI Phantom 3, 2.67 lb, between arms, 61 fps, angled frontal; subject #3; front of the head; time-history summary

Test 19 – A(58F)-71

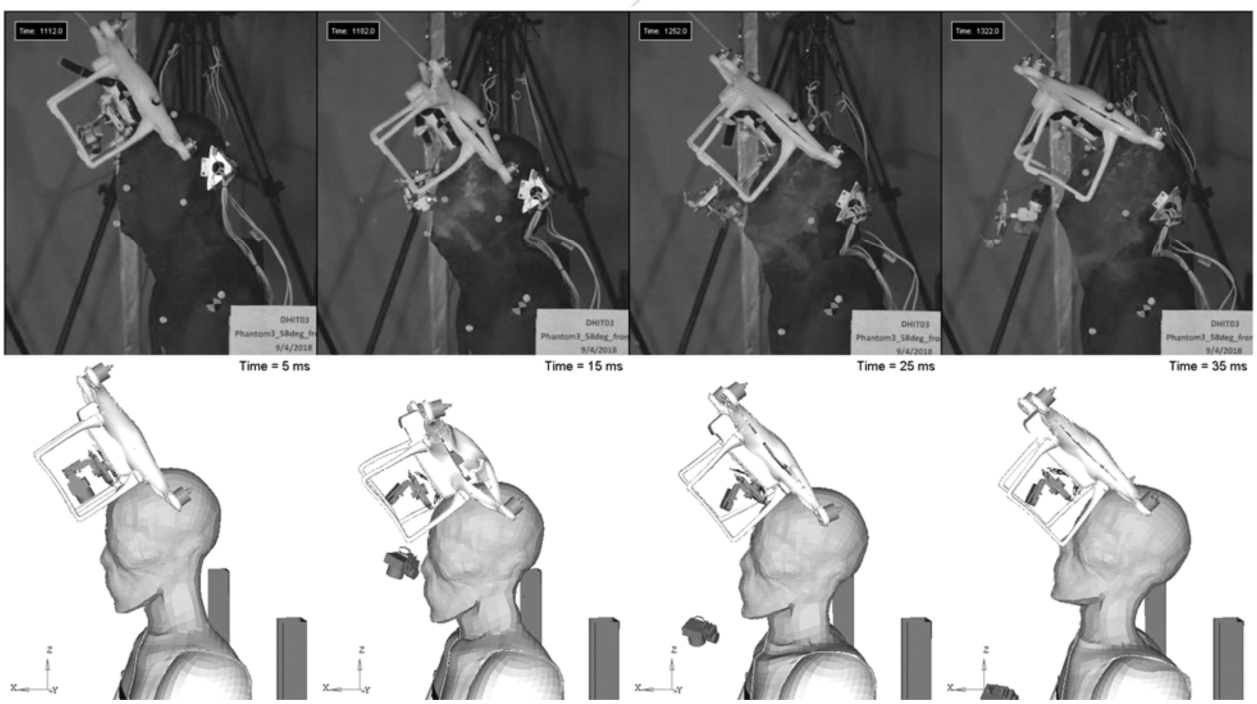

Figure 361. PMHS test 19 vs simulation comparison; DJI Phantom 3, 2.67 lb, between arms, 71 fps, angled frontal; subject #3; front of the head; kinematics

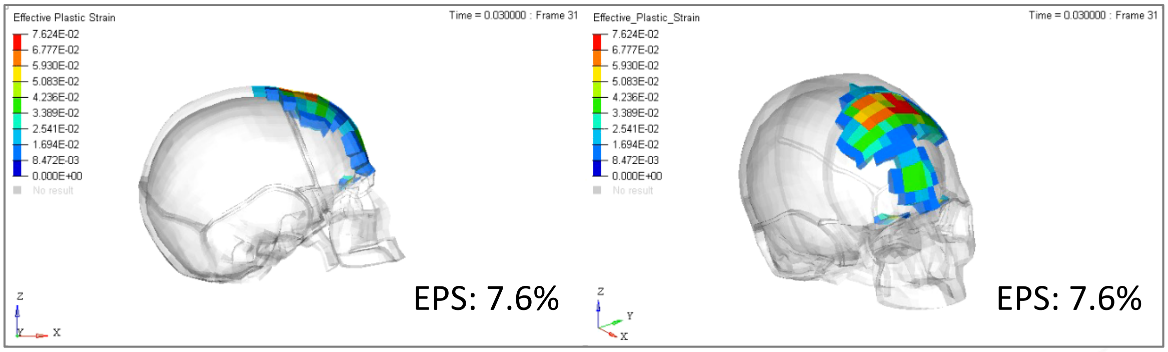

Figure 362. PMHS test 19 vs simulation comparison; DJI Phantom 3, 2.67 lb, between arms, 71 fps, angled frontal; subject #3; front of the head; EPS contour plot of skull

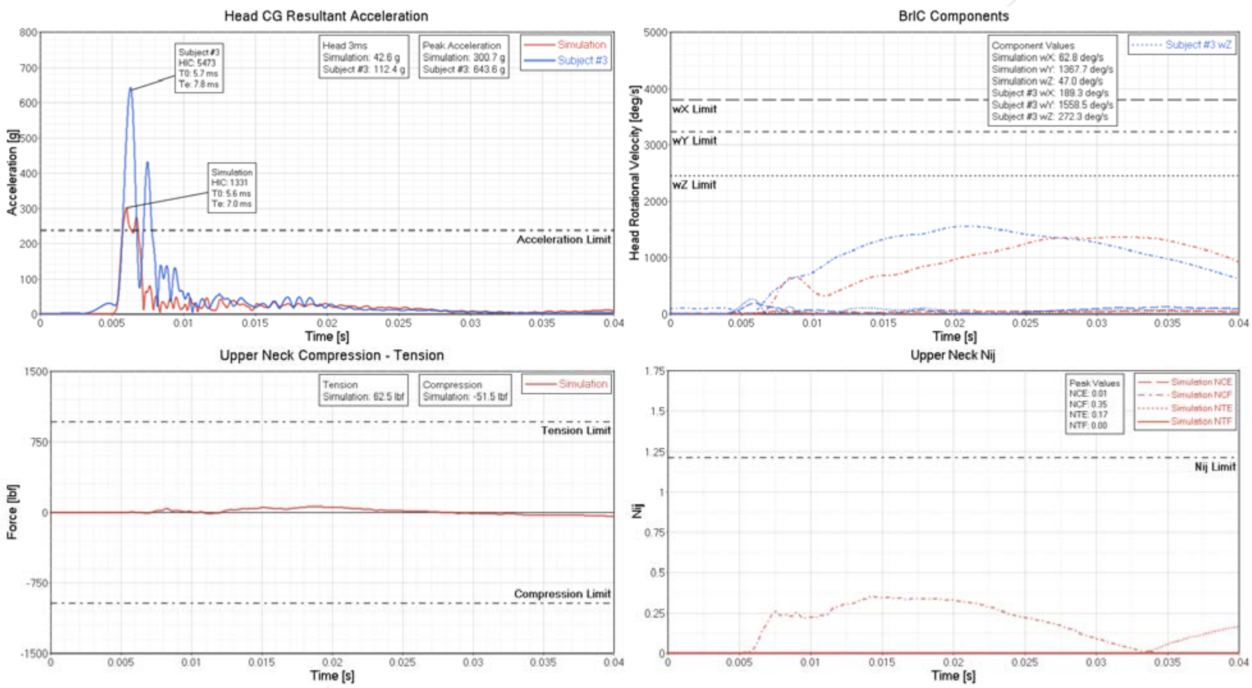

Figure 363. PMHS test 19 vs simulation comparison; DJI Phantom 3, 2.67 lb, between arms, 71 fps, angled frontal; subject #3; front of the head; time-history summary

Test 22 – V(90)-64

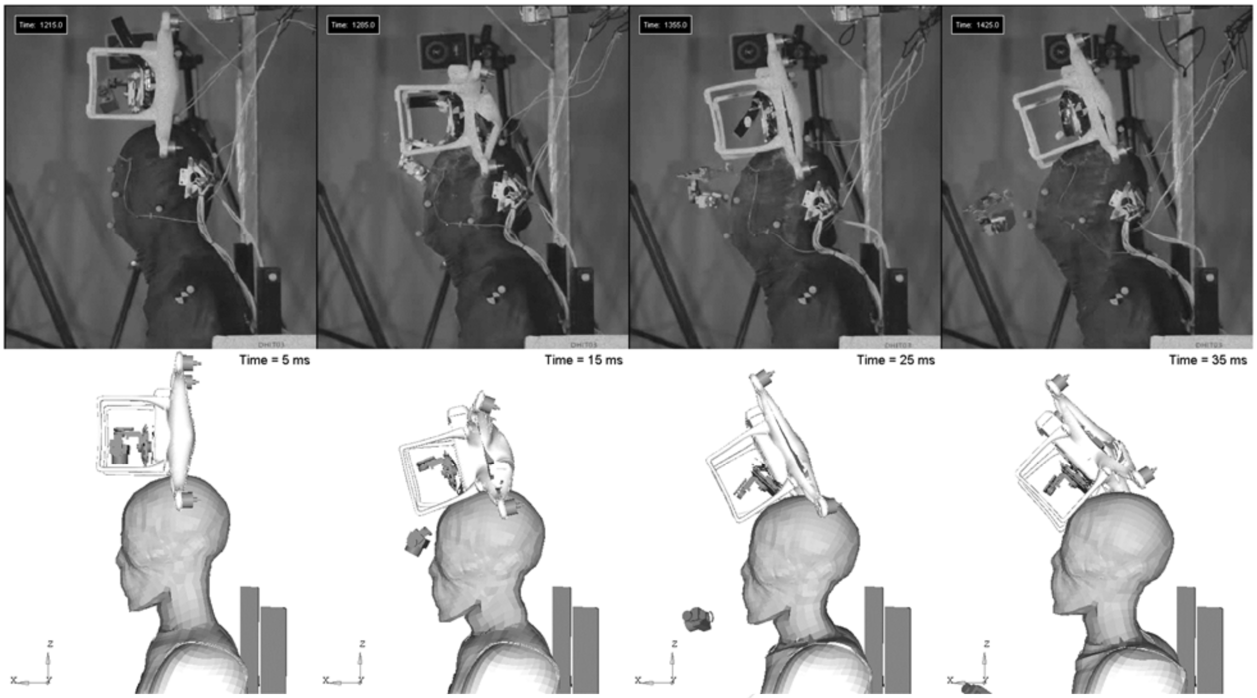

Figure 364. PMHS test 22 vs simulation comparison; DJI Phantom 3, 2.67 lb, between arms, 61 fps, vertical; subject #3; top of the head; kinematics

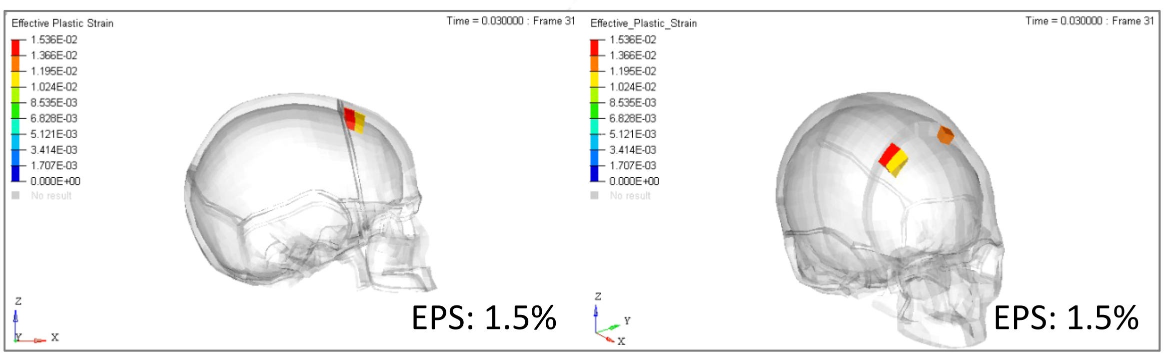

Figure 365. PMHS test 22 vs simulation comparison; DJI Phantom 3, 2.67 lb, between arms, 61 fps, vertical; subject #3; top of the head; EPS contour plot of skull

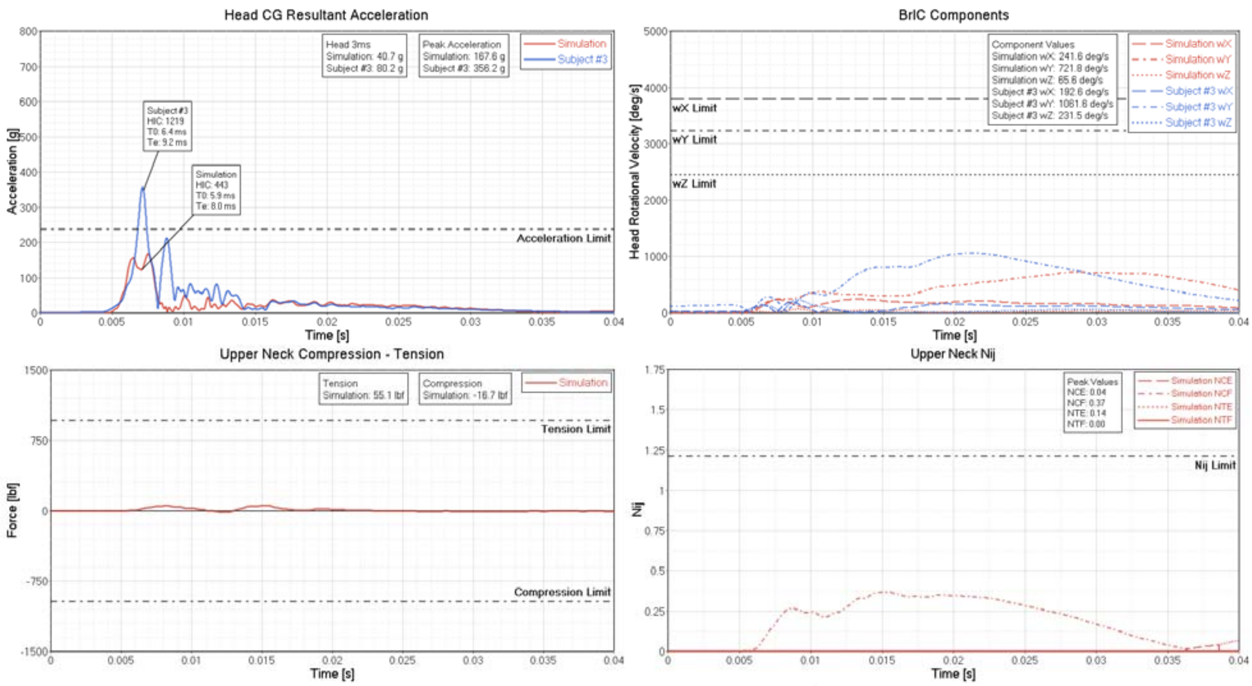

Figure 366. PMHS test 22 vs simulation comparison; DJI Phantom 3, 2.67 lb, between arms, 61 fps, vertical; subject #3; top of the head; time-history summary

<u>Test 23 – V(90)-71</u>

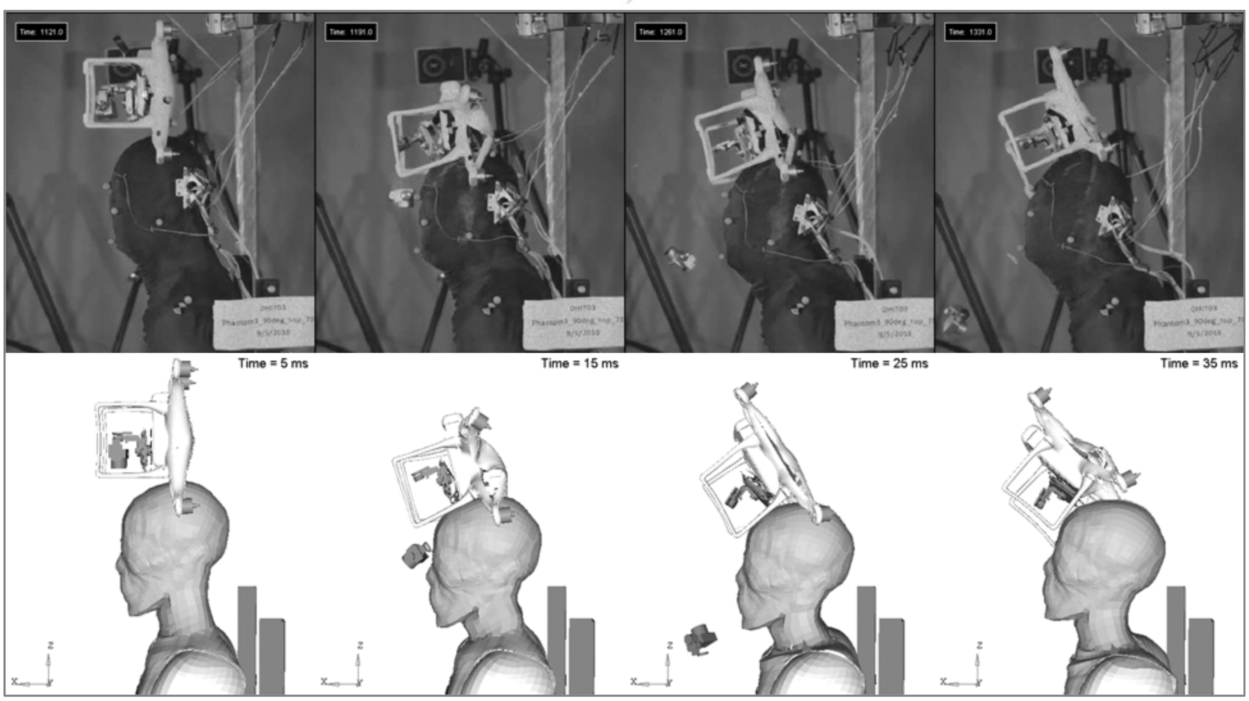

Figure 367. PMHS test 23 vs simulation comparison; DJI Phantom 3, 2.67 lb, between arms, 71 fps, vertical; subject #3; top of the head; kinematics

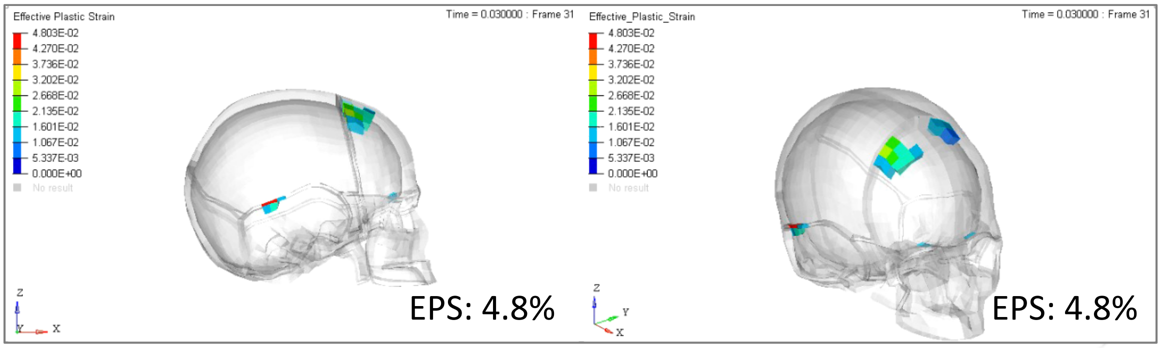

Figure 368. PMHS test 23 vs simulation comparison; DJI Phantom 3, 2.67 lb, between arms, 71 fps, vertical; subject #3; top of the head; EPS contour plot of skull

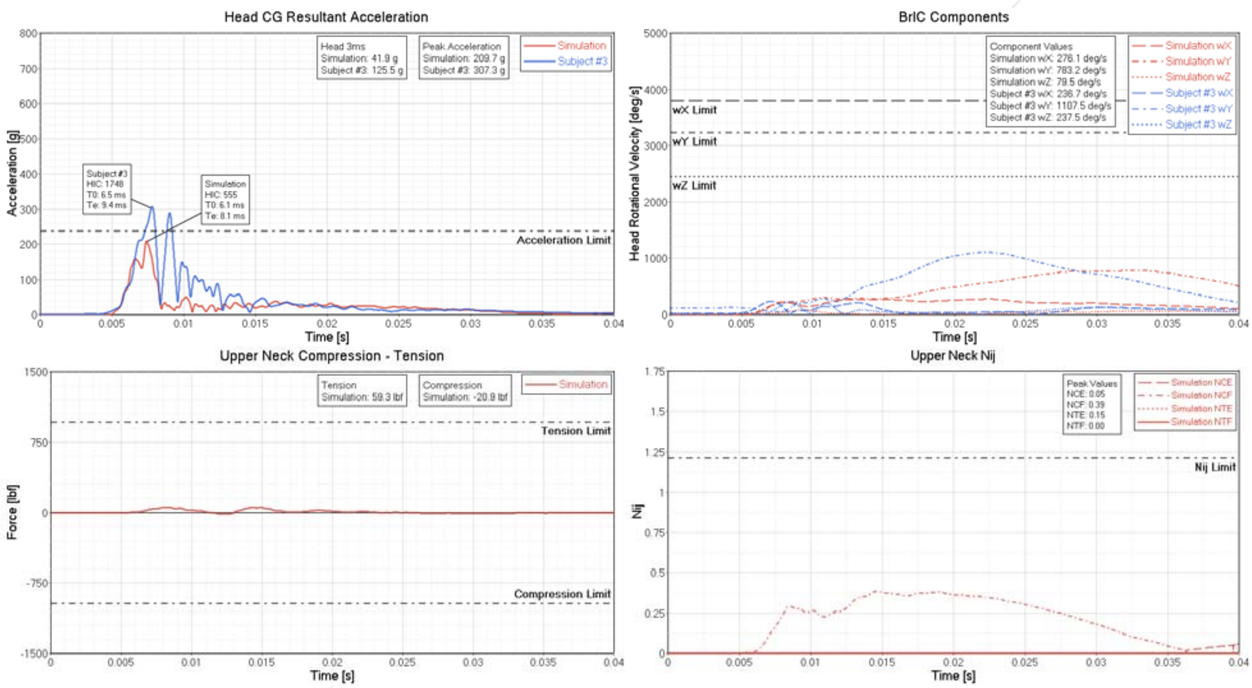

Figure 369. PMHS test 23 vs simulation comparison; DJI Phantom 3, 2.67 lb, between arms, 71 fps, vertical; subject #3; top of the head; time-history summary